Dissertation zur Erlangung des Doktorgrades
der Fakultät Chemie und Pharmazie der
Ludwig–Maximilians–Universität München

Development of Efficient Methods for the Computation of Ground State Energies, Nuclear Gradients, and Nuclear Magnetic Resonance Shieldings Based on the Adiabatic-Connection Fluctuation-Dissipation Theorem

Viktoria Drontschenko
aus
Njagan, Russland

2024

Erklärung

Diese Dissertation wurde im Sinne von §7 der Promotionsordnung vom 28. November 2011 von Herrn Prof. Dr. Christian Ochsenfeld betreut.

Eidesstattliche Versicherung

Diese Dissertation wurde eigenständig und ohne unerlauble Hilfsmittel erarbeitet.

München, 07.01.2025

Viktoria Drontschenko

Dissertation eingereicht am:	06.11.2024
Erstgutachter:	Prof. Dr. Christian Ochsenfeld
Zweitgutachter:	Prof. Dr. Benjamin P. Fingerhut
Mündliche Prüfung am:	04.12.2024

Danksagung

Zuallererst bedanke ich mich bei Prof. Dr. Christian Ochsenfeld für die Möglichkeit meine Doktorarbeit in seinem Arbeitskreis anfertigen zu können, die interessanten Projekte und die Unterstützung im Laufe der Jahre.

Des Weiteren bedanke ich mich bei Prof. Dr. Benjamin P. Fingerhut für die Anfertigung des Zweitgutachtens.

Beim gesamten Arbeitskreis Ochsenfeld bedanke ich mich herzlich für das schöne Arbeitsklima sowie den zahlreichen Freizeitaktivitäten. Insbesondere bedanke ich mich für die produktive Zusammenarbeit bei Dr. Henryk Laqua, Dr. Daniel Graf, Felix Bangerter, Prof. Dr. Andreas Görling und Steffen Fauser.

Bei meiner Familie und meinen Freunden bedanke ich mich für die Unterstützung während meiner Promotion.

Summary

One of the primary goals in quantum chemistry is to develop efficient and accurate methods for the computation of energetic parameters and molecular properties across a broad range of system sizes and complexities, enabling reliable predictions of experimental data. In this regard, the random phase approximation (RPA), a post-Kohn–Sham method derived from the adiabatic-connection fluctuation-dissipation theorem, has emerged as a highly promising method.

This thesis comprises a collection of novel methods for the computation of RPA energies as well as properties, derived from first- and second-order derivatives of the energy. The memory limitation problem, a common problem for electronic structure methods, is alleviated for the calculation of RPA energies by introducing a minimal overhead batching method based on a Lagrangian formalism, thereby extending RPA's applicability to very large systems that were out of reach before on a single compute node. This method facilitates efficient balancing between memory demands and resource utilization. Moreover, it is widely applicable and can be adapted for related electronic structure methods.

For RPA nuclear gradients—the first derivative of the RPA energy with respect to nuclear coordinates—an efficient method for incorporating the frozen-core approximation is introduced. This approach not only yields performance improvements but also ensures accurate results using atomic and auxiliary basis sets specifically designed to correlate valence electrons only, as is the case for most basis sets.

Furthermore, in previous work it has been shown, using numerical derivatives, that nuclear magnetic resonance (NMR) shieldings—the second mixed derivative of the energy with respect to the nuclear magnetic moment and the magnetic field—based on RPA yield accuracies comparable to coupled cluster singles and doubles. Motivated by this good performance, the thesis introduces, for the first time, the derivation and implementation of analytical NMR shieldings within RPA. Furthermore, to increase the efficiency of the method, a local resolution-of-the-identity (RI) metric is employed to introduce sparsity in the RI tensors, which is efficiently exploited using sparse matrix algebra techniques. Additionally, Cholesky decomposed density type matrices and an efficient batching scheme for memory intensive intermediates are utilized, thereby extending the applicability of the method to even larger systems.

Another promising method that improves upon many of the shortcomings of RPA, are σ-functionals. While they have been shown to achieve high accuracies for energetic data, nuclear gradients, and vibrational frequencies, NMR shieldings have not been comprehensively studied so far. This work closes that gap by carrying out an extensive benchmark study to investigate the accuracy of σ-functionals for NMR shieldings.

List of Publications

This is a cumulative dissertation, comprising five articles in peer-reviewed journals (I-V). In the following, all articles are stated together with the author's contribution to each of them.

I. **V. Drontschenko**, D. Graf, H. Laqua, C. Ochsenfeld
"Lagrangian-Based Minimal-Overhead Batching Scheme for the Efficient Integral-Direct Evaluation of the RPA Correlation Energy"
J. Chem. Theory Comput., **17**, 5623 (2021).
Contribution by the Author: *Development of the theory in cooperation with D. Graf and H. Laqua. All of the implementation, all of the calculations and writing.*

II. **V. Drontschenko**, D. Graf, H. Laqua, C. Ochsenfeld
"Efficient Method for the Computation of Frozen-Core Nuclear Gradients within the Random Phase Approximation"
J. Chem. Theory Comput., **18**, 7359 (2022).
Contribution by the Author: *All of the theory, most of the implementation, all of the calculations and writing.*

III. **V. Drontschenko**, F. H. Bangerter, C. Ochsenfeld
"Analytical Second-Order Properties for the Random Phase Approximation: Nuclear Magnetic Resonance Shieldings"
J. Chem. Theory Comput., **19**, 7542 (2023).
Contribution by the Author: *Shared first authorship with F. H. Bangerter. Most of the theory, parts of the implementation, most of the calculations and writing.*

IV. **V. Drontschenko**, C. Ochsenfeld
"Low-Scaling, Efficient and Memory Optimized Computation of Nuclear Magnetic Resonance Shieldings within the Random Phase Approximation Using Cholesky-Decomposed Densities and an Attenuated Coulomb Metric"
J. Phys. Chem. A, **128**, 7950 (2024).
Contribution by the Author: *All of the theory, all of the implementation, all of the calculations and writing.*

V. S. Fauser, **V. Drontschenko**, C. Ochsenfeld, A. Görling
"Accurate NMR Shieldings with σ-Functionals"
J. Chem. Theory Comput., **20**, 6028 (2024).
Contribution by the Author: *Shared first authorship with S. Fauser. All of the benchmark calculations. Contributions to the manuscript.*

Contents

Chapter 1

Introduction

The field of quantum chemistry has emerged as an important area for scientific explorations within chemistry, biochemistry, solid-state and molecular physics, as well as material science. Its central equation is the Schrödinger equation [1] providing an exact description of a non-relativistic system of interacting particles. However, the exact analytical solution to the time-independent Schrödinger equation for multi-electron systems within the Born–Oppenheimer approximation [2] requires the solution of differential equations describing interacting electrons, which cannot be solved with the methods and computational means available today. [3,4] While numerically exact solutions [3] employing the full-configuration interaction approach have been known for a long time, its huge computational effort prohibits to treat systems beyond a few atoms. Thus, for practical applications approximate solutions to the Schrödinger equation are necessary. In this context, one of the fundamental objectives in quantum chemistry is the development of accurate and efficient methods for the computation of observable quantities such as energetic or spectroscopic parameters to accurately predict experimental data.

Approximate methods for solving the Schrödinger equation can generally be categorized into wave function based approaches and density functional theory (DFT). Wave-function-based methods expand upon the Hartree-Fock (HF) approximation, [5–7] which typically lacks sufficient accuracy on its own. In this regard, Møller–Plesset perturbation theory of second order [8] (MP2) provides moderate accuracy, while coupled cluster variants, such as coupled cluster singles and doubles (CCSD) and CCSD with additional perturbative triples (CCSD(T)), are among the most accurate methods for energetic data as well as molecular properties. An advantage of wave-function-based correlation methods is that their accuracy can be systematically improved, which, however, comes with a comparably high computational cost.

On the other hand, DFT methods within the Kohn–Sham [9] (KS) framework provide reasonable accuracy at moderate computational cost, thus, making it the method of choice for computational applications in quantum chemistry. Within KS-DFT, the only unknown quantity is the exchange-correlation energy, which has to be approximated. Approximations for the exchange-correlation functional are based on mathematical functions containing a number of parameters, leading to nonempirical functionals if the parameters are chosen by considering the constraints derived for the exact KS functional, or empirical functionals by fitting the parameters to selected experimental or ab initio data. [10] As there are many different approaches

for modeling both nonempirical and empirical functionals, a very large number of functionals exist today, which may differ in performance based on the system and property being investigated. This necessitates benchmarking the performance of different exchange-correlation functionals with respect to classes of molecular systems as well as molecular properties.[11] Therefore, a functional that exhibits a high degree of transferability across various types of chemical systems and properties is highly desirable.

One class of methods that shows high potential in this regard and has regained popularity in recent years constitutes methods based on the adiabatic-connection fluctuation-dissipation theorem[12–14] (ACFDT). Within this framework, the physically exact exchange-correlation energy is expressed through the response function of the non-interacting Kohn–Sham system as well as the response function of fully-interacting (correlated) particles. However, the latter quantity contains the exchange-correlation kernel—the functional derivative of the exchange-correlation potential with respect to the density—which is not known. Thus, rather than approximating the exchange-correlation energy, the kernel must be approximated, which shifts the problem and creates a framework of equations for the exchange-correlation energy. The simplest approximation for the kernel is to neglect it entirely, resulting in the (direct) random phase approximation (RPA). RPA, as derived in the context of DFT from the ACFDT, can be classified as a fifth-rung functional on Jacob's ladder of density functional approximations.[15] It does not have any empirical parameters and is usually implemented as a post-KS method. Nonetheless, RPA can be derived from several different approaches,[16] such as coupled cluster theory,[17] many-body Green's function theory,[18] or, as originally introduced, in the framework of solid-state physics.[19–21] While all these avenues lead to the same final quantity, the different equations and intermediates provide valuable physical insights to different aspects of the underlying theory.

RPA was originally introduced within solid-state physics by D. Bohm and D. Pines in a series of papers[19–21] between 1951 and 1953. In these works, the homogeneous electron gas was investigated using the Hamiltonian of the coupled harmonic oscillator to describe the long-ranged collective motion of all electrons, termed plasma oscillations, along with a short-range correction term arising from random thermal motions of the electrons.[20] The plasma oscillations could be accurately described by neglecting the coupling of oscillations in different plasmon phases.[20] As the coupling term depends on the coordinates of the particles, which are randomly distributed throughout the system, their contributions can be assumed to average out to zero in the high-density limit.[22] In this case, the method—termed the 'random phase approximation'—provides an accurate description.

Years later, D. C. Langreth and J. P. Perdew derived RPA in the framework of the ACFDT, which has become the most well-established formulation in today's research. However, the corresponding formulation in a molecular-orbital (MO) basis showed an $\mathcal{O}(M^6)$ scaling of the computational cost with the system size M,[23] limiting its applicability to only small systems and basis sets. By introducing the resolution-of-the-identity (RI) approximation and a numerical quadrature for the imaginary frequency integration, Furche and co-workers[24] were able to reduce the scaling to $\mathcal{O}(M^4)$, thus making RPA one of the formally lowest scaling correlation methods. An effective linear scaling RPA energy implementation was obtained by recasting the RPA correlation energy expression in the atomic-orbital basis and

utilizing a local RI metric to exploit the introduced sparsity using sparse matrix algebra techniques.[25] Further efficiency improvements, that is, pivoted Cholesky decomposition[26] of density matrices[27] and optimized minimax grids[27,28] for the numerical frequency integration, extended the applicability of RPA to even larger systems. However, for very large system sizes and/or basis sets the memory requirements of the method exceed the available system memory and, thus, become the limiting factor. Here, the three-center integral tensors have to be stored in memory during the calculation of the response function together with other memory demanding intermediates arising during the calculation. To overcome these memory limitation problems, **Publication I** presents a minimal overhead batching scheme for the computation of the response function by batching over the atomic-orbital and auxiliary-function index as well as the numerical quadrature points. A Lagrangian formalism is employed to minimize floating point operations within the given system memory. This provides the best trade-off between memory demand and program runtime, thus alleviating the memory limitation problem. Since electron correlation methods generally suffer from memory limitation issues, the method introduced in **Publication I** can also be applied outside of RPA, specifically to related methods such as MP2 or coupled cluster variants.[29]

Electron correlation methods are usually implemented within the frozen-core approximation, where the correlation of core electrons—which occupy, by definition, the lowest lying MOs—is neglected, and only the correlation of valence electrons is considered. This aligns with the intuitive view in chemistry where core electrons are generally seen as inert in chemical reactions, which are primarily governed by the behavior of valence electrons. For relative RPA energies the error has been reported to be minimal,[30] while the computational gain is considerable. The frozen-core approximation has further advantages considering the choice of atomic and auxiliary basis sets, since many basis sets are designed to correlate the valence electrons only and do not describe the core region sufficiently. Implementing the frozen-core approximation for energies is straightforward, involving only the consideration of valence orbitals within the coefficient matrix, such as for constructing the density matrix. For properties, however, the implementation is very involved.[31,32]

While the description of energetic data is crucial in quantum chemistry, practical applications also require accurate and efficient methods to predict molecular properties. Many important properties can be obtained from the derivative of the total energy of the system. For example, molecular forces, which are crucial for describing dynamics, are determined by the negative derivative of the energy with respect to the nuclear coordinates. Much progress has been made in this regard for RPA, where efficient implementations have been introduced.[33–40] However, RPA gradients within the frozen-core approximation had not been considered prior to **Publication II**. Here, the frozen-core approximation was introduced within the low-scaling gradient implementation of Ref. [36] based on a formulation in the atomic-orbital basis with an attenuated Coulomb RI metric and Cholesky decomposed densities. The difficulty lies in evaluating derivatives of the occupied and frozen-core density matrices, where the latter is only present when applying the frozen-core approximation. An efficient method for the evaluation of both density matrix responses is introduced in **Publication II**, leading to performance gains of 20-30%, depending on the basis set, and an accurate description when utilizing basis sets that were optimized within the frozen-core approximation. Given that the description of core electrons does not sig-

nificantly affect the accuracy of nuclear gradients, the utilization of the frozen-core approximation is justified and employing basis sets that were optimized within the frozen-core approximation—thus not containing additional core functions—results in further performance gains due to the smaller size of the basis sets.

Another property of high importance is the nuclear magnetic resonance (NMR) shielding tensor. NMR spectroscopy has emerged as an important tool in the structure determination in the fields of chemistry and biochemistry. Since interpreting experimental spectra to determine molecular or solid-state structures can be challenging, computational methods can be very helpful for predicting spectra and assisting in the interpretation of experimental data. Methods for the computation of the NMR shielding tensor—the second mixed derivative of the energy with respect to the nuclear magnetic moment and the magnetic field—range from HF [41–45] and DFT [46–48] to wave-function-based methods, such as MP2, [49,50] coupled cluster variants, [51–53] and multiconfigurational self-consistent field [54] (MCSCF) methods. Here, HF and DFT offer moderate accuracy with generally low computational cost, while CC methods such as CCSD and CCSD(T) are among the most accurate methods for predicting NMR data but are also the most computationally expensive. MP2 has demonstrated higher accuracy than HF and DFT, however, it is more computationally demanding than both methods.

In a benchmark study employing numerical second derivatives, [55] RPA based on a HF reference has been shown to achieve high accuracy comparable to CCSD, but with significantly lower computational cost. Moreover, it has been found to outperform MP2 and achieve higher computational efficiency. Due to this good performance of RPA NMR, analytical NMR shieldings were derived and implemented in **Publication III**. This is the first account of analytical second derivatives for the computation of NMR shieldings for RPA defined as a post-KS method derived from the ACFDT. The formulation of **Publication III** employs an atomic-orbital formalism and the Coulomb RI metric. This implementation serves as an optimal foundation for further improvements in efficiency. In fact, **Publication IV** makes use of a local RI metric and Cholesky decomposed density type matrices together with sparse matrix algebra techniques to increase the computational efficiency and lower the scaling of RPA NMR calculations, and, furthermore a batching scheme for the memory efficient computation of intermediates to extend the applicability of RPA NMR calculations to even larger systems and basis sets.

RPA not only performs well for NMR data, [55] it also yields accurate interaction energies, [56] barrier heights, [56] isogyric and isodesmic reaction energies, [16,56,57] and it is able to capture static correlation to some degree. [56,58,59] Further, RPA seamlessly incorporates the description of dispersion interactions, which are based on the long-range interactions between spontaneous dipole moment fluctuations and is also able to treat small gap systems. Thus, RPA is applicable to a wide range of systems, such as metallic systems, surfaces, crystals, as well as molecular systems. However, RPA is not free of limitations, which can be traced back to the non-self consistent nature of RPA and/or the lacking description of the exchange-correlation kernel. The latter point leads to self-interaction in RPA, causing it to fail for cases such as H_2^+ and He_2^+. [56] For short interaction distances RPA leads to overcorrelation of electrons, which explains its poor performance for atomization energies and spin-flip processes, i.e., processes that separate electron pairs, resulting in substantial changes in the short-range correlation energy. [16] While there are many beyond-RPA methods, e.g.,

Refs. [56, 60–80], aiming to correct the shortcomings, the introduced accuracy comes with an increased computational cost.

A method that significantly improves upon the mentioned limitations of RPA while maintaining the same computational cost are the σ-functionals, which were recently introduced by A. Görling and co-workers.[81,82] A σ-functional implementation builds upon an RPA implementation but contains an additional term that depends on the eigenvalues of the frequency dependent KS-response function. This term is modeled by cubic splines containing parameters that are fitted to energetic data. Here, the different possibilities in the fitting approach lead to different parametrizations for σ-functionals.[80–84] It was found that σ-functionals perform very well for energetic data,[81,82] nuclear gradients, and vibrational frequencies.[85] First results on the accuracy for NMR shieldings have been promising.[55] Thus, in **Publication V**, an extensive benchmark study using numerical second derivatives was carried out to study the accuracy of σ-functionals using different parametrizations as well as various reference functionals. It was found that σ-functionals based on the S1 parametrization[83] yield isotropic NMR shielding constants comparable in accuracy to CCSD(T) and outperforming all tested density functionals. Thus, the results of **Publication V** indicate that analytical NMR shieldings based on σ-functionals would be highly desirable, as it revealed itself to be a cost-efficient and highly accurate NMR method. As with σ-functional energies, the NMR implementation could be implemented with reasonable programming effort based on an existing RPA NMR implementation.

This thesis is structured as follows: in Chapter 2, the theoretical framework of the work is established. Chapter 3 is the main part of this cumulative dissertation where **Publications I-V** are reproduced in their entirety. Finally, in Chapter 4, a conclusion is presented.

Chapter 2

Theoretical Background

2.1 The Schrödinger Equation

The non-relativistic time-independent electronic Schrödinger equation[1] within the Born-Oppenheimer[2] approximation is given by

$$\hat{H}\Psi = E\Psi \tag{2.1}$$

with the electronic energy E and the wave function Ψ. The Hamiltonian is defined as

$$\hat{H} = \hat{T} + \hat{V}_{\text{en}} + \hat{V}_{\text{ee}} \tag{2.2}$$

with the kinetic energy operator $\hat{T}$, the operator for the Coulombic attraction between electrons and nuclei $\hat{V}_{\text{en}}$, and the electron-electron interaction operator $\hat{V}_{\text{ee}}$, all defined in atomic units according to

$$\hat{T} = -\sum_{i}^{N_{\text{el}}} \frac{1}{2}\nabla_i^2 \tag{2.3}$$

$$\hat{V}_{\text{en}} = -\sum_{i}^{N_{\text{el}}} \sum_{A}^{N_{\text{at}}} \frac{Z_A}{r_{iA}} \tag{2.4}$$

$$\hat{V}_{\text{ee}} = \sum_{i<j}^{N_{\text{el}}} \frac{1}{r_{ij}} \tag{2.5}$$

where N_{el} denotes the number of electrons of the system and N_{at} the number of atoms. Further, r_{iA} specifies the distance between electron i and nucleus A, r_{ij} the distance between electrons i and j, and Z_A is the charge of nucleus A. The exact wave function of the system can be expanded in a complete set of N_{el}-electron wave functions $\{\Phi_\alpha\}$ according to

$$\Psi(\mathbf{x}_1, \mathbf{x}_2, ..., \mathbf{x}_{N_{\text{el}}}) = \sum_{\alpha}^{\infty} a_\alpha \Phi_\alpha(\mathbf{x}_1, \mathbf{x}_2, ..., \mathbf{x}_{N_{\text{el}}}) \tag{2.6}$$

where Ψ and $\{\Phi_\alpha\}$ depend on the electronic coordinates $\mathbf{x}_i = (\mathbf{r}_i, \sigma_i)$ ($i \in [1, N_{\text{el}}]$) containing both space coordinates $\mathbf{r}_i$ and spin coordinates σ_i. For an accurate description of the fermionic system, the many-electron wave function Φ has to comply

with the antisymmetry principle,[86,87] which is a generalization of the Pauli exclusion principle.[88,89] It states that the wave function has to be antisymmetric with respect to the interchange of two electronic coordinates. This is captured by the Slater determinant of one-electron molecular orbitals (spin orbitals) $\{\phi_i\}$ defined as

$$\Phi = \frac{1}{\sqrt{N_{\mathrm{el}}!}} \begin{vmatrix} \phi_1(\mathbf{x}_1) & \phi_2(\mathbf{x}_1) & \cdots & \phi_{N_{\mathrm{el}}}(\mathbf{x}_1) \\ \phi_1(\mathbf{x}_2) & \phi_2(\mathbf{x}_2) & \cdots & \phi_{N_{\mathrm{el}}}(\mathbf{x}_2) \\ \vdots & \vdots & \ddots & \vdots \\ \phi_1(\mathbf{x}_{N_{\mathrm{el}}}) & \phi_2(\mathbf{x}_{N_{\mathrm{el}}}) & \cdots & \phi_{N_{\mathrm{el}}}(\mathbf{x}_{N_{\mathrm{el}}}) \end{vmatrix} \tag{2.7}$$

Thus, the exact wave function can be obtained by a linear combination of Slater determinants $\{\Phi_\alpha\}$, where each Φ_α defines a specific configuration of spin-orbitals, therefore, the method is termed full configuration interaction (FCI), or, simply CI for an incomplete expansion in Eq. (2.6). While the FCI method is highly accurate, its application is limited to systems with a small number of electrons due to its huge computational cost.

2.2 The Hartree–Fock Approximation

The simplest antisymmetrized wave function suitable to describe the ground state of a many-electron system is a single Slater determinant (Eq. (2.7)). This approximation to the wave function constitutes the basis of the Hartree–Fock approximation,[5–7] providing typically moderate accuracy and serving as the starting point for more accurate wave function methods.

The Hartree–Fock energy E_{HF} can be expressed as the expectation value of the Hamiltonian according to[90]

$$E_{\mathrm{HF}}[\Phi] = \langle \Phi | \hat{H} | \Phi \rangle = \sum_i^{N_{\mathrm{el}}} h_i + \frac{1}{2} \sum_{ij}^{N_{\mathrm{el}}} (J_{ij} - K_{ij}); \quad \langle \Phi | \Phi \rangle = 1 \tag{2.8}$$

where the wave function Φ is chosen to be orthonormal and the bra-ket notation is employed. Further, h_i denotes the MO representation of the one-electron Hamiltonian $\hat{h}$, and J_{ij} as well as K_{ij} the MO representations of the Coulomb operator $\hat{J}$ and exchange operator $\hat{K}$, respectively. The introduced quantities are defined as

$$h_i := \int \mathrm{d}\mathbf{x}_1 \; \phi_i(\mathbf{x}_1) \left[-\frac{1}{2}\nabla_1^2 - \sum_A^{N_{\mathrm{at}}} \frac{Z_A}{r_{1A}} \right] \phi_i(\mathbf{x}_1) =: (\phi_i | \hat{h} | \phi_i) \tag{2.9}$$

$$J_{ij} := \iint \mathrm{d}\mathbf{x}_1 \mathrm{d}\mathbf{x}_2 \; \phi_i^*(\mathbf{x}_1) \phi_i(\mathbf{x}_1) \frac{1}{r_{12}} \phi_j^*(\mathbf{x}_2) \phi_j(\mathbf{x}_2) =: (\phi_i \phi_i | \phi_j \phi_j) \tag{2.10}$$

$$K_{ij} := \iint \mathrm{d}\mathbf{x}_1 \mathrm{d}\mathbf{x}_2 \; \phi_i^*(\mathbf{x}_1) \phi_j(\mathbf{x}_1) \frac{1}{r_{12}} \phi_j^*(\mathbf{x}_2) \phi_i(\mathbf{x}_2) =: (\phi_i \phi_j | \phi_j \phi_i) \tag{2.11}$$

where the Mulliken notation was employed. According to the variational principle, the energy obtained from an approximate wave function constitutes an upper bound to the exact energy of the system. Thus, it follows for the Hartree–Fock energy that $E_{\mathrm{HF}}[\Phi[\{\phi_i\}]] \geq E$ and the optimal molecular orbitals can be obtained by Lagrangian minimization of Eq. (2.8) with respect to the set of molecular orbitals $\{\phi_i\}$ subject

to the orthonormality constraint $\langle\phi_i|\phi_j\rangle = \delta_{ij}$. This leads to the canonical Hartree–Fock equations[90]

$$\hat{F}\phi_i(\mathbf{x}_1) = \epsilon_i\phi_i(\mathbf{x}_1) \tag{2.12}$$

where ϵ_i denotes the HF orbital energy for the molecular orbital ϕ_i and the Fock operator $\hat{F}$ is given by

$$\hat{F} = \hat{h} + \sum_{j}^{N_{\mathrm{el}}}(\hat{J}_j - \hat{K}_j) \tag{2.13}$$

$$\hat{J}_j := \int \mathrm{d}\mathbf{x}_2\ \phi_j^*(\mathbf{x}_2)\frac{1}{r_{12}}\phi_j(\mathbf{x}_2) \tag{2.14}$$

$$\hat{K}_j := \int \mathrm{d}\mathbf{x}_2\ \phi_j^*(\mathbf{x}_2)\frac{\hat{P}_{12}}{r_{12}}\phi_j(\mathbf{x}_2) \tag{2.15}$$

with the permutation operator $\hat{P}_{12}$, which interchanges the coordinates of electron one and two.

For practical implementations, the molecular orbital basis functions can be expanded in an atomic orbital basis set—a procedure termed linear combination of atomic orbitals (LCAO)—thereby transforming the HF equations into the Roothaan–Hall[91,92] matrix eigenvalue equations, which can be solved by diagonalization within a self-consistent-field (SCF) procedure. As a result, the optimal HF orbitals comprising the single determinant wave function are obtained together with the corresponding HF energy. However, while electrons with parallel spin are correlated through the exchange operator, the interaction of electrons with opposite spin is only accounted for in an average way. Thus, the HF approximation is referred to as an uncorrelated wave function method. In the next section, an approach is introduced with the aim of capturing electron correlation effects—density functional theory—which utilizes the electron density, rather than wave function, to describe the state of the electronic system.

2.3 Density Functional Theory

Density functional theory (DFT) is based on a formulation of the energy in terms of the one-electron density

$$\rho(\mathbf{r}_1) = N_{\mathrm{el}}\int ... \int \mathrm{d}\sigma_1\ \mathrm{d}\mathbf{x}_2\ ...\ \mathrm{d}\mathbf{x}_{N_{\mathrm{el}}}\ |\Psi(\mathbf{x}_1, \mathbf{x}_2, ..., \mathbf{x}_{N_{\mathrm{el}}})|^2 \tag{2.16}$$

which is normalized to the number of electrons $\int \mathrm{d}\mathbf{r}\ \rho(\mathbf{r}) = N_{\mathrm{el}}$. This is validated by the first Hohenberg–Kohn theorem.[93] It states that the external potential $v_{\mathrm{ext}}(\mathbf{r})$, which is usually the potential generated by the nuclei, is uniquely determined, within an additive constant, by the electron density. Thus, the electron density determines the ground-state wave function as well as all other properties of the electronic system.[94] Specifically, the ground-state energy can be expressed as a functional of the density according to

$$E[\rho] = T[\rho] + V_{\mathrm{ee}}[\rho] + \int \mathrm{d}\mathbf{r}\ v_{\mathrm{ext}}(\mathbf{r})\rho(\mathbf{r}) \tag{2.17}$$

with the kinetic energy functional $T[\rho] = \langle\Psi[\rho]|\,\hat{T}\,|\Psi[\rho]\rangle$ and the electron-electron interaction energy functional $V_{\mathrm{ee}}[\rho] = \langle\Psi[\rho]|\,\hat{V}_{\mathrm{ee}}\,|\Psi[\rho]\rangle$. The optimal density can be obtained by variational minimization of the energy functional with respect to the density, which is validated by the second Hohenberg–Kohn theorem.[93]

The expression of the energy in terms of the three-dimensional density, rather than $4N_{\mathrm{el}}$-dimensional wave function, is a substantial simplification and it is still in the realm of the exact theory. However, the explicit form of $(T[\rho] + V_{\mathrm{ee}}[\rho])$ is not known and accurate approximations are necessary, which have shown to be challenging especially for the approximation of the kinetic energy term. In light thereof, W. Kohn and L. J. Sham[9] proposed the reintroduction of single-particle spin-orbitals $\{\phi_i\}$, the KS orbitals, which describe a reference system of non-interacting electrons in a potential, the KS potential v_{KS}, that insures that the electron density defined by the KS-orbitals

$$\rho(\mathbf{r}) = \sum_{i}^{N_{\mathrm{el}}} |\phi_i(\mathbf{r})|^2 \tag{2.18}$$

reproduces the exact ground-state density, that is the density of a system with interacting electrons. The Hamiltonian describing the non-interacting system is given by[95]

$$\hat{H}_{\mathrm{KS}} = \hat{T} + \hat{V}_{\mathrm{KS}} \tag{2.19}$$

$$\hat{V}_{\mathrm{KS}} = \sum_{i}^{N_{\mathrm{el}}} v_{\mathrm{KS}}(\mathbf{r}_i) \tag{2.20}$$

This KS system can then be described by a single determinant wave function $\Phi[\rho]$, the KS wave function, that is fully determined by the electron density. This allows to express the ground-state energy according to[94]

$$E[\rho] = \langle\Phi[\rho]|\,\hat{H}_{\mathrm{KS}}\,|\Phi[\rho]\rangle = T_{\mathrm{s}}[\rho] + V_{\mathrm{KS}}[\rho] \tag{2.21}$$

where the following quantities are introduced:

$$T_{\mathrm{s}}[\rho] = \langle\Phi[\rho]|\,\hat{T}\,|\Phi[\rho]\rangle = -\frac{1}{2}\sum_{i}^{N_{\mathrm{el}}} \langle\phi_i|\,\nabla_1^2\,|\phi_i\rangle \tag{2.22}$$

$$V_{\mathrm{KS}}[\rho] = \langle\Phi[\rho]|\,\hat{V}_{\mathrm{KS}}\,|\Phi[\rho]\rangle = V_{\mathrm{ext}}[\rho] + E_{\mathrm{H}}[\rho] + E_{\mathrm{xc}}[\rho] \tag{2.23}$$

$$E_{\mathrm{H}}[\rho] = \frac{1}{2}\iint \mathrm{d}\mathbf{r}_1\mathrm{d}\mathbf{r}_2 \frac{\rho(\mathbf{r}_1)\rho(\mathbf{r}_2)}{r_{12}} \tag{2.24}$$

$$E_{\mathrm{xc}}[\rho] = \big(T[\rho] - T_{\mathrm{s}}[\rho]\big) + \big(V_{\mathrm{ee}}[\rho] - E_{\mathrm{H}}[\rho]\big) \tag{2.25}$$

thereby building the foundation of KS-DFT. This formulation is still in the realm of the exact theory: the non-interacting kinetic energy is expressed by $T_{\mathrm{s}}[\rho]$, which is defined in terms of non-interacting orbitals, while its correction $(T[\rho] - T_{\mathrm{s}}[\rho])$ to the physically exact kinetic energy $T[\rho]$ is contained in the exchange-correlation energy $E_{\mathrm{xc}}[\rho]$. The Hartree energy contribution $E_{\mathrm{H}}[\rho]$ describes the classical electrostatic Coulomb repulsion of the density ρ, and the remaining electron-electron interaction energy is contained in $E_{\mathrm{xc}}[\rho]$. Variational minimization of the energy functional given by Eq. (2.21) leads to the KS equations[94]

$$\hat{h}_{\mathrm{KS}}\phi_i = \epsilon_i\phi_i \tag{2.26}$$

where ϵ_i defines the KS orbital energy of the molecular orbital ϕ_i and the KS Hamiltonian $\hat{h}_{\mathrm{KS}}$ is defined according to

$$\hat{h}_{\mathrm{KS}} = -\frac{1}{2}\nabla^2 + v_{\mathrm{KS}}(\mathbf{r}) \tag{2.27}$$

$$v_{\mathrm{KS}}(\mathbf{r}) = v_{\mathrm{ext}}(\mathbf{r}) + v_{\mathrm{H}}(\mathbf{r}) + v_{\mathrm{xc}}(\mathbf{r}) \tag{2.28}$$

$$v_{\mathrm{H}}(\mathbf{r}) = \frac{\partial E_{\mathrm{H}}[\rho]}{\partial \rho(\mathbf{r})} = \int \mathrm{d}\mathbf{r}_2 \frac{\rho(\mathbf{r}_2)}{r_{12}} \tag{2.29}$$

$$v_{\mathrm{xc}}(\mathbf{r}) = \frac{\partial E_{\mathrm{xc}}[\rho]}{\partial \rho(\mathbf{r})} \tag{2.30}$$

Within KS-DFT all terms except for the exchange-correlation energy and potential are known. Hence, the central challenge constitutes the determination of accurate and efficient approximations for E_{xc} and v_{xc}. One possible way to address this challenge is described in the next section.

2.4 Adiabatic-Connection Fluctuation-Dissipation Approach

An exact expression for the exchange-correlation energy of ground-state density functional theory can be derived employing the adiabatic-connection fluctuation-dissipation theorem,[12–14] as will be demonstrated in this section. This opens the way for another class of electron correlation methods—that is, methods based on the ACFDT theorem—which will be described following this section.

From this point onward, all equations will be derived for the general case of complex-valued orbitals. This is crucial to this work as computing second-order derivatives for NMR parameters, a central aspect of this work, requires the use of complex-valued orbitals. This derivation is novel, as existing literature commonly assumes real-valued orbitals.

2.4.1 Adiabatic-Connection

The adiabatic-connection method, introduced by D. C. Langreth and J. P. Perdew,[12,13] is based on the following premise: a continuous connection is created between a system with non-interacting electrons and the physical system with fully interacting electrons, while the density is kept constant at the exact (physical) ground-state density. This is accomplished by introducing a modified Hamiltonian $\hat{H}^\lambda$ dependent on a coupling parameter λ according to[13]

$$\hat{H}^\lambda = \hat{T} + \hat{V}^\lambda + \lambda \hat{V}_{\mathrm{ee}}; \quad \lambda \in [0,1] \tag{2.31}$$

$$\hat{H}^\lambda = \begin{cases} \hat{H} & = \hat{T} + \hat{V}_{\mathrm{ext}} + \hat{V}_{\mathrm{ee}} \quad | \ \lambda = 1 \\ \hat{H}_{\mathrm{KS}} & = \hat{T} + \hat{V}_{\mathrm{KS}} \quad | \ \lambda = 0 \end{cases} \tag{2.32}$$

where $\hat{V}^\lambda$ is an external potential operator keeping the density constant at the physical value, thereby reducing to the external potential for $\lambda = 1$, while for $\lambda = 0$ it takes the value of the KS potential. Thus, for $\lambda = 1$ the physical Hamiltonian is recovered, where the electron-electron interaction is described by $\hat{V}_{\mathrm{ee}}$, while $\lambda = 0$

corresponds to the KS Hamiltonian, where the electron-electron interaction is contained within the KS potential operator $\hat{V}_{\mathrm{KS}}$.

By increasing the coupling parameter λ adiabatically slowly, the electron-electron interaction is gradually increased connecting the non-interacting system to the physical system, while the density is kept constant along the adiabatic path.

To derive an expression for the correlation energy, first, the energy difference of the physical to the KS system is evaluated by integration along the adiabatic path according to[13]

$$0 = E^{\lambda=1} - E^{\lambda=0} = \int_0^1 \mathrm{d}\lambda \; \frac{\partial E^\lambda}{\partial \lambda} \tag{2.33}$$

where $E^\lambda = \langle \Psi^\lambda | \, \hat{H}^\lambda \, | \Psi^\lambda \rangle$; inserting this expression into the above equation and utilizing the Hellman-Feynman theorem,[96] that is valid for a full set of eigenfunctions, yields[95]

$$0 = E^{\lambda=1} - E^{\lambda=0} = \int_0^1 \mathrm{d}\lambda \; \langle \Psi^\lambda | \, \frac{\partial \hat{H}^\lambda}{\partial \lambda} \, | \Psi^\lambda \rangle \tag{2.34}$$

$$= \int_0^1 \mathrm{d}\lambda \; \langle \Psi^\lambda | \, \hat{V}_{\mathrm{ee}} + \frac{\partial \hat{V}^\lambda}{\partial \lambda} \, | \Psi^\lambda \rangle \tag{2.35}$$

Since $\hat{V}^\lambda$ describes a local multiplicative potential and the density is kept constant along the path, the above equation simplifies to

$$0 = E^{\lambda=1} - E^{\lambda=0} = \int_0^1 \mathrm{d}\lambda \; \langle \Psi^\lambda | \, \hat{V}_{\mathrm{ee}} \, | \Psi^\lambda \rangle + \int_0^1 \mathrm{d}V^\lambda \tag{2.36}$$

$$= \int_0^1 \mathrm{d}\lambda \; \langle \Psi^\lambda | \, \hat{V}_{\mathrm{ee}} \, | \Psi^\lambda \rangle + V_{\mathrm{ext}} - V_{\mathrm{KS}} \tag{2.37}$$

By inserting Eq. (2.23) for V_{KS}, an expression for the exchange-correlation energy can be obtained according to

$$E_{\mathrm{xc}} = \int_0^1 \mathrm{d}\lambda \; \langle \Psi^\lambda | \, \hat{V}_{\mathrm{ee}} \, | \Psi^\lambda \rangle - E_{\mathrm{H}} \tag{2.38}$$

Next, the exchange energy $E_{\mathrm{x}} = \langle \Phi | \, \hat{K} \, | \Phi \rangle$ can be subtracted from the above equation leading to

$$E_{\mathrm{c}} = \int_0^1 \mathrm{d}\lambda \; \langle \Psi^\lambda | \, \hat{V}_{\mathrm{ee}} \, | \Psi^\lambda \rangle - E_{\mathrm{H}} - E_{\mathrm{x}} \tag{2.39}$$

The term $(E_{\mathrm{H}} + E_{\mathrm{x}})$ is known in terms of one-electron orbitals from HF theory and can be further expressed using the KS wave function Φ according to

$$E_{\mathrm{H}} + E_{\mathrm{x}} = \langle \Phi | \, \hat{V}_{\mathrm{ee}} \, | \Phi \rangle \tag{2.40}$$

Inserting the above expression into Eq. (2.39) yields[56]

$$E_{\mathrm{c}} = \int_0^1 \mathrm{d}\lambda \; \langle \Psi^\lambda | \, \hat{V}_{\mathrm{ee}} \, | \Psi^\lambda \rangle - \langle \Phi | \, \hat{V}_{\mathrm{ee}} \, | \Phi \rangle \tag{2.41}$$

The above equation provides an exact expression for the correlation energy, however, while the second term on the right-hand side, i.e. $\langle \Phi | \, \hat{V}_{\mathrm{ee}} \, | \Phi \rangle$, is known exactly, the first term is not known and remains to be evaluated. This is the subject of the next section.

2.4.2 Density Fluctuations

To derive an expression for the term $\langle\Psi^\lambda|\,\hat{V}_{\mathrm{ee}}\,|\Psi^\lambda\rangle$ in Eq (2.41), first, the electron-electron interaction operator is expressed in terms of the density operator

$$\hat{\rho}(\mathbf{x}) = \sum_i^{N_{\mathrm{el}}} \delta(\mathbf{x}-\mathbf{x}_i); \quad \langle\Psi|\,\hat{\rho}(\mathbf{x})\,|\Psi\rangle = \rho(\mathbf{x}) \tag{2.42}$$

resulting in[95]

$$\hat{V}_{\mathrm{ee}} = \frac{1}{2}\iint \mathrm{d}\mathbf{x}_1\mathrm{d}\mathbf{x}_2 \frac{\hat{\rho}(\mathbf{x}_1)\hat{\rho}(\mathbf{x}_2) - \hat{\rho}(\mathbf{x}_1)\delta(\mathbf{x}_1-\mathbf{x}_2)}{r_{12}} \tag{2.43}$$

Next, by introducing the density fluctuation operator $\Delta\hat{\rho}(\mathbf{x})$ defined as

$$\Delta\hat{\rho}(\mathbf{x}) := \hat{\rho}(\mathbf{x}) - \rho(\mathbf{x}) \tag{2.44}$$

$\hat{V}_{\mathrm{ee}}$ can be formulated as

$$\begin{aligned}\hat{V}_{\mathrm{ee}} = \frac{1}{2}\iint \mathrm{d}\mathbf{x}_1\mathrm{d}\mathbf{x}_2\ \frac{1}{r_{12}}\Big[&\Delta\hat{\rho}(\mathbf{x}_1)\Delta\hat{\rho}(\mathbf{x}_2) + \hat{\rho}(\mathbf{x}_1)\rho(\mathbf{x}_2) + \rho(\mathbf{x}_1)\hat{\rho}(\mathbf{x}_2) \\ &- \rho(\mathbf{x}_1)\rho(\mathbf{x}_2) - \delta(\mathbf{x}_1-\mathbf{x}_2)\hat{\rho}(\mathbf{x}_1)\Big]\end{aligned} \tag{2.45}$$

Inserting this expression into Eq. (2.41) results in an expression for the correlation energy in terms of density fluctuations according to[56]

$$E_{\mathrm{c}} = \frac{1}{2}\int_0^1 \mathrm{d}\lambda\ \iint \mathrm{d}\mathbf{x}_1\mathrm{d}\mathbf{x}_2\ \frac{\langle\Psi^\lambda|\,\Delta\hat{\rho}(\mathbf{x}_1)\Delta\hat{\rho}(\mathbf{x}_2)\,|\Psi^\lambda\rangle - \langle\Phi|\,\Delta\hat{\rho}(\mathbf{x}_1)\Delta\hat{\rho}(\mathbf{x}_2)\,|\Phi\rangle}{r_{12}} \tag{2.46}$$

According to this equation, density fluctuations at a position $\mathbf{r}_1$ are correlated with fluctuations at $\mathbf{r}_2$ and these density fluctuations are associated with the correlation energy.[97]

2.4.3 Adiabatic-Connection Fluctuation-Dissipation Theorem

In this section, the correlation energy expression within the adiabatic-connection approach given by Eq. (2.46) is further reformulated utilizing response theory to introduce the fluctuation-dissipation theorem leading to the adiabatic-connection fluctuation-dissipation formalism.

Electron Correlation Energy in Terms of Transition Densities

The correlation energy expression in Eq. (2.46) can be further rewritten using the completeness relation of the electronic states $\{\Psi_n^\lambda\}$

$$\sum_n |\Psi_n^\lambda\rangle\langle\Psi_n^\lambda| = \mathbf{1}; \quad \forall\ \lambda \in [0,1] \tag{2.47}$$

where $n = 0$ denotes the ground-state wave function. In the following, the subscript '0' will be added to highlight ground-state quantities for clarity, i.e. $\Psi_0^\lambda = \Psi^\lambda, \Phi_0 = \Phi$, and $E_0 = E$. Inserting Eq. (2.47) into Eq. (2.46) yields[56]

$$E_\mathrm{c} = \frac{1}{2}\int_0^1 \mathrm{d}\lambda \iint \mathrm{d}\mathbf{x}_1\mathrm{d}\mathbf{x}_2 \, \frac{\sum_{n\neq 0}\rho_{0n}^\lambda(\mathbf{x}_1)\rho_{n0}^\lambda(\mathbf{x}_2) - \sum_{n\neq 0}\rho_{0n}^{\lambda=0}(\mathbf{x}_1)\rho_{n0}^{\lambda=0}(\mathbf{x}_2)}{r_{12}} \tag{2.48}$$

where the transition densities $\rho_{0n}^\lambda(\mathbf{x})$ and $\rho_{n0}^\lambda(\mathbf{x})$ are defined according to[56]

$$\begin{aligned}
\rho_{0n}^\lambda(\mathbf{x}) &= \langle\Psi_0^\lambda|\,\Delta\hat{\rho}(\mathbf{x})\,|\Psi_n^\lambda\rangle && (2.49)\\
&= \langle\Psi_0^\lambda|\,\hat{\rho}(\mathbf{x})\,|\Psi_n^\lambda\rangle\,; \quad \forall\ n \neq 0 && (2.50)\\
\rho_{n0}^\lambda(\mathbf{x}) &= \langle\Psi_n^\lambda|\,\Delta\hat{\rho}(\mathbf{x})\,|\Psi_0^\lambda\rangle && (2.51)\\
&= \langle\Psi_n^\lambda|\,\hat{\rho}(\mathbf{x})\,|\Psi_0^\lambda\rangle\,; \quad \forall\ n \neq 0 && (2.52)
\end{aligned}$$

For complex-valued wave functions it follows that $\rho_{0n}^\lambda(\mathbf{x}) = \big(\rho_{n0}^\lambda(\mathbf{x})\big)^*$, which simplifies for real-valued wave functions to $\rho_{0n}^\lambda(\mathbf{x}) = \rho_{n0}^\lambda(\mathbf{x})$. Further, in the summations of Eq. (2.48) the case $n = 0$ is excluded since $\rho_{00}^\lambda(\mathbf{x}) = 0$ due to the consistency of the ground-state density along the adiabatic path.

Linear Density-Density Response Function

In previous sections, it was established that electron correlation arises as a result of random density fluctuations within an electronic system. An alternative perspective on electron correlation lies in response theory. Within this framework, the behavior of the fully interacting system can be elucidated by comparing it to a reference system that is subjected to a small external perturbation giving rise to density fluctuations. The reaction of the electronic density to this perturbation is then captured by the linear density–density response function. Specifically, it describes the density response at a position $\mathbf{r}_1$ caused by the perturbations at a position $\mathbf{r}_2$ due to a small external potential oscillating at a certain frequency.[95]

As will be shown in the following, density fluctuations of a system—also captured in the transition densities—can be related to the integral of the linear density–density response function over the frequency,[56] which is given within the Lehmann representation,[98] also called spectral decomposition, by

$$\chi^\lambda(\omega, \mathbf{x}_1, \mathbf{x}_2) = \lim_{\eta\to 0^+}\sum_{n\neq 0}\left(\frac{\rho_{0n}^\lambda(\mathbf{x}_1)\rho_{n0}^\lambda(\mathbf{x}_2)}{\omega - \Omega_{0n}^\lambda - \mathrm{i}\eta} - \frac{\rho_{0n}^\lambda(\mathbf{x}_2)\rho_{n0}^\lambda(\mathbf{x}_1)}{\omega + \Omega_{0n}^\lambda + \mathrm{i}\eta}\right) \tag{2.53}$$

with the frequency ω and the excitation energies $\Omega_{0n}^\lambda = E_n^\lambda - E_0^\lambda$. The positive real number η shifts the poles at $\omega = \pm\Omega_{0n}^\lambda$ infinitesimally away from the real axis making the response function analytical in the upper right and lower left complex frequency plane (see Fig. 2.1). Nevertheless, the pole structure of the response function poses challenges for the integration along the real frequency axis

$$\int_{-\infty}^{+\infty}\mathrm{d}\omega\ \chi^\lambda(\omega, \mathbf{x}_1, \mathbf{x}_2) = \int_{-\infty}^{0}\mathrm{d}\omega\ \chi^\lambda(\omega, \mathbf{x}_1, \mathbf{x}_2) + \int_0^{+\infty}\mathrm{d}\omega\ \chi^\lambda(\omega, \mathbf{x}_1, \mathbf{x}_2) \tag{2.54}$$

To avoid that, each integral along the real frequency axis in Eq. (2.54) may be expressed by an integral along the imaginary frequency axis, as the response function

does not have any poles in the imaginary frequency domain. Thus, a relation between the real and imaginary frequency integral is necessary, which can be best rationalized by considering the respective integration on the complex ω-plane. First, the integral in the interval $[0, +\infty]$ is considered, i.e. the second term on the right-hand side of Eq. (2.54). As can be seen in Fig. 2.1, a closed contour can be created from $0 \to +\infty$ along the real frequency axis (path I), from the real to the imaginary axis (path II), and finally from $+\infty \to 0$ on the imaginary axis (path III). According to Cauchy's residue theorem,[99] which states that the integral over a closed contour containing no poles evaluates to zero, it follows that $\int_{\text{path I}} \mathrm{d}\omega\ \chi^\lambda = \int_{\text{path III}} \mathrm{d}\omega\ \chi^\lambda$. This gives the following relation

$$\int_0^{+\infty} \mathrm{d}\omega\ \chi^\lambda(\omega, \mathbf{x}_1, \mathbf{x}_2) = \int_{+\infty}^{0} \mathrm{d}\omega\ \chi^\lambda(\mathrm{i}\omega, \mathbf{x}_1, \mathbf{x}_2) = -\int_0^{+\infty} \mathrm{d}\omega\ \chi^\lambda(\mathrm{i}\omega, \mathbf{x}_1, \mathbf{x}_2) \quad (2.55)$$

The same reasoning can be applied for the first term in Eq. (2.54) resulting in the relation

$$\int_{-\infty}^{0} \mathrm{d}\omega\ \chi^\lambda(\omega, \mathbf{x}_1, \mathbf{x}_2) = \int_{0}^{-\infty} \mathrm{d}\omega\ \chi^\lambda(\mathrm{i}\omega, \mathbf{x}_1, \mathbf{x}_2) = -\int_0^{+\infty} \mathrm{d}\omega\ \chi^\lambda(-\mathrm{i}\omega, \mathbf{x}_1, \mathbf{x}_2) \quad (2.56)$$

Combining the results of Eq. (2.55) and Eq. (2.56) allows to express the integral $\int_{-\infty}^{+\infty} \mathrm{d}\omega\ \chi^\lambda(\omega, \mathbf{x}_1, \mathbf{x}_2)$ using the response function in the imaginary frequency domain as

$$\begin{aligned}
\int_{-\infty}^{+\infty} \mathrm{d}\omega\ \chi^\lambda(\omega, \mathbf{x}_1, \mathbf{x}_2) &= -\int_{-\infty}^{+\infty} \mathrm{d}\omega\ \chi^\lambda(\mathrm{i}\omega, \mathbf{x}_1, \mathbf{x}_2) && (2.57)\\
&= -\int_0^{+\infty} \mathrm{d}\omega\ \left[\chi^\lambda(\mathrm{i}\omega, \mathbf{x}_1, \mathbf{x}_2) + \chi^\lambda(-\mathrm{i}\omega, \mathbf{x}_1, \mathbf{x}_2)\right] && (2.58)
\end{aligned}$$

Inserting Eq. (2.53) in terms of imaginary frequencies into Eq. (2.58) results in

$$\begin{aligned}
&-\int_0^{+\infty} \mathrm{d}\omega\ \left[\chi^\lambda(\mathrm{i}\omega, \mathbf{x}_1, \mathbf{x}_2) + \chi^\lambda(-\mathrm{i}\omega, \mathbf{x}_1, \mathbf{x}_2)\right]\\
&= \int_0^{+\infty} \mathrm{d}\omega\ \frac{2\Omega_{0n}^\lambda}{\omega^2 + \left(\Omega_{0n}^\lambda\right)^2} \left(\sum_{n\neq 0} \rho_{0n}^\lambda(\mathbf{x}_1)\rho_{n0}^\lambda(\mathbf{x}_2) + \rho_{0n}^\lambda(\mathbf{x}_2)\rho_{n0}^\lambda(\mathbf{x}_1) \right) \quad (2.59)
\end{aligned}$$

The frequency integration can be carried out using the relation $\int_0^{+\infty} \mathrm{d}\omega \frac{\mathcal{R}}{\mathcal{R}^2+\omega^2} = \frac{\pi}{2} (\forall\ \mathcal{R} > 0)$ to yield

$$\begin{aligned}
&-\int_0^{+\infty} \mathrm{d}\omega\ \left[\chi^\lambda(\mathrm{i}\omega, \mathbf{x}_1, \mathbf{x}_2) + \chi^\lambda(-\mathrm{i}\omega, \mathbf{x}_1, \mathbf{x}_2)\right]\\
&= \pi \left(\sum_{n\neq 0} \rho_{0n}^\lambda(\mathbf{x}_1)\rho_{n0}^\lambda(\mathbf{x}_2) + \rho_{0n}^\lambda(\mathbf{x}_2)\rho_{n0}^\lambda(\mathbf{x}_1) \right) && (2.60)\\
&= \pi \left(\sum_{n\neq 0} \rho_{0n}^\lambda(\mathbf{x}_1)\rho_{n0}^\lambda(\mathbf{x}_2) + \left(\rho_{0n}^\lambda(\mathbf{x}_1)\right)^* \left(\rho_{n0}^\lambda(\mathbf{x}_2)\right)^* \right) && (2.61)\\
&= 2\pi \sum_{n\neq 0} \mathrm{Re}\left(\rho_{0n}^\lambda(\mathbf{x}_1)\rho_{n0}^\lambda(\mathbf{x}_2)\right) && (2.62)
\end{aligned}$$

In Eq. (2.62), the term $\mathrm{Re}\big(\rho_{0n}^{\lambda}(\mathbf{x}_1)\rho_{n0}^{\lambda}(\mathbf{x}_2)\big)$ denotes the real part of the product of two transition densities. It should be noted that for complex-valued orbitals the real part of this product also contains contributions from the imaginary part of each transition density.

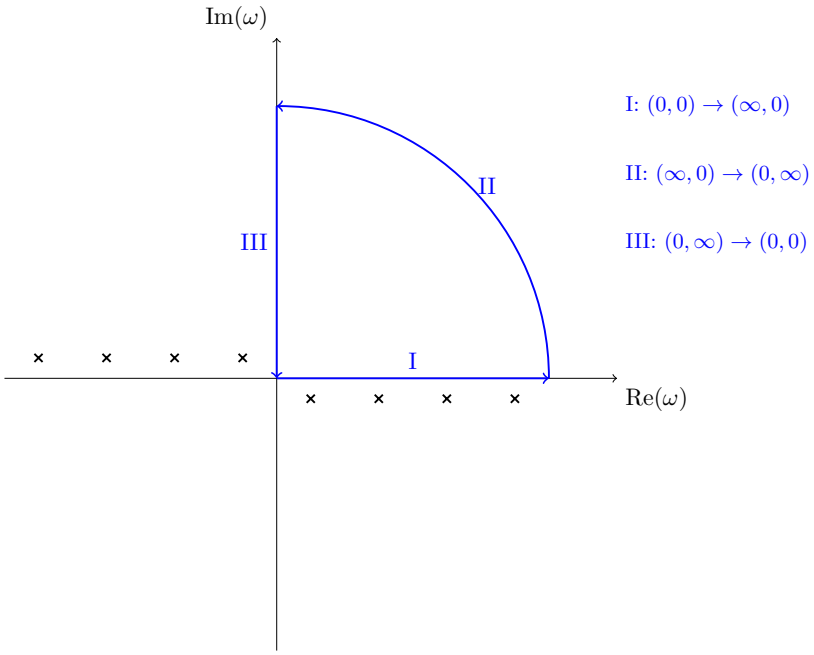

Figure 2.1: Graphical representation of the pole structure of the response function $\chi^{\lambda}(\omega, \mathbf{x}_1, \mathbf{x}_2)$ given by Eq. (2.53) in the complex frequency plane. The poles are denoted by '×' and a closed contour is given by the path I→II→III.

Fluctuation-Dissipation Theorem

Combining Eq. (2.62) with Eq. (2.49) and Eq. (2.51) yields the following relation

$$-\frac{1}{2\pi}\int_{-\infty}^{+\infty} \mathrm{d}\omega\ \chi^{\lambda}(\mathrm{i}\omega, \mathbf{x}_1, \mathbf{x}_2) = \sum_{n\neq 0} \mathrm{Re}\big(\rho_{0n}^{\lambda}(\mathbf{x}_1)\rho_{n0}^{\lambda}(\mathbf{x}_2)\big) = \langle \Psi_0^{\lambda}|\, \Delta\hat{\rho}(\mathbf{x}_1)\Delta\hat{\rho}(\mathbf{x}_2)\, |\Psi_0^{\lambda}\rangle \tag{2.63}$$

which is known as the zero temperature fluctuation-dissipation theorem.[14] Thus, the response function in the imaginary frequency domain, which describes energy absorption, i.e., dissipation,[97] of the system subject to an external perturbation oscillating with a certain frequency ω, is tied to density fluctuations.

Electron Correlation Energy within the Adiabatic-Connection Fluctuation-Dissipation Formalism

The fluctuation-dissipation theorem (Eq. (2.63)) allows to reformulate the correlation energy expression given by Eq. (2.48) in terms of the response function by recognizing that only the real component of the product of transition densities in Eq. (2.48) is relevant since the correlation energy is a real-valued quantity. Thus,

combining Eq. (2.62) with Eq. (2.48) yields

$$E_{\mathrm{c}} = -\frac{1}{4\pi}\int_0^1 \mathrm{d}\lambda \iint \mathrm{d}\mathbf{x}_1\mathrm{d}\mathbf{x}_2 \, \frac{1}{r_{12}} \int_{-\infty}^{+\infty} \mathrm{d}\omega \, \left[\chi^{\lambda}(\mathrm{i}\omega, \mathbf{x}_1, \mathbf{x}_2) - \chi^{\lambda=0}(\mathrm{i}\omega, \mathbf{x}_1, \mathbf{x}_2)\right] \tag{2.64}$$

In the above equation, the response function at coupling strength $\lambda = 0$, i.e., the KS response function $\chi_{\mathrm{KS}} = \chi^{\lambda=0} = \chi^0$, is known in terms of the KS orbitals, while the interacting response function χ^{λ} is accessible from time-dependent density functional theory (TDDFT) as will be shown in the next section.

2.4.4 Density Response from Time-Dependent Density Functional Theory

Within the framework of time-dependent density functional theory, the electronic system starts in its ground-state and an external perturbation in form of a potential oscillating with a given frequency ω is applied according to[97]

$$v_{\mathrm{ext}}(\omega, \mathbf{x}) = v_{\mathrm{ext}}(\mathbf{x}) + v^{(1)}_{\mathrm{ext}}(\omega, \mathbf{x}) \tag{2.65}$$

The corresponding density response can be expanded in a Taylor series with respect to $v^{(1)}_{\mathrm{ext}}(\omega, \mathbf{x})$ as[97]

$$\rho(\omega, \mathbf{x}) = \rho_0(\mathbf{x}) + \rho_1(\omega, \mathbf{x}) + \rho_2(\omega, \mathbf{x}) + ... \tag{2.66}$$

The linear response is given by[97]

$$\rho_1(\omega, \mathbf{x}_1) = \int \mathrm{d}\mathbf{x}_2 \chi(\omega, \mathbf{x}_1, \mathbf{x}_2) v^{(1)}_{\mathrm{ext}}(\mathbf{x}_2, \omega) \tag{2.67}$$

where the linear response function can be expressed by the Fourier transform of[95]

$$\chi(\mathbf{x}_1, t_1, \mathbf{x}_2, t_2) = \left.\frac{\partial \rho(\mathbf{x}_1, t_1)}{\partial v_{\mathrm{ext}}(\mathbf{x}_2, t_2)}\right|_{v_{\mathrm{ext}}(\mathbf{x}_2, t_2) = v_{\mathrm{ext}}(\mathbf{x}_2)} \tag{2.68}$$

Since the external potential of the ground-state, $v_{\mathrm{ext}}(\mathbf{x})$, is a functional of the ground-state density $\rho_0(\mathbf{x})$, the above equation implies that the linear response function is a functional of the ground-state density only.[95]

The linear response can be equivalently expressed within the KS system with the KS potential

$$v_{\mathrm{KS}}(\omega, \mathbf{x}) = v_{\mathrm{KS}}(\mathbf{x}) + v^{(1)}_{\mathrm{KS}}(\omega, \mathbf{x}) \tag{2.69}$$

according to[97]

$$\rho_1(\omega, \mathbf{x}_1) = \int \mathrm{d}\mathbf{x}_2 \chi^0(\omega, \mathbf{x}_1, \mathbf{x}_2) v^{(1)}_{\mathrm{KS}}(\mathbf{x}, \omega) \tag{2.70}$$

The first-order change in the time-dependent KS potential is given by[97]

$$v^{(1)}_{\mathrm{KS}}(\omega, \mathbf{x}) = v^{(1)}_{\mathrm{ext}}(\omega, \mathbf{x}) + v^{(1)}_{\mathrm{H}}(\omega, \mathbf{x}) + v^{(1)}_{\mathrm{xc}}(\omega, \mathbf{x}_1) \tag{2.71}$$

$$v^{(1)}_{\mathrm{H}}(\omega, \mathbf{x}_1) = \int \mathrm{d}\mathbf{x}_2 \frac{\rho^{(1)}(\omega, \mathbf{x}_2)}{r_{12}} = \int \mathrm{d}\mathbf{x}_2 \; f_{\mathrm{H}}(\mathbf{x}_1, \mathbf{x}_2) \rho^{(1)}(\omega, \mathbf{x}_2) \tag{2.72}$$

$$v^{(1)}_{\mathrm{xc}}(\omega, \mathbf{x}_1) = \int \mathrm{d}\mathbf{x}_2 f_{\mathrm{xc}}(\omega, \mathbf{x}_1, \mathbf{x}_2) \rho^{(1)}(\omega, \mathbf{x}_2) \tag{2.73}$$

where $f_{\mathrm{H}}(\mathbf{x}_1, \mathbf{x}_2) := \frac{1}{r_{12}}$ is the Hartree kernel and $f_{\mathrm{xc}}(\omega, \mathbf{x}_1, \mathbf{x}_2)$ is the exchange-correlation kernel, which can be expressed by the Fourier transform of

$$f_{\mathrm{xc}}(\mathbf{x}_1, t_1, \mathbf{x}_2, t_2) = \left.\frac{\partial v_{\mathrm{xc}}(\mathbf{x}_1, t_1)}{\partial \rho(\mathbf{x}_2, t_2)}\right|_{\rho(\mathbf{x}_2,t_2)=\rho_0(\mathbf{x}_2)} \tag{2.74}$$

Using Eq. (2.67) with Eq. (2.70) and Eq. (2.71) leads to the Dyson-like equation for the interacting response function[100]

$$\begin{aligned}&\chi(\omega, \mathbf{x}_1, \mathbf{x}_2)\\ &= \chi^0(\omega, \mathbf{x}_1, \mathbf{x}_2)\\ &\quad + \iint \mathrm{d}\mathbf{x}_3 \mathrm{d}\mathbf{x}_4 \; \chi^0(\omega, \mathbf{x}_1, \mathbf{x}_3)\big[f_{\mathrm{H}}(\mathbf{x}_3, \mathbf{x}_4) + f_{\mathrm{xc}}(\omega, \mathbf{x}_3, \mathbf{x}_4)\big]\chi(\omega, \mathbf{x}_4, \mathbf{x}_2)\end{aligned} \tag{2.75}$$

This allows to express the interacting response function in terms of the KS response function, which is known, and the exchange-correlation kernel, which, like the exchange-correlation potential, is unknown.

The findings from this section can now be applied to the electron correlation energy expression within the ACFDT as given by Eq. (2.64). The interacting response function in the imaginary time domain can be expressed using Eq. (2.75) as

$$\begin{aligned}&\chi^\lambda(\mathrm{i}\omega, \mathbf{x}_1, \mathbf{x}_2)\\ &= \chi^0(\mathrm{i}\omega, \mathbf{x}_1, \mathbf{x}_2)\\ &\quad + \iint \mathrm{d}\mathbf{x}_3 \mathrm{d}\mathbf{x}_4 \; \chi^0(\mathrm{i}\omega, \mathbf{x}_1, \mathbf{x}_3)\Big(\lambda f_{\mathrm{H}}(\mathbf{x}_3, \mathbf{x}_4) + f^\lambda_{\mathrm{xc}}(\mathrm{i}\omega, \mathbf{x}_3, \mathbf{x}_4)\Big)\chi^\lambda(\mathrm{i}\omega, \mathbf{x}_4, \mathbf{x}_2)\end{aligned} \tag{2.76}$$

where the Hartree kernel is linear in λ. The KS response function can be expressed using Eq. (2.53) as

$$\chi^0(\mathrm{i}\omega, \mathbf{x}_1, \mathbf{x}_2) = \sum_i^{N_{\mathrm{occ}}} \sum_a^{N_{\mathrm{virt}}} \left(\frac{\phi_i^*(\mathbf{x}_1)\phi_a(\mathbf{x}_1)\phi_a^*(\mathbf{x}_2)\phi_i(\mathbf{x}_2)}{\mathrm{i}\omega - (\epsilon_a - \epsilon_i)} - \frac{\phi_a^*(\mathbf{x}_1)\phi_i(\mathbf{x}_1)\phi_i^*(\mathbf{x}_2)\phi_a(\mathbf{x}_2)}{\mathrm{i}\omega + (\epsilon_a - \epsilon_i)} \right) \tag{2.77}$$

where the summations run over all occupied MOs i up to the total number of occupied orbitals N_{occ} as well as over all virtual orbitals a up to the total number of virtual orbitals N_{virt}.

2.5 The Random Phase Approximation

2.5.1 Real-Space Representation

The simplest approximation to the exchange-correlation kernel constitutes the (direct) random phase approximation where

$$f^\lambda_{\mathrm{xc}}(\mathrm{i}\omega, \mathbf{x}_3, \mathbf{x}_4) = 0 \tag{2.78}$$

Thus, only the Hartree kernel is considered for the computation of the RPA response function, which takes the form

$$\begin{aligned}\chi^\lambda_{\mathrm{RPA}}(\mathrm{i}\omega, \mathbf{x}_1, \mathbf{x}_2) &= \chi^0(\mathrm{i}\omega, \mathbf{x}_1, \mathbf{x}_2)\\ &\quad + \iint \mathrm{d}\mathbf{x}_3 \mathrm{d}\mathbf{x}_4 \; \chi^0(\mathrm{i}\omega, \mathbf{x}_1, \mathbf{x}_3)\lambda f_{\mathrm{H}}(\mathbf{x}_3, \mathbf{x}_4)\chi^\lambda_{\mathrm{RPA}}(\mathrm{i}\omega, \mathbf{x}_4, \mathbf{x}_2)\end{aligned} \tag{2.79}$$

To obtain an expression for the RPA correlation energy, first, the above equation is rewritten to obtain an expression for $\chi^{\lambda}_{\mathrm{RPA}}(\mathrm{i}\omega, \mathbf{x}_1, \mathbf{x}_2)$ according to[97]

$$\chi^{\lambda}_{\mathrm{RPA}}(\mathrm{i}\omega) = \chi^0(\mathrm{i}\omega) + \chi^0(\mathrm{i}\omega) \otimes \lambda f_{\mathrm{H}} \otimes \chi^{\lambda}_{\mathrm{RPA}}(\mathrm{i}\omega) \tag{2.80}$$

where the dependence on the space and spin coordinates was omitted and the multiplication of two functions in the real-space representation is given by

$$\chi^0(\mathrm{i}\omega) \otimes f_{\mathrm{H}} = \int \mathrm{d}\mathbf{x}_3 \chi^0(\mathrm{i}\omega, \mathbf{x}_1, \mathbf{x}_3) f_{\mathrm{H}}(\mathbf{x}_3, \mathbf{x}_4) \tag{2.81}$$

By rearranging the terms, the RPA response function can be expressed according to

$$\chi^{\lambda}_{\mathrm{RPA}}(\mathrm{i}\omega) = \left(\hat{1} - \chi^0(\mathrm{i}\omega) \otimes \lambda f_{\mathrm{H}}\right)^{-1} \otimes \chi_{\mathrm{KS}}(\mathrm{i}\omega) \tag{2.82}$$

where $\hat{1}$ denotes the identity function. Using the above expression for the RPA response function with the ACFDT correlation energy expression given by Eq. (2.64) yields the RPA correlation energy

$$E_{\mathrm{c}}^{\mathrm{RPA}} = -\frac{1}{4\pi} \int_0^1 \mathrm{d}\lambda \int_{-\infty}^{+\infty} \mathrm{d}\omega \ \mathrm{Tr}\left[f_{\mathrm{H}} \otimes \left\{\left(\hat{1} - \chi^0(\mathrm{i}\omega) \otimes \lambda f_{\mathrm{H}}\right)^{-1} \otimes \chi^0(\mathrm{i}\omega) - \chi^0(\mathrm{i}\omega)\right\}\right] \tag{2.83}$$

where the trace of a product of two functions $f(\mathbf{x}_1, \mathbf{x}_2)$ and $g(\mathbf{x}_1, \mathbf{x}_2)$ in the real-space representation is defined as

$$\mathrm{Tr}(f \otimes g) = \iint \mathrm{d}\mathbf{x}_1 \mathrm{d}\mathbf{x}_2 \ f(\mathbf{x}_1, \mathbf{x}_2) g(\mathbf{x}_1, \mathbf{x}_2) \tag{2.84}$$

After analytical coupling strength integration, the RPA correlation energy reads

$$E_{\mathrm{c}}^{\mathrm{RPA}} = \frac{1}{4\pi} \int_{-\infty}^{+\infty} \mathrm{d}\omega \ \mathrm{Tr}\left[\ln\left\{\hat{1} - \chi^0(\mathrm{i}\omega) \otimes f_{\mathrm{H}}\right\} + \chi^0(\mathrm{i}\omega) \otimes f_{\mathrm{H}}\right] \tag{2.85}$$

2.5.2 Molecular-Orbital Representation

For computational implementations within quantum chemistry it is more common to work within the molecular orbital space, rather than the real-space. Therefore, Eq. (2.85) can be reformulated for the general case of complex-valued orbitals according to[55]

$$\begin{aligned} E_{\mathrm{c}}^{\mathrm{RPA}} = \frac{1}{4\pi} \int_{-\infty}^{+\infty} \mathrm{d}\omega \ \sum_{i}^{N_{\mathrm{occ}}} \sum_{a}^{N_{\mathrm{virt}}} \Big[& \ln\left\{1 - \left(\Pi^{0,-}_{ia,ia}(\mathrm{i}\omega) V_{ia,ai} - \Pi^{0,+}_{ia,ia}(\mathrm{i}\omega) V^*_{ia,ai}\right)\right\} \\ & + \left(\Pi^{0,-}_{ia,ia}(\mathrm{i}\omega) V_{ia,ai} - \Pi^{0,+}_{ia,ia}(\mathrm{i}\omega) V^*_{ia,ai}\right)\Big] \end{aligned} \tag{2.86}$$

$$\begin{aligned} = \frac{1}{4\pi} \int_{-\infty}^{+\infty} \mathrm{d}\omega \ \mathrm{Tr}\Big[& \ln\left\{\mathbf{1} - \left(\mathbf{\Pi}^{0,-}(\mathrm{i}\omega)\mathbf{V} - \mathbf{\Pi}^{0,+}(\mathrm{i}\omega)\mathbf{V}^*\right)\right\} \\ & + \left(\mathbf{\Pi}^{0,-}(\mathrm{i}\omega)\mathbf{V} - \mathbf{\Pi}^{0,+}(\mathrm{i}\omega)\mathbf{V}^*\right)\Big] \end{aligned} \tag{2.87}$$

with the polarization propagator $\mathbf{\Pi}^0(\mathrm{i}\omega)$ given by[55]

$$\mathbf{\Pi}^0(\mathrm{i}\omega) = \mathbf{\Pi}^{0,-}(\mathrm{i}\omega) - \mathbf{\Pi}^{0,+}(\mathrm{i}\omega) \tag{2.88}$$

$$\Pi^{0,-}_{ia,ia}(\mathrm{i}\omega) = \frac{1}{\mathrm{i}\omega - (\epsilon_a - \epsilon_i)} \tag{2.89}$$

$$\Pi^{0,+}_{ia,ia}(\mathrm{i}\omega) = \frac{1}{\mathrm{i}\omega + (\epsilon_a - \epsilon_i)} \tag{2.90}$$

and the MO representation of the Hartree kernel $\mathbf{V}$:

$$V_{ia,ai} = \iint \mathrm{d}\mathbf{x}_1 \mathrm{d}\mathbf{x}_2 \; \frac{\phi_i^*(\mathbf{x}_1)\phi_a(\mathbf{x}_1)\phi_a^*(\mathbf{x}_2)\phi_i(\mathbf{x}_2)}{r_{12}} \tag{2.91}$$

$$V_{ia,ai}^* = \iint \mathrm{d}\mathbf{x}_1 \mathrm{d}\mathbf{x}_2 \; \frac{\phi_a^*(\mathbf{x}_1)\phi_i(\mathbf{x}_1)\phi_i^*(\mathbf{x}_2)\phi_a(\mathbf{x}_2)}{r_{12}} \tag{2.92}$$

For real-valued wave functions it follows that $\mathbf{V} = \mathbf{V}^*$ and the polarization propagator is an even function in the iω-space. Thus, the RPA correlation energy given by Eq. (2.87) reduces to[75]

$$E_\mathrm{c}^\mathrm{RPA} = \frac{1}{2\pi} \int_0^{+\infty} \mathrm{d}\omega \; \mathrm{Tr}\big[\ln\big\{\mathbf{1} - \mathbf{\Pi}^0(\mathrm{i}\omega)\mathbf{V}\big\} + \mathbf{\Pi}^0(\mathrm{i}\omega)\mathbf{V}\big] \tag{2.93}$$

and the polarization propagator for real-valued orbitals reduces to[75]

$$\Pi_{ia,ia}^0(\mathrm{i}\omega) = \frac{-2(\epsilon_a - \epsilon_i)}{\omega^2 + (\epsilon_a - \epsilon_i)^2} \tag{2.94}$$

2.5.3 Molecular-Orbital Resolution-of-the-Identity RPA

Calculating the RPA correlation energy within the molecular orbital basis (Eq. (2.87)) requires storing the four-dimensional electron repulsion integral (ERI) tensor, which restricts its applicability to small systems. Thus, in the next section, the resolution-of-the-identity (RI) approach—which provides one possible avenue to factorize the four center integrals into lower rank tensors—is introduced and subsequently applied to the computation of the MO-RPA energy expression, thereby reducing the computational cost.

Resolution-of-the-Identity

The RI approach[101–106] allows to factorize the four-center ERI tensor into tensors of second- and third-order. The RI approach is frequently used interchangeably with the density fitting (DF) method. Although both approaches yield the same results, they are not identical, as they are based on different conceptual frameworks.[107] The following derivation is based on the DF formalism.

The four-center two-electron integral tensor in the atomic orbital basis $\{\varphi_\mu\}$ is given by

$$(\mu\nu|\lambda\sigma) = \iint \mathrm{d}\mathbf{x}_1 \mathrm{d}\mathbf{x}_2 \; \varphi_\mu^*(\mathbf{x}_1)\varphi_\nu(\mathbf{x}_1)\frac{1}{r_{12}}\varphi_\lambda^*(\mathbf{x}_2)\varphi_\sigma(\mathbf{x}_2) \tag{2.95}$$

where the indices μ, ν, λ, and σ denote atomic orbital indices, with a total of N_basis AO basis functions. The charge densities $|\lambda\sigma)$ are now approximated by expanding them in an auxiliary basis set $\{P\}$ according to

$$|\lambda\sigma) \approx |\widetilde{\lambda\sigma}) = \sum_M^{N_\mathrm{aux}} \tilde{C}_{\lambda\sigma}^P |P) \tag{2.96}$$

where N_aux denotes the total number of auxiliary functions and the fitting coefficients $\tilde{C}_{\lambda\sigma}^P$ can be determined by minimizing the error

$$0 \stackrel{!}{=} \frac{\partial}{\partial \tilde{C}_{\lambda\sigma}^P} (\lambda\sigma - \widetilde{\lambda\sigma}|m_{12}|\lambda\sigma - \widetilde{\lambda\sigma}) \tag{2.97}$$

within a metric m_{12} leading to

$$\tilde{C}^P_{\lambda\sigma} = \sum_{Q}^{N_{\text{aux}}} (\lambda\sigma|m_{12}|Q)(Q|m_{12}|P)^{-1} \tag{2.98}$$

where matrix operations are performed prior to indexing. Using this result allows to factorize the ERI tensor according to

$$(\mu\nu|\lambda\sigma) \approx \sum_{PQ}^{N_{\text{aux}}} \tilde{C}^P_{\mu\nu}(P|Q)\tilde{C}^Q_{\lambda\sigma} \tag{2.99}$$

$$= \sum_{PQRS}^{N_{\text{aux}}} (\mu\nu|m_{12}|P)(P|m_{12}|Q)^{-1}(Q|R)(R|m_{12}S)^{-1}(S|m_{12}|\lambda\sigma) \tag{2.100}$$

$$= \sum_{PS}^{N_{\text{aux}}} \mathbb{B}^P_{\mu\nu}\tilde{V}_{PS}\mathbb{B}^S_{\lambda\sigma} \tag{2.101}$$

where the following second- and third-order tensors have been introduced

$$\mathbb{B}^P_{\mu\nu} := (\mu\nu|m_{12}|P) \tag{2.102}$$

$$\tilde{V}_{PS} := \sum_{QR}^{N_{\text{aux}}} (P|m_{12}|Q)^{-1}(Q|R)(R|m_{12}S)^{-1} \tag{2.103}$$

The choice of the metric m_{12} is important for the accuracy of the approximation. The Coulomb metric $m_{12} = \frac{1}{r_{12}}$ has been shown to be well suited for fitting density-like repulsions.[106] Other choices include the overlap metric as well as the Coulomb metric attenuated by the complementary error function.[26,108,109] While those metrics are less accurate than the Coulomb metric, they introduce sparsity into the respective matrices which can be exploited for efficiency, which will be discussed further in section 2.5.5.

MO-RI-RPA Energy

For the general case of complex-valued orbitals, $\mathbf{V}$ (Eq. (2.91)) and $\mathbf{V}^*$ (Eq. (2.92)) can be factorized according to Eq. (2.101) to yield

$$V_{ia,ai} = \sum_{PQ}^{N_{\text{aux}}} \mathbb{B}^P_{ia}\tilde{V}_{PQ}\mathbb{B}^Q_{ai} \tag{2.104}$$

$$V^*_{ia,ai} = \sum_{PQ}^{N_{\text{aux}}} \left(\mathbb{B}^P_{ia}\right)^*\tilde{V}_{PQ}\left(\mathbb{B}^Q_{ai}\right)^* \tag{2.105}$$

this allows to rewrite $\mathbf{\Pi}^{0,-}(\mathrm{i}\omega)\mathbf{V} - \mathbf{\Pi}^{0,+}(\mathrm{i}\omega)\mathbf{V}^*$ according to

$$\sum_{i}^{N_{\text{occ}}}\sum_{a}^{N_{\text{virt}}} \Pi^{0,-}_{ia,ia}(\mathrm{i}\omega)V_{ia,ai} - \Pi^{0,+}_{ia,ia}(\mathrm{i}\omega)V^*_{ia,ai} = \sum_{PQ}^{N_{\text{aux}}} \left[\tilde{X}^-_{0,PQ}(\mathrm{i}\omega) - \tilde{X}^+_{0,PQ}(\mathrm{i}\omega)\right]\tilde{V}_{PQ} \tag{2.106}$$

with the polarization propagator in the auxiliary basis

$$\tilde{\mathbf{X}}_0(\mathrm{i}\omega) = \tilde{\mathbf{X}}_0^-(\mathrm{i}\omega) - \tilde{\mathbf{X}}_0^+(\mathrm{i}\omega) \tag{2.107}$$

$$\tilde{X}_{0,PQ}^-(\mathrm{i}\omega) = \sum_i^{N_\mathrm{occ}} \sum_a^{N_\mathrm{virt}} \mathbb{B}_{ia}^P \Pi_{ia,ia}^{0,-}(\mathrm{i}\omega) \mathbb{B}_{ai}^Q \tag{2.108}$$

$$\tilde{X}_{0,PQ}^+(\mathrm{i}\omega) = \sum_i^{N_\mathrm{occ}} \sum_a^{N_\mathrm{virt}} \left(\mathbb{B}_{ia}^P\right)^* \Pi_{ia,ia}^{0,+}(\mathrm{i}\omega) \left(\mathbb{B}_{ai}^Q\right)^* \tag{2.109}$$

Combining these results with Eq. (2.87) yields

$$E_\mathrm{c}^\mathrm{RPA} = \frac{1}{4\pi} \int_{-\infty}^{+\infty} \mathrm{d}\omega \ \mathrm{Tr}\left[\ln\left\{\mathbf{1} - \tilde{\mathbf{X}}_0(\mathrm{i}\omega)\tilde{\mathbf{V}}\right\} + \tilde{\mathbf{X}}_0(\mathrm{i}\omega)\tilde{\mathbf{V}}\right] \tag{2.110}$$

It should be noted that for real-valued orbitals $\tilde{\mathbf{X}}_0(\mathrm{i}\omega)$ reduces to

$$\tilde{\mathbf{X}}_{0,PQ}(\mathrm{i}\omega) = \sum_i^{N_\mathrm{occ}} \sum_a^{N_\mathrm{virt}} \mathbb{B}_{ia}^P \frac{-2(\epsilon_a - \epsilon_i)}{\omega^2 + (\epsilon_a - \epsilon_i)^2} \mathbb{B}_{ia}^Q \tag{2.111}$$

and the corresponding energy expression reads[24]

$$E_\mathrm{c}^\mathrm{RPA} = \frac{1}{2\pi} \int_0^{+\infty} \mathrm{d}\omega \ \mathrm{Tr}\left[\ln\left\{\mathbf{1} - \tilde{\mathbf{X}}_0(\mathrm{i}\omega)\tilde{\mathbf{V}}\right\} + \tilde{\mathbf{X}}_0(\mathrm{i}\omega)\tilde{\mathbf{V}}\right] \tag{2.112}$$

Introducing the RI approximation and a numerical frequency integration for the MO-RPA correlation energy computation—which was accomplished by Furche and co-workers[24]—reduces the formal scaling of the method from $\mathcal{O}(M^6)$ to $\mathcal{O}(M^4)$, thereby making RPA one of the formally lowest-scaling electron correlation methods.

2.5.4 Atomic-Orbital Resolution-of-the-Identity RPA

The computationally most intensive step within RPA is the computation of the response function in the auxiliary basis as given by Eqs. (2.107)–(2.109) formally scaling as $\mathcal{O}(N_\mathrm{aux}^2 N_\mathrm{virt} N_\mathrm{occ} \propto M^4)$. Thus, an atomic orbital formulation will be derived for this step to benefit from locality in the electronic structure.

In a first step, the response function in the imaginary frequency domain is expressed by its Fourier transform according to[28]

$$\tilde{\mathbf{X}}_0(\mathrm{i}\omega) = \int_{-\infty}^{+\infty} \mathrm{d}\tau \mathbf{X}_0(\mathrm{i}\tau) \exp(\mathrm{i}\tau\omega) \tag{2.113}$$

For real-valued orbitals, $\tilde{\mathbf{X}}_0(\mathrm{i}\omega)$ is an even function in the $\mathrm{i}\omega$-space and the Fourier transform reduces to a cosine transform,[27,28] or, equivalently a double Laplace transform.[25] To obtain an expression for $\mathbf{X}_0(\mathrm{i}\tau)$, the inverse Fourier transform given by

$$\mathbf{X}_0(\mathrm{i}\tau) = \frac{1}{2\pi} \int_{-\infty}^{+\infty} \mathrm{d}\omega \tilde{\mathbf{X}}_0(\mathrm{i}\omega) \exp(-\mathrm{i}\tau\omega) \tag{2.114}$$

$$= \int_0^{+\infty} \mathrm{d}\omega \left[\exp(\mathrm{i}\tau\omega)\tilde{\mathbf{X}}_0(-\mathrm{i}\omega) + \exp(-\mathrm{i}\tau\omega)\tilde{\mathbf{X}}_0(\mathrm{i}\omega)\right] \tag{2.115}$$

can be evaluated. For this, $\tilde{\mathbf{X}}_0(\mathrm{i}\omega)$ can be rewritten according to

$$\begin{aligned}&\tilde{X}_{0,PQ}(\mathrm{i}\omega)\\&=\sum_{i}^{N_{\mathrm{occ}}}\sum_{a}^{N_{\mathrm{virt}}}\frac{-\left[\mathbb{B}_{ia}^{P}\mathbb{B}_{ai}^{Q}-(\mathbb{B}_{ia}^{P}\mathbb{B}_{ai}^{Q})^{*}\right]\mathrm{i}\omega}{\omega^{2}+(\epsilon_{a}-\epsilon_{i})^{2}}-\frac{\left[\mathbb{B}_{ia}^{P}\mathbb{B}_{ai}^{Q}+(\mathbb{B}_{ia}^{P}\mathbb{B}_{ai}^{Q})^{*}\right](\epsilon_{a}-\epsilon_{i})}{\omega^{2}+(\epsilon_{a}-\epsilon_{i})^{2}}\end{aligned}\tag{2.116}$$

and inserted into Eq. (2.115). Further, using Euler's formula to express the exponential function, $\exp(\mathrm{i}x)=\cos(x)+\mathrm{i}\sin(x)$ $(x\in\mathbb{R})$, yields

$$\begin{aligned}X_{0,PQ}(\mathrm{i}\tau)=\sum_{i}^{N_{\mathrm{occ}}}\sum_{a}^{N_{\mathrm{virt}}}-\frac{1}{\pi}\Bigg[&\int_{0}^{+\infty}\mathrm{d}\omega\,\cos(\omega\tau)\frac{\left[\mathbb{B}_{ia}^{P}\mathbb{B}_{ai}^{Q}+(\mathbb{B}_{ia}^{P}\mathbb{B}_{ai}^{Q})^{*}\right](\epsilon_{a}-\epsilon_{i})}{\omega^{2}+(\epsilon_{a}-\epsilon_{i})^{2}}\\&+\int_{0}^{+\infty}\mathrm{d}\omega\,\mathrm{i}\sin(\omega\tau)\frac{\left[\mathbb{B}_{ia}^{P}\mathbb{B}_{ai}^{Q}-(\mathbb{B}_{ia}^{P}\mathbb{B}_{ai}^{Q})^{*}\right]\mathrm{i}\omega}{\omega^{2}+(\epsilon_{a}-\epsilon_{i})^{2}}\Bigg]\end{aligned}\tag{2.117}$$

The cosine and sine transforms can be evaluated according to[110]

$$\int_{0}^{+\infty}\mathrm{d}\omega\,\cos(\omega\tau)\frac{(\epsilon_{a}-\epsilon_{i})}{\omega^{2}+(\epsilon_{a}-\epsilon_{i})^{2}}=\frac{\pi}{2}\exp(-\omega\tau);\quad\forall\,\tau\geq0\tag{2.118}$$

$$\int_{0}^{+\infty}\mathrm{d}\omega\,\sin(\omega\tau)\frac{\omega}{\omega^{2}+(\epsilon_{a}-\epsilon_{i})^{2}}=\frac{\pi}{2}\exp(-\omega\tau);\quad\forall\,\tau\geq0\tag{2.119}$$

yielding

$$X_{0,PQ}(\mathrm{i}\tau)=\sum_{i}^{N_{\mathrm{occ}}}\sum_{a}^{N_{\mathrm{virt}}}\exp(-(\epsilon_{a}-\epsilon_{i})\tau)(\mathbb{B}_{ia}^{P}\mathbb{B}_{ai}^{Q});\quad\forall\,\tau\geq0\tag{2.120}$$

Since the response function in the imaginary time domain is a Hermitian function, it has the following property[111]

$$\mathbf{X}_0(-\mathrm{i}\tau)=\mathbf{X}_0(\mathrm{i}\tau)^{*}\tag{2.121}$$

which provides an expression for $\mathbf{X}_0(\mathrm{i}\tau)$ for negative imaginary times. Thus, it can be summarized as

$$X_{0,PQ}(\mathrm{i}\tau)=\begin{cases}\sum_{i}^{N_{\mathrm{occ}}}\sum_{a}^{N_{\mathrm{virt}}}\exp(-(\epsilon_{a}-\epsilon_{i})\tau)(\mathbb{B}_{ia}^{P}\mathbb{B}_{ai}^{Q}) & \mid t\geq0\\ \sum_{i}^{N_{\mathrm{occ}}}\sum_{a}^{N_{\mathrm{virt}}}\exp(-(\epsilon_{a}-\epsilon_{i})\tau)(\mathbb{B}_{ia}^{P}\mathbb{B}_{ai}^{Q})^{*} & \mid t<0\end{cases}\tag{2.122}$$

Compared to Eq. (2.116) where a straightforward AO formulation is not possible due to the squared orbital energy denominator, the above equation has decoupled orbital energies which allows a transformation into the atomic orbital space. For positive imaginary times it follows that

$$X_{0,PQ}(\mathrm{i}\tau)=\sum_{\mu\nu\lambda\sigma}^{N_{\mathrm{basis}}}\sum_{i}^{N_{\mathrm{occ}}}\sum_{a}^{N_{\mathrm{virt}}}\exp(-(\epsilon_{a}-\epsilon_{i})\tau)C_{\mu i}^{*}C_{\nu a}C_{\lambda a}^{*}C_{\sigma i}\mathbb{B}_{\mu\nu}^{P}\mathbb{B}_{\lambda\sigma}^{Q};\quad\forall\,\tau\geq0\tag{2.123}$$

$$=\sum_{\mu\nu\lambda\sigma}^{N_{\mathrm{basis}}}\underline{G}_{0,\mu\sigma}(-\mathrm{i}\tau)\mathbb{B}_{\mu\nu}^{P}\overline{G}_{0,\nu\lambda}(\mathrm{i}\tau)\mathbb{B}_{\lambda\sigma}^{Q};\quad\forall\,\tau\geq0\tag{2.124}$$

where $\{C_{\mu i}\}$ and $\{C_{\nu a}\}$ denote occupied and virtual MO coefficients, respectively, and the non-interacting one-particle Green's function is defined as

$$\mathbf{G}_0(\mathrm{i}\tau) = \Theta(-\tau)\underline{\mathbf{G}}_0(\mathrm{i}\tau) + \Theta(\tau)\overline{\mathbf{G}}_0(\mathrm{i}\tau) \tag{2.125}$$

$$\underline{G}_{0,\mu\nu}(\mathrm{i}\tau) = \sum_{i}^{N_{\mathrm{occ}}} C^*_{\mu i} C_{\nu i} \exp(-\tau\epsilon_i) = \left[\mathbf{P}\exp(-\tau\mathbf{H}_{\mathrm{KS}}\mathbf{P})\right]_{\mu\nu} \tag{2.126}$$

$$\overline{G}_{0,\mu\nu}(\mathrm{i}\tau) = -\sum_{a}^{N_{\mathrm{virt}}} C^*_{\mu a} C_{\nu a} \exp(-\tau\epsilon_a) = \left[\mathbf{P}_{\mathrm{virt}}\exp(-\tau\mathbf{H}_{\mathrm{KS}}\mathbf{P}_{\mathrm{virt}})\right]_{\mu\nu} \tag{2.127}$$

with the Heaviside step-function Θ, as well as the occupied and virtual one-particle density matrix given by $\mathbf{P}$ and $\mathbf{P}_{\mathrm{virt}}$, respectively. Accordingly, an expression for the response function in the negative imaginary time domain can be derived leading to the final expression

$$X_{0,PQ}(\mathrm{i}\tau) = \begin{cases} \sum_{\mu\nu\lambda\sigma}^{N_{\mathrm{basis}}} \underline{G}_{0,\mu\sigma}(-\mathrm{i}\tau)\mathbb{B}^P_{\mu\nu}\overline{G}_{0,\nu\lambda}(\mathrm{i}\tau)\mathbb{B}^Q_{\lambda\sigma} | \tau \geq 0 \\ \sum_{\mu\nu\lambda\sigma}^{N_{\mathrm{basis}}} \underline{G}_{0,\nu\lambda}(-\mathrm{i}\tau)\mathbb{B}^P_{\mu\nu}\overline{G}_{0,\mu\sigma}(\mathrm{i}\tau)\mathbb{B}^Q_{\lambda\sigma} | \tau < 0 \end{cases} \tag{2.128}$$

Again, for real-valued orbitals the response function is an even function in the iτ-domain, that is $\mathbf{X}_0(\mathrm{i}\tau) = \mathbf{X}_0(-\mathrm{i}\tau)$.

The general RPA energy expression in terms of complex-valued orbitals given by Eq. (2.87) with the evaluation of the response function in the imaginary time domain was employed in **Publication III** as the starting point for the derivation of analytical second-order derivatives for the computation of NMR shielding tensors. Then, in **Publication IV**, further improvements were made for the computational efficiency using a low-scaling RPA energy formulation. In the next section, strategies for low-scaling RPA methods are introduced and subsequently applied to the computation of RPA correlation energies.

2.5.5 Strategies for Low-Scaling

In the following, two strategies for an efficient and low-scaling implementation will be described, specifically the utilization of a local RI metric and pivoted Cholesky decomposition (CD) of density type matrices.

As mentioned in the previous section, the choice of the RI metric constitutes a crucial factor for increasing the computational efficiency and lower the scaling of the method. While the Coulomb metric $m_{12} = \frac{1}{r_{12}}$ has shown to be very accurate,[106] no sparsity can be gained from the corresponding matrix representations. Considering, for instance, the three-center integrals $(\mu\nu|r_{12}^{-1}|P)$ it becomes apparent, that the charge distribution $(\mu\nu)$ is coupled to the auxiliary function P over effectively infinite distances due to the very slow decay of the metric. By comparison, the overlap metric $m_{12} = \delta(r_{12})$ is very local due to the exponential decay of Gaussian basis functions, and, thus, its matrix representations are very sparse. However, this metric has been shown to be rather inaccurate.[106] A metric that encompasses both accuracy and sparsity is the Coulomb metric attenuated by the complementary error function (erfc)[26,108,109] given by

$$m_{12} = \frac{\mathrm{erfc}(\omega_{\mathrm{att}} r_{12})}{r_{12}} \tag{2.129}$$

where the attenuation parameter ω_{att} determines the attenuation strength, thereby varying the sparsity and accuracy. In the limiting cases, the Coulomb metric is recovered as $\omega_{\text{att}} \to 0$, and the overlap metric is recovered as $\omega_{\text{att}} \to \infty$. Specifically, for RPA it has been shown that the parameter $\omega_{\text{att}} = 0.1$ a.u. provides a good compromise between accuracy and sparsity.[26,36]

Another strategy that can be employed to increase computational efficiency is pivoted Cholesky decomposition of density type matrices. While the computational scaling can be reduced significantly within the AO framework, the scaling with the basis set size (for a fixed system size) increases. This introduces an overhead for systems that are not sparse. To remedy this, pivoted Cholesky decomposition of density type matrices has shown to be very useful. In this context, the pivoted Cholesky decomposition of a positive semi-definite matrix $\boldsymbol{\mathcal{R}}$ is given by

$$\boldsymbol{\mathcal{R}} = \boldsymbol{\mathcal{L}}\boldsymbol{\mathcal{L}}^{\mathrm{T}} \tag{2.130}$$

where $\boldsymbol{\mathcal{L}}$ is a lower triangular matrix, having the same number of rows as $\boldsymbol{\mathcal{R}}$, while the number of columns corresponds to rank($\boldsymbol{\mathcal{R}}$). Here, the CD of the occupied one-particle density matrix $\mathbf{P}$ according to

$$\mathbf{P} = \mathbf{L}\mathbf{L}^{\mathrm{T}} \tag{2.131}$$

is very beneficial since its rank corresponds to the number of occupied orbitals N_{occ}, which is significantly less than the number of basis functions. Further, the Cholesky matrices usually retain the sparsity of the original matrix. To apply this to the framework of AO-RI-RPA, it can be considered that the Green's function in the negative imaginary time domain is invariant to projections onto the occupied subspace, which gives rise to the CD of the occupied density matrix according to[27]

$$\underline{\mathbf{G}}_0(-\mathrm{i}\tau) = \mathbf{P}\mathbf{S}\underline{\mathbf{G}}_0(-\mathrm{i}\tau)\mathbf{S}\mathbf{P} \tag{2.132}$$

$$= \mathbf{L}\mathbf{L}^{\mathrm{T}}\mathbf{S}\underline{\mathbf{G}}_0(-\mathrm{i}\tau)\mathbf{S}\mathbf{L}\mathbf{L}^{\mathrm{T}} \tag{2.133}$$

Next, the Cholesky decomposition of the Green's function in the positive imaginary time domain can be considered directly

$$-\overline{\mathbf{G}}_0(\mathrm{i}\tau) = \mathbf{L}_{\text{virt}}(\mathrm{i}\tau)\mathbf{L}_{\text{virt}}^{\mathrm{T}}(\mathrm{i}\tau) \tag{2.134}$$

Since this Green's function is negative semi-definite, CD is applied to $-\overline{\mathbf{G}}_0(\mathrm{i}\tau)$, which is positive semi-definite. The number of columns of $\mathbf{L}_{\text{virt}}(\mathrm{i}\tau)$, and, thus, the rank of $\overline{\mathbf{G}}_0(\mathrm{i}\tau)$, is dependent on the τ-quadrature point. It follows that the rank decreases with increasing τ, thus, capturing the decay of the exponential function within the Green's function. This decomposition is somewhat more beneficial than projecting the Green's function onto the virtual subspace and using the CD of the virtual density, whose rank always corresponds to the number of virtual orbitals.

In **Publications I-II**, Eq. (2.133) was used together with the attenuated Coulomb metric, while **Publication IV** employs both, Eqs. (2.133) and (2.134).

2.5.6 Low-Scaling Atomic-Orbital Resolution-of-the-Identity RPA

To derive a low-scaling formulation for the response function in the imaginary time domain—the time-determining step within RI-RPA—it can be first expressed as a

trace over the AO-indices according to

$$X_{0,PQ}(\mathrm{i}\tau) = \mathrm{Tr}\big(\underline{\mathbf{G}}_0(-\mathrm{i}\tau)\mathbb{B}^P\overline{\mathbf{G}}_0(\mathrm{i}\tau)\mathbb{B}^Q\big) \tag{2.135}$$

Next, employing the attenuated Coulomb metric for the two- and three-center integrals as well as the CD given by Eq. (2.124) yields[27]

$$\begin{aligned} X_{0,PQ}(\mathrm{i}\tau) &= \mathrm{Tr}\big(\mathbf{L}\mathbf{L}^{\mathrm{T}}\mathbf{S}\underline{\mathbf{G}}_0(-\mathrm{i}\tau)\mathbf{S}\mathbf{L}\mathbf{L}^{\mathrm{T}}\mathbb{B}^P\overline{\mathbf{G}}_0(\mathrm{i}\tau)\mathbb{B}^Q\big) && (2.136)\\ &= \mathrm{Tr}\big([\mathbf{L}^{\mathrm{T}}\mathbf{S}\underline{\mathbf{G}}_0(-\mathrm{i}\tau)\mathbf{S}\mathbf{L}][\mathbf{L}^{\mathrm{T}}\mathbb{B}^P]\overline{\mathbf{G}}_0(\mathrm{i}\tau)[\mathbb{B}^Q\mathbf{L}^{\mathrm{T}}]\big) && (2.137)\\ &= \sum_{\underline{ij}}^{N_{\mathrm{occ}}}\sum_{\mu\nu}^{N_{\mathrm{basis}}} \underline{\tilde{G}}_{0,\underline{ij}}(-\mathrm{i}\tau)\tilde{\mathbb{B}}^P_{\mu\underline{j}}\overline{G}_{0,\mu\nu}(\mathrm{i}\tau)\tilde{\mathbb{B}}^Q_{\nu\underline{i}} && (2.138) \end{aligned}$$

In Eq. (2.137) the invariance of the trace under cyclic permutation was utilized and in Eq. (2.138), the following quantities have been introduced

$$\begin{aligned} \underline{\tilde{G}}_{0,\underline{ij}}(-\mathrm{i}\tau) &= \big(\mathbf{L}^{\mathrm{T}}\mathbf{S}\underline{\mathbf{G}}_0(-\mathrm{i}\tau)\mathbf{S}\mathbf{L}\big)_{\underline{ij}} && (2.139)\\ \tilde{\mathbb{B}}^P_{\mu\underline{j}} &= \big(\mathbb{B}^P\mathbf{L}^{\mathrm{T}}\big)_{\mu\underline{j}} && (2.140) \end{aligned}$$

which are represented (partially) in the Cholesky MO basis with the occupied Cholesky indices denoted by $\underline{i}$ and $\underline{j}$.

For molecular systems with a local electronic structure all matrices become sparse allowing an asymptotically linear scaling computation of the response function in the imaginary time domain, which constitutes the time determining step.[25–27]

Further, the memory requirements of the method—which are dominated by the memory requirements of the three-center integral tensor—were reduced significantly by utilizing CD from $N_{\mathrm{aux}}N_{\mathrm{basis}}^2$ to $N_{\mathrm{aux}}N_{\mathrm{basis}}N_{\mathrm{occ}}$. However, for larger molecular systems and/or basis sets, the memory requirements of the method, comprising the memory of the three-center integrals as well as intermediate quantities arising during the calculation, quickly exceed the available system memory on a single compute node. This problem was solved in **Publication I**, where the low-scaling RPA energy expression derived in this section was used within a real-valued atomic orbital basis to introduce an optimized batching scheme for the computation of $\mathbf{X}_0(\mathrm{i}\tau)$. Using a Lagrangian formalism, the number of batches was computed by minimizing the batching overhead while not exceeding the available system memory, thus providing the optimal compromise between program runtime and memory demand.

2.6 σ-Functionals

Another approach based on the ACFD theorem that is closely related to RPA are σ-functionals, which were recently introduced by Görling and co-workers.[81,82] To derive the corresponding correlation energy expression, first, the RPA correlation energy is considered as given by Eq. (2.87). To obtain a symmetric expression for the term $\tilde{\mathbf{X}}_0(\mathrm{i}\omega)\tilde{\mathbf{V}}$, the matrix $\tilde{\mathbf{V}}$ can be decomposed as $\tilde{\mathbf{V}} = \tilde{\mathbf{V}}^{\frac{1}{2}}\tilde{\mathbf{V}}^{\frac{1}{2}}$ (alternatively the Cholesky matrix of $\tilde{\mathbf{V}}$ may be employed). Next, the first trace in Eq. (2.87) is

considered, where the series representation of the matrix logarithm is used together with the invariance of the trace with respect to cyclic permutation yielding

$$\mathrm{Tr}\big[\ln\big(\mathbf{1}-\tilde{\mathbf{X}}_0(\mathrm{i}\omega)\tilde{\mathbf{V}}\big)\big] = \mathrm{Tr}\bigg[\sum_{n=1}^{\infty}\big(\tilde{\mathbf{X}}_0(\mathrm{i}\omega)\tilde{\mathbf{V}}^{\frac{1}{2}}\tilde{\mathbf{V}}^{\frac{1}{2}}\big)\bigg] \tag{2.141}$$

$$= \mathrm{Tr}\bigg[\sum_{n=1}^{\infty}\big(\tilde{\mathbf{V}}^{\frac{1}{2}}\tilde{\mathbf{X}}_0(\mathrm{i}\omega)\tilde{\mathbf{V}}^{\frac{1}{2}}\big)\bigg] \tag{2.142}$$

$$= \mathrm{Tr}\big[\ln\big(\mathbf{1}-\tilde{\mathbf{V}}^{\frac{1}{2}}\tilde{\mathbf{X}}_0(\mathrm{i}\omega)\tilde{\mathbf{V}}^{\frac{1}{2}}\big)\big] \tag{2.143}$$

Accordingly, the second trace in Eq. (2.87) can be expressed as $\mathrm{Tr}\big[\tilde{\mathbf{X}}_0(\mathrm{i}\omega)\tilde{\mathbf{V}}\big] = \mathrm{Tr}\big[\tilde{\mathbf{V}}^{\frac{1}{2}}\tilde{\mathbf{X}}_0(\mathrm{i}\omega)\tilde{\mathbf{V}}^{\frac{1}{2}}\big)\big]$. Next, the positive semi-definite matrix $-\tilde{\mathbf{V}}^{\frac{1}{2}}\tilde{\mathbf{X}}_0(\mathrm{i}\omega)\tilde{\mathbf{V}}^{\frac{1}{2}}$ is expressed in the spectral representation as

$$-\tilde{\mathbf{V}}^{\frac{1}{2}}\tilde{\mathbf{X}}_0(\mathrm{i}\omega)\tilde{\mathbf{V}}^{\frac{1}{2}} = \mathbf{V}_\sigma(\mathrm{i}\omega)\boldsymbol{\sigma}(\mathrm{i}\omega)\mathbf{V}_\sigma^\dagger(\mathrm{i}\omega) \tag{2.144}$$

where $\boldsymbol{\sigma}(\mathrm{i}\omega)$ denotes the eigenvalue matrix of the expression on the left-hand side and $\mathbf{V}_\sigma(\mathrm{i}\omega)$ the corresponding eigenvector matrix. Thus, the RPA correlation energy can now be expressed in terms of the eigenvalues $\boldsymbol{\sigma}(\mathrm{i}\omega)$ according to

$$E_\mathrm{c}^\mathrm{RPA} = \frac{1}{4\pi}\int_{-\infty}^{+\infty}\mathrm{d}\omega\ \mathrm{Tr}\big[\ln\big\{\mathbf{1}+\boldsymbol{\sigma}(\mathrm{i}\omega)\big\}-\boldsymbol{\sigma}(\mathrm{i}\omega)\big] \tag{2.145}$$

The σ-functional correlation energy is obtained by using the RPA correlation energy and adding an additional term[81,82]

$$E_\mathrm{c}^\sigma = \frac{1}{4\pi}\int_{-\infty}^{+\infty}\mathrm{d}\omega\ \big\{\mathrm{Tr}\big[\ln\big\{\mathbf{1}+\boldsymbol{\sigma}(\mathrm{i}\omega)\big\}-\boldsymbol{\sigma}(\mathrm{i}\omega)\big]-\mathrm{Tr}\big[H\big(\boldsymbol{\sigma}(\mathrm{i}\omega)\big)\big]\big\} \tag{2.146}$$

where $H\big(\boldsymbol{\sigma}(\mathrm{i}\omega)\big)$ is defined by cubic splines which are optimized using a set of benchmark datasets. A number of parametrizations exist for σ-functionals which are characterized by the setting of the optimization as well as the chosen benchmark sets.[80–82]

In **Publication V**, the σ-functional correlation energy expression was used as the starting point for the computation of NMR shielding tensors using numerical second-order derivatives within a finite-field approach.

2.7 Molecular Properties from Derivatives of the Energy

The computation of energy derivatives is of central importance in quantum chemistry as many molecular properties can be obtained directly from these derivatives. In this context, many properties can be defined as the response of the energy to a perturbation. The energy of a system subjected to a weak perturbation, characterized by the perturbation strength α, can be expanded in a Taylor series around $\alpha = 0$ according to[112]

$$E(\alpha) = E(0) + \frac{\partial E}{\partial\alpha}\bigg|_{\alpha=0}\lambda + \frac{1}{2}\frac{\partial^2 E}{\partial\alpha^2}\bigg|_{\alpha=0}\alpha^2 + \frac{1}{6}\frac{\partial^3 E}{\partial\alpha^3}\bigg|_{\alpha=0}\alpha^3 + \ldots \tag{2.147}$$

where the n^{th}-order property is defined by the n^{th}-order derivative of the energy $\frac{\partial^n E}{\partial \alpha^n}$. Furthermore, a system can also be subject to multiple perturbations, e.g., for two perturbations α and β, the Taylor expansion around $\alpha = 0$ and $\beta = 0$ of the multivariable function $E(\alpha, \beta)$ leads to[113]

$$E(\alpha,\beta) = E(0,0) + \left[\frac{\partial E}{\partial \alpha}\alpha + \frac{\partial E}{\partial \beta}\beta\right]_{\alpha=0,\beta=0} + \frac{1}{2}\left[\frac{\partial^2 E}{\partial \alpha^2}\alpha^2 + 2\frac{\partial^2 E}{\partial \alpha \partial \beta}\alpha\beta + \frac{\partial^2 E}{\partial \beta^2}\beta^2\right]_{\alpha=0,\beta=0} + \ldots \tag{2.148}$$

thus, giving rise to mixed derivatives.

Examples for such properties are the derivative of the energy with respect to the positions of the nuclei (nuclear gradients) and the mixed second derivative of the energy with respect to the nuclear magnetic moment and magnetic field yielding the NMR shielding tensor. Both properties are of central importance in quantum chemistry, and will be described in the next sections.

2.7.1 Analytical and Numerical Derivatives

Derivatives of the energy can be obtained either analytically, by differentiating the corresponding energy expression with respect to the perturbation(s), or by employing numerical techniques, where the energy is perturbed by an infinitesimal amount and the corresponding difference quotient is computed from this data. However, in practice, a finite difference has to be employed to avoid numerical instabilities, thus, decreasing the accuracy. Further, numerical derivatives are usually computationally much more demanding than analytical derivatives as it requires a number of energy calculations in the presence of the perturbation(s). Therefore, analytical derivatives are generally preferred.[114,115] However, in the absence of an analytical implementation, numerical approaches can be useful for benchmark studies since the computational implementation is usually straightforward.[114,115] An exception is perturbations of the magnetic field, which require the use of complex algebra due to the nature of the perturbation.[115] In **Publication V**, the accuracy of σ-functionals for the computation of NMR shielding parameters was investigated in detail using numerical second derivatives. The results of this investigation are crucial for determining the viability of implementing analytical second-order derivatives for σ-functionals.

2.7.2 Analytical Derivative Techniques

For the evaluation of the analytical derivative of a quantum chemical energy expression, there is a distinct difference between methods with variationally optimized wavefunctions, such as HF or multi-configurational self-consistent field (MCSCF), and nonvariational wavefunctions, e.g., MP2 or RPA. Thus, different techniques are required for their computation. In this context, the energy of a system can be expressed as[115]

$$E = E(\mathcal{R}, \mathcal{C}) \tag{2.149}$$

depending on an external parameter $\mathcal{R}$ representing a coordinate of the perturbation and the internal parameters summarized in the variable $\mathcal{C}$, which may also

implicitly depend on $\mathcal{R}$, i.e., $\mathcal{C}(\mathcal{R})$. The parameters $\mathcal{C}$ are determined within a quantum chemical approach for fixed $\mathcal{R}$, which are contained in the Hamiltonian of the corresponding method. E.g., in case of nuclear gradients within HF theory, $\mathcal{R}$ corresponds to a nuclear coordinate and $\mathcal{C}$ to the orbital coefficients. For the general case of Eq. (2.149) the derivative of the energy with respect to $\mathcal{R}$ can be expressed as

$$\frac{\mathrm{d}E(\mathcal{R},\mathcal{C}(\mathcal{R}))}{\mathrm{d}\mathcal{R}} = \frac{\partial E}{\partial \mathcal{R}} + \frac{\partial E}{\partial \mathcal{C}}\frac{\partial C}{\partial \mathcal{R}} \tag{2.150}$$

If the wavefunction is variationally optimized with respect to the internal parameters $\mathcal{C}$, the last term in the above equation vanishes. In this context it can further be shown that the n^{th}-order wavefunction response is required for the energy derivative of order $2n + 1$.[116] This concept is commonly referred to as the Wigner $2n + 1$ rule.[116] For methods with nonvariational wavefunctions, the first-order response with respect to $\mathcal{C}$ is required for the first-order derivative. However, by employing the Z-vector technique[117] only one response equation has to be solved as opposed to one response equation for each component of the perturbation. E.g., for a nuclear gradient, instead of $3N_{\text{at}}$ equations, only one response equation has to be solved. This is usually combined with the Lagrangian formulation,[118] where a Lagrange function is constructed which is fully variational in all parameters and leads to the same energy as the nonvariational energy expression. This formalism also requires the solution of only one response equation. The Lagrangian formalism has been employed in Ref. [34] for the computation of RPA nuclear gradients within the molecular orbital basis. For the RPA nuclear gradient expression within the atomic-orbital basis,[36] that forms the basis of **Publication II**, a different approach has been employed, as discussed in the next section.

2.8 Nuclear Gradients within the Random Phase Approximation

To compute the first-order derivative of the RPA energy with respect to a perturbation, the total RPA energy given by the sum of the Hartree–Fock energy functional evaluated with KS orbitals and the RPA correlation according to

$$E_{\text{total}}^{\text{RPA}}[\mathbf{P}] = E_{\text{HF}}[\mathbf{P}] + E_{\text{c}}^{\text{RPA}}[\mathbf{P}] \tag{2.151}$$

has to be differentiated. Since the electronic one-particle density matrix $\mathbf{P}$ that enters the energy expression stems from a preceding KS-DFT calculation, neither the HF functional nor the RPA correlation energy functional is stationary with respect to the KS orbitals. Thus, the first-order derivative requires the first-order response of the density matrix to the perturbation. As explained in the previous section, in this case the Z-vector technique can be applied for an efficient evaluation of the derivative. Differentiating the total RPA energy with respect to one nuclear coordinate denoted by x yields

$$\frac{\partial E_{\text{total}}^{\text{RPA}}}{\partial x} = \frac{\partial E_{\text{HF}}}{\partial x} + \frac{\partial E_{\text{c}}^{\text{RPA}}}{\partial x} \tag{2.152}$$

The derivative can be evaluated by employing partial derivatives of $E_\mathrm{c}^\mathrm{RPA}$ with respect to $\tilde{\mathbf{X}}_0(\mathrm{i}\omega), \tilde{\mathbf{V}}, \mathbb{B}$, and $\mathbf{G}_0(\mathrm{i}\tau)$ and considering the trace according to[36]

$$\begin{aligned}\frac{\partial E_\mathrm{c}^\mathrm{RPA}}{\partial x} = &\mathrm{Tr}\left(\int_0^{+\infty} \mathrm{d}\omega \frac{\partial E_\mathrm{c}^\mathrm{RPA}(\mathrm{i}\omega)}{\partial \tilde{\mathbf{X}}_0(\mathrm{i}\omega)} \frac{\partial \tilde{\mathbf{X}}_0(\mathrm{i}\omega)}{\partial \tilde{\mathbf{V}}} \frac{\partial \tilde{\mathbf{V}}}{\partial x}\right) \\ &+ \mathrm{Tr}\left(\int_0^{+\infty} \mathrm{d}\omega \frac{\partial E_\mathrm{c}^\mathrm{RPA}(\mathrm{i}\omega)}{\partial \tilde{\mathbf{X}}_0(\mathrm{i}\omega)} \frac{\partial \tilde{\mathbf{X}}_0(\mathrm{i}\omega)}{\partial \mathbb{B}} \frac{\partial \mathbb{B}}{\partial x}\right) \\ &+ \mathrm{Tr}\left(\int_{-\infty}^{+\infty} \mathrm{d}\omega \frac{\partial E_\mathrm{c}^\mathrm{RPA}(\mathrm{i}\omega)}{\partial \tilde{\mathbf{X}}_0(\mathrm{i}\omega)} \frac{\partial \tilde{\mathbf{X}}_0(\mathrm{i}\omega)}{\partial \mathbf{G}_0(\mathrm{i}\tau)} \frac{\partial \mathbf{G}_0(\mathrm{i}\tau)}{\partial x}\right)\end{aligned} \tag{2.153}$$

Here, the RPA correlation energy expression for one imaginary frequency is denoted as $E_\mathrm{c}^\mathrm{RPA}(\mathrm{i}\omega)$. Further, the AO-RI-RPA expression is considered in terms of real-valued orbitals. From the above equation, intermediate quantities can now be identified:

$$\frac{\partial E_\mathrm{c}^\mathrm{RPA}(\mathrm{i}\omega)}{\partial \tilde{\mathbf{X}}_0(\mathrm{i}\omega)} = -\frac{1}{4\pi} \tilde{\mathbf{W}}_\mathrm{c}(\mathrm{i}\omega) \tag{2.154}$$

$$\int_{-\infty}^{+\infty} \mathrm{d}\omega \ \frac{\partial E_\mathrm{c}^\mathrm{RPA}(\mathrm{i}\omega)}{\partial \tilde{\mathbf{X}}_0(\mathrm{i}\omega)} \frac{\partial \tilde{\mathbf{X}}_0(\mathrm{i}\omega)}{\partial \mathbf{G}_0(\mathrm{i}\tau)} = \int_{-\infty}^{+\infty} \mathrm{d}\tau \ \boldsymbol{\Sigma}(\mathrm{i}\tau) \tag{2.155}$$

with the correlated screened Coulomb interaction in the auxiliary basis $\tilde{\mathbf{W}}_\mathrm{c}(\mathrm{i}\omega)$ and the correlated self-energy in the imaginary time domain $\boldsymbol{\Sigma}(\mathrm{i}\tau)$ defined as

$$\tilde{\mathbf{W}}_\mathrm{c}(\mathrm{i}\omega) = \tilde{\mathbf{V}}\left[\left(\mathbf{1} - \tilde{\mathbf{X}}_0(\mathrm{i}\omega)\tilde{\mathbf{V}}\right)^{-1} - \mathbf{1}\right] \tag{2.156}$$

$$\Sigma_{\nu\lambda}(\mathrm{i}\tau) = -\sum_{PQ}^{N_\mathrm{aux}} \sum_{\mu\sigma}^{N_\mathrm{basis}} \tilde{W}_{\mathrm{c},PQ}(\mathrm{i}\tau) \mathbb{B}_{\mu\nu}^P G_{0,\mu\sigma}(\mathrm{i}\tau) \mathbb{B}_{\lambda\sigma}^Q; \quad \forall\ \tau \in [-\infty, +\infty] \tag{2.157}$$

The correlated screened Coulomb interaction in the imaginary time domain is defined by the Fourier transform

$$\tilde{\mathbf{W}}_\mathrm{c}(\mathrm{i}\tau) = \frac{1}{2\pi} \int_{-\infty}^{+\infty} \mathrm{d}\omega \ \exp(-\mathrm{i}\omega\tau) \tilde{\mathbf{W}}_\mathrm{c}(\mathrm{i}\omega) \tag{2.158}$$

Since only real-valued basis functions are considered in this section, the Fourier transform simplifies to a cosine transform as $\tilde{\mathbf{W}}_\mathrm{c}(\mathrm{i}\omega)$ is an even function in the $\mathrm{i}\omega$-domain[36]

$$\tilde{\mathbf{W}}_\mathrm{c}(\mathrm{i}\tau) = \frac{1}{2\pi} \int_0^{+\infty} \mathrm{d}\omega \ \cos(\omega\tau) \tilde{\mathbf{W}}_\mathrm{c}(\mathrm{i}\omega) \tag{2.159}$$

The evaluation of the first two terms on the right-hand side of Eq. (2.153) is not as involved, since it only requires integral derivatives. In contrast, the last term contains the derivative of the density matrix, which is more involved. It can be further expressed according to

$$\int_{-\infty}^{+\infty} \mathrm{d}\tau \ \boldsymbol{\Sigma}(\mathrm{i}\tau) \frac{\partial \mathbf{G}_0(\mathrm{i}\tau)}{\partial x} = \int_{-\infty}^{+\infty} \mathrm{d}\tau \ \boldsymbol{\Sigma}(\mathrm{i}\tau) \left(\frac{\partial \mathbf{G}_0(\mathrm{i}\tau)}{\partial \mathbf{h}_\mathrm{KS}} \frac{\partial \mathbf{h}_\mathrm{KS}}{\partial x} + \frac{\partial \mathbf{G}_0(\mathrm{i}\tau)}{\partial \mathbf{P}} \frac{\partial \mathbf{P}}{\partial x}\right) \tag{2.160}$$

The partial derivatives of the Green's functions can be obtained by expanding the exponential function in its series representation and subsequently differentiating the

corresponding expression.[36,119–121] Further, in the above expression the derivative of the occupied density matrix could be identified and isolated. It should be noted that the Green's function in the imaginary time domain can be expressed in terms of the occupied density for both, positive and negative imaginary times. For positive imaginary times, the Green's function depends on the virtual density matrix. However, the virtual density matrix can be expressed by the occupied density using the following identity

$$\mathbf{1} = \mathbf{PS} + \mathbf{P}_{\text{virt}}\mathbf{S} \tag{2.161}$$

$$\mathbf{P}_{\text{virt}} = \big(\mathbf{1} - \mathbf{PS}\big)\mathbf{S}^{-1} \tag{2.162}$$

Thus, only the derivative of the occupied density matrix is required.[119] Eq. (2.160) can be further summarized as

$$\int_{-\infty}^{+\infty} \mathrm{d}\tau\ \boldsymbol{\Sigma}(\mathrm{i}\tau)\left(\frac{\partial \mathbf{G}_0(\mathrm{i}\tau)}{\partial \mathbf{h}_{\text{KS}}}\frac{\partial \mathbf{h}_{\text{KS}}}{\partial x} + \frac{\partial \mathbf{G}_0(\mathrm{i}\tau)}{\partial \mathbf{P}}\frac{\partial \mathbf{P}}{\partial x}\right) = \mathbf{P}_{\text{RPA}}\frac{\partial \mathbf{h}_{\text{KS}}}{\partial x} + \mathbf{V}_{\text{RPA}}\frac{\partial \mathbf{P}}{\partial x} \tag{2.163}$$

The derivative of the HF functional in Eq. (2.151) can be obtain by tracing over the partial derivatives in an analogous manner, yielding

$$\frac{\partial E_{\text{HF}}}{\partial x} = E_{\text{HF}}^{(x)} + E_{\text{HF}}^{x} \tag{2.164}$$

where a shorthand notation for derivatives was introduced: the derivative of a quantity O with respect to a perturbation ξ is denoted by O^{ξ}. Further, to highlight that a derivative contains only integral derivatives and not the derivative of the density matrix the following notation is adopted $O^{(\xi)}$. The last term in the above equation can be expressed according to

$$E_{\text{HF}}^{x} = \mathrm{Tr}\big(\mathbf{H}_{\text{HF}}\mathbf{P}^{x}\big) \tag{2.165}$$

$$\mathbf{H}_{\text{HF}} = \mathbf{h} + \mathbf{J}[\mathbf{P}] + \mathbf{K}[\mathbf{P}] \tag{2.166}$$

Summarizing the derivative of the density matrix stemming from the derivative of the HF functional (Eq. (2.165)) and the RPA correlation energy part (Eq. (2.163)) yields[36]

$$\mathrm{Tr}\big([\mathbf{H}_{\text{HF}} + \mathbf{V}_{\text{RPA}}]\mathbf{P}^{x}\big) \tag{2.167}$$

This is now amendable to the Z-vector technique, where an AO-based formalism for the Z-vector approach is adopted.[119] In this context, the density matrix based Laplace transformed (DL) coupled-perturbed Kohn–Sham (CPKS) approach is utilized.[122] Further, for a low-scaling RPA gradient implementation the techniques introduced in section 2.5.5 can be applied, thus, reducing the formal $\mathcal{O}(M^4)$ scaling to an asymptotic $\mathcal{O}(M^2)$ scaling.[36]

The results from this section constitute the foundation of **Publication II**, where a formalism was derived for RPA gradients within the frozen-core approximation. Within the AO formalism, the frozen-core approximation is introduced through the density matrix used for the RPA correlation contribution. Thus, the total RPA energy is given within the frozen-core approximation according to

$$E_{\text{total}}^{\text{RPA}}[\mathbf{P}] = E_{\text{HF}}[\mathbf{P}] + E_{\text{c}}^{\text{RPA}}[\mathbf{P}_{\text{fc}}] \tag{2.168}$$

Here, the density matrix within the frozen-core approximation $\mathbf{P}_{\mathrm{fc}}$ does not contain contributions from core electrons and is defined according to

$$P_{\mathrm{fc},\mu\nu} = \sum_{i=N_{\mathrm{core}}}^{N_{\mathrm{occ}}} C_{\mu i} C_{\nu i} \tag{2.169}$$

where N_{core} denotes the number of core electrons. That is, the correlation of core electrons is neglected and only the contribution of valence electrons is considered. While the implementation of the frozen-core RPA energy expression is rather simple, the corresponding gradient implementation is very involved. In this context, the contribution of the response of the occupied and frozen-core density matrix has to be considered:

$$\mathrm{Tr}\big(\mathbf{H}_{\mathrm{HF}}\mathbf{P}^x + \mathbf{V}_{\mathrm{RPA}}\mathbf{P}^x_{\mathrm{fc}}\big) \tag{2.170}$$

An efficient method for the evaluation of the above equation is derived in **Publication II**.

2.9 Nuclear Magnetic Resonance Shielding Tensor within the Random Phase Approximation and σ-Functionals

The description of nuclear magnetic resonance phenomena with computational methods is accomplished by employing a phenomenological Hamiltonian [11,123]

$$\hat{H}^{\mathrm{NMR}} = -\sum_A \mathbf{m}^A(\mathbf{1} - \tilde{\boldsymbol{\sigma}}^A)\mathbf{B} + \frac{1}{2}\sum_{A\neq B} \mathbf{m}^A(\mathbf{D}^{AB} + \mathbf{J}^{AB})\mathbf{m}^B \tag{2.171}$$

that describes the effect of a perturbation of the nuclear magnetic moment of nucleus A, $\mathbf{m}^A$, and magnetic field, $\mathbf{B}$, on an electronic system, thus, reproducing the relevant interactions present in most NMR spectra.[123] In Eq. (2.171), $\tilde{\boldsymbol{\sigma}}^A$ represents the NMR shielding tensor, $\mathbf{D}^{AB}$ and $\mathbf{J}^{AB}$ are the dipolar and indirect nuclear spin-spin coupling tensors, respectively.[123] In the context of NMR spectra, $\mathbf{D}^{AB}$ and $\mathbf{J}^{AB}$ determine the magnitude of peak splitting that arise from the coupling of pairs of nuclei, while $\tilde{\boldsymbol{\sigma}}^A$ determines the shape and shift of the peak. From a physical point of view, $\tilde{\boldsymbol{\sigma}}^A$ describes how the applied field is altered by the electronic environment as perceived by the nuclear magnetic moment.[11,123] The focus in this work lies in the computation of the NMR shielding tensor, which will be described in the following.

The NMR shielding tensor can be obtained from the second mixed derivative of the energy E with respect to the nuclear magnetic moment $\mathbf{m}^A$, and the magnetic field $\mathbf{B}$, both evaluated at zero. Thus, one component of the NMR shielding tensor is given by

$$\tilde{\sigma}^A_{rs} = \frac{\partial^2}{\partial B_s \partial m^A_r} E\bigg|_{\mathbf{m}^A=\mathbf{0},\mathbf{B}=\mathbf{0}} \qquad \forall\, r,s \in \{x,y,z\} \tag{2.172}$$

However, for theoretical benchmark studies instead of the NMR shielding tensor, often the isotropic NMR shielding constants are studied, given by

$$\tilde{\sigma}^A_{\mathrm{iso}} = \frac{1}{3}\big(\tilde{\sigma}^A_{xx} + \tilde{\sigma}^A_{yy} + \tilde{\sigma}^A_{zz}\big) \tag{2.173}$$

as they can be observed (relative to some reference compound) by experiment in liquids. Isotropic NMR shielding constants were also employed for the benchmark studies in **Publication V**.

To insure gauge origin independence, gauge-including atomic orbitals (GIAOs)[42,43,124,125] are employed, defined as

$$\varphi_\mu(\mathbf{r},\mathbf{B}) = \varphi_\mu(\mathbf{r},\mathbf{B}=\mathbf{0})\exp\Big(-\frac{\mathrm{i}}{2}\big[\mathbf{B}(\mathbf{R}_\mu-\mathbf{R}_0)\big]\mathbf{r}\Big) \tag{2.174}$$

where $\varphi_\mu(\mathbf{r},\mathbf{B}=\mathbf{0})$ is the field-independent atomic-orbital basis function centered at $\mathbf{R}_\mu$, and $\mathbf{R}_0$ is the gauge origin. For the implementation of analytical derivatives all intermediates are either purely real or purely imaginary. Thus, the implementation does not require the utilization of complex matrix algebra routines. Instead, real valued matrices can be used; however, it should be considered that the matrix product of two imaginary matrices yields the square of the imaginary unit, thus leading to a prefactor of -1.

In the following, two approaches for the computation of the NMR shielding tensor at the RPA level of theory are presented: numerical derivatives,[55] employed for **Publication V**, and analytical derivatives subject of **Publication III** and **IV**.

2.9.1 Numerical Second-Order Derivatives

In **Publication V** an extensive benchmark study was conducted to investigate the accuracy of σ-functionals for the computation of isotropic NMR shielding constants using numerical second-order derivatives employing the approach of Ref. [55]. In this section the underlying equations are briefly summarized.

The computation of the NMR shielding tensor using a finite-field method requires various computations of the energy in the presence of perturbations of the magnetic field and nuclear magnetic moment, $E(\mathbf{B},\mathbf{m})$. One component of the NMR shielding tensor, e.g. $\tilde{\sigma}^A_{xy}$, can be computed according to[55,126]

$$\tilde{\sigma}^A_{xy} \approx \frac{1}{2m^A_y B_x}\big[E\big((B_x,0,0)^\mathrm{T},(0,m^A_y,0)^\mathrm{T}\big) - E\big((B_x,0,0)^\mathrm{T},(0,-m^A_y,0)^\mathrm{T}\big] \tag{2.175}$$

Next, both B_x and m^A_y can be set to a constant value of δ yielding

$$\tilde{\sigma}^A_{xy} \approx \frac{1}{2\delta^2}\big[E\big((\delta,0,0)^\mathrm{T},(0,\delta,0)^\mathrm{T}\big) - E\big((\delta,0,0)^\mathrm{T},(0,-\delta,0)^\mathrm{T}\big] \tag{2.176}$$

Using the above equations allows to compute the perturbed total RPA energy or σ-functional energy using GIAOs, which requires complex matrix algebra routines. Since this is usually not part of a quantum chemical program package, considerable implementation effort has to be spend for the implementation of numerical NMR shieldings. The implementation of Ref. [55] employs the MO-RI-RPA correlation energy expression in terms of complex-valued orbitals given by Eq. (2.87). This allowed the first extensive benchmark study on the accuracy of RPA for NMR shieldings; furthermore first results for σ-functionals were presented as well. In **Publication V** a more comprehensive benchmark study is conducted to investigate the accuracy of σ-functionals for the computation of NMR shielding tensors.

For RPA NMR shieldings, the good accuracy determined by the results of

Ref. [55] motivated the implementation of analytical NMR shielding tensors of **Publications III** and **IV**, thus extending the applicability of RPA NMR to larger systems. The next section presents the key concepts that contributed to the development of analytical second-order derivatives for RPA.

2.9.2 Analytical Second-Order Derivatives

The NMR shielding tensor within RPA can be obtained by taking the second mixed derivative of the total RPA energy given by Eq. (2.168) with respect to $\mathbf{m}^A$ and $\mathbf{B}$. The first derivative of the AO-RI-RPA correlation energy in terms of complex valued orbitals with respect to $\mathbf{m}^A$ reads

$$\frac{\partial E_\mathrm{c}^\mathrm{RPA}}{\partial \mathbf{m}^A} = \mathrm{Tr}\left(\int_{-\infty}^{+\infty} \mathrm{d}\omega \frac{\partial E_\mathrm{c}^\mathrm{RPA}(\mathrm{i}\omega)}{\partial \tilde{\mathbf{X}}_0(\mathrm{i}\omega)} \frac{\partial \tilde{\mathbf{X}}_0(\mathrm{i}\omega)}{\partial \mathbf{G}_0(\mathrm{i}\tau)} \frac{\mathbf{G}_0(\mathrm{i}\tau)}{\partial \mathbf{m}^A} \right) \tag{2.177}$$

As shown for the derivative with respect to a nuclear coordinate in Eq. (2.163), the above equation can be expressed in terms of the derivative of the KS-Hamiltonian and the density matrix according to

$$\frac{\partial E_\mathrm{c}^\mathrm{RPA}}{\partial \mathbf{m}^A} = \mathrm{Tr}\left(\mathbf{P}_\mathrm{RPA} \frac{\partial \mathbf{h}}{\partial \mathbf{m}^A} \right) + \mathrm{Tr}\left(\mathbf{V}_\mathrm{RPA} \frac{\partial \mathbf{P}}{\partial \mathbf{m}^A} \right) \tag{2.178}$$

Here, the derivative of the KS-Hamiltonian with respect to $\mathbf{m}^A$ reduces to the derivative of the core Hamiltonian $\mathbf{h}$, since the derivatives of the remaining terms evaluate to zero. Next, differentiating with respect to the magnetic field results in

$$\begin{aligned} \frac{\partial^2 E_\mathrm{c}^\mathrm{RPA}}{\partial \mathbf{B} \partial \mathbf{m}^A} = &\mathrm{Tr}\left(\frac{\partial \mathbf{P}_\mathrm{RPA}}{\partial \mathbf{B}} \frac{\partial \mathbf{h}}{\partial \mathbf{m}^A} \right) + \mathrm{Tr}\left(\mathbf{P}_\mathrm{RPA} \frac{\partial^2 \mathbf{h}}{\partial \mathbf{B} \partial \mathbf{m}^A} \right) + \mathrm{Tr}\left(\frac{\partial \mathbf{V}_\mathrm{RPA}}{\partial \mathbf{B}} \frac{\partial \mathbf{P}}{\partial \mathbf{m}^A} \right) \\ &+ \mathrm{Tr}\left(\mathbf{V}_\mathrm{RPA} \frac{\partial^2 \mathbf{P}}{\partial \mathbf{B} \partial \mathbf{m}^A} \right) \end{aligned} \tag{2.179}$$

At this point, the similarities between Laplace-transformed atomic-orbital MP2 NMR shieldings[127,128] can be leveraged. The general form of the second mixed derivative of Laplace-transformed atomic-orbital MP2 energy $E_\mathrm{c}^\mathrm{MP2}$ can be expressed as[128]

$$\begin{aligned} \frac{\partial^2 E_\mathrm{c}^\mathrm{MP2}}{\partial \mathbf{B} \partial \mathbf{m}^A} = &\mathrm{Tr}\left(\frac{\partial \mathbf{P}_\mathrm{MP2}}{\partial \mathbf{B}} \frac{\partial \mathbf{h}}{\partial \mathbf{m}^A} \right) + \mathrm{Tr}\left(\mathbf{P}_\mathrm{MP2} \frac{\partial^2 \mathbf{h}}{\partial \mathbf{B} \partial \mathbf{m}^A} \right) + \mathrm{Tr}\left(\frac{\partial \mathbf{V}_\mathrm{MP2}}{\partial \mathbf{B}} \frac{\partial \mathbf{P}}{\partial \mathbf{m}^A} \right) \\ &+ \mathrm{Tr}\left(\mathbf{V}_\mathrm{MP2} \frac{\partial^2 \mathbf{P}}{\partial \mathbf{B} \partial \mathbf{m}^A} \right) \end{aligned} \tag{2.180}$$

with the mixed second derivatives of $\mathbf{h}$ and $\mathbf{P}$ as well as intermediate quantities $\mathbf{P}_\mathrm{MP2}$ and $\mathbf{V}_\mathrm{MP2}$ and their magnetic field derivatives. Thus, for the computation of $\mathbf{P}^{\mathbf{B}\mathbf{m}^A}$ and $\mathbf{h}^{\mathbf{B}\mathbf{m}^A}$ the same strategies as used for MP2 can also be applied for RPA. Specifically, the nested Z-vector equations[127,128] for the efficient computation of the second derivative of the density matrix.

The quantities that remain to be evaluated are the magnetic field derivatives of the intermediates $\mathbf{P}_\mathrm{RPA}$ and $\mathbf{V}_\mathrm{RPA}$. Alongside this, the efficient evaluation of the second mixed derivative of the HF-energy together with the RPA correlation energy part to form the NMR shielding tensor at the RPA level of theory is subject of

Publication III. Further, in **Publication IV** an efficient and low-scaling RPA NMR implementation is presented, combining the results of **Publication III** with the techniques introduced in section 2.5.5. This extends the applicability of RPA NMR to even larger systems and allows an efficient and low-scaling computation.

Chapter 3

Publications

3.1 Publication I: Lagrangian-Based Minimal-Overhead Batching Scheme for the Efficient Integral-Direct Evaluation of the RPA Correlation Energy

V. Drontschenko, D. Graf, H. Laqua, C. Ochsenfeld
J. Chem. Theory Comput., **17**, 5623 (2021).

Abstract

A highly memory-efficient integral-direct random phase approximation (RPA) method based on our ω-CDGD-RI-RPA method [Graf, D. et al. *J. Chem. Theory Comput.* **2018**, *14*, 2505] is presented that completely alleviates the memory bottleneck of storing the multidimensional three-center integral tensor, which severely limited the tractable system sizes. Based on a Lagrangian formulation, we introduce an optimized batching scheme over the auxiliary and basis-function indices, which allows to compute the optimal number of batches for a given amount of system memory, while minimizing the batching overhead. Thus, our optimized batching constitutes the best tradeoff between program runtime and memory demand. Within this batching scheme, the half-transformed three-center integral tensor $B_{i\mu}^{M}$ is recomputed for each batch of auxiliary and basis functions. This allows the computation of systems that were out of reach before. The largest system within this work consists of a DNA fragment comprising 1052 atoms and 11 230 basis functions calculated on a single node, which emphasizes the new possibilities of our integral-direct RPA method.

JCTC Journal of Chemical Theory and Computation

pubs.acs.org/JCTC Article

Lagrangian-Based Minimal-Overhead Batching Scheme for the Efficient Integral-Direct Evaluation of the RPA Correlation Energy

Viktoria Drontschenko, Daniel Graf, Henryk Laqua, and Christian Ochsenfeld*

Cite This: *J. Chem. Theory Comput.* 2021, 17, 5623−5634 Read Online

ACCESS | Metrics & More | Article Recommendations

ABSTRACT: A highly memory-efficient integral-direct random phase approximation (RPA) method based on our ω-CDGD-RI-RPA method [Graf, D. et al. *J. Chem. Theory Comput.* **2018**, *14*, 2505] is presented that completely alleviates the memory bottleneck of storing the multidimensional three-center integral tensor, which severely limited the tractable system sizes. Based on a Lagrangian formulation, we introduce an optimized batching scheme over the auxiliary and basis-function indices, which allows to compute the optimal number of batches for a given amount of system memory, while minimizing the batching overhead. Thus, our optimized batching constitutes the best tradeoff between program runtime and memory demand. Within this batching scheme, the half-transformed three-center integral tensor $B_{i\mu}^{M}$ is recomputed for each batch of auxiliary and basis functions. This allows the computation of systems that were out of reach before. The largest system within this work consists of a DNA fragment comprising 1052 atoms and 11 230 basis functions calculated on a single node, which emphasizes the new possibilities of our integral-direct RPA method.

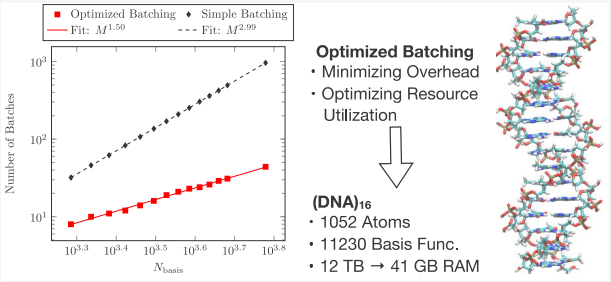

1. INTRODUCTION

Density-functional theory (DFT) has become one of the most applied theoretical techniques for electronic structure calculations of molecules,[1−3] surfaces,[4−6] and crystals[7−9] in the fields of solid-state physics, computational chemistry, and materials science.[10] Its remarkable success can be largely attributed to the excellent cost performance ratios and good accuracies for various properties and compounds, which make DFT applicable to systems containing up to several thousand atoms.[11,12] However, despite the vast benefits of DFT, it is subject to several well-known deficiencies. The accurate description of long-range electron correlation, particularly including van der Waals (vdW) interactions, represents a challenging task in the modeling of molecules and materials.[11,13−18] This makes the development of more broadly applicable correlation models a necessity.

The random phase approximation (RPA) is one of the most promising methods to obtain accurate correlation energies,[19,20] which is reflected by the increased interest over the last decades.[13,21−34] It yields a good description of bonding types, including covalent, ionic, and metallic bonding.[19] Additionally, due to its nonlocality, RPA correlation is able to describe vdW interactions exceptionally well.[35]

RPA is usually implemented as a post-Kohn−Sham method[36] and was first introduced by Bohm and Pines in 1953.[37] It was later formulated within the framework of DFT using the adiabatic-connection fluctuation-dissipation theorem.[20,38,39] However, in its original formulation, the calculation of RPA correlation energies scales as $O(M^6)$ with the system size M, limiting its applicability to systems comprising only tens of atoms. In 2010, Furche and co-workers introduced the resolution-of-the-identity (RI) approximation to RPA, reducing the scaling to $O(M^4)$.[27,40,41] This opened the way for applications beyond the few atoms scale. In 2016, Schurkus and Ochsenfeld[32] reformulated the RPA correlation energy in the atomic orbital (AO) space, thus extending the applicability of the RPA to molecules comprising thousands of atoms. Further improvements were introduced by Luenser et al.[33] and later by Graf et al.[34] by employing an attenuated Coulomb metric, Cholesky decomposition of the ground-state density matrix, and an improved quadrature for the cosine transform in the framework of the ω-CDGD-RI-RPA method.

Within the ω-CDGD-RI-RPA method, the most demanding step regarding the computational effort and memory requirements constitutes the calculation of the response function in the auxiliary basis. For this step, the half-transformed three-center integral tensor $B_{i\mu}^{M}$, whose storage requirements formally scale as $O(N_{\text{aux}}N_{\text{basis}}N_{\text{occ}})$ with the number of auxiliary

Received: May 18, 2021
Published: August 25, 2021

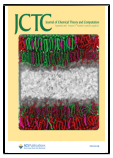

functions N_{aux}, AO basis functions N_{basis}, and occupied molecular orbitals (MOs) N_{occ}, has to be stored in memory. Consequently, when approaching large systems, the memory requirement of the three-center integral tensor easily exceeds the available system memory on a single computing node, thereby severely limiting the tractable system sizes. This memory bottleneck was previously addressed by Graf et al.[34] utilizing a hybrid parallelization scheme, thus reducing the memory requirements of the three-center integral tensor per node. However, depending on the targeted system size, this requires medium to large computing clusters. To avoid these demanding computing requirements, a method utilizing a single server or workstation, which is readily available in research groups, is desirable.

In this work, we introduce a Lagrange formulation for a minimal batching overhead and an optimal exploitation of computing resources. The memory-efficient integral-direct RPA method completely eliminates the storage bottleneck of the three-center integral tensor by computing the response function within an optimized batching scheme over both the auxiliary and AO basis-function index at the same time. The available system memory is utilized in the most efficient way and with minimal overhead. The three-center integral tensor is recomputed and transformed "on the fly" for only the respective batch (integral-direct), thereby reducing its memory requirement by a factor of $b_{aux}b_{AO}$, where b_{aux} denotes the number of auxiliary function batches and b_{AO} the number of AO basis-function batches. This redundant on the fly recomputation comes, however, at the cost of an increased program runtime. Hence, a compromise between memory demand and program runtime has to be made. In this context, the here presented optimized batching represents, by design, the optimal compromise requiring the smallest amount of recomputation, and consequently the lowest runtime, for any given amount of available system memory. In this way, our integral-direct RPA implementation extends the applicability of RPA to considerably larger systems.

This work is structured as follows: We begin with a brief review of the ω-CDGD-RI-RPA method in Section 2. Next, we derive a batching method for the calculation of the response function in Section 3. In this regard, we begin with the trivial approach of batching with respect to auxiliary functions in Section 3.1 and subsequently extend this batching scheme by additionally including batching over the AO basis functions and Laplace quadrature points in Section 3.2, where we arrive at the optimal batching formalism. We proceed to compare both batching methods in Section 3.3 and present calculations to support our considerations. In Section 4, we first establish why integral-direct RPA is best suited to reach very large systems by addressing two approaches typically used for the assessment of large integral tensors such as the three-center integrals, namely, the integral-direct approach and retrieving the three-center integrals from disk in Section 4.1. In Section 4.2, the scaling for integral-direct RPA is analyzed and systematically improved using shell pair and integral screening methods, sparse matrix algebra as well as switching from the Coulomb metric to the Coulomb metric attenuated by a complementary error function. Furthermore, calculations are presented to support our theoretical considerations. Computational details are given in Section 5 and the performance of our integral-direct RPA implementation is evaluated for chemically relevant systems in Section 6. Finally, the conclusion and outlook are presented in Section 7.

2. ω-CDGD-RI-RPA THEORY

In this section, we intend to give a brief overview of the theory underlying the ω-CDGD-RI-RPA method.[34] For a more detailed derivation, we refer the reader to previous publications.[27,32−34,40,41]

Throughout, the following notation has been adopted: μ, ν, λ, and σ denote atomic orbitals (AOs); i and j refer to occupied molecular orbitals (MOs); a and b refer to virtual MOs; $\underline{i}$ and $\underline{j}$ denote Cholesky orbitals, and M, N, P, and Q denote auxiliary functions. The number of auxiliary functions is represented by N_{aux}, the number of AO basis functions by N_{basis}, the number of Laplace quadrature points by N_τ, and the numbers of occupied and virtual MOs by N_{occ} and N_{virt}, respectively. For two-, three-, and four-center integrals, the Mulliken notation is used. Furthermore, Einstein's sum convention[42] is employed. The spin index is dropped for convenience and matrix operations are to be taken before indexing in this work.

The total energy of the electronic ground state can be expressed within the adiabatic-connection formalism[39] as[20,38]

$$E = E_h[\{\phi_{KS}\}] + E_J[\{\phi_{KS}\}] + E_X[\{\phi_{KS}\}] + E_C \tag{1}$$

where E_h, E_J, and E_X denote the one-electron, Coulomb, and exact exchange energies, respectively. An expression for the correlation energy[24] E_C can be derived by applying the zero-temperature fluctuation-dissipation theorem and the RPA[34] as well as the RI approximation[27,40,41]

$$E_C = \frac{1}{2\pi}\int_0^{+\infty} d\omega \mathrm{Tr}[\ln(\mathbf{1}-\mathbf{X}_0(i\omega)\mathbf{V}) + \mathbf{X}_0(i\omega)\mathbf{V}] \tag{2}$$

with the electron−electron interaction operator in the auxiliary basis

$$V_{MN} = (M|m_{12}|P)^{-1}(P|r_{12}^{-1}|Q)(Q|m_{12}|N)^{-1} \tag{3}$$

where m_{12} denotes the RI metric and r_{12} the interelectronic distance. $\mathbf{X}_0$ represents the noninteracting density−density response function in the auxiliary basis in the zero-temperature case.[43] For efficiency reasons, the response function is calculated in the imaginary time domain according to[29,34]

$$X_{0,MN}(i\tau) = \mathrm{Tr}[\underline{\mathbf{G}}_0(-i\tau)\mathbf{B}^M\bar{\mathbf{G}}_0(i\tau)\mathbf{B}^N] \tag{4}$$

$$X_{0,MN}(i\tau) = \underline{G}_{0,\mu\nu}(-i\tau)B^M_{\nu\lambda}\bar{G}_{0,\lambda\sigma}(i\tau)B^N_{\sigma\mu} \tag{5}$$

with the one-particle Green's function in the imaginary time domain

$$\mathbf{G}_0(i\tau) = \Theta(-i\tau)\underline{\mathbf{G}}_0(i\tau) + \Theta(i\tau)\bar{\mathbf{G}}_0(i\tau) \tag{6}$$

$$\underline{\mathbf{G}}_{0,\mu\nu}(i\tau) = C_{\mu i}C_{\nu i}\exp(-(\epsilon_i - \epsilon_F)\tau) \tag{7}$$

$$\bar{\mathbf{G}}_{0,\mu\nu}(i\tau) = -C_{\mu a}C_{\nu a}\exp(-(\epsilon_a - \epsilon_F)\tau) \tag{8}$$

where $C_{\mu i}$ and $C_{\mu a}$ denote the occupied and unoccupied MO coefficients, respectively, and ϵ_F the Fermi level. The three-center integral matrix $\mathbf{B}^M$ is given by

$$B^M_{\nu\lambda} = (\nu\lambda|m_{12}|M) \tag{9}$$

A drawback of AO compared to MO formulations is the increased scaling with the size of the atom-centered basis. However, this drawback can be addressed by utilizing pivoted Cholesky decomposition of density-type matrices, thereby reintroducing the occupied index.[33] Furthermore, a memory-

https://doi.org/10.1021/acs.jctc.1c00494
J. Chem. Theory Comput. 2021, 17, 5623−5634

efficient expression for $\mathbf{X}_0(\mathrm{i}\tau)$ can be obtained using the idempotency relation of the ground-state density matrix $\mathbf{P}$

$$\mathbf{P} = \mathbf{PSP} \tag{10}$$

with the two-center overlap matrix $\mathbf{S}$, and the analogous expression for the one-particle Green's function in the negative imaginary time domain

$$\underline{\mathbf{G}}_0(-\mathrm{i}\tau) = \underline{\mathbf{G}}_0(-\mathrm{i}\tau)\mathbf{SP} \tag{11}$$

leading to[34]

$$X_{0,MN}(\mathrm{i}\tau) = \mathrm{Tr}[\mathbf{L}^{\mathrm{T}}\mathbf{S}\underline{\mathbf{G}}_0(-\mathrm{i}\tau)\mathbf{S}\mathbf{L}\underline{\mathbf{L}}^{\mathrm{T}}\mathbf{B}^M\overline{\mathbf{G}}_0(\mathrm{i}\tau)\mathbf{B}^N\mathbf{L}] \tag{12}$$

$$X_{0,MN}(\mathrm{i}\tau) = \underline{G}_{0,\underline{j}\,\underline{i}}(-\mathrm{i}\tau)B^M_{\underline{i}\nu}\overline{G}_{0,\nu\mu}(\mathrm{i}\tau)B^N_{\mu\underline{j}} \tag{13}$$

where the pivoted Cholesky factorization of a matrix $\mathbf{A}$ is abbreviated by $\mathbf{A} = \mathbf{LL}^{\mathrm{T}}$. Each $\mathbf{B}^M$ is precontracted with the Cholesky factor $\mathbf{L}$ of the occupied one-particle density $\mathbf{P}$, which is independent of the Laplace points. This reduces the memory requirement for storing the three-center integrals from $(N_{\mathrm{aux}}N^2_{\mathrm{basis}})$ to $(N_{\mathrm{aux}}N_{\mathrm{basis}}N_{\mathrm{occ}})$. The final expression for $\mathbf{X}_0(\mathrm{i}\tau)$ reads

$$X_{0,MN}(\mathrm{i}\tau) = B^M_{\underline{j}\mu}(\mathrm{i}\tau)B^N_{\mu\underline{j}} \tag{14}$$

with

$$B^M_{\underline{j}\mu}(\mathrm{i}\tau) = \underline{G}_{0,\underline{j}\,\underline{i}}(-\mathrm{i}\tau)B^M_{\underline{i}\nu}\overline{G}_{0,\nu\mu}(\mathrm{i}\tau) \tag{15}$$

and the transformed three-center integrals[32−34]

$$B^N_{\mu\underline{j}} = B^N_{\mu\nu}L_{\nu\underline{j}} \tag{16}$$

From here on, we will refer to the transformed three-center integrals $B^N_{\mu\underline{i}}$ (eq 16) also as the three-center integrals.

After obtaining the response function in the imaginary time domain, it is transformed into the imaginary frequency domain with a contracted double-Laplace[32,34] or cosine transform[44] according to

$$\mathbf{X}_0(\mathrm{i}\omega) = \int_{-\infty}^{+\infty} \mathrm{d}\tau\, \cos(\omega\tau)\mathbf{X}_0(\mathrm{i}\tau) \tag{17}$$

The ω-CDGD-RI-RPA method scales formally as $O(N^2_{\mathrm{aux}}N_{\mathrm{basis}}N_{\mathrm{occ}} \propto M^4)$; it can, however, be implemented in an asymptotically linear scaling fashion.[34]

3. MINIMAL-OVERHEAD BATCHING

Within the calculation of the RPA correlation energy, the most demanding step in terms of memory requirements is the calculation of the response function in the imaginary time domain. The response function $\mathbf{X}_0(\mathrm{i}\tau)$ is calculated within the standard algorithm according to eq 14 for one Laplace point at a time. Therefore, the Laplace point-dependent three-center integrals $B^M_{\underline{j}\mu}(\mathrm{i}\tau)$ as well as the three-center integrals $B^N_{\mu\underline{i}}$ have to be stored in memory, which requires $(2N_{\mathrm{aux}}N_{\mathrm{basis}}N_{\mathrm{occ}})$ memory. Further, taking into account the memory requirements of the response function with dimensions $(N_{\mathrm{aux}} \times N_{\mathrm{aux}} \times N_\tau)$, it becomes apparent that for large systems the memory requirements easily exceed the available system memory on a workstation or server. Thus, to overcome the limiting storage requirements within the calculation of the response function, a batching algorithm is necessary.

In this section, we first derive a simple batching method where only batching over the auxiliary function index is employed. Subsequently, we increase the complexity of our batching method by additionally batching over the AO basis-function index as well as the Laplace quadrature points. For the latter method, we derive an expression for the optimal number of batches using a Lagrange formalism. Finally, we compare both algorithms in terms of their scaling behavior and present computational results supporting our theoretical studies. Please note that we use the def2-SVP basis set for the calculations in this and the subsequent section (Sections 3 and 4) for illustration purposes only. Since our objective is to, first, demonstrate the scaling with the system size, the completeness of the basis set is not relevant in this context. However, for practical applications, where the objective is to obtain high-quality results, larger basis sets are typically required, which are presented in Section 6.

3.1. Trivial Batching.

In the following, we introduce the approach of batching over the auxiliary function index, which we will refer to as trivial batching. The pseudocode for this implementation is shown in Algorithm 1.

Algorithm 1 Trivial Batching

```
1:  for aux-batch1 do
2:    for M ∈ aux-batch1 do
3:      read/recalculate B^M_{j̲ν}   ∀j̲, ν
4:      for all τ do
5:        B^M_{i̲μ}(iτ) = G̲_{0,i̲j̲}(−iτ) B^M_{j̲ν} Ḡ_{0,νμ}(iτ)   ∀i̲, μ
6:      end for
7:    end for
8:    for aux-batch2 ≥ aux-batch1 do
9:      for N ∈ aux-batch2 do
10:       read/recalculate B^N_{i̲μ}   ∀i̲, μ
11:     end for
12:     for all τ do
13:       for M ∈ aux-batch1 do
14:         for N ∈ aux-batch2 do
15:           X_{0,MN}(iτ) = B^M_{i̲μ}(iτ) B^N_{i̲μ}
16:         end for
17:       end for
18:     end for
19:   end for
20:   for M ∈ aux-batch1 do
21:     for all τ do
22:       write on disk X_{0,MN}(iτ)   ∀N
23:     end for
24:   end for
25: end for
```

In the context of index batching, reading from disk or recomputing from scratch are analogous. That is, both variants yield a given set of tensor elements at a cost that is proportional to the amount of requested elements. Thus, the two possible variants for accessing the three-center integrals, namely, reading or recalculating (lines 3 and 10) both require the same batching and can therefore be discussed separately in Section 4.

In Algorithm 1, first, the tensor elements of the three-center integrals $B^M_{\underline{j}\nu}$ are accessed for one auxiliary function within the respective auxiliary batch (aux-batch) (line 3) and subsequently used to compute $B^M_{\underline{j}\mu}(\mathrm{i}\tau)$ (line 5). Next, within the second aux-batch loop (line 8), the tensor elements of the three-center integrals $B^N_{\underline{i}\mu}$ are accessed for a second time (line 10) and subsequently contracted with $B^M_{\underline{i}\mu}(\mathrm{i}\tau)$ for each Laplace point τ to form $X_{0,MN}(\mathrm{i}\tau)$ (line 15). Please note that, due to the symmetry of the response function, only $\frac{b'_{\mathrm{aux}}+1}{2}$ aux-batches are considered for the second aux-batch loop (line 8), where b'_{aux} denotes the number of aux-batches. Further, for performance reasons, the operations in line 5 as well as lines 13−17 are implemented as matrix multiplications to utilize the high performance of dense matrix algebra routines provided by

https://doi.org/10.1021/acs.jctc.1c00494
J. Chem. Theory Comput. 2021, 17, 5623−5634

basic linear algebra subroutine (BLAS) libraries. To further reduce the memory requirements of the algorithm, the response function is written on disk (line 22) by batching over the first auxiliary function index. However, the storage of the response function only becomes problematic for extremely large systems, since the memory demand scales as $O(M^2)$ compared to the $O(M^3)$ scaling of the three-center integral tensor.

3.2. Optimized Batching. In this section, we extend the trivial batching algorithm: First, in addition to batching with respect to auxiliary functions, we also incorporate batching with respect to basis functions as well as Laplace points. Second, we use the method of Lagrange multipliers to minimize the number of three-center integral tensor accesses for a given amount of available memory. This allows the optimal utilization of the available memory with minimal overhead. Thus, we refer to this batching algorithm as optimized batching. The pseudocode for the optimized batching algorithm is shown in Algorithm 2.

Algorithm 2 Optimized Batching

```
1: for aux-batch1 do
2:   for AO-batch do
3:     for τ-batch do
4:       for M ∈ aux-batch1 do
5:         read/recalculate B^M_{j̲ν}   ∀j̲, ν
6:         for τ ∈ τ-batch do
7:           B^M_{j̲μ'}(iτ) = G̲_{0,j̲j̲}(−iτ) B^M_{j̲ν} G̅_{0,νμ'}(iτ)   ∀j̲, μ' ∈ AO-batch
8:         end for
9:       end for
10:      for aux-batch2 ≥ aux-batch1 do
11:        for N ∈ aux-batch2 do
12:          read/recalculate B^N_{j̲μ'}   ∀j̲, μ' ∈ AO-batch
13:        end for
14:        for τ ∈ τ-batch do
15:          for M ∈ aux-batch1 do
16:            for N ∈ aux-batch2 do
17:              X_{0,MN}(iτ) += B^M_{j̲μ'}(iτ) B^N_{j̲μ'}
18:            end for
19:          end for
20:        end for
21:      end for
22:    end for
23:  end for
24:  for M ∈ aux-batch1 do
25:    for all τ do
26:      write on disk X_{0,MN}(iτ)   ∀N
27:    end for
28:  end for
29: end for
```

In this work, the following abbreviations are introduced: The number of aux-batches is denoted by b_{aux}, the number of AO-batches by b_{AO}, and the number of τ-batches by b_τ. Please note that b_{aux} denotes the number of aux-batches within the optimized batching, while b'_{aux} represents the number of aux-batches within the trivial batching algorithm. Further, the following approximations are used for simplicity: The number of auxiliary functions in an aux-batch is given by $\frac{N_{\text{aux}}}{b_{\text{aux}}}$, the number of basis functions in an AO-batch by $\frac{N_{\text{basis}}}{b_{\text{AO}}}$, and the number of Laplace points in a τ-batch is given by $\frac{N_\tau}{b_\tau}$. Please note that within this approximation, the number of functions in the respective batches constitutes a rational number; therefore, it needs to be rounded down to an integer for practical applications. For large systems, however, this rounding makes little difference.

In Algorithm 2, the most prominent changes compared to the trivial batching in Algorithm 1 include the loop over the basis-function batches ranging from lines 2 to 23. Accordingly, $B^M_{j\mu'}(i\tau)$ (line 7) and $B^N_{j\mu'}$ (line 12) show decreased memory requirements, considering the batched aux- and basis-function index. Further, $B^M_{j\mu'}(i\tau)$ (line 7) as well as $X_{0,MN}(i\tau)$ (line 17) are evaluated for one τ-batch.

In Table 1, the memory requirements for an implementation without any batching, the trivial batching, as well as the optimized batching scheme are compared. It follows that the memory requirements of the largest quantities within the response function calculation can be significantly reduced by employing either of the batching schemes. However, the optimized batching scheme provides a larger range of batching configurations for the same ratio, while for the trivial batching there is only one possibility to achieve a specific ratio.

As seen in Algorithm 1 (lines 3 and 10) and Algorithm 2 (lines 5 and 12), each element $B^M_{j\mu}$ needs to be read/recalculated redundantly. Therefore, the reduced memory requirements come at the cost of a batching overhead, which is proportional to the number of batches. Consequently, a minimal amount of batches is required to minimize the batching overhead for a fixed amount of the available system memory. This can be achieved by employing the method of Lagrange multipliers. Please note that for the rest of this section we will refer to the amount of redundant integral reads or recalculations more generally as redundant integral tensor accesses.

Therefore, the rest of this section is structured as follows: At first, an expression for the number of redundant integral tensor element accesses is derived, followed by an expression for the constraint function. Subsequently, the number of redundant tensor accesses is minimized with respect to the number of

Table 1. Largest Quantities within the Response Function Calculation with Their Respective Memory Requirements for an Implementation without Any Batching, the Trivial Batching Algorithm (Algorithm 1), and the Optimized Batching Algorithm (Algorithm 2)[a]

quantity	memory			ratio	
	not batched[b]	trivial[c]	optimized[d]	trivial	optimized
$B^M_{j\mu}(i\tau)$	$N_{\text{occ}}N_{\text{aux}}N_{\text{basis}}$	$\frac{N_{\text{aux}}}{b'_{\text{aux}}}N_{\text{basis}}N_{\text{occ}}N_\tau$	$\frac{N_{\text{aux}}}{b_{\text{aux}}}\frac{N_{\text{basis}}}{b_{\text{AO}}}\frac{N_\tau}{b_\tau}N_{\text{occ}}$	$\frac{N_\tau}{b'_{\text{aux}}}$	$\frac{N_\tau}{b_{\text{aux}}b_{\text{AO}}b_\tau}$
$B^N_{j\mu}$	$N_{\text{aux}}N_{\text{basis}}N_{\text{occ}}$	$\frac{N_{\text{aux}}}{b'_{\text{aux}}}N_{\text{basis}}N_{\text{occ}}$	$\frac{N_{\text{aux}}}{b_{\text{aux}}}\frac{N_{\text{basis}}}{b_{\text{AO}}}N_{\text{occ}}$	$\frac{1}{b'_{\text{aux}}}$	$\frac{1}{b_{\text{aux}}b_{\text{AO}}}$
$X_{0,MN}(i\tau)$	$N_{\text{aux}}N_{\text{aux}}N_\tau$	$\frac{N_{\text{aux}}}{b'_{\text{aux}}}N_{\text{aux}}N_\tau$	$\frac{N_{\text{aux}}}{b_{\text{aux}}}N_{\text{aux}}N_\tau$	$\frac{1}{b'_{\text{aux}}}$	$\frac{1}{b_{\text{aux}}}$

[a]The ratio of the memory for the trivial batching and optimized batching algorithm to an algorithm without any batching is given for each quantity. For illustrative purposes, all tensors are represented by their tensor elements. [b]Evaluated according to eq 14 per Laplace point. [c]Evaluated according to Algorithm 1. [d]Evaluated according to Algorithm 2.

https://doi.org/10.1021/acs.jctc.1c00494
J. Chem. Theory Comput. 2021, 17, 5623−5634

aux-, AO-, and τ-batches using the method of Lagrange multipliers to comply with the constraint.

3.2.1. Number of Integral Tensor Accesses. According to Algorithm 2, the number of integral tensor accesses $N'_{\mathrm{acc}}(b_{\mathrm{aux}}, b_{\mathrm{AO}}, b_\tau)$ for the elements of $B^M_{j\nu}$ (line 5) is given by

$$N'_{\mathrm{acc}}(b_{\mathrm{aux}}, b_{\mathrm{AO}}, b_\tau) = b_{\mathrm{AO}} b_\tau N_{\mathrm{aux}} N_{\mathrm{basis}} N_{\mathrm{occ}} \tag{18}$$

and the number of integral tensor accesses N''_{acc} for $B^{N}_{j\mu'}$ (line 12) is given by

$$N''_{\mathrm{acc}}(b_{\mathrm{aux}}, b_{\mathrm{AO}}, b_\tau) = \frac{b_{\mathrm{aux}}+1}{2} b_\tau N_{\mathrm{aux}} N_{\mathrm{basis}} N_{\mathrm{occ}} \tag{19}$$

where the term $\frac{b_{\mathrm{aux}}+1}{2}$ stems from exploiting the symmetry of the response function in line 10. The total number of integral tensor accesses $N^{\mathrm{total}}_{\mathrm{acc}}(b_{\mathrm{aux}}, b_{\mathrm{AO}}, b_\tau)$ can be obtained by adding eqs 18 and 19, which leads to

$$N^{\mathrm{total}}_{\mathrm{acc}}(b_{\mathrm{aux}}, b_{\mathrm{AO}}, b_\tau) = \bar{N} b_\tau \left(\frac{b_{\mathrm{aux}}+1}{2} + b_{\mathrm{AO}} \right) \tag{20}$$

with

$$\bar{N} = N_{\mathrm{aux}} N_{\mathrm{basis}} N_{\mathrm{occ}} \tag{21}$$

3.2.2. Constraint Function. The constraint function $C(b_{\mathrm{aux}}, b_{\mathrm{AO}}, b_\tau)$ can be expressed as

$$C(b_{\mathrm{aux}}, b_{\mathrm{AO}}, b_\tau) = \mathrm{mem}_{\mathrm{avail}} - \mathrm{mem}_{\mathrm{req}}(b_{\mathrm{aux}}, b_{\mathrm{AO}}, b_\tau) = 0 \tag{22}$$

where $\mathrm{mem}_{\mathrm{avail}}$ denotes the available system memory and $\mathrm{mem}_{\mathrm{req}}(b_{\mathrm{aux}}, b_{\mathrm{AO}}, b_\tau)$ the memory required for the algorithm. For the latter, the relevant quantities that have to be stored in memory during the algorithm are shown along with their memory requirements in Table 2. Please note that the memory requirements of the batched response function are not considered in Table 2 since its size is not significant as explained in Section 3.1. Using Table 2, $\mathrm{mem}_{\mathrm{req}}(b_{\mathrm{aux}}, b_{\mathrm{AO}}, b_\tau)$ can be written as

Table 2. Quantities That have to be Stored in Memory during the Calculation of the Response Function with Their Respective Memory Requirements[a]

quantity	memory
$B^M_{j\mu'}(\mathrm{i}\tau)$	$\frac{N_{\mathrm{aux}}}{b_{\mathrm{aux}}}\frac{N_{\mathrm{basis}}}{b_{\mathrm{AO}}}\frac{N_\tau}{b_\tau}N_{\mathrm{occ}}$
$B^N_{j\mu'}$	$\frac{N_{\mathrm{aux}}}{b_{\mathrm{aux}}}\frac{N_{\mathrm{basis}}}{b_{\mathrm{AO}}}N_{\mathrm{occ}}$
$\underline{G}_{0,\mu\nu}(-\mathrm{i}\tau)$	$N^2_{\mathrm{basis}}\, N_\tau$
$\overline{G}_{0,\mu\nu}(\mathrm{i}\tau)$	$N^2_{\mathrm{basis}}\, N_\tau$
V_{MN}	N^2_{aux}

[a]For illustrative purposes, all tensors are represented by their tensor elements. Note that $B^M_{j\mu'}(\mathrm{i}\tau)$ and $B^N_{j\mu'}$ are evaluated within Algorithm 2, lines 7 and 12, respectively.

$$\mathrm{mem}_{\mathrm{req}}(b_{\mathrm{aux}}, b_{\mathrm{AO}}, b_\tau) = \frac{N_{\mathrm{aux}}}{b_{\mathrm{aux}}}\frac{N_{\mathrm{basis}}}{b_{\mathrm{AO}}}N_{\mathrm{occ}}\left(\frac{N_\tau}{b_\tau}+1\right) + N^2_{\mathrm{aux}} + 2N^2_{\mathrm{basis}}N_\tau \tag{23}$$

$$\mathrm{mem}_{\mathrm{req}}(b_{\mathrm{aux}}, b_{\mathrm{AO}}, b_\tau) = \frac{\bar{N}}{b_{\mathrm{aux}} b_{\mathrm{AO}}}\left(\frac{N_\tau}{b_\tau}+1\right) + \overline{\overline{N}} \tag{24}$$

with

$$\overline{\overline{N}} = N^2_{\mathrm{aux}} + 2N^2_{\mathrm{basis}}N_\tau \tag{25}$$

By inserting eq 24 into eq 22, the constraint function can be expressed as

$$C(b_{\mathrm{aux}}, b_{\mathrm{AO}}, b_\tau) = \overline{\mathrm{mem}}_{\mathrm{avail}} - \frac{\bar{N}}{b_{\mathrm{aux}} b_{\mathrm{AO}}}\left(\frac{N_\tau}{b_\tau}+1\right) = 0 \tag{26}$$

where

$$\overline{\mathrm{mem}}_{\mathrm{avail}} = \mathrm{mem}_{\mathrm{avail}} - \overline{\overline{N}} \tag{27}$$

3.2.3. Minimizing the Number of Integral Tensor Accesses using the Method of Lagrange Multipliers. To obtain the optimal number of batches, the total number of integral tensor accesses $N^{\mathrm{total}}_{\mathrm{acc}}$ (eq 20) has to be minimized with respect to the number of aux-, AO-, and τ-batches, while not exceeding the available memory. The Lagrange function hence reads

$$\mathcal{L}(b_{\mathrm{aux}}, b_{\mathrm{AO}}, b_\tau, \lambda) = N^{\mathrm{total}}_{\mathrm{acc}}(b_{\mathrm{aux}}, b_{\mathrm{AO}}, b_\tau) - \lambda C(b_{\mathrm{aux}}, b_{\mathrm{AO}}, b_\tau) \tag{28}$$

where λ denotes the Lagrange multiplier. Inserting the expression for $N^{\mathrm{total}}_{\mathrm{acc}}$ according to eq 20 and $C(b_{\mathrm{aux}}, b_{\mathrm{AO}}, b_\tau)$ according to eq 26 yields

$$\mathcal{L}(b_{\mathrm{aux}}, b_{\mathrm{AO}}, b_\tau, \lambda) = \bar{N} b_\tau \left(\frac{b_{\mathrm{aux}}+1}{2} + b_{\mathrm{AO}}\right) - \lambda\left(\overline{\mathrm{mem}}_{\mathrm{avail}} - \frac{\bar{N}}{b_{\mathrm{aux}} b_{\mathrm{AO}}}\left(\frac{N_\tau}{b_\tau}+1\right)\right) \tag{29}$$

Partial differentiation of eq 29 with respect to b_{aux}, b_{AO}, and λ gives the first-order conditions for the minimization

$$\frac{\partial \mathcal{L}}{\partial b_{\mathrm{aux}}} = \frac{\bar{N}}{2} b_\tau - \lambda\left(\frac{\bar{N}}{b^2_{\mathrm{aux}} b_{\mathrm{AO}}}\left(\frac{N_\tau}{b_\tau}+1\right)\right) \overset{!}{=} 0 \tag{30}$$

$$\frac{\partial \mathcal{L}}{\partial b_{\mathrm{AO}}} = \bar{N} b_\tau - \lambda\frac{\bar{N}}{b_{\mathrm{aux}} b^2_{\mathrm{AO}}}\left(\frac{N_\tau}{b_\tau}+1\right) \overset{!}{=} 0 \tag{31}$$

$$\frac{\partial \mathcal{L}}{\partial \lambda} = -\overline{\mathrm{mem}}_{\mathrm{avail}} + \frac{\bar{N}}{b_{\mathrm{aux}} b_{\mathrm{AO}}}\left(\frac{N_\tau}{b_\tau}+1\right) + \frac{N^2_{\mathrm{aux}}}{b_{\mathrm{aux}}}\frac{N_\tau}{b_\tau} \overset{!}{=} 0 \tag{32}$$

To obtain a relation between b_{aux} and b_{AO}, eq 31 can be rewritten as

$$\bar{N} b_\tau = \lambda\frac{\bar{N}}{b_{\mathrm{aux}} b^2_{\mathrm{AO}}}\left(\frac{N_\tau}{b_\tau}+1\right) \tag{33}$$

and inserted into eq 30, which leads to the following relation

$$b_{\mathrm{AO}} = \frac{1}{2} b_{\mathrm{aux}} \tag{34}$$

An expression for b_{aux} can be obtained by inserting eq 34 into eq 32 according to

$$\overline{\mathrm{mem}}_{\mathrm{avail}} - \frac{2\bar{N}}{b^2_{\mathrm{aux}}}\left(\frac{N_\tau}{b_\tau}+1\right) = 0 \tag{35}$$

leading to

https://doi.org/10.1021/acs.jctc.1c00494
J. Chem. Theory Comput. 2021, 17, 5623−5634

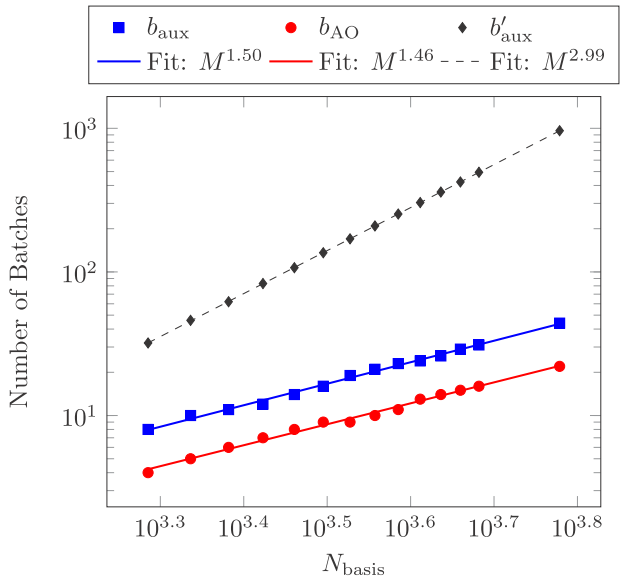

Figure 1. Log−log plot of the number of aux-batches b_{aux} and AO-batches b_{AO} for the optimized batching and number of aux-batches b'_{aux} for the trivial batching against the number of basis functions. In addition, the scaling fits are given. Note that for illustrative purposes, mem_{avail} = 10 GB as well as $\overline{\overline{N}} = 0$ (eq 25) was used.

$$b_{aux} = \pm\sqrt{2}\sqrt{\bar{N}\left(\frac{N_\tau}{b_\tau} + 1\right)\frac{1}{\overline{mem}_{avail}}} \tag{36}$$

However, eq 36 is still dependent on b_τ. To derive an expression for b_τ, eq 34 can be inserted into eq 29

$$\mathcal{L}(b_{aux}, b_\tau, \lambda) = \bar{N}b_\tau\left(b_{aux} + \frac{1}{2}\right) - \lambda\left(\overline{mem}_{avail} - \frac{2\bar{N}}{b_{aux}^2}\left(\frac{N_\tau}{b_\tau} + 1\right)\right) \tag{37}$$

and using eq 36 leads to

$$\mathcal{L}(b_\tau) = \bar{N}\sqrt{2}\sqrt{\frac{\bar{N}}{\overline{mem}_{avail}}b_\tau(N_\tau + b_\tau)} + \frac{1}{2}\bar{N}b_\tau \tag{38}$$

Equation 38 is minimized if b_τ is minimal. Therefore, it follows that

$$b_\tau = 1 \tag{39}$$

Inserting eq 39 into eq 36, the final expression for b_{aux} reads

$$b_{aux} = \sqrt{2}\sqrt{\frac{\bar{N}}{\overline{mem}_{avail}}(N_\tau + 1)} \tag{40}$$

$$b_{aux} = \sqrt{2}\sqrt{\frac{N_{aux}N_{basis}N_{occ}}{\overline{mem}_{avail}}(N_\tau + 1)} \quad \propto O(M^{3/2}) \tag{41}$$

and b_{AO} can be written using the relation in eq 34 as

$$b_{AO} = \frac{1}{\sqrt{2}}\sqrt{\frac{\bar{N}}{\overline{mem}_{avail}}(N_\tau + 1)} \tag{42}$$

$$b_{AO} = \frac{1}{\sqrt{2}}\sqrt{\frac{N_{aux}N_{basis}N_{occ}}{\overline{mem}_{avail}}(N_\tau + 1)} \quad \propto O(M^{3/2}) \tag{43}$$

It follows from eqs 41 and 43 that the number of batches scales as $O(M^{3/2})$ or, equivalently, $O(M^{1.5})$ with the system size and $O(mem_{avail}^{-0.5})$ with respect to the available system memory, since the number of Laplace points N_τ is independent of the system size.

To summarize the results of the optimization, the optimal setting employs one τ-batch containing all Laplace points (eq 39), there are twice as many aux-batches as AO-batches (eq 34), and the number of batches scales as $O(mem_{avail}^{-0.5})$ with respect to the available system memory and $O(M^{1.5})$ with respect to the system size (eqs 41 and 43).

3.3. Comparing the Optimized Batching and the Trivial Batching. In the following, the scaling behavior for the number of batches as well as the number of integral tensor accesses is analyzed for the trivial and the optimized batching.

3.3.1. Number of Batches. In the context of optimizing the batch sizes, the previously introduced trivial batching scheme can be regarded as a nonoptimal variant, where b_{AO} and b_τ were set equal to 1. Thus, for the trivial batching, the number of aux-batches b'_{aux} can be obtained using the constraint function in eq 26. Setting b_{AO} and b_τ equal to 1 leads to

$$C(b'_{aux}) = \overline{mem}_{avail} - \frac{\bar{N}}{b'_{aux}}(N_\tau + 1) = 0 \tag{44}$$

Rewriting eq 44 gives the optimal number of aux-batches b'_{aux}

$$b'_{aux} = \frac{\bar{N}}{\overline{mem}_{avail}}(N_\tau + 1) \tag{45}$$

For the trivial batching, the optimal number of batches grows as $O(M^{3.0})$, while the optimized batching shows a more favorable scaling of $O(M^{1.5})$ (eqs 41 and 43).

To verify these theoretical considerations, we first carried out calculations on simple linear *n*-alkanes of increasing size using the def2-SVP basis set.[45−47] In Figure 1, a log−log plot of the numbers of aux- and AO-batches against the number of

https://doi.org/10.1021/acs.jctc.1c00494
J. Chem. Theory Comput. 2021, 17, 5623−5634

AO basis functions is shown. The obtained scaling behavior is in very good agreement with the theoretical scaling. The fluctuations around the optimized batching arise solely from the rounding of the batch dimension to the nearest lower integer.

3.3.2. Number of Integral Tensor Accesses. The scaling behavior for both batching algorithms can be obtained using the expression for the number of integral tensor accesses in eq 20 and inserting the expression for the optimized number of batches.

For the optimized batching, we insert the expressions for b_{aux} (eq 41), b_{AO} (eq 43), and b_τ (eq 39) leading to

$$N_{\text{acc}}^{\text{opt}}(b_{\text{aux}}, b_{\text{AO}}, b_\tau) = \bar{N}\sqrt{2}\sqrt{\frac{\bar{N}}{\overline{\text{mem}}_{\text{avail}}}(N_\tau + 1)} + \frac{\bar{N}}{2} \tag{46}$$

It follows that the number of integral tensor accesses grows as $O(M^{4.5})$.

Analogously, for the trivial batching, the number of integral tensor accesses N'_{acc} can be obtained by inserting b'_{aux} (eq 45) into eq 20 as well as setting b_{AO} and b_τ equal to 1, resulting in

$$N_{\text{acc}}^{\text{triv}} = \frac{\bar{N}^2}{\overline{\text{mem}}_{\text{avail}}}(N_\tau + 1) + \frac{3}{2}\bar{N} \tag{47}$$

For the trivial batching, the number of integral tensor accesses thus grows as $O(M^{6.0})$.

In Figure 2, the corresponding log−log plot of the number of integral tensor accesses against the number of AO basis functions is shown for the trivial and the optimized batching, which confirms the theoretical scaling of $O(M^{4.5})$ for the optimized batching (eq 46) and $O(M^{6.0})$ for the trivial batching (eq 47).

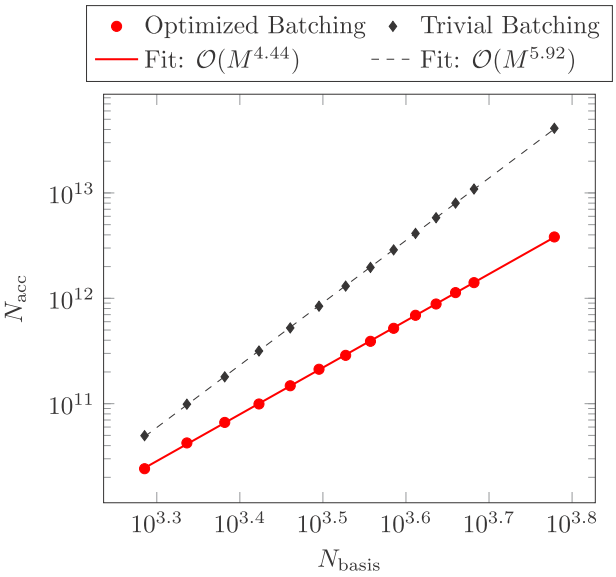

Figure 2. Log−log plot of the number of integral tensor accesses N_{acc} for the optimized batching and the trivial batching against the number of basis functions. In addition, the scaling fits are given. Note that for illustrative purposes, $\text{mem}_{\text{avail}}$ = 10 GB as well as $\overline{\overline{N}} = 0$ (eq 25) was uesd.

In conclusion, the optimized batching shows a more favorable scaling with respect to the number of batches as well as the number of integral tensor accesses compared to the trivial batching. Since the number of integral tensor accesses is proportional to the batching overhead, we can also conclude that our optimized batching is more effective in reducing the batching overhead than the trivial batching. Especially when aiming for very large systems requiring a high number of batches, the advantages of our optimized batching become apparent. In essence, the optimized batching represents the best compromise between program runtime and demand for system memory.

4. INTEGRAL-DIRECT RPA

As mentioned in Section 3.1, there are two approaches for accessing the elements of the three-center integral tensor $B^M_{i\mu}$, namely, reading and recomputing (Algorithm 1, lines 3 and 10 and Algorithm 2, lines 5 and 12). In this section, we will first compare both approaches and establish why integral-direct RPA (recomputation) is best suited for the computation of very large systems. We will then analyze the scaling behavior for integral-direct RPA and systematically improve upon it.

4.1. Hard-Disk IO vs On the Fly Computation of the three-center Integrals. For the first approach to access the elements of the three-center integrals, the integrals are stored on disk and the tensor elements $B^M_{i\mu}$ are read into memory in batches. Thus, the batching overhead is determined by the amount of input/output operations on a physical disk (disk I/O). However, since the three-center integrals with dimensions ($N_{\text{aux}} \times N_{\text{basis}} \times N_{\text{occ}}$) have to be stored on disk, the algorithm is limited by the available disk space. The storage limitation problem can be overcome entirely using an integral-direct scheme for the three-center integrals, which we will refer to as integral-direct RPA.

In Table 3, both approaches as well as an implementation without any batching are compared with regard to the feasible system size. To this end, the memory and disk space requirements for all methods are shown for different system sizes using the def2-SVP basis set.[45−47] Please note again that we use this basis set for illustration purposes only. Further, to demonstrate the scope of the methods from a practical viewpoint, it is noted whether the respective system is accessible on a computing node using 200 GB of memory space and 2500 GB of disk space. As expected, when reading the three-center integrals from disk, we are able to access much larger system sizes than without utilizing any batching, since this approach is not limited by the available system memory. However, this shifts the bottleneck to the disk space requirements such that storing the three-center integrals becomes the limiting factor and, therefore, larger systems are not accessible. In contrast to that, integral-direct RPA opens the way to access all listed systems, since this method is not limited by the disk space requirements of the three-center integral tensor. Within integral-direct RPA, only the response function has to be stored on disk. However, the response function with dimensions ($N_{\text{aux}} \times N_{\text{aux}} \times N_\tau$) is orders of magnitude smaller than the three-center integral tensor with dimensions ($N_{\text{aux}} \times N_{\text{basis}} \times N_{\text{occ}}$). Thus, it does not constitute the limiting factor for the systems shown in Table 3.

4.2. Scaling. The calculation of the response function comprises four major steps: The computation of the three-center integrals in the AO basis $B^M_{\mu\nu}$ and its subsequent

https://doi.org/10.1021/acs.jctc.1c00494
J. Chem. Theory Comput. 2021, 17, 5623−5634

Table 3. Required Memory and Disk Space for Various Systems Utilizing an Implementation without any Batching (NB) and the Reading Variant of the RPA Batching Routine (Read) as well as the Integral-Direct RPA (Int-Dir)[a]

	memory (GB)		disk space (GB)		accessibility[f]		
system	NB[b,c]	Read/Int-Dir[c]	Read[d,e]	Int-Dir[d]	NB	Read	Int-Dir
$C_{100}H_{202}$	96.3	1.6	50.3	6.1	√	√	√
$C_{110}H_{222}$	127.1	2.0	66.2	7.3	√	√	√
$C_{120}H_{242}$	163.8	2.4	85.1	8.7	√	√	√
$C_{130}H_{262}$	207.0	2.8	107.2	10.2	×	√	√
$C_{300}H_{602}$	1177.9	15.0	608.6	54.2	×	√	√
$C_{400}H_{802}$	2373.3	26.6	1221.5	96.3	×	√	√
$C_{500}H_{1002}$	4145.3	41.6	2127.1	150.4	×	√	√
$C_{600}H_{1202}$	9123.7	59.8	4640.2	216.5	×	×	√
$C_{1000}H_{2002}$	62 189.4	166.1	31 312.2	601.1	×	×	√
$(DNA)_4$	183.4	2.5	95.5	9.9	√	√	√
$(DNA)_8$	1488.3	10.2	759.6	41.0	×	√	√
$(DNA)_{16}$	11 987.0	41.4	6056.1	166.5	×	×	√

[a]Note that the disk space requirements for an implementation without batching are not shown, since no quantities are stored on disk. Further, it is assessed whether the respective system is accessible, employing either method on a computing node using 200 GB of memory space and 2500 GB of disk space. [b]For storing $B_{j\mu}{}^{M}(i\tau)$ per Laplace point (eq 14). [c]For storing $\underline{G}_{0,\mu\nu}(-i\tau)$, $\overline{G}_{0,\mu\nu}(i\tau)$, and V_{MN} (Table 2). [d]For storing the response function. [e]For storing the three-center integrals. [f]Memory: 200 GB; disk space: 2500 GB.

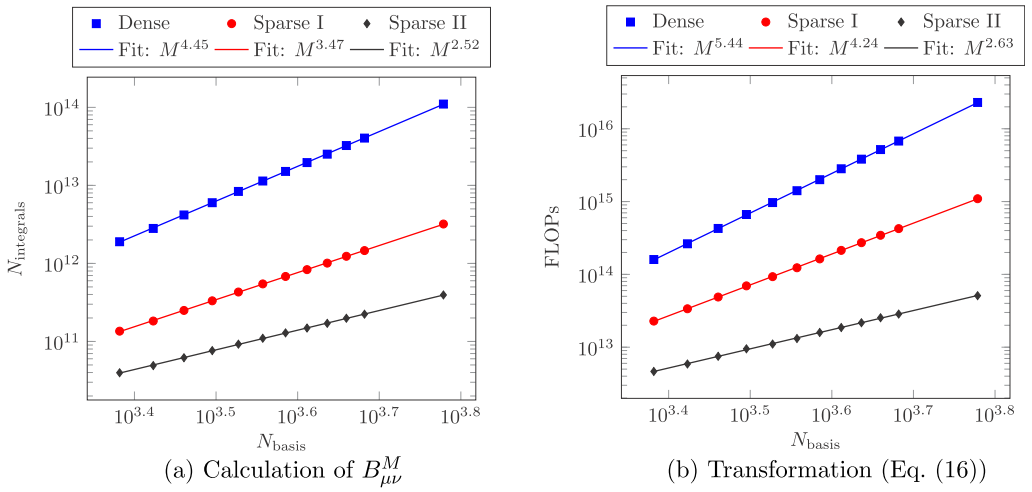

(a) Calculation of $B^{M}_{\mu\nu}$ (b) Transformation (Eq. (16))

Figure 3. Log−log plots of the number of calculated primitive integrals $N_{\text{integrals}}$ against the number of basis functions (a) and the number of FLOPs needed for the transformation of the three-center integrals (b). In addition, the scaling fits are given. Note that for illustrative purposes, $\text{mem}_{\text{avail}}$ = 10 GB as well as $\overline{\overline{N}} = 0$ (eq 25) was used.

transformation (eq 16) as well as the matrix multiplications to obtain $B^{M}_{j\mu}(i\tau)$ (eq 15) and $X_{0,MN}(i\tau)$ (eq 14).

4.2.1. Without Batching. When no batching is employed, the calculation of the three-center integrals $B^{M}_{\mu\nu}$ formally scales as $O(N_{\text{aux}}N^{2}_{\text{basis}} \propto M^{3.0})$, while the transformation shows an $O(N_{\text{aux}}N^{2}_{\text{basis}}N_{\text{occ}} \propto M^{4.0})$ scaling. The matrix multiplications both scale as $O(M^{4.0})$. As mentioned in Section 2, the calculation of the response function can also be implemented in an asymptotically linear scaling fashion,[34] which, however, will not be discussed further in this work.

4.2.2. Dense. When there is not enough available system memory, batching has to be employed (integral-direct RPA). Please note that for our integral-direct RPA implementation, we use dense matrix algebra and hence presently do not aim for linear scaling. Our method could also be implemented using sparse matrix algebra; however, this would significantly complicate the determination of optimal batch sizes since the exact memory demand is not known a priori in case of sparse matrices.

Within integral-direct RPA, the response function is calculated in the batching routine (Algorithm 2), where the three-center integral tensor is recomputed on the fly. The recomputation (lines 5 and 12) is comprised of the computation of the three-center integrals in the AO basis $B^{M}_{\mu\nu}$ and the subsequent transformation with the Cholesky factor of the occupied one-particle density matrix (eq 16) for each batch only. It follows that the formal scaling for the computation of $B^{M}_{\mu\nu}$ as well as the transformation is increased by a factor of $O(M^{1.5})$, which accounts for the scaling with respect to the numbers of batches (eqs 41 and 43). The scaling for the matrix multiplications in lines 7 and 17, however, remains unchanged since it is independent of the batching as can be deduced from Algorithm 2. Thus, within integral-direct RPA, the integral calculation formally scales as $O(M^{4.5})$ and the transformation as $O(M^{5.5})$. To confirm these considerations, we carried out

https://doi.org/10.1021/acs.jctc.1c00494
J. Chem. Theory Comput. 2021, 17, 5623−5634

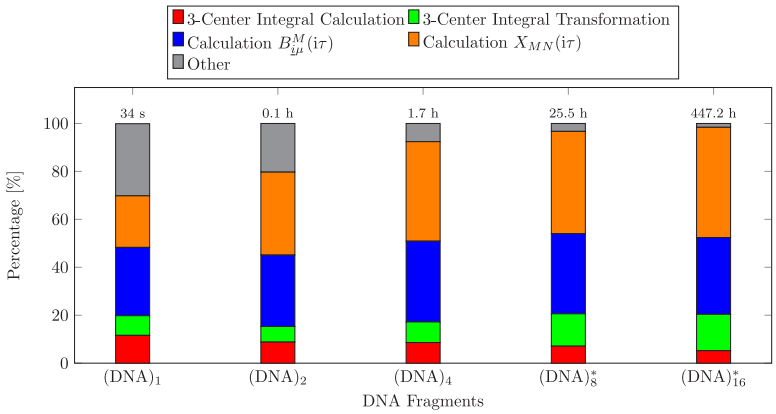

Figure 4. Contributions to the total time for the integral-direct calculation of the RPA correlation energy for DNA fragments using the def2-SVP basis set. Specifically, timings for the following operations are shown: three-center integral calculation (Algorithm 2, lines 5 and 12), three-center integral transformation (Algorithm 2, lines 5 and 12), calculation of $B^M_{i\mu}(i\tau)$ (Algorithm 2, line 7), and calculation of $X_{MN}(i\tau)$ (Algorithm 2, line 17). Systems that are marked with an asterisk (*) can only be computed using our integral-direct RPA method since the memory requirements for the unbatched variant would exceed the available system memory.

calculations on linear *n*-alkanes of increasing size using the def2-SVP basis set.[45−47] The results are summarized in Figure 3 in the blue graphs (denoted by "Dense"), where a log−log plot of the number of primitive integral calculations against the number of basis functions (a) as well as a log−log plot of the numbers of floating point operations (FLOPs) needed for the transformation of the three-center integrals against the number of basis functions (b) are shown.

4.2.3. Sparse I. Due to the exponential decay of the overlapping Gaussian-type basis functions of the charge distribution $(\mu\nu)$, the number of significant three-center integrals $B^M_{\mu\nu}$ scales asymptotically only as $O(M^{3.5})$ with a relatively early onset of the reduced scaling (only a few Ångström coupling distance between the AO basis functions μ and ν). Furthermore, the sparsity of $(\mu\nu)$ can also be exploited in the transformation of the three-center integrals using block-sparse matrix multiplication. This reduces the scaling for the calculation and transformation by a factor of M, leading to an asymptotic scaling of $O(M^{3.5})$ for the calculation and $O(M^{4.5})$ for the transformation. To verify this, we edited the code of our implementation by incorporating shell pair screening for the integral calculation and using sparse matrix algebra for the transformation, where we only exploit the sparsity of the charge distribution $(\mu\nu)$. The results are summarized in the red graphs (denoted by "Sparse I") in Figure 3. It can be observed that the obtained scaling for the calculation (Figure 3a) and the transformation (Figure 3b) are in good agreement with the theoretical scaling.

4.2.4. Sparse II. The scaling for the calculation can be further reduced by employing the Coulomb metric attenuated by the complementary error function (see eq 9 with $m_{12} = \frac{\mathrm{erfc}(\omega_{\mathrm{att}} r_{12})}{r_{12}}$), which decreases the range of coupling between the charge distribution $(\mu\nu)$ and the auxiliary functions. This reduces the asymptotic scaling for the calculation of the three-center integrals $B^M_{\mu\nu}$ to $O(M^{2.5})$. Furthermore, the scaling for the transformation of the three-center integrals can be reduced by additionally exploiting the sparsity of the Cholesky factor, leading to an asymptotic $O(M^{2.5})$ scaling. For our implementation, we switched to the Coulomb metric attenuated by the complementary error function with the attenuation parameter w_{att} = 0.1 a.u.[33] and used the approximate integral partition bounds (aIPBs)[48] developed by our group for screening the three-center integral computation. The results are shown in the black graphs (denoted by "Sparse II") in Figure 3.

To summarize, within integral-direct RPA, the computation of $B^M_{\mu\nu}$ scales formally as $O(M^{4.5})$, the subsequent transformation as $O(M^{5.5})$, albeit with a small prefactor depending on the available system memory, and the matrix multiplications for obtaining $B^M_{i\mu}(i\tau)$ (line 7) and $X_{0,MN}(i\tau)$ (line 17) scale formally as $O(M^{4.0})$. However, the scaling for the calculation and transformation of the three-center integral tensor can be reduced to $O(M^{2.5})$ by employing shell pair screening, a local metric for the three-center integral tensor, and integral screening, as well as using sparse matrix algebra for the transformation of the three-center integrals. As a result, these redundant on the fly recomputations of the three-center integrals do not represent a significant bottleneck compared to the computation of $B^M_{i\mu}(i\tau)$ (line 7) and $X_{0,MN}(i\tau)$ (line 17) in practice.

5. COMPUTATIONAL DETAILS

Our new integral-direct RPA method was implemented in the FermiONs++ program package.[49−51] The Kohn−Sham orbitals used for the RPA energy calculations were obtained by preceding DFT calculations employing the generalized gradient approximation of Perdew, Burke, and Ernzerhof (PBE).[52,53] The atomic basis sets def2-SVP and def2-QZVP are used.[45,46] The RI approximation, which is applied to the four-center integrals in the correlation part of the RPA energy, employs the corresponding auxiliary basis sets[47,54] with the attenuated Coulomb metric and the attenuation parameter ω_{att} = 0.1 a.u.[33] For the Laplace expansion, 13−15 quadrature points were used.[34] All calculations were carried out on an Intel Xeon E5-2667 processor using 16 threads.

6. PERFORMANCE

In the following, we investigate the performance of our integral-direct RPA method by considering the contribution of the batching overhead to the total computation time. In respect thereof, we calculated DNA fragments of increasing

https://doi.org/10.1021/acs.jctc.1c00494
J. Chem. Theory Comput. 2021, 17, 5623−5634

size. To obtain physically meaningful energies, we carried out calculations using the def2-QZVP basis set, which has shown to yield very accurate results within RPA.[13,27,32−34,55−58] Furthermore, for illustration purposes, we carried out calculations using the def2-SVP basis set to compute large systems in a reasonable amount of time.

In Figure 4, the contributions of the most time-consuming operations to the overall time are shown for DNA fragments using the def2-SVP basis set. The timings for the integral calculation and transformation as well as its contribution to the total time are considerably lower and grow less rapidly with increased system size as compared to the calculation of $B^M_{i\mu}(i\tau)$ (line 7) and $X_{MN}(i\tau)$ (line 17). It follows that the timings for the calculation and transformation observed for the largest systems in Figure 4 are a direct consequence of exploiting the sparsity of the system as explained in Section 4. Thus, the contribution of the batching overhead is relatively low and the total computation time is dominated by the calculation of $B^M_{i\mu}(i\tau)$ (Algorithm 2, line 7) and $X_{MN}(i\tau)$ (Algorithm 2 line 17).

In Figure 5, the corresponding results for DNA fragments using the def2-QZVP basis set are shown. Without batching

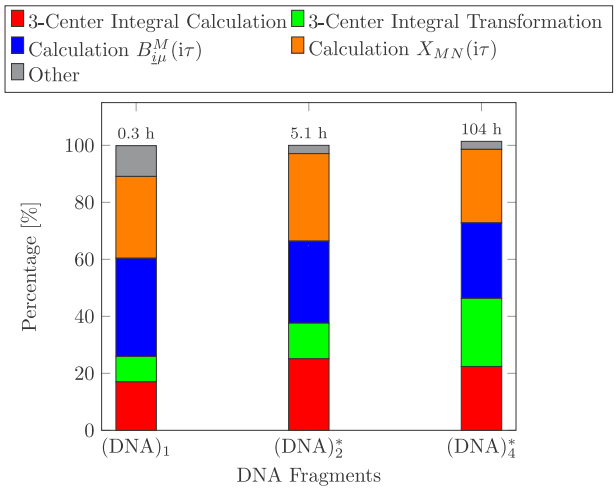

Figure 5. Contributions to the total time for the integral-direct calculation of the RPA correlation energy for DNA fragments using the def2-QZVP basis set. Specifically, timings for the following operations are shown: three-center integral calculation (Algorithm 2, lines 5 and 12), three-center integral transformation (Algorithm 2, lines 5 and 12), calculation of $B^M_{i\mu}(i\tau)$ (Algorithm 2, line 7), and calculation of $X_{MN}(i\tau)$ (Algorithm 2, line 17). Systems that are marked with an asterisk (*) can only be computed using our integral-direct RPA method, since the memory requirements for the unbatched variant would exceed the available system memory.

(integral-direct RPA), we would only be able to compute $(DNA)_1$, since for larger systems the memory demand for the unbatched variant already exceeds the available system memory. In contrast, using the def2-SVP basis (Figure 4), systems up to $(DNA)_4$ were accessible without batching. Consequently, our integral-direct RPA method is of even higher relevance for large basis set calculations (which are required to obtain high-quality results in practice), where the memory limitation problem (which our proposed batching solves in an optimized fashion) already emerges for much smaller molecules. The timings shown in Figure 5 indicate that the calculation of the three-center integrals is considerably more demanding compared to the def2-SVP basis set results (Figure 4). For larger basis sets, the three-center integrals $B^M_{\mu\nu}$ show less sparsity and thus the computational cost increases since shell pair screening and integral screening methods cannot significantly decrease the number of significant elements for the present systems.

7. CONCLUSIONS AND OUTLOOK

We presented a memory-efficient integral-direct RPA algorithm based on our ω-CDGD-RI-RPA method by employing an optimized batching scheme, which, by construction via a Lagrangian formalism, allows for the most effective utilization of the available system memory, while minimizing the number of three-center integral tensor calculations.

We showed that our optimized batching scheme over the auxiliary and basis functions is able to minimize the batching overhead for a given amount of memory considerably better than an implementation where only batching with respect to auxiliary functions is employed by considering their scaling behavior with the system size M. For our optimized batching, the number of batches, which are proportional to the batching overhead, scale only as $O(M^{1.5})$, which is a considerable improvement compared to the $O(M^{3.0})$ scaling for a simple batching implementation over the auxiliary functions only. Furthermore, we have shown that the utilization of an integral-direct scheme for the three-center integral tensor, as opposed to reading the three-center integrals from disk, completely alleviates the storage bottleneck of the three-center integral tensor, thereby allowing the calculation of large systems, which were previously intractable. For the performance assessment of our integral-direct RPA method, we calculated DNA fragments of increasing size, showing that the batching overhead has a relatively small contribution on the total time. In this regard, we calculated the DNA fragment $(DNA)_{16}$ comprised of 1052 atoms and 11 230 basis functions.

In the future, our method could in principle be extended to asymptotically linear scaling schemes using sparse matrix algebra. However, for the computation of the optimized number of batches, the precise sparsity of the relevant matrices has to be known beforehand, which is only determined at program runtime, so that efficient estimates will be required.

Moreover, it has been shown that significant performance gains can be obtained by porting computer-intensive code to the graphics processing unit (GPU). However, special algorithms are necessary for the optimal exploitation of the scarce memory resources of GPUs as well as to reduce the high-cost data transfer between the GPU and the central processing unit (CPU). Our integral-direct RPA method is able to address both challenges: We compute the optimal amount of batches for a given amount of GPU memory. Further, all quantities needed for the computation of the response function could be computed directly on the GPU, thereby minimizing the data transfer between the GPU and CPU. Since the computation of the response function is the computationally most expensive part of the total calculation, significant performance gains are expected by porting our integral-direct RPA algorithm to the GPU.

Lastly, we would like to emphasize the applicability of the underlying concepts of our integral-direct RPA method (such as the derivation of the optimized batching method using the

https://doi.org/10.1021/acs.jctc.1c00494
J. Chem. Theory Comput. 2021, 17, 5623−5634

method of Lagrange multipliers) to related correlation methods such as SOS-MP2 and Coupled-Cluster variants.

AUTHOR INFORMATION

Corresponding Author

Christian Ochsenfeld − *Chair of Theoretical Chemistry, Department of Chemistry, University of Munich (LMU), 81377 Munich, Germany; Max Planck Institute for Solid State Research, D-70569 Stuttgart, Germany;* orcid.org/0000-0002-4189-6558; Email: christian.ochsenfeld@cup.uni-muenchen.de

Authors

Viktoria Drontschenko − *Chair of Theoretical Chemistry, Department of Chemistry, University of Munich (LMU), 81377 Munich, Germany*

Daniel Graf − *Chair of Theoretical Chemistry, Department of Chemistry, University of Munich (LMU), 81377 Munich, Germany*

Henryk Laqua − *Chair of Theoretical Chemistry, Department of Chemistry, University of Munich (LMU), 81377 Munich, Germany*

Complete contact information is available at: https://pubs.acs.org/10.1021/acs.jctc.1c00494

Notes

The authors declare no competing financial interest.

ACKNOWLEDGMENTS

The authors acknowledge financial support by the Deutsche Forschungsgemeinschaft (DFG) within the cluster of excellence (EXC2111-390814868) "Munich Center for Quantum Science and Technology", MCQST. C.O. further acknowledges financial support as Max-Planck Fellow at the MPI-FKF Stuttgart.

REFERENCES

(1) Ciofini, I.; Daul, C. A. DFT calculations of molecular magnetic properties of coordination compounds. *Coord. Chem. Rev.* **2003**, *238*−*239*, 187.

(2) Li, X.; Cai, Z.; Sevilla, M. D. Investigation of proton transfer within DNA base pair anion and cation radicals by density functional theory (DFT). *J. Phys. Chem. B* **2001**, *105*, 10115.

(3) Jacquemin, D.; Wathelet, V.; Perpete, E. A.; Adamo, C. Extensive TD-DFT benchmark: singlet-excited states of organic molecules. *J. Chem. Theory Comput.* **2009**, *5*, 2420−2435.

(4) Armiento, R.; Mattsson, A. E. Functional designed to include surface effects in self-consistent density functional theory. *Phys. Rev. B* **2005**, *72*, No. 085108.

(5) Nolan, M.; Grigoleit, S.; Sayle, D. C.; Parker, S. C.; Watson, G. W. Density functional theory studies of the structure and electronic structure of pure and defective low index surfaces of ceria. *Surf. Sci.* **2005**, *576*, 217.

(6) Buchwald, J.; Hennes, M. Adsorption and diffusion of Au, Pt, and Co adatoms on SrTiO3 (001) surfaces: A density functional theory study. *Surf. Sci.* **2020**, No. 121683.

(7) Widdifield, C. M.; Farrell, J. D.; Cole, J. C.; Howard, J. A.; Hodgkinson, P. Resolving alternative organic crystal structures using density functional theory and NMR chemical shifts. *Chem. Sci.* **2020**, *11*, 2987.

(8) Sasmal, A.; Shit, S.; Rizzoli, C.; Wang, H.; Desplanches, C.; Mitra, S. Framework solids based on copper (II) halides (Cl/Br) and methylene-bridged bis (1-hydroxybenzotriazole): Synthesis, crystal structures, magneto-structural correlation, and density functional theory (DFT) studies. *Inorg. Chem.* **2012**, *51*, 10148.

(9) Campbell, J.; Mercier, H. P.; Franke, H.; Santry, D. P.; Dixon, D. A.; Schrobilgen, G. J. Syntheses, Crystal Structures, and Density Functional Theory Calculations of the c loso-[1-M (CO) 3 (η4-E9)] 4-(E= Sn, Pb; M= Mo, W) Cluster Anions and Solution NMR Spectroscopic Characterization of [1-M (CO) 3 (η4-Sn9)] 4-(M= Cr, Mo, W). *Inorg. Chem.* **2002**, *41*, 86.

(10) Schleder, G. R.; Padilha, A. C.; Acosta, C. M.; Costa, M.; Fazzio, A. From DFT to machine learning: recent approaches to materials science−a review. *J. Phys. Mater.* **2019**, *2*, No. 032001.

(11) Stöhr, M.; Van Voorhis, T.; Tkatchenko, A. Theory and practice of modeling van der Waals interactions in electronic-structure calculations. *Chem. Soc. Rev* **2019**, *48*, 4118.

(12) Kussmann, J.; Beer, M.; Ochsenfeld, C. Linear-scaling self-consistent field methods for large molecules. *Wiley Interdiscip. Rev.: Comput. Mol. Sci.* **2013**, *3*, 614.

(13) Ren, X.; Rinke, P.; Joas, C.; Scheffler, M. Random-phase approximation and its applications in computational chemistry and materials science. *J. Mater. Sci.* **2012**, *47*, 7447.

(14) Zhu, W.; Toulouse, J.; Savin, A.; Ángyán, J. G. Range-separated density-functional theory with random phase approximation applied to noncovalent intermolecular interactions. *J. Chem. Phys.* **2010**, *132*, No. 244108.

(15) Ehrlich, S.; Moellmann, J.; Reckien, W.; Bredow, T.; Grimme, S. System-Dependent Dispersion Coefficients for the DFT-D3 Treatment of Adsorption Processes on Ionic Surfaces. *ChemPhysChem.* **2011**, *12*, 3414.

(16) Caldeweyher, E.; Bannwarth, C.; Grimme, S. Extension of the D3 dispersion coefficient model. *J. Chem. Phys.* **2017**, *147*, No. 034112.

(17) Moellmann, J.; Grimme, S. DFT-D3 study of some molecular crystals. *J. Phys. Chem. C* **2014**, *118*, 7615.

(18) Sure, R.; Antony, J.; Grimme, S. Blind prediction of binding affinities for charged supramolecular host−guest systems: achievements and shortcomings of DFT-D3. *J. Phys. Chem. B* **2014**, *118*, 3431.

(19) Kaltak, M.; Klimeš, J.; Kresse, G. Cubic scaling algorithm for the random phase approximation: Self-interstitials and vacancies in Si. *Phys. Rev. B* **2014**, *90*, No. 054115.

(20) Langreth, D. C.; Perdew, J. P. Exchange-correlation energy of a metallic surface: Wave-vector analysis. *Phys. Rev. B* **1977**, *15*, No. 2884.

(21) Kurth, S.; Perdew, J. P. Density-functional correction of random-phase-approximation correlation with results for jellium surface energies. *Phys. Rev. B* **1999**, *59*, No. 10461.

(22) Furche, F. Molecular tests of the random phase approximation to the exchange-correlation energy functional. *Phys. Rev. B* **2001**, *64*, No. 195120.

(23) Fuchs, M.; Gonze, X. Accurate density functionals: Approaches using the adiabatic-connection fluctuation-dissipation theorem. *Phys. Rev. B* **2002**, *65*, No. 235109.

(24) Niquet, Y.; Fuchs, M.; Gonze, X. Exchange-correlation potentials in the adiabatic connection fluctuation-dissipation framework. *Phys. Rev. A* **2003**, *68*, No. 032507.

(25) Fuchs, M.; Niquet, Y.-M.; Gonze, X.; Burke, K. Describing static correlation in bond dissociation by Kohn−Sham density functional theory. *J. Chem. Phys.* **2005**, *122*, No. 094116.

(26) Furche, F.; Van Voorhis, T. Fluctuation-dissipation theorem density-functional theory. *J. Chem. Phys.* **2005**, *122*, No. 164106.

(27) Eshuis, H.; Furche, F. Basis set convergence of molecular correlation energy differences within the random phase approximation. *J. Chem. Phys.* **2012**, *136*, No. 084105.

(28) Heßelmann, A.; Görling, A. Random phase approximation correlation energies with exact Kohn−Sham exchange. *Mol. Phys.* **2010**, *108*, 359−372.

(29) Graf, D.; Beuerle, M.; Ochsenfeld, C. Low-Scaling Self-Consistent Minimization of a Density Matrix Based Random Phase Approximation Method in the Atomic Orbital Space. *J. Chem. Theory Comput.* **2019**, *15*, 4468.

(30) Beuerle, M.; Graf, D.; Schurkus, H. F.; Ochsenfeld, C. Efficient calculation of beyond RPA correlation energies in the dielectric matrix formalism. *J. Chem. Phys.* **2018**, *148*, No. 204104.
(31) Graf, D.; Ochsenfeld, C. A range-separated generalized Kohn−Sham method including a long-range nonlocal random phase approximation correlation potential. *J. Chem. Phys.* **2020**, *153*, No. 244118.
(32) Schurkus, H. F.; Ochsenfeld, C. Communication: An effective linear-scaling atomic-orbital reformulation of the random-phase approximation using a contracted double-Laplace transformation. *J. Chem. Phys.* **2016**, *144*, No. 031101.
(33) Luenser, A.; Schurkus, H. F.; Ochsenfeld, C. Vanishing-overhead linear-scaling random phase approximation by Cholesky decomposition and an attenuated Coulomb-metric. *J. Chem. Theory Comput.* **2017**, *13*, 1647.
(34) Graf, D.; Beuerle, M.; Schurkus, H. F.; Luenser, A.; Savasci, G.; Ochsenfeld, C. Accurate and Efficient Parallel Implementation of an Effective Linear-Scaling Direct Random Phase Approximation Method. *J. Chem. Theory Comput.* **2018**, *14*, 2505.
(35) Paier, J.; Janesko, B. G.; Henderson, T. M.; Scuseria, G. E.; Grüneis, A.; Kresse, G. Hybrid functionals including random phase approximation correlation and second-order screened exchange. *J. Chem. Phys.* **2010**, *132*, No. 094103.
(36) Kohn, W.; Sham, L. J. Self-consistent equations including exchange and correlation effects. *Phys. Rev.* **1965**, *140*, No. A1133.
(37) Bohm, D.; Pines, D. A collective description of electron interactions: III. Coulomb interactions in a degenerate electron gas. *Phys. Rev.* **1953**, *92*, No. 609.
(38) Langreth, D. C.; Perdew, J. P. The exchange-correlation energy of a metallic surface. *Solid State Commun.* **1975**, *17*, 1425.
(39) Gunnarsson, O.; Lundqvist, B. I. Exchange and correlation in atoms, molecules, and solids by the spin-density-functional formalism. *Phys. Rev. B* **1976**, *13*, No. 4274.
(40) Furche, F. Developing the random phase approximation into a practical post-Kohn−Sham correlation model. *J. Chem. Phys.* **2008**, *129*, No. 114105.
(41) Eshuis, H.; Yarkony, J.; Furche, F. Fast computation of molecular random phase approximation correlation energies using resolution of the identity and imaginary frequency integration. *J. Chem. Phys.* **2010**, *132*, No. 234114.
(42) Einstein, A. The foundation of the general theory of relativity. *Ann. Phys.* **1916**, *354*, 769.
(43) Ullrich, C. A. *Time-Dependent Density-Functional Theory: Concepts and Applications*; Oxford University Press: Oxford, 2011.
(44) Kaltak, M.; Klimes, J.; Kresse, G. Low scaling algorithms for the random phase approximation: Imaginary time and Laplace transformations. *J. Chem. Theory Comput.* **2014**, *10*, 2498.
(45) Weigend, F.; Furche, F.; Ahlrichs, R. Gaussian basis sets of quadruple zeta valence quality for atoms H−Kr. *J. Chem. Phys.* **2003**, *119*, 12753−12762.
(46) Weigend, F.; Ahlrichs, R. Balanced basis sets of split valence, triple zeta valence and quadruple zeta valence quality for H to Rn: Design and assessment of accuracy. *Phys. Chem. Chem. Phys.* **2005**, *7*, 3297−3305.
(47) Weigend, F.; Häser, M.; Patzelt, H.; Ahlrichs, R. RI-MP2: optimized auxiliary basis sets and demonstration of efficiency. *Chem. Phys. Lett.* **1998**, *294*, 143−152.
(48) Thompson, T. H.; Ochsenfeld, C. Integral partition bounds for fast and effective screening of general one-, two-, and many-electron integrals. *J. Chem. Phys.* **2019**, *150*, No. 044101.
(49) Kussmann, J.; Ochsenfeld, C. Pre-selective screening for matrix elements in linear-scaling exact exchange calculations. *J. Chem. Phys.* **2013**, *138*, No. 134114.
(50) Kussmann, J.; Ochsenfeld, C. Preselective screening for linear-scaling exact exchange-gradient calculations for graphics processing units and general strong-scaling massively parallel calculations. *J. Chem. Theory Comput.* **2015**, *11*, 918.
(51) Kussmann, J.; Ochsenfeld, C. Hybrid CPU/GPU integral engine for strong-scaling ab initio methods. *J. Chem. Theory Comput.* **2017**, *13*, 3153−3159.
(52) Perdew, J. P.; Burke, K.; Ernzerhof, M. Generalized gradient approximation made simple. *Phys. Rev. Lett.* **1996**, *77*, No. 3865.
(53) Perdew, J. P.; Burke, K.; Ernzerhof, M. Generalized gradient approximation made simple [Phys. Rev. Lett. 77, 3865 (1996)]. *Phys. Rev. Lett* **1997**, *78*, No. 1396.
(54) Hättig, C. Optimization of auxiliary basis sets for RI-MP2 and RI-CC2 calculations: Core−valence and quintuple-ζ basis sets for H to Ar and QZVPP basis sets for Li to Kr. *Phys. Chem. Chem. Phys.* **2005**, *7*, 59−66.
(55) Kreppel, A.; Graf, D.; Laqua, H.; Ochsenfeld, C. Range-separated density-functional theory in combination with the random phase approximation: An accuracy benchmark. *J. Chem. Theory Comput.* **2020**, *16*, 2985−2994.
(56) Yang, Y.; van Aggelen, H.; Steinmann, S. N.; Peng, D.; Yang, W. Benchmark tests and spin adaptation for the particle-particle random phase approximation. *J. Chem. Phys.* **2013**, *139*, No. 174110.
(57) Mussard, B.; Reinhardt, P.; Ángyán, J. G.; Toulouse, J. Spin-unrestricted random-phase approximation with range separation: Benchmark on atomization energies and reaction barrier heights. *J. Chem. Phys.* **2015**, *142*, No. 154123.
(58) Heßelmann, A.; Görling, A. Random-phase approximation correlation methods for molecules and solids. *Mol. Phys.* **2011**, *109*, 2473−2500.

https://doi.org/10.1021/acs.jctc.1c00494
J. Chem. Theory Comput. 2021, 17, 5623−5634

3.2 Publication II: Efficient Method for the Computation of Frozen-Core Nuclear Gradients within the Random Phase Approximation

V. Drontschenko, D. Graf, H. Laqua, C. Ochsenfeld
J. Chem. Theory Comput., **18**, 7359 (2022).

Abstract

A method for the evaluation of analytical frozen-core gradients within the random phase approximation is presented. We outline an efficient way to evaluate the response of the density of active electrons arising only when introducing the frozen-core approximation and constituting the main difficulty, together with the response of the standard Kohn–Sham density. The general framework allows to extend the outlined procedure to related electron correlation methods in the atomic orbital basis that require the evaluation of density responses, such as second-order Møller–Plesset perturbation theory or coupled cluster variants. By using Cholesky decomposed densities—which reintroduce the occupied index in the time-determining steps—we are able to achieve speedups of 20-30% (depending on the size of the basis set) by using the frozen-core approximation, which is of similar magnitude as for molecular orbital formulations. We further show that the errors introduced by the frozen-core approximation are practically insignificant for molecular geometries.

JCTC Journal of Chemical Theory and Computation

pubs.acs.org/JCTC Article

Efficient Method for the Computation of Frozen-Core Nuclear Gradients within the Random Phase Approximation

Viktoria Drontschenko, Daniel Graf, Henryk Laqua, and Christian Ochsenfeld*

Cite This: J. Chem. Theory Comput. 2022, 18, 7359−7372 Read Online

ACCESS | Metrics & More | Article Recommendations

ABSTRACT: A method for the evaluation of analytical frozen-core gradients within the random phase approximation is presented. We outline an efficient way to evaluate the response of the density of active electrons arising only when introducing the frozen-core approximation and constituting the main difficulty, together with the response of the standard Kohn−Sham density. The general framework allows to extend the outlined procedure to related electron correlation methods in the atomic orbital basis that require the evaluation of density responses, such as second-order Møller−Plesset perturbation theory or coupled cluster variants. By using Cholesky decomposed densities—which reintroduce the occupied index in the time-determining steps—we are able to achieve speedups of 20−30% (depending on the size of the basis set) by using the frozen-core approximation, which is of similar magnitude as for molecular orbital formulations. We further show that the errors introduced by the frozen-core approximation are practically insignificant for molecular geometries.

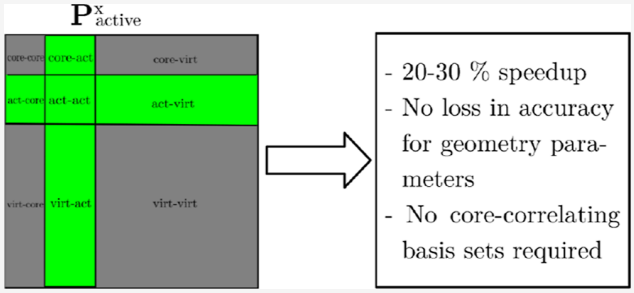

1. INTRODUCTION

The accurate and efficient calculation of the electron correlation energy is one of the most challenging tasks in quantum chemistry for approaching the Schrödinger equation. One of the most widely applied approaches to solve the Schrödinger equation is density functional theory (DFT)[1,2] due to its excellent cost performance ratios and good accuracies for various compounds and properties. However, the vast number of available functionals makes the choice for a specific application difficult and severely limits the predictive power of density functionals.[3−5] Other methods to describe electron correlation include wave function-based methods such as second-order Møller−Plesset (MP2) perturbation theory,[6] coupled cluster (CC) theory,[7,8] or configuration interaction (CI) methods,[9,10] which, however, come with a much higher computational effort.

A very promising method, that has gained increased popularity in the last decades, is the random phase approximation (RPA)[5,11−42] as a post-Kohn−Sham method. It does not contain any empirical parameters and in connection with DFT can be assigned to the fifth rung on Jacob's ladder of density functional approximations.[43] Most notably, RPA is able to describe noncovalent interactions exceptionally well[44] without the need to introduce semi-empirical corrections, which makes it stand out from empirical dispersion correction methods.[45−55] Furthermore, it is able to describe systems with vanishing electronic gaps,[56] where methods such as MP2 fail. In addition, the recently developed RPA-like σ-functionals[60−63] introduced by the Görling group look especially promising in that regard. Much progress has been made in terms of the computational efficiency of RPA since it was first proposed by Bohm and Pines in 1953.[57] By introducing the resolution-of-the-identity (RI) approximation to RPA, Furche and coworkers[16,18,20] were able to reduce the scaling from $O(M^6)$ to $O(M^4)$ with the system size M, which opened the way for practical applications beyond a few atoms. Further improvements in the efficiency of RPA followed,[31,32,34,39,58,59] extending the applicability of RPA to systems with more than 1000 atoms.[31,32,34,39,59] Furthermore, for practical applications, the computation of electronic properties beyond ground-state energies is necessary, such as the determination of equilibrium geometries, which requires the analytical evaluation of nuclear gradients. Much progress has been made in the development of efficient methods for the computation of molecular gradients within RPA in recent years as well:[22,40,41,64−69] for example, the molecular orbital (MO) RI-RPA implementation of Burow et al.,[22] the work of Kresse and coworkers,[67] as well as the work in our group by Beuerle and Ochsenfeld,[68] the latter presenting an atomic orbital (AO)

Received: July 26, 2022
Published: November 4, 2022

implementation with Cholesky-decomposed ground-state densities.

A very widely applied approximation for electron correlation methods (including RPA) is the frozen-core approximation, whereby the lowest lying MOs are "frozen", prohibiting excitations from these orbitals and only including excitations from valence or "active" orbitals. This approximation also coincides with an intuitive chemist's picture where the core electrons are considered to be less sensitive to changes in the environment and chemical reactions are determined by valence electrons. In fact, it has been found that the error introduced by the frozen-core approximation is minimal in terms of relative energies for RPA[16] and additionally for geometries of related methods.[70,71] Furthermore, for practical applications, the use of the frozen-core approximation is preferred since most of the commonly used basis sets are designed to correlate the valence electrons only. Specifically, most AO and auxiliary basis sets are not equipped to describe the core region sufficiently and special basis functions, that is, Gaussians with large exponents, would have to be added to the basis sets in order to describe the correlation between core electrons as well as core and active electrons,[72] such as, for example, in Dunning's cc-pCV*X*Z[73] and cc-pwCV*X*Z[74] basis sets (where *X* = D, T, Q, 5, ...). The problem with auxiliary basis sets is even more obvious since they are often developed within the frozen-core approximation and, thus, do not contain any core functions. One possible solution is the use of automatically generated auxiliary basis sets, for example, developed by Neese and coworkers.[75] However, these basis sets are usually about twice the size of optimized basis sets, which makes the computation much more expensive. Another possible solution lies in the utilization of optimized auxiliary basis sets in combination with the frozen-core approximation for the underlying electron correlation method, which allows to overcome the restrictions on the basis set selection. A further advantage when using the frozen-core approximation comes with the increased computational efficiency since the active occupied space excludes the core electrons. Thus, the limited availability of all-electron basis sets together with the higher computational cost for larger basis sets makes the use of the frozen-core approximation preferable within electron correlation methods. In addition, the frozen-core approximation entails no significant loss of accuracy for quantities such as structural parameters or relative energies.

While the implementation of the frozen-core approximation for ground-state energies is a trivial matter, the corresponding implementation for analytical gradients is far from trivial. In the literature, the frozen-core approximation has been derived and implemented within an MO formalism for MP2 gradients,[70,71,76,77] CC gradients,[71,78−80] as well as CI gradients.[76,81,82] However, there are no accounts for RPA gradients within the frozen-core approximation (to the best of our knowledge).

In this work, we give a detailed derivation of the frozen-core approximation within our RPA gradient implementation.[68] Since the main difficulty lies in the evaluation of the response of the density stemming from active electrons, we will show how to do this in the most efficient way. The proposed approach could further be used for the implementation of σ-functional gradients and, furthermore, applied for related AO-based electron correlation methods that require the evaluation of density responses (which is done most efficiently using the Z-vector method),[83,84] such as MP2 gradients.[84] As will be shown, the loss in accuracy in structures resulting from the introduction of the frozen-core approximation is minimal, while the gain in performance is 20−30%, depending on the size of the chosen basis set.

2. NOTATION

We adopt the Mulliken notation for two- and three-center integrals. Furthermore, we use a generalized notation for the trace: coordinates that appear twice within a trace are implicitly integrated over. The notation and abbreviations used in this work are summarized in Table 1. Additionally, the following definitions are used for various densities

$$P_{\mu\nu} = \sum_{i}^{N_{\mathrm{occ}}} C_{\mu i} C_{\nu i} \tag{1}$$

$$P_{\mathrm{virt},\mu\nu} = \sum_{a}^{N_{\mathrm{virt}}} C_{\mu a} C_{\nu a} \tag{2}$$

$$P_{\mathrm{act},\mu\nu} = \sum_{i'}^{N_{\mathrm{act}}} C_{\mu i'} C_{\nu i'} \tag{3}$$

Table 1. Notation and Abbreviations Adopted in This Work

orbital indices		scalars	
$\mu, \nu, \lambda, \sigma$	atomic orbitals	N_{basis}	number of AO basis functions
M, N, P, Q	auxiliary functions	N_{aux}	number of auxiliary functions
i, j	occupied MOs	N_{occ}	number of occupied MOs
a, b	virtual MOs	N_{virt}	number of virtual MOs
$\underline{i}, \underline{j}$	Cholesky orbitals		
I, J	frozen-core orbitals	N_{core}	number of frozen-core orbitals
i', j'	active orbitals	N_{act}	number of active, occupied orbitals
p, q	any orbitals (occupied or virtual)	N_{all}	number of occupied and virtual orbitals
		N_{atoms}	number of atoms
		N_{r}	number of Laplace quadrature points

density matrices		subscripts	
$\mathbf{P}$	all-electron, KS density (eq 1)	oo	occupied−occupied subspace
$\mathbf{P}_{\mathrm{virt}}$	virtual density (eq 2)	ov	occupied−virtual subspace
$\mathbf{P}_{\mathrm{act}}$	active density (eq 3)	cc	core−core subspace
$\mathbf{P}^{x}$	derivative of the KS density	aa	active−active subspace
$\mathbf{P}^{x}_{\mathrm{act}}$	derivative of the active density	ac	active−core subspace
$\mathbf{P}^{x}_{\mathrm{virt}}$	derivative of the virtual density	av	active−virtual subspace

derivatives			
$O^{(x)}$	derivatives of a quantity O with respect to a perturbation x containing only integral derivatives	O^{x}	derivatives of a quantity O with respect to a perturbation x with a functional dependence on the perturbed density

3. THEORY

We will start by reviewing the expressions for the RPA total energy within the AO basis. We will first present the equations within the all-electron formalism and subsequently derive the expressions for the frozen-core approximation. Next, we will continue with a review of RPA gradients in the AO basis: we will begin by briefly summarizing RPA gradients in the original all-electron formalism[68] and then derive the incorporation of the frozen-core approximation in detail. Since the difficulty lies

https://doi.org/10.1021/acs.jctc.2c00774
J. Chem. Theory Comput. 2022, 18, 7359−7372

in the additional evaluation of the active perturbed density, we will derive and explain how to obtain the corresponding expressions. And lastly, we will use pivoted Cholesky decomposition (CD) of the (active) ground-state density within the energy and force calculation to reintroduce the occupied (active) orbital index, which is an important step to achieve increased performance when using the frozen-core approximation within an AO formalism.

Please note that in Sections 3.1.1 and 3.2.1, we will only give a brief summary of the most important equations, which will be relevant in the main part of this paper. For more detailed derivations, we refer the reader to previous publications related to RPA energies[16,18,20,31,32,34] and gradients.[68,84]

3.1. RPA Total Energies. *3.1.1. All-Electron Energy Expression.* The total energy within the adiabatic-connection fluctuation−dissipation theorem and the RPA[15,85] can be expressed as[86,87]

$$E_{\text{total}}[\mathbf{P}] = E^{\text{HF}}[\mathbf{P}] + E_{\text{C}}^{\text{RPA}}[\mathbf{P}] \tag{4}$$

where $E^{\text{HF}}[\mathbf{P}]$ denotes the Hartree−Fock energy evaluated with KS orbitals, stemming from a prior DFT calculation.

The RPA correlation energy $E_{\text{C}}^{\text{RPA}}$ can be expressed within the RI approximation[16,18,20] as

$$E_{\text{C}}^{\text{RPA}} = \frac{1}{2\pi}\int_0^{+\infty} \mathrm{d}\omega \text{Tr}(\ln[\mathbf{1} - \mathbf{X}_0(\mathrm{i}\omega)\mathbf{V}] + \mathbf{X}_0(\mathrm{i}\omega)\mathbf{V}) \tag{5}$$

with the noninteracting density−density response function $\mathbf{X}_0$ and the electron−electron interaction operator in the auxiliary basis employing a short-range RI metric[32]

$$V_{PQ} = \sum_{R,S}^{N_{\text{aux}}} (P|m_{12}|R)^{-1}(R|r_{12}^{-1}|S)(S|m_{12}|Q)^{-1} \tag{6}$$

with m_{12} denoting the RI-metric and r_{12} the interelectronic distance. For efficiency reasons, the response function is computed in the imaginary time domain according to[31,32,34]

$$X_{0,MN}(\mathrm{i}\tau) = \sum_{\mu,\nu,\lambda,\sigma}^{N_{\text{basis}}} \underline{G}_{0,\mu\nu}(-\mathrm{i}\tau)B_{\nu\lambda}^{M}\overline{G}_{0,\lambda\sigma}(\mathrm{i}\tau)B_{\sigma\mu}^{N} \tag{7}$$

where the three-center integral tensor $\mathbf{B}^M$ is defined as

$$B_{\mu\nu}^{M} = (\mu\nu|m_{12}|M) \tag{8}$$

The one-particle Green's function in the imaginary time domain is given by

$$\mathbf{G}_0(\mathrm{i}\tau) = \Theta(-\mathrm{i}\tau)\underline{\mathbf{G}}_0(\mathrm{i}\tau) + \Theta(\mathrm{i}\tau)\overline{\mathbf{G}}_0(\mathrm{i}\tau) \tag{9}$$

with $\underline{\mathbf{G}}_0(\mathrm{i}\tau)$ defined as

$$\underline{\mathbf{G}}_0(\mathrm{i}\tau) = \mathbf{P}\ \exp(-\tau(\mathbf{H}_{\text{KS}} - \epsilon_{\text{F}}\mathbf{S})\mathbf{P}) \tag{10}$$

$$\underline{G}_{0,\mu\nu}(\mathrm{i}\tau) = \sum_{i}^{N_{\text{occ}}} C_{\mu i}C_{\nu i}\ \exp(-(\epsilon_i - \epsilon_{\text{F}})\tau) \tag{11}$$

and $\overline{\mathbf{G}}_0(\mathrm{i}\tau)$ as

$$\overline{\mathbf{G}}_0(\mathrm{i}\tau) = -\mathbf{P}_{\text{virt}}\ \exp(-\tau(\mathbf{H}_{\text{KS}} - \epsilon_{\text{F}}\mathbf{S})\mathbf{P}_{\text{virt}}) \tag{12}$$

$$\overline{G}_{0,\mu\nu}(\mathrm{i}\tau) = -\sum_{a}^{N_{\text{virt}}} C_{\mu a}C_{\nu a}\ \exp(-(\epsilon_a - \epsilon_{\text{F}})\tau) \tag{13}$$

where $C_{\mu i}$ and $C_{\mu a}$ denote occupied and virtual MO coefficients, respectively. ϵ_i and ϵ_a denote the occupied and virtual orbital energies, respectively. The Fermi level ϵ_{F} is defined as $\frac{1}{2}(\epsilon_{\text{HOMO}} + \epsilon_{\text{LUMO}})$ where ϵ_{HOMO} and ϵ_{LUMO} are the orbital energies of the highest occupied MO and the lowest unoccupied MO, respectively.[32,88] $\Theta(\mathrm{i}\tau)$ is the Heaviside step function and $\mathbf{S}$ is the overlap matrix. The Kohn−Sham Hamiltonian $\mathbf{H}_{\text{KS}}$ is defined as

$$\mathbf{H}_{\text{KS}} = \mathbf{h} + \mathbf{J}[\mathbf{P}] + \mathbf{V}_{\text{xc}}[\mathbf{P}] \tag{14}$$

with the matrix representation of the one-electron potential $\mathbf{h}$, the Coulomb potential $\mathbf{J}$, and the exchange−correlation potential $\mathbf{V}_{\text{xc}}$. Subsequently, the response function (eq 7) is transformed into the imaginary frequency domain by a cosine transform,[58] or, equivalently, a contracted double-Laplace transform[31,34] according to

$$\mathbf{X}_0(\mathrm{i}\omega) = 2\int_0^{+\infty} \mathrm{d}\tau\ \cos(\omega\tau)\mathbf{X}_0(\mathrm{i}\tau) \tag{15}$$

in order to carry out the frequency integration in eq 5.

3.1.2. Frozen-Core Energy Expression. Within the frozen-core approximation, only the correlation of active electrons is considered. Thus, the frozen-core approximation can be implemented for RPA correlation energies by considering excitations from active electrons only, which can be easily achieved by restricting the sum over occupied orbitals in the construction of $\underline{\mathbf{G}}_0(-\mathrm{i}\tau)$ to active occupied orbitals according to

$$\underline{G}_{0,\mu\nu}^{\text{act}}(-\mathrm{i}\tau) = \sum_{i'}^{N_{\text{act}}} C_{\mu i'}C_{\nu i'}\ \exp(\tau(\epsilon_{i'} - \epsilon_{\text{F}})) \tag{16}$$

$$\underline{\mathbf{G}}_0^{\text{act}}(-\mathrm{i}\tau) = \mathbf{P}_{\text{act}}\ \exp(\tau(\mathbf{H}_{\text{KS}} - \epsilon_{\text{F}}\mathbf{S})\mathbf{P}_{\text{act}}) \tag{17}$$

This way, the general expression for the active Green's function within the frozen-core approximation reads

$$\mathbf{G}_0^{\text{act}}(\mathrm{i}\tau) = \Theta(-\mathrm{i}\tau)\underline{\mathbf{G}}_0^{\text{act}}(\mathrm{i}\tau) + \Theta(\mathrm{i}\tau)\overline{\mathbf{G}}_0(\mathrm{i}\tau) \tag{18}$$

Thus, by using the active Green's function as defined above in the computation of the response function (eq 7), we obtain the active response function

$$X_{0,MN}^{\text{act}}(\mathrm{i}\tau) = \sum_{\mu,\nu,\lambda,\sigma}^{N_{\text{basis}}} \underline{G}_{0,\mu\nu}^{\text{act}}(-\mathrm{i}\tau)B_{\nu\lambda}^{M}\overline{G}_{0,\lambda\sigma}(\mathrm{i}\tau)B_{\sigma\mu}^{N} \tag{19}$$

which allows to compute the RPA correlation energy within the frozen-core approximation.

3.2. RPA Gradients in the AO Basis. The first derivative of the RPA total energy (eq 4) with respect to perturbations caused by nuclear displacements can be expressed as

$$E_{\text{total}}^{x}[\mathbf{P}] = E^{\text{HF},x}[\mathbf{P}] + E_{\text{C}}^{\text{RPA},x}[\mathbf{P}] \tag{20}$$

The contribution of the HF functional can be further separated according to

$$E^{\text{HF},x}[\mathbf{P}] = E^{\text{HF},(x)}[\mathbf{P}] + E^{\text{HF}}[\mathbf{P}^x] \tag{21}$$

Please note that at this stage, the response of the KS density has to be evaluated (which is most efficiently accomplished using the Z-vector method)[83,84] since the HF functional is not stationary with respect to the KS orbitals. This differs from regular HF force calculations, where the response of the HF orbitals can be expressed with the derivative of the overlap matrix and the energy-weighted one-particle density matrix.[89] The first contribution in eq 21 is given by

https://doi.org/10.1021/acs.jctc.2c00774
J. Chem. Theory Comput. 2022, 18, 7359−7372

$$E^{\mathrm{HF},(x)}[\mathbf{P}] = \mathrm{Tr}(\mathbf{P}\mathbf{h}^{(x)} + 0.5(\mathbf{P}\mathbf{J}^{(x)}[\mathbf{P}] + \mathbf{P}\mathbf{K}^{(x)}[\mathbf{P}])) \quad (22)$$

and the second one by

$$E^{\mathrm{HF}}[\mathbf{P}^x] = \mathrm{Tr}(\mathbf{H}_{\mathrm{HF}}\mathbf{P}^x) \quad (23)$$

with

$$\mathbf{H}_{\mathrm{HF}} = \mathbf{h} + \mathbf{J}[\mathbf{P}] + \mathbf{K}[\mathbf{P}] \quad (24)$$

where $\mathbf{K}$ denotes the HF exchange matrix. In the following, we will first present the all-electron formulation for $E_{\mathrm{C}}^{\mathrm{RPA},x}$ and subsequently derive the corresponding frozen-core expressions.

3.2.1. All-Electron Gradient Expression. The derivative of the RPA correlation energy can be expressed according to

$$E_{\mathrm{C}}^{\mathrm{RPA},x}[\mathbf{V}, \mathbf{B}, \mathbf{G}_0] = \mathrm{Tr}\left(\frac{\partial E_{\mathrm{C}}^{\mathrm{RPA}}}{\partial \mathbf{V}}\frac{\partial \mathbf{V}}{\partial x}\right) + \mathrm{Tr}\left(\frac{\partial E_{\mathrm{C}}^{\mathrm{RPA}}}{\partial \mathbf{X}_0(\mathrm{i}\omega)}\frac{\partial \mathbf{X}_0(\mathrm{i}\omega)}{\partial \mathbf{B}}\frac{\partial \mathbf{B}}{\partial x}\right) + \mathrm{Tr}\left(\frac{\partial E_{\mathrm{C}}^{\mathrm{RPA}}}{\partial \mathbf{G}_0(\mathrm{i}\tau)}\frac{\partial \mathbf{G}_0(\mathrm{i}\tau)}{\partial x}\right) \quad (25)$$

The first term in eq 25 can be evaluated as[68]

$$\frac{\partial E_{\mathrm{C}}^{\mathrm{RPA}}}{\partial \mathbf{V}} = \frac{1}{2\pi}\int_0^{+\infty} \mathrm{d}\omega(-[(\mathbf{1} - \mathbf{X}_0(\mathrm{i}\omega)\mathbf{V})^{-1} - \mathbf{1}]\mathbf{X}_0(\mathrm{i}\omega)) \quad (26)$$

$$\left(\frac{\partial \mathbf{V}}{\partial x}\right)_{PQ} = -(P|m_{12}|M)^{-1}(M|m_{12}|N)^{(x)}(N|m_{12}|R)^{-1}(R|r_{12}^{-1}|S)(S|m_{12}|Q)^{-1} + (P|m_{12}|M)^{-1}(M|r_{12}^{-1}|N)^{(x)}(N|m_{12}|Q)^{-1} - (P|m_{12}|M)^{-1}(M|r_{12}|N)(N|m_{12}|R)^{-1}(R|m_{12}|S)^{(x)}(S|m_{12}|Q)^{-1} \quad (27)$$

The contribution from the three-center integrals to the RPA gradient (second term, eq 25) can be evaluated in the imaginary time domain according to[68]

$$\begin{aligned}&\mathrm{Tr}\left(\frac{\partial E_{\mathrm{C}}^{\mathrm{RPA}}}{\partial \mathbf{X}_0(\mathrm{i}\omega)}\frac{\partial \mathbf{X}_0(\mathrm{i}\omega)}{\partial \mathbf{B}^M}\frac{\partial \mathbf{B}^M}{\partial x}\right)\\ &= \mathrm{Tr}\left(-\frac{2}{\pi}\int_0^{+\infty}\int_0^{+\infty}\mathrm{d}\omega\,\mathrm{d}\tau\,\cos(\omega\tau)\left[\sum_N^{N_{\mathrm{aux}}} W_{\mathrm{c},MN}(\mathrm{i}\omega)\underline{\mathbf{G}}_0(-\mathrm{i}\tau)\mathbf{B}^N\bar{\mathbf{G}}_0(\mathrm{i}\tau)(\mathbf{B}^M)^x\right]\right)\\ &= \mathrm{Tr}\left(-2\int_0^{+\infty}\mathrm{d}\tau\left[\sum_N^{N_{\mathrm{aux}}} W_{\mathrm{c},MN}(\mathrm{i}\tau)\underline{\mathbf{G}}_0(-\mathrm{i}\tau)\mathbf{B}^N\bar{\mathbf{G}}_0(\mathrm{i}\tau)(\mathbf{B}^M)^x\right]\right)\end{aligned} \quad (28)$$

where the correlated screened Coulomb interaction in the auxiliary basis is defined as

$$\mathbf{W}_{\mathrm{c}}(\mathrm{i}\omega) = \mathbf{V}(\mathbf{1} - \mathbf{X}_0(\mathrm{i}\omega)\mathbf{V})^{-1} - \mathbf{1} \quad (29)$$

Lastly, the contribution of the Green's function to the RPA gradient (third term, eq 25) can be evaluated in the imaginary time domain as well yielding

$$\mathrm{Tr}\left(\frac{\partial E_{\mathrm{C}}^{\mathrm{RPA}}}{\partial \mathbf{G}_0(\mathrm{i}\tau)}\frac{\partial \mathbf{G}_0(\mathrm{i}\tau)}{\partial x}\right) = \mathrm{Tr}\left(\int_0^{+\infty}\mathrm{d}\tau[\mathbf{\Sigma}(-\mathrm{i}\tau)\bar{\mathbf{G}}_0^x(\mathrm{i}\tau) + \mathbf{\Sigma}(\mathrm{i}\tau)\underline{\mathbf{G}}_0^x(-\mathrm{i}\tau)]\right) \quad (30)$$

with the correlated self-energy defined as[67,90,91]

$$\Sigma_{\mu\nu}(\mathrm{i}\tau) = \sum_{P,Q}^{N_{\mathrm{aux}}}\sum_{\lambda,\sigma}^{N_{\mathrm{basis}}} -W_{\mathrm{c},PQ}(\mathrm{i}\tau)B_{\mu\lambda}^Q G_{0,\lambda\sigma}(\mathrm{i}\tau)B_{\sigma\nu}^P \quad (31)$$

The detailed derivation for the evaluation of $\mathbf{G}_0^x(\mathrm{i}\tau)$ arising in eq 30 can be found in ref 68. Here, we only want to note the most important steps in the evaluation: starting with the representation of the Green's function given in eqs 10 and 12 together with the power series representation of the exponential function[84,88,92] allows to take the derivative with respect to a perturbation x. Furthermore, to avoid the derivative of the virtual density, which arises in the evaluation of $\bar{\mathbf{G}}_0^x(\mathrm{i}\tau)$, $\mathbf{P}_{\mathrm{virt}}^x$ can be expressed in terms of $\mathbf{P}^x$ by taking the derivative of the completeness relation $\mathbf{1} = \mathbf{PS} + \mathbf{P}_{\mathrm{virt}}\mathbf{S}$. Thus, the final expression for the contribution of the Green's function to the RPA gradient reads[68]

$$\mathrm{Tr}\left(\frac{\partial E_{\mathrm{C}}^{\mathrm{RPA}}}{\partial \mathbf{G}_0}\frac{\partial \mathbf{G}_0}{\partial x}\right) = \mathrm{Tr}(\mathbf{P}_{\mathrm{RPA}}(\mathbf{H}_{\mathrm{KS}}^{(x)} - \epsilon_{\mathrm{F}}\mathbf{S}^{(x)}) + \mathbf{V}_{\mathrm{RPA}}\mathbf{P}^x + \mathbf{S}^{-1}\bar{\mathbf{\Sigma}}^+\mathbf{S}^{-1}\mathbf{S}^{(x)}) \quad (32)$$

where we have introduced the following quantities

$$\mathbf{V}_{\mathrm{RPA}} = \bar{\mathbf{\Sigma}} + \mathbf{J}[\mathbf{P}_{\mathrm{RPA}}] + \mathbf{V}_{\mathrm{xc}}[\mathbf{P}_{\mathrm{RPA}}] \quad (33)$$

$$\mathbf{P}_{\mathrm{RPA}} = \int_0^{\infty}\mathrm{d}\tau(\mathbf{P}\underline{\mathbf{Y}}(-\mathrm{i}\tau) - \mathbf{P}_{\mathrm{virt}}\bar{\mathbf{Y}}(\mathrm{i}\tau)) \quad (34)$$

$$\bar{\mathbf{\Sigma}} = \bar{\mathbf{\Sigma}}^- + \bar{\mathbf{\Sigma}}^+ \quad (35)$$

$$\bar{\mathbf{\Sigma}}^- = \int_0^{+\infty}\mathrm{d}\tau(\underline{\mathbf{Y}}(-\mathrm{i}\tau)(\mathbf{H}_{\mathrm{KS}} - \epsilon_{\mathrm{F}}\mathbf{S}) + \exp(-\tau(\mathbf{H}_{\mathrm{KS}} - \epsilon_{\mathrm{F}}\mathbf{S})\mathbf{P})\mathbf{\Sigma}(\mathrm{i}\tau)) \quad (36)$$

$$\bar{\mathbf{\Sigma}}^+ = \int_0^{+\infty}\mathrm{d}\tau(\bar{\mathbf{Y}}(\mathrm{i}\tau)(\mathbf{H}_{\mathrm{KS}} - \epsilon_{\mathrm{F}}\mathbf{S}) + \exp(-\tau(\mathbf{H}_{\mathrm{KS}} - \epsilon_{\mathrm{F}}\mathbf{S})\mathbf{P}_{\mathrm{virt}})\mathbf{\Sigma}(-\mathrm{i}\tau)) \quad (37)$$

$$\mathbf{Y}(\mathrm{i}\tau) = \Theta(-\mathrm{i}\tau)\underline{\mathbf{Y}}(\mathrm{i}\tau) + \Theta(\mathrm{i}\tau)\bar{\mathbf{Y}}(\mathrm{i}\tau) \quad (38)$$

$$\underline{\mathbf{Y}}(-\mathrm{i}\tau) = \sum_{n=1}^{\infty}\sum_{k=0}^{n-1}\frac{(\tau)^n}{n!}((\mathbf{H}_{\mathrm{KS}} - \epsilon_{\mathrm{F}}\mathbf{S})\mathbf{P})^{n-k-1}\mathbf{\Sigma}(\mathrm{i}\tau)\mathbf{P}((\mathbf{H}_{\mathrm{KS}} - \epsilon_{\mathrm{F}}\mathbf{S})\mathbf{P})^k \quad (39)$$

$$\bar{\mathbf{Y}}(\mathrm{i}\tau) = \sum_{n=1}^{\infty}\sum_{k=0}^{n-1}\frac{(-\tau)^n}{n!}((\mathbf{H}_{\mathrm{KS}} - \epsilon_{\mathrm{F}}\mathbf{S})\mathbf{P}_{\mathrm{virt}})^{n-k-1}\mathbf{\Sigma}(-\mathrm{i}\tau)\mathbf{P}_{\mathrm{virt}}((\mathbf{H}_{\mathrm{KS}} - \epsilon_{\mathrm{F}}\mathbf{S})\mathbf{P}_{\mathrm{virt}})^k \quad (40)$$

Now, the only remaining quantity to be determined is the derivative of the occupied one-particle density $\mathbf{P}^x$. The density response can be determined by solving the coupled-perturbed KS (CPKS) equations for all $3N_{\mathrm{atoms}}$ perturbations, which, however, becomes very expensive. A better approach is to first summarize all terms containing density derivatives, specifically, the contribution stemming from $E^{\mathrm{HF}}[\mathbf{P}^x]$ (eq 23) and from the Green's function (eq 32), resulting in

$$\mathrm{Tr}([\mathbf{H}_{\mathrm{HF}} + \mathbf{V}_{\mathrm{RPA}}]\mathbf{P}^x) \quad (41)$$

and use the Z-vector technique[83,84] on eq 41, which requires solving only one CPKS equation instead of $3N_{\mathrm{atoms}}$ equations. Within an AO-formalism, the response of the density can be evaluated by considering its subspace projections. The

https://doi.org/10.1021/acs.jctc.2c00774
J. Chem. Theory Comput. 2022, 18, 7359−7372

occupied−virtual and virtual−occupied subspace projections of $\mathbf{P}^x$ can be solved using the density matrix-based Laplace transformed (DL) CPKS equations.[93] The occupied−occupied subspace projection can be easily evaluated according to

$$\mathbf{P}^x_{oo} = -\mathbf{P}\mathbf{S}^x\mathbf{P} \tag{42}$$

3.2.2. Frozen-Core Gradient Expression. Within the frozen-core approximation, the derivative of the RPA correlation energy reads

$$\begin{aligned} E_C^{\mathrm{RPA},x}[\mathbf{V}, \mathbf{B}, \mathbf{G}_0^{\mathrm{act}}] &= \mathrm{Tr}\left(\frac{\partial E_C^{\mathrm{RPA}}}{\partial \mathbf{V}}\frac{\partial \mathbf{V}}{\partial x}\right) + \mathrm{Tr}\left(\frac{\partial E_C^{\mathrm{RPA}}}{\partial \mathbf{X}_0^{\mathrm{act}}(\mathrm{i}\omega)}\frac{\partial \mathbf{X}_0^{\mathrm{act}}(\mathrm{i}\omega)}{\partial \mathbf{B}}\frac{\partial \mathbf{B}}{\partial x}\right) \\ &\quad + \mathrm{Tr}\left(\frac{\partial E_C^{\mathrm{RPA}}}{\partial \mathbf{G}_0^{\mathrm{act}}(\mathrm{i}\tau)}\frac{\partial \mathbf{G}_0^{\mathrm{act}}(\mathrm{i}\tau)}{\partial x}\right) \end{aligned} \tag{43}$$

where we use the active Green's function (eq 18). Upon closer inspection, it becomes apparent that for the evaluation of the first two terms, the equations derived for the all-electron case can be used, however, replacing the Green's function with the active Green's function throughout the complete computation. Therefore, the contribution of the electron−electron operator to the RPA gradient (first term, eq 43) can be computed using eqs 26 and 27, however, using the active response function (eq 19) and for the contribution of the three-center integrals to the RPA gradient (second term, eq 43), eq 28 can be employed using the active Green's function.

The task ahead is now to compute the contribution of the active Green's function to the RPA gradient (third term, eq 43). We can start by following the same steps as for the all-electron Green's function bringing us to the following expression

$$\begin{aligned} &\mathrm{Tr}\left(\frac{\partial E_C^{\mathrm{RPA}}}{\partial \mathbf{G}_0^{\mathrm{act}}(\mathrm{i}\tau)}\frac{\partial \mathbf{G}_0^{\mathrm{act}}(\mathrm{i}\tau)}{\partial x}\right) \\ &= \mathrm{Tr}\left(\int_0^{+\infty} \mathrm{d}\tau[\boldsymbol{\Sigma}_{\mathrm{act}}(-\mathrm{i}\tau)\bar{\mathbf{G}}_0^x(\mathrm{i}\tau) + \boldsymbol{\Sigma}_{\mathrm{act}}(\mathrm{i}\tau)\underline{\mathbf{G}}_0^{\mathrm{act},x}(-\mathrm{i}\tau)]\right) \end{aligned} \tag{44}$$

where we introduced the active self-energy $\boldsymbol{\Sigma}_{\mathrm{act}}$ which is constructed according to eq 31 employing the active Green's function (eq 18). The contribution of the active Green's function in the negative imaginary time domain can be evaluated using eq 17 following the same procedure as outlined for the all-electron case in ref 68. Here, it is important to note that the active Green's function (eq 17) is dependent not only on the active density but also on the all-electron KS density $\mathbf{P}$ through the KS Hamiltonian (eq 14). Therefore, $\underline{\mathbf{G}}_0^{\mathrm{act},x}(-\mathrm{i}\tau)$ depends explicitly on the response of the active density $\mathbf{P}^x_{\mathrm{act}}$, but it also depends implicitly on the response of the all-electron KS density $\mathbf{P}^x$ through $\mathbf{H}^x_{\mathrm{KS}}$ (eq 14).

The derivative of the Green's function in the positive imaginary time domain is computed as in the all-electron case and is thus only dependent on the response of the all-electron KS density.

Finally, after collecting all terms, we arrive at the following expression for the contribution of the active Green's function

$$\begin{aligned} &\mathrm{Tr}\left(\frac{\partial E_C^{\mathrm{RPA}}}{\partial \mathbf{G}_0^{\mathrm{act}}(\mathrm{i}\tau)}\frac{\partial \mathbf{G}_0^{\mathrm{act}}(\mathrm{i}\tau)}{\partial x}\right) \\ &= \mathrm{Tr}(\mathbf{P}^{\mathrm{act}}_{\mathrm{RPA}}(\mathbf{H}^{(x)}_{\mathrm{KS}} - \epsilon_F\mathbf{S}^{(x)}) + \mathbf{V}^{\mathrm{act}}_{\mathrm{RPA}}\mathbf{P}^x + \bar{\boldsymbol{\Sigma}}^-_{\mathrm{act}}\mathbf{P}^x_{\mathrm{act}} \\ &\quad + \mathbf{S}^{-1}\bar{\boldsymbol{\Sigma}}^+_{\mathrm{act}}\mathbf{S}^{-1}\mathbf{S}^{(x)}) \end{aligned} \tag{45}$$

where we have introduced the following quantities

$$\mathbf{V}^{\mathrm{act}}_{\mathrm{RPA}} = \bar{\boldsymbol{\Sigma}}^+_{\mathrm{act}} + \mathbf{J}[\mathbf{P}^{\mathrm{act}}_{\mathrm{RPA}}] + \mathbf{V}_{\mathrm{xc}}[\mathbf{P}^{\mathrm{act}}_{\mathrm{RPA}}] \tag{46}$$

$$\mathbf{P}^{\mathrm{act}}_{\mathrm{RPA}} = \int_0^{\infty} \mathrm{d}\tau(\mathbf{P}\underline{\mathbf{Y}}_{\mathrm{act}}(-\mathrm{i}\tau) - \mathbf{P}_{\mathrm{virt}}\bar{\mathbf{Y}}_{\mathrm{act}}(\mathrm{i}\tau)) \tag{47}$$

$$\begin{aligned} \bar{\boldsymbol{\Sigma}}^-_{\mathrm{act}} = \int_0^{+\infty} \mathrm{d}\tau(&\underline{\mathbf{Y}}_{\mathrm{act}}(-\mathrm{i}\tau)(\mathbf{H}_{\mathrm{KS}} - \epsilon_F\mathbf{S}) \\ &+ \exp(-\tau(\mathbf{H}_{\mathrm{KS}} - \epsilon_F\mathbf{S})\mathbf{P}_{\mathrm{act}})\boldsymbol{\Sigma}_{\mathrm{act}}(\mathrm{i}\tau)) \end{aligned} \tag{48}$$

$$\begin{aligned} \bar{\boldsymbol{\Sigma}}^+_{\mathrm{act}} = \int_0^{+\infty} \mathrm{d}\tau(&\bar{\mathbf{Y}}_{\mathrm{act}}(\mathrm{i}\tau)(\mathbf{H}_{\mathrm{KS}} - \epsilon_F\mathbf{S}) \\ &+ \exp(-\tau(\mathbf{H}_{\mathrm{KS}} - \epsilon_F\mathbf{S})\mathbf{P}_{\mathrm{virt}})\boldsymbol{\Sigma}_{\mathrm{act}}(-\mathrm{i}\tau)) \end{aligned} \tag{49}$$

$$\mathbf{Y}_{\mathrm{act}}(\mathrm{i}\tau) = \Theta(-\mathrm{i}\tau)\underline{\mathbf{Y}}_{\mathrm{act}}(\mathrm{i}\tau) + \Theta(\mathrm{i}\tau)\bar{\mathbf{Y}}_{\mathrm{act}}(\mathrm{i}\tau) \tag{50}$$

where $\underline{\mathbf{Y}}_{\mathrm{act}}(-\mathrm{i}\tau)$ can be computed using eq 39 utilizing the active density and active self-energy and $\bar{\mathbf{Y}}_{\mathrm{act}}(\mathrm{i}\tau)$ according to eq 40 using the active self-energy.

When comparing the expression within the frozen-core approximation (eq 45) with the all-electron expression (eq 32), it becomes clear that within the frozen-core approximation, we have to evaluate not only the response of the KS density but also the response of the active density. This fact makes the evaluation of gradients within the frozen-core approximation nontrivial.

To eventually make use of the Z-vector technique for the computation of perturbed densities, we start by summarizing all terms containing density responses, such as the contribution stemming from $E^{\mathrm{HF}}[\mathbf{P}^x]$ (eq 23) and from the active Green's function (eq 45) resulting in

$$\mathrm{Tr}([\mathbf{H}_{\mathrm{HF}} + \mathbf{V}^{\mathrm{act}}_{\mathrm{RPA}}]\mathbf{P}^x + \bar{\boldsymbol{\Sigma}}^-_{\mathrm{act}}\mathbf{P}^x_{\mathrm{act}}) \tag{51}$$

While the evaluation of $\mathbf{P}^x$ is not new and can, in principle, be done as in the all-electron case, we do require an expression for $\mathbf{P}^x_{\mathrm{act}}$. The next section is structured as follows: we will start by reviewing important equations from MO response theory. Subsequently, we will derive an expression for both densities in terms of MO quantities. Lastly, we will derive the final Z-vector equation for the efficient evaluation of both density responses.

Please note that for the implementation of the frozen-core approximation for related AO-based electron correlation methods (such as MP2 or CC variants), the equivalent of eq 51 has to be derived, that is, an expression that depends on the response of the active and all-electron density. After that expression is obtained, the density responses can be computed as outlined in the next section.

3.3. Evaluating the Contribution of Density Responses to the RPA Gradient. *3.3.1. MO-Response Theory.* In this section, we will review some important equations from MO response theory[94] that will become very useful and relevant in the upcoming sections.

The derivative of the MO coefficient matrix can be expressed as

https://doi.org/10.1021/acs.jctc.2c00774
J. Chem. Theory Comput. 2022, 18, 7359−7372

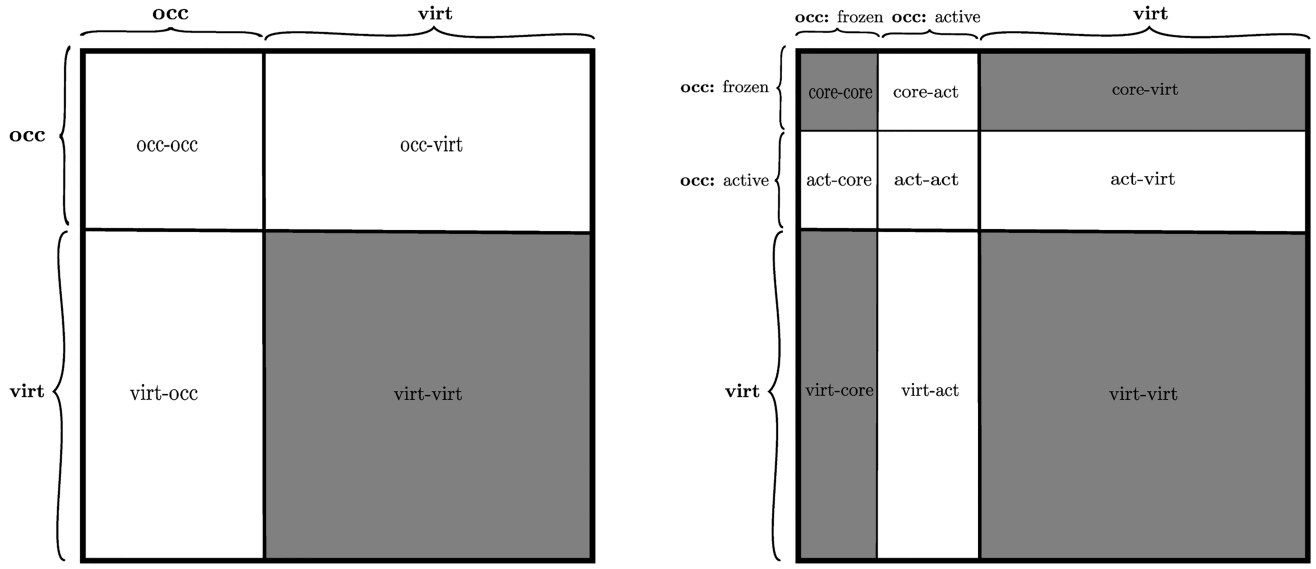

Figure 1. Schematic representation of the different subspace projections of the all-electron perturbed density (left) and the active perturbed density (right). The gray blocks evaluate to zero.

$$C^x_{\mu p} = \sum_{q}^{N_{all}} C_{\mu q} U^x_{qp} \tag{52}$$

where we used the unitary matrix $\mathbf{U}^x$ to express the perturbed MO coefficient matrix as a linear combination of the unperturbed quantities. In the quest to obtain an expression for $\mathbf{U}^x$, the CPKS equations can be derived—specifically by taking the derivative of the off-diagonal elements of the Fock matrix.[95] The CPKS equations within the MO formalism read

$$\sum_{i}^{N_{occ}} \sum_{a}^{N_{virt}} (\delta_{ab}\delta_{ij}(\epsilon_i - \epsilon_a) - A_{aibj}) U^x_{ai} = B^x_{bj} \tag{53}$$

where we introduced the following quantities

$$A'_{aibj} = \delta_{ab}\delta_{ij}(\epsilon_i - \epsilon_a) - A_{aibj} \tag{54}$$

$$A_{pqrs} = 2(pq|rs) - (pr|f_{xc}|qs) - (ps|f_{xc}|qr) \tag{55}$$

$$B^x_{pq} = F^{(x)}_{pq} - S^{(x)}_{pq}\epsilon_q - \frac{1}{2}\sum_{kl}^{N_{occ}} S^{(x)}_{kl} A_{pqlk} \tag{56}$$

with the exchange−correlation kernel f_{xc}. It should be noted that by construction, the CPKS equations solve only for the occupied−virtual block of $\mathbf{U}^x$ ($\{U^x_{ai}\}$). However, to obtain an arbitrary block U^x_{pq}, the following equation can be used[95]

$$U^x_{pq} = \frac{1}{\epsilon_q - \epsilon_p}\left(\sum_{a}^{N_{virt}} \sum_{i}^{N_{occ}} A_{pqai} U^x_{ai} + B^x_{pq}\right) \tag{57}$$

3.3.2. Evaluating Density Responses ($\mathbf{P}^x_{act}$ and $\mathbf{P}^x$). In order to evaluate $\mathbf{P}^x_{act}$ and $\mathbf{P}^x$, we may start by visualizing the different subspace projections of each density response. This is shown in Figure 1, where the subspace projections of $\mathbf{P}^x$ are shown on the left and those of $\mathbf{P}^x_{act}$ on the right. For $\mathbf{P}^x_{act}$, the core−core as well as the core−virtual (virtual−core) blocks evaluate to zero as has been shown in Appendix B. Therefore, using Figure 1, the response of the all-electron and the active density can now be expressed in terms of their subspace projections. This allows us to break down the task of evaluating the complete density responses ($\mathbf{P}^x_{act}$ and $\mathbf{P}^x$) into the evaluations of each individual subspace projection. This can be accomplished by utilizing quantities from MO response theory (Section 3.3.1) to express each subspace projection in terms of $\mathbf{U}^x$. As shown in Appendices A and B, the resulting equations for $\mathbf{P}^x$ read

$$P^x_{\mu\nu} = (\mathbf{P}^x_{oo})_{\mu\nu} + (\mathbf{P}^x_{vo})_{\mu\nu} + (\mathbf{P}^x_{ov})_{\mu\nu} \tag{58}$$

$$= \left(\sum_{i}^{N_{occ}} \sum_{j}^{N_{occ}} C_{\mu j} U^x_{ji} C_{\nu i} + \sum_{i}^{N_{occ}} \sum_{j}^{N_{occ}} C_{\mu i} C_{\nu j} U^x_{ji}\right) + \left(\sum_{i}^{N_{occ}} \sum_{a}^{N_{virt}} C_{\mu a} U^x_{ai} C_{\nu i}\right) + \left(\sum_{i}^{N_{occ}} \sum_{a}^{N_{virt}} C_{\mu i} C_{\nu a} U^x_{ai}\right) \tag{59}$$

and for $\mathbf{P}^x_{act}$

$$P^x_{act,\mu\nu} = \mathbf{P}^x_{act,ca} + \mathbf{P}^x_{act,ac} + \mathbf{P}^x_{act,aa} + \mathbf{P}^x_{act,va} + \mathbf{P}^x_{act,av} \tag{60}$$

$$= \left(\sum_{i'}^{N_{act}} \sum_{I}^{N_{core}} C_{\mu I} U^x_{Ii'} C_{\nu i'}\right) + \left(\sum_{i'}^{N_{act}} \sum_{I}^{N_{core}} C_{\mu i'} C_{\nu I} U^x_{Ii'}\right) + \left(\sum_{i'}^{N_{act}} \sum_{j'}^{N_{act}} C_{\mu j'} U^x_{j'i'} C_{\nu i'} + \sum_{i'}^{N_{act}} \sum_{j'}^{N_{act}} C_{\mu i'} C_{\nu j'} U^x_{j'i'}\right) + \left(\sum_{i'}^{N_{act}} \sum_{a}^{N_{virt}} C_{\mu a} U^x_{ai'} C_{\nu i'}\right) + \left(\sum_{i'}^{N_{act}} \sum_{a}^{N_{virt}} C_{\mu i'} C_{\nu a} U^x_{ai'}\right) \tag{61}$$

where $\{U^x_{Ii'}\}$ is defined according to eq 57.

3.3.3. Efficient Evaluation of Perturbed Densities: RPA-Lagrangian, Z-Vector Technique. We may recall that the term depending on density responses is given by eq 51. In this section, we aim to combine the observations made in the last two sections to efficiently solve eq 51 using the Z-vector technique.[83,84] To accomplish this, we can start by inserting the expressions for $\mathbf{P}^x$ (eq 58) and $\mathbf{P}^x_{act}$ (eq 60) into eq 51 according to

https://doi.org/10.1021/acs.jctc.2c00774
J. Chem. Theory Comput. 2022, 18, 7359−7372

$$\begin{aligned}\mathrm{Tr}([\mathbf{V}^{\mathrm{act}}_{\mathrm{RPA}} + \mathbf{H}_{\mathrm{HF}}]\mathbf{P}^x + \bar{\boldsymbol{\Sigma}}^-_{\mathrm{act}}\mathbf{P}^x_{\mathrm{act}}) &= \mathrm{Tr}([\mathbf{V}^{\mathrm{act}}_{\mathrm{RPA}} + \mathbf{H}_{\mathrm{HF}}]\mathbf{P}^x_{\mathrm{oo}}) + \mathrm{Tr}(\bar{\boldsymbol{\Sigma}}^-_{\mathrm{act}}\mathbf{P}^x_{\mathrm{act,aa}}) \\ &+ \mathrm{Tr}([\mathbf{V}^{\mathrm{act}}_{\mathrm{RPA}} + \mathbf{H}_{\mathrm{HF}}]\mathbf{P}^x_{\mathrm{vo}}) + \mathrm{Tr}([\mathbf{V}^{\mathrm{act}}_{\mathrm{RPA}} + \mathbf{H}_{\mathrm{HF}}]\mathbf{P}^x_{\mathrm{ov}}) \\ &+ \mathrm{Tr}(\bar{\boldsymbol{\Sigma}}^-_{\mathrm{act}}\mathbf{P}^x_{\mathrm{act,va}}) + \mathrm{Tr}(\bar{\boldsymbol{\Sigma}}^-_{\mathrm{act}}\mathbf{P}^x_{\mathrm{act,av}}) + \mathrm{Tr}(\bar{\boldsymbol{\Sigma}}^-_{\mathrm{act}}\mathbf{P}^x_{\mathrm{act,ca}}) \\ &+ \mathrm{Tr}(\bar{\boldsymbol{\Sigma}}^-_{\mathrm{act}}\mathbf{P}^x_{\mathrm{act,ac}}) \end{aligned} \tag{62}$$

The contribution stemming from $\mathbf{P}^x_{\mathrm{oo}}$ (eq 42) as well as the contribution from $\mathbf{P}^x_{\mathrm{act,aa}}$ can be easily evaluated according to

$$\mathrm{Tr}([\mathbf{V}^{\mathrm{act}}_{\mathrm{RPA}} + \mathbf{H}_{\mathrm{HF}}]\mathbf{P}^x_{\mathrm{oo}}) = \mathrm{Tr}(-[\mathbf{V}^{\mathrm{act}}_{\mathrm{RPA}} + \mathbf{H}_{\mathrm{HF}}]\mathbf{P}\mathbf{S}^x\mathbf{P}) \tag{63}$$

$$\mathrm{Tr}(\bar{\boldsymbol{\Sigma}}^-_{\mathrm{act}}\mathbf{P}^x_{\mathrm{act,aa}}) = \mathrm{Tr}(-\bar{\boldsymbol{\Sigma}}^-_{\mathrm{act}}\mathbf{P}_{\mathrm{act}}\mathbf{S}^x\mathbf{P}_{\mathrm{act}}) \tag{64}$$

The contribution of the remaining subspaces can be evaluated utilizing their expressions given in eqs 59 and 61. As shown in the detailed derivation in Appendix C, the final expression reads

$$\begin{aligned}\mathrm{Tr}([\mathbf{V}^{\mathrm{act}}_{\mathrm{RPA}} + \mathbf{H}_{\mathrm{HF}}]\mathbf{P}^x_{\mathrm{vo}}) + \mathrm{Tr}(\bar{\boldsymbol{\Sigma}}^-_{\mathrm{act}}\mathbf{P}^x_{\mathrm{act,va}}) + \mathrm{Tr}(\bar{\boldsymbol{\Sigma}}^-_{\mathrm{act}}\mathbf{P}^x_{\mathrm{act,ac}}) \\ = \sum_{i}^{N_{\mathrm{occ}}}\sum_{a}^{N_{\mathrm{virt}}} Q_{ai}U^x_{ai} + \sum_{i'}^{N_{\mathrm{act}}}\sum_{I}^{N_{\mathrm{core}}} \tilde{Z}_{Ii'}B^x_{Ii'}\end{aligned} \tag{65}$$

with

$$\tilde{Z}_{Ii'} = \frac{(\bar{\boldsymbol{\Sigma}}^-_{\mathrm{act}})_{Ii'}}{\epsilon_I - \epsilon_{i'}} \tag{66}$$

and the RPA Lagrangian $\mathbf{Q}$ is defined as

$$Q_{ai} = (\mathbf{V}^{\mathrm{act}}_{\mathrm{RPA}} + \mathbf{H}_{\mathrm{HF}})_{ai} + (\bar{\boldsymbol{\Sigma}}^-_{\mathrm{act}})_{ai}I^{\mathrm{act}}_i + L_{ai} \tag{67}$$

$$L_{ai} = \sum_{i'}^{N_{\mathrm{act}}}\sum_{I}^{N_{\mathrm{core}}} (\bar{\boldsymbol{\Sigma}}^-_{\mathrm{act}})_{Ii'}\frac{A_{i'Iai}}{\epsilon_I - \epsilon_{i'}} \tag{68}$$

where we introduced

$$I^{\mathrm{act}}_i = \begin{cases} 0 & \text{if } i \in [1, N_{\mathrm{core}}] \\ 1 & \text{if } i \in (N_{\mathrm{core}}, N_{\mathrm{occ}}] \end{cases} \tag{69}$$

Using eq 65, we are able to simultaneously determine the contributions stemming from the virtual−occupied subspace of $\mathbf{P}^x$ as well as the virtual−active and active−core subspaces of $\mathbf{P}^x_{\mathrm{act}}$. Now, we can apply the Z-vector technique on the right hand side of eq 65 giving the final expression

$$\mathrm{Tr}(\mathbf{Q}^{\mathrm{T}}\mathbf{U}^x + \tilde{\mathbf{Z}}^{\mathrm{T}}\mathbf{B}^x) = \mathrm{Tr}([\mathbf{Z}^{\mathrm{T}} + \tilde{\mathbf{Z}}^{\mathrm{T}}]\mathbf{B}^x) \tag{70}$$

with

$$\mathbf{Z}^{\mathrm{T}} = \mathbf{Q}^{\mathrm{T}}(\mathbf{A}')^{-1} \tag{71}$$

Accordingly, only one CPKS equation has to be solved to obtain the perturbation-independent matrix $\mathbf{Z}$.

3.4. Cholesky Decomposition. An important technique used in AO-based theories to achieve rank reduction is the CD with complete pivoting of positive semi-definite density matrices,[96−100] which allows to overcome the unfavorable scaling with the size of the atom-centered basis by reintroducing the occupied index. When the frozen-core approximation is used, instead of the aforementioned occupied index, the active-orbital index is introduced. Thus, by using the CD within an AO-based theory, the frozen-core approximation becomes profitable also in terms of increased computational efficiency and memory requirements.

The most demanding steps within the calculation of RPA gradients in terms of memory and computational resources are the computation of the response function (eq 7), which formally scales as $O(N^2_{\mathrm{aux}}N^2_{\mathrm{basis}})$, and the computation of the self-energy (eq 31), where the most demanding step is the contraction of the screened Coulomb interaction with the three-center integrals formally scaling as $O(N^2_{\mathrm{aux}}N^2_{\mathrm{basis}})$. Thus, we will use the CD of ground-state densities to reduce the scaling and memory requirements for both steps.

3.4.1. All-Electron Formalism. To introduce the CD, we make use of the fact that the Green's function in negative imaginary time is invariant with respect to projections onto the occupied subspace

$$\underline{\mathbf{G}}_0(-\mathrm{i}\tau) = \underline{\mathbf{G}}_0(-\mathrm{i}\tau)\mathbf{S}\mathbf{P} \tag{72}$$

Using eq 72 together with the CD of the occupied ground-state density, $\mathbf{P} = \mathbf{L}\mathbf{L}^{\mathrm{T}}$ allows to express the response function as[32,34]

$$X_{0,MN}(\mathrm{i}\tau) = [\mathbf{L}^{\mathrm{T}}\mathbf{S}\underline{\mathbf{G}}_0(-\mathrm{i}\tau)\mathbf{S}\mathbf{L}][\mathbf{L}^{\mathrm{T}}\mathbf{B}^M]\bar{\mathbf{G}}_0(\mathrm{i}\tau)[\mathbf{B}^N\mathbf{L}] \tag{73}$$

$$X_{0,MN}(\mathrm{i}\tau) = \sum_{\underline{j},\underline{i}}^{N_{\mathrm{occ}}}\sum_{\nu,\mu}^{N_{\mathrm{basis}}} [\underline{G}_{0,\underline{j}\,\underline{i}}(-\mathrm{i}\tau)B^M_{\underline{i}\nu}\bar{G}_{0,\mu\nu}(\mathrm{i}\tau)]B^N_{\mu\underline{j}} \tag{74}$$

$$X_{0,MN}(\mathrm{i}\tau) = \sum_{\underline{j}}^{N_{\mathrm{occ}}}\sum_{\mu}^{N_{\mathrm{basis}}} B^M_{\underline{j}\mu}(\mathrm{i}\tau)B^N_{\mu\underline{j}} \tag{75}$$

This reduces the formal scaling for the computation of the response function to $O(N^2_{\mathrm{aux}}N_{\mathrm{basis}}N_{\mathrm{occ}})$.

For the computation of the self-energy in negative imaginary time, we can use eq 72 together with the CD of the ground-state density to yield

$$\boldsymbol{\Sigma}(-\mathrm{i}\tau) = \sum_{M,N}^{N_{\mathrm{aux}}} [-\mathbf{B}^M\mathbf{L}][\mathbf{L}^{\mathrm{T}}\mathbf{S}\underline{\mathbf{G}}_0(-\mathrm{i}\tau)\mathbf{S}\mathbf{L}][\mathbf{L}^{\mathrm{T}}\mathbf{B}^N]W_{\mathrm{c},NM}(-\mathrm{i}\tau) \tag{76}$$

$$\Sigma_{\mu\nu}(-\mathrm{i}\tau) = \sum_{M,N}^{N_{\mathrm{aux}}}\sum_{\underline{i},\underline{j}}^{N_{\mathrm{occ}}} B^M_{\mu\underline{i}}\underline{G}_{0,\underline{i},\underline{j}}(-\mathrm{i}\tau)B^N_{\underline{j}\nu}W_{\mathrm{c},NM}(-\mathrm{i}\tau) \tag{77}$$

The scaling for the expensive contraction can thus be reduced to $O(N^2_{\mathrm{aux}}N_{\mathrm{basis}}N_{\mathrm{occ}})$.

For the self-energy in the positive imaginary time domain, instead of computing $\boldsymbol{\Sigma}(\mathrm{i}\tau)$ directly, we can also compute $\mathbf{S}\mathbf{P}\boldsymbol{\Sigma}(\mathrm{i}\tau)$ without changing the final result of the gradient calculation. The details and reasoning for this approach can be found in ref 68. This gives rise to the CD of the occupied density. Thus, we obtain the following expression

$$\mathbf{S}\mathbf{P}\boldsymbol{\Sigma}(\mathrm{i}\tau) = \sum_{M,N}^{N_{\mathrm{aux}}} W_{\mathrm{c},MN}(\mathrm{i}\tau)[\mathbf{S}\mathbf{L}][\mathbf{L}^{\mathrm{T}}\mathbf{B}^M]\bar{\mathbf{G}}_0(\mathrm{i}\tau)\mathbf{B}^N \tag{78}$$

$$(\mathbf{S}\mathbf{P}\boldsymbol{\Sigma}(\mathrm{i}\tau))_{\mu\nu} = \sum_{M,N}^{N_{\mathrm{aux}}}\sum_{\underline{i}}^{N_{\mathrm{occ}}}\sum_{\sigma,\kappa}^{N_{\mathrm{basis}}} S_{\mu\,\underline{i}}W_{\mathrm{c},NM}(\mathrm{i}\tau)B^M_{\underline{i}\sigma}\bar{G}_{0,\sigma\kappa}(\mathrm{i}\tau)B^N_{\kappa\nu} \tag{79}$$

scaling as $O(N^2_{\mathrm{aux}}N_{\mathrm{basis}}N_{\mathrm{occ}})$.

3.4.2. Frozen-Core Formalism. We can derive the frozen-core equivalent of eq 72 as

https://doi.org/10.1021/acs.jctc.2c00774
J. Chem. Theory Comput. 2022, 18, 7359−7372

$$\underline{\mathbf{G}}_0^{\mathrm{act}}(-\mathrm{i}\tau) = \underline{\mathbf{G}}_0^{\mathrm{act}}(-\mathrm{i}\tau)\mathbf{S}\mathbf{P}_{\mathrm{act}} \tag{80}$$

and use the pivoted CD of the active density $\mathbf{P}_{\mathrm{act}} = \tilde{\mathbf{L}}\tilde{\mathbf{L}}^{\mathrm{T}}$ to reformulate the active response function and active self-energy using the approaches presented in the last section. This reduces the scaling for the computation of the response function and for the expensive contraction within the calculation of the self-energy to $O(N_{\mathrm{aux}}^2 N_{\mathrm{basis}} N_{\mathrm{act}})$. Thus, within the frozen-core approximation, we are able to reduce the computational effort and memory requirement for the two most costly steps by a factor of $N_{\mathrm{occ}}/N_{\mathrm{act}}$.

4. COMPUTATIONAL DETAILS

The frozen-core approximation was implemented for RPA forces in the FermiONs++ program package,[101−103] which was compiled with the GNU Compiler Collection (GCC) version 8.1. Kohn−Sham orbitals required for the RPA calculations were obtained from preceeding DFT calculations using the generalized gradient approximation of Perdew, Burke, and Ernzerhof[104,105] provided by the libXC library.[106] For atomic basis sets, we use the def2-SVP, def2-TZVP, and def2-QZVP basis sets[107,108] as well as Dunning's augmented correlation-consistent basis sets with core-weighted functions (aug-cc-pwCVQZ).[74] For the RI approximation, which is applied to the four-center integrals in the correlation part of the RPA energy, the corresponding RI basis sets are employed.[109,110] For the time and frequency grid, we used 13−15 grid points.[34] When using the frozen-core approximation, the following number of orbitals was kept frozen: H−Be: 0, B−Mg: 1, Al−Zn: 5, and Ga−Kr: 9. All calculations were carried out on a CPU compute node containing 2 AMD EPYC 7302 16-core processors (in total, 32 cores/64 threads @ 3.0 GHz). Since the most compute intensive steps involve dense linear algebra, we use the high performance of the Math Kernel Library (version 2021). Thus, the speedup from the frozen-core approximation is the result of smaller matrix dimensions—and therefore a lower number of floating point operations—in the time-determining steps.

5. RESULTS AND DISCUSSION

5.1. Validation of the Implementation. First, we will validate our implementation by comparing our analytical frozen-core gradients to numerical results, which we obtained using the five-point stencil method with a step size of 10^{-5} Å. For the computations, we used the molecules in the G2 test set since it includes various main-group elements (specifically, elements from the first to third row), which allows us to investigate an assortment of systems with a broad range of frozen-core orbitals. However, since the geometries of the G2 test set were already optimized and consequently comprised very small gradient vectors, we decided to distort one atom in each molecule by 0.2 Å in order to obtain larger gradients to asses. Please note that the small size of the gradient vector for preoptimized geometries serves as the first consistency check of our new implementation. We computed the analytical and numerical frozen-core gradients for the molecules in the distorted G2 test set using the def2-QZVP basis set and the corresponding RI basis set. The results are shown in Table 2 where we denoted the mean-absolute deviation (MAD) as well as the number of frozen-core orbitals compared to the total number of occupied orbitals for each system. As can be observed, the MADs are on the order of 10^{-6} to 10^{-4} a.u., which is within the error of numerical differentiation. Therefore we can conclude that our implementation is correct.

Table 2. Comparison of Analytical and Numerical Frozen-Core RPA Forces for the Distorted G2 Test Set Using the def2-QZVP Basis Set with the Corresponding RI Basis Set[a]

system	$N_{\mathrm{core}}/N_{\mathrm{occ}}$	MAD	system	$N_{\mathrm{core}}/N_{\mathrm{occ}}$	MAD
CO	2/7	0.470	P_2	10/15	0.040
SiO	6/11	0.268	CH_4	1/5	0.164
H_2N-NH_2	2/9	0.216	Na_2	4/11	0.003
Cl_2	10/17	0.054	HOCl	6/13	0.071
PH_3	5/9	0.175	H_3C-SH	6/13	0.200
CH_3-OH	2/9	0.186	H_3C-CH_3	2/9	0.120
H_2S	5/9	0.112	NH_3	1/5	0.038
CS	6/11	0.607	HCl	5/9	0.077
LiF	1/6	0.016	SiH_2	5/8	0.154
$H_3Si-SiH_3$	10/17	0.294	N_2	2/7	0.433
SiH_4	5/9	0.364	ClF	6/13	0.076
CH_2	1/4	0.265	HO−OH	2/9	0.154
NaCl	6/14	0.075	HCN	2/7	0.876
H_2O	1/5	0.069	HF	1/5	0.025
CO_2	3/11	0.461	formaldehyde	2/8	0.150
ethylene	2/8	0.157	CH_3Cl	6/13	0.141
C_2H_2	2/7	0.230	F_2	2/9	0.056

[a]MADs are given in units of 10^{-3} a.u.

5.2. Accuracy of RPA Frozen-Core Forces Compared to All-Electron Forces. In this section, we will investigate the error that is introduced when using the frozen-core approximation or, equivalently, the effect of neglecting the electron correlation of core electrons for molecular geometries. Dunning's augmented correlation-consistent basis sets with core-weighted functions (aug-cc-pwCVQZ) are used as well as the corresponding RI basis sets in order to obtain accurate results when all electrons are correlated. In Table 3, the equilibrium bond lengths and angles for small main-group molecules as optimized with and without the frozen-core approximation are summarized. As can be seen, the deviation in bond lengths is below 0.5 pm and the deviation in bond angles is below 0.2°. Those deviations are in very good agreement with results obtained for related electron correlation methods; for example, in ref 71, the effect of core correlation was investigated using CC and many-body perturbation theory and the largest deviations for bond lengths were found to be 0.3 pm and for bond angles 0.1°. Thus, our work extends these findings (ref 71) to RPA. That is, the correlation of core electrons has minimal effect on molecular geometries for RPA as well, meaning that the frozen-core method has indeed shown to be a very accurate approximation in the scope of this study.

5.3. Timings. In this section, we will investigate the efficiency of our frozen-core RPA forces as compared to all-electron forces. For this, we have computed a DNA fragment as well as linear alkanes of increasing length using the def2-SVP and def2-TZVP basis sets with the corresponding RI basis sets with and without the frozen-core approximation. In Table 4, the speedups obtained by using the frozen-core approximation compared to the all-electron timings are shown. As can be seen, depending on the size of the basis set, we obtain a speedup of 20−30%. The decreased speedup when moving to larger basis sets can be rationalized by the increased number of virtual orbitals, which are not influenced by the frozen-core approximation and, therefore, other steps in the calculation

https://doi.org/10.1021/acs.jctc.2c00774
J. Chem. Theory Comput. 2022, 18, 7359−7372

Table 3. Comparison of Equilibrium Bond Distances r (pm) and Angles α (deg) for Small Main-Group Molecules Obtained Using All-Electron RPA Forces and Frozen-Core RPA Forces[a]

system	param.	all-electron	frozen-core	system	param.	all-electron	frozen-core
H_2O	r	96.34	0.08	NH_3	r	101.64	0.11
	α	103.901	−0.102		α	106.064	−0.171
CO	r	113.53	0.25	CS	r	154.32	0.36
Cl_2	r	201.33	0.45	HCl	r	127.71	0.15
HCN	r(C−N)	115.86	0.20	C_2H_2	r(C−H)	106.46	0.11
	r(C−H)	106.80	0.12		r(C−C)	120.70	0.20
H_2S	r	133.84	0.20	PH_3	r	141.44	0.30
	α	92.165	−0.013		α	93.333	0.014
SiH_4	r	151.41	0.34	CH_4	r	108.96	0.15
	α	92.394	0.035		α	109.471	0.000
HF	r	92.28	0.06	SiO	r	151.824	0.36
CH_2O	r(C−O)	121.11	0.21	HOCl	r(O−H)	96.91	−0.09
	r(C−H)	110.32	0.11		r(O−Cl)	171.17	−0.38
	α(H−C−O)	121.702	−0.012		α	102.176	0.097
	α(H−C−H)	116.596	−0.024	F_2	r	143.87	0.19
H_2O_2	r(O−H)	96.82	0.09	N_2	r	110.35	0.20
	r(O−O)	147.23	0.28	SiH_2	r	151.41	−0.38
	α(O−O−H)	99.389	0.088		α	92.358	0.035
	α(H−O−O−H)	−113.225	0.167				

[a]The frozen-core RPA results are displayed as differences to the corresponding all-electron results. The geometry optimizations were carried out using the aug-cc-pwCVQZ basis set and the corresponding RI basis set.

Table 4. Speedups (%) for the Computation of Frozen-Core Forces Compared to All-Electron Results for a DNA Fragment and the Average Speedup for Five Linear Alkanes ($C_{10}H_{22}$−$C_{50}H_{102}$)

basis Set	alkanes	$(DNA)_1$
def2-SVP	31	29
def2-TZVP	22	26

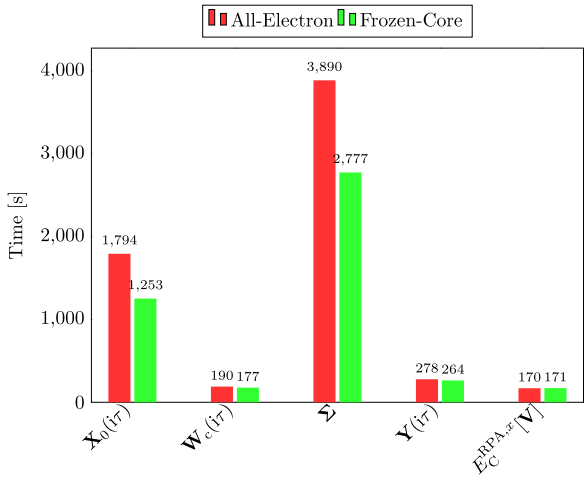

Figure 2. Timings for the most time-consuming steps during the computation of the all-electron (red) and frozen-core (green) RPA forces for $(DNA)_1$ (61 atoms, N_{occ} = 130, N_{act} = 95) using the def2-SVP basis set. For a detailed description of the steps and symbols, we refer to the text.

become more computationally demanding. For heavier elements with more frozen-core electrons, we of course expect larger speedups.

For a more detailed analysis, we have summarized timings for the most time-consuming steps within the gradient calculation for a DNA fragment using the def2-SVP basis set. Specifically, we summarized the timings for the computation of the response function $[\mathbf{X}_0(i\tau)$, eq 75] of the screened Coulomb interaction $[\mathbf{W}_c(i\tau)$, eq 29], the self-energy $[\mathbf{\Sigma}(\pm i\tau)$; eqs 76 and 78], the auxiliary matrix $\mathbf{Y}(i\tau)$ (eq 38), as well as the contribution from $\partial E_C^{RPA}/\partial \mathbf{V}$ (eqs 26 and 27). The results are shown in Figure 2. As expected, the biggest speedups are obtained for the two most computationally demanding steps, that is, the calculation of the response function as well as the computation of the self-energy, since for the computation of those terms, we made use of Cholesky decomposed densities as explained in Section 3.4.

6. CONCLUSIONS

In this work, we have presented a detailed derivation of the frozen-core approximation within RPA gradients in the AO formalism. The main difficulty lies in the evaluation of the response of the active density in addition to the response of the all-electron KS density, for which we have outlined an efficient way to account for both density responses. By comparing our analytical frozen-core RPA gradients to numerical results, we demonstrated the validity and correctness of our implementation. Furthermore, we investigated the error introduced by the frozen-core approximation on molecular geometries for small main-group molecules. We found that the deviation in bond lengths lies below 0.5 pm and that in bond angles lies below 0.2°. Lastly, we have shown that by using the frozen-core approximation, we are able to achieve speedups of 20−30% depending on the size of the chosen basis set. We expect these speedups to be larger for systems with more frozen-core electrons. By introducing the frozen-core approximation to RPA gradients, we extended RPA to practical applications by improving the computational efficiency with practically negligible loss in accuracy and removing the limitation in the basis set selection.

Finally, we would also like to emphasize that the presented derivation in the AO framework allows us to easily adopt the

https://doi.org/10.1021/acs.jctc.2c00774
J. Chem. Theory Comput. 2022, 18, 7359−7372

outlined procedure to related electron correlation methods formulated in the AO basis that require the evaluation of density responses, such as MP2 or CC variants.

APPENDICES

A. Relationship between $\mathbf{P}^x$ and $\mathbf{U}^x$

The KS density $\mathbf{P}$ is defined as

$$P_{\mu\nu} = \sum_{i}^{N_{occ}} C_{\mu i} C_{\nu i} \tag{81}$$

Taking the derivative of eq 81 gives

$$P^x_{\mu\nu} = \sum_{i}^{N_{occ}} (C^x_{\mu i} C_{\nu i} + C_{\mu i} C^x_{\nu i}) \tag{82}$$

Inserting eq 52 into eq 82 gives an expression for the perturbed density entirely in terms of $\mathbf{U}^x$ and $\mathbf{C}$

$$P^x_{\mu\nu} = \sum_{i}^{N_{occ}} \left(\sum_{p}^{N_{all}} C_{\mu p} U^x_{pi} C_{\nu i} + \sum_{p}^{N_{all}} C_{\mu i} C_{\nu p} U^x_{pi} \right) \tag{83}$$

Splitting the summation over all orbitals into occupied and virtual orbitals gives the subspace projections of $\mathbf{P}^x$ in terms of the respective blocks of $\mathbf{U}^x$

$$\begin{aligned} P^x_{\mu\nu} &= \left(\sum_{i}^{N_{occ}} \sum_{j}^{N_{occ}} C_{\mu j} U^x_{ji} C_{\nu i} + \sum_{i}^{N_{occ}} \sum_{j}^{N_{occ}} C_{\mu i} C_{\nu j} U^x_{ji} \right) \\ &\quad + \left(\sum_{i}^{N_{occ}} \sum_{a}^{N_{virt}} C_{\mu a} U^x_{ai} C_{\nu i} \right) + \left(\sum_{i}^{N_{occ}} \sum_{a}^{N_{virt}} C_{\mu i} C_{\nu a} U^x_{ai} \right) \\ &= (\mathbf{P}^x_{oo})_{\mu\nu} + (\mathbf{P}^x_{vo})_{\mu\nu} + (\mathbf{P}^x_{ov})_{\mu\nu} \end{aligned} \tag{84}$$

It follows that the first term in eq 84 corresponds to the occupied−occupied subspace projection of $\mathbf{P}^x$ and can be easily determined using eq 42. The second and third terms in eq 84 correspond to the virtual−occupied and occupied−virtual subspace projections of $\mathbf{P}^x$, respectively, and can be obtained using the CPKS equations. The subspace projections of $\mathbf{P}^x$ (eq 85) are also illustrated in Figure 1 (left).

B. Relationship between $\mathbf{P}^x_{act}$ and $\mathbf{U}^x$

To determine the relation between the active perturbed density $\mathbf{P}^x_{act}$ and $\mathbf{U}^x$, we first note that the KS density can be expressed as a sum of the active and core density as

$$P_{\mu\nu} = \sum_{i}^{N_{occ}} C_{\mu i} C_{\nu i} \tag{85}$$

$$= \sum_{I}^{N_{core}} C_{\mu I} C_{\nu I} + \sum_{i'}^{N_{act}} C_{\mu i'} C_{\nu i'} \tag{86}$$

$$= P_{act,\mu\nu} + P_{core,\mu\nu} \tag{87}$$

where the summation over all occupied orbitals was split into the summation over core orbitals and active orbitals.

In a similar way, we can determine the perturbed active density $\mathbf{P}^x_{act}$ from the perturbed KS density $\mathbf{P}^x$. Starting with eq 82, we can split the summation over the occupied space into core and active subspaces

$$\begin{aligned} P^x_{\mu\nu} &= \sum_{I}^{N_{core}} \left(\sum_{p}^{N_{all}} C_{\mu p} U^x_{pI} C_{\nu I} + \sum_{p}^{N_{all}} C_{\mu I} C_{\nu p} U^x_{pI} \right) \\ &\quad + \sum_{i'}^{N_{act}} \left(\sum_{p}^{N_{all}} C_{\mu p} U^x_{pi'} C_{\nu i'} + \sum_{p}^{N_{all}} C_{\mu i'} C_{\nu p} U^x_{pi'} \right) \end{aligned} \tag{88}$$

$$= P^x_{core,\mu\nu} + P^x_{act,\mu\nu} \tag{89}$$

and we can identify $\mathbf{P}^x_{act}$ as

$$P^x_{act,\mu\nu} = \sum_{i'}^{N_{act}} \left(\sum_{p}^{N_{all}} C_{\mu p} U^x_{pi'} C_{\nu i'} + \sum_{p}^{N_{all}} C_{\mu i'} C_{\nu p} U^x_{pi'} \right) \tag{90}$$

Next, we can proceed to split the summations over all orbitals into core, active, and virtual subspaces according to

$$\begin{aligned} P^x_{act,\mu\nu} &= \left(\sum_{i'}^{N_{act}} \sum_{I}^{N_{core}} C_{\mu I} U^x_{Ii'} C_{\nu i'} \right) + \left(\sum_{i'}^{N_{act}} \sum_{I}^{N_{core}} C_{\mu i'} C_{\nu I} U^x_{Ii'} \right) \\ &\quad + \left(\sum_{i'}^{N_{act}} \sum_{j'}^{N_{act}} C_{\mu j'} U^x_{j'i'} C_{\nu i'} + \sum_{i'}^{N_{act}} \sum_{j'}^{N_{act}} C_{\mu i'} C_{\nu j'} U^x_{j'i'} \right) \\ &\quad + \left(\sum_{i'}^{N_{act}} \sum_{a}^{N_{virt}} C_{\mu a} U^x_{ai'} C_{\nu i'} \right) + \left(\sum_{i'}^{N_{act}} \sum_{a}^{N_{virt}} C_{\mu i'} C_{\nu a} U^x_{ai'} \right) \end{aligned} \tag{91}$$

$$= (\mathbf{P}^x_{act,ca})_{\mu\nu} + (\mathbf{P}^x_{act,ac})_{\mu\nu} + (\mathbf{P}^x_{act,aa})_{\mu\nu} + (\mathbf{P}^x_{act,va})_{\mu\nu} + (\mathbf{P}^x_{act,av})_{\mu\nu} \tag{92}$$

which reveals the different subspace projections of $\mathbf{P}^x_{act}$ that are also illustrated in Figure 1 (right). Thus, the task ahead is to evaluate the different subspace projections.

Upon closer inspection, it becomes apparent that the active−active subspace can be computed according to

$$\mathbf{P}^x_{act,aa} = -\mathbf{P}_{act} \mathbf{S}^x \mathbf{P}_{act} \tag{93}$$

and the active−virtual (virtual−active) subspace can be determined using the CPKS equations. The only undetermined subspace is the active−core (core−active) subspace. To derive an expression for $\mathbf{P}^x_{act,ca}$ and $\mathbf{P}^x_{act,ac}$, we can express the active−core (core−active) block of $\mathbf{U}^x$ using equation eq 57

$$U^x_{i'I} = \frac{1}{\epsilon_I - \epsilon_{i'}} \left(\sum_{a}^{N_{virt}} \sum_{i}^{N_{occ}} A_{i'Iai} U^x_{ai} + B^x_{i'I} \right) \tag{94}$$

C. Efficient Computation of Perturbed Densities: RPA-Lagrangian, Z-Vector Technique

Inserting the expression for $\mathbf{P}^x$ (eq 88) and for $\mathbf{P}^x_{act}$ (eq 91) into eq 51 yields

$$\begin{aligned} &\mathrm{Tr}([\mathbf{V}^{act}_{RPA} + \mathbf{H}_{HF}]\mathbf{P}^x + \bar{\boldsymbol{\Sigma}}^-_{act}\mathbf{P}^x_{act}) \\ &= \mathrm{Tr}([\mathbf{V}^{act}_{RPA} + \mathbf{H}_{HF}]\mathbf{P}^x_{oo}) + \mathrm{Tr}(\bar{\boldsymbol{\Sigma}}^-_{act}\mathbf{P}^x_{act,aa}) \\ &\quad + \mathrm{Tr}([\mathbf{V}^{act}_{RPA} + \mathbf{H}_{HF}]\mathbf{P}^x_{vo}) + \mathrm{Tr}([\mathbf{V}^{act}_{RPA} + \mathbf{H}_{HF}]\mathbf{P}^x_{ov}) \\ &\quad + \mathrm{Tr}(\bar{\boldsymbol{\Sigma}}^-_{act}\mathbf{P}^x_{act,va}) + \mathrm{Tr}(\bar{\boldsymbol{\Sigma}}^-_{act}\mathbf{P}^x_{act,av}) + \mathrm{Tr}(\bar{\boldsymbol{\Sigma}}^-_{act}\mathbf{P}^x_{act,ca}) \\ &\quad + \mathrm{Tr}(\bar{\boldsymbol{\Sigma}}^-_{act}\mathbf{P}^x_{act,ac}) \end{aligned} \tag{95}$$

https://doi.org/10.1021/acs.jctc.2c00774
J. Chem. Theory Comput. 2022, 18, 7359−7372

The first two terms can be readily evaluated using eqs 42 and 93, respectively. For the evaluation of the remaining terms, we use the following symmetries

$$\mathbf{P}^x_{\mathrm{vo}} = (\mathbf{P}^x_{\mathrm{ov}})^{\mathrm{T}} \tag{96}$$

$$\mathbf{P}^x_{\mathrm{act,va}} = (\mathbf{P}^x_{\mathrm{act,av}})^{\mathrm{T}} \tag{97}$$

$$\mathbf{P}^x_{\mathrm{act,ac}} = (\mathbf{P}^x_{\mathrm{act,ca}})^{\mathrm{T}} \tag{98}$$

which require the evaluation of only one of each subspaces. Furthermore, inserting the specific expressions for each subspace projection (eqs 84 and 91) and using matrix index notation for the trace result in the following contributions

$$\begin{aligned}
&\mathrm{Tr}([\mathbf{V}^{\mathrm{act}}_{\mathrm{RPA}} + \mathbf{H}_{\mathrm{HF}}]\mathbf{P}^x_{\mathrm{vo}}) + \mathrm{Tr}(\bar{\boldsymbol{\Sigma}}^-_{\mathrm{act}}\mathbf{P}^x_{\mathrm{act,va}}) + \mathrm{Tr}(\bar{\boldsymbol{\Sigma}}^-_{\mathrm{act}}\mathbf{P}^x_{\mathrm{act,ac}}) \\
&= \sum_{i}^{N_{\mathrm{occ}}}\sum_{a}^{N_{\mathrm{virt}}} (\mathbf{V}^{\mathrm{act}}_{\mathrm{RPA}} + \mathbf{H}_{\mathrm{HF}})_{\mu\nu} C_{\mu a} U^x_{ai} C_{\nu i} \\
&\quad + \sum_{i'}^{N_{\mathrm{act}}}\sum_{a}^{N_{\mathrm{virt}}} (\bar{\boldsymbol{\Sigma}}^-_{\mathrm{act}})_{\mu\nu} C_{\mu a} U^x_{ai'} C_{\nu i'} \\
&\quad + \sum_{i'}^{N_{\mathrm{act}}}\sum_{I}^{N_{\mathrm{core}}} (\bar{\boldsymbol{\Sigma}}^-_{\mathrm{act}})_{\mu\nu} C_{\mu I} U^x_{i'I} C_{\nu i'}
\end{aligned} \tag{99}$$

Next, we can extend the summation range in the second term to all occupied orbitals (since the core−virtual block is zero), transform the first terms of each trace expression into the MO basis, and insert eq 94 into the third term yielding the final expression

$$\sum_{i}^{N_{\mathrm{occ}}}\sum_{a}^{N_{\mathrm{virt}}} Q_{ai} U^x_{ai} + \sum_{i'}^{N_{\mathrm{act}}}\sum_{I}^{N_{\mathrm{core}}} \tilde{Z}_{Ii'} B^x_{Ii'} \tag{100}$$

with

$$\tilde{Z}_{Ii'} = \frac{(\bar{\boldsymbol{\Sigma}}^-_{\mathrm{act}})_{Ii'}}{\epsilon_I - \epsilon'_i} \tag{101}$$

and the RPA Lagrangian $\mathbf{Q}$ defined as

$$Q_{ai} = (\mathbf{V}^{\mathrm{act}}_{\mathrm{RPA}} + \mathbf{H}_{\mathrm{HF}})_{ai} + (\bar{\boldsymbol{\Sigma}}^-_{\mathrm{act}})_{ai} I^{\mathrm{act}}_i + L_{ai} \tag{102}$$

$$L_{ai} = \sum_{i'}^{N_{\mathrm{act}}}\sum_{I}^{N_{\mathrm{core}}} (\bar{\boldsymbol{\Sigma}}^-_{\mathrm{act}})_{Ii'} \frac{A_{i'Iai}}{\epsilon_I - \epsilon'_i} \tag{103}$$

where we introduced

$$I^{\mathrm{act}}_i = \begin{cases} 0 & \text{if } i \in [1, N_{\mathrm{core}}] \\ 1 & \text{if } i \in (N_{\mathrm{core}}, N_{\mathrm{occ}}] \end{cases} \tag{104}$$

Now, we can use the Z-vector technique for the first term in eq 65. Using eq 53, we can express $\mathbf{U}^x$ as

$$\mathbf{U}^x = (\mathbf{A}')^{-1}\mathbf{B}^x \tag{105}$$

This allows us to express $\mathbf{Q}^{\mathrm{T}}\mathbf{U}^x$ in eq 100 as

$$\mathbf{Q}^{\mathrm{T}}\mathbf{U}^x = \mathbf{Z}^{\mathrm{T}}\mathbf{B}^x \tag{106}$$

with

$$\mathbf{Z}^{\mathrm{T}} = \mathbf{Q}^{\mathrm{T}}(\mathbf{A}')^{-1} \tag{107}$$

Thus, inserting eq 106 into eq 100 yields

$$\mathrm{Tr}([\mathbf{Z}^{\mathrm{T}} + \tilde{\mathbf{Z}}^{\mathrm{T}}]\mathbf{B}^x) \tag{108}$$

AUTHOR INFORMATION

Corresponding Author

Christian Ochsenfeld − *Chair of Theoretical Chemistry, Department of Chemistry, University of Munich (LMU), 81377 Munich, Germany; Max Planck Institute for Solid State Research, D-70569 Stuttgart, Germany;* orcid.org/0000-0002-4189-6558; Email: christian.ochsenfeld@cup.uni-muenchen.de

Authors

Viktoria Drontschenko − *Chair of Theoretical Chemistry, Department of Chemistry, University of Munich (LMU), 81377 Munich, Germany*

Daniel Graf − *Chair of Theoretical Chemistry, Department of Chemistry, University of Munich (LMU), 81377 Munich, Germany*

Henryk Laqua − *Chair of Theoretical Chemistry, Department of Chemistry, University of Munich (LMU), 81377 Munich, Germany*

Complete contact information is available at: https://pubs.acs.org/10.1021/acs.jctc.2c00774

Notes

The authors declare no competing financial interest.

ACKNOWLEDGMENTS

The authors acknowledge financial support by the Deutsche Forschungsgemeinschaft (DFG) within the cluster of excellence (EXC2111-390814868) "Munich Center for Quantum Science and Technology", MCQST, and SFB 1309-325871075 "Chemical Biology of Epigenetic Modifications". C.O. further acknowledges financial support as Max-Planck-Fellow at the MPI-FKF Stuttgart.

REFERENCES

(1) Hohenberg, P.; Kohn, W. Inhomogeneous electron gas. *Phys. Rev.* **1964**, *136*, B864.

(2) Kohn, W.; Sham, L. J. Self-consistent equations including exchange and correlation effects. *Phys. Rev.* **1965**, *140*, A1133.

(3) Mardirossian, N.; Head-Gordon, M. Thirty years of density functional theory in computational chemistry: an overview and extensive assessment of 200 density functionals. *Mol. Phys.* **2017**, *115*, 2315−2372.

(4) Burke, K. Perspective on density functional theory. *J. Chem. Phys.* **2012**, *136*, 150901.

(5) Chen, G. P.; Voora, V. K.; Agee, M. M.; Balasubramani, S. G.; Furche, F. Random-phase approximation methods. *Annu. Rev. Phys. Chem.* **2017**, *68*, 421−445.

(6) Møller, C.; Plesset, M. S. Note on an approximation treatment for many-electron systems. *Phys. Rev.* **1934**, *46*, 618.

(7) Čížek, J. On the correlation problem in atomic and molecular systems. Calculation of wavefunction components in Ursell-type expansion using quantum-field theoretical methods. *J. Chem. Phys.* **1966**, *45*, 4256−4266.

(8) Čížek, J.; Paldus, J.; Šroubková, L. Cluster expansion analysis for delocalized systems. *Int. J. Quantum Chem.* **1969**, *3*, 149−167.

(9) Ritz, W. Über eine neue Methode zur Lösung gewisser Variationsprobleme der mathematischen Physik. *J. Reine Angew. Math.* **1909**, *135*, 1−61.

(10) Kellner, G. W. Die Ionisierungsspannung des Heliums nach der Schrödingerschen Theorie. *Z. Phys.* **1927**, *44*, 91.

(11) Furche, F. Molecular tests of the random phase approximation to the exchange-correlation energy functional. *Phys. Rev. B: Condens. Matter Mater. Phys.* **2001**, *64*, 195120.

(12) Fuchs, M.; Gonze, X. Accurate density functionals: Approaches using the adiabatic-connection fluctuation-dissipation theorem. *Phys. Rev. B: Condens. Matter Mater. Phys.* **2002**, *65*, 235109.
(13) Niquet, Y. M.; Fuchs, M.; Gonze, X. Exchange-correlation potentials in the adiabatic connection fluctuation-dissipation framework. *Phys. Rev. A: At., Mol., Opt. Phys.* **2003**, *68*, 032507.
(14) Fuchs, M.; Niquet, Y.-M.; Gonze, X.; Burke, K. Describing static correlation in bond dissociation by Kohn−Sham density functional theory. *J. Chem. Phys.* **2005**, *122*, 094116.
(15) Furche, F.; Van Voorhis, T. Fluctuation-dissipation theorem density-functional theory. *J. Chem. Phys.* **2005**, *122*, 164106.
(16) Eshuis, H.; Furche, F. Basis set convergence of molecular correlation energy differences within the random phase approximation. *J. Chem. Phys.* **2012**, *136*, 084105.
(17) Eshuis, H.; Bates, J. E.; Furche, F. Electron correlation methods based on the random phase approximation. *Theor. Chem. Acc.* **2012**, *131*, 1084.
(18) Eshuis, H.; Yarkony, J.; Furche, F. Fast computation of molecular random phase approximation correlation energies using resolution of the identity and imaginary frequency integration. *J. Chem. Phys.* **2010**, *132*, 234114.
(19) Bates, J. E.; Furche, F. Communication: Random phase approximation renormalized many-body perturbation theory. *J. Chem. Phys.* **2013**, *139*, 171103.
(20) Furche, F. Developing the random phase approximation into a practical post-Kohn−Sham correlation model. *J. Chem. Phys.* **2008**, *129*, 114105.
(21) Voora, V. K.; Balasubramani, S. G.; Furche, F. Variational generalized Kohn-Sham approach combining the random-phase-approximation and Green's-function methods. *Phys. Rev. A* **2019**, *99*, 012518.
(22) Burow, A. M.; Bates, J. E.; Furche, F.; Eshuis, H. Analytical first-order molecular properties and forces within the adiabatic connection random phase approximation. *J. Chem. Theory Comput.* **2014**, *10*, 180−194.
(23) Eshuis, H.; Furche, F. A parameter-free density functional that works for noncovalent interactions. *J. Phys. Chem. Lett.* **2011**, *2*, 983−989.
(24) Heßelmann, A.; Görling, A. Random phase approximation correlation energies with exact Kohn−Sham exchange. *Mol. Phys.* **2010**, *108*, 359−372.
(25) Heßelmann, A.; Görling, A. Correct description of the bond dissociation limit without breaking spin symmetry by a random-phase-approximation correlation functional. *Phys. Rev. Lett.* **2011**, *106*, 093001.
(26) Paier, J.; Ren, X.; Rinke, P.; Scuseria, G. E.; Grüneis, A.; Kresse, G.; Scheffler, M. Assessment of correlation energies based on the random-phase approximation. *New J. Phys.* **2012**, *14*, 043002.
(27) Ren, X.; Tkatchenko, A.; Rinke, P.; Scheffler, M. Beyond the random-phase approximation for the electron correlation energy: The importance of single excitations. *Phys. Rev. Lett.* **2011**, *106*, 153003.
(28) Bleiziffer, P.; Heßelmann, A.; Görling, A. Resolution of identity approach for the Kohn-Sham correlation energy within the exact-exchange random-phase approximation. *J. Chem. Phys.* **2012**, *136*, 134102.
(29) Ren, X.; Rinke, P.; Joas, C.; Scheffler, M. Random-phase approximation and its applications in computational chemistry and materials science. *J. Mater. Sci.* **2012**, *47*, 7447.
(30) Scuseria, G. E.; Henderson, T. M.; Sorensen, D. C. The ground state correlation energy of the random phase approximation from a ring coupled cluster doubles approach. *J. Chem. Phys.* **2008**, *129*, 231101.
(31) Schurkus, H. F.; Ochsenfeld, C. Communication: An effective linear-scaling atomic-orbital reformulation of the random-phase approximation using a contracted double-Laplace transformation. *J. Chem. Phys.* **2016**, *144*, 031101.
(32) Luenser, A.; Schurkus, H. F.; Ochsenfeld, C. Vanishing-overhead linear-scaling random phase approximation by Cholesky decomposition and an attenuated Coulomb-metric. *J. Chem. Theory Comput.* **2017**, *13*, 1647.
(33) Beuerle, M.; Ochsenfeld, C. Short-range second order screened exchange correction to RPA correlation energies. *J. Chem. Phys.* **2017**, *147*, 204107.
(34) Graf, D.; Beuerle, M.; Schurkus, H. F.; Luenser, A.; Savasci, G.; Ochsenfeld, C. Accurate and Efficient Parallel Implementation of an Effective Linear-Scaling Direct Random Phase Approximation Method. *J. Chem. Theory Comput.* **2018**, *14*, 2505.
(35) Beuerle, M.; Graf, D.; Schurkus, H. F.; Ochsenfeld, C. Efficient calculation of beyond RPA correlation energies in the dielectric matrix formalism. *J. Chem. Phys.* **2018**, *148*, 204104.
(36) Graf, D.; Beuerle, M.; Ochsenfeld, C. Low-Scaling Self-Consistent Minimization of a Density Matrix Based Random Phase Approximation Method in the Atomic Orbital Space. *J. Chem. Theory Comput.* **2019**, *15*, 4468.
(37) Kreppel, A.; Graf, D.; Laqua, H.; Ochsenfeld, C. Range-separated density-functional theory in combination with the random phase approximation: An accuracy benchmark. *J. Chem. Theory Comput.* **2020**, *16*, 2985−2994.
(38) Graf, D.; Ochsenfeld, C. A range-separated generalized Kohn−Sham method including a long-range nonlocal random phase approximation correlation potential. *J. Chem. Phys.* **2020**, *153*, 244118.
(39) Drontschenko, V.; Graf, D.; Laqua, H.; Ochsenfeld, C. Lagrangian-Based Minimal-Overhead Batching Scheme for the Efficient Integral-Direct Evaluation of the RPA Correlation Energy. *J. Chem. Theory Comput.* **2021**, *17*, 5623−5634.
(40) Thierbach, A.; Görling, A. Analytic energy gradients for the exact exchange Kohn−Sham method. *Chem. Phys.* **2020**, *152*, 114113.
(41) Thierbach, A.; Görling, A. Analytic energy gradients for the self-consistent direct random phase approximation. *J. Chem. Phys.* **2020**, *153*, 134113.
(42) Glasbrenner, M.; Graf, D.; Ochsenfeld, C. Benchmarking the Accuracy of the Direct Random Phase Approximation and σ-Functionals for NMR Shieldings. *J. Chem. Theory Comput.* **2021**, *18*, 192−205.
(43) Perdew, J. P.; Schmidt, K. Jacob's ladder of density functional approximations for the exchange-correlation energy. *AIP Conf. Proc.* **2001**, *577*, 1−20.
(44) Dobson, J. F.; Gould, T. Calculation of dispersion energies. *J. Condens. Matter Phys.* **2012**, *24*, 073201.
(45) Dion, M.; Rydberg, H.; Schröder, E.; Langreth, D. C.; Lundqvist, B. I. Van der Waals density functional for general geometries. *Phys. Rev. Lett.* **2004**, *92*, 246401.
(46) Vydrov, O. A.; Wu, Q.; Van Voorhis, T. Self-consistent implementation of a nonlocal van der Waals density functional with a Gaussian basis set. *Chem. Phys.* **2008**, *129*, 014106.
(47) Lee, K.; Murray, É. D.; Kong, L.; Lundqvist, B. I.; Langreth, D. C. Higher-accuracy van der Waals density functional. *Phys. Rev. B: Condens. Matter Mater. Phys.* **2010**, *82*, 081101.
(48) Vydrov, O. A.; Van Voorhis, T. Nonlocal van der Waals density functional made simple. *Phys. Rev. Lett.* **2009**, *103*, 063004.
(49) Vydrov, O. A.; Van Voorhis, T. Implementation and assessment of a simple nonlocal van der Waals density functional. *Chem. Phys.* **2010**, *132*, 164113.
(50) Vydrov, O. A.; Van Voorhis, T. Nonlocal van der Waals density functional: The simpler the better. *Chem. Phys.* **2010**, *133*, 244103.
(51) Sabatini, R.; Gorni, T.; De Gironcoli, S. Nonlocal van der Waals density functional made simple and efficient. *Phys. Rev. B: Condens. Matter Mater. Phys.* **2013**, *87*, No. 041108(R).
(52) Ehrlich, S.; Moellmann, J.; Reckien, W.; Bredow, T.; Grimme, S. System-Dependent Dispersion Coefficients for the DFT-D3 Treatment of Adsorption Processes on Ionic Surfaces. *J. Chem. Phys.* **2011**, *12*, 3414.
(53) Caldeweyher, E.; Bannwarth, C.; Grimme, S. Extension of the D3 dispersion coefficient model. *J. Chem. Phys.* **2017**, *147*, 034112.
(54) Moellmann, J.; Grimme, S. DFT-D3 study of some molecular crystals. *J. Phys. Chem. C* **2014**, *118*, 7615.

https://doi.org/10.1021/acs.jctc.2c00774
J. Chem. Theory Comput. 2022, 18, 7359−7372

(55) Sure, R.; Antony, J.; Grimme, S. Blind prediction of binding affinities for charged supramolecular host−guest systems: achievements and shortcomings of DFT-D3. *J. Phys. Chem. B* **2014**, *118*, 3431.
(56) Harl, J.; Kresse, G. Accurate bulk properties from approximate many-body techniques. *Phys. Rev. Lett.* **2009**, *103*, 056401.
(57) Bohm, D.; Pines, D. A collective description of electron interactions: III. Coulomb interactions in a degenerate electron gas. *Phys. Rev.* **1953**, *92*, 609.
(58) Kaltak, M.; Klimeš, J.; Kresse, G. Low scaling algorithms for the random phase approximation: Imaginary time and Laplace transformations. *J. Chem. Theory Comput.* **2014**, *10*, 2498.
(59) Kállay, M. Linear-scaling implementation of the direct random-phase approximation. *J. Chem. Phys.* **2015**, *142*, 204105.
(60) Trushin, E.; Thierbach, A.; Görling, A. Toward chemical accuracy at low computational cost: Density-functional theory with σ-functionals for the correlation energy. *J. Chem. Phys.* **2021**, *154*, 014104.
(61) Fauser, S.; Trushin, E.; Neiss, C.; Görling, A. Chemical accuracy with σ-functionals for the Kohn−Sham correlation energy optimized for different input orbitals and eigenvalues. *J. Chem. Phys.* **2021**, *155*, 134111.
(62) Lemke, Y.; Graf, D.; Kussmann, J.; Ochsenfeld, C. An assessment of orbital energy corrections for the direct random phase approximation and explicit σ-functionals. *Mol. Phys.* **2022**, No. e2098862.
(63) Erhard, J.; Fauser, S.; Trushin, E.; Görling, A. Scaled σ-functionals for the Kohn−Sham correlation energy with scaling functions from the homogeneous electron gas. *J. Chem. Phys.* **2022**, *157*, 114105.
(64) Gotoh, M.; Tachikawa, M.; Ryuo, K.; Sasagane, K.; Suzuki, K.; Mori, K.; Nakamura, S. The first and second derivative matrices in the random phase approximation scheme by using the Lagrangian technique. *Int. J. Quantum Chem.* **2005**, *105*, 225−231.
(65) Rekkedal, J.; Coriani, S.; Iozzi, M. F.; Teale, A. M.; Helgaker, T.; Pedersen, T. B. Communication: Analytic gradients in the random-phase approximation. *J. Chem. Phys.* **2013**, *139*, 081101.
(66) Mussard, B.; Szalay, P. G.; Ángyán, J. G. Analytical energy gradients in range-separated hybrid density functional theory with random phase approximation. *J. Chem. Theory Comput.* **2014**, *10*, 1968−1979.
(67) Ramberger, B.; Schäfer, T.; Kresse, G. Analytic interatomic forces in the random phase approximation. *Phys. Rev. Lett.* **2017**, *118*, 106403.
(68) Beuerle, M.; Ochsenfeld, C. Low-scaling analytical gradients for the direct random phase approximation using an atomic orbital formalism. *J. Chem. Phys.* **2018**, *149*, 244111.
(69) Tahir, M. N.; Zhu, T.; Shang, H.; Li, J.; Blum, V.; Ren, X. Localized Resolution of Identity Approach to the Analytical Gradients of Random-Phase Approximation Ground-State Energy: Algorithm and Benchmarks. *J. Chem. Theory Comput.* **2022**, *18*, 5297−5311.
(70) Distasio, R. A., Jr; Steele, R. P.; Rhee, Y. M.; Shao, Y.; Head-Gordon, M. An improved algorithm for analytical gradient evaluation in resolution-of-the-identity second-order Møller-Plesset perturbation theory: Application to alanine tetrapeptide conformational analysis. *J. Comput. Chem.* **2007**, *28*, 839−856.
(71) Baeck, K. K.; Watts, J. D.; Bartlett, R. J. Analytic energy gradients with frozen molecular orbitals in coupled-cluster and many-body perturbation theory methods: Systematic study of the magnitude and trends of the effects of frozen molecular orbitals. *J. Chem. Phys.* **1997**, *107*, 3853−3863.
(72) Demaison, J.; Vogt, N. *Accurate Structure Determination of Free Molecules*; Springer, 2020.
(73) Woon, D. E.; Dunning, T. H., Jr. Gaussian basis sets for use in correlated molecular calculations. V. Core-valence basis sets for boron through neon. *J. Chem. Phys.* **1995**, *103*, 4572−4585.
(74) Peterson, K. A.; Dunning, T. H., Jr. Accurate correlation consistent basis sets for molecular core−valence correlation effects: The second row atoms Al−Ar, and the first row atoms B−Ne revisited. *J. Chem. Phys.* **2002**, *117*, 10548−10560.
(75) Stoychev, G. L.; Auer, A. A.; Neese, F. Automatic generation of auxiliary basis sets. *J. Chem. Theory Comput.* **2017**, *13*, 554−562.
(76) Handy, N.; Amos, R.; Gaw, J.; Rice, J.; Simandiras, E. The elimination of singularities in derivative calculations. *Chem. Phys. Lett.* **1985**, *120*, 151−158.
(77) Aikens, C. M.; Webb, S. P.; Bell, R. L.; Fletcher, G. D.; Schmidt, M. W.; Gordon, M. S. A derivation of the frozen-orbital unrestricted open-shell and restricted closed-shell second-order perturbation theory analytic gradient expressions. *Theor. Chem. Acc.* **2003**, *110*, 233−253.
(78) Scheiner, A. C.; Scuseria, G. E.; Rice, J. E.; Lee, T. J.; Schaefer, H. F., III Analytic evaluation of energy gradients for the single and double excitation coupled cluster (CCSD) wave function: Theory and application. *J. Chem. Phys.* **1987**, *87*, 5361−5373.
(79) Rendell, A. P.; Lee, T. J. An efficient formulation and implementation of the analytic energy gradient method to the single and double excitation coupled-cluster wave function: Application to Cl2O2. *J. Chem. Phys.* **1991**, *94*, 6219−6228.
(80) Lee, T. J.; Rendell, A. P. Analytic gradients for coupled-cluster energies that include noniterative connected triple excitations: Application to cis-and trans-HONO. *J. Chem. Phys.* **1991**, *94*, 6229−6236.
(81) Rice, J. E.; Amos, R. D.; Handy, N. C.; Lee, T. J.; Schaefer, H. F., III The analytic configuration interaction gradient method: Application to the cyclic and open isomers of the S3 molecule. *J. Chem. Phys.* **1986**, *85*, 963−968.
(82) Lee, T. J.; Allen, W. D.; Schaefer, H. F., III The analytic evaluation of energy first derivatives for two-configuration self-consistent-field configuration interaction (TCSCF-CI) wave functions. Application to ozone and ethylene. *J. Chem. Phys.* **1987**, *87*, 7062−7075.
(83) Handy, N. C.; Schaefer, H. F., III On the evaluation of analytic energy derivatives for correlated wave functions. *J. Chem. Phys.* **1984**, *81*, 5031−5033.
(84) Schweizer, S.; Doser, B.; Ochsenfeld, C. An atomic orbital-based reformulation of energy gradients in second-order Møller−Plesset perturbation theory. *J. Chem. Phys.* **2008**, *128*, 154101.
(85) Gunnarsson, O.; Lundqvist, B. I. Exchange and correlation in atoms, molecules, and solids by the spin-density-functional formalism. *Phys. Rev. B: Solid State* **1976**, *13*, 4274.
(86) Langreth, D. C.; Perdew, J. P. The exchange-correlation energy of a metallic surface. *Solid State Commun.* **1975**, *17*, 1425.
(87) Langreth, D. C.; Perdew, J. P. Exchange-correlation energy of a metallic surface: Wave-vector analysis. *Phys. Rev. B: Solid State* **1977**, *15*, 2884.
(88) Ayala, P. Y.; Scuseria, G. E. Linear scaling second-order Moller−Plesset theory in the atomic orbital basis for large molecular systems. *Chem. Phys.* **1999**, *110*, 3660−3671.
(89) Pulay, P. Ab initio calculation of force constants and equilibrium geometries in polyatomic molecules: I. Theory. *Mol. Phys.* **1969**, *17*, 197−204.
(90) Liu, P.; Kaltak, M.; Klimeš, J.; Kresse, G. Cubic scaling G W: Towards fast quasiparticle calculations. *Phys. Rev. B* **2016**, *94*, 165109.
(91) Wilhelm, J.; Golze, D.; Talirz, L.; Hutter, J.; Pignedoli, C. A. Toward GW calculations on thousands of atoms. *J. Phys. Chem. Lett.* **2018**, *9*, 306−312.
(92) Surján, P. R. The MP2 energy as a functional of the Hartree−Fock density matrix. *Chem. Phys. Lett.* **2005**, *406*, 318−320.
(93) Beer, M.; Ochsenfeld, C. Efficient linear-scaling calculation of response properties: Density matrix-based Laplace-transformed coupled-perturbed self-consistent field theory. *J. Chem. Phys.* **2008**, *128*, 221102.
(94) Pople, J. A.; Krishnan, R.; Schlegel, H.; Binkley, J. S. Derivative studies in hartree-fock and møller-plesset theories. *Int. J. Quantum Chem.* **1979**, *16*, 225−241.
(95) Yamaguchi, Y.; Schaefer, H. F.; Osamura, Y.; Goddard, J.; et al. *A New Dimension to Quantum Chemistry: Analytic Derivative Methods*

https://doi.org/10.1021/acs.jctc.2c00774
J. Chem. Theory Comput. 2022, 18, 7359−7372

in Ab Initio Molecular Electronic Structure Theory; Oxford University Press: USA, 1994.
(96) Koch, H.; Sánchez de Merás, A.; Pedersen, T. B. Reduced scaling in electronic structure calculations using Cholesky decompositions. *J. Chem. Phys.* **2003**, *118*, 9481.
(97) Higham, N. J. Cholesky factorization. *Wiley Interdiscip. Rev. Comput. Stat.* **2009**, *1*, 251.
(98) Harbrecht, H.; Peters, M.; Schneider, R. On the low-rank approximation by the pivoted Cholesky decomposition. *Appl. Numer. Math.* **2012**, *62*, 428.
(99) Zienau, J.; Clin, L.; Doser, B.; Ochsenfeld, C. Cholesky-decomposed densities in Laplace-based second-order Møller−Plesset perturbation theory. *J. Chem. Phys.* **2009**, *130*, 204112.
(100) Maurer, S. A.; Clin, L.; Ochsenfeld, C. Cholesky-decomposed density MP2 with density fitting: Accurate MP2 and double-hybrid DFT energies for large systems. *J. Chem. Phys.* **2014**, *140*, 224112.
(101) Kussmann, J.; Ochsenfeld, C. Pre-selective screening for matrix elements in linear-scaling exact exchange calculations. *J. Chem. Phys.* **2013**, *138*, 134114.
(102) Kussmann, J.; Ochsenfeld, C. Preselective screening for linear-scaling exact exchange-gradient calculations for graphics processing units and general strong-scaling massively parallel calculations. *J. Chem. Theory Comput.* **2015**, *11*, 918.
(103) Kussmann, J.; Ochsenfeld, C. Hybrid CPU/GPU integral engine for strong-scaling ab initio methods. *J. Chem. Theory Comput.* **2017**, *13*, 3153−3159.
(104) Perdew, J. P.; Burke, K.; Ernzerhof, M. Generalized gradient approximation made simple. *Phys. Rev. Lett.* **1996**, *77*, 3865.
(105) Perdew, J. P.; Burke, K.; Ernzerhof, M. Generalized gradient approximation made simple [Phys. Rev. Lett. 77, 3865 (1996)]. *Phys. Rev. Lett.* **1997**, *78*, 1396.
(106) Marques, M. A.; Oliveira, M. J.; Burnus, T. Libxc: A library of exchange and correlation functionals for density functional theory. *Comput. Phys. Commun.* **2012**, *183*, 2272−2281.
(107) Weigend, F.; Furche, F.; Ahlrichs, R. Gaussian basis sets of quadruple zeta valence quality for atoms H−Kr. *J. Chem. Phys.* **2003**, *119*, 12753−12762.
(108) Weigend, F.; Ahlrichs, R. Balanced basis sets of split valence, triple zeta valence and quadruple zeta valence quality for H to Rn: Design and assessment of accuracy. *Phys. Chem. Chem. Phys.* **2005**, *7*, 3297−3305.
(109) Weigend, F.; Köhn, A.; Hättig, C. Efficient use of the correlation consistent basis sets in resolution of the identity MP2 calculations. *J. Chem. Phys.* **2002**, *116*, 3175−3183.
(110) Hättig, C. Optimization of auxiliary basis sets for RI-MP2 and RI-CC2 calculations: Core−valence and quintuple-ζ basis sets for H to Ar and QZVPP basis sets for Li to Kr. *Phys. Chem. Chem. Phys.* **2005**, *7*, 59−66.

https://doi.org/10.1021/acs.jctc.2c00774
J. Chem. Theory Comput. 2022, 18, 7359−7372

3.3 Publication III: Analytical Second-Order Properties for the Random Phase Approximation: Nuclear Magnetic Resonance Shieldings

V. Drontschenko, F. H. Bangerter, C. Ochsenfeld
J. Chem. Theory Comput., **19**, 7542 (2023).

Abstract

A method for the analytical computation of nuclear magnetic resonance (NMR) shieldings within the direct random phase approximation (RPA) is presented. As a starting point, we use the RPA ground-state energy expression within the resolution-of-the-identity approximation in the atomic-orbital formalism. As has been shown in a recent benchmark study using numerical second derivatives [Glasbrenner, M. et al. *J. Chem. Theory Comput.* **2022**, *18*, 192], RPA based on a Hartree–Fock reference shows accuracies comparable to coupled cluster singles and doubles (CCSD) for NMR chemical shieldings. Together with the much lower computational cost of RPA, it has emerged as an accurate method for the computation of NMR shieldings. Therefore, we aim to extend the applicability of RPA NMR to larger systems by introducing analytical second-order derivatives, making it a viable method for the accurate and efficient computation of NMR chemical shieldings.

JCTC Journal of Chemical Theory and Computation

pubs.acs.org/JCTC Article

Analytical Second-Order Properties for the Random Phase Approximation: Nuclear Magnetic Resonance Shieldings

Viktoria Drontschenko,[§] Felix H. Bangerter,[§] and Christian Ochsenfeld*

Cite This: *J. Chem. Theory Comput.* 2023, 19, 7542−7554 Read Online

ACCESS | Metrics & More | Article Recommendations | Supporting Information

ABSTRACT: A method for the analytical computation of nuclear magnetic resonance (NMR) shieldings within the direct random phase approximation (RPA) is presented. As a starting point, we use the RPA ground-state energy expression within the resolution-of-the-identity approximation in the atomic-orbital formalism. As has been shown in a recent benchmark study using numerical second derivatives [Glasbrenner, M. et al. *J. Chem. Theory Comput.* **2022**, *18*, 192], RPA based on a Hartree−Fock reference shows accuracies comparable to coupled cluster singles and doubles (CCSD) for NMR chemical shieldings. Together with the much lower computational cost of RPA, it has emerged as an accurate method for the computation of NMR shieldings. Therefore, we aim to extend the applicability of RPA NMR to larger systems by introducing analytical second-order derivatives, making it a viable method for the accurate and efficient computation of NMR chemical shieldings.

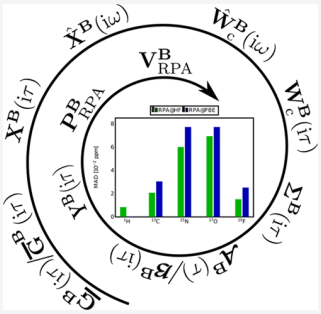

1. INTRODUCTION

Nuclear magnetic resonance (NMR) spectroscopy has emerged as an important tool for the structure determination of organic, inorganic, and macromolecular compounds in the field of chemistry and biochemistry.[1−4] However, the precise determination of molecular or solid state structures from experimental NMR spectra can be tedious due to the difficulty of assigning the signals.[2,5] In these cases, employing quantum chemical methods for the computation of NMR shielding tensors can aid in the interpretation of experimental spectra and, thus, help in the elucidation of structures.[2,6] Hence, a lot of effort has been put into the development of such methods, e.g., refs 2,7−10.

Methods for the computation of molecular NMR shifts range from Hartree−Fock (HF)[11−15] and density functional theory (DFT)[16−18] to wave function-based post-HF methods such as Møller−Plesset perturbation theory (MP2),[19,20] coupled cluster (CC) variants,[21−23] and multiconfigurational self-consistent field (MCSCF).[24] Among these methods, HF and DFT have the lowest computational cost, with comparably moderate accuracy. Nonetheless, the development of low-scaling implementations has made the computation of systems with over 1000 atoms possible.[25,26] MP2 has been shown to yield more accurate results than HF and DFT[20,27,28] while also being computationally more demanding. However, significant advancements have been made in the development of efficient methods for the computation of MP2 NMR shifts to alleviate this issue.[29−39] The most accurate methods for the computation of NMR shifts are coupled cluster singles and doubles (CCSD) as well as with additional perturbative triples (CCSD(T)).[40] However, the CC methods are accompanied by the highest computational cost among the above-mentioned methods and are, if no further approximations are applied, only feasible for very small systems.

A method that has proven to combine both high accuracy and low computational cost is the random phase approximation (RPA).[41] In a recent benchmark study,[41] it was shown that RPA provides comparable accuracy for NMR chemical shieldings as CCSD, albeit with reduced computational effort, also when compared to MP2.

RPA, originally introduced by Bohm and Pines in 1953,[42] is usually implemented as a post-Kohn−Sham (KS)[43] method. It stands on the fifth and highest rung of Jacob's ladder[44] and does not contain any empirical parameters. The expression for the RPA ground-state energy can be derived in the context of DFT[43,45] using the adiabatic-connection fluctuation−dissipation theorem (ACFDT).[46−48] However, the original formulation[46,48] has an $O(M^6)$ scaling with the system size M, making it only feasible for small systems. By introducing the resolution-of-the-identity (RI)[49−53] approximation, Furche and co-workers[54] lowered the formal scaling to $O(M^4)$, rendering RPA as one of the formally lowest scaling correlation methods. Further improvements for the computational efficiency of the RPA ground-state energies followed,[54−63] paving the way for the investigation of systems with more than 1000 atoms.[58−63]

Received: May 23, 2023
Published: October 20, 2023

For the investigation of many molecular properties, derivatives of the ground-state energy are necessary. In this regard, there are two routes to obtain higher-order derivatives, either numerically or analytically. Generally, analytical derivatives are superior to numerical schemes since they are significantly more efficient and avoid errors stemming from a finite step size.[8,64] It is worth noting here that mixed schemes, e.g., calculating the first derivative analytically and the second derivative numerically, are also conceivable and in fact often applied, e.g., for vibrational frequency calculations, as a trade-off between computational efficiency and development effort. While various methods have been developed for the analytical evaluation of first-order properties at the RPA level of theory,[65−71] to the best of our knowledge, no analytical second-order properties such as NMR shieldings with post-KS methods based on the ACFDT exist. A first step in this direction was taken by Glasbrenner et al.[41] by introducing a numerical implementation of RPA shielding tensors for benchmarking the performance of RPA and the closely related σ-functionals.[72] It has been found that RPA calculations based on a HF reference provide NMR shieldings comparable to the CCSD accuracy. Based on these promising results, we aim to extend the applicability of RPA NMR by deriving the expression for the RPA NMR shielding tensor as an analytical second derivative of the RPA energy. This enables the accurate prediction of NMR shieldings of large molecules with a low formal scaling behavior.

We want to note that refs 8,73−78, which describe RPA NMR, use RPA synonymously with coupled-perturbed HF as well as time-dependent HF. However, in our work, RPA stands for an ACFDT-based post-KS method and gives different results than coupled-perturbed HF and time-dependent HF. Therefore, the methods described in these references differ from the method introduced in this work.

This work is structured as follows: after establishing the notation used throughout this work in Section 2, we will derive the analytical mixed second derivative of the total RPA energy with respect to the nuclear magnetic moment and an external magnetic field to obtain the NMR shielding tensor in Section 3. To accomplish this, we will start by reviewing the expression for the RPA correlation energy within the atomic-orbital basis in Section 3.1 and subsequently derive its first derivative with respect to the nuclear magnetic moment in Section 3.2. In the main part of the theory in Section 3.3, we will derive the second derivative with respect to the magnetic field. Due to the close relation of RPA and MP2, we will make use of several methods used for the Laplace transformed atomic-orbital MP2 NMR method, as introduced by us earlier. Finally, after providing the computational details in Section 4, we will present the validation of our theory and implementation.

2. NOTATION

Throughout this work, we adopt the following notation:

- μ, ν, λ, σ: atomic-orbital indices; N: total number of AO-basis functions
- P, Q: auxiliary function indices; N_{aux}: total number of auxiliary functions

We use the Mulliken notation for two- and three-center integrals. Furthermore, Einstein's sum convention is employed.[79] For general intermediates containing both integrals and densities, the derivative with respect to a general perturbation ξ is denoted as O^{ξ}, while intermediate derivatives containing only the differentiated integrals are denoted as $O^{(\xi)}$. In all other cases, O^{ξ} is used as a short-hand notation for $\frac{\partial}{\partial \xi} O$.

3. THEORY

The elements of the NMR shielding tensor σ_{rs}^{A} of a nucleus A can be expressed as the mixed second derivative of the electronic energy E with respect to a coordinate of the nuclear magnetic moment m_s^A and the magnetic field B_r evaluated at zero according to

$$\sigma_{rs}^{A} = \frac{\partial^2}{\partial B_r \partial m_s^A} E \Big|_{\mathbf{m}^A=\mathbf{0},\mathbf{B}=\mathbf{0}} \qquad \forall\, r, s \in \{x, y, z\} \tag{1}$$

In this work, the focus is on NMR shieldings based on RPA, which are derived as the analytical second derivatives of the total RPA energy with respect to $\mathbf{B}$ and $\mathbf{m}$. To ensure gauge origin independence, we employ gauge-including atomic orbitals (GIAOs)[12,13,80−83] defined as

$$\chi_\mu(\mathbf{r}, \mathbf{B}) = \chi_\mu(\mathbf{r}, \mathbf{B} = \mathbf{0}) \exp\left(-\frac{\mathrm{i}}{2}[\mathbf{B} \times (\mathbf{R}_\mu - \mathbf{R}_0)]\mathbf{r}\right) \tag{2}$$

where i is the imaginary unit, $\chi_\mu(\mathbf{r}, \mathbf{B} = \mathbf{0})$ denotes the field-independent atomic-orbital basis function centered at $\mathbf{R}_\mu$, and $\mathbf{R}_0$ is the gauge origin. Through the utilization of GIAOs, we, therefore, formally introduce complex quantities.

The remainder of this section is structured as follows: we will first give a brief review of the RPA total energy in the atomic-orbital basis formulation and subsequently continue with the first derivative with respect to the nuclear magnetic moment $\mathbf{m}$. We derive both in terms of complex-valued orbitals without any assumptions on the symmetry of functions in the time and frequency domain. This general formulation of the RPA energy and first-order properties differs from the derivation presented by Beuerle and Ochsenfeld[68] for molecular gradients since it was carried out for real-valued orbitals only. Subsequently, the second derivative of the RPA energy with respect to the magnetic field $\mathbf{B}$ is derived and evaluated at $\mathbf{m} = \mathbf{0}$ and $\mathbf{B} = \mathbf{0}$. This leads to a simplification of the expressions, such that no complex-valued matrices enter the final equations. All matrices are either purely real and symmetric or purely imaginary and skew-symmetric. Further, all time- and frequency-dependent quantities are either odd or even functions in the time or frequency domain.

Please note that in the following sections, we will provide only a brief summary for RPA energies and gradients, which serve as a starting point for the second derivative. For a more detailed account, we refer the reader to previous publications on RPA energies[54−56,59−61] and gradients.[68,84]

3.1. AO-RPA Total Energies.

Within the adiabatic-connection formalism,[47] the total energy of the electronic ground state can be expressed as[46,48]

$$E^{\text{total}}[\mathbf{P}] = E^{\text{HF}}[\mathbf{P}] + E_{\text{c}}[\mathbf{P}] \tag{3}$$

where the total electronic energy E^{total}, the Hartree−Fock energy E^{HF}, and the correlation energy E_{c} are evaluated with the density $\mathbf{P}$ obtained from a prior DFT or HF calculation. Please note that the following derivations will be carried out for the more general case of a KS-DFT reference calculation. However, we will note necessary changes for an HF reference calculation where needed. The correlation energy can be

https://doi.org/10.1021/acs.jctc.3c00542
J. Chem. Theory Comput. 2023, 19, 7542−7554

expressed within the zero-temperature fluctuation−dissipation theorem and the RPA[85] as well as the RI approximation[54−56] after analytical coupling-strength integration as

$$E_c^{\mathrm{RPA}} = \frac{1}{4\pi}\int_{-\infty}^{+\infty} \mathrm{d}\omega \mathrm{Tr}[\ln(\mathbf{1} - \hat{\mathbf{X}}_0(\mathrm{i}\omega)\mathbb{V}) + \hat{\mathbf{X}}_0(\mathrm{i}\omega)\mathbb{V}] \tag{4}$$

Here, the electron−electron interaction operator in the auxiliary basis is given as

$$\mathbb{V}_{PQ} = (P|r_{12}^{-1}|Q)^{-1} \tag{5}$$

within the RI approximation with the r_{12}^{-1} Coulomb metric, where r_{12} is the interelectronic distance. For efficiency reasons, the noninteracting response function is computed in the imaginary time domain and transformed into the imaginary frequency domain using the Fourier transform

$$\hat{\mathbf{X}}_0(\mathrm{i}\omega) = \int_{-\infty}^{+\infty} \mathrm{d}\tau \exp(\mathrm{i}\omega\tau)\mathbf{X}_0(\mathrm{i}\tau) \tag{6}$$

The Fourier transform simplifies to a cosine transform[57,61] or, equivalently, to a double Laplace transform[59,60] if $\mathbf{X}_0(\mathrm{i}\tau)$ is an even function in the imaginary time domain. The response function in the imaginary time domain is given by[86]

$$\mathbf{X}_0(\mathrm{i}\tau) = \Theta(-\tau)\mathbf{X}_0^-(\mathrm{i}\tau) + \Theta(\tau)\mathbf{X}_0^+(\mathrm{i}\tau) \tag{7}$$

$$X_{0,\mathrm{PQ}}^-(\mathrm{i}\tau) = \underline{G}_{0,\lambda\nu}(-\mathrm{i}\tau)\mathbb{B}_{\mu\nu}^P \overline{G}_{0,\mu\sigma}(\mathrm{i}\tau)\mathbb{B}_{\lambda\sigma}^Q \tag{8}$$

$$X_{0,\mathrm{PQ}}^+(\mathrm{i}\tau) = \underline{G}_{0,\mu\sigma}(-\mathrm{i}\tau)\mathbb{B}_{\mu\nu}^P \overline{G}_{0,\lambda\nu}(\mathrm{i}\tau)\mathbb{B}_{\lambda\sigma}^Q \tag{9}$$

where the three-center RI integrals are defined as

$$\mathbb{B}_{\mu\nu}^P = (\mu\nu|r_{12}^{-1}|P) \tag{10}$$

and the noninteracting Green's functions are defined as

$$\mathbf{G}_0(\mathrm{i}\tau) = \Theta(-\tau)\underline{\mathbf{G}}_0(\mathrm{i}\tau) + \Theta(\tau)\overline{\mathbf{G}}_0(\mathrm{i}\tau) \tag{11}$$

$$\underline{\mathbf{G}}_0(\mathrm{i}\tau) = \mathbf{P}\exp(-\tau(\mathbf{H} - \epsilon_F\mathbf{S})\mathbf{P}) \tag{12}$$

$$\overline{\mathbf{G}}_0(\mathrm{i}\tau) = -\mathbf{P}_{\mathrm{virt}}\exp(-\tau(\mathbf{H} - \epsilon_F\mathbf{S})\mathbf{P}_{\mathrm{virt}}) \tag{13}$$

with the Fermi level ϵ_F,[60,87] the Heaviside step function $\Theta(\tau)$, the occupied density $\mathbf{P}$, and the virtual density $\mathbf{P}_{\mathrm{virt}}$. Further, the Hamiltonian $\mathbf{H}$ is defined according to

$$\mathbf{H} = \mathbf{h} + \mathbf{G}[\mathbf{P}] \tag{14}$$

where $\mathbf{h}$ denotes the matrix representation of the one-electron Hamiltonian, and $\mathbf{G}[\mathbf{P}]$ is defined as

$$\mathbf{G}[\mathbf{P}] = \mathbf{J}[\mathbf{P}] + \mathbf{V}_{\mathrm{xc}}[\mathbf{P}] \tag{15}$$

with the matrix representation of the Coulomb potential $\mathbf{J}$ and the exchange-correlation potential $\mathbf{V}_{\mathrm{xc}}$. Please note that for a RPA calculation based on a Hartree−Fock reference, $\mathbf{V}_{\mathrm{xc}}$ is replaced by the Hartree−Fock exchange $\mathbf{K}$.

3.2. First Derivative with Respect to the Nuclear Magnetic Moment.

The first derivative of the RPA total energy in eq 3 with respect to the nuclear magnetic moment $\mathbf{m}$ reads

$$\frac{\partial E^{\mathrm{total}}[\mathbf{P}]}{\partial \mathbf{m}} = \frac{\partial E^{\mathrm{HF}}[\mathbf{P}]}{\partial \mathbf{m}} + \frac{\partial E_c^{\mathrm{RPA}}[\mathbf{P}]}{\partial \mathbf{m}} \tag{16}$$

In the following sections, we will first review the expression for $\frac{\partial E^{\mathrm{HF}}[\mathbf{P}]}{\partial \mathbf{m}}$ and subsequently derive an expression for the derivative of the RPA correlation energy E_c^{RPA} with respect to $\mathbf{m}$.

3.2.1. First Derivative of the HF Functional with Respect to the Nuclear Magnetic Moment. The derivative of the HF energy with respect to the nuclear magnetic moment $\mathbf{m}$, given by the first term in eq 16, can be written as

$$\frac{\partial E^{\mathrm{HF}}[\mathbf{P}]}{\partial \mathbf{m}} = \mathrm{Tr}(\mathbf{P}\mathbf{h}^{\mathbf{m}}) + \mathrm{Tr}(\mathbf{H}_{\mathrm{HF}}\mathbf{P}^{\mathbf{m}}) \tag{17}$$

with

$$\mathrm{Tr}(\mathbf{H}_{\mathrm{HF}}\mathbf{P}^{\mathbf{m}}) = \mathrm{Tr}(\mathbf{P}^{\mathbf{m}}\mathbf{h} + \mathbf{P}^{\mathbf{m}}\mathbf{J}[\mathbf{P}] + \mathbf{P}^{\mathbf{m}}\mathbf{K}[\mathbf{P}]) \tag{18}$$

It is important to note that the HF energy is not stationary with respect to the KS density. Therefore, the density response, i.e., the last term in eq 17, has to be evaluated explicitly and cannot be avoided as in regular HF gradient calculations.[88] A most efficient alternative is to use the Z-vector method, as outlined later in this work.[84,89]

3.2.2. First Derivative of the RPA Correlation Energy with Respect to the Nuclear Magnetic Moment. The first derivative of the RPA correlation energy (eq 4) with respect to a general perturbation ξ is given by[68]

$$\frac{\partial E_c^{\mathrm{RPA}}}{\partial \xi} = \mathrm{Tr}\left(\frac{\partial E_c^{\mathrm{RPA}}}{\partial \mathbb{V}}\frac{\partial \mathbb{V}}{\partial \xi}\right) + \mathrm{Tr}\left(\frac{\partial E_c^{\mathrm{RPA}}}{\partial \mathbb{B}}\frac{\partial \mathbb{B}}{\partial \xi}\right) + \mathrm{Tr}\left(\frac{\partial E_c^{\mathrm{RPA}}}{\partial \mathbf{G}_0}\frac{\partial \mathbf{G}_0}{\partial \xi}\right) \tag{19}$$

When considering the derivative with respect to the nuclear magnetic moment $\mathbf{m}$, the above equation reduces to

$$\frac{\partial E_c^{\mathrm{RPA}}}{\partial \mathbf{m}} = \mathrm{Tr}\left(\int_{-\infty}^{+\infty} \mathrm{d}\omega \frac{\partial E_c^{\mathrm{RPA}}(\mathrm{i}\omega)}{\partial \hat{\mathbf{X}}_0(\mathrm{i}\omega)}\frac{\partial \hat{\mathbf{X}}_0(\mathrm{i}\omega)}{\partial \mathbf{G}_0(\mathrm{i}\tau)}\frac{\partial \mathbf{G}_0(\mathrm{i}\tau)}{\partial \mathbf{m}}\right) \tag{20}$$

since both the electron−electron interaction operator in the auxiliary basis $\mathbb{V}$ and the three-center integral tensor $\mathbb{B}$ are independent of $\mathbf{m}$, and thus their derivative is zero.

For a given imaginary frequency, the first term in eq 20 evaluates to

$$\frac{\partial E_c^{\mathrm{RPA}}(\mathrm{i}\omega)}{\partial \hat{\mathbf{X}}_0(\mathrm{i}\omega)} = -\frac{1}{4\pi}\hat{\mathbf{W}}_c(\mathrm{i}\omega) \tag{21}$$

where the correlated screened Coulomb interaction, which is also one of the central quantities in the GW-approximation,[67,90,91] is defined as

$$\hat{\mathbf{W}}_c(\mathrm{i}\omega) = \mathbb{V}[(\mathbf{1} - \hat{\mathbf{X}}_0(\mathrm{i}\omega)\mathbb{V})^{-1} - \mathbf{1}] \tag{22}$$

To evaluate the derivative of the RPA correlation energy with respect to $\mathbf{m}$ entirely in the imaginary time domain, eq 6 can be inserted into eq 20 to yield

$$\frac{\partial E_c^{\mathrm{RPA}}}{\partial \mathbf{m}} = \mathrm{Tr}\left(-\frac{1}{4\pi}\int_{-\infty}^{+\infty}\mathrm{d}\omega\int_{-\infty}^{+\infty}\mathrm{d}\tau\hat{\mathbf{W}}_c(\mathrm{i}\omega)\exp(\mathrm{i}\omega\tau)\frac{\partial \mathbf{X}_0(\mathrm{i}\tau)}{\partial \mathbf{G}_0(\mathrm{i}\tau)}\frac{\partial \mathbf{G}_0(\mathrm{i}\tau)}{\partial \mathbf{m}}\right) \tag{23}$$

https://doi.org/10.1021/acs.jctc.3c00542
J. Chem. Theory Comput. 2023, 19, 7542−7554

Next, $\hat{\mathbf{W}}_c(i\omega)$ has to be transformed into the imaginary time domain. Therefore, we consider the expression for its inverse Fourier transform

$$\mathbf{W}_c(i\tau) = \frac{1}{2\pi}\int_{-\infty}^{+\infty} d\omega \hat{\mathbf{W}}_c(i\omega)\exp(-i\omega\tau) \tag{24}$$

When comparing the right-hand side of eq 24 with eq 23, it becomes apparent that eq 23 cannot be rewritten directly in terms of $\mathbf{W}_c(i\tau)$. However, $\mathbf{W}_c(i\tau)$ can be expressed in terms of its even and odd part as $\mathbf{W}_c(i\tau) = \mathbf{W}_c^{\text{even}}(i\tau) + \mathbf{W}_c^{\text{odd}}(i\tau)$, which allows us to rewrite the first two terms in eq 23 as

$$\begin{aligned}\tilde{\mathbf{W}}_c(i\tau) &:= \frac{1}{2\pi}\int_{-\infty}^{+\infty} d\omega \hat{\mathbf{W}}_c(i\omega)\exp(i\omega\tau)\\ &= \mathbf{W}_c^{\text{even}}(i\tau) - \mathbf{W}_c^{\text{odd}}(i\tau)\end{aligned} \tag{25}$$

with

$$\mathbf{W}_c^{\text{even}}(i\tau) = \frac{1}{\pi}\int_0^{+\infty} d\omega \cos(\omega\tau)\hat{\mathbf{W}}_c(i\omega) \tag{26}$$

$$\mathbf{W}_c^{\text{odd}}(i\tau) = -\frac{i}{\pi}\int_0^{+\infty} d\omega \sin(\omega\tau)\hat{\mathbf{W}}_c(i\omega) \tag{27}$$

Inserting eq 25 into eq 23 finally yields

$$\frac{\partial E_c^{\text{RPA}}}{\partial \mathbf{m}} = \frac{1}{2}\text{Tr}\left(-\int_{-\infty}^{+\infty} d\tau \tilde{\mathbf{W}}_c(i\tau)\frac{\partial \mathbf{X}_0(i\tau)}{\partial \mathbf{G}_0(i\tau)}\frac{\partial \mathbf{G}_0(i\tau)}{\partial \mathbf{m}}\right) \tag{28}$$

$$\begin{aligned}&= \frac{1}{2}\text{Tr}\left(-\int_0^{+\infty} d\tau \tilde{\mathbf{W}}_c(i\tau)\frac{\partial \mathbf{X}_0(i\tau)}{\partial \mathbf{G}_0(i\tau)}\frac{\partial \mathbf{G}_0(i\tau)}{\partial \mathbf{m}}\right)\\ &+ \frac{1}{2}\text{Tr}\left(-\int_0^{+\infty} d\tau \tilde{\mathbf{W}}_c(-i\tau)\frac{\partial \mathbf{X}_0(-i\tau)}{\partial \mathbf{G}_0(-i\tau)}\right.\\ &\left.\frac{\partial \mathbf{G}_0(-i\tau)}{\partial \mathbf{m}}\right)\end{aligned} \tag{29}$$

After the evaluation of $\frac{\partial \mathbf{X}_0(i\tau)}{\partial \mathbf{G}_0(i\tau)}$, the following expression is obtained

$$\frac{\partial E_c^{\text{RPA}}}{\partial \mathbf{m}} = \frac{1}{2}\text{Tr}\left(\int_0^{+\infty} d\tau \boldsymbol{\Sigma}(i\tau)\underline{\mathbf{G}}_0^{\mathbf{m}}(-i\tau) + \boldsymbol{\Sigma}(-i\tau)\bar{\mathbf{G}}_0^{\mathbf{m}}(i\tau)\right) \tag{30}$$

where the correlated self-energy $\boldsymbol{\Sigma}$ is introduced, which is another central quantity in the GW-approximation.[67] For positive and negative imaginary times, $\boldsymbol{\Sigma}(i\tau)$ is defined as

$$\Sigma_{\nu\lambda}(i\tau) = -\tilde{W}_{c,PQ}(-i\tau)\mathbb{B}_{\mu\nu}^P G_{0,\mu\sigma}(i\tau)\mathbb{B}_{\lambda\sigma}^Q \tag{31}$$

The last term that remains to be evaluated in eq 30 is the derivative of the Green's functions with respect to $\mathbf{m}$. A detailed derivation can be found in ref 68. In the following, only the most important steps of the derivation are shown. Differentiating the Green's functions given in eqs 12 and 13 yields

$$\begin{aligned}\frac{\partial \underline{\mathbf{G}}_0(i\tau)}{\partial \mathbf{m}} &= \mathbf{P}^{\mathbf{m}}\exp(-\tau(\mathbf{H}-\epsilon_F\mathbf{S})\mathbf{P})\\ &+ \mathbf{P}(\exp(-\tau(\mathbf{H}-\epsilon_F\mathbf{S})\mathbf{P}))^{\mathbf{m}}\end{aligned} \tag{32}$$

$$\begin{aligned}\frac{\partial \bar{\mathbf{G}}_0(i\tau)}{\partial \mathbf{m}} &= -\mathbf{P}_{\text{virt}}^{\mathbf{m}}\exp(-\tau(\mathbf{H}-\epsilon_F\mathbf{S})\mathbf{P}_{\text{virt}})\\ &+ \mathbf{P}_{\text{virt}}(\exp(-\tau(\mathbf{H}-\epsilon_F\mathbf{S})\mathbf{P}_{\text{virt}}))^{\mathbf{m}}\end{aligned} \tag{33}$$

The occupied and virtual densities are related through the completeness relation

$$\mathbf{1} = \mathbf{PS} + \mathbf{P}_{\text{virt}}\mathbf{S} \tag{34}$$

By differentiating the above identity with respect to the nuclear magnetic moment,[84] the following relation is obtained: $\mathbf{P}_{\text{virt}}^{\mathbf{m}} = -\mathbf{P}^{\mathbf{m}}$, which only requires the evaluation of the occupied density. The derivative of the matrix exponentials can be evaluated by differentiating the corresponding series expansion.[84,87,92]

The final expression reads

$$\frac{\partial E_c^{\text{RPA}}}{\partial \mathbf{m}} = \text{Tr}\left(\frac{\partial E_c^{\text{RPA}}}{\partial \mathbf{X}_0(i\omega)}\frac{\partial \hat{\mathbf{X}}_0(i\omega)}{\partial \mathbf{G}_0(i\tau)}\frac{\partial \mathbf{G}_0(i\tau)}{\partial \mathbf{m}}\right) \tag{35}$$

$$= \text{Tr}(\mathbf{V}_{\text{RPA}}\mathbf{P}^{\mathbf{m}} + \mathbf{P}_{\text{RPA}}\mathbf{h}^{\mathbf{m}}) \tag{36}$$

where the following intermediates are introduced

$$\mathbf{V}_{\text{RPA}} = \frac{1}{2}(\mathbf{M} + \mathbf{G}[\mathbf{P}_{\text{RPA}}]) \tag{37}$$

$$\mathbf{P}_{\text{RPA}} = \frac{1}{2}\int_0^{+\infty} d\tau(\mathbf{P}\underline{\mathbf{Y}}(-i\tau) - \mathbf{P}_{\text{virt}}\bar{\mathbf{Y}}(i\tau)) \tag{38}$$

as well as

$$\mathbf{M} = \bar{\mathbf{M}} + \underline{\mathbf{M}} \tag{39}$$

$$\begin{aligned}\bar{\mathbf{M}} = \int_0^{+\infty} d\tau(&\bar{\mathbf{Y}}(i\tau)(\mathbf{H}-\epsilon_F\mathbf{S})\\ &+ \exp(-\tau(\mathbf{H}-\epsilon_F\mathbf{S})\mathbf{P}_{\text{virt}})\boldsymbol{\Sigma}(-i\tau))\end{aligned} \tag{40}$$

$$\begin{aligned}\underline{\mathbf{M}} = \int_0^{+\infty} d\tau(&\underline{\mathbf{Y}}(-i\tau)(\mathbf{H}-\epsilon_F\mathbf{S})\\ &+ \exp(\tau(\mathbf{H}-\epsilon_F\mathbf{S})\mathbf{P})\boldsymbol{\Sigma}(i\tau))\end{aligned} \tag{41}$$

and the matrices

$$\mathbf{Y}(i\tau) = \Theta(-\tau)\underline{\mathbf{Y}}(i\tau) + \Theta(\tau)\bar{\mathbf{Y}}(i\tau) \tag{42}$$

$$\bar{\mathbf{Y}}(i\tau) = \sum_{k=1}^{\infty}\sum_{l=0}^{k-1}\frac{1}{k!}\bar{\mathcal{A}}^{k-l-1}(\tau)\bar{\mathcal{B}}(i\tau)\bar{\mathcal{A}}^{l}(\tau) \tag{43}$$

$$\underline{\mathbf{Y}}(i\tau) = \sum_{k=1}^{\infty}\sum_{l=0}^{k-1}\frac{1}{k!}\underline{\mathcal{A}}^{k-l-1}(\tau)\underline{\mathcal{B}}(i\tau)\underline{\mathcal{A}}^{l}(\tau) \tag{44}$$

with $\mathcal{A}(\tau)$ defined as

$$\mathcal{A}(\tau) = \Theta(-\tau)\underline{\mathcal{A}}(\tau) + \Theta(\tau)\bar{\mathcal{A}}(\tau) \tag{45}$$

$$\underline{\mathcal{A}}(\tau) = -\tau(\mathbf{H}-\epsilon_F\mathbf{S})\mathbf{P} \tag{46}$$

$$\bar{\mathcal{A}}(\tau) = -\tau(\mathbf{H}-\epsilon_F\mathbf{S})\mathbf{P}_{\text{virt}} \tag{47}$$

and $\mathcal{B}(i\tau)$ as

$$\mathcal{B}(i\tau) = \Theta(-\tau)\underline{\mathcal{B}}(i\tau) + \Theta(\tau)\bar{\mathcal{B}}(i\tau) \tag{48}$$

$$\underline{\mathcal{B}}(i\tau) = -\tau\boldsymbol{\Sigma}(-i\tau)\mathbf{P} \tag{49}$$

https://doi.org/10.1021/acs.jctc.3c00542
J. Chem. Theory Comput. 2023, 19, 7542−7554

$$\bar{\mathcal{B}}(i\tau) = -\tau\boldsymbol{\Sigma}(-i\tau)\mathbf{P}_{\text{virt}} \tag{50}$$

The $\mathbf{Y}$ matrices are most efficiently evaluated using a recursion scheme according to[34,84]

$$\mathbf{Y}(i\tau) = \sum_{k=0}^{\infty} \mathbf{Y}_k(i\tau) \tag{51}$$

$$\mathbf{Y}_k(i\tau) = \begin{cases} 0 & k = 0 \\ \frac{1}{k}(\mathcal{A}(\tau)\mathbf{Y}_{k-1}(i\tau) + \mathcal{B}(i\tau)\mathcal{A}_{k-1}(\tau)) & k > 0 \end{cases} \tag{52}$$

with

$$\mathcal{A}_k(\tau) = \frac{1}{k!}\mathcal{A}^k(\tau) \tag{53}$$

3.3. Second Derivative with Respect to the Magnetic Field. The mixed second derivative of the total RPA energy with respect to $\mathbf{m}$ and $\mathbf{B}$ reads

$$\begin{aligned}\boldsymbol{\sigma} &= \left.\frac{\partial^2 E^{\text{total}}[\mathbf{P}]}{\partial\mathbf{B}\partial\mathbf{m}}\right|_{\mathbf{m}=\mathbf{0},\mathbf{B}=\mathbf{0}} \\ &= \left.\frac{\partial^2 E^{\text{HF}}[\mathbf{P}]}{\partial\mathbf{B}\partial\mathbf{m}}\right|_{\mathbf{m}=\mathbf{0},\mathbf{B}=\mathbf{0}} + \left.\frac{\partial^2 E_c^{\text{RPA}}[\mathbf{P}]}{\partial\mathbf{B}\partial\mathbf{m}}\right|_{\mathbf{m}=\mathbf{0},\mathbf{B}=\mathbf{0}}\end{aligned} \tag{54}$$

In the following sections, the mixed second derivative of the HF energy, given by the first term in eq 54, is reviewed. Subsequently the second derivative of the RPA correlation energy, given by the second term in eq 54, is derived, and finally both components are combined to form the total shielding tensor.

3.3.1. Second Derivative of the HF Energy with Respect to the Magnetic Field. The second derivative of the HF energy with respect to $\mathbf{m}$ and $\mathbf{B}$ can be obtained by differentiating eq 17 with respect to $\mathbf{B}$ yielding

$$\begin{aligned}\left.\frac{\partial^2 E^{\text{HF}}[\mathbf{P}]}{\partial\mathbf{B}\partial\mathbf{m}}\right|_{\mathbf{m}=\mathbf{0},\mathbf{B}=\mathbf{0}} &= \text{Tr}(\mathbf{P}^{\mathbf{B}}\mathbf{h}^{\mathbf{m}}) + \text{Tr}(\mathbf{P}\mathbf{h}^{\mathbf{Bm}}) \\ &\quad + \text{Tr}(\mathbf{H}_{\text{HF}}^{\mathbf{B}}\mathbf{P}^{\mathbf{m}}) \\ &\quad + \text{Tr}(\mathbf{H}_{\text{HF}}\mathbf{P}^{\mathbf{Bm}})\end{aligned} \tag{55}$$

$$\begin{aligned}&= \tilde{\boldsymbol{\sigma}}^{\text{HF}} + \text{Tr}(\mathbf{H}_{\text{HF}}^{\mathbf{B}}\mathbf{P}^{\mathbf{m}}) \\ &\quad + \text{Tr}(\mathbf{H}_{\text{HF}}\mathbf{P}^{\mathbf{Bm}})\end{aligned} \tag{56}$$

For simplicity in the following, the first two contributions from the HF functional are summarized in the intermediate $\tilde{\boldsymbol{\sigma}}^{\text{HF}}$. We note here that the contributions from $\text{Tr}(\mathbf{H}_{\text{HF}}^{\mathbf{B}}\mathbf{P}^{\mathbf{m}})$ and $\text{Tr}(\mathbf{H}_{\text{HF}}\mathbf{P}^{\mathbf{Bm}})$ do not arise in the case of a HF reference, as explained in detail in Appendix A. The magnetic field derivative of the HF Hamiltonian $\mathbf{H}_{\text{HF}}^{\mathbf{B}}$ is given by

$$\mathbf{H}_{\text{HF}}^{\mathbf{B}} = \mathbf{h}^{\mathbf{B}} + \mathbf{J}^{\mathbf{B}}[\mathbf{P}] + \mathbf{K}^{\mathbf{B}}[\mathbf{P}] + \mathbf{K}[\mathbf{P}^{\mathbf{B}}] \tag{57}$$

where the term $\mathbf{J}[\mathbf{P}^{\mathbf{B}}]$ is zero, due to the skew symmetry of the purely imaginary $\mathbf{B}$-field derivative of the density matrix.

3.3.2. Second Derivative of the RPA Correlation Energy with Respect to the Magnetic Field. The second derivative of the RPA correlation energy with respect to the magnetic field $\mathbf{B}$ can be obtained by differentiating eq 36

$$\begin{aligned}\left.\frac{\partial^2 E_c^{\text{RPA}}[\mathbf{P}]}{\partial\mathbf{B}\partial\mathbf{m}}\right|_{\mathbf{m}=\mathbf{0},\mathbf{B}=\mathbf{0}} &= \text{Tr}(\mathbf{V}_{\text{RPA}}^{\mathbf{B}}\mathbf{P}^{\mathbf{m}}) + \text{Tr}(\mathbf{V}_{\text{RPA}}\mathbf{P}^{\mathbf{Bm}}) \\ &\quad + \text{Tr}(\mathbf{P}_{\text{RPA}}^{\mathbf{B}}\mathbf{h}^{\mathbf{m}}) + \text{Tr}(\mathbf{P}_{\text{RPA}}\mathbf{h}^{\mathbf{Bm}})\end{aligned} \tag{58}$$

The derivative of the density with respect to the nuclear magnetic moment in the first term of eq 58 can, in principle, be evaluated by solving the coupled-perturbed KS (CPKS) equations for all perturbations of the nuclear magnetic moment. However, the response of the density can be obtained more efficiently using the Z-vector technique,[84,89] which requires the evaluation of only one CPKS equation. Within the AO-based formulation, the density matrix-based Laplace transformed CPKS method[93] developed by our group is employed.

In the next sections, the derivation of the $\mathbf{B}$-field derivatives of the $\mathbf{P}_{\text{RPA}}$ and the $\mathbf{V}_{\text{RPA}}$ intermediates is explained in detail. Figure 1 provides a schematic overview of the necessary steps

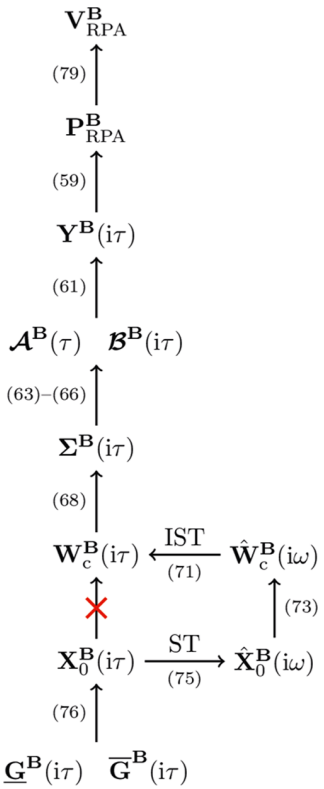

Figure 1. Schematic representation of the derivation of $\mathbf{V}_{\text{RPA}}^{\mathbf{B}}$ and $\mathbf{P}_{\text{RPA}}^{\mathbf{B}}$. ST denotes a sine transform and IST denotes an inverse sine transform. All arrows are labeled with the corresponding equations from the text.

to derive an expression for the central intermediates $\mathbf{P}_{\text{RPA}}^{\mathbf{B}}$ and $\mathbf{V}_{\text{RPA}}^{\mathbf{B}}$. The next section starts with the evaluation of $\mathbf{P}_{\text{RPA}}^{\mathbf{B}}$, which will lead to an expression for the magnetic field derivative of the correlated self-energy $\boldsymbol{\Sigma}^{\mathbf{B}}$. As can be seen in Figure 1, this requires the $\mathbf{B}$-field differentiated correlated screened Coulomb interaction $\mathbf{W}_c^{\mathbf{B}}$, which in turn contains the derivative of the noninteracting response function $\mathbf{X}_0^{\mathbf{B}}$. Subsequently, the evaluation of $\mathbf{V}_{\text{RPA}}^{\mathbf{B}}$ will be detailed, and finally, the contributions from the HF functional and the RPA correlation energy are combined to formulate the final equation for the computation of the total RPA NMR shieldings.

https://doi.org/10.1021/acs.jctc.3c00542
J. Chem. Theory Comput. 2023, 19, 7542−7554

3.3.3. Derivative of P_{RPA} with Respect to the Magnetic Field. Differentiation of eq 38 with respect to the magnetic field yields

$$\mathbf{P}^{\mathbf{B}}_{\mathrm{RPA}} = \frac{1}{2}\int_0^{+\infty} \mathrm{d}\tau(\mathbf{P}^{\mathbf{B}}\underline{\mathbf{Y}}(-\mathrm{i}\tau) + \mathbf{P}\underline{\mathbf{Y}}^{\mathbf{B}}(-\mathrm{i}\tau) - \mathbf{P}^{\mathbf{B}}_{\mathrm{virt}}\overline{\mathbf{Y}}(\mathrm{i}\tau) - \mathbf{P}_{\mathrm{virt}}\overline{\mathbf{Y}}^{\mathbf{B}}(\mathrm{i}\tau)) \tag{59}$$

The direct evaluation of $\mathbf{P}^{\mathbf{B}}_{\mathrm{virt}}$ can again be avoided by differentiation of the completeness relation given in eq 34 with respect to the **B**-field

$$\mathbf{P}^{\mathbf{B}}_{\mathrm{virt}} = \mathbf{P}^{\mathbf{B}} - \mathbf{S}^{-1}\mathbf{S}^{\mathbf{B}}\mathbf{S}^{-1} \tag{60}$$

Here, we note that at this stage the density response $\mathbf{P}^{\mathbf{B}}$ is evaluated directly by solving the CPKS equations for all **B**-field perturbations without utilizing the Z-vector technique. Since there are only three perturbations in total, this does not constitute a considerable overhead.

Apart from $\mathbf{P}^{\mathbf{B}}$, the evaluation of eq 59 requires the **B**-field derivative of the **Y** intermediates. Since the derivative of the **Y** matrices also arises in the evaluation of Laplace transformed atomic-orbital MP2 NMR shieldings,[33,34,38] the approach recently introduced by Glasbrenner et al.[34] is adopted for the evaluation of $\mathbf{Y}^{\mathbf{B}}(\mathrm{i}\tau)$. Differentiating the recursion formula for $\mathbf{Y}(\mathrm{i}\tau)$ given in eq 51 with respect to the **B**-field yields

$$\mathbf{Y}^{\mathbf{B}}(\mathrm{i}\tau) = \sum_{k=0}^{\infty} \mathbf{Y}^{\mathbf{B}}_k(\mathrm{i}\tau) \tag{61}$$

$$\mathbf{Y}^{\mathbf{B}}_k(\mathrm{i}\tau) = \frac{1}{k}(\mathcal{A}^{\mathbf{B}}(\tau)\mathbf{Y}_{k-1}(\mathrm{i}\tau) + \mathcal{A}(\tau)\mathbf{Y}^{\mathbf{B}}_{k-1}(\mathrm{i}\tau) + \mathcal{B}^{\mathbf{B}}(\mathrm{i}\tau)\mathcal{A}_{k-1}(\tau) + \mathcal{B}(\mathrm{i}\tau)\mathcal{A}^{\mathbf{B}}_{k-1}(\tau)) \quad \forall\, k > 0 \tag{62}$$

At this point the derivatives of $\mathcal{A}(\tau)$ and $\mathcal{B}(\mathrm{i}\tau)$ are required. Differentiation of the respective expressions given in eqs 46−50 results in

$$\underline{\mathcal{A}}^{\mathbf{B}}(\tau) = -\tau(\mathbf{H}^{\mathbf{B}} - \epsilon_{\mathrm{F}}\mathbf{S}^{\mathbf{B}})\mathbf{P} - \tau(\mathbf{H} - \epsilon_{\mathrm{F}}\mathbf{S})\mathbf{P}^{\mathbf{B}} \tag{63}$$

$$\overline{\mathcal{A}}^{\mathbf{B}}(\tau) = -\tau(\mathbf{H}^{\mathbf{B}} - \epsilon_{\mathrm{F}}\mathbf{S}^{\mathbf{B}})\mathbf{P}_{\mathrm{virt}} - \tau(\mathbf{H} - \epsilon_{\mathrm{F}}\mathbf{S})\mathbf{P}^{\mathbf{B}}_{\mathrm{virt}} \tag{64}$$

$$\underline{\mathcal{B}}^{\mathbf{B}}(\mathrm{i}\tau) = -\tau\mathbf{\Sigma}^{\mathbf{B}}(-\mathrm{i}\tau)\mathbf{P} - \tau\mathbf{\Sigma}(-\mathrm{i}\tau)\mathbf{P}^{\mathbf{B}} \tag{65}$$

$$\overline{\mathcal{B}}^{\mathbf{B}}(\mathrm{i}\tau) = -\tau\mathbf{\Sigma}^{\mathbf{B}}(-\mathrm{i}\tau)\mathbf{P}_{\mathrm{virt}} - \tau\mathbf{\Sigma}(-\mathrm{i}\tau)\mathbf{P}^{\mathbf{B}}_{\mathrm{virt}} \tag{66}$$

where the **B**-field derivative of the Hamiltonian (eq 14) is given by

$$\mathbf{H}^{\mathbf{B}} = \mathbf{h}^{\mathbf{B}} + \mathbf{G}^{\mathbf{B}}[\mathbf{P}] + \mathbf{G}[\mathbf{P}^{\mathbf{B}}] \tag{67}$$

Up to this point, the only unknown quantity is the **B**-field derivative of the correlated self-energy, which is the focus of the next section.

3.3.4. Derivative of the Correlated Self-Energy with Respect to the Magnetic Field. The derivative of the self-energy, i.e.,

$$\left.\frac{\partial\Sigma_{\nu\lambda}(\mathrm{i}\tau)}{\partial\mathbf{B}}\right|_{\mathbf{B}=\mathbf{0}} = \left.\frac{\partial}{\partial\mathbf{B}}(-\tilde{W}_{\mathrm{c,PQ}}(-\mathrm{i}\tau)\mathbb{B}^{P}_{\mu\nu}G_{0,\mu\sigma}(\mathrm{i}\tau)\mathbb{B}^{Q}_{\lambda\sigma})\right|_{\mathbf{B}=\mathbf{0}} \tag{68}$$

can be obtained by differentiating eq 31 using the product rule. Further simplifications can be made by considering the symmetries of all quantities when evaluating at $\mathbf{B} = \mathbf{0}$. Since the vector potential that describes the magnetic field is purely imaginary, any associated **B**-field differentiated Hermitian matrix will necessarily be purely imaginary and therefore skew-symmetric in the time domain. Furthermore, both the magnetic field derivative of the noninteracting response function $\mathbf{X}^{\mathbf{B}}_0(\mathrm{i}\tau)$ and the derivative of the correlated screened Coulomb interaction $\mathbf{W}^{\mathbf{B}}_{\mathrm{c}}(\mathrm{i}\tau)$ are odd functions in the imaginary time domain. All remaining, nondifferentiated quantities are purely real, symmetric, and even functions in the imaginary time domain. A detailed derivation is shown in Appendix B, while here only the resulting working equations are presented

$$\begin{aligned}\Sigma^{\mathbf{B}}_{\nu\lambda}(\mathrm{i}\tau) = &-\frac{\partial W_{\mathrm{c,PQ}}(\mathrm{i}\tau)}{\partial\mathbf{B}}\mathbb{B}^{P}_{\mu\nu}\overline{G}_{0,\mu\sigma}(\mathrm{i}\tau)\mathbb{B}^{Q}_{\lambda\sigma}\\ &- W_{\mathrm{c,PQ}}(\mathrm{i}\tau)\frac{\partial\mathbb{B}^{P}_{\mu\nu}}{\partial\mathbf{B}}\overline{G}_{0,\mu\sigma}(\mathrm{i}\tau)\mathbb{B}^{Q}_{\lambda\sigma}\\ &- W_{\mathrm{c,PQ}}(\mathrm{i}\tau)\mathbb{B}^{P}_{\mu\nu}\frac{\partial\overline{G}_{0,\mu\sigma}(\mathrm{i}\tau)}{\partial\mathbf{B}}\mathbb{B}^{Q}_{\lambda\sigma}\\ &- W_{\mathrm{c,PQ}}(\mathrm{i}\tau)\mathbb{B}^{P}_{\mu\nu}G_{0,\mu\sigma}(\mathrm{i}\tau)\frac{\partial\mathbb{B}^{Q}_{\lambda\sigma}}{\partial\mathbf{B}}\end{aligned} \tag{69}$$

$$\begin{aligned}\Sigma^{\mathbf{B}}_{\nu\lambda}(-\mathrm{i}\tau) = &+\frac{\partial W_{\mathrm{c,PQ}}(\mathrm{i}\tau)}{\partial\mathbf{B}}\mathbb{B}^{P}_{\mu\nu}\underline{G}_{0,\mu\sigma}(-\mathrm{i}\tau)\mathbb{B}^{Q}_{\lambda\sigma}\\ &- W_{\mathrm{c,PQ}}(\mathrm{i}\tau)\frac{\partial\mathbb{B}^{P}_{\mu\nu}}{\partial\mathbf{B}}\underline{G}_{0,\mu\sigma}(-\mathrm{i}\tau)\mathbb{B}^{Q}_{\lambda\sigma}\\ &- W_{\mathrm{c,PQ}}(\mathrm{i}\tau)\mathbb{B}^{P}_{\mu\nu}\frac{\partial\underline{G}_{0,\mu\sigma}(-\mathrm{i}\tau)}{\partial\mathbf{B}}\mathbb{B}^{Q}_{\lambda\sigma}\\ &- W_{\mathrm{c,PQ}}(\mathrm{i}\tau)\mathbb{B}^{P}_{\mu\nu}\underline{G}_{0,\mu\sigma}(-\mathrm{i}\tau)\frac{\partial\mathbb{B}^{Q}_{\lambda\sigma}}{\partial\mathbf{B}}\end{aligned} \tag{70}$$

If done stepwise, the computation of the self-energy and its **B**-field derivative formally scale as $O(N^2_{\mathrm{aux}}N^2)$ and thus constitute the steepest scaling steps in the computation of RPA NMR shieldings.

In the following sections, first the **B**-field derivative of the correlated screened Coulomb interaction $\mathbf{W}_{\mathrm{c}}(\mathrm{i}\tau)$ is evaluated and subsequently the derivative of the Green's functions is evaluated.

Since no simple closed expression for the correlated screened Coulomb interaction in the imaginary time domain exists, the **B**-field derivative is evaluated in the imaginary frequency domain $\hat{\mathbf{W}}^{\mathbf{B}}_{\mathrm{c}}(\mathrm{i}\omega)$ and subsequently transformed back into the imaginary time domain using an inverse sine transform

$$\mathbf{W}^{\mathbf{B}}_{\mathrm{c}}(\mathrm{i}\tau) = 2\mathrm{i}\int_0^{+\infty}\mathrm{d}\omega\,\sin(\omega\tau)\hat{\mathbf{W}}^{\mathbf{B}}_{\mathrm{c}}(\mathrm{i}\omega) \tag{71}$$

$\hat{\mathbf{W}}^{\mathbf{B}}_{\mathrm{c}}(\mathrm{i}\omega)$ can be obtained by differentiating eq 22 with respect to the **B**-field yielding

$$\frac{\partial\hat{\mathbf{W}}_{\mathrm{c}}(\mathrm{i}\omega)}{\partial\mathbf{B}} = \frac{\partial}{\partial\mathbf{B}}(\mathbb{V}([\mathbf{1} - \hat{\mathbf{X}}_0(\mathrm{i}\omega)\mathbb{V}]^{-1} - \mathbf{1})) \tag{72}$$

$$= \mathbb{V}([\mathbf{1} - \hat{\mathbf{X}}_0(\mathrm{i}\omega)\mathbb{V}]^{-1}[\hat{\mathbf{X}}^{\mathbf{B}}_0(\mathrm{i}\omega)\mathbb{V}][\mathbf{1} - \hat{\mathbf{X}}_0(\mathrm{i}\omega)\mathbb{V}]^{-1}) \tag{73}$$

where the following identity for the derivative of matrix inverses of a general matrix $\mathcal{R}$ is used

$$\frac{\partial(\mathcal{R}^{-1})}{\partial\xi} = -\mathcal{R}^{-1}\frac{\partial\mathcal{R}}{\partial\xi}\mathcal{R}^{-1} \tag{74}$$

https://doi.org/10.1021/acs.jctc.3c00542
J. Chem. Theory Comput. 2023, 19, 7542−7554

As can be seen from eq 73, for the computation of $\hat{\mathbf{W}}_c^{\mathbf{B}}(i\omega)$, the **B**-field derivative of the response function in the imaginary frequency domain $\hat{\mathbf{X}}_0^{\mathbf{B}}(i\omega)$ is needed. For efficiency reasons, the **B**-field derivative of the response function is computed in the imaginary time domain and transformed back into the imaginary frequency domain using the sine transform

$$\hat{\mathbf{X}}_0^{\mathbf{B}}(i\omega) = 2i\int_0^{+\infty} d\tau\, \sin(\omega\tau)\mathbf{X}_0^{\mathbf{B}}(i\tau) \tag{75}$$

By differentiating eq 9 using the product rule, an expression for $\mathbf{X}_0^{\mathbf{B}}(i\tau)$ is obtained according to

$$\begin{aligned}\frac{\partial X^{+}_{0,PQ}(i\tau)}{\partial \mathbf{B}} = {}& \frac{\partial \underline{G}_{0,\mu\sigma}(-i\tau)}{\partial \mathbf{B}}\mathbb{B}^P_{\mu\nu}\overline{G}_{0,\lambda\nu}(i\tau)\mathbb{B}^Q_{\lambda\sigma} \\ &+ \underline{G}_{0,\mu\sigma}(-i\tau)\frac{\partial \mathbb{B}^P_{\mu\nu}}{\partial \mathbf{B}}\overline{G}_{0,\lambda\nu}(i\tau)\mathbb{B}^Q_{\lambda\sigma} \\ &+ \underline{G}_{0,\mu\sigma}(-i\tau)\mathbb{B}^P_{\mu\nu}\frac{\partial \overline{G}_{0,\lambda\nu}(i\tau)}{\partial \mathbf{B}}\mathbb{B}^Q_{\lambda\sigma} \\ &+ \underline{G}_{0,\mu\sigma}(-i\tau)\mathbb{B}^P_{\mu\nu}\overline{G}_{0,\lambda\nu}(i\tau)\frac{\partial \mathbb{B}^Q_{\lambda\sigma}}{\partial \mathbf{B}}\end{aligned} \tag{76}$$

Finally, to complete the evaluation of $\mathbf{\Sigma}(i\tau)$, the **B**-field derivative of the Green's function is needed. Differentiating eqs 12 and 13 yields

$$\begin{aligned}\frac{\partial \underline{\mathbf{G}}_0(i\tau)}{\partial \mathbf{B}} = {}& \mathbf{P}^{\mathbf{B}}\exp(-\tau(\mathbf{H}-\epsilon_F\mathbf{S})\mathbf{P}) \\ &+ \mathbf{P}(\exp(-\tau(\mathbf{H}-\epsilon_F\mathbf{S})\mathbf{P}))^{\mathbf{B}}\end{aligned} \tag{77}$$

$$\begin{aligned}\frac{\partial \overline{\mathbf{G}}_0(i\tau)}{\partial \mathbf{B}} = {}& -\mathbf{P}^{\mathbf{B}}_{\mathrm{virt}}\exp(-\tau(\mathbf{H}-\epsilon_F\mathbf{S})\mathbf{P}_{\mathrm{virt}}) \\ &- \mathbf{P}_{\mathrm{virt}}(\exp(-\tau(\mathbf{H}-\epsilon_F\mathbf{S})\mathbf{P}_{\mathrm{virt}}))^{\mathbf{B}}\end{aligned} \tag{78}$$

The **B**-field derivative of the matrix exponentials in the above equations can be obtained, as explained in Section 3.2.[68]

3.3.5. Derivative of V_{RPA} with Respect to the Magnetic Field. Differentiating eq 37 yields

$$\mathbf{V}^{\mathbf{B}}_{\mathrm{RPA}} = \frac{1}{2}(\mathbf{M}^{\mathbf{B}} + \mathbf{G}^{\mathbf{B}}[\mathbf{P}_{\mathrm{RPA}}] + \mathbf{G}[\mathbf{P}^{\mathbf{B}}_{\mathrm{RPA}}]) \tag{79}$$

The evaluation of $\mathbf{P}^{\mathbf{B}}_{\mathrm{RPA}}$ was described in detail in the last section. An expression for $\mathbf{M}^{\mathbf{B}} = \overline{\mathbf{M}}^{\mathbf{B}} + \underline{\mathbf{M}}^{\mathbf{B}}$ can be obtained by differentiating eqs 40 and 41 using the product rule yielding

$$\begin{aligned}\overline{\mathbf{M}}^{\mathbf{B}} = {}& \int_0^{+\infty} d\tau(\overline{\mathbf{Y}}^{\mathbf{B}}(i\tau)(\mathbf{H}-\epsilon_F\mathbf{S}) \\ &+ \overline{\mathbf{Y}}(i\tau)(\mathbf{H}^{\mathbf{B}}-\epsilon_F\mathbf{S}^{\mathbf{B}}) + [\exp(-\tau(\mathbf{H}-\epsilon_F\mathbf{S})\mathbf{P}_{\mathrm{virt}})]^{\mathbf{B}}\mathbf{\Sigma} \\ &(-i\tau) + \exp(-\tau(\mathbf{H}-\epsilon_F\mathbf{S})\mathbf{P}_{\mathrm{virt}})\mathbf{\Sigma}^{\mathbf{B}}(-i\tau))\end{aligned} \tag{80}$$

$$\begin{aligned}\underline{\mathbf{M}}^{\mathbf{B}} = {}& \int_0^{+\infty} d\tau(\underline{\mathbf{Y}}^{\mathbf{B}}(-i\tau)(\mathbf{H}-\epsilon_F\mathbf{S}) \\ &+ \underline{\mathbf{Y}}(-i\tau)(\mathbf{H}^{\mathbf{B}}-\epsilon_F\mathbf{S}^{\mathbf{B}}) \\ &+ [\exp(\tau(\mathbf{H}-\epsilon_F\mathbf{S})\mathbf{P})]^{\mathbf{B}}\mathbf{\Sigma}(i\tau) \\ &+ \exp(\tau(\mathbf{H}-\epsilon_F\mathbf{S})\mathbf{P})\mathbf{\Sigma}^{\mathbf{B}}(i\tau))\end{aligned} \tag{81}$$

The evaluation of all **B**-field derivatives in the above expression has been described in the previous section.

3.3.6. Second Derivative of the Total RPA Energy. By combining eqs 56 and 58, an expression for the total RPA energy can be obtained according to

$$\begin{aligned}\left.\frac{\partial^2 E^{\mathrm{total}}[\mathbf{P}]}{\partial \mathbf{B}\partial \mathbf{m}}\right|_{\mathbf{m}=\mathbf{0},\mathbf{B}=\mathbf{0}} = {}& \mathrm{Tr}([\mathbf{V}^{\mathbf{B}}_{\mathrm{RPA}} + \mathbf{H}^{\mathbf{B}}_{\mathrm{HF}}]\mathbf{P}^{\mathbf{m}}) \\ &+ \mathrm{Tr}([\mathbf{V}_{\mathrm{RPA}} + \mathbf{H}_{\mathrm{HF}}]\mathbf{P}^{\mathbf{Bm}}) \\ &+ \mathrm{Tr}(\mathbf{P}^{\mathbf{B}}_{\mathrm{RPA}}\mathbf{h}^{\mathbf{m}}) + \mathrm{Tr}(\mathbf{P}_{\mathrm{RPA}}\mathbf{h}^{\mathbf{Bm}}) + \tilde{\boldsymbol{\sigma}}^{\mathrm{HF}}\end{aligned} \tag{82}$$

For simplicity, the contribution $\tilde{\boldsymbol{\sigma}}^{\mathrm{HF}}$ is treated separately with the usual techniques used for the computation of HF and DFT shifts. The contribution of the remaining terms will be described in detail in the next section.

3.3.7. Final Equation for RPA NMR Shieldings: Nested Z-Vector Approach for Avoiding P^{Bm}. The nested Z-vector approach provides an efficient way to evaluate $\mathbf{P}^{\mathbf{Bm}}$ with a reduced number of CPKS equations. It was first introduced by Maurer and Ochsenfeld[33] for AO-MP2 NMR shieldings and recently improved by Glasbrenner et al.[34] Here, we want to stress that Gauss had already introduced the respective MO-based Z-vector equations in the framework of MO-MP2 in 1992.[19]

In the following, the basic idea for the nested Z-vector method is reviewed, and subsequently the final equations are presented. A detailed derivation can be found in ref 34.

The objective is to evaluate $\mathrm{Tr}([\mathbf{V}_{\mathrm{RPA}} + \mathbf{H}_{\mathrm{HF}}]\mathbf{P}^{\mathbf{Bm}})$, i.e., the second term in eq 82. For this, we first consider the CPKS equation for the **B**-field derivative of the density

$$\mathbf{A}\mathbf{P}^{\mathbf{B}} = \mathbf{b}^{\mathbf{B}} \tag{83}$$

where **A** is the KS Hessian matrix and $\mathbf{b}^{\mathbf{B}}$ is the right-hand side of the CPKS equation. Next, eq 83 is differentiated with respect to **m** and rearranged to obtain an expression for $\mathbf{P}^{\mathbf{Bm}}$ according to

$$\mathbf{P}^{\mathbf{Bm}} = \mathbf{A}^{-1}(\mathbf{b}^{\mathbf{Bm}} - \mathbf{A}^{\mathbf{m}}[\mathbf{P}^{\mathbf{B}}]) \tag{84}$$

Using eq 84 together with the Z-vector ansatz allows to rewrite $\mathrm{Tr}([\mathbf{V}_{\mathrm{RPA}} + \mathbf{H}_{\mathrm{HF}}]\mathbf{P}^{\mathbf{Bm}})$ as

$$\mathrm{Tr}([\mathbf{V}_{\mathrm{RPA}} + \mathbf{H}_{\mathrm{HF}}]\mathbf{P}^{\mathbf{Bm}}) = \mathrm{Tr}(\mathbf{Z}(\mathbf{b}^{\mathbf{Bm}} - \mathbf{A}^{\mathbf{m}}[\mathbf{P}^{\mathbf{B}}])) \tag{85}$$

where **Z** is computed by solving one CPKS equation $\mathbf{AZ} = \mathbf{V}_{\mathrm{RPA}} + \mathbf{H}_{\mathrm{HF}}$. Next, all terms in $\mathrm{Tr}(\mathbf{Z}(\mathbf{b}^{\mathbf{Bm}} - \mathbf{A}^{\mathbf{m}}[\mathbf{P}^{\mathbf{B}}]))$ need to be reordered, such that only terms of the form $\mathrm{Tr}[\cdots\mathbf{P}^{\mathbf{m}}]$ result, which renders the expression amenable to another Z-vector step. The reordering is performed analogously to eqs D12–D28 in ref 34. It was shown that this, in combination with the terms $\mathrm{Tr}[\mathbf{V}^{\mathbf{B}}_{\mathrm{RPA}}\mathbf{P}^{\mathbf{m}}]$ from eq 58 and $\mathrm{Tr}[\mathbf{H}^{\mathbf{B}}_{\mathrm{HF}}\mathbf{P}^{\mathbf{m}}]$ from eq 56, leads to

$$\begin{aligned}&\mathrm{Tr}(\mathbf{Z}(\mathbf{b}^{\mathbf{Bm}} - \mathbf{A}^{\mathbf{m}}[\mathbf{P}^{\mathbf{B}}])) + \mathrm{Tr}([\mathbf{V}^{\mathbf{B}}_{\mathrm{RPA}} + \mathbf{H}^{\mathbf{B}}_{\mathrm{HF}}]\mathbf{P}^{\mathbf{m}}) \\ &\quad = \mathrm{Tr}(\mathbf{O}_{\mathbf{F}^{\mathbf{m}}}\mathbf{h}^{\mathbf{m}}) + \mathrm{Tr}(\mathbf{O}_{\mathbf{Y}^{\mathbf{m}}}\mathbf{h}^{\mathbf{m}}) + \mathrm{Tr}(\mathbf{O}\mathbf{P}^{\mathbf{m}})\end{aligned} \tag{86}$$

Applying eqs 85 and 86 to eq 82 and rearranging terms, yields the final expression for the RPA NMR shieldings as

$$\begin{aligned}\boldsymbol{\sigma} = {}& \mathrm{Tr}([\mathbf{P}_{\mathrm{RPA}} + \mathbf{O}_{\mathbf{Y}^{\mathbf{m}}}]\mathbf{h}^{\mathbf{Bm}}) + \mathrm{Tr}([\mathbf{P}^{\mathbf{B}}_{\mathrm{RPA}} + \mathbf{O}_{\mathbf{F}^{\mathbf{m}}}]\mathbf{h}^{\mathbf{m}}) \\ &+ \mathrm{Tr}(\mathbf{Z}_{\mathbf{O}}\mathbf{b}^{\mathbf{m}}) + \tilde{\boldsymbol{\sigma}}^{\mathrm{HF}}\end{aligned} \tag{87}$$

The introduced quantities $\mathbf{O}_{\mathbf{Y}^{\mathbf{m}}}$, $\mathbf{O}_{\mathbf{F}^{\mathbf{m}}}$, **O**, and $\mathbf{Z}_{\mathbf{O}}$ are defined in ref 34. Here, we note that following the notation of ref 34 in the context of the AO-MP2 NMR shieldings, the intermediates $\mathbf{P}_{\mathrm{RPA}}$ and $(\mathbf{V}_{\mathrm{RPA}} + \mathbf{H}_{\mathrm{HF}})$ correspond to the intermediates $\mathcal{F}$ and $\mathcal{P}$, respectively, and likewise for the differentiated intermediates. In essence, for an efficient treatment of the

https://doi.org/10.1021/acs.jctc.3c00542
J. Chem. Theory Comput. 2023, 19, 7542−7554

contributions from the HF Hamiltonian, i.e., $\mathrm{Tr}(\mathbf{H}_{\mathrm{HF}}\,\mathbf{P}^{\mathbf{Bm}})$ and $\mathrm{Tr}(\mathbf{H}^{\mathbf{B}}_{\mathrm{HF}}\,\mathbf{P}^{\mathbf{m}})$ from eq 56, $\mathbf{H}_{\mathrm{HF}}$ needs to be added to the $\mathbf{V}_{\mathrm{RPA}}$ intermediate, and likewise for the **B**-field differentiated quantities, to avoid the solution of two nested Z-vector equations. Finally, an overview of all necessary steps to compute NMR chemical shieldings at the RPA level of theory is provided in the Supporting Information.

4. COMPUTATIONAL DETAILS

Analytical NMR shifts at the RPA level of theory were implemented within our quantum chemistry package FermiONs++.[94−96] As a starting point for the RPA calculations, DFT with the generalized gradient approximation of Perdew−Burke−Ernzerhof (PBE),[97] as provided by the Libxc library version 5.1.1,[98] as well as the Hartree−Fock method, are employed. For all PBE reference calculations, an uncoupled DFT scheme is used.[99,100] The frozen core approximation is not utilized. Further, dense matrix algebra routines from the Intel Math Kernel Library (version 2022.0.0) are employed. Dunning's correlation-consistent basis sets with core weighted functions (cc-pwCVDZ, cc-pwCVTZ)[101] are used in combination with the corresponding RI basis sets.[102] For the time and frequency integration[57,61] as well as the cosine[57,61] and sine transformation[90] to switch between two domains, optimized minimax grids[57] are employed. For this, we use 15 grid points, which is proven to be sufficiently accurate, as shown in Section 5.2. The derivatives of numerical integration roots and weights used for the numerical imaginary time and frequency quadratures are neglected. This is justified by earlier work on RPA gradients,[67,68] which employ the same integration grids and for which it was found that this approximation yields sufficiently accurate results. Further, the validity of the gauge origin independence was confirmed by carrying out calculations after shifting each coordinate of the gauge origin by 5 Å. The isotropic shieldings showed deviations that did not exceed 0.05 ppm. Detailed results are provided in the Supporting Information. As commonly done in implementations of NMR shieldings, the explicit use of complex-valued matrices is avoided by treating purely imaginary matrices using skew-symmetric, real-valued matrices.

To validate our implementation, we further computed numerical RPA NMR shifts that were recently presented by our group.[41] In this context, the RPA correlation energy is computed within the RI approximation using the method of Furche and co-workers.[54] For the numerical frequency integration, we employ the Clenshaw−Curtis scheme[54,103] with 120 grid points, which was confirmed to provide accurate results in ref 41.

5. RESULTS AND DISCUSSION

5.1. Validation of the Implementation. For the validation of our implementation of analytical RPA NMR shifts, the shifts are compared against the results obtained with the numerical RPA NMR reference implementation.[41] Therefore, analytical and numerical RPA NMR shifts based on a preceding PBE reference calculation (RPA@PBE) and based on a HF reference (RPA@HF) were computed for the molecules in the test set assembled by Gauss and co-workers[104] as well as the test set of Flaig et al.[27] For the Gauss benchmark set, the molecules SO_2 and O_3 are excluded, as in ref 104, as well as PN, which is a difficult case for theoretical computations in general.[105]

The results for the Gauss benchmark set are shown in Figure 2 and in more detail in Table 1, where the mean

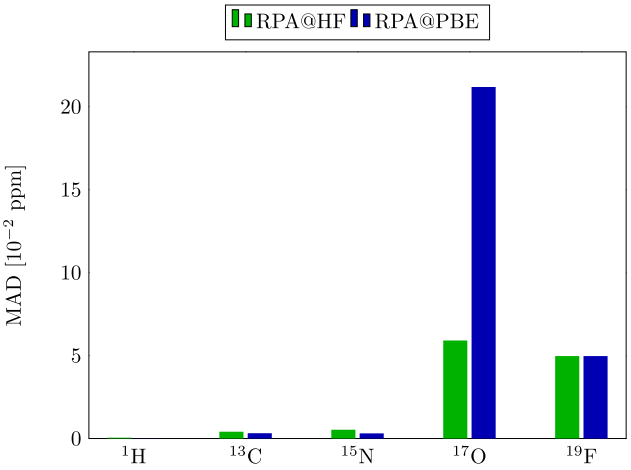

Figure 2. MADs in 10^{-2} ppm of analytical to numerical isotropic NMR shifts for the ^{1}H, ^{13}C, ^{15}N, ^{17}O, and ^{19}F nuclei at the RPA@HF and RPA@PBE levels of theory for the molecules in the Gauss[104] benchmark set. All calculations were carried out using the cc-pwCVTZ basis set with the corresponding RI basis set.

Table 1. Comparison of MADs in 10^{-2} ppm of Analytical to Numerical Isotropic NMR Shifts for the ^{1}H, ^{13}C, ^{15}N, ^{17}O, and ^{19}F Nuclei at the RPA@HF and RPA@PBE Levels of Theory[a]

benchmark	reference	^{1}H	^{13}C	^{15}N	^{17}O	^{19}F
Gauss	HF	0.05	0.41	0.53	5.91	4.97
	PBE	0.01	0.32	0.31	21.19	6.44
Flaig	HF	0.84	2.08	6.01	6.94	1.52
	PBE	0.04	3.05	7.73	7.73	2.52

[a]All Calculations were carried out with the cc-pwCVTZ basis set for the Gauss benchmark set and with the cc-pwCVDZ basis set for the Flaig benchmark set.

absolute deviations (MADs) of the analytical istropic NMR shifts with respect to the numerical results are shown for the most common nuclei in the test set, i.e., ^{1}H, ^{13}C, ^{15}N, ^{17}O, and ^{19}F, at the RPA@HF and RPA@PBE levels of theory using the cc-pwCVTZ basis set with the corresponding RI basis set. As can be seen, the MADs for the different nuclei at the RPA@HF and RPA@PBE levels of theory are all on the order of 10^{-2} ppm, which is well within the error of numerical differentiation.

The corresponding results for the Flaig benchmark set are provided in Figure 3 and in more detail in Table 1 for the nuclei ^{1}H, ^{13}C, ^{15}N, ^{17}O, and ^{19}F. All calculations were carried out using the cc-pwCVDZ basis set with the corresponding RI basis set. Evidently, for this benchmark set, all MADs are also on the order of 10^{-2} ppm and comparable with the results obtained for the Gauss benchmark set. Since the errors are well within the error of numerical differentiation, it is safe to conclude that the presented theory and the implementation thereof are correct.

5.2. Accuracy: Convergence of the Minimax Grid. To motivate the choice for the number of numerical integration points for the minimax grids in the previous section, NMR shift calculations on the benchmark set by Gauss and co-workers[104] are performed at the RPA@HF level of theory

https://doi.org/10.1021/acs.jctc.3c00542
J. Chem. Theory Comput. 2023, 19, 7542−7554

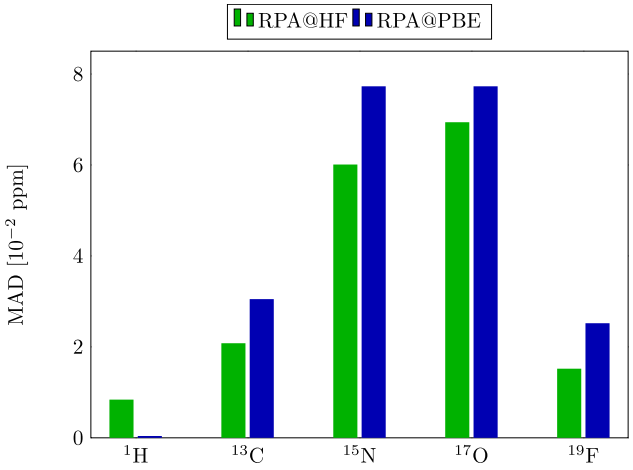

Figure 3. MADs in 10^{-2} ppm of analytical to numerical isotropic NMR shifts for the ^{1}H, ^{13}C, ^{15}N, ^{17}O, and ^{19}F nuclei at the RPA@HF and RPA@PBE levels of theory for the molecules in the Flaig[27] benchmark set. All calculations were carried out using the cc-pwCVDZ basis set with the corresponding RI basis set.

using the cc-pwCVTZ basis set for a varying number of integration points. The MADs with respect to the results obtained with the largest available integration grid are presented in Table 2 for the most represented nuclei in this benchmark set, i.e., ^{1}H, ^{13}C, ^{15}N, ^{17}O, and ^{19}F.

Table 2. Analysis of the RPA NMR Shift Convergence for the ^{1}H, ^{13}C, ^{15}N, ^{17}O, and ^{19}F Nuclei with the Number of Minimax Grid Points N_g[a]

N_g	^{1}H	^{13}C	^{15}N	^{17}O	^{19}F
10	0.01	0.62	1.75	3.20	0.97
11	0.01	0.50	1.40	2.57	0.77
12	0.01	0.41	1.14	2.07	0.61
13	0.01	0.36	0.91	1.73	0.49
14	0.00	0.26	0.70	1.31	0.42
15	0.00	0.24	0.54	1.07	0.31
16	0.00	0.15	0.39	0.75	0.23
17	0.00	0.13	0.26	0.53	0.39
18	0.00	0.09	0.14	0.32	0.34
19	0.00	0.04	0.07	0.15	0.08
20	-	-	-	-	-

[a]All values are given as MADs in 10^{-2} ppm with respect to the results obtained for N_g = 20 at the RPA@HF level of theory. All calculations were carried out using the cc-pwCVTZ basis set with the corresponding RI basis set.

The results in Table 2 show that the numerical integration grids allow to smoothly converge the obtained chemical shifts. For lighter elements, such as ^{1}H, the errors are almost independent of the grid size and smaller than 10^{-3} ppm. For heavier elements, such as ^{17}O, a grid size of 15 integration points allows one to obtain an accuracy on the order of 10^{-2} ppm, compared to the converged result obtained with 20 integration points. In conclusion, based on the obtained results, the choice of 15 integration points provides a good compromise between accuracy and computational cost, which is why this number of grid points was employed in all presented calculations.

6. CONCLUSIONS

An analytical expression for NMR chemical shieldings at the direct RPA level of theory as a post-KS method based on ACFDT is presented for the first time. By taking the mixed second derivative of the RPA ground-state energy expression with respect to the nuclear magnetic moment and an external magnetic field, the NMR shielding tensor is obtained. For this, a rigorous derivation for the analytical expression is presented, with which the evaluation of the shielding tensor is possible with formal $O(N^4)$ time complexity, in contrast to the higher-scaling of other correlation methods such as MP2 or CC. The derived expressions and the implementation are sensibly verified by comparing the obtained chemical shifts against the numerical implementation by Glasbrenner et al.[41] For this, calculations on established NMR benchmark sets were carried out with both HF and a commonly used representative for DFT functionals, i.e., PBE, as reference. While the employed implementation is only preliminarily optimized in terms of computational efficiency and not yet optimized in terms of memory requirements, the presented equations represent an ideal stepping stone toward a low-scaling and efficient implementation of NMR shieldings at the RPA level of theory in future work. Similar to the AO-RPA gradients, the evaluation of the noninteracting response function and the correlated self-energy in the imaginary time domain represent the formally highest scaling steps, and the necessity to compute their magnetic field derivatives adds additional $O(N^4)$ scaling steps. However, efficient techniques, such as the attenuated Coulomb RI approximation[60] and Cholesky molecular orbitals, to treat the involved integral contractions can be leveraged for a low-scaling implementation at reduced cost in future work. The application of these low-scaling techniques therefore provides a valuable route toward NMR shift calculations on large molecules with good accuracy and affordable cost.

Furthermore, the derived expression for the analytical second derivative of the RPA energy can easily be extended to the related σ-functionals[72] to profit from the reduced errors not only for atomization, reaction, and noncovalent interaction energies but possibly also for NMR shifts.

APPENDICES

A. Derivation of the Hartree−Fock Energy Functional Shielding Contribution

The Hartree−Fock energy functional is given as

$$E^{\mathrm{HF}}[\mathbf{P}] = \mathrm{Tr}\left(\mathbf{Ph} + \frac{1}{2}\mathbf{PG}[\mathbf{P}]\right) \tag{88}$$

To compute the HF contribution to the total NMR shielding tensor, this expression is first differentiated with respect to the nuclear magnetic moment $\mathbf{m}$ given by

$$\frac{\partial E^{\mathrm{HF}}[\mathbf{P}]}{\partial \mathbf{m}} = \mathrm{Tr}(\mathbf{P}^{\mathbf{m}}\mathbf{h} + \mathbf{Ph}^{\mathbf{m}} + \mathbf{P}^{\mathbf{m}}\mathbf{G}[\mathbf{P}]) \tag{89}$$

As the basis functions are independent of $\mathbf{m}$, the contribution from the differentiated integrals, i.e., $\mathbf{G}^{\mathbf{m}}[\mathbf{P}]$ is zero. The terms contracted with the response of the density matrix $\mathbf{P}^{\mathbf{m}}$ can be collected in the HF Hamiltonian $\mathbf{H}_{\mathrm{HF}}$ to yield

$$\frac{\partial E^{\mathrm{HF}}[\mathbf{P}]}{\partial \mathbf{m}} = \mathrm{Tr}(\mathbf{Ph}^{\mathbf{m}} + \mathbf{P}^{\mathbf{m}}\mathbf{H}_{\mathrm{HF}}) \tag{90}$$

https://doi.org/10.1021/acs.jctc.3c00542
J. Chem. Theory Comput. 2023, 19, 7542−7554

Since the occupied−occupied part of $\mathbf{P}^{\mathbf{m}}$ is given by $\mathbf{P}^{\mathbf{m}}_{\mathrm{oo}} = -\mathbf{PS}^{\mathbf{m}}\mathbf{P} = \mathbf{0}$ and the virtual−virtual part is necessarily zero, the density response is given by the nonzero occupied−virtual and virtual−occupied blocks as

$$\mathbf{P}^{\mathbf{m}} = \mathbf{PSP}^{\mathbf{m}}(\mathbf{1} - \mathbf{SP}) + (\mathbf{1} - \mathbf{PS})\mathbf{P}^{\mathbf{m}}\mathbf{SP} \quad (91)$$

$$= \mathbf{P}^{\mathbf{m}}_{\mathrm{ov}} + \mathbf{P}^{\mathbf{m}}_{\mathrm{vo}} \quad (92)$$

At the same time the occupied−virtual and virtual−occupied parts of the HF Hamiltonian, given by the following subspace projections,

$$\mathbf{SPH}_{\mathrm{HF}}(\mathbf{1} - \mathbf{PS}) = (\mathbf{1} - \mathbf{SP})\mathbf{H}_{\mathrm{HF}}\mathbf{PS} = \mathbf{0} \quad (93)$$

$$\mathbf{H}_{\mathrm{HF,ov}} = \mathbf{H}_{\mathrm{HF,vo}} = \mathbf{0} \quad (94)$$

vanish for a matching converged HF density. Therefore, the trace of $\mathbf{P}^{\mathbf{m}}\mathbf{H}_{\mathrm{HF}}$ is zero and the HF contribution to the total shielding tensor, after second differentiation with respect to $\mathbf{B}$, is given by

$$\frac{\partial^2 E^{\mathrm{HF}}[\mathbf{P}]}{\partial \mathbf{B}\partial \mathbf{m}} = \mathrm{Tr}(\mathbf{P}^{\mathbf{B}}\mathbf{h}^{\mathbf{m}}) + \mathrm{Tr}(\mathbf{Ph}^{\mathbf{Bm}}) \quad (95)$$

However, in the case of a KS reference density, the HF energy functional is nonstationary with respect to the density and thus the occupied−virtual and virtual−occupied parts of the HF Hamiltonian are nonzero. Therefore, in this case, the HF contribution to the total shielding tensor is given by

$$\frac{\partial^2 E^{\mathrm{HF}}[\mathbf{P}]}{\partial \mathbf{B}\partial \mathbf{m}} = \mathrm{Tr}(\mathbf{P}^{\mathbf{B}}\mathbf{h}^{\mathbf{m}}) + \mathrm{Tr}(\mathbf{Ph}^{\mathbf{Bm}}) + \mathrm{Tr}(\mathbf{H}^{\mathbf{B}}_{\mathrm{HF}}\mathbf{P}^{\mathbf{m}}) + \mathrm{Tr}(\mathbf{H}_{\mathrm{HF}}\mathbf{P}^{\mathbf{Bm}}) \quad (96)$$

B. Derivative of the Self-Energy with Respect to the Magnetic Field

Carrying out the differentiation in eq 68 for the self-energy $\mathbf{\Sigma}(-\mathrm{i}\tau)$ in the negative imaginary time domain yields

$$\left.\frac{\partial \Sigma_{\nu\lambda}(-\mathrm{i}\tau)}{\partial \mathbf{B}}\right|_{\mathbf{B}=\mathbf{0}} = -\frac{\partial \tilde{W}_{\mathrm{c,PQ}}(+\mathrm{i}\tau)}{\partial \mathbf{B}}\mathbb{B}^{P}_{\mu\nu}\underline{G}_{0,\mu\sigma}(-\mathrm{i}\tau)\mathbb{B}^{Q}_{\lambda\sigma} - \tilde{W}_{\mathrm{c,PQ}}(+\mathrm{i}\tau)\frac{\partial \mathbb{B}^{P}_{\mu\nu}}{\partial \mathbf{B}}\underline{G}_{0,\mu\sigma}(-\mathrm{i}\tau)\mathbb{B}^{Q}_{\lambda\sigma} - \tilde{W}_{\mathrm{c,PQ}}(+\mathrm{i}\tau)\mathbb{B}^{P}_{\mu\nu}\frac{\partial \underline{G}_{0,\mu\sigma}(-\mathrm{i}\tau)}{\partial \mathbf{B}}\mathbb{B}^{Q}_{\lambda\sigma} - \tilde{W}_{\mathrm{c,PQ}}(+\mathrm{i}\tau)\mathbb{B}^{P}_{\mu\nu}\underline{G}_{0,\mu\sigma}(-\mathrm{i}\tau)\frac{\partial \mathbb{B}^{Q}_{\lambda\sigma}}{\partial \mathbf{B}} \quad (97)$$

When evaluating the above expression at $\mathbf{B} = \mathbf{0}$, all quantities that are not $\mathbf{B}$-field derivatives evaluate to real-valued matrices (symmetric) and even functions in the imaginary time domain. All $\mathbf{B}$-field derivatives are purely imaginary quantities (skew-symmetric) and odd functions in the imaginary time domain. With this in mind, $\frac{\partial \tilde{W}_{\mathrm{c,PQ}}(+\mathrm{i}\tau)}{\partial \mathbf{B}}$ can further be simplified by using the definition in eq 25 and the fact that it is an odd function in the imaginary time domain:

$$\frac{\partial \tilde{W}_{\mathrm{c,PQ}}(+\mathrm{i}\tau)}{\partial \mathbf{B}} = \frac{\partial \mathbf{W}^{\mathrm{even}}_{\mathrm{c}}(\mathrm{i}\tau)}{\partial \mathbf{B}} - \frac{\partial \mathbf{W}^{\mathrm{odd}}_{\mathrm{c}}(\mathrm{i}\tau)}{\partial \mathbf{B}} \quad (98)$$

$$= -\frac{\partial \mathbf{W}^{\mathrm{odd}}_{\mathrm{c}}(\mathrm{i}\tau)}{\partial \mathbf{B}} = -\frac{\partial \mathbf{W}_{\mathrm{c}}(\mathrm{i}\tau)}{\partial \mathbf{B}} \quad (99)$$

Inserting the above expression into eq 97 yields the final expression given in eq 70.

By analogy, the self-energy in the positive time domain can be written according to

$$\left.\frac{\partial \Sigma_{\nu\lambda}(+\mathrm{i}\tau)}{\partial \mathbf{B}}\right|_{\mathbf{B}=\mathbf{0}} = -\frac{\partial \tilde{W}_{\mathrm{c,PQ}}(-\mathrm{i}\tau)}{\partial \mathbf{B}}\mathbb{B}^{P}_{\mu\nu}\overline{G}_{0,\mu\sigma}(\mathrm{i}\tau)\mathbb{B}^{Q}_{\lambda\sigma} - \tilde{W}_{\mathrm{c,PQ}}(-\mathrm{i}\tau)\frac{\partial \mathbb{B}^{P}_{\mu\nu}}{\partial \mathbf{B}}\overline{G}_{0,\mu\sigma}(\mathrm{i}\tau)\mathbb{B}^{Q}_{\lambda\sigma} - \tilde{W}_{\mathrm{c,PQ}}(-\mathrm{i}\tau)\mathbb{B}^{P}_{\mu\nu}\frac{\partial \overline{G}_{0,\mu\sigma}(\mathrm{i}\tau)}{\partial \mathbf{B}}\mathbb{B}^{Q}_{\lambda\sigma} - \tilde{W}_{\mathrm{c,PQ}}(-\mathrm{i}\tau)\mathbb{B}^{P}_{\mu\nu}\overline{G}_{0,\mu\sigma}(\mathrm{i}\tau)\frac{\partial \mathbb{B}^{Q}_{\lambda\sigma}}{\partial \mathbf{B}} \quad (100)$$

Again, rewriting $\frac{\partial \tilde{W}_{\mathrm{c,PQ}}(-\mathrm{i}\tau)}{\partial \mathbf{B}}$ using eq 25 and considering that it is an odd function in the imaginary time domain yields

$$\frac{\partial \tilde{W}_{\mathrm{c,PQ}}(-\mathrm{i}\tau)}{\partial \mathbf{B}} = \frac{\partial \mathbf{W}^{\mathrm{even}}_{\mathrm{c}}(-\mathrm{i}\tau)}{\partial \mathbf{B}} - \frac{\partial \mathbf{W}^{\mathrm{odd}}_{\mathrm{c}}(-\mathrm{i}\tau)}{\partial \mathbf{B}} \quad (101)$$

$$= +\frac{\partial \mathbf{W}^{\mathrm{odd}}_{\mathrm{c}}(\mathrm{i}\tau)}{\partial \mathbf{B}} = +\frac{\partial \mathbf{W}_{\mathrm{c}}(\mathrm{i}\tau)}{\partial \mathbf{B}} \quad (102)$$

Finally, inserting the above equation into eq 100 yields eq 69.

■ ASSOCIATED CONTENT

Supporting Information

The Supporting Information is available free of charge at https://pubs.acs.org/doi/10.1021/acs.jctc.3c00542.

Algorithm for the presented RPA NMR method, detailed results for the demonstration of the validity of the gauge origin independence, and detailed results for the Gauss[104] and Flaig[27] benchmark set as well as for the minimax convergence analysis (PDF)

■ AUTHOR INFORMATION

Corresponding Author

Christian Ochsenfeld − *Chair of Theoretical Chemistry, Department of Chemistry, University of Munich (LMU), D-81377 Munich, Germany; Max Planck Institute for Solid State Research, D-70569 Stuttgart, Germany;* orcid.org/0000-0002-4189-6558; Email: christian.ochsenfeld@cup.uni-muenchen.de

Authors

Viktoria Drontschenko − *Chair of Theoretical Chemistry, Department of Chemistry, University of Munich (LMU), D-81377 Munich, Germany*

Felix H. Bangerter − *Chair of Theoretical Chemistry, Department of Chemistry, University of Munich (LMU), D-81377 Munich, Germany;* orcid.org/0000-0001-5649-1599

https://doi.org/10.1021/acs.jctc.3c00542
J. Chem. Theory Comput. 2023, 19, 7542−7554

Complete contact information is available at:
https://pubs.acs.org/10.1021/acs.jctc.3c00542

Author Contributions

[§]V.D. and F.H.B. contributed equally to this work.

Notes

The authors declare no competing financial interest.

■ ACKNOWLEDGMENTS

The authors acknowledge the financial support by the "Deutsche Forschungsgemeinschaft" (DFG) under Grant TRR325 "Assembly Controlled Chemical Photocatalysis" (Grant No. 444632635) and the cluster of excellence (EXC2111-390814868) "Munich Center for Quantum Science and Technology" (MCQST). C.O. acknowledges the additional support as Max-Planck-Fellow at the MPI-FKF Stuttgart. F.H.B. thanks the "Fonds der Chemischen Industrie" (FCI) for a graduate fellowship. The authors thank Y. Lemke (LMU Munich) for helpful discussions and Dr. J. Kussmann (LMU Munich) for providing a development version of the FermiONs++ program package.

■ REFERENCES

(1) Schmidt-Rohr, K.; Spiess, H. W. *Multidimensional Solid-State NMR and Polymers*; Academic Press, 1994.
(2) Bühl, M.; van Mourik, T. NMR spectroscopy: quantum-chemical calculations. *Wiley Interdiscip. Rev.: Comput. Mol. Sci.* **2011**, *1*, 634−647.
(3) James, T. *Nuclear Magnetic Resonance in Biochemistry*; Elsevier, 2012.
(4) Hodgkinson, P. *Nuclear Magnetic Resonance Vol. 47*; Nuclear Magnetic Resonance; Royal Society of Chemistry, 2021.
(5) Hodgkinson, P. *Nuclear Magnetic Resonance Vol. 46*; SPR Nuclear Magnetic Resonance; Royal Society of Chemistry, 2020.
(6) Harris, R.; Wasylishen, R.; Duer, M. *NMR Crystallography*; eMagRes Books; Wiley, 2009.
(7) Gauss, J. Effects of electron correlation in the calculation of nuclear magnetic resonance chemical shifts. *J. Chem. Phys.* **1993**, *99*, 3629−3643.
(8) Helgaker, T.; Jaszunski, M.; Ruud, K. Ab initio methods for the calculation of NMR shielding and indirect spin-spin coupling constants. *Chem. Rev.* **1999**, *99*, 293−352.
(9) Casabianca, L. B.; De Dios, A. C. Ab initio calculations of NMR chemical shifts. *J. Chem. Phys.* **2008**, *128*, No. 052201.
(10) Lodewyk, M. W.; Siebert, M. R.; Tantillo, D. J. Computational prediction of 1H and 13C chemical shifts: a useful tool for natural product, mechanistic, and synthetic organic chemistry. *Chem. Rev.* **2012**, *112*, 1839−1862.
(11) Stevens, R. M.; Pitzer, R.; Lipscomb, W. Perturbed Hartree−Fock Calculations. I. Magnetic Susceptibility and Shielding in the LiH Molecule. *J. Chem. Phys.* **1963**, *38*, 550−560.
(12) Ditchfield, R. Self-consistent perturbation theory of diamagnetism: I. A gauge-invariant LCAO method for NMR chemical shifts. *Mol. Phys.* **1974**, *27*, 789−807.
(13) Wolinski, K.; Hinton, J. F.; Pulay, P. Efficient implementation of the gauge-independent atomic orbital method for NMR chemical shift calculations. *J. Am. Chem. Soc.* **1990**, *112*, 8251−8260.
(14) Häser, M.; Ahlrichs, R.; Baron, H.; Weis, P.; Horn, H. Direct computation of second-order SCF properties of large molecules on workstation computers with an application to large carbon clusters. *Theor. Chim. Acta* **1992**, *83*, 455−470.
(15) Larsen, H.; Helgaker, T.; Olsen, J.; Jørgensen, P. Geometrical derivatives and magnetic properties in atomic-orbital density-based Hartree−Fock theory. *J. Chem. Phys.* **2001**, *115*, 10344−10352.
(16) Schreckenbach, G.; Ziegler, T. Calculation of NMR shielding tensors using gauge-including atomic orbitals and modern density functional theory. *J. Phys. Chem. A* **1995**, *99*, 606−611.
(17) Cheeseman, J. R.; Trucks, G. W.; Keith, T. A.; Frisch, M. J. A comparison of models for calculating nuclear magnetic resonance shielding tensors. *J. Chem. Phys.* **1996**, *104*, 5497−5509.
(18) Rauhut, G.; Puyear, S.; Wolinski, K.; Pulay, P. Comparison of NMR shieldings calculated from Hartree- Fock and density functional wave functions using gauge-including atomic orbitals. *J. Phys. Chem. A* **1996**, *100*, 6310−6316.
(19) Gauss, J. Calculation of NMR chemical shifts at second-order many-body perturbation theory using gauge-including atomic orbitals. *Chem. Phys. Lett.* **1992**, *191*, 614−620.
(20) Gauss, J.; Stanton, J. F. Electron-correlated approaches for the calculation of NMR chemical shifts. *Adv. Chem. Phys.* **2002**, *123*, 355−422.
(21) Gauss, J.; Stanton, J. F. Gauge-invariant calculation of nuclear magnetic shielding constants at the coupled−cluster singles and doubles level. *J. Chem. Phys.* **1995**, *102*, 251−253.
(22) Gauss, J.; Stanton, J. F. Perturbative treatment of triple excitations in coupled-cluster calculations of nuclear magnetic shielding constants. *J. Chem. Phys.* **1996**, *104*, 2574−2583.
(23) Kállay, M.; Gauss, J. Analytic second derivatives for general coupled-cluster and configuration-interaction models. *J. Chem. Phys.* **2004**, *120*, 6841−6848.
(24) Ruud, K.; Helgaker, T.; Kobayashi, R.; Jørgensen, P.; Bak, K. L.; Jensen, H. J. A. Multiconfigurational self-consistent field calculations of nuclear shieldings using London atomic orbitals. *J. Chem. Phys.* **1994**, *100*, 8178−8185.
(25) Ochsenfeld, C.; Kussmann, J.; Koziol, F. Ab initio NMR spectra for molecular systems with a thousand and more atoms: a linear-scaling method. *Angew. Chem.* **2004**, *116*, 4585−4589.
(26) Kussmann, J.; Ochsenfeld, C. Linear-scaling method for calculating nuclear magnetic resonance chemical shifts using gauge-including atomic orbitals within Hartree-Fock and density-functional theory. *J. Chem. Phys.* **2007**, *127*, No. 054103.
(27) Flaig, D.; Maurer, M.; Hanni, M.; Braunger, K.; Kick, L.; Thubauville, M.; Ochsenfeld, C. Benchmarking hydrogen and carbon NMR chemical shifts at HF, DFT, and MP2 levels. *J. Chem. Theory Comput.* **2014**, *10*, 572−578.
(28) Stoychev, G. L.; Auer, A. A.; Neese, F. Efficient and accurate prediction of nuclear magnetic resonance shielding tensors with double-hybrid density functional theory. *J. Chem. Theory Comput.* **2018**, *14*, 4756−4771.
(29) Kollwitz, M.; Gauss, J. A direct implementation of the GIAO-MBPT (2) method for calculating NMR chemical shifts. Application to the naphthalenium and anthracenium ions. *Chem. Phys. Lett.* **1996**, *260*, 639−646.
(30) Kollwitz, M.; Häser, M.; Gauss, J. Non-Abelian point group symmetry in direct second-order many-body perturbation theory calculations of NMR chemical shifts. *J. Chem. Phys.* **1998**, *108*, 8295−8301.
(31) Gauss, J.; Werner, H.-J. NMR chemical shift calculations within local correlation methods: the GIAO-LMP2 approach. *Phys. Chem. Chem. Phys.* **2000**, *2*, 2083−2090.
(32) Loibl, S.; Schütz, M. NMR shielding tensors for density fitted local second-order Møller-Plesset perturbation theory using gauge including atomic orbitals. *J. Chem. Phys.* **2012**, *137*, No. 084107.
(33) Maurer, M.; Ochsenfeld, C. A linear-and sublinear-scaling method for calculating NMR shieldings in atomic orbital-based second-order Møller-Plesset perturbation theory. *J. Chem. Phys.* **2013**, *138*, No. 174104.
(34) Glasbrenner, M.; Vogler, S.; Ochsenfeld, C. Efficient low-scaling computation of NMR shieldings at the second-order Møller−Plesset perturbation theory level with Cholesky-decomposed densities and an attenuated Coulomb metric. *J. Chem. Phys.* **2021**, *155*, No. 224107.
(35) Burger, S.; Lipparini, F.; Gauss, J.; Stopkowicz, S. NMR chemical shift computations at second-order Møller−Plesset

perturbation theory using gauge-including atomic orbitals and Cholesky-decomposed two-electron integrals. *J. Chem. Phys.* **2021**, *155*, No. 074105.
(36) Stoychev, G. L.; Auer, A. A.; Gauss, J.; Neese, F. DLPNO-MP2 second derivatives for the computation of polarizabilities and NMR shieldings. *J. Chem. Phys.* **2021**, *154*, No. 164110.
(37) Grimme, S. Improved second-order Møller−Plesset perturbation theory by separate scaling of parallel-and antiparallel-spin pair correlation energies. *J. Chem. Phys.* **2003**, *118*, 9095−9102.
(38) Maurer, M.; Ochsenfeld, C. Spin Component-Scaled Second-Order Møller−Plesset Perturbation Theory for Calculating NMR Shieldings. *J. Chem. Theory Comput.* **2015**, *11*, 37−44.
(39) Jung, Y.; Lochan, R. C.; Dutoi, A. D.; Head-Gordon, M. Scaled opposite-spin second order Møller−Plesset correlation energy: An economical electronic structure method. *J. Chem. Phys.* **2004**, *121*, 9793−9802.
(40) Gauss, J.; Stanton, J. F. Analytic CCSD(T) second derivatives. *Chem. Phys. Lett.* **1997**, *276*, 70−77.
(41) Glasbrenner, M.; Graf, D.; Ochsenfeld, C. Benchmarking the Accuracy of the Direct Random Phase Approximation and σ-Functionals for NMR Shieldings. *J. Chem. Theory Comput.* **2022**, *18*, 192−205.
(42) Bohm, D.; Pines, D. A collective description of electron interactions: III. Coulomb interactions in a degenerate electron gas. *Phys. Rev.* **1953**, *92*, 609.
(43) Kohn, W.; Sham, L. J. Self-consistent equations including exchange and correlation effects. *Phys. Rev.* **1965**, *140*, A1133.
(44) Perdew, J. P.; Schmidt, K. Jacob's ladder of density functional approximations for the exchange-correlation energy. *AIP Conf. Proc.* **2001**, *577*, 1−20.
(45) Hohenberg, P.; Kohn, W. Inhomogeneous electron gas. *Phys. Rev.* **1964**, *136*, B864.
(46) Langreth, D. C.; Perdew, J. P. The exchange-correlation energy of a metallic surface. *Solid State Commun.* **1975**, *17*, 1425−1429.
(47) Gunnarsson, O.; Lundqvist, B. I. Exchange and correlation in atoms, molecules, and solids by the spin-density-functional formalism. *Phys. Rev. B* **1976**, *13*, 4274.
(48) Langreth, D. C.; Perdew, J. P. Exchange-correlation energy of a metallic surface: Wave-vector analysis. *Phys. Rev. B* **1977**, *15*, 2884.
(49) Whitten, J. L. Coulombic potential energy integrals and approximations. *J. Chem. Phys.* **1973**, *58*, 4496.
(50) Dunlap, B. I.; Connolly, J. W. D.; Sabin, J. R. On some approximations in applications of Xα theory. *J. Chem. Phys.* **1979**, *71*, 3396.
(51) Feyereisen, M.; Fitzgerald, G.; Komornicki, A. Use of approximate integrals in ab initio theory. An application in MP2 energy calculations. *Chem. Phys. Lett.* **1993**, *208*, 359−363.
(52) Eichkorn, K.; Treutler, O.; Öhm, H.; Häser, M.; Ahlrichs, R. Auxiliary basis sets to approximate Coulomb potentials. *Chem. Phys. Lett.* **1995**, *240*, 283−290.
(53) Eichkorn, K.; Weigend, F.; Treutler, O.; Ahlrichs, R. Auxiliary basis sets for main row atoms and transition metals and their use to approximate Coulomb potentials. *Theor. Chem. Acc.* **1997**, *97*, 119−124.
(54) Eshuis, H.; Yarkony, J.; Furche, F. Fast computation of molecular random phase approximation correlation energies using resolution of the identity and imaginary frequency integration. *J. Chem. Phys.* **2010**, *132*, No. 234114.
(55) Furche, F. Developing the random phase approximation into a practical post-Kohn-Sham correlation model. *J. Chem. Phys.* **2008**, *129*, No. 114105.
(56) Eshuis, H.; Furche, F. Basis set convergence of molecular correlation energy differences within the random phase approximation. *J. Chem. Phys.* **2012**, *136*, No. 084105.
(57) Kaltak, M.; Klimes, J.; Kresse, G. Low scaling algorithms for the random phase approximation: Imaginary time and Laplace transformations. *J. Chem. Theory Comput.* **2014**, *10*, No. 2498.
(58) Kállay, M. Linear-scaling implementation of the direct random-phase approximation. *J. Chem. Phys.* **2015**, *142*, No. 204105.
(59) Schurkus, H. F.; Ochsenfeld, C. Communication: An effective linear-scaling atomic-orbital reformulation of the random-phase approximation using a contracted double-Laplace transformation. *J. Chem. Phys.* **2016**, *144*, No. 031101.
(60) Luenser, A.; Schurkus, H. F.; Ochsenfeld, C. Vanishing-overhead linear-scaling random phase approximation by Cholesky decomposition and an attenuated Coulomb-metric. *J. Chem. Theory Comput.* **2017**, *13*, 1647.
(61) Graf, D.; Beuerle, M.; Schurkus, H. F.; Luenser, A.; Savasci, G.; Ochsenfeld, C. Accurate and Efficient Parallel Implementation of an Effective Linear-Scaling Direct Random Phase Approximation Method. *J. Chem. Theory Comput.* **2018**, *14*, 2505.
(62) Drontschenko, V.; Graf, D.; Laqua, H.; Ochsenfeld, C. Lagrangian-based minimal-overhead batching scheme for the efficient integral-direct evaluation of the RPA correlation energy. *J. Chem. Theory and Comput.* **2021**, *17*, 5623−5634.
(63) Wilhelm, J.; Seewald, P.; Del Ben, M.; Hutter, J. Large-scale cubic-scaling random phase approximation correlation energy calculations using a Gaussian basis. *J. Chem. Theory Comput.* **2016**, *12*, 5851−5859.
(64) Gauss, J. Molecular properties. *Modern Methods and Algorithms of Quantum Chemistry* **2000**, *3*, 541−592.
(65) Rekkedal, J.; Coriani, S.; Iozzi, M. F.; Teale, A. M.; Helgaker, T.; Pedersen, T. B. Communication: Analytic gradients in the random-phase approximation. *J. Chem. Phys.* **2013**, *139*, No. 081101.
(66) Burow, A. M.; Bates, J. E.; Furche, F.; Eshuis, H. Analytical first-order molecular properties and forces within the adiabatic connection random phase approximation. *J. Chem. Theory Comput.* **2014**, *10*, 180−194.
(67) Ramberger, B.; Schäfer, T.; Kresse, G. Analytic interatomic forces in the random phase approximation. *Phys. Rev. Lett.* **2017**, *118*, 106403.
(68) Beuerle, M.; Ochsenfeld, C. Low-scaling analytical gradients for the direct random phase approximation using an atomic orbital formalism. *J. Chem. Phys.* **2018**, *149*, No. 244111.
(69) Thierbach, A.; Görling, A. Analytic energy gradients for the exact exchange Kohn−Sham method. *J. Chem. Phys.* **2020**, *152*, No. 114113.
(70) Tahir, M. N.; Zhu, T.; Shang, H.; Li, J.; Blum, V.; Ren, X. Localized resolution of identity approach to the analytical gradients of random-phase approximation ground-state energy: algorithm and benchmarks. *J. Chem. Theory Comput.* **2022**, *18*, 5297−5311.
(71) Drontschenko, V.; Graf, D.; Laqua, H.; Ochsenfeld, C. Efficient Method for the Computation of Frozen-Core Nuclear Gradients within the Random Phase Approximation. *J. Chem. Theory Comput.* **2022**, *18*, 7359−7372.
(72) Trushin, E.; Thierbach, A.; Görling, A. Toward chemical accuracy at low computational cost: Density-functional theory with σ-functionals for the correlation energy. *J. Chem. Phys.* **2021**, *154*, No. 014104.
(73) Hansen, A. E.; Bouman, T. D. Localized orbital/local origin method for calculation and analysis of NMR shieldings. Applications to 13C shielding tensors. *J. Chem. Phys.* **1985**, *82*, 5035−5047.
(74) Tossell, J. A.; Lazzeretti, P. Ab initio calculation of 77Se NMR shielding constants in H2Se and SeF6 and other second-order properties of H2Se. *J. Magn. Reson. (1969)* **1988**, *80*, 39−44.
(75) Tossell, J. A. Calculation of the 29 Si NMR shielding tensor in forsterite. *Phys. Chem. Miner.* **1992**, *19*, 338−342.
(76) Sauer, S. P.; Špirko, V.; Paidarová, I.; Kraemer, W. P. The vibrational dependence of the hydrogen and oxygen nuclear magnetic shielding constants in OH- and OH-· H2O. *Chem. Phys.* **1997**, *214*, 91−101.
(77) Visscher, L.; Enevoldsen, T.; Saue, T.; Jensen, H. J. A.; Oddershede, J. Full four-component relativistic calculations of NMR shielding and indirect spin-spin coupling tensors in hydrogen halides. *J. Comput. Chem.* **1999**, *20*, 1262−1273.
(78) Gimenez, C. A.; Kozioł, K.; Aucar, G. A. Quantum electrodynamics effects on NMR magnetic shielding constants of

https://doi.org/10.1021/acs.jctc.3c00542
J. Chem. Theory Comput. 2023, 19, 7542−7554

He-like and Be-like atomic systems. *Phys. Rev. A* **2016**, *93*, No. 032504.
(79) Einstein, A. The foundation of the general theory of relativity. *Ann. Phys.* **1916**, *354*, 769.
(80) Hameka, H. F. Theory of Magnetic Properties of Molecules with Particular Emphasis on the Hydrogen Molecule. *Rev. Mod. Phys.* **1962**, *34*, 87−101.
(81) Zeroka, D.; Hameka, H. F. Calculation of Magnetic Shielding Constants of Diatomic Molecules. I. General Theory and Application to HF Molecule. *J. Chem. Phys.* **1966**, *45*, 300−311.
(82) London, F. Théorie quantique des courants interatomiques dans les combinaisons aromatiques. *J. Phys. Radium* **1937**, *8*, 397−409.
(83) Helgaker, T.; Jørgensen, P. An electronic Hamiltonian for origin independent calculations of magnetic properties. *J. Chem. Phys.* **1991**, *95*, 2595−2601.
(84) Schweizer, S.; Doser, B.; Ochsenfeld, C. An atomic orbital-based reformulation of energy gradients in second-order Møller−Plesset perturbation theory. *J. Chem. Phys.* **2008**, *128*, No. 154101.
(85) Furche, F.; Van Voorhis, T. Fluctuation-dissipation theorem density-functional theory. *J. Chem. Phys.* **2005**, *122*, No. 164106.
(86) Hedin, L. New method for calculating the one-particle Green's function with application to the electron-gas problem. *Phys. Rev.* **1965**, *139*, A796.
(87) Ayala, P. Y.; Scuseria, G. E. Linear scaling second-order M? ller−Plesset theory in the atomic orbital basis for large molecular systems. *J. Chem. Phys.* **1999**, *110*, 3660−3671.
(88) Pulay, P. Ab initio calculation of force constants and equilibrium geometries in polyatomic molecules: I. Theory. *Mol. Phys.* **1969**, *17*, 197−204.
(89) Handy, N. C.; Schaefer, H. F., III On the evaluation of analytic energy derivatives for correlated wave functions. *J. Chem. Phys.* **1984**, *81*, 5031−5033.
(90) Liu, P.; Kaltak, M.; Klimeš, J.; Kresse, G. Cubic scaling G W: Towards fast quasiparticle calculations. *Phys. Rev. B* **2016**, *94*, 165109.
(91) Wilhelm, J.; Golze, D.; Talirz, L.; Hutter, J.; Pignedoli, C. A. Toward GW calculations on thousands of atoms. *J. Phys. Chem. Lett.* **2018**, *9*, 306−312.
(92) Surján, P. R. The MP2 energy as a functional of the Hartree−Fock density matrix. *Chem. Phys. Lett.* **2005**, *406*, 318−320.
(93) Beer, M.; Ochsenfeld, C. Efficient linear-scaling calculation of response properties: Density matrix-based Laplace-transformed coupled-perturbed self-consistent field theory. *J. Chem. Phys.* **2008**, *128*, No. 221102.
(94) Kussmann, J.; Ochsenfeld, C. Pre-selective screening for matrix elements in linear-scaling exact exchange calculations. *J. Chem. Phys.* **2013**, *138*, No. 134114.
(95) Kussmann, J.; Ochsenfeld, C. Preselective screening for linear-scaling exact exchange-gradient calculations for graphics processing units and general strong-scaling massively parallel calculations. *J. Chem. Theory Comput.* **2015**, *11*, 918−922.
(96) Kussmann, J.; Ochsenfeld, C. Hybrid CPU/GPU Integral Engine for Strong-Scaling Ab Initio Methods. *J. Chem. Theory Comput.* **2017**, *13*, 3153−3159.
(97) Perdew, J. P.; Burke, K.; Ernzerhof, M. Generalized gradient approximation made simple. *Phys. Rev. Lett.* **1996**, *77*, 3865.
(98) Marques, M. A.; Oliveira, M. J.; Burnus, T. Libxc: A library of exchange and correlation functionals for density functional theory. *Comput. Phys. Commun.* **2012**, *183*, 2272−2281.
(99) Malkin, V. G.; Malkina, O. L.; Salahub, D. R. Calculations of NMR Shielding Constants by Uncoupled Density Functional Theory. *Chem. Phys. Lett.* **1993**, *204*, 80−86.
(100) Beer, M.; Kussmann, J.; Ochsenfeld, C. Nuclei-selected NMR shielding calculations: A sublinear-scaling quantum-chemical method. *J. Chem. Phys.* **2011**, *134*, No. 074102.
(101) Peterson, K. A.; Dunning, T. H., Jr Accurate correlation consistent basis sets for molecular core-valence correlation effects: The second row atoms Al−Ar, and the first row atoms B−Ne revisited. *J. Chem. Phys.* **2002**, *117*, 10548−10560.
(102) Hättig, C. Optimization of auxiliary basis sets for RI-MP2 and RI-CC2 calculations: Core-valence and quintuple-ζ basis sets for H to Ar and QZVPP basis sets for Li to Kr. *Phys. Chem. Chem. Phys.* **2005**, *7*, 59−66.
(103) Boyd, J. P. Exponentially convergent Fourier-Chebshev quadrature schemes on bounded and infinite intervals. *J. Sci. Comput.* **1987**, *2*, 99−109.
(104) Teale, A. M.; Lutnæs, O. B.; Helgaker, T.; Tozer, D. J.; Gauss, J. Benchmarking density-functional theory calculations of NMR shielding constants and spin-rotation constants using accurate coupled-cluster calculations. *J. Chem. Phys.* **2013**, *138*, No. 024111.
(105) Kupka, T.; Leszczyńska, M.; Ejsmont, K.; Mnich, A.; Broda, M.; Thangavel, K.; Kaminskỳ, J. Phosphorus mononitride: A difficult case for theory. *Int. J. Quantum Chem.* **2019**, *119*, No. e26032.

https://doi.org/10.1021/acs.jctc.3c00542
J. Chem. Theory Comput. 2023, 19, 7542−7554

Supporting Information: Analytical Second-Order Properties for the Random Phase Approximation: Nuclear Magnetic Resonance Shieldings

Viktoria Drontschenko,[†] Felix H. Bangerter,[†] and Christian Ochsenfeld[*,†,‡]

†*Chair of Theoretical Chemistry, Department of Chemistry, University of Munich (LMU), D-81377 Munich, Germany*

‡*Max Planck Institute for Solid State Research, D-70569 Stuttgart, Germany*

E-mail: christian.ochsenfeld@cup.uni-muenchen.de

Contents

1 Implementation

The following algorithm summarizes the necessary steps for computing NMR chemical shieldings at the RPA level of theory.

Algorithm 1 Compute RPA NMR chemical shieldings.

compute $\mathbf{H}$, $\mathbf{S}$, $\mathbf{P}$, $\mathbf{P}_{\text{virt}}$, $\mathbb{V}$, and $\mathbb{B}$ ▷ SCF intermediates
compute $\mathbf{h}^{\mathbf{m}}$, $\mathbf{h}^{\mathbf{Bm}}$, $\mathbf{S}^{\mathbf{B}}$, $\mathbf{H}^{(\mathbf{B})}$, and $\mathbb{B}^{\mathbf{B}}$
solve CPSCF for $\mathbf{P}^{\mathbf{B}}$
compute $\mathbf{P}^{\mathbf{B}}_{\text{virt}}$
compute $\mathbf{H}^{\mathbf{B}}$
if not Hartree–Fock reference **then**
  compute $\mathbf{H}_{\text{HF}}$ and $\mathbf{H}^{\mathbf{B}}_{\text{HF}}$
end if
compute $\mathbf{G}_0(\mathrm{i}\tau)$ ▷ first derivative intermediates
compute $\mathbf{X}_0(\mathrm{i}\tau)$
cosine transform of $\mathbf{X}_0(\mathrm{i}\tau)$ to $\hat{\mathbf{X}}_0(\mathrm{i}\omega)$
compute $\hat{\mathbf{W}}_{\text{c}}(\mathrm{i}\omega)$
inverse cosine transform of $\hat{\mathbf{W}}_{\text{c}}(\mathrm{i}\omega)$ to $\mathbf{W}_{\text{c}}(\mathrm{i}\tau)$
compute $\boldsymbol{\Sigma}(\mathrm{i}\tau)$
compute $\mathbf{Y}(\mathrm{i}\tau)$ by recursion with $\boldsymbol{\mathcal{A}}(\tau)$ and $\boldsymbol{\mathcal{B}}(\mathrm{i}\tau)$
integrate $\mathbf{Y}(\mathrm{i}\tau)$ to form $\mathbf{P}_{\text{RPA}}$
integrate $\mathbf{Y}(\mathrm{i}\tau)$ and $\boldsymbol{\Sigma}(\mathrm{i}\tau)$ to form $\mathbf{M}$
compute $\mathbf{V}_{\text{RPA}}$
for every $\mathbf{B}$-field component **do** ▷ second derivative intermediates
  compute $\mathbf{G}^{\mathbf{B}}_0(\mathrm{i}\tau)$
  compute $\mathbf{X}^{\mathbf{B}}_0(\mathrm{i}\tau)$
  sine transform of $\mathbf{X}^{\mathbf{B}}_0(\mathrm{i}\tau)$ to $\hat{\mathbf{X}}^{\mathbf{B}}_0(\mathrm{i}\omega)$
  compute $\hat{\mathbf{W}}^{\mathbf{B}}_{\text{c}}(\mathrm{i}\omega)$
  inverse sine transform of $\hat{\mathbf{W}}^{\mathbf{B}}_{\text{c}}(\mathrm{i}\omega)$ to $\mathbf{W}^{\mathbf{B}}_{\text{c}}(\mathrm{i}\tau)$
  compute $\boldsymbol{\Sigma}^{\mathbf{B}}(\mathrm{i}\tau)$
  compute $\mathbf{Y}^{\mathbf{B}}(\mathrm{i}\tau)$ by recursion with $\boldsymbol{\mathcal{A}}^{\mathbf{B}}(\tau)$ and $\boldsymbol{\mathcal{B}}^{\mathbf{B}}(\mathrm{i}\tau)$
  integrate $\mathbf{Y}(\mathrm{i}\tau)$ and $\mathbf{Y}^{\mathbf{B}}(\mathrm{i}\tau)$ to form $\mathbf{P}^{\mathbf{B}}_{\text{RPA}}$
  integrate $\mathbf{Y}(\mathrm{i}\tau)$, $\mathbf{Y}^{\mathbf{B}}(\mathrm{i}\tau)$, $\boldsymbol{\Sigma}(\mathrm{i}\tau)$, and $\boldsymbol{\Sigma}^{\mathbf{B}}(\mathrm{i}\tau)$ to form $\mathbf{M}^{\mathbf{B}}$
  compute $\mathbf{V}^{\mathbf{B}}_{\text{RPA}}$
end for
solve Z-vector equation $\mathbf{Z}_{\mathbf{V}_{\text{RPA}}} = \mathbf{A}^{-1}(\mathbf{V}_{\text{RPA}} + \mathbf{H}_{\text{HF}})$ ▷ nested Z-vector/final shieldings
compute $\mathbf{O}$, $\mathbf{O}_{\mathbf{F}^{\mathbf{m}}}$, and $\mathbf{O}_{\mathbf{Y}^{\mathbf{m}}}$
solve Z-vector equation $\mathbf{Z}_{\mathbf{O}} = \mathbf{A}^{-1}\mathbf{O}$
compute $\boldsymbol{\sigma} = \mathrm{Tr}([\mathbf{P}_{\text{RPA}} + \mathbf{O}_{\mathbf{Y}^{\mathbf{m}}}]\mathbf{h}^{\mathbf{Bm}}) + \mathrm{Tr}([\mathbf{P}^{\mathbf{B}}_{\text{RPA}} + \mathbf{O}_{\mathbf{F}^{\mathbf{m}}}]\mathbf{h}^{\mathbf{m}}) + \mathrm{Tr}(\mathbf{Z}_{\mathbf{O}}\mathbf{b}^{\mathbf{m}}) + \tilde{\boldsymbol{\sigma}}^{\text{HF}}$

The algorithm can roughly be grouped into four stages. First, the computation of all

intermediates also present in HF NMR shieldings, i.e., the densities, the Hamiltonian, the integrals, etc., as well as their derivatives. Second, the formation of all intermediates also occurring in the first derivative of the RPA equations, which are independent of the magnetic field. Third, **B**-field derivatives of the intermediates of the first derivative, and lastly the nested Z-vector step to obtain the final intermediates for the NMR shieldings.

The most involved steps in terms of computational effort are the computation of the response function $\mathbf{X}_0(\mathrm{i}\tau)$ and the self-energy $\mathbf{\Sigma}(\mathrm{i}\tau)$ in the imaginary time domain, as well as their **B**-field derivatives. Here, $\mathbf{X}_0(\mathrm{i}\tau)$ is most efficiently computed according to, e.g., Ref. S1 by premultiplying the Green's functions with the three-center integrals and then using a matrix multiplication to multiply both third-order tensors. The same approach can be used for the **B**-field derivative of the response function. The self-energy is computed as explained in Ref. S2 and its SI. For the **B**-field derivative of the self-energy we use the same approach. Here, we want to note that for the matrix multiplications we use the high parallel performance of the MKL library for dense matrix algebra routines.

2 Gauge Invariance

Table S1: Testing the gauge origin independence at the RPA@HF level of theory using the def2-SVP and cc-pwCVTZ basis sets with the corresponding RI basis sets for the molecules in the Gauss benchmark set. For each basis set the NMR shifts are given in ppm for the initial geometry (reference) and after each atom has been translated by 5 Å(transl.) as well as the resulting absolute deviation (abs. err.).

		def2-SVP [ppm]			cc-pwCVTZ [ppm]		
molecule	element	transl.	reference	abs. err.	transl.	reference	abs. err.
AlF							
	Al	-4.1606	-4.1605	0.0001	-4.8933	-4.8936	0.0002
	F	3.7843	3.7823	0.0020	-2.5863	-2.5871	0.0008
C_2H_4							
	C	13.5843	13.5850	0.0007	8.0167	8.0169	0.0003
	C	13.5843	13.5850	0.0007	8.0172	8.0169	0.0003
	H	0.3400	0.3400	0.0000	0.1530	0.1499	0.0031
	H	0.3400	0.3400	0.0000	0.1466	0.1499	0.0033
	H	0.3400	0.3400	0.0000	0.1531	0.1499	0.0032
	H	0.3400	0.3400	0.0000	0.1468	0.1499	0.0031
C_3H_4							
	C	-0.8958	-0.8959	0.0001	-2.3976	-2.3762	0.0213
	C	16.5324	16.5323	0.0001	10.5089	10.5229	0.0140
	C	16.5324	16.5323	0.0001	10.5468	10.5229	0.0239
	H	0.7695	0.7695	0.0000	0.5412	0.5476	0.0064
	H	0.7695	0.7695	0.0000	0.5391	0.5476	0.0085
	H	0.1390	0.1390	0.0000	0.0055	0.0054	0.0000
	H	0.1390	0.1390	0.0000	0.0001	0.0054	0.0053
CH_2O							
	O	120.5025	120.5017	0.0008	82.7901	82.7902	0.0000
	C	21.1176	21.1176	0.0000	12.2381	12.2387	0.0006
	H	0.3273	0.3273	0.0000	0.1245	0.1186	0.0058
	H	0.3273	0.3273	0.0000	0.1126	0.1186	0.0060
CH_3F							
	C	0.6198	0.6197	0.0001	-1.3122	-1.3128	0.0007
	F	-9.1903	-9.1894	0.0009	-7.9269	-7.9254	0.0016
	H	0.0139	0.0139	0.0000	-0.1095	-0.1076	0.0019
	H	0.0139	0.0139	0.0000	-0.1051	-0.1076	0.0025
	H	0.0139	0.0139	0.0000	-0.1083	-0.1076	0.0007
CH_4							
	C	1.1768	1.1747	0.0021	1.3187	1.3182	0.0005
	H	0.0179	0.0180	0.0001	-0.0461	-0.0460	0.0001
	H	0.0180	0.0180	0.0000	-0.0460	-0.0460	0.0000
	H	0.0180	0.0180	0.0000	-0.0460	-0.0460	0.0000

	H	0.0180	0.0180	0.0001	-0.0459	-0.0460	0.0001
CO							
	C	34.8474	34.8478	0.0004	24.6474	24.6476	0.0002
	O	49.7149	49.7178	0.0028	33.9522	33.9530	0.0008
FCCH							
	C	4.5935	4.5934	0.0001	2.0948	2.0918	0.0030
	C	2.7262	2.7263	0.0001	-0.2682	-0.2672	0.0010
	H	0.3649	0.3649	0.0000	0.2173	0.2173	0.0000
	F	-0.1199	-0.1190	0.0009	-3.9647	-3.9823	0.0176
FCN							
	F	7.1241	7.1225	0.0016	-0.2682	-0.2703	0.0021
	C	8.2799	8.2794	0.0005	5.3903	5.3900	0.0003
	N	30.1391	30.1381	0.0010	20.9845	20.9848	0.0003
H_2C_2O							
	C	4.3011	4.3010	0.0001	2.2121	2.2113	0.0009
	C	15.1969	15.1970	0.0001	8.7411	8.7352	0.0059
	O	42.7184	42.7181	0.0003	26.3746	26.3681	0.0064
	H	0.4432	0.4432	0.0000	0.1693	0.1673	0.0021
	H	0.4432	0.4432	0.0000	0.1646	0.1673	0.0026
H_2O							
	O	6.1048	6.1066	0.0018	5.8646	5.8657	0.0011
	H	0.5146	0.5146	0.0000	0.4335	0.4339	0.0004
	H	0.5146	0.5146	0.0000	0.4333	0.4339	0.0006
H_2S							
	S	8.2477	8.2485	0.0009	8.7821	8.7865	0.0044
	H	0.5157	0.5157	0.0000	0.2848	0.2857	0.0009
	H	0.5157	0.5157	0.0000	0.2845	0.2857	0.0012
H_4C_2O							
	O	-11.4164	-11.4150	0.0014	-14.9307	-14.8794	0.0513
	C	0.2379	0.2380	0.0001	-1.7721	-1.7721	0.0000
	C	0.2381	0.2380	0.0000	-1.7677	-1.7721	0.0045
	H	-0.0084	-0.0084	0.0000	-0.1355	-0.1444	0.0088
	H	-0.0084	-0.0084	0.0000	-0.1488	-0.1444	0.0044
	H	-0.0084	-0.0084	0.0000	-0.1346	-0.1444	0.0098
	H	-0.0084	-0.0084	0.0000	-0.1479	-0.1444	0.0035
HCN							
	H	0.1919	0.1919	0.0000	0.0776	0.0776	0.0000
	C	15.7958	15.7957	0.0001	11.5072	11.5071	0.0000
	N	43.4703	43.4703	0.0000	32.1927	32.1927	0.0000
HCP							
	H	-0.0709	-0.0709	0.0000	-0.1727	-0.1727	0.0000
	C	26.8904	26.8920	0.0015	18.0367	18.0369	0.0002
	P	48.7256	48.7297	0.0041	32.5252	32.5260	0.0008

HF							
	H	0.8963	0.8964	0.0001	0.8973	0.8972	0.0001
	F	3.4654	3.4627	0.0027	3.0933	3.0962	0.0029
HFCO							
	O	59.6156	59.6138	0.0017	37.5707	37.5889	0.0182
	C	11.8853	11.8851	0.0002	6.0880	6.0736	0.0144
	F	2.8728	2.8736	0.0008	-7.2110	-7.2375	0.0266
	H	0.0653	0.0653	0.0000	-0.1022	-0.0882	0.0140
HOF							
	O	94.8495	94.8534	0.0039	73.5406	73.5422	0.0017
	H	1.9550	1.9549	0.0001	1.5882	1.5875	0.0007
	F	-66.9284	-66.9253	0.0031	-76.2030	-76.2082	0.0052
LiF							
	Li	-0.8679	-0.8679	0.0000	-0.8239	-0.8239	0.0000
	F	-12.5098	-12.5098	0.0001	-1.8842	-1.8845	0.0004
LiH							
	H	0.4265	0.4265	0.0000	0.3036	0.3036	0.0000
	Li	0.3786	0.3786	0.0000	-0.1106	-0.1107	0.0001
N_2							
	N	60.9736	60.9742	0.0005	46.4441	46.4434	0.0007
	N	60.9736	60.9742	0.0005	46.4441	46.4434	0.0007
N_2O							
	N	47.6472	47.6460	0.0011	37.0936	37.0939	0.0003
	N	47.6002	47.5990	0.0011	37.8976	37.8977	0.0001
	O	34.7642	34.7621	0.0021	22.7467	22.7465	0.0003
NH_3							
	N	3.8785	3.8787	0.0002	4.0256	4.0258	0.0002
	H	0.2181	0.2181	0.0000	0.1343	0.1341	0.0002
	H	0.2181	0.2181	0.0000	0.1344	0.1341	0.0003
	H	0.2180	0.2181	0.0000	0.1345	0.1341	0.0004
OCS							
	O	32.8266	32.8281	0.0015	19.9120	19.9142	0.0022
	C	25.1191	25.1194	0.0002	17.9478	17.9482	0.0004
	S	24.1941	24.1940	0.0001	9.8036	9.8036	0.0000
OF_2							
	O	68.5144	68.5128	0.0016	34.5995	34.6088	0.0093
	F	3.3360	3.3362	0.0002	-18.4908	-18.4840	0.0068
	F	3.3412	3.3362	0.0049	-18.5005	-18.4840	0.0165

3 Detailed Validation Results

In the following section detailed results for the Gauss[S3] and the Flaig[S4] benchmark set are presented. The order of the nuclei corresponds to the order given in the geometry files of the respective molecules obtained from the SI in the case of the Gauss[S3] benchmark set and from the download section of the Ochsenfeld group website[S5] in the case of the Flaig[S4] benchmark set. Shifts of nuclei which are not chemically equivalent are labeled appropriately for an unambiguous assignment. For smaller molecules the respective functional group, and if necessary the orientation, is given and for aromatics numbering according to the IUPAC nomenclature is chosen.

3.1 Detailed Validation Results: Gauss Benchmark Set

Table S2: Detailed results of the RPA NMR shifts for all molecules in the Gauss benchmark set[S3] at the RPA@HF/cc-pwCVTZ level of theory for the numerical reference implementation (reference) as well as the analytical implementation (result). All shifts and the resulting deviations are given in ppm.

molecule	element	result	reference	abs. err.
AlF				
	Al	-4.8936	-4.8950	0.0015
	F	-2.5871	-2.4875	0.0995
C_2H_4				
	C	8.0169	8.0204	0.0035
	C	8.0169	8.0204	0.0035
	H	0.1499	0.1503	0.0004
	H	0.1499	0.1503	0.0004
	H	0.1499	0.1503	0.0004
	H	0.1499	0.1503	0.0004
C_3H_4				
	C	-2.3762	-2.3758	0.0005
	C	10.5229	10.5281	0.0051
	C	10.5229	10.5281	0.0051
	H	0.5476	0.5463	0.0013
	H	0.5476	0.5463	0.0012
	H	0.0054	0.0058	0.0004
	H	0.0054	0.0058	0.0004
CH_2O				

	O	82.7902	82.6459	0.1443
	C	12.2387	12.2425	0.0038
	H	0.1186	0.1195	0.0009
	H	0.1186	0.1195	0.0008
CH_3F				
	C	-1.3128	-1.3089	0.0039
	F	-7.9254	-7.9222	0.0032
	H	-0.1076	-0.1071	0.0005
	H	-0.1076	-0.1071	0.0005
	H	-0.1076	-0.1071	0.0005
CH_4				
	C	1.3182	1.3200	0.0019
	H	-0.0460	-0.0460	0.0000
	H	-0.0460	-0.0460	0.0000
	H	-0.0460	-0.0460	0.0000
	H	-0.0460	-0.0460	0.0000
CO				
	C	24.6476	24.6488	0.0011
	O	33.9530	33.9399	0.0131
FCCH				
	C	2.0918	2.0954	0.0036
	C	-0.2672	-0.2641	0.0031
	H	0.2173	0.2161	0.0012
	F	-3.9823	-3.9386	0.0437
FCN				
	F	-0.2703	-0.2593	0.0110
	C	5.3900	5.3935	0.0034
	N	20.9848	20.9702	0.0146
H_2C_2O				
	C	2.2113	2.2086	0.0026
	C	8.7352	8.7477	0.0125
	O	26.3681	26.3467	0.0215
	H	0.1673	0.1676	0.0003
	H	0.1673	0.1675	0.0002
H_2O				
	O	5.8657	5.8665	0.0008
	H	0.4339	0.4339	0.0000
	H	0.4339	0.4339	0.0000
H_2S				
	S	8.7865	8.7782	0.0083
	H	0.2857	0.2858	0.0001
	H	0.2857	0.2858	0.0001
H_4C_2O				

	O	-14.8794	-14.8979	0.0185
	C	-1.7721	-1.7677	0.0044
	C	-1.7721	-1.7677	0.0044
	H	-0.1444	-0.1437	0.0006
	H	-0.1444	-0.1437	0.0006
	H	-0.1444	-0.1437	0.0006
	H	-0.1444	-0.1437	0.0006
HCN				
	H	0.0776	0.0761	0.0015
	C	11.5071	11.5120	0.0048
	N	32.1927	32.1900	0.0027
HCP				
	H	-0.1727	-0.1741	0.0014
	C	18.0369	18.0328	0.0041
	P	32.5260	32.4875	0.0385
HF				
	H	0.8972	0.8971	0.0001
	F	3.0962	3.0949	0.0013
HFCO				
	O	37.5889	37.5400	0.0489
	C	6.0736	6.0813	0.0077
	F	-7.2375	-7.2411	0.0036
	H	-0.0882	-0.0875	0.0007
HOF				
	O	73.5422	73.4006	0.1416
	H	1.5875	1.5873	0.0002
	F	-76.2082	-76.0488	0.1594
LiF				
	Li	-0.8239	-0.8231	0.0008
	F	-1.8845	-1.8240	0.0605
LiH				
	H	0.3036	0.3036	0.0000
	Li	-0.1107	-0.1096	0.0011
N_2				
	N	46.4434	46.4436	0.0002
	N	46.4434	46.4437	0.0003
N_2O				
	N	37.0939	37.0826	0.0113
	N	37.8977	37.8925	0.0052
	O	22.7465	22.7367	0.0097
NH_3				
	N	4.0258	4.0283	0.0025
	H	0.1341	0.1341	0.0000

	H	0.1341	0.1341	0.0000
	H	0.1341	0.1341	0.0000
OCS				
	O	19.9142	19.9108	0.0034
	C	17.9482	17.9512	0.0031
	S	9.8036	9.7461	0.0575
OF_2				
	O	34.6088	34.4193	0.1895
	F	-18.4840	-18.4269	0.0571
	F	-18.4840	-18.4266	0.0574

Table S3: Detailed results of the RPA NMR shifts for all molecules in the Gauss benchmark set[S3] at the RPA@PBE/cc-pwCVTZ level of theory for the numerical reference implementation (reference) as well as the analytical implementation (result). All shifts and the resulting deviations are given in ppm.

molecule	element	result	reference	abs. err.
AlF				
	Al	-12.5395	-12.5407	0.0012
	F	-25.8208	-25.8211	0.0003
C_2H_4				
	C	20.7298	20.7377	0.0079
	C	20.7298	20.7377	0.0079
	H	0.3384	0.3386	0.0002
	H	0.3384	0.3386	0.0002
	H	0.3384	0.3386	0.0002
	H	0.3384	0.3386	0.0002
C_3H_4				
	C	-2.9284	-2.9238	0.0046
	C	21.3029	21.3117	0.0088
	C	21.3029	21.3117	0.0088
	H	0.9359	0.9361	0.0002
	H	0.9359	0.9361	0.0002
	H	-0.1389	-0.1389	0.0000
	H	-0.1389	-0.1389	0.0000
CH_2O				
	O	220.4304	219.8347	0.5958
	C	31.8927	31.8966	0.0039
	H	0.0714	0.0715	0.0001
	H	0.0714	0.0715	0.0001
CH_3F				
	C	-1.9967	-1.9966	0.0001
	F	-20.7658	-20.7645	0.0013
	H	-0.4794	-0.4794	0.0000
	H	-0.4794	-0.4794	0.0000
	H	-0.4794	-0.4794	0.0000
CH_4				
	C	1.8436	1.8456	0.0020
	H	-0.0590	-0.0590	0.0000
	H	-0.0590	-0.0590	0.0000
	H	-0.0590	-0.0590	0.0000
	H	-0.0590	-0.0590	0.0000
CO				
	C	52.3831	52.3850	0.0019
	O	71.6005	71.5951	0.0055

FCCH				
	C	8.9862	8.9872	0.0010
	C	5.0325	5.0352	0.0027
	H	0.4341	0.4343	0.0002
	F	-5.5674	-5.5578	0.0096
FCN				
	F	-9.4155	-9.4147	0.0008
	C	18.3118	18.3125	0.0006
	N	50.2996	50.2937	0.0058
H_2C_2O				
	C	3.7803	3.7816	0.0013
	C	26.7004	26.7042	0.0038
	O	61.5271	61.4990	0.0281
	H	0.2732	0.2732	0.0001
	H	0.2732	0.2732	0.0001
H_2O				
	O	4.0511	4.0525	0.0014
	H	0.8537	0.8537	0.0000
	H	0.8537	0.8537	0.0000
H_2S				
	S	10.5790	10.5488	0.0301
	H	0.4957	0.4957	0.0000
	H	0.4957	0.4957	0.0000
H_4C_2O				
	O	-19.6393	-19.6391	0.0002
	C	-2.9245	-2.9235	0.0009
	C	-2.9245	-2.9236	0.0009
	H	-0.5762	-0.5762	0.0000
	H	-0.5762	-0.5762	0.0000
	H	-0.5762	-0.5762	0.0000
	H	-0.5762	-0.5762	0.0000
HCN				
	H	-0.1525	-0.1526	0.0000
	C	27.2219	27.2264	0.0045
	N	65.8816	65.8822	0.0006
HCP				
	H	-0.4788	-0.4788	0.0000
	C	43.6045	43.6065	0.0019
	P	100.7949	100.7578	0.0372
HF				
	H	1.7421	1.7421	0.0000
	F	0.5872	0.5846	0.0026
HFCO				

	O	100.6239	100.5588	0.0651
	C	19.8154	19.8164	0.0010
	F	-29.0573	-29.0556	0.0017
	H	-0.3361	-0.3361	0.0000
HOF				
	O	121.8165	121.2863	0.5303
	H	2.2540	2.2541	0.0001
	F	-71.9220	-72.1018	0.1798
LiF				
	Li	-2.0030	-2.0031	0.0000
	F	-15.1874	-15.1811	0.0063
LiH				
	H	-0.0427	-0.0428	0.0000
	Li	1.3533	1.3550	0.0018
N_2				
	N	80.3644	80.3690	0.0046
	N	80.3644	80.3690	0.0046
N_2O				
	N	59.5667	59.5670	0.0003
	N	66.8380	66.8419	0.0038
	O	38.3326	38.3284	0.0042
NH_3				
	N	3.6714	3.6733	0.0019
	H	0.2822	0.2822	0.0000
	H	0.2822	0.2822	0.0000
	H	0.2822	0.2822	0.0000
OCS				
	O	38.5240	38.5158	0.0082
	C	41.5165	41.5165	0.0000
	S	13.8466	13.8308	0.0158
OF_2				
	O	55.7934	54.9134	0.8800
	F	-28.0742	-28.2949	0.2206
	F	-28.0742	-28.2949	0.2206

3.2 Detailed Validation Results: Flaig Benchmark Set

Table S4: Detailed results of the RPA NMR shifts for all molecules in the Flaig benchmark set[S4] at the RPA@HF/cc-pwCVDZ level of theory for the numerical reference implementation (reference) as well as the analytical implementation (result). All shifts and the resulting deviations are given in ppm.

molecule	element	result	reference	abs. err.
Acetylene (C_2H_2)				
	H	0.0861	0.0859	0.0002
	C	8.4582	8.4780	0.0198
	C	8.4582	8.4781	0.0198
	H	0.0861	0.0859	0.0002
Ethylene (C_2H_4)				
	H	0.3076	0.3084	0.0009
	H	0.3076	0.3084	0.0009
	C	13.4627	13.4998	0.0371
	H	0.3076	0.3084	0.0009
	C	13.4626	13.4998	0.0372
	H	0.3076	0.3084	0.0009
Ethane (C_2H_6)				
	H	-0.0524	-0.0522	0.0001
	H	-0.0524	-0.0522	0.0001
	H	-0.0524	-0.0522	0.0001
	C	1.4695	1.4784	0.0089
	H	-0.0524	-0.0522	0.0001
	H	-0.0524	-0.0523	0.0001
	C	1.4694	1.4784	0.0090
	H	-0.0524	-0.0523	0.0001
Benzene (C_6H_6)				
	H	0.2580	0.2591	0.0011
	H	0.2580	0.2591	0.0011
	C	11.9683	12.0091	0.0409
	H	0.2580	0.2591	0.0011
	C	11.9683	12.0092	0.0410
	H	0.2580	0.2591	0.0011
	C	11.9683	12.0092	0.0410
	H	0.2580	0.2591	0.0011
	C	11.9683	12.0092	0.0410
	C	11.9683	12.0092	0.0410
	C	11.9683	12.0091	0.0409
	H	0.2580	0.2591	0.0011
Tetrachloromethane (CCl_4)				
	C	-0.9163	-0.9147	0.0016
	Cl	-10.1405	-10.1198	0.0207

	Cl	-10.1405	-10.1198	0.0207
	Cl	-10.1405	-10.1198	0.0207
	Cl	-10.1405	-10.1198	0.0207
Tetrafluoromethane (CF_4)				
	F	1.3975	1.4164	0.0188
	F	1.3975	1.4166	0.0191
	F	1.3975	1.4166	0.0191
	C	-5.6193	-5.6128	0.0064
	F	1.3975	1.4165	0.0189
Propadiene (CH_2CCH_2)				
	H	0.1796	0.1802	0.0006
	H	0.1796	0.1802	0.0006
	$\underline{C}H_2$	6.2350	6.2590	0.0239
	C=$\underline{C}$=C	20.6112	20.6644	0.0532
	H	0.1796	0.1802	0.0006
	$\underline{C}H_2$	6.2351	6.2589	0.0239
	H	0.1796	0.1802	0.0006
Acetaldehyde (CH_3CHO)				
	O	77.9944	78.1373	0.1429
	C$\underline{H}$O	0.1444	0.1452	0.0008
	$\underline{C}$HO	20.9302	20.9626	0.0324
	C$\underline{H}_3$, out of CCO plane	0.0217	0.0219	0.0002
	C$\underline{H}_3$, out of CCO plane	0.0217	0.0219	0.0002
	$\underline{C}H_3$	2.4229	2.4315	0.0086
	C$\underline{H}_3$, in CCO plane	0.2397	0.2399	0.0002
Chloroform (CH_3Cl)				
	C	2.9458	2.9462	0.0003
	Cl	-21.6412	-21.6328	0.0084
	H	0.1091	0.1091	0.0000
	H	0.1091	0.1091	0.0000
	H	0.1091	0.1091	0.0000
Acetonitrile (CH_3CN)				
	N	42.4969	42.5614	0.0645
	$\underline{C}$N	14.4076	14.4328	0.0252
	H	0.0640	0.0641	0.0001
	H	0.0655	0.0655	0.0001
	$\underline{C}H_3$	0.9050	0.9119	0.0069
	H	0.0653	0.0654	0.0001
Acetone (CH_3COCH_3)				
	H, in CCC plane	0.2100	0.2101	0.0002
	H, out of CCC plane	-0.0359	-0.0357	0.0002
	H, out of CCC plane	-0.0359	-0.0354	0.0005
	$\underline{C}H_3$	2.2390	2.2466	0.0075
	O	59.2885	59.4418	0.1533

	$\underline{C}$O	21.0772	21.1097	0.0325
	H, out of CCC plane	-0.0359	0.2102	0.2461
	H, out of CCC plane	-0.0359	-0.0357	0.0002
	$\underline{C}H_3$	2.2390	2.2468	0.0078
	H, in CCC plane	0.2100	-0.0360	0.2460
Fluoromethane (CH_3F)				
	F	-9.8763	-9.8764	0.0001
	H	-0.0009	-0.0009	0.0001
	H	-0.0009	-0.0009	0.0001
	C	1.0363	1.0428	0.0065
	H	-0.0009	-0.0008	0.0001
Methylamine (CH_3NH_2)				
	N$\underline{H}_2$	0.0521	0.0521	0.0001
	N$\underline{H}_2$	0.0521	0.0521	0.0001
	N	2.1892	2.2004	0.0112
	C$\underline{H}_3$, antiperiplanar to lone pair	-0.1745	-0.0625	0.1120
	C$\underline{H}_3$, gauche to lone pair	-0.0626	-0.0625	0.0001
	C	0.7933	0.8019	0.0086
	C$\underline{H}_3$, gauche to lone pair	-0.0626	-0.1744	0.1118
Dimethyl ether (CH_3OCH_3)				
	H, in COC plane	-0.0900	-0.0898	0.0001
	H, out of COC plane	-0.1058	-0.1057	0.0001
	H, out of COC plane	-0.1058	-0.1057	0.0001
	C	0.2035	0.2118	0.0083
	O	-6.7843	-6.7804	0.0039
	H, out of COC plane	-0.1058	-0.1057	0.0001
	H, out of COC plane	-0.1058	-0.1057	0.0001
	C	0.2035	0.2118	0.0082
	H, in COC plane	-0.0900	-0.0898	0.0001
Methanol (CH_3OH)				
	O$\underline{H}$	0.3536	0.3535	0.0001
	O	-0.8619	-0.8536	0.0082
	C$\underline{H}_3$, gauche to OH	-0.1264	-0.0263	0.1001
	C$\underline{H}_3$, gauche to OH	-0.1264	-0.1263	0.0001
	C	0.4881	0.4958	0.0077
	C$\underline{H}_3$, antiperiplanar to OH	-0.0264	-0.1263	0.0999
Methylphosphine (CH_3PH_2)				
	C	1.6790	1.6800	0.0011
	P	6.7592	6.7706	0.0114
	P$\underline{H}_2$	0.1609	0.1609	0.0001
	P$\underline{H}_2$	0.1609	0.1609	0.0001
	C$\underline{H}_3$, gauche to lone pair	-0.0006	-0.0006	0.0000
	C$\underline{H}_3$, gauche to lone pair	-0.0006	-0.0006	0.0000
	C$\underline{H}_3$, antiperiplanar to lone pair	-0.0018	-0.0017	0.0000

Methanethiol (CH_3SH)				
	C	1.3876	1.3884	0.0008
	S	4.3638	4.3698	0.0060
	S$\underline{H}$	0.3022	0.3022	0.0000
	C$\underline{H}_3$, antiperiplanar to SH	0.0278	0.0278	0.0000
	C$\underline{H}_3$, gauche to SH	0.0002	0.0003	0.0000
	C$\underline{H}_3$, gauche to SH	0.0002	0.0003	0.0000
Methane (CH_4)				
	H	0.0182	0.0184	0.0002
	H	0.0182	0.0184	0.0002
	H	0.0182	0.0184	0.0002
	C	1.9054	1.9133	0.0079
	H	0.0182	0.0184	0.0002
Carbon dioxide (CO_2)				
	O	19.3097	19.3454	0.0357
	C	13.4738	13.4891	0.0152
	O	19.3097	19.3453	0.0356
Carbon monoxide (CO)				
	O	47.7924	47.8807	0.0883
	C	35.0061	35.0445	0.0384
Furan (C_4H_4O)				
	3-H	0.2051	0.2057	0.0005
	2-H	0.2082	0.2087	0.0005
	3C	9.5302	9.5488	0.0185
	4-H	0.2051	0.2057	0.0005
	2C	12.4641	12.4850	0.0209
	4C	9.5302	9.5488	0.0186
	1O	10.3533	10.4096	0.0562
	5C	12.4642	12.4851	0.0209
	5-H	0.2082	0.2087	0.0005
Glycine (NH_2CH_2COOH)				
	N$\underline{H}_2$	0.0221	0.0222	0.0001
	N$\underline{H}_2$	0.0592	0.0593	0.0001
	N	1.5762	1.5853	0.0091
	C$\underline{H}_2$	0.0746	0.0747	0.0001
	C$\underline{H}_2$	0.0224	0.0224	0.0000
	$\underline{C}H_2$	1.2177	1.2256	0.0079
	C=$\underline{O}$	37.2847	37.3778	0.0931
	$\underline{C}$OOH	14.9177	14.9401	0.0224
	$\underline{O}$H	9.7918	9.8330	0.0412
	O$\underline{H}$	0.3915	0.3921	0.0006
Formaldehyde (H_2CO)				
	O	111.0888	111.1752	0.0864
	H	0.2826	0.2836	0.0009

	C	21.1961	21.2295	0.0333
	H	0.2826	0.2836	0.0010
Hydrogen cyanide (HCN)				
	H	0.0601	0.0598	0.0003
	C	16.3948	16.4221	0.0273
	N	42.1806	42.2535	0.0729
Formamide ($HCONH_2$)				
	N$\underline{H}_2$	0.3538	0.3543	0.0005
	N$\underline{H}_2$	0.3662	0.3667	0.0005
	N	7.2581	7.2796	0.0215
	C$\underline{H}$O	0.0740	0.0743	0.0003
	C	16.7315	16.7528	0.0213
	O	34.4261	34.5238	0.0976
Formic acid (HCOOH)				
	O$\underline{H}$	0.5611	0.5616	0.0005
	$\underline{O}$H	9.1381	9.1754	0.0373
	C$\underline{H}$	0.1191	0.1194	0.0003
	C	14.8579	14.8790	0.0211
	C=$\underline{O}$	41.7052	41.7970	0.0918
Imidazole ($C_3H_4N_2$)				
	3-H	0.1194	0.1202	0.0008
	2-H	0.4273	0.4280	0.0007
	3N	10.7744	10.8151	0.0406
	4-H	0.3158	0.3165	0.0007
	2C	17.1388	17.1675	0.0287
	4C	10.9611	10.9867	0.0256
	1N	35.5496	35.6308	0.0813
	5C	12.2712	12.2994	0.0282
	5-H	0.3522	0.3530	0.0008
Pyridine (C_5H_5N)				
	2-H	0.3683	0.3695	0.0012
	1N	42.2988	42.4102	0.1114
	6-H	0.3683	0.3695	0.0012
	2C	15.5825	15.6170	0.0345
	3-H	0.1291	0.1297	0.0006
	6C	15.5825	15.6170	0.0345
	5-H	0.1291	0.1297	0.0006
	3C	7.3790	7.4037	0.0248
	5C	7.3790	7.4037	0.0248
	4C	15.7400	15.7658	0.0259
	4-H	0.3905	0.3912	0.0007
Pyrimidine ($C_4H_4N_2$)				
	6-H	0.3878	0.3888	0.0010
	1N	24.1426	24.2371	0.0944

	2-H	0.2580	0.2592	0.0012
	6C	18.0969	18.1322	0.0353
	5-H	0.0596	0.0604	0.0008
	1C	16.0559	16.0916	0.0357
	5C	4.4116	4.4397	0.0281
	3N	24.1424	24.2367	0.0943
	4C	18.0960	18.1311	0.0351
	4-H	0.3875	0.3885	0.0010
Tetramethylsilane ($Si(CH_3)_4$)				
	H	-0.0658	-0.0658	0.0000
	H	-0.0658	-0.0658	0.0000
	H	-0.0658	-0.0658	0.0000
	H	-0.0658	-0.0658	0.0000
	H	-0.0658	-0.0658	0.0000
	H	-0.0658	-0.0658	0.0000
	H	-0.0658	-0.0658	0.0000
	H	-0.0658	-0.0658	0.0000
	H	-0.0658	-0.0658	0.0000
	C	2.0029	2.0043	0.0014
	C	2.0029	2.0043	0.0014
	C	2.0029	2.0043	0.0014
	Si	-11.3421	-11.3278	0.0144
	H	-0.0658	-0.0658	0.0000
	H	-0.0658	-0.0658	0.0000
	C	2.0029	2.0043	0.0014
	H	-0.0658	-0.0658	0.0000

Table S5: Detailed results of the RPA NMR shifts for all molecules in the Flaig benchmark set[S4] at the RPA@PBE/cc-pwCVDZ level of theory for the numerical reference implementation (reference) as well as the analytical implementation (result). All shifts and the resulting deviations are given in ppm.

molecule	element	result	reference	abs. err.
Acetylene (C_2H_2)				
	H	0.0787	0.0784	0.0003
	C	19.1544	19.1837	0.0292
	C	19.1544	19.1837	0.0292
	H	0.0787	0.0784	0.0003
Ethylene (C_2H_4)				
	H	0.5381	0.5391	0.0010
	H	0.5381	0.5391	0.0010
	C	27.1906	27.2432	0.0526
	H	0.5451	0.5461	0.0010
	C	27.2817	27.3347	0.0530
	H	0.5451	0.5461	0.0010
Ethane (C_2H_6)				
	H	-0.1615	-0.1614	0.0001
	H	-0.1615	-0.1614	0.0001
	H	-0.1615	-0.1614	0.0001
	C	1.6414	1.6559	0.0145
	H	-0.1618	-0.1616	0.0001
	H	-0.1618	-0.1616	0.0001
	C	1.6159	1.6304	0.0146
	H	-0.1618	-0.1616	0.0001
Benzene (C_6H_6)				
	H	0.4910	0.4922	0.0012
	H	0.4910	0.4922	0.0013
	C	24.1266	24.1809	0.0542
	H	0.4910	0.4922	0.0013
	C	24.1267	24.1809	0.0543
	H	0.4910	0.4922	0.0013
	C	24.1267	24.1809	0.0543
	H	0.4910	0.4922	0.0013
	C	24.1267	24.1809	0.0543
	C	24.1267	24.1809	0.0543
	C	24.1266	24.1809	0.0542
	H	0.4910	0.4922	0.0013
Tetrachloromethane (CCl_4)				
	C	7.7902	7.7945	0.0043
	Cl	-36.5447	-36.5615	0.0168
	Cl	-36.5447	-36.5615	0.0168
	Cl	-36.5447	-36.5615	0.0168

	Cl	-36.5447	-36.5615	0.0168
Tetrafluoromethane (CF_4)				
	F	-6.0114	-5.9824	0.0290
	F	-6.0116	-5.9817	0.0299
	F	-6.0116	-5.9817	0.0299
	C	-4.0609	-4.0475	0.0134
	F	-6.0117	-5.9821	0.0296
Propadiene (CH_2CCH_2)				
	H	0.2550	0.2557	0.0007
	H	0.2765	0.2772	0.0007
	$\underline{C}H_2$	14.4060	14.4407	0.0347
	C=$\underline{C}$=C	41.5436	41.6158	0.0722
	H	0.2658	0.2664	0.0007
	$\underline{C}H_2$	14.4060	14.4399	0.0339
	H	0.2658	0.2664	0.0007
Acetaldehyde (CH_3CHO)				
	O	205.4081	205.4133	0.0052
	C$\underline{H}$O	0.0321	0.0334	0.0013
	$\underline{C}$HO	41.5548	41.6041	0.0494
	C$\underline{H}_3$, out of CCO plane	-0.0362	-0.0359	0.0003
	C$\underline{H}_3$, out of CCO plane	-0.0362	-0.0359	0.0003
	$\underline{C}H_3$	4.5204	4.5366	0.0162
	C$\underline{H}_3$, in CCO plane	0.4048	0.4052	0.0003
Chloroform (CH_3Cl)				
	C	4.2965	4.2981	0.0016
	Cl	-41.3884	-41.3727	0.0157
	H	-0.0046	-0.0045	0.0000
	H	-0.0046	-0.0045	0.0000
	H	-0.0046	-0.0045	0.0000
Acetonitrile (CH_3CN)				
	N	71.8026	71.8871	0.0845
	$\underline{C}$N	30.2404	30.2746	0.0342
	H	-0.0142	-0.0141	0.0001
	H	-0.0118	-0.0117	0.0001
	$\underline{C}H_3$	0.5402	0.5514	0.0112
	H	-0.0120	-0.0119	0.0001
Acetone (CH_3COCH_3)				
	H, in CCC plane	0.3530	0.3532	0.0002
	H, out of CCC plane	-0.2379	-0.2377	0.0003
	H, out of CCC plane	-0.2379	-0.2377	0.0003
	$\underline{C}H_3$	4.5256	4.5392	0.0136
	O	174.4594	174.5093	0.0499
	$\underline{C}$O	41.1737	41.2223	0.0486
	H, out of CCC plane	-0.2479	-0.2476	0.0004

	H, out of CCC plane	-0.2479	-0.2476	0.0004
	$\underline{C}H_3$	4.4580	4.4728	0.0148
	H, in CCC plane	0.3383	0.3386	0.0003
Fluoromethane (CH_3F)				
	F	-26.8766	-26.8692	0.0074
	H	-0.3595	-0.3594	0.0001
	H	-0.3595	-0.3594	0.0001
	C	0.9788	0.9902	0.0114
	H	-0.3595	-0.3594	0.0001
Methylamine (CH_3NH_2)				
	$N\underline{H}_2$	-0.0521	-0.0521	0.0000
	$N\underline{H}_2$	-0.0521	-0.0521	0.0000
	N	0.4456	0.4641	0.0186
	$C\underline{H}_3$, antiperiplanar to lone pair	-0.7037	-0.7036	0.0001
	$C\underline{H}_3$, gauche to lone pair	-0.2410	-0.2408	0.0001
	C	0.6955	0.7109	0.0154
	$C\underline{H}_3$, gauche to lone pair	-0.2410	-0.2408	0.0001
Dimethyl ether (CH_3OCH_3)				
	H, in COC plane	-0.3361	-0.3360	0.0002
	H, out of COC plane	-0.4440	-0.4439	0.0001
	H, out of COC plane	-0.4440	-0.4439	0.0001
	C	0.6376	0.6523	0.0147
	O	-14.9422	-14.9251	0.0171
	H, out of COC plane	-0.4440	-0.4439	0.0001
	H, out of COC plane	-0.4440	-0.4439	0.0001
	C	0.6373	0.6523	0.0149
	H, in COC plane	-0.3361	-0.3360	0.0002
Methanol (CH_3OH)				
	$O\underline{H}$	0.3781	0.3777	0.0003
	O	-7.8372	-7.8206	0.0165
	$C\underline{H}_3$, gauche to OH	-0.6123	-0.6121	0.0001
	$C\underline{H}_3$, gauche to OH	-0.6123	-0.6121	0.0001
	C	0.1934	0.2073	0.0139
	$C\underline{H}_3$, antiperiplanar to OH	-0.2089	-0.2088	0.0001
Methylphosphine (CH_3PH_2)				
	C	1.0495	1.0519	0.0024
	P	14.2332	14.2472	0.0140
	$P\underline{H}_2$	0.0468	0.0468	0.0001
	$P\underline{H}_2$	0.0468	0.0468	0.0001
	$C\underline{H}_3$, gauche to lone pair	-0.1364	-0.1363	0.0000
	$C\underline{H}_3$, gauche to lone pair	-0.1364	-0.1363	0.0000
	$C\underline{H}_3$, antiperiplanar to lone pair	-0.1528	-0.1528	0.0001
Methanethiol (CH_3SH)				
	C	0.9706	0.9728	0.0022

	S	4.3320	4.3284	0.0036
	S$\underline{H}$	0.3438	0.3439	0.0001
	C$\underline{H}_3$, antiperiplanar to SH	-0.0761	-0.0761	0.0000
	C$\underline{H}_3$, gauche to SH	-0.1995	-0.1995	0.0000
	C$\underline{H}_3$, gauche to SH	-0.1995	-0.1995	0.0000
Methane (CH_4)				
	H	0.0014	0.0016	0.0002
	H	0.0014	0.0016	0.0002
	H	0.0014	0.0016	0.0002
	C	2.2800	2.2920	0.0120
	H	0.0014	0.0016	0.0002
Carbon dioxide (CO_2)				
	O	29.8121	29.8546	0.0425
	C	27.1710	27.1911	0.0201
	O	29.8121	29.8546	0.0425
Carbon monoxide (CO)				
	O	87.4544	87.5640	0.1096
	C	63.0853	63.1363	0.0509
Furan (C_4H_4O)				
	3-H	0.4369	0.4375	0.0006
	2-H	0.4133	0.4139	0.0006
	3C	20.4635	20.4898	0.0263
	4-H	0.4369	0.4375	0.0006
	2C	25.2926	25.3221	0.0296
	4C	20.4633	20.4898	0.0265
	1O	41.2453	41.3227	0.0774
	5C	25.2923	25.3221	0.0299
	5-H	0.4133	0.4139	0.0006
Glycine (NH_2CH_2COOH)				
	N$\underline{H}_2$	-0.3357	-0.3356	0.0001
	N$\underline{H}_2$	-0.1692	-0.1691	0.0001
	N	-2.9521	-2.9364	0.0158
	C$\underline{H}_2$	-0.1440	-0.1439	0.0001
	C$\underline{H}_2$	-0.1341	-0.1341	0.0000
	$\underline{C}H_2$	3.1432	3.1575	0.0143
	C=$\underline{O}$	107.4834	107.5693	0.0859
	$\underline{C}$OOH	32.4836	32.5163	0.0328
	$\underline{O}$H	13.1910	13.2577	0.0666
	O$\underline{H}$	0.3283	0.3291	0.0008
Formaldehyde (H_2CO)				
	O	270.1876	269.8305	0.3571
	H	0.4016	0.4033	0.0017
	C	43.2373	43.2921	0.0548
	H	0.4018	0.4035	0.0017

Hydrogen cyanide (HCN)				
	H	-0.1398	-0.1402	0.0004
	C	32.4556	32.4908	0.0352
	N	77.7749	77.8627	0.0878
Formamide ($HCONH_2$)				
	N$\underline{H}_2$	0.5833	0.5839	0.0006
	N$\underline{H}_2$	0.4932	0.4939	0.0006
	N	13.5060	13.5393	0.0334
	C$\underline{H}$O	0.0313	0.0317	0.0005
	C	37.0433	37.0737	0.0304
	O	106.7358	106.8051	0.0692
Formic acid (HCOOH)				
	O$\underline{H}$	0.7453	0.7460	0.0007
	$\underline{O}$H	8.1066	8.1726	0.0660
	C$\underline{H}$	0.1891	0.1895	0.0004
	C	34.6067	34.6384	0.0317
	C=$\underline{O}$	112.0754	112.1526	0.0772
Imidazole ($C_3H_4N_2$)				
	3-H	0.4304	0.4314	0.0010
	2-H	0.6165	0.6173	0.0008
	3N	29.9086	29.9642	0.0556
	4-H	0.4904	0.4912	0.0008
	2C	28.2279	28.2661	0.0382
	4C	23.6096	23.6444	0.0349
	1N	73.2228	73.3188	0.0960
	5C	24.7178	24.7582	0.0404
	5-H	0.6076	0.6085	0.0010
Pyridine (C_5H_5N)				
	2-H	0.4742	0.4757	0.0015
	1N	85.5818	85.7092	0.1273
	6-H	0.4742	0.4757	0.0015
	2C	27.1182	27.1686	0.0504
	3-H	0.4988	0.4998	0.0010
	6C	27.1182	27.1687	0.0505
	5-H	0.4988	0.4998	0.0010
	3C	20.3647	20.4059	0.0412
	5C	20.3647	20.4059	0.0412
	4C	26.3408	26.3839	0.0431
	4-H	0.5778	0.5787	0.0010
Pyrimidine ($C_4H_4N_2$)				
	6-H	0.5046	0.5060	0.0014
	1N	70.4828	70.6091	0.1263
	2-H	0.2864	0.2881	0.0017
	6C	29.3256	29.3789	0.0533
	5-H	0.5507	0.5516	0.0009

	1C	27.3475	27.4033	0.0558
	5C	17.7443	17.7867	0.0424
	3N	70.4820	70.6095	0.1275
	4C	29.3232	29.3762	0.0530
	4-H	0.5041	0.5055	0.0013
Tetramethylsilane ($Si(CH_3)_4$)				
	H	-0.2583	-0.2582	0.0001
	H	-0.2583	-0.2582	0.0000
	H	-0.2583	-0.2582	0.0000
	H	-0.2583	-0.2582	0.0000
	H	-0.2583	-0.2582	0.0001
	H	-0.2583	-0.2582	0.0000
	H	-0.2582	-0.2582	0.0000
	H	-0.2582	-0.2582	0.0000
	H	-0.2582	-0.2582	0.0000
	C	1.6427	1.6451	0.0024
	C	1.6426	1.6452	0.0026
	C	1.6420	1.6452	0.0032
	Si	-13.0176	-12.9900	0.0275
	H	-0.2583	-0.2582	0.0000
	H	-0.2583	-0.2582	0.0001
	C	1.6426	1.6452	0.0026
	H	-0.2583	-0.2582	0.0001

3.3 Detailed Validation Results: Summary For All Nuclei

Table S6: Comparison of MADs in ppm of the analytical to the numerical isotropic NMR shifts for all nuclei in the Gauss benchmark set[S3] at the RPA@HF/cc-pwCVTZ and RPA@PBE/cc-pwCVTZ level of theory. Additionally, the number of occurrences $N_{\text{nuc}}^{\text{test}}$ of a given element within the benchmark set is given.

reference	^{1}H	^{7}Li	^{13}C	^{15}N	^{17}O	^{19}F	^{27}Al	^{31}P	^{33}S
$N_{\text{nuc}}^{\text{test}}$	37	2	20	8	15	10	1	2	3
HF	0.0005	0.0009	0.0041	0.0053	0.0591	0.0497	0.0015	0.0385	0.0329
PBE	0.0001	0.0009	0.0032	0.0031	0.2119	0.0644	0.0012	0.0372	0.0230

Table S7: Comparison of MADs in ppm of the analytical to the numerical isotropic NMR shifts for all nuclei in the Flaig benchmark set[S4] at the RPA@HF/cc-pwCVDZ and RPA@PBE/cc-pwCVDZ level of theory. Additionally, the number of occurrences $N_{\text{nuc}}^{\text{test}}$ of a given element within the benchmark set is given.

reference	^{1}H	^{13}C	^{15}N	^{17}O	^{19}F	^{29}Si	^{31}P	^{33}S	^{35}Cl
$N_{\text{nuc}}^{\text{test}}$	111	61	10	14	5	1	1	1	5
HF	0.0084	0.0208	0.0601	0.0694	0.0152	0.0144	0.0114	0.0060	0.0183
PBE	0.0004	0.0305	0.0773	0.0773	0.0252	0.0275	0.0140	0.0036	0.0166

4 Detailed Results for the Convergence of the Minimax Grid

Table S8: Detailed results of the RPA NMR shift convergence for all nuclei in the Gauss benchmark set[S3] with the number of minimax integration points N_g. All values are given as MADs in ppm in comparison to the results obtained with $N_g = 20$ at the RPA@HF level of theory using the cc-pwCVTZ/cc-pwCVTZ-RI basis sets.

N_g	^{1}H	^{7}Li	^{13}C	^{15}N	^{17}O	^{19}F	^{27}Al	^{31}P	^{33}S
10	0.0001	0.0003	0.0062	0.0175	0.0320	0.0097	0.0108	0.0366	0.0166
11	0.0001	0.0002	0.0050	0.0140	0.0257	0.0077	0.0075	0.0297	0.0130
12	0.0001	0.0002	0.0041	0.0114	0.0207	0.0061	0.0059	0.0244	0.0103
13	0.0001	0.0001	0.0036	0.0091	0.0173	0.0049	0.0049	0.0190	0.0084
14	0.0000	0.0001	0.0026	0.0070	0.0131	0.0042	0.0040	0.0156	0.0066
15	0.0000	0.0000	0.0024	0.0054	0.0107	0.0031	0.0029	0.0114	0.0053
16	0.0000	0.0000	0.0015	0.0039	0.0075	0.0023	0.0021	0.0088	0.0039
17	0.0000	0.0000	0.0013	0.0026	0.0053	0.0039	0.0015	0.0058	0.0027
18	0.0000	0.0000	0.0009	0.0014	0.0032	0.0034	0.0010	0.0039	0.0015
19	0.0000	0.0000	0.0004	0.0007	0.0015	0.0008	0.0005	0.0022	0.0006
20	–	–	–	–	–	–	–	–	–

References

(S1) Graf, D.; Beuerle, M.; Schurkus, H. F.; Luenser, A.; Savasci, G.; Ochsenfeld, C. Accurate and Efficient Parallel Implementation of an Effective Linear-Scaling Direct Random Phase Approximation Method. *J. Chem. Theory Comput.* **2018**, *14*, 2505–2515.

(S2) Beuerle, M.; Ochsenfeld, C. Low-scaling analytical gradients for the direct random phase approximation using an atomic orbital formalism. *J. Chem. Phys.* **2018**, *149*, 244111.

(S3) Teale, A. M.; Lutnæs, O. B.; Helgaker, T.; Tozer, D. J.; Gauss, J. Benchmarking density-functional theory calculations of NMR shielding constants and spin–rotation constants using accurate coupled-cluster calculations. *J. Chem. Phys.* **2013**, *138*, 024111.

(S4) Flaig, D.; Maurer, M.; Hanni, M.; Braunger, K.; Kick, L.; Thubauville, M.; Ochsenfeld, C. Benchmarking hydrogen and carbon NMR chemical shifts at HF, DFT, and MP2 levels. *J. Chem. Theory Comp.* **2014**, *10*, 572–578.

(S5) `https://www.cup.uni-muenchen.de/pc/ochsenfeld/download/`.

3.4 Publication IV: Low-Scaling, Efficient and Memory Optimized Computation of Nuclear Magnetic Resonance Shieldings within the Random Phase Approximation Using Cholesky-Decomposed Densities and an Attenuated Coulomb Metric

V. Drontschenko, C. Ochsenfeld
J. Phys. Chem. A, **128**, 7950 (2024).

Abstract

An efficient method for the computation of nuclear magnetic resonance (NMR) shielding tensors within the random phase approximation (RPA) is presented based on our recently introduced resolution-of-the-identity (RI) atomic orbital RPA NMR method [Drontschenko, V. et al. *J. Chem. Theory Comput.* **2023**, *19*, 7542–7554] utilizing Cholesky decomposed density type matrices and employing an attenuated Coulomb RI metric. The introduced sparsity is efficiently exploited using sparse matrix algebra. This allows for an efficient and low-scaling computation of RPA NMR shielding tensors. Furthermore, we introduce a batching method for the computation of memory demanding intermediates that accounts for their sparsity. This extends the applicability of our method to even larger systems that would have been out of reach before, such as, e.g., a DNA strand with 260 atoms and 3408 atomic orbital basis functions.

THE JOURNAL OF PHYSICAL CHEMISTRY A
A JOURNAL OF THE AMERICAN CHEMICAL SOCIETY

pubs.acs.org/JPCA
Article

Low-Scaling, Efficient and Memory Optimized Computation of Nuclear Magnetic Resonance Shieldings within the Random Phase Approximation Using Cholesky-Decomposed Densities and an Attenuated Coulomb Metric

Published as part of The Journal of Physical Chemistry A special issue "Gustavo Scuseria Festschrift".

Viktoria Drontschenko and Christian Ochsenfeld*

Cite This: *J. Phys. Chem. A* 2024, 128, 7950−7965
Read Online

ABSTRACT: An efficient method for the computation of nuclear magnetic resonance (NMR) shielding tensors within the random phase approximation (RPA) is presented based on our recently introduced resolution-of-the-identity (RI) atomic orbital RPA NMR method [Drontschenko, V. et al. *J. Chem. Theory Comput.* **2023**, *19*, 7542−7554] utilizing Cholesky decomposed density type matrices and employing an attenuated Coulomb RI metric. The introduced sparsity is efficiently exploited using sparse matrix algebra. This allows for an efficient and low-scaling computation of RPA NMR shielding tensors. Furthermore, we introduce a batching method for the computation of memory demanding intermediates that accounts for their sparsity. This extends the applicability of our method to even larger systems that would have been out of reach before, such as, e.g., a DNA strand with 260 atoms and 3408 atomic orbital basis functions.

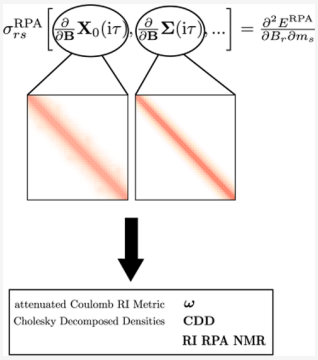

1. INTRODUCTION

The accurate and efficient prediction of nuclear magnetic resonance (NMR) shielding tensors from quantum chemical calculations has emerged as an important technique to assist experimental NMR spectroscopy in structure determination.[1−7] Methods for the computation of NMR shielding tensors providing reasonable accuracy at moderate computational cost include Hartree−Fock (HF)[8−12] theory and density functional theory (DFT).[13−15] Here, the development of low-scaling methods allowed the computation of systems with over 1000 atoms.[16,17] In general a higher level of accuracy can be achieved by wave function based post HF-methods such as Møller−Plesset perturbation theory (MP2),[18,19] multiconfigurational self-consistent field (MCSCF) methods,[20] and coupled cluster (CC) variants.[21−23] MP2 has been shown to be more accurate than HF and DFT,[19,24,25] while coupled cluster singles and doubles (CCSD) as well as CCSD with additional perturbative triples (CCSD(T)) are among the most accurate methods.[26] However, the increased accuracy comes at an increased computational cost, which makes the development of efficient and low-scaling techniques an important task in the development of wave function based NMR methods. Specifically, much progress has been made in this regard for MP2 and its related methods.[27−36]

A method that has recently been shown to combine both accuracy and low computational cost is the random phase approximation (RPA). In a recent benchmark study it was shown that RPA based on a HF reference calculation is able to provide NMR shielding tensors comparable in accuracy to CCSD.[37] Due to these promising results, we successfully derived and implemented a method for the computation of analytical RPA NMR shielding tensors.[38]

RPA is usually implemented as a post-Kohn−Sham (KS)[39] method. It stands on the fifth rung on Jacob's ladder[40] of density functional approximations, and does not contain any empirical parameters. The RPA ground state energy can be obtained within the framework of DFT[39,41] by applying the adiabatic-connection fluctuation−dissipation theorem (ACFDT).[42−44] The ACDFT provides an exact expression for the electron correlation energy in terms of the KS response function and the response function of the system of fully interacting electrons. However, the latter quantity contains the exchange-correlation kernel, the functional derivative of the exchange-correlation potential with respect to the density, which is not known. The simplest approximation is to neglect

Received: April 28, 2024
Revised: August 12, 2024
Accepted: August 19, 2024
Published: September 6, 2024

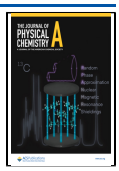

https://doi.org/10.1021/acs.jpca.4c02773
J. Phys. Chem. A 2024, 128, 7950−7965

this contribution, which leads to the (direct) random phase approximation. From its formal derivation, RPA is able to seamlessly incorporate the description of mid- to long-range dispersion interactions, eliminating the need for empirical corrections, and, furthermore, it can also be employed for metallic systems.[45−48] However, in its original form, the computation of RPA energies scales as $O(M^6)$ with the system size M, limiting its applicability to small systems. Furche and co-workers extended the applicability of RPA by utilizing the resolution-of-the-identity (RI)[49] approximation achieving an $O(M^4)$ scaling, which makes RPA one of the formally lowest scaling correlation methods. Further, by reformulating the RPA ground state energy expression in the atomic orbital (AO) basis[50] and using an attenuated Coulomb RI metric,[51] Cholesky decomposed ground state densities,[52] and sparse matrix algebra we were able to obtain asymptotically linear scaling with the system size. These techniques were also applied to the computation of first-order properties within RPA, specifically analytical nuclear gradients, thereby achieving an $O(M^2)$ scaling.[53]

In ref 38 we introduced a method for the calculation of analytical RPA NMR shielding tensors for the first time. We used an atomic orbital formalism as well as the RI approximation with the Coulomb RI metric. This provides an optimal starting point to improve the computational efficiency as well as scaling behavior. In this work we switch to the attenuated Coulomb RI metric, thereby introducing sparsity in the three-center integral tensors, and use Cholesky decomposition (CD) of ground state densities as well as CD of the Green's function in the positive imaginary time domain. The introduced sparsity is efficiently exploited using sparse matrix algebra.

While these techniques are able to improve the computational efficiency of the method, another challenge has to be addressed. For the computation of NMR shielding tensors, the three-center RI tensors as well as their **B**-field derivatives have to be stored in memory. Together with the memory requirements of intermediates arising during the calculation, the memory required for the method easily exceeds the available random access memory (RAM), which limits the tractable system sizes. For the computation of RPA energies, we solved this problem in ref 54 by developing an optimized batching scheme for the computation of the response function by batching over auxiliary function indices, atomic orbital indices, as well as time quadrature points. The three-center integral tensor was recomputed for each batch (integral-direct) and transformed on the fly. The optimal number of batches was computed by minimizing the number of integral calculations, under the constraint of not exceeding the system memory using a Lagrange formalism. This constitutes the best trade off between program runtime and memory demand. However, the optimized batching was so far implemented only for dense matrices and, thus, the sparsity of matrices was not exploited when computing the number of batches. When utilizing sparse matrices, the challenge lies in approximating their memory demand, which is not known beforehand and only determined at program runtime. In this context, we want to note that the most common batching approach within electron correlation methods in literature is batching over one index only, such as the auxiliary function index,[52,76−78] AO index,[79,80] or molecular orbital index[81,82] (virtual or occupied). The number of batches is chosen to be as low as possible without exceeding the available memory. Since dense matrices are employed, the memory demand can be easily approximated.

In this work, we introduce a sparse batching method by approximating the memory demand of sparse matrices by sampling the auxiliary function space and precomputing a number of intermediates. As will be demonstrated, the overhead for the precomputations is practically insignificant. Since there is a considerable number of intermediates within RPA NMR that have to be computed by batching, we opted for a simple batching scheme over auxiliary function indices. The three-center integrals and their magnetic field derivatives are stored on disk and read into memory for each batch and transformed on the fly. While this batching scheme is not optimal yet, it constitutes a starting point for the development of sparse batching methods. In a next step, our sparse sample batching method could be combined with optimal batching, however, we leave this for future work.

The present work is structured as follows: We start with a brief review of the atomic orbital RI-RPA-NMR method in Section 2.2 and continue in Section 2.3 with the description of our new ω-CDD-RI-RPA-NMR method. The theory is concluded in Section 2.4 with the description of our new batching method to achieve a memory efficient implementation. Next, after establishing the computational details in Section 3, we start the results section by considering the accuracy of the introduced approximations in Section 4.1. The scaling is analyzed in Section 4.2. In Section 4.3 the performance of our method is examined, by considering the timings for the most computationally demanding steps within ω-CDD-RI-RPA-NMR (Section 4.3.1) and analyzing the batching in detail for sparse systems in Section 4.3.2 and in Section 4.3.3 for dense systems that are more representative of potential applications. Finally, the conclusion is given in Section 5.

2. THEORY

The NMR shielding tensor $\boldsymbol{\sigma}^A$ of a nucleus A is given by the mixed second derivative of the electronic Energy E with respect to the components of the nuclear magnetic moment $\mathbf{m}^A$ and the magnetic field $\mathbf{B}$ evaluated at zero

$$\sigma_{rs}^A = \frac{\partial^2}{\partial B_r \partial m_s^A} E \Big|_{\mathbf{m}^A=0,\mathbf{B}=0} \qquad \forall\, r, s \in \{x, y, z\} \tag{1}$$

In this work, we will compute the NMR shielding tensor at the RPA level of theory: we start by introducing the notation used throughout this work and subsequently, in Section 2.2, we give a short summary of the RPA NMR method introduced in ref 38. The theory for the low-scaling RPA NMR method is detailed in Section 2.3 and memory efficient batching implementation is provided in Section 2.4.

2.1. Notation. The following notation is used in this work:

- μ, ν, λ, σ: Atomic orbitals (total number: N).
- P, Q, R, S: Auxiliary functions (total number: N_{aux}).
- $\underline{i}$, $\underline{j}$: Occupied Cholesky orbitals (total number: N_{occ}).
- $\underline{a}$, $\underline{b}$: Virtual Cholesky orbitals (total number: $N_{\text{virt}}(i\tau)$).

Mulliken notation is used for two- and three-center integrals. Einstein's sum convention is employed.[55] The derivative of a quantity O with respect to a perturbation ξ, i.e., $\frac{\partial}{\partial \xi} O$, is abbreviated as O^{ξ}.

https://doi.org/10.1021/acs.jpca.4c02773
J. Phys. Chem. A 2024, 128, 7950−7965

2.2. Atomic Orbital RI-RPA Nuclear Magnetic Resonance Shieldings. *2.2.1. AO-RI-RPA Total Energy.* The total energy of the electronic ground state can be expressed within the adiabatic-connection formalism[43] as[42,44]

$$E[\mathbf{P}] = E^{\mathrm{HF}}[\mathbf{P}] + E_{\mathrm{c}}[\mathbf{P}] \tag{2}$$

where the Hartree−Fock energy E^{HF} and the correlation energy E_{c} are evaluated with the density matrix $\mathbf{P}$ from a preceding KS-DFT or HF calculation. Further, by applying the zero-temperature fluctuation−dissipation theorem, the random phase approximation,[56] as well as the RI approximation,[57−59] the correlation energy can be expressed as

$$E_{\mathrm{c}}^{\mathrm{RPA}} = \frac{1}{4\pi}\int_{-\infty}^{+\infty} \mathrm{d}\omega \mathrm{Tr}[\ln(\mathbf{1} - \hat{\mathbf{X}}_0(\mathrm{i}\omega)\mathbb{V}) + \hat{\mathbf{X}}_0(\mathrm{i}\omega)\mathbb{V}] \tag{3}$$

The RI approximation employed in the above equation allows to factorize four-center-two-electron integrals within an arbitrary metric m_{12} as

$$(\mu\nu|r_{12}^{-1}|\lambda\sigma) \approx (\mu\nu|m_{12}|P)(P|m_{12}|R)^{-1}(R|r_{12}^{-1}|S) (S|m_{12}|Q)^{-1}(Q|m_{12}|\lambda\sigma) \tag{4}$$

$$:= \mathbb{B}^{P}_{\mu\nu}\mathbb{V}_{PQ}\mathbb{B}^{Q}_{\lambda\sigma} \tag{5}$$

leaving behind three-center integral tensors $\mathbb{B}^{P}_{\mu\nu}$ as well as two-center integral tensors summarized in the electron−electron interaction operator $\mathbb{V}_{PQ}$, both defined as

$$\mathbb{B}^{P}_{\mu\nu} = (\mu\nu|m_{12}|P) \tag{6}$$

$$\mathbb{V}_{PQ} = (P|m_{12}|R)^{-1}(R|r_{12}^{-1}|S)(S|m_{12}|Q)^{-1} \tag{7}$$

Please note that matrix operations are to be taken before indexing in this work. The noninteracting response function in the imaginary frequency domain $\hat{\mathbf{X}}_0(\mathrm{i}\omega)$ in eq 3 is obtained by the Fourier transform

$$\hat{\mathbf{X}}_0(\mathrm{i}\omega) = \int_{-\infty}^{+\infty} \mathrm{d}\tau \exp(\mathrm{i}\omega\tau)\mathbf{X}_0(\mathrm{i}\tau) \tag{8}$$

which simplifies to a cosine transform,[52,60] or, equivalently to a double Laplace transform[50,51] in case $\mathbf{X}_0(\mathrm{i}\tau)$ is an even function in the imaginary time domain. The response function in the imaginary time domain is given by[61]

$$\mathbf{X}_0(\mathrm{i}\tau) = \Theta(-\tau)\mathbf{X}_0^{-}(\mathrm{i}\tau) + \Theta(\tau)\mathbf{X}_0^{+}(\mathrm{i}\tau) \quad \forall\ \tau \in (-\infty, +\infty) \tag{9}$$

$$X_{0,PQ}^{-}(\mathrm{i}\tau) = \underline{G}_{0,\lambda\nu}(-\mathrm{i}\tau)\mathbb{B}^{P}_{\mu\nu}\overline{G}_{0,\mu\sigma}(\mathrm{i}\tau)\mathbb{B}^{Q}_{\lambda\sigma} \tag{10}$$

$$X_{0,PQ}^{+}(\mathrm{i}\tau) = \underline{G}_{0,\mu\sigma}(-\mathrm{i}\tau)\mathbb{B}^{P}_{\mu\nu}\overline{G}_{0,\lambda\nu}(\mathrm{i}\tau)\mathbb{B}^{Q}_{\lambda\sigma} \tag{11}$$

with the noninteracting Green's function defined as

$$\mathbf{G}_0(\mathrm{i}\tau) = \Theta(-\tau)\underline{\mathbf{G}}_0(\mathrm{i}\tau) + \Theta(\tau)\overline{\mathbf{G}}_0(\mathrm{i}\tau) \quad \forall\ \tau \in (-\infty, +\infty) \tag{12}$$

$$\underline{\mathbf{G}}_0(\mathrm{i}\tau) = \mathbf{P}\exp(-\tau(\mathbf{H} - \epsilon_{\mathrm{F}}\mathbf{S})\mathbf{P}) \tag{13}$$

$$\overline{\mathbf{G}}_0(\mathrm{i}\tau) = -\mathbf{P}_{\mathrm{virt}}\exp(-\tau(\mathbf{H} - \epsilon_{\mathrm{F}}\mathbf{S})\mathbf{P}_{\mathrm{virt}}) \tag{14}$$

here ϵ_{F} denotes the Fermi level,[51,62] $\Theta(\tau)$ the Heaviside step function, and $\mathbf{S}$ is the overlap matrix. The occupied and virtual density matrix is given by $\mathbf{P}$ and $\mathbf{P}_{\mathrm{virt}}$, respectively. The Hamiltonian $\mathbf{H}$ is defined according to

$$\mathbf{H} = \mathbf{h} + \mathbf{G}[\mathbf{P}] \tag{15}$$

$$\mathbf{G}[\mathbf{P}] = \mathbf{J}[\mathbf{P}] + \mathbf{V}_{\mathrm{xc}}[\mathbf{P}] \tag{16}$$

with the matrix representation of the one-electron Hamiltonian $\mathbf{h}$, the Coulomb potential $\mathbf{J}$, and exchange-correlation potential $\mathbf{V}_{\mathrm{xc}}$. Computing the response function in the imaginary time domain and Fourier transforming into the imaginary frequency domain (rather than direct computation in the (iω)-domain) allows for an atomic orbital formulation opening the way for linear scaling RPA implementations.[50−52]

2.2.2. First Derivative with Respect to the Nuclear Magnetic Moment. The first derivative of the total RPA energy, i.e., eq 2, with respect to the nuclear magnetic moment $\mathbf{m}$ is given by[38,53]

$$\frac{\partial E[\mathbf{P}]}{\partial \mathbf{m}} = \frac{\partial E^{\mathrm{HF}}[\mathbf{P}]}{\partial \mathbf{m}} + \frac{\partial E_{\mathrm{c}}^{\mathrm{RPA}}[\mathbf{P}]}{\partial \mathbf{m}} \tag{17}$$

The derivative of the HF energy with respect to $\mathbf{m}$ can be expressed as

$$\frac{\partial E^{\mathrm{HF}}[\mathbf{P}]}{\partial \mathbf{m}} = \mathrm{Tr}(\mathbf{P}\mathbf{h}^{\mathbf{m}}) + \mathrm{Tr}(\mathbf{H}_{\mathrm{HF}}\mathbf{P}^{\mathbf{m}}) \tag{18}$$

$$\mathrm{Tr}(\mathbf{H}_{\mathrm{HF}}\mathbf{P}^{\mathbf{m}}) = \mathrm{Tr}(\mathbf{P}^{\mathbf{m}}\mathbf{h} + \mathbf{P}^{\mathbf{m}}\mathbf{J}[\mathbf{P}] + \mathbf{P}^{\mathbf{m}}\mathbf{K}[\mathbf{P}]) \tag{19}$$

with the matrix representation of the Hartree−Fock exchange $\mathbf{K}$. Since the HF energy is not stationary with respect to the KS density matrix, the response $\mathbf{P}^{\mathbf{m}}$ has to be evaluated, which differs from regular HF gradient calculations where it can be avoided.[63]

Next, differentiating the RPA correlation energy given in eq 3 with respect to $\mathbf{m}$ results in[38,53]

$$\frac{\partial E_{\mathrm{c}}^{\mathrm{RPA}}}{\partial \mathbf{m}} = \mathrm{Tr}(\mathbf{V}_{\mathrm{RPA}}\mathbf{P}^{\mathbf{m}} + \mathbf{P}_{\mathrm{RPA}}\mathbf{h}^{\mathbf{m}}) \tag{20}$$

It is important to note that the density matrix response $\mathbf{P}^{\mathbf{m}}_{\mathrm{virt}}$ could be avoided in this expression using the relation $\mathbf{P}^{\mathbf{m}}_{\mathrm{virt}} = -\mathbf{P}^{\mathbf{m}}$.[38,53,64]

The central intermediates $\mathbf{V}_{\mathrm{RPA}}$ and $\mathbf{P}_{\mathrm{RPA}}$ are defined as

$$\mathbf{V}_{\mathrm{RPA}} = \frac{1}{2}(\mathbf{M} + \mathbf{G}[\mathbf{P}_{\mathrm{RPA}}]) \tag{21}$$

$$\mathbf{P}_{\mathrm{RPA}} = \frac{1}{2}\int_{0}^{+\infty} \mathrm{d}\tau(\mathbf{P}\underline{\mathbf{Y}}(-\mathrm{i}\tau) - \mathbf{P}_{\mathrm{virt}}\overline{\mathbf{Y}}(\mathrm{i}\tau)) \tag{22}$$

Further, $\mathbf{M}$ is given by

$$\mathbf{M} = \overline{\mathbf{M}} + \underline{\mathbf{M}} \tag{23}$$

$$\overline{\mathbf{M}} = \int_{0}^{+\infty} \mathrm{d}\tau(\overline{\mathbf{Y}}(\mathrm{i}\tau)(\mathbf{H} - \epsilon_{\mathrm{F}}\mathbf{S}) + \exp(-\tau(\mathbf{H} - \epsilon_{\mathrm{F}}\mathbf{S})\mathbf{P}_{\mathrm{virt}}) \mathbf{\Sigma}(-\mathrm{i}\tau)) \tag{24}$$

$$\underline{\mathbf{M}} = \int_{0}^{+\infty} \mathrm{d}\tau(\underline{\mathbf{Y}}(-\mathrm{i}\tau)(\mathbf{H} - \epsilon_{\mathrm{F}}\mathbf{S}) + \exp(\tau(\mathbf{H} - \epsilon_{\mathrm{F}}\mathbf{S})\mathbf{P}) \mathbf{\Sigma}(\mathrm{i}\tau)) \tag{25}$$

and $\mathbf{Y}(\mathrm{i}\tau)$ is expressed according to

$$\mathbf{Y}(\mathrm{i}\tau) = \Theta(-\tau)\underline{\mathbf{Y}}(\mathrm{i}\tau) + \Theta(\tau)\overline{\mathbf{Y}}(\mathrm{i}\tau) \tag{26}$$

https://doi.org/10.1021/acs.jpca.4c02773
J. Phys. Chem. A 2024, 128, 7950−7965

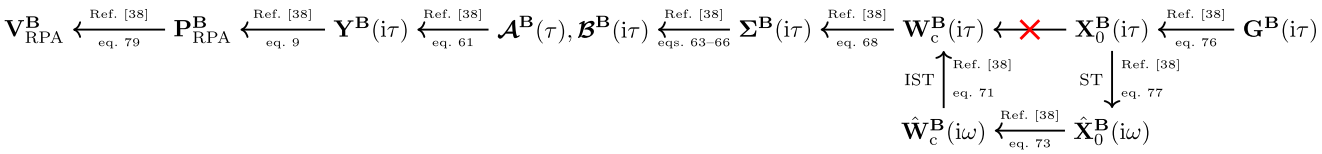

Figure 1. Schematic representation of the derivation of the intermediates $\mathbf{V}^{\mathrm{B}}_{\mathrm{RPA}}$ and $\mathbf{P}^{\mathrm{B}}_{\mathrm{RPA}}$. ST denotes a sine transform and IST an inverse sine transform. All arrows are labeled with the corresponding equations from ref 38. (Reproduced from ref 38. Copyright 2023 American Chemical Society).

$$\overline{\mathbf{Y}}(\mathrm{i}\tau) = \sum_{k=1}^{\infty}\sum_{l=0}^{k-1}\frac{1}{k!}\overline{\mathcal{A}}^{k-l-1}(\tau)\overline{\mathcal{B}}(\mathrm{i}\tau)\overline{\mathcal{A}}^{l}(\tau) \tag{27}$$

$$\underline{\mathbf{Y}}(\mathrm{i}\tau) = \sum_{k=1}^{\infty}\sum_{l=0}^{k-1}\frac{1}{k!}\underline{\mathcal{A}}^{k-l-1}(\tau)\underline{\mathcal{B}}(\mathrm{i}\tau)\underline{\mathcal{A}}^{l}(\tau) \tag{28}$$

with $\mathcal{A}(\tau)$ defined as

$$\mathcal{A}(\tau) = \Theta(-\tau)\underline{\mathcal{A}}(\tau) + \Theta(\tau)\overline{\mathcal{A}}(\tau) \tag{29}$$

$$\underline{\mathcal{A}}(\tau) = -\tau(\mathbf{H} - \epsilon_{\mathrm{F}}\mathbf{S})\mathbf{P} \tag{30}$$

$$\overline{\mathcal{A}}(\tau) = -\tau(\mathbf{H} - \epsilon_{\mathrm{F}}\mathbf{S})\mathbf{P}_{\mathrm{virt}} \tag{31}$$

and $\mathcal{B}(\mathrm{i}\tau)$ as

$$\mathcal{B}(\mathrm{i}\tau) = \Theta(-\tau)\underline{\mathcal{B}}(\mathrm{i}\tau) + \Theta(\tau)\overline{\mathcal{B}}(\mathrm{i}\tau) \tag{32}$$

$$\underline{\mathcal{B}}(\mathrm{i}\tau) = -\tau\mathbf{\Sigma}(-\mathrm{i}\tau)\mathbf{P} \tag{33}$$

$$\overline{\mathcal{B}}(\mathrm{i}\tau) = -\tau\mathbf{\Sigma}(-\mathrm{i}\tau)\mathbf{P}_{\mathrm{virt}} \tag{34}$$

The $\mathbf{Y}$ matrices are most efficiently evaluated using a recursion scheme. The detailed procedure and corresponding equations can be found in refs 34 and 64.

Furthermore, the correlated self-energy $\mathbf{\Sigma}(\mathrm{i}\tau)$, which is of central importance in this work, is defined as

$$\Sigma_{\nu\lambda}(\mathrm{i}\tau) = -\tilde{W}_{\mathrm{c},PQ}(-\mathrm{i}\tau)\mathbb{B}^{P}_{\mu\nu}G_{0,\mu\sigma}(\mathrm{i}\tau)\mathbb{B}^{Q}_{\lambda\sigma} \quad \forall\ \tau \in (-\infty, +\infty) \tag{35}$$

with the intermediate

$$\tilde{\mathbf{W}}_{\mathrm{c}}(\mathrm{i}\tau) = \frac{1}{\pi}\int_{0}^{+\infty}\mathrm{d}\omega(\cos(\omega\tau)\hat{\mathbf{W}}_{\mathrm{c}}(\mathrm{i}\omega) + \mathrm{i}\sin(\omega\tau)\hat{\mathbf{W}}_{\mathrm{c}}(\mathrm{i}\omega)) \tag{36}$$

defined in terms of the correlated screened Coulomb interaction

$$\hat{\mathbf{W}}_{\mathrm{c}}(\mathrm{i}\omega) = \mathbb{V}[(\mathbf{1} - \hat{\mathbf{X}}_{0}(\mathrm{i}\omega)\mathbb{V})^{-1} - \mathbf{1}] \tag{37}$$

2.2.3. Second Derivative with Respect to the Magnetic Field: NMR Shielding Tensor. The NMR shielding tensor, i.e., the second mixed derivative of the total RPA energy with respect to $\mathbf{m}$ and $\mathbf{B}$, is defined as[38]

$$\boldsymbol{\sigma} = \left.\frac{\partial^2 E^{\mathrm{total}}[\mathbf{P}]}{\partial\mathbf{B}\partial\mathbf{m}}\right|_{\mathbf{m}=\mathbf{0},\mathbf{B}=\mathbf{0}} = \left.\frac{\partial^2 E^{\mathrm{HF}}[\mathbf{P}]}{\partial\mathbf{B}\partial\mathbf{m}}\right|_{\mathbf{m}=\mathbf{0},\mathbf{B}=\mathbf{0}} + \left.\frac{\partial^2 E_{\mathrm{c}}^{\mathrm{RPA}}[\mathbf{P}]}{\partial\mathbf{B}\partial\mathbf{m}}\right|_{\mathbf{m}=\mathbf{0},\mathbf{B}=\mathbf{0}} \tag{38}$$

Evaluating the above equation by forming the second derivative of the HF energy and of the RPA correlation energy with respect to $\mathbf{m}$ and $\mathbf{B}$ results in[38]

$$\boldsymbol{\sigma} = \left.\frac{\partial^2 E^{\mathrm{total}}[\mathbf{P}]}{\partial\mathbf{B}\partial\mathbf{m}}\right|_{\mathbf{m}=\mathbf{0},\mathbf{B}=\mathbf{0}} = \mathrm{Tr}([\mathbf{V}^{\mathbf{B}}_{\mathrm{RPA}} + \mathbf{H}^{\mathbf{B}}_{\mathrm{HF}}]\mathbf{P}^{\mathbf{m}}) + \mathrm{Tr}([\mathbf{V}_{\mathrm{RPA}} + \mathbf{H}_{\mathrm{HF}}]\mathbf{P}^{\mathbf{Bm}}) + \mathrm{Tr}(\mathbf{P}^{\mathbf{B}}_{\mathrm{RPA}}\mathbf{h}^{\mathbf{m}}) + \mathrm{Tr}(\mathbf{P}_{\mathrm{RPA}}\mathbf{h}^{\mathbf{Bm}}) + \tilde{\boldsymbol{\sigma}}^{\mathrm{HF}} \tag{39}$$

$$\mathbf{H}^{\mathbf{B}}_{\mathrm{HF}} = \mathbf{h}^{\mathbf{B}} + \mathbf{J}^{\mathbf{B}}[\mathbf{P}] + \mathbf{K}^{\mathbf{B}}[\mathbf{P}] + \mathbf{K}[\mathbf{P}^{\mathbf{B}}] \tag{40}$$

It should be noted that the term $\mathbf{J}[\mathbf{P}^{\mathbf{B}}]$ in the above equation is zero, due to the skew-symmetry of the purely imaginary density matrix derivative and the contribution $\tilde{\boldsymbol{\sigma}}^{\mathrm{HF}} = \mathrm{Tr}(\mathbf{P}^{\mathbf{B}}\mathbf{h}^{\mathbf{m}}) + \mathrm{Tr}(\mathbf{P}\mathbf{h}^{\mathbf{Bm}})$ is treated separately with the usual techniques used for the computation of HF and DFT shifts for simplicity. The perturbed density matrix $\mathbf{P}^{\mathbf{m}}$, given in the first term of eq 39, can, in principle, be computed by solving the coupled perturbed KS (CPKS) equations for all perturbations of the nuclear magnetic moment. However, a more efficient route is to use the Z-vector technique,[64,65] which requires the solution of only one CPKS equation. We employ the density matrix-based Laplace-transformed CPKS method[66] developed by our group within our AO formulation.

At this point, the challenging terms from eq 39 that remain to be evaluated are the $\mathbf{B}$-field derivatives of the RPA intermediates $\mathbf{V}_{\mathrm{RPA}}$ and $\mathbf{P}_{\mathrm{RPA}}$ as well as the second derivative of the density matrix $\mathbf{P}^{\mathbf{Bm}}$. In this context the second derivative of the density matrix, $\mathbf{P}^{\mathbf{Bm}}$, can be computed using a nested Z-vector approach[32,34] which was introduced in the framework of Laplace-transformed MP2 NMR. Employing the efficient approach of ref 34 allows to derive the final equations for the computation the NMR shielding tensor within RPA (in terms of $\mathbf{V}^{\mathbf{B}}_{\mathrm{RPA}}$ and $\mathbf{P}^{\mathbf{B}}_{\mathrm{RPA}}$) as detailed in ref 38. The central task in RPA NMR is, however, the evaluation of $\mathbf{V}^{\mathbf{B}}_{\mathrm{RPA}}$ and $\mathbf{P}^{\mathbf{B}}_{\mathrm{RPA}}$, which is the subject of the next section.

2.2.4. Computation of RPA NMR Intermediates: $\mathbf{V}^{\mathbf{B}}_{RPA}$ and $\mathbf{P}^{\mathbf{B}}_{RPA}$. The detailed evaluation of the intermediates $\mathbf{V}^{\mathbf{B}}_{\mathrm{RPA}}$ and $\mathbf{P}^{\mathbf{B}}_{\mathrm{RPA}}$ has been presented in ref 38 and we refer to this reference for a complete derivation and the corresponding equations. Figure 1 provides an overview over the important intermediates that have to be differentiated in order to obtain $\mathbf{V}^{\mathbf{B}}_{\mathrm{RPA}}$ and $\mathbf{P}^{\mathbf{B}}_{\mathrm{RPA}}$. The equation numbers from ref 38 corresponding to the specific steps are provided and we intend to only review the detailed equations for the two most demanding steps, specifically, the computation of $\mathbf{\Sigma}^{\mathbf{B}}(\mathrm{i}\tau)$ and $\mathbf{X}^{\mathbf{B}}_{0}(\mathrm{i}\tau)$.

The $\mathbf{B}$-field derivative of the self-energy can be obtained by either directly differentiating eq 35 using the product rule, as has been done in ref 38, or by taking the partial derivatives of $\mathbf{\Sigma}(\mathrm{i}\tau)$ with respect to $\tilde{\mathbf{W}}_{\mathrm{c}}(\mathrm{i}\tau)$, $\mathbb{B}$, and $\mathbf{G}_{0}(\mathrm{i}\tau)$ multiplied by the respective $\mathbf{B}$-field derivative of each quantity. This results in

https://doi.org/10.1021/acs.jpca.4c02773
J. Phys. Chem. A 2024, 128, 7950−7965

$$\frac{\partial \boldsymbol{\Sigma}(i\tau)}{\partial \mathbf{B}} = \frac{\partial \boldsymbol{\Sigma}(i\tau)}{\partial \tilde{W}_{c,PQ}(-i\tau)}\frac{\partial \tilde{W}_{c,PQ}(-i\tau)}{\partial \mathbf{B}} + \frac{\partial \boldsymbol{\Sigma}(i\tau)}{\partial \mathbf{G}_0(i\tau)}\frac{\partial \mathbf{G}_0(i\tau)}{\partial \mathbf{B}} + \frac{\partial \boldsymbol{\Sigma}(i\tau)}{\partial \mathbb{B}^P}\frac{\partial \mathbb{B}^P}{\partial \mathbf{B}} \quad \forall\ \tau \in (-\infty, +\infty) \tag{41}$$

For the **B**-field derivative of the self-energy in the positive imaginary time domain it follows for the partial derivatives of eq 41 (for $\tau > 0$)

$$\left(\frac{\partial \boldsymbol{\Sigma}(i\tau)}{\partial \tilde{W}_{c,PQ}(-i\tau)}\frac{\partial \tilde{W}_{c,PQ}(-i\tau)}{\partial \mathbf{B}}\right)_{\nu\lambda} = -\frac{\partial W_{c,PQ}(i\tau)}{\partial \mathbf{B}}\mathbb{B}^P_{\mu\nu}\overline{G}_{0,\mu\sigma}(i\tau)B^Q_{\lambda\sigma} \tag{42}$$

$$\left(\frac{\partial \boldsymbol{\Sigma}(i\tau)}{\partial \overline{\mathbf{G}}_0(i\tau)}\frac{\partial \overline{\mathbf{G}}_0(i\tau)}{\partial \mathbf{B}}\right)_{\nu\lambda} = -W_{c,PQ}(i\tau)\mathbb{B}^P_{\mu\nu}\frac{\partial \overline{G}_{0,\mu\sigma}(i\tau)}{\partial \mathbf{B}}\mathbb{B}^Q_{\lambda\sigma} \tag{43}$$

$$\left(\frac{\partial \boldsymbol{\Sigma}(i\tau)}{\partial \mathbb{B}^P}\frac{\partial \mathbb{B}^P}{\partial \mathbf{B}}\right)_{\nu\lambda} = -W_{c,PQ}(i\tau)\mathbb{B}^Q_{\mu\nu}\overline{G}_{0,\mu\sigma}(i\tau)\frac{\partial \mathbb{B}^P_{\lambda\sigma}}{\partial \mathbf{B}} + \text{ct} \tag{44}$$

In eq 44 the abbreviation "ct" denotes the conjugate transpose of the first term on the right-hand site, a notation that will be employed from now on. The terms $\mathbf{W}_c(i\tau)$ and $\mathbf{W}^{\mathbf{B}}_c(i\tau)$ are given by the cosine and sine transforms, respectively, as

$$\mathbf{W}_c(i\tau) = \frac{1}{\pi}\int_0^{+\infty} d\omega \hat{\mathbf{W}}_c(i\omega)\cos(\omega\tau) \tag{45}$$

$$\mathbf{W}^{\mathbf{B}}_c(i\tau) = 2i\int_0^{+\infty} d\omega \hat{\mathbf{W}}^{\mathbf{B}}_c(i\omega)\sin(\omega\tau) \tag{46}$$

The partial derivatives for the self-energy in the negative imaginary time domain are given for $\tau \geq 0$ by

$$\left(\frac{\partial \boldsymbol{\Sigma}(-i\tau)}{\partial \tilde{W}_{c,PQ}(i\tau)}\frac{\partial \tilde{W}_{c,PQ}(i\tau)}{\partial \mathbf{B}}\right)_{\nu\lambda} = \frac{\partial W_{c,PQ}(i\tau)}{\partial \mathbf{B}}\mathbb{B}^P_{\mu\nu}\underline{G}_{0,\mu\sigma}(-i\tau)\mathbb{B}^Q_{\lambda\sigma} \tag{47}$$

$$\left(\frac{\partial \boldsymbol{\Sigma}(-i\tau)}{\partial \underline{\mathbf{G}}_0(-i\tau)}\frac{\partial \underline{\mathbf{G}}_0(-i\tau)}{\partial \mathbf{B}}\right)_{\nu\lambda} = -W_{c,PQ}(i\tau)\mathbb{B}^P_{\mu\nu}\frac{\partial \underline{G}_{0,\mu\sigma}(-i\tau)}{\partial \mathbf{B}}\mathbb{B}^Q_{\lambda\sigma} \tag{48}$$

$$\left(\frac{\partial \boldsymbol{\Sigma}(-i\tau)}{\partial \mathbb{B}^P}\frac{\partial \mathbb{B}^P}{\partial \mathbf{B}}\right)_{\nu\lambda} = -W_{c,PQ}(i\tau)\mathbb{B}^Q_{\mu\nu}\underline{G}_{0,\mu\sigma}(-i\tau)\frac{\partial \mathbb{B}^P_{\lambda\sigma}}{\partial \mathbf{B}} + \text{ct} \tag{49}$$

The **B**-field derivative of the response function, i.e., eq 11, can be obtained using the same strategy yielding

$$\frac{\partial \mathbf{X}^+_0(i\tau)}{\partial \mathbf{B}} = \frac{\partial \mathbf{X}^+_0(i\tau)}{\partial \underline{\mathbf{G}}_0(-i\tau)}\frac{\partial \underline{\mathbf{G}}_0(-i\tau)}{\partial \mathbf{B}} + \frac{\partial \mathbf{X}^+_0(i\tau)}{\partial \overline{\mathbf{G}}_0(i\tau)}\frac{\partial \overline{\mathbf{G}}_0(i\tau)}{\partial \mathbf{B}} + \frac{\partial \mathbf{X}^+_0(i\tau)}{\partial \mathbb{B}^P}\frac{\partial \mathbb{B}^P}{\partial \mathbf{B}} \quad \forall\ \tau \geq 0 \tag{50}$$

with the partial derivatives

$$\left(\frac{\partial \mathbf{X}^+_0(i\tau)}{\partial \underline{\mathbf{G}}_0(-i\tau)}\frac{\partial \underline{\mathbf{G}}_0(-i\tau)}{\partial \mathbf{B}}\right)_{QP} = \frac{\partial \underline{G}_{0,\mu\sigma}(-i\tau)}{\partial \mathbf{B}}\mathbb{B}^Q_{\mu\nu}\overline{G}_{0,\lambda\nu}(i\tau)\mathbb{B}^P_{\lambda\sigma} \tag{51}$$

$$\left(\frac{\partial \mathbf{X}^+_0(i\tau)}{\partial \overline{\mathbf{G}}_0(i\tau)}\frac{\partial \overline{\mathbf{G}}_0(i\tau)}{\partial \mathbf{B}}\right)_{QP} = \underline{G}_{0,\mu\sigma}(-i\tau)\mathbb{B}^Q_{\mu\nu}\frac{\partial \overline{G}_{0,\lambda\nu}(i\tau)}{\partial \mathbf{B}}\mathbb{B}^P_{\lambda\sigma} \tag{52}$$

$$\left(\frac{\partial \mathbf{X}^+_0(i\tau)}{\partial \mathbb{B}^P}\frac{\partial \mathbb{B}^P}{\partial \mathbf{B}}\right)_{QP} = \underline{G}_{0,\mu\sigma}(-i\tau)\mathbb{B}^Q_{\mu\nu}\overline{G}_{0,\lambda\nu}(i\tau)\frac{\partial \mathbb{B}^P_{\lambda\sigma}}{\partial \mathbf{B}} + \text{ct} \tag{53}$$

The self-energy and response function as well as their **B**-field derivatives can be computed with a formal scaling of $O(N^2_{aux}N^2 \propto M^4)$ and thus are the steepest scaling steps in the computation of RPA NMR shieldings. Further, since these steps require the three-center integrals as well as their **B**-field derivatives, they are also the most demanding steps in terms of memory requirements. Thus, for an efficient implementation of RPA NMR it is necessary to optimize these steps in terms of computational effort as well as memory requirements. The former is described in the next section, where we employ a local RI metric and Cholesky decomposition together with sparse matrix algebra to reduce the computational effort as well as lower the scaling. Then, in Section 2.4, those computational optimizations are combined with a batching scheme to achieve a memory efficient implementation.

2.3. Low-Scaling RPA NMR Method: ω-CDD-RI-RPA-NMR.

2.3.1. Strategies for Low-Scaling: Local RI Metric and Cholesky Decomposition of Density Type Matrices. The computation of the response function and self-energy as well as their respective **B**-field derivatives constitute the most computationally demanding steps in the calculation of RPA NMR shieldings. In this section we describe several methods to optimize these steps and lower their scaling.

As mentioned in Section 2.2.1 we employ the RI approximation which allows to avoid the four-center-two-electron integrals and instead work with lower rank tensors, specifically three-center and two-center integral tensors (see eqs 4 and 5). The crucial factor to decrease computational effort and lower the scaling in extended molecular systems is the choice of the RI metric m_{12}. The Coulomb metric $m_{12} = \frac{1}{r_{12}}$ has proven to be optimal for modeling density type repulsions.[67] However, due to the very slow decay, it couples the charge distributions $(\mu\nu)$ with the auxiliary functions P in the three-center integral tensor $(\mu\nu|m_{12}|P)$ over effectively infinite distances. Thus, no sparsity can be gained in their matrix representation. In contrast to that, the overlap metric $m_{12} = \delta(r_{12})$ is very local since it decays as $\exp(-r^2_{12})$ for Gaussian basis sets. The introduced sparsity comes, however, at the cost of decreased accuracy.[67] A metric that combines both, accuracy and sparsity, is the Coulomb metric attenuated by the complementary error function (erfc)[51,68,69] expressed as

$$m_{12} = \frac{\text{erfc}(w_{att}r_{12})}{r_{12}} \tag{54}$$

The attenuation parameter w_{att} determines the attenuation strength. By varying this parameter the sparsity and loss in accuracy can be controlled. In the limiting cases of $w_{att} \to 0$ and $w_{att} \to \infty$ the Coulomb metric and overlap metric are

https://doi.org/10.1021/acs.jpca.4c02773
J. Phys. Chem. A 2024, 128, 7950−7965

retrieved, respectively. It has been shown in ref 51 that the attenuation parameter $w_{att} = 0.1$ au gives very good results for RPA energy calculations by balancing accuracy and sparsity. Further, ref 53 reports the same for RPA nuclear gradients. In this work we will further investigate if these findings can be extended to second order properties, specifically RPA NMR shieldings.

Another strategy we will employ, is pivoted Cholesky decomposition (CD)[50−52,70−74] of density type matrices. In this context the pivoted Cholesky decomposition of a positive semidefinite $(N_R \times N_R)$ matrix $\mathcal{R}$ is given by

$$\mathcal{R} = \mathcal{L}\mathcal{L}^T \tag{55}$$

where $\mathcal{L}$ is a lower triangular matrix with dimensions $(N_R \times \mathrm{rank}(\mathcal{R}))$. Thus, if the rank of a matrix is significantly less than its dimensions then substantial savings in computational effort and memory requirements can be achieved. In order to make use of that, we start by considering that the Green's function in the negative imaginary time domain is invariant to projection onto the occupied space, which gives rise to the Cholesky decomposition of the occupied ground state density matrix $\mathbf{P} = \mathbf{L}\mathbf{L}^T$ resulting in[52]

$$\underline{\mathbf{G}}_0(-i\tau) = \mathbf{P}\mathbf{S}\underline{\mathbf{G}}_0(-i\tau)\mathbf{S}\mathbf{P} \tag{56}$$

$$= \mathbf{L}\mathbf{L}^T\mathbf{S}\underline{\mathbf{G}}_0(-i\tau)\mathbf{S}\mathbf{L}\mathbf{L}^T \tag{57}$$

where the Cholesky matrix $\mathbf{L}$ has dimensions $(N \times N_{occ})$. It should be noted that the CD of the virtual density matrix is of not much use since its rank corresponds to the number of virtual orbitals N_{virt}, which is not significantly less than the number of basis functions. Next, the CD of the Green's function in the positive imaginary time domain is considered according to

$$-\bar{\mathbf{G}}_0(i\tau) = \mathbf{L}_{virt}(i\tau)\mathbf{L}_{virt}^T(i\tau) \tag{58}$$

Since $\bar{\mathbf{G}}_0(i\tau)$ is a negative semidefinite matrix it is made positive semidefinite by multiplication with -1. The rank of $\bar{\mathbf{G}}_0(i\tau)$, which corresponds to the columns of $\mathbf{L}_{virt}(i\tau)$, is time dependent and decreases with increasing time, that is $\mathrm{rank}(\bar{\mathbf{G}}_0(i\tau)) \leq N_{virt}$.

It is important to note that CD of the **B**-field derivative of the Green's function and density matrix is not possible since both matrices are not positive semidefinite.

2.3.2. Calculation of the Self-Energy and Its B-Field Derivative. For the calculation of the self-energy given by eq 35 we can insert eq 58 for the computation of $\boldsymbol{\Sigma}(i\tau)$ and eq 57 for the computation of $\boldsymbol{\Sigma}(-i\tau)$ leading to

$$\Sigma_{\nu\lambda}(i\tau) = W_{c,PQ}(-i\tau)\bar{\mathbb{B}}^P_{\mu\underline{a}}(i\tau)\bar{\mathbb{B}}^Q_{\lambda\underline{a}}(i\tau) \quad \forall\ \tau \geq 0 \tag{59}$$

$$\Sigma_{\nu\lambda}(-i\tau) = -W_{c,PQ}(i\tau)\underline{\mathbb{B}}^P_{\nu\underline{i}}\underline{G}_{0,\underline{i}\underline{j}}(-i\tau)\underline{\mathbb{B}}^Q_{\lambda\underline{j}} \quad \forall\ \tau \geq 0 \tag{60}$$

where we have used the fact that the unperturbed correlated screened Coulomb interaction is an even function in the $(i\tau)$-space. Further, the following notation for transformed quantities has been introduced

$$\underline{G}_{0,\underline{i}\underline{j}}(-i\tau) := (\mathbf{L}^T\mathbf{S}\underline{\mathbf{G}}_0(-i\tau)\mathbf{S}\mathbf{L})_{\underline{i}\underline{j}} \tag{61}$$

$$\underline{\mathbb{B}}^P_{\mu\underline{i}} := (\mathbb{B}^P\mathbf{L})_{\mu\underline{i}} \tag{62}$$

$$\bar{\mathbb{B}}^Q_{\mu\underline{a}}(i\tau) := (\mathbb{B}^Q\mathbf{L}_{virt}(i\tau))_{\mu\underline{a}} \tag{63}$$

Next, for the **B**-field derivative of the self-energy we start by considering the partial derivatives of the self-energy in the positive imaginary time domain. For the partial derivative with respect to $\tilde{\mathbf{W}}_c(i\tau)$, i.e., eq 42, and for the partial derivative with respect to the three-center integrals, i.e., eq 44, we can employ eq 55 leading to

$$\left(\frac{\partial\boldsymbol{\Sigma}(i\tau)}{\partial\tilde{W}_{c,PQ}(-i\tau)}\frac{\partial\tilde{W}_{c,PQ}(-i\tau)}{\partial\mathbf{B}}\right)_{\nu\lambda} = \frac{\partial W_{c,PQ}(i\tau)}{\partial\mathbf{B}}\bar{\mathbb{B}}^P_{\nu\underline{a}}(i\tau)\bar{\mathbb{B}}^Q_{\lambda\underline{a}}(i\tau) \tag{64}$$

$$\left(\frac{\partial\boldsymbol{\Sigma}(i\tau)}{\partial\mathbb{B}^P}\frac{\partial\mathbb{B}^P}{\partial\mathbf{B}}\right)_{\nu\lambda} = W_{c,PQ}(i\tau)\bar{\mathbb{B}}^P_{\nu\underline{a}}(i\tau)\left(\mathbf{L}^T_{virt}(i\tau)\frac{\partial\mathbb{B}^P}{\partial\mathbf{B}}\right)_{\lambda\underline{a}} + \mathrm{ct} \tag{65}$$

For the term containing the derivative of the Green's function, that is eq 43, CD cannot be used since $\mathbf{G}_0^{\mathbf{B}}$ is not positive semidefinite.

Similarly, for the self-energy in the negative imaginary time domain eq 56 can be inserted into the partial derivative term containing $\mathbf{W}_c^{\mathbf{B}}(i\tau)$, i.e., eq 47, and the term containing $\mathbb{B}^{\mathbf{B}}$, i.e., eq 49, resulting in

$$\left(\frac{\partial\boldsymbol{\Sigma}(-i\tau)}{\partial\tilde{W}_{c,PQ}(i\tau)}\frac{\partial\tilde{W}_{c,PQ}(i\tau)}{\partial\mathbf{B}}\right)_{\nu\lambda} = \frac{\partial W_{c,PQ}(i\tau)}{\partial\mathbf{B}}\underline{\mathbb{B}}^P_{\nu\underline{i}}\underline{G}_{0,\underline{i}\underline{j}}(-i\tau)\underline{\mathbb{B}}^Q_{\lambda\underline{j}} \tag{66}$$

$$\left(\frac{\partial\boldsymbol{\Sigma}(-i\tau)}{\partial\mathbb{B}^P}\frac{\partial\mathbb{B}^P}{\partial\mathbf{B}}\right)_{\nu\lambda} = -W_{c,PQ}(i\tau)\underline{\mathbb{B}}^P_{\nu\underline{i}}\underline{G}_{0,\underline{i}\underline{j}}(-i\tau)\left(\mathbf{L}^T\frac{\partial\mathbb{B}^P}{\partial\mathbf{B}}\right)_{\lambda\underline{j}} + \mathrm{ct} \tag{67}$$

Again, the term containing the derivative of the Green's function eq 48 cannot be transformed using CD.

2.3.3. Calculation of the Response Function and its B-Field Derivative. The evaluation of the response function can be restricted to positive imaginary times, that is eq 11, since the unperturbed response function is an even function in the $(i\tau)$-domain. Using eqs 56 and 58 allows to express the response function according to

$$X^+_{0,PQ}(i\tau) = (\mathbf{L}^T\mathbb{B}^P\mathbf{L}_{virt}(i\tau))_{\underline{j}\underline{a}}(\mathbf{L}^T\mathbf{S}\underline{\mathbf{G}}_0(-i\tau)\mathbf{S}\mathbf{L})_{\underline{i}\underline{j}} (\mathbf{L}^T_{virt}(i\tau)\mathbb{B}^Q\mathbf{L})_{\underline{a}\underline{i}} \tag{68}$$

$$= \bar{\mathbb{B}}^P_{\underline{a}\underline{j}}(i\tau)\underline{G}_{0,\underline{i}\underline{j}}(-i\tau)\bar{\mathbb{B}}^Q_{\underline{a}\underline{i}}(i\tau) \tag{69}$$

where

$$\bar{\mathbb{B}}^Q_{\underline{i}\underline{a}}(i\tau) := (\mathbf{L}^T\mathbb{B}^Q\mathbf{L}_{virt}(i\tau))_{\underline{i}\underline{a}} \tag{70}$$

For the **B**-field derivative of the response function eq 50 its partial derivatives given by eqs 51−53 can be considered. Inserting eq 56 into eq 52 and into eq 53; furthermore inserting eq 58 into eq 51 and into eq 53 yields

https://doi.org/10.1021/acs.jpca.4c02773
J. Phys. Chem. A 2024, 128, 7950−7965

$$\left(\frac{\partial \mathbf{X}_0^+(\mathrm{i}\tau)}{\partial \underline{\mathbf{G}}_0(-\mathrm{i}\tau)}\frac{\partial \underline{\mathbf{G}}_0(-\mathrm{i}\tau)}{\partial \mathbf{B}}\right)_{QP} = -\frac{\partial \underline{G}_{0,\mu\sigma}(-\mathrm{i}\tau)}{\partial \mathbf{B}}\overline{\mathbb{B}}^{Q}_{\mu\underline{a}}(\mathrm{i}\tau)\overline{\mathbb{B}}^{P}_{\sigma\underline{a}}(\mathrm{i}\tau) \tag{71}$$

$$\left(\frac{\partial \mathbf{X}_0^+(\mathrm{i}\tau)}{\partial \overline{\mathbf{G}}_0(\mathrm{i}\tau)}\frac{\partial \overline{\mathbf{G}}_0(\mathrm{i}\tau)}{\partial \mathbf{B}}\right)_{QP} = \underline{G}_{0,\underline{i}\,\underline{j}}(-\mathrm{i}\tau)\underline{\mathbb{B}}^{Q}_{\nu\,\underline{i}}\frac{\partial \overline{G}_{0,\lambda\nu}(\mathrm{i}\tau)}{\partial \mathbf{B}}\underline{\mathbb{B}}^{P}_{\lambda\,\underline{j}} \tag{72}$$

$$\left(\frac{\partial \mathbf{X}_0^+(\mathrm{i}\tau)}{\partial \mathbb{B}^P}\frac{\partial \mathbb{B}^P}{\partial \mathbf{B}}\right)_{QP} = -\underline{G}_{0,\underline{i}\,\underline{j}}(-\mathrm{i}\tau)\overline{\underline{\mathbb{B}}}^{Q}_{\underline{i}\,\underline{a}}(\mathrm{i}\tau)\left(\mathbf{L}^{\mathrm{T}}_{\mathrm{virt}}(\mathrm{i}\tau)\frac{\partial \mathbb{B}^P}{\partial \mathbf{B}}\mathbf{L}\right)_{\underline{a}\,\underline{j}} + \mathrm{ct} \tag{73}$$

2.3.4. Scaling. When discussing the scaling in this section, we refer to the asymptotic scaling in the limit of very large system sizes. In this context a distinction is made for the theoretical scaling of the ω-CDD-RI-RPA method employing dense matrix algebra, which is generally denoted as "formal scaling" and the method is referred to as "dense method", and the same method employing sparse matrix algebra which is discussed in the context of computing sparse systems, which is denoted as "sparse method".

As noted earlier, our AO-RI-RPA-NMR implementation of ref 38 has a formal scaling of $O(N_{\mathrm{aux}}^2N^2)$ and scales as $O(M^4)$ with the system size. In this section we investigate the asymptotic scaling of the dense and sparse implementation for the computation of the self-energy and response function as well as their **B**-field derivatives using our new ω-CDD-RI-RPA-NMR formulation as introduced in the previous sections. The results are shown in Table 1. The asymptotic scaling of the sparse method for the response function and its **B**-field derivative can be reduced to linear provided that the matrices $\mathbf{G}_0(\mathrm{i}\tau)$ and $\mathbb{B}$ as well as their **B**-field derivatives are sparse. The asymptotic scaling for the self-energy and its **B**-field derivative can be reduced only to quadratic at this stage, since the correlated screened Coulomb interaction is in general a dense matrix as it contains the $\frac{1}{r_{12}}$ term.[53] Thus, for sparse systems generally a quadratic scaling with the system size would be expected for the ω-CDD-RI-RPA-NMR method.

2.4. Memory Efficient Implementation. As a starting point for the implementation of our new ω-CDD-RI-RPA-NMR method, we used the framework of our AO-RI-RPA-NMR method.[38] An overview containing all steps of the calculation is provided in the Supporting Information of ref 38. However, the steps involving the computation of the response function and self-energy as well as their **B**-field derivatives will be replaced by the memory efficient method introduced below. We employ the following directives for a memory efficient implementation:

- $\mathbf{\Sigma}(\mathrm{i}\tau)$, $\mathbf{X}_0(\mathrm{i}\tau)$, $\mathbf{\Sigma}^{\mathbf{B}}(\mathrm{i}\tau)$, and $\mathbf{X}_0^{\mathbf{B}}(\mathrm{i}\tau)$ are computed for one τ quadrature point at a time.
- Each partial derivative term corresponding to $\mathbf{\Sigma}^{\mathbf{B}}(\mathrm{i}\tau)$, and $\mathbf{X}_0^{\mathbf{B}}(\mathrm{i}\tau)$ is computed within a separate batching scheme.
- The partial derivative terms for the magnetic field derivative of the self-energy are computed for the positive and negative imaginary time domain within the same batching scheme.
- The three-center integrals and their **B**-field derivatives are stored on disk in a compact matrix format, where only elements (with a significant contribution) from the upper triangular matrix are stored for each auxiliary function. When the integrals and their derivatives are needed within the calculation they are copied back into a regular matrix format for one auxiliary function at a time and the lower triangular matrix is filled by considering the symmetry of the three-center integrals and the skew-symmetry of its **B**-field derivative.
- Intermediates that are stored on disk are read into memory for one aux-batch for efficient read performance.
- Integrals are transformed for one auxiliary function at a time.
- For efficiency, common intermediates are precomputed and stored on disk to be reused.
- The loops over auxiliary function indices are parallelized.

With these guidelines in mind, a memory efficient implementation for the computation of $\mathbf{\Sigma}(\mathrm{i}\tau)$ and $\mathbf{X}_0(\mathrm{i}\tau)$ as well as their magnetic field derivatives is possible. The detailed algorithms and technical details of the implementations are provided in the Supporting Information.

2.4.1. Computation of Batches: Accounting for Sparsity. In the previous section, batching schemes were described for the computation of the self-energy and response function as well as their **B**-field derivatives. The task ahead is to develop a method for the computation of the number of batches by

Table 1. Asymptotic Scaling for the Computation of the Self-Energy and Response Function As Well As Their B-Field Derivatives within the ω-CDD-RI-RPA-NMR Method Utilizing Dense Matrix Algebra (Dense) and Using Sparse Matrix Algebra (Sparse) Assuming Sparse Systems[a]

		scaling	
quantity	equation nr.	dense	sparse
$\mathbf{\Sigma}(\mathrm{i}\tau)$	59	$O(N_{\mathrm{aux}}^2NN_{\mathrm{virt}}(\mathrm{i}\tau))$	$O(M^2)$
$\mathbf{\Sigma}^{\mathbf{B}}(\mathrm{i}\tau)$			
$\frac{\partial \mathbf{\Sigma}(\mathrm{i}\tau)}{\partial \tilde{\mathbf{W}}_c(-\mathrm{i}\tau)}\frac{\partial \tilde{\mathbf{W}}_c(-\mathrm{i}\tau)}{\partial \mathbf{B}}$	64	$O(N_{\mathrm{aux}}^2NN_{\mathrm{virt}}(\mathrm{i}\tau))$	$O(M^2)$
$\frac{\partial \mathbf{\Sigma}(\mathrm{i}\tau)}{\partial \overline{\mathbf{G}}_0(\mathrm{i}\tau)}\frac{\partial \overline{\mathbf{G}}_0(\mathrm{i}\tau)}{\partial \mathbf{B}}$	43	$O(N_{\mathrm{aux}}^2N^2)$	$O(M^2)$
$\frac{\partial \mathbf{\Sigma}(\mathrm{i}\tau)}{\partial \mathbb{B}}\frac{\partial \mathbb{B}}{\partial \mathbf{B}}$	65	$O(N_{\mathrm{aux}}^2NN_{\mathrm{virt}}(\mathrm{i}\tau))$	$O(M^2)$
$\mathbf{\Sigma}(-\mathrm{i}\tau)$	60	$O(N_{\mathrm{aux}}^2NN_{\mathrm{occ}})$	$O(M^2)$
$\mathbf{\Sigma}^{\mathbf{B}}(-\mathrm{i}\tau)$			
$\frac{\partial \mathbf{\Sigma}(-\mathrm{i}\tau)}{\partial \tilde{\mathbf{W}}_c(\mathrm{i}\tau)}\frac{\partial \tilde{\mathbf{W}}_c(\mathrm{i}\tau)}{\partial \mathbf{B}}$	66	$O(N_{\mathrm{aux}}^2NN_{\mathrm{occ}})$	$O(M^2)$
$\frac{\partial \mathbf{\Sigma}(-\mathrm{i}\tau)}{\partial \underline{\mathbf{G}}_0(-\mathrm{i}\tau)}\frac{\partial \underline{\mathbf{G}}_0(-\mathrm{i}\tau)}{\partial \mathbf{B}}$	48	$O(N_{\mathrm{aux}}^2N^2)$	$O(M^2)$
$\frac{\partial \mathbf{\Sigma}(-\mathrm{i}\tau)}{\partial \mathbb{B}}\frac{\partial \mathbb{B}}{\partial \mathbf{B}}$	67	$O(N_{\mathrm{aux}}^2NN_{\mathrm{occ}})$	$O(M^2)$
$\mathbf{X}_0(\mathrm{i}\tau)$	69	$O(N_{\mathrm{aux}}^2NN_{\mathrm{occ}})$	$O(M)$
$\mathbf{X}_0^{\mathbf{B}}(\mathrm{i}\tau)$			
$\frac{\partial \mathbf{X}_0(\mathrm{i}\tau)}{\partial \underline{\mathbf{G}}_0(-\mathrm{i}\tau)}\frac{\partial \underline{\mathbf{G}}_0(-\mathrm{i}\tau)}{\partial \mathbf{B}}$	71	$O(N_{\mathrm{aux}}^2NN_{\mathrm{virt}}(\mathrm{i}\tau))$	$O(M)$
$\frac{\partial \mathbf{X}_0(\mathrm{i}\tau)}{\partial \overline{\mathbf{G}}_0(\mathrm{i}\tau)}\frac{\partial \overline{\mathbf{G}}_0(\mathrm{i}\tau)}{\partial \mathbf{B}}$	72	$O(N_{\mathrm{aux}}^2NN_{\mathrm{occ}})$	$O(M)$
$\frac{\partial \mathbf{X}_0(\mathrm{i}\tau)}{\partial \mathbb{B}}\frac{\partial \mathbb{B}}{\partial \mathbf{B}}$	73	$O(N_{\mathrm{aux}}^2N_{\mathrm{virt}}(\mathrm{i}\tau)N_{\mathrm{occ}})$	$O(M)$

[a]For the **B**-field derivatives, the scaling for all partial derivative terms is provided. Further, the equation numbers for each term are noted.

https://doi.org/10.1021/acs.jpca.4c02773
J. Phys. Chem. A 2024, 128, 7950−7965

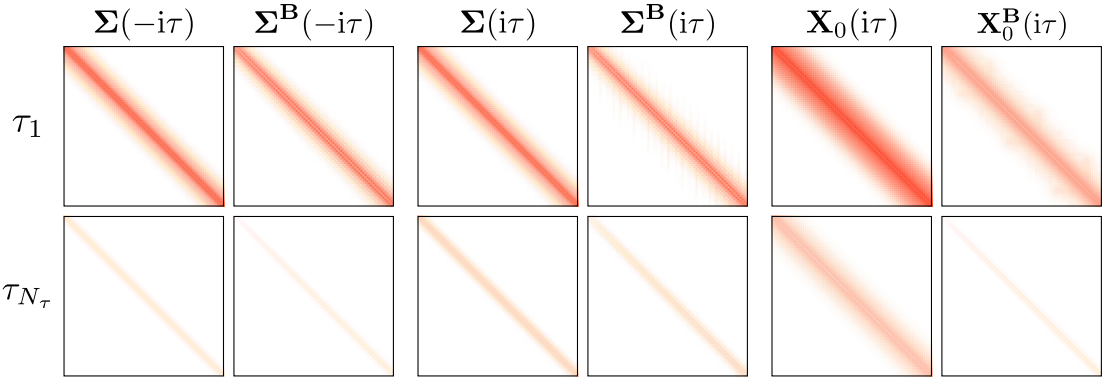

Figure 2. Sparsity patterns of the self-energy and the response function as well as their **B**-field derivatives (for one direction of the magnetic field) for the first time grid point (τ_1) and the last one (τ_{N_τ}) for the linear alkane $C_{80}H_{162}$ using the cc-pwCVDZ basis set with the corresponding RI basis set.

accounting for the sparsity of all matrices within a step of the calculation. In this context a general framework for the computation of batches will be presented.

First, the dependence of the sparsity on the time quadrature point τ is investigated for the self-energy, response function, and their **B**-field derivatives. In Figure 2 the sparsity patterns for all of the mentioned quantities are shown for the linear alkane $C_{80}H_{162}$ in a cc-pwCVDZ basis set. As can be seen, the sparsity shows a strong dependence on the τ quadrature point for all quantities, increasing with the value of τ. Presumably, this can be traced back to the exponential functions within the Green's functions eqs 13 and14 which decay with increasing τ. This indicates that the sparsity associated with this exponential decay is present in both, sparse and dense systems. Due to this observation, the number of batches is recomputed for each τ quadrature point.

Next, an approximation for the memory demands of sparse matrices is necessary, since they are not previously known and only determined at program runtime. In our implementation sparse matrices are implemented in a block-sparse format, where the matrices are divided into blocks of constant size. Upon allocation of the sparse matrix, the blocks are screened. Each block with an L2-norm lower than a threshold value ϑ_a is removed. A second screening threshold ϑ_m is used for the matrix−matrix multiplication. If the product of the L2-norms of two matrix-blocks is below ϑ_m the matrix−matrix multiplication of those blocks is not preformed. More information about block-sparse matrices, their matrix−matrix multiplication routine, as well as the memory allocation technique is given in the Supporting Information of ref 75.

For the computation of batches the relevant memory demands that need to be approximated are those of third-order tensors $\mathcal{R}_{kl}^{m}$ with dimension $(N_k \times N_l \times N_m)$. In our implementation third-order tensors are generally represented by a vector containing a number of N_m sparse matrices of size $(N_k \times N_l)$. Thus, the total memory demand of the tensor is given by the sum of the memory demands of the respective sparse matrix associated with each m. Specifically in this work the third index m refers to the auxiliary function index. To approximate the total memory demand of these tensors, we sample the auxiliary function space by precomputing intermediate quantities for a number of auxiliary functions to determine their memory demands. Subsequently, the average memory demand for one auxiliary function is computed from the sampling and multiplied by the total number of auxiliary functions to approximate the memory demands of the tensor. Further, for **B**-field derivatives of third order tensors, we carry out the sampling for all **B**-field directions, compute the approximate memory demands, and determine the maximum memory out of all **B**-field directions. The maximum memory is then used for the computation of batches. In this work, we sample the auxiliary function space in steps of 100, which provides reliable results while not significantly increasing the computational effort of the method. Thus, together with the available system memory, the number of batches can be easily determined. By recomputing the batches for each τ quadrature point and approximating the sparsity of all matrices as described, we are able to account for sparsity in the computation of the number of batches for each batching scheme.

3. COMPUTATIONAL DETAILS

Our new method was implemented in the FermiONs++ program package.[83−85] The RPA NMR shieldings computed in this work are based on preceding Hartree−Fock calculations. In ref 37 this setup was shown to provide accurate NMR shieldings of about CCSD quality. Optimized minimax grids[60] for the time and frequency integration[52,60] as well as the cosine and sine[86] transformation are employed with 15 grid points, which has been shown in ref 38 to yield accurate results. For our new method, in the following denoted as ω-CDD-RI-RPA-NMR, we employ sparse matrix algebra ($\vartheta_a = 10^{-7}$, $\vartheta_m = 10^{-9}$, block size (96×96)) and the attenuated Coulomb metric with the attenuation parameter ω_{att} = 0.1 au. The truncation tolerance used for the pivoted Cholesky decomposition is 10^{-11}. The implementation introduced in ref 38 is denoted as AO-RI-RPA-NMR and utilizes the Coulomb metric as well as dense matrix algebra routines as provided by the Math Kernel Library (version 2022.0.0). The frozen core approximation is not applied. The atomic orbital basis sets cc-pwCVDZ[87] and cc-pwCVTZ[87] were used with their corresponding RI basis set.[88]

4. RESULTS AND DISCUSSION

4.1. Accuracy. Several techniques have been employed to improve the efficiency and the scaling of our RPA NMR method.[38] To test the accuracy of our ω-CDD-RI-RPA-NMR method, calculations have been performed for the molecules in the test set assembled by Gauss and co-workers,[89] excluding the molecules SO_2 and O_3 as has been done in ref 89 as well as

https://doi.org/10.1021/acs.jpca.4c02773
J. Phys. Chem. A 2024, 128, 7950−7965

PN as done in ref 38. Further, the test set of Flaig et al.[24] was used. To analyze the deviations for more extended systems the monomers in the L7 test set[90] (excluding C3GC monomer B and C2PD monomer A due to the high computing demands of the AO-RI-RPA-NMR method) as well as a set of three linear alkanes with 10−30 carbon atoms have been computed. NMR shieldings computed using the new ω-CDD-RI-RPA-NMR method are compared to the results obtained with the AO-RI-RPA-NMR method,[38] which employs the Coulomb RI metric and dense matrix algebra. By this comparison, the error introduced through the local RI metric, the utilization of sparse matrix algebra, as well as Cholesky decomposition can be assessed for the ω-CDD-RI-RPA-NMR method. The cc-pwCVDZ and cc-pwCVTZ basis sets were used with the corresponding RI basis sets for the Gauss and Flaig test set. For the L7 test set and the set of linear alkanes the cc-pwCVDZ basis set was used due to the high computing demands of the AO-RI-RPA-NMR method that is used as the reference. The results are shown in Table 2, where the mean absolute errors

Table 2. MAEs (ppm) and SDs (ppm) of Isotropic NMR Shielding Constants Obtained Using the ω-CDD-RI-RPA-NMR Method with Respect to the AO-RI-RPA-NMR Results for the Molecules in the Gauss Benchmark Set, the Flaig Benchmark Set, the L7 Test Set, and a Set of Linear Alkanes[a]

benchmark set	basis set	MAE [10^{-3} ppm]	SD [10^{-3} ppm]
Gauss	cc-pwCVDZ	2.40	4.9
	cc-pwCVTZ	0.90	1.54
Flaig	cc-pwCVDZ	1.42	3.04
	cc-pwCVTZ	1.04	2.98
L7	cc-pwCVDZ	1.34	2.6
linear alkanes	cc-pwCVDZ	0.59	0.91

[a]The cc-pwCVDZ and cc-pwCVTZ basis sets were used with the corresponding RI basis set.

(MAEs) and the standard deviations (SDs) of the ω-CDD-RI-RPA-NMR method compared to the AO-RI-RPA-NMR method are displayed for different test sets. As can be seen, the MAEs and SDs are on the order of 10^{-3} ppm for all considered test sets. Therefore, we can conclude that the introduced techniques do not compromise the accuracy of the method.

Given that the ω-CDD-RI-RPA-NMR method does not introduce any significant error, it is preferred over the AO-RI-RPA-NMR method due to its superior computational efficiency. In this context dense matrix algebra may be employed for smaller systems, while sparse matrix algebra is more efficient for larger systems and especially sparse systems. As shown in the Supporting Information for linear alkanes, an early crossover for $C_{10}H_{22}$ with the dense method is observed.

4.2. Scaling Behavior with the System Size. To analyze the effective scaling of our method with the system size, we carried out calculations on linear alkanes of increasing length using the cc-pwCVDZ basis set with the corresponding RI basis set. This system was chosen as an optimal test case due to its local electronic structure and the ability to systematically increase the system size. The calculations were performed on a compute node with AMD EPYC 9334 processors with 128 threads, 1.5 TB of RAM, and 4.7 TB of disk space. No batching was employed for the calculations.

The computation of the **B**-field derivative of the response function and the self-energy are the computationally most demanding steps and are among the formally steepest scaling steps of the calculation. Thus, to analyze the effective scaling behavior with the system size of both steps, we measure the number of floating point operations (FLOPs) that are required for their computation. The results are given in Figure 3. As can

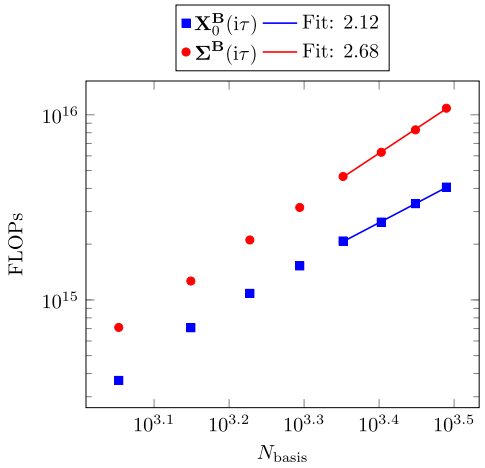

Figure 3. Log−log plot of the FLOPs for the calculation of $\mathbf{X}_0^{\mathbf{B}}(i\tau)$ (blue) and $\mathbf{\Sigma}^{\mathbf{B}}(i\tau)$ (red) against the number of atomic orbital basis functions for linear alkanes of increasing size employing the ω-CDD-RI-RPA-NMR method.

be seen, a quadratic scaling is obtained for the computation of $\mathbf{X}_0^{\mathbf{B}}(i\tau)$, which is higher than the expected asymptotic linear scaling that was discussed in Section 2.3.4. In comparison, in ref 52 an effective scaling of $M^{1.39}$ was determined for the (non differentiated) response function by computing linear alkanes with 2170−7210 atomic orbital basis functions. Presumably, similar behavior could be obtained for the **B**-field derivative of the response function for larger systems. This would indicate a later onset of linear scaling behavior for larger systems. However, without batching the computation of ω-CDD-RI-RPA-NMR is limited to linear alkanes with up to 3090 atomic orbital basis functions on a compute node with 1.5 TB of RAM. A similar discussion can be applied to the computation of the **B**-field derivative of the self-energy. The observed scaling is also higher than the expected asymptotic quadratic scaling, which was discussed in Section 2.3.4. For the (non differentiated) self-energy an effective scaling of $M^{2.43}$ was obtained in ref 53 using linear alkanes with 1930−4810 atomic orbital basis functions. Thus, we would expect to converge to the expected quadratic scaling for the **B**-field derivative of the self-energy for larger systems as well.

4.3. Performance. *4.3.1. Timings.* In the following, the timings for the most time-consuming steps within the calculation of ω-CDD-RI-RPA-NMR shieldings are investigated. Please note that the total timings refer to the time for the RPA NMR correlation contribution only, that is, excluding the time for the preceding HF NMR calculation. We computed a DNA fragment with two adenine-thymine base pairs (128 atoms; 580 electrons) using the cc-pwCVDZ basis set (N = 1646) with the corresponding RI basis set. Further, as an example of sparse systems, we computed the linear alkane $C_{60}H_{122}$ (182 atoms; 482 electrons) using the same basis set (N = 1690). No batching was employed for the calculations,

https://doi.org/10.1021/acs.jpca.4c02773
J. Phys. Chem. A 2024, 128, 7950−7965

which were carried out on a compute node with AMD EPYC 7452 processors with 128 threads, 1 TB of RAM, and 4.7 TB of disk space. The results are shown in Figure 4. For both

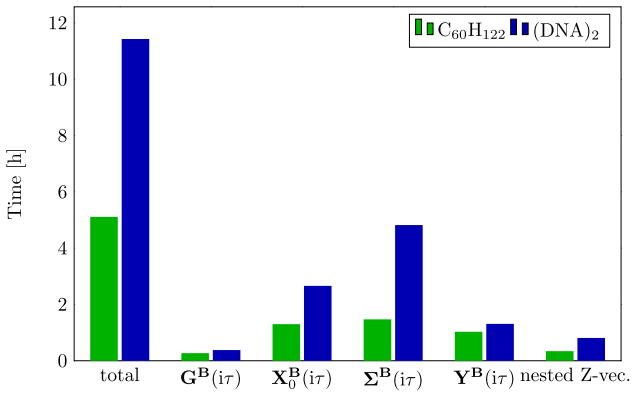

Figure 4. Timings for the computationally most demanding steps within the ω-CDD-RI-RPA-NMR calculation for the DNA fragment $(DNA)_2$ computed using dense matrix algebra and a linear alkane which was computed using sparse matrix algebra. The cc-pwCVDZ basis set with the corresponding RI basis set was used. Note that the timings for the **B**-field derivative of the self-energy in the positive and negative imaginary time domain are summarized in $\mathbf{\Sigma}^{\mathbf{B}}(i\tau)$. Calculations were performed on a compute node with 1 TB of RAM without employing batching.

systems the computation of the **B**-field derivative of the self-energy is the most compute intensive step, followed by the computation of $\mathbf{X}_0^{\mathbf{B}}(i\tau)$ as well as $\mathbf{Y}^{\mathbf{B}}(i\tau)$. However, for the sparse system, i.e., $C_{60}H_{122}$, the timings for all three steps are on the same order while for the dense system, i.e., $(DNA)_2$, the computation of $\mathbf{\Sigma}^{\mathbf{B}}(i\tau)$ is still dominating. This demonstrates that for the linear alkane the sparsity of $\mathbf{\Sigma}^{\mathbf{B}}(i\tau)$ is efficiently exploited using sparse matrix algebra.

Next, detailed timings for the partial derivatives within the calculation of $\mathbf{\Sigma}^{\mathbf{B}}(i\tau)$ $(\forall\tau \in (-\infty, +\infty))$ and $\mathbf{X}_0^{\mathbf{B}}(i\tau)$ are investigated. The results are shown in Figure 5. Starting with the timings for $\mathbf{\Sigma}^{\mathbf{B}}(\pm i\tau)$ given on the left-hand side of Figure 5, it can be observed that the dominating step is the partial derivative term containing the derivative of the Green's function. Since CD cannot be applied to this term, it is the most demanding step in terms of computational resources as well as memory requirements. However, for the linear alkane the sparsity introduced through the local metric in the three-center integral tensor is exploited using sparse algebra, which lowers its contribution to the total time compared to the dense DNA fragment. Further, it is evident that the computation of the **B**-field derivative of the self-energy is more efficient for the negative imaginary time domain than for the positive imaginary time domain. This is due to the very efficient CD of the ground state density matrix within the calculation of $\mathbf{\Sigma}^{\mathbf{B}}(-i\tau)$, while the CD of the Green's function in the positive imaginary time domain within the calculation of $\mathbf{\Sigma}^{\mathbf{B}}(i\tau)$ is less effective. For the computation of $\mathbf{X}_0^{\mathbf{B}}(i\tau)$, shown on the right-hand side of Figure 5, the partial derivative term containing $\underline{\mathbf{G}}_0^{\mathbf{B}}(-i\tau)$ requires over 50% of the total time for both systems. For this term only the CD of $\overline{\mathbf{G}}_0(i\tau)$ can be used, while the more efficient CD of the ground state density matrix can only be used for the remaining terms.

4.3.2. Batching: Linear Alkanes. As described in Section 2.4.1, the introduced batching method was designed to account for the sparsity of intermediates when computing the number of batches. To test this aspect of our batching method, we performed calculations on linear alkanes of increasing length using the cc-pwCVDZ atomic orbital basis set with the corresponding RI basis set. All calculations were performed on a compute note with AMD EPYC 7302 processors using 64 threads, 250 GB of RAM, and 1.7 TB of disk space.

As has been shown in Section 2.4.1, the sparsity of intermediates has a dependence on the τ quadrature point, typically increasing with the τ quadrature points. To account for this, we recompute the number of batches for each τ quadrature point. Since the number of batches is dependent on the memory demands of intermediates it would be expected

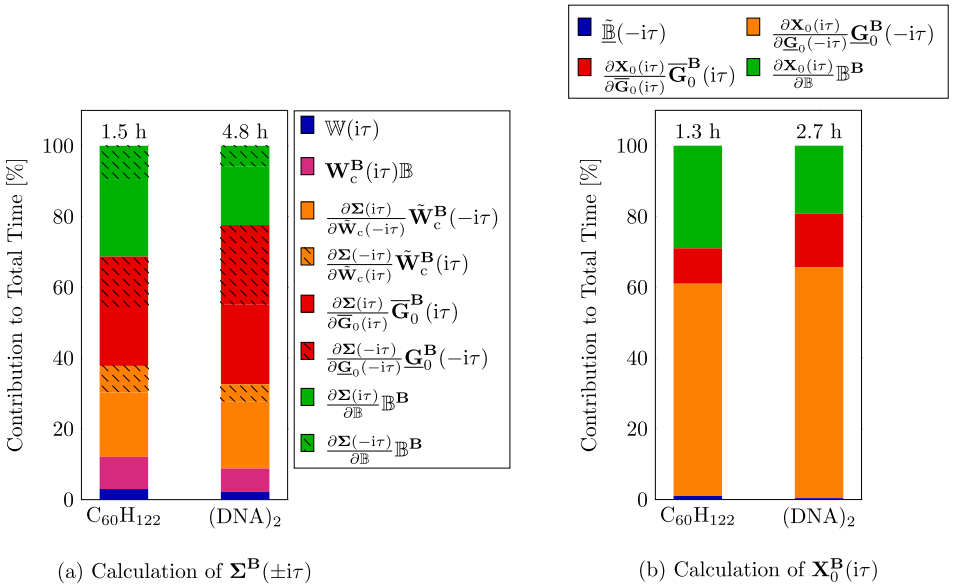

(a) Calculation of $\mathbf{\Sigma}^{\mathbf{B}}(\pm i\tau)$ (b) Calculation of $\mathbf{X}_0^{\mathbf{B}}(i\tau)$

Figure 5. Contribution of the partial derivative terms (a) for the computation of $\mathbf{\Sigma}^{\mathbf{B}}(i\tau)$ (nonshaded bars) and $\mathbf{\Sigma}^{\mathbf{B}}(-i\tau)$ (shaded bars) as well as (b) for the computation of $\mathbf{X}_0^{\mathbf{B}}(i\tau)$ to the total time required for the computation of $\mathbf{\Sigma}^{\mathbf{B}}(\pm i\tau)$ and $\mathbf{X}_0^{\mathbf{B}}(i\tau)$, respectively.

https://doi.org/10.1021/acs.jpca.4c02773
J. Phys. Chem. A 2024, 128, 7950−7965

that the number of batches also decreases with the τ quadrature point. Thus, we start our investigation by considering the number of batches for all intermediates for each τ quadrature point using the linear alkane $C_{100}H_{202}$. The results are displayed in Figure 6. It can be observed that the

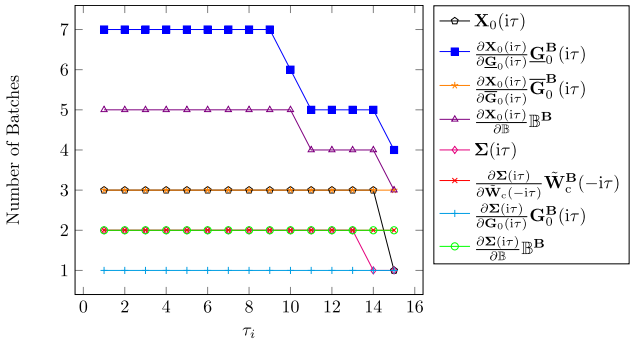

Figure 6. Number of aux-batches for the calculation of the most memory demanding steps per τ quadrature point for the linear alkane $C_{100}H_{202}$. Note that τ_i denotes the ith τ quadrature point. Calculations were carried out on a compute node using 250 GB of RAM.

computation of the partial derivative term $\frac{\partial \mathbf{X}_0(i\tau)}{\partial \underline{\mathbf{G}}_0(i\tau)} \underline{\mathbf{G}}_0^{\mathbf{B}}(i\tau)$ requires the highest number of batches, which was expected since this term has the highest memory demand given that CD of the ground state density matrix is not possible for that term. However, the number of batches does decrease significantly with increasing τ points due to the increasing sparsity for which our batching is able to accommodate for. The decrease in batches can be observed for all terms except for $\frac{\partial \mathbf{\Sigma}(i\tau)}{\partial \tilde{\mathbf{W}}_c(i\tau)} \tilde{\mathbf{W}}_c^{\mathbf{B}}(i\tau)$, $\frac{\partial \mathbf{X}_0(i\tau)}{\partial \overline{\mathbf{G}}_0(i\tau)} \overline{\mathbf{G}}_0^{\mathbf{B}}(i\tau)$, and $\frac{\partial \mathbf{\Sigma}(i\tau)}{\partial \mathbb{B}} \mathbb{B}^{\mathbf{B}}$. For the first term it is due to the fact that $\tilde{\mathbf{W}}_c^{\mathbf{B}}(i\tau)$ is in general a dense matrix, while for the second term the memory demand is dominated by the memory required for the batched three-center integrals in the AO basis as well as the three-center integrals transformed with $\mathbf{L}$, which are independent of τ. For the last term the batched $\mathbf{B}$-field derivatives of the three-center integrals are loaded into memory for all three magnetic field directions, whose memory is also independent of τ. To summarize, in general the sparsity of intermediates increases with the τ quadrature points, which our batching is able to account for. As demonstrated, the number of computed batches decreases with increasing τ.

Next, we investigate the total number of batches (for the first τ quadrature point) for each intermediate with increasing system sizes. The results are given in Figure 7. Since the number of batches overlap for some intermediates, the results are also summarized in the Supporting Information for clarity. It can be observed again, that the partial derivative term $\frac{\partial \mathbf{X}_0(i\tau)}{\partial \underline{\mathbf{G}}_0(i\tau)} \underline{\mathbf{G}}_0^{\mathbf{B}}(i\tau)$ requires the highest number of batches and increases the strongest with the system size. Further, for the partial derivative terms within the calculation of $\mathbf{\Sigma}^{\mathbf{B}}(i\tau)$ the number of batches is lower compared to the partial derivative terms for $\mathbf{X}_0^{\mathbf{B}}(i\tau)$. For the calculation of $\mathbf{\Sigma}^{\mathbf{B}}(i\tau)$ the batching over auxiliary functions is very beneficial, since various memory demanding intermediates can be computed for one auxiliary function at a time.

For the computation of batches we approximated the memory demands of sparse matrices by sampling the auxiliary

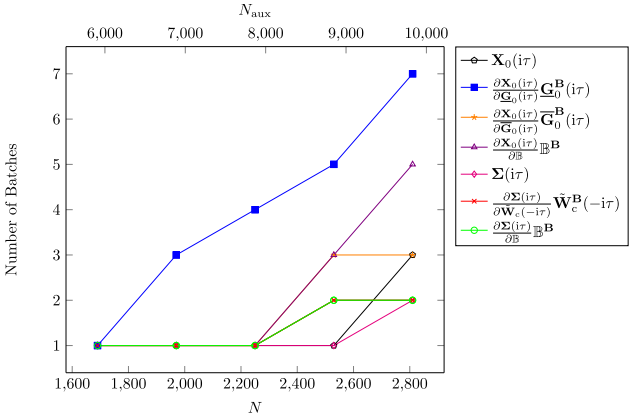

Figure 7. Number of auxiliary function batches for the computation of the partial derivative terms within the calculation of $\mathbf{\Sigma}^{\mathbf{B}}(i\tau)$ $(\forall \tau \in (-\infty, +\infty))$ and $\mathbf{X}_0^{\mathbf{B}}(i\tau)$ for linear alkanes of increasing size. Note that only the partial derivative terms are displayed, for which the number of batches is larger than 1. Calculations were performed on a compute node with 250 GB of RAM.

function space and precomputing a number of intermediates, which introduces an overhead. To investigate the extend of the overhead, we examine the total time for the computation of batches for increasing system sizes and consider the contribution to the total computation time for the correlation part of the RPA NMR calculation. The results are displayed in Figure 8. The computation time for the sample batching of the

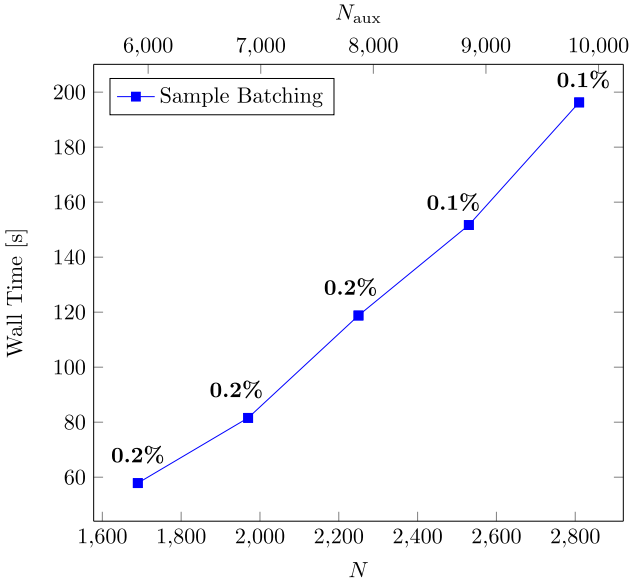

Figure 8. Wall time (s) for the computation of batches using the sample batching method for systems of increasing size with their contribution to the total time for the correlation part of the ω-CDD-RI-RPA-NMR calculation.

largest system size is still under 5 min and the total contribution does not exceed 1% of the total computation time. Therefore, it can be concluded, that the overhead that comes with the sample batching method is practically insignificant.

Another overhead that comes with the batching method is associated with disk input/output (I/O) operations. When using the batching method certain quantities, such as the three-

https://doi.org/10.1021/acs.jpca.4c02773
J. Phys. Chem. A 2024, 128, 7950−7965

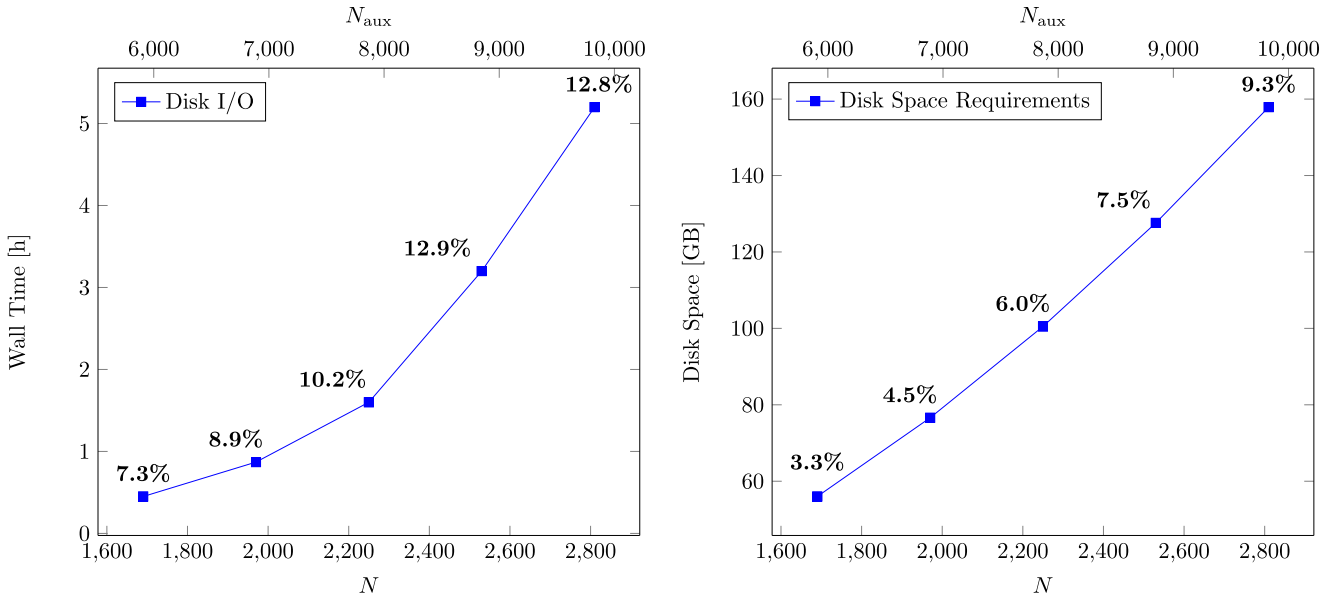

Figure 9. Wall time (h) required for disk I/O operations for increasing system sizes with the contribution to the total time for the correlation part of the ω-CDD-RI-RPA-NMR calculation (left). Further, disk space requirements (GB) for increasing system sizes with the contribution to the total disk space are displayed on the right-hand side.

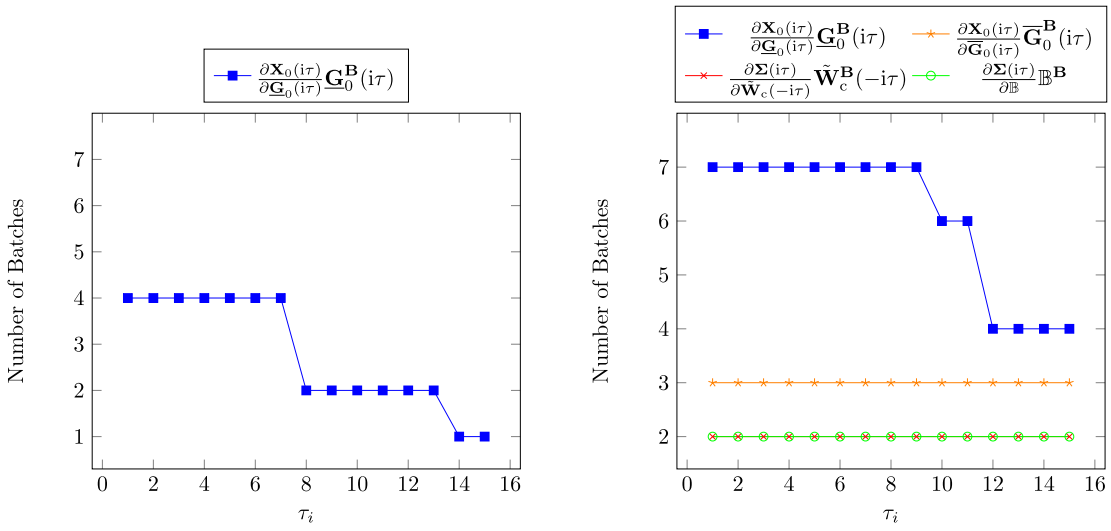

(a) Tweezer Complex (b) $(DNA)_4$

Figure 10. Number of aux-batches for the calculation of intermediates per τ quadrature point for (a) the tweezer complex and (b) $(DNA)_4$. Note that τ_i denotes the ith τ quadrature point. Calculations were carried out on a compute node using 1 TB of RAM.

center integrals and their **B**-field derivatives, are stored on disk and read into memory within the respective batching scheme. On the left-hand side of Figure 9 the total time for disk I/O operations as well as the contribution to the total time for the correlation part of the ω-CDD-RI-RPA-NMR calculation is shown for increasing system sizes. As can be seen, the contribution does increase with the system size, due to the increasing number of batches. For the largest system the disk I/O contribution is less than 15% of the total time, which is still acceptable. However, for efficiency reasons an integral direct computation of the three-center integrals and their **B**-field derivatives would certainly be beneficial, but we leave this to future work on this topic.

Lastly, we investigate the maximum disk space requirements of the method for increasing system sizes. The results are summarized on the right-hand side of Figure 9. As can be seen, the disk space demands are low compared to the total disk space, due to the compact storage format we adopted for the three-center integrals and their derivatives as explained in Section 2.4. Therefore, it can be concluded that currently the disk space does not yet constitute a bottleneck in the computation of large system sizes.

In summary, we can conclude this section with the following points:

- The sparsity of intermediates increases with the number of τ quadrature points, which our sparse sample batching is able to account for.

https://doi.org/10.1021/acs.jpca.4c02773
J. Phys. Chem. A 2024, 128, 7950−7965

- The time for the computation of batches within the sample batching method is practically insignificant (<1% of the total time).
- The disk space demands are relatively low and currently do not hinder the calculation of large systems.
- Disk I/O operations have a significant contribution to the total time for larger systems, thus, an integral-direct scheme for the three-center integrals and their **B**-field derivatives would be beneficial to explore in future work.

4.3.3. Batching: Illustrative Applications. We further test our batching method on chemically relevant systems representative for potential applications. All calculations were performed on a compute node with AMD EPYC 7452 processors using 128 threads, 1 TB of RAM, and 4.7 TB of disk space.

First, we test the performance of our method for a tweezer host−guest complex (92 atoms; 374 electrons) which has been investigated in literature from an application point of view[91] as well as for performance analysis within NMR calculations.[35,36] The structure was taken from refs 35,36. The calculation was carried out using a cc-pwCVTZ AO basis set (N = 2912) with the corresponding RI basis set. The correlation part of the RPA NMR calculation took 4 days. Here, disk I/O operations accounted for 6.1% of that time and the computation of batches for 0.2%. While disk I/O operations have a significant contribution to the total time, the time for the computation of batches is practically insignificant. The calculation required 541.0 GB of disk space, which is clearly under the available 4.7 TB. Further, on the left-hand side of Figure 10 the number of batches per τ quadrature point is given for all intermediates with a batch number larger than 1. It is interesting to note that for the dense system the number of batches for the intermediate $\frac{\partial \mathbf{X}_0(i\tau)}{\partial \underline{\mathbf{G}}_0(i\tau)} \underline{\mathbf{G}}_0^{\mathbf{B}}(i\tau)$ is also dependent on the τ quadrature point and decreases significantly with increasing τ, which was also observed for sparse systems in the previous section. This shows that our sample batching method is also beneficial for dense systems.

Next, we performed calculations on a DNA strand with four adenine-thymine base pairs, denoted as $(DNA)_4$ (260 atoms; 1220 electrons), using a cc-pwCVDZ AO basis set (N = 3408) with the corresponding RI basis set. The correlation part of the RPA NMR calculation required 7.5 days in total. Out of that time 5.3% was spend on disk I/O operations, while the sample batching only took 0.2% of the total time. Thus, the time needed for the sample batching method is practically insignificant in this case as well. The time spend on disk I/O operations is not the dominating part, but has still a significant contribution to the total time. The required disk space was 687.3 GB which amount to 14.6% of the available disk space. Next, the number of batches is investigated for all τ quadrature points. The results are given on the right-hand side of Figure 10. Here, only terms are displayed for which the batch count exceeds 1. It can be observed again that the number of batches for the intermediate $\frac{\partial \mathbf{X}_0(i\tau)}{\partial \underline{\mathbf{G}}_0(i\tau)} \underline{\mathbf{G}}_0^{\mathbf{B}}(i\tau)$ shows a strong dependence on the τ quadrature point, making our sample batching relevant for dense systems as well.

5. CONCLUSIONS

An efficient and low-scaling method for the computation of RPA NMR shielding tensors has been presented that is based on our AO-RI-RPA-NMR method introduced in ref 38. We utilize Cholesky decomposed ground state densities as well as Cholesky decomposed Green's functions in the positive imaginary time domain. Further, the attenuated Coulomb RI metric was employed to introduce sparsity in the three-center integral tensors, which was efficiently exploited using sparse matrix algebra. Specifically, these techniques were employed for the computation of the response function, self-energy and their **B**-field derivatives which constitute the steepest scaling and most demanding steps in terms of computational effort and memory requirements. It was shown that the introduced approximations do not deteriorate the accuracy of the method. The scaling with the system size was analyzed using linear alkanes, which revealed close to a quadratic scaling.

To lower the memory demand of the method and, thus, extend its applicability to even larger systems, we introduced a batching method for memory demanding intermediates. Here, the memory demand of sparse matrices was approximated by sampling the auxiliary function space and used to compute the number of batches for each τ quadrature point. It was shown that the overhead related to the sampling method has only a small contribution to the total time (<1%) and, thus, is practically insignificant. Further, we analyzed the number of batches for each τ quadrature point for, both, sparse systems and dense systems. We found, that there is a decrease in batches with increasing τ quadrature points for sparse and dense systems. This shows, that our batching method is beneficial for both sparse and dense systems. Further, within the batching method, the three-center integrals and their **B**-field derivatives were stored on disk and read into memory within the respective batching scheme and transformed on the fly. As has been shown, the contribution from disk I/O operations is not the dominating step but it does have a significant contribution to the total time.

In future work, the efficiency of our method could be further improved by utilizing an integral-direct scheme for the integrals and their derivatives and combining the sparse sample batching method with an optimized batching scheme as introduced in ref 54.

The importance of our new NMR method is further highlighted by the possibility to use it as a basis for the implementation of NMR shieldings based on a method that is closely related to RPA, that is σ-functionals.[92,93] Due to the close relation of σ-functionals and RPA, it should be possible to implement analytical σ-functional NMR shieldings using our efficient RPA NMR implementation. This would provide another accurate and efficient method for the computation of NMR shieldings. Since σ-functionals[92,93] and extensions thereof[94−96] are being developed it would be interesting to explore these possibilities in future work.

■ ASSOCIATED CONTENT

Supporting Information

The Supporting Information is available free of charge at https://pubs.acs.org/doi/10.1021/acs.jpca.4c02773.

Batching algorithms and implementation details for all intermediates; detailed results for the batching of linear alkanes; timings for linear alkanes with dense and sparse matrix algebra employing the ω-CDD-RI-RPA-NMR method, and isotropic NMR shielding constants for $(DNA)_4$ (PDF)

https://doi.org/10.1021/acs.jpca.4c02773
J. Phys. Chem. A 2024, 128, 7950−7965

AUTHOR INFORMATION

Corresponding Author

Christian Ochsenfeld − *Chair of Theoretical Chemistry, Department of Chemistry, University of Munich (LMU), D-81377 Munich, Germany; Max Planck Institute for Solid State Research, D-70569 Stuttgart, Germany;* orcid.org/0000-0002-4189-6558; Email: christian.ochsenfeld@cup.uni-muenchen.de

Author

Viktoria Drontschenko − *Chair of Theoretical Chemistry, Department of Chemistry, University of Munich (LMU), D-81377 Munich, Germany*

Complete contact information is available at: https://pubs.acs.org/10.1021/acs.jpca.4c02773

Funding

Open access funded by Max Planck Society.

Notes

The authors declare no competing financial interest.

ACKNOWLEDGMENTS

The authors acknowledge financial support by the "Deutsche Forschungsgemeinschaft" (DFG) under Grant TRR325 "Assembly Controlled Chemical Photocatalysis" (grant No. 444632635) and the cluster of excellence (EXC2111-390814868) "Munich Center for Quantum Science and Technology" (MCQST). C.O. acknowledges additional support as Max-Planck-Fellow at the MPI-FKF Stuttgart. The authors thank Dr. H. Laqua (LMU Munich), F. Sacchetta (LMU Munich), and F. H. Bangerter (LMU Munich) for helpful discussions as well as Dr. J. Kussmann (LMU Munich) for providing a development version of the FERMIONS++ program package.

REFERENCES

(1) Gauss, J. Effects of electron correlation in the calculation of nuclear magnetic resonance chemical shifts. *J. Chem. Phys.* **1993**, *99*, 3629−3643.

(2) Helgaker, T.; Jaszunski, M.; Ruud, K. Ab initio methods for the calculation of NMR shielding and indirect spin-spin coupling constants. *Chem. Rev.* **1999**, *99*, 293−352.

(3) Casabianca, L. B.; De Dios, A. C. Ab initio calculations of NMR chemical shifts. *J. Chem. Phys.* **2008**, *128*, No. 052201.

(4) Bühl, M.; van Mourik, T. NMR spectroscopy: quantum-chemical calculations. *WIREs Comput. Mol. Sci.* **2011**, *1*, 634−647.

(5) Facelli, J. C. Chemical shift tensors: Theory and application to molecular structural problems. *Prog. Nucl. Magn. Reson. Spectrosc.* **2011**, *58*, 176−201.

(6) Harding, M. E.; Gauss, J.; von Ragué Schleyer, P. Why benchmark-quality computations are needed to reproduce 1-adamantyl cation NMR chemical shifts accurately. *J. Phys. Chem. A* **2011**, *115*, 2340−2344.

(7) Lodewyk, M. W.; Siebert, M. R.; Tantillo, D. J. Computational prediction of 1H and 13C chemical shifts: a useful tool for natural product, mechanistic, and synthetic organic chemistry. *Chem. Rev.* **2012**, *112*, 1839−1862.

(8) Stevens, R. M.; Pitzer, R.; Lipscomb, W. Perturbed Hartree−Fock Calculations. I. Magnetic Susceptibility and Shielding in the LiH Molecule. *J. Chem. Phys.* **1963**, *38*, 550−560.

(9) Ditchfield, R. Self-consistent perturbation theory of diamagnetism: I. A gauge-invariant LCAO method for NMR chemical shifts. *Mol. Phys.* **1974**, *27*, 789−807.

(10) Wolinski, K.; Hinton, J. F.; Pulay, P. Efficient implementation of the gauge-independent atomic orbital method for NMR chemical shift calculations. *J. Am. Chem. Soc.* **1990**, *112*, 8251−8260.

(11) Häser, M.; Ahlrichs, R.; Baron, H.; Weis, P.; Horn, H. Direct computation of second-order SCF properties of large molecules on workstation computers with an application to large carbon clusters. *Theor. Chim. Acta* **1992**, *83*, 455−470.

(12) Larsen, H.; Helgaker, T.; Olsen, J.; Jørgensen, P. Geometrical derivatives and magnetic properties in atomic-orbital density-based Hartree−Fock theory. *J. Chem. Phys.* **2001**, *115*, 10344−10352.

(13) Schreckenbach, G.; Ziegler, T. Calculation of NMR shielding tensors using gauge-including atomic orbitals and modern density functional theory. *J. Phys. Chem. A* **1995**, *99*, 606−611.

(14) Cheeseman, J. R.; Trucks, G. W.; Keith, T. A.; Frisch, M. J. A comparison of models for calculating nuclear magnetic resonance shielding tensors. *J. Chem. Phys.* **1996**, *104*, 5497−5509.

(15) Rauhut, G.; Puyear, S.; Wolinski, K.; Pulay, P. Comparison of NMR shieldings calculated from Hartree- Fock and density functional wave functions using gauge-including atomic orbitals. *J. Phys. Chem. A* **1996**, *100*, 6310−6316.

(16) Ochsenfeld, C.; Kussmann, J.; Koziol, F. Ab initio NMR spectra for molecular systems with a thousand and more atoms: a linear-scaling method. *Angew. Chem.* **2004**, *116*, 4585−4589.

(17) Kussmann, J.; Ochsenfeld, C. Linear-scaling method for calculating nuclear magnetic resonance chemical shifts using gauge-including atomic orbitals within Hartree-Fock and density-functional theory. *J. Chem. Phys.* **2007**, *127*, No. 054103.

(18) Gauss, J. Calculation of NMR chemical shifts at second-order many-body perturbation theory using gauge-including atomic orbitals. *Chem. Phys. Lett.* **1992**, *191*, 614−620.

(19) Gauss, J.; Stanton, J. F.Electron-Correlated Approaches for the Calculation of NMR Chemical Shifts. In *Advances in Chemical Physics*; John Wiley & Sons, 2002; Vol. *123*, pp 355−422.

(20) Ruud, K.; Helgaker, T.; Kobayashi, R.; Jørgensen, P.; Bak, K. L.; Jensen, H. J. A. Multiconfigurational self-consistent field calculations of nuclear shieldings using London atomic orbitals. *J. Chem. Phys.* **1994**, *100*, 8178−8185.

(21) Gauss, J.; Stanton, J. F. Gauge-invariant calculation of nuclear magnetic shielding constants at the coupled−cluster singles and doubles level. *J. Chem. Phys.* **1995**, *102*, 251−253.

(22) Gauss, J.; Stanton, J. F. Perturbative treatment of triple excitations in coupled-cluster calculations of nuclear magnetic shielding constants. *J. Chem. Phys.* **1996**, *104*, 2574−2583.

(23) Kállay, M.; Gauss, J. Analytic second derivatives for general coupled-cluster and configuration-interaction models. *J. Chem. Phys.* **2004**, *120*, 6841−6848.

(24) Flaig, D.; Maurer, M.; Hanni, M.; Braunger, K.; Kick, L.; Thubauville, M.; Ochsenfeld, C. Benchmarking hydrogen and carbon NMR chemical shifts at HF, DFT, and MP2 levels. *J. Chem. Theory Comput.* **2014**, *10*, 572−578.

(25) Stoychev, G. L.; Auer, A. A.; Neese, F. Efficient and accurate prediction of nuclear magnetic resonance shielding tensors with double-hybrid density functional theory. *J. Chem. Theory Comput.* **2018**, *14*, 4756−4771.

(26) Gauss, J.; Stanton, J. F. Analytic CCSD(T) second derivatives. *Chem. Phys. Lett.* **1997**, *276*, 70−77.

(27) Kollwitz, M.; Gauss, J. A direct implementation of the GIAO-MBPT (2) method for calculating NMR chemical shifts. Application to the naphthalenium and anthracenium ions. *Chem. Phys. Lett.* **1996**, *260*, 639−646.

(28) Gauss, J.; Werner, H.-J. NMR chemical shift calculations within local correlation methods: the GIAO-LMP2 approach. *Phys. Chem. Chem. Phys.* **2000**, *2*, 2083−2090.

(29) Grimme, S. Improved second-order Møller−Plesset perturbation theory by separate scaling of parallel-and antiparallel-spin pair correlation energies. *J. Chem. Phys.* **2003**, *118*, 9095−9102.

(30) Jung, Y.; Lochan, R. C.; Dutoi, A. D.; Head-Gordon, M. Scaled opposite-spin second order Møller−Plesset correlation energy: An

economical electronic structure method. *J. Chem. Phys.* **2004**, *121*, 9793−9802.
(31) Loibl, S.; Schütz, M. NMR shielding tensors for density fitted local second-order Møller-Plesset perturbation theory using gauge including atomic orbitals. *J. Chem. Phys.* **2012**, *137*, No. 084107.
(32) Maurer, M.; Ochsenfeld, C. A linear-and sublinear-scaling method for calculating NMR shieldings in atomic orbital-based second-order Møller-Plesset perturbation theory. *J. Chem. Phys.* **2013**, *138*, No. 174104.
(33) Maurer, M.; Ochsenfeld, C. Spin Component-Scaled Second-Order Møller−Plesset Perturbation Theory for Calculating NMR Shieldings. *J. Chem. Theory Comput.* **2015**, *11*, 37−44.
(34) Glasbrenner, M.; Vogler, S.; Ochsenfeld, C. Efficient low-scaling computation of NMR shieldings at the second-order Møller−Plesset perturbation theory level with Cholesky-decomposed densities and an attenuated Coulomb metric. *J. Chem. Phys.* **2021**, *155*, No. 224107.
(35) Burger, S.; Lipparini, F.; Gauss, J.; Stopkowicz, S. NMR chemical shift computations at second-order Møller−Plesset perturbation theory using gauge-including atomic orbitals and Cholesky-decomposed two-electron integrals. *J. Chem. Phys.* **2021**, *155*, No. 074105.
(36) Stoychev, G. L.; Auer, A. A.; Gauss, J.; Neese, F. DLPNO-MP2 second derivatives for the computation of polarizabilities and NMR shieldings. *J. Chem. Phys.* **2021**, *154*, No. 164110.
(37) Glasbrenner, M.; Graf, D.; Ochsenfeld, C. Benchmarking the Accuracy of the Direct Random Phase Approximation and σ-Functionals for NMR Shieldings. *J. Chem. Theory Comput.* **2022**, *18*, 192−205.
(38) Drontschenko, V.; Bangerter, F. H.; Ochsenfeld, C. Analytical second-order properties for the random phase approximation: Nuclear magnetic resonance shieldings. *J. Chem. Theory Comput.* **2023**, *19*, 7542−7554.
(39) Kohn, W.; Sham, L. J. Self-consistent equations including exchange and correlation effects. *Phys. Rev.* **1965**, *140*, No. A1133.
(40) Perdew, J. P.; Schmidt, K. In *Jacob's Ladder of Density Functional Approximations for the Exchange-Correlation Energy*, AIP Conference Proccedings; AIP Publishing, 2001; pp 1−20.
(41) Hohenberg, P.; Kohn, W. Inhomogeneous electron gas. *Phys. Rev.* **1964**, *136*, No. B864.
(42) Langreth, D. C.; Perdew, J. P. The exchange-correlation energy of a metallic surface. *Solid State Commun.* **1975**, *17*, 1425−1429.
(43) Gunnarsson, O.; Lundqvist, B. I. Exchange and correlation in atoms, molecules, and solids by the spin-density-functional formalism. *Phys. Rev. B* **1976**, *13*, No. 4274.
(44) Langreth, D. C.; Perdew, J. P. Exchange-correlation energy of a metallic surface: Wave-vector analysis. *Phys. Rev. B* **1977**, *15*, No. 2884.
(45) Chen, G. P.; Voora, V. K.; Agee, M. M.; Balasubramani, S. G.; Furche, F. Random-phase approximation methods. *Annu. Rev. Phys. Chem.* **2017**, *68*, 421−445.
(46) Ren, X.; Rinke, P.; Joas, C.; Scheffler, M. Random-phase approximation and its applications in computational chemistry and materials science. *J. Mater. Sci.* **2012**, *47*, 7447−7471.
(47) Heßelmann, A.; Görling, A. Random-phase approximation correlation methods for molecules and solids. *Mol. Phys.* **2011**, *109*, 2473−2500.
(48) Co', G. Introducing the random phase approximation theory. *Universe* **2023**, *9*, No. 141.
(49) Feyereisen, M.; Fitzgerald, G.; Komornicki, A. Use of approximate integrals in ab initio theory. An application in MP2 energy calculations. *Chem. Phys. Lett.* **1993**, *208*, 359−363.
(50) Schurkus, H. F.; Ochsenfeld, C. Communication: An effective linear-scaling atomic-orbital reformulation of the random-phase approximation using a contracted double-Laplace transformation. *J. Chem. Phys.* **2016**, *144*, No. 031101.
(51) Luenser, A.; Schurkus, H. F.; Ochsenfeld, C. Vanishing-overhead linear-scaling random phase approximation by Cholesky decomposition and an attenuated Coulomb-metric. *J. Chem. Theory Comput.* **2017**, *13*, 1647−1655.
(52) Graf, D.; Beuerle, M.; Schurkus, H. F.; Luenser, A.; Savasci, G.; Ochsenfeld, C. Accurate and Efficient Parallel Implementation of an Effective Linear-Scaling Direct Random Phase Approximation Method. *J. Chem. Theory Comput.* **2018**, *14*, 2505−2515.
(53) Beuerle, M.; Ochsenfeld, C. Low-scaling analytical gradients for the direct random phase approximation using an atomic orbital formalism. *J. Chem. Phys.* **2018**, *149*, No. 244111.
(54) Drontschenko, V.; Graf, D.; Laqua, H.; Ochsenfeld, C. Lagrangian-based minimal-overhead batching scheme for the efficient integral-direct evaluation of the RPA correlation energy. *J. Chem. Theory Comput.* **2021**, *17*, 5623−5634.
(55) Einstein, A. The foundation of the general theory of relativity. *Ann. Phys.* **1916**, *354*, No. 769.
(56) Furche, F.; Van Voorhis, T. Fluctuation-dissipation theorem density-functional theory. *J. Chem. Phys.* **2005**, *122*, No. 164106.
(57) Furche, F. Developing the random phase approximation into a practical post-Kohn-Sham correlation model. *J. Chem. Phys.* **2008**, *129*, No. 114105.
(58) Eshuis, H.; Yarkony, J.; Furche, F. Fast computation of molecular random phase approximation correlation energies using resolution of the identity and imaginary frequency integration. *J. Chem. Phys.* **2010**, *132*, No. 234114.
(59) Eshuis, H.; Furche, F. Basis set convergence of molecular correlation energy differences within the random phase approximation. *J. Chem. Phys.* **2012**, *136*, No. 084105.
(60) Kaltak, M.; Klimes, J.; Kresse, G. Low scaling algorithms for the random phase approximation: Imaginary time and Laplace transformations. *J. Chem. Theory Comput.* **2014**, *10*, 2498−2507.
(61) Hedin, L. New method for calculating the one-particle Green's function with application to the electron-gas problem. *Phys. Rev.* **1965**, *139*, No. A796.
(62) Ayala, P. Y.; Scuseria, G. E. Linear scaling second-order M? ller−Plesset theory in the atomic orbital basis for large molecular systems. *J. Chem. Phys.* **1999**, *110*, 3660−3671.
(63) Pulay, P. Ab initio calculation of force constants and equilibrium geometries in polyatomic molecules: I. Theory. *Mol. Phys.* **1969**, *17*, 197−204.
(64) Schweizer, S.; Doser, B.; Ochsenfeld, C. An atomic orbital-based reformulation of energy gradients in second-order Møller−Plesset perturbation theory. *J. Chem. Phys.* **2008**, *128*, No. 154101.
(65) Handy, N. C.; Schaefer, H. F., III On the evaluation of analytic energy derivatives for correlated wave functions. *J. Chem. Phys.* **1984**, *81*, 5031−5033.
(66) Beer, M.; Ochsenfeld, C. Efficient linear-scaling calculation of response properties: Density matrix-based Laplace-transformed coupled-perturbed self-consistent field theory. *J. Chem. Phys.* **2008**, *128*, No. 221102.
(67) Vahtras, O.; Almlöf, J.; Feyereisen, M. Integral approximations for LCAO-SCF calculations. *Chem. Phys. Lett.* **1993**, *213*, 514−518.
(68) Jung, Y.; Sodt, A.; Gill, P. M.; Head-Gordon, M. Auxiliary basis expansions for large-scale electronic structure calculations. *Proc. Natl. Acad. Sci. U.S.A.* **2005**, *102*, 6692−6697.
(69) Jung, Y.; Shao, Y.; Head-Gordon, M. Fast evaluation of scaled opposite spin second-order Møller−Plesset correlation energies using auxiliary basis expansions and exploiting sparsity. *J. Comput. Chem.* **2007**, *28*, 1953−1964.
(70) Koch, H.; de Merás, A. S.; Pedersen, T. B. Reduced scaling in electronic structure calculations using Cholesky decompositions. *J. Chem. Phys.* **2003**, *118*, 9481−9484.
(71) Higham, N. J. Cholesky factorization. *WIREs Comput. Stat.* **2009**, *1*, 251−254.
(72) Harbrecht, H.; Peters, M.; Schneider, R. On the low-rank approximation by the pivoted Cholesky decomposition. *Appl. Numer. Math.* **2012**, *62*, 428−440.
(73) Zienau, J.; Clin, L.; Doser, B.; Ochsenfeld, C. Cholesky-decomposed densities in Laplace-based second-order Møller−Plesset perturbation theory. *J. Chem. Phys.* **2009**, *130*, No. 204112.

https://doi.org/10.1021/acs.jpca.4c02773
J. Phys. Chem. A 2024, 128, 7950−7965

(74) Maurer, S. A.; Clin, L.; Ochsenfeld, C. Cholesky-decomposed density MP2 with density fitting: Accurate MP2 and double-hybrid DFT energies for large systems. *J. Chem. Phys.* **2014**, *140*, No. 224112.
(75) Sacchetta, F.; Graf, D.; Laqua, H.; Ambroise, M.; Kussmann, J.; Dreuw, A.; Ochsenfeld, C. An effective sub-quadratic scaling atomic-orbital reformulation of the scaled opposite-spin RI-CC2 ground-state model using Cholesky-decomposed densities and an attenuated Coulomb metric. *J. Chem. Phys.* **2022**, *157*, No. 104104.
(76) Beran, G. J. O.; Head-Gordon, M.; Gwaltney, S. R. Second-order correction to perfect pairing: An inexpensive electronic structure method for the treatment of strong electron-electron correlations. *J. Chem. Phys.* **2006**, *124*, No. 114107.
(77) Head-Gordon, M.; Beran, G. J.; Sodt, A.; Jung, Y. Fast electronic structure methods for strongly correlated molecular systems. *J. Phys.: Conf. Ser.* **2005**, *16*, No. 233.
(78) Beran, G. J. O.; Austin, B.; Sodt, A.; Head-Gordon, M. Unrestricted perfect pairing: The simplest wave-function-based model chemistry beyond mean field. *J. Phys. Chem. A* **2005**, *109*, 9183−9192.
(79) Schmitz, G.; Madsen, N. K.; Christiansen, O. Atomic-batched tensor decomposed two-electron repulsion integrals. *J. Chem. Phys.* **2017**, *146*, No. 134112.
(80) Schmitz, G.; Christiansen, O. Assessment of the overlap metric in the context of RI-MP2 and atomic batched tensor decomposed MP2. *Chem. Phys. Lett.* **2018**, *701*, 7−14.
(81) Stocks, R.; Palethorpe, E.; Barca, G. M. High-performance multi-GPU analytic RI-MP2 energy gradients. *J. Chem. Theory Comput.* **2024**, *20*, 2505−2519.
(82) Rhee, Y. M.; Head-Gordon, M. Scaled second-order perturbation corrections to configuration interaction singles: Efficient and reliable excitation energy methods. *J. Phys. Chem. A* **2007**, *111*, 5314−5326.
(83) Kussmann, J.; Ochsenfeld, C. Pre-selective screening for matrix elements in linear-scaling exact exchange calculations. *J. Chem. Phys.* **2013**, *138*, No. 134114.
(84) Kussmann, J.; Ochsenfeld, C. Preselective screening for linear-scaling exact exchange-gradient calculations for graphics processing units and general strong-scaling massively parallel calculations. *J. Chem. Theory Comput.* **2015**, *11*, 918−922.
(85) Kussmann, J.; Ochsenfeld, C. Hybrid CPU/GPU Integral Engine for Strong-Scaling Ab Initio Methods. *J. Chem. Theory Comput.* **2017**, *13*, 3153−3159.
(86) Liu, P.; Kaltak, M.; Klimeš, J.; Kresse, G. Cubic scaling G W: Towards fast quasiparticle calculations. *Phys. Rev. B* **2016**, *94*, No. 165109.
(87) Peterson, K. A.; Dunning, T. H., Jr Accurate correlation consistent basis sets for molecular core-valence correlation effects: The second row atoms Al-Ar, and the first row atoms B-Ne revisited. *J. Chem. Phys.* **2002**, *117*, 10548−10560.
(88) Hättig, C. Optimization of auxiliary basis sets for RI-MP2 and RI-CC2 calculations: Core-valence and quintuple-ζ basis sets for H to Ar and QZVPP basis sets for Li to Kr. *Phys. Chem. Chem. Phys.* **2005**, *7*, 59−66.
(89) Teale, A. M.; Lutnæs, O. B.; Helgaker, T.; Tozer, D. J.; Gauss, J. Benchmarking density-functional theory calculations of NMR shielding constants and spin−rotation constants using accurate coupled-cluster calculations. *J. Chem. Phys.* **2013**, *138*, No. 024111.
(90) Sedlak, R.; Janowski, T.; Pitonak, M.; Rezac, J.; Pulay, P.; Hobza, P. Accuracy of quantum chemical methods for large noncovalent complexes. *J. Chem. Theory Comput.* **2013**, *9*, 3364−3374.
(91) Brown, S. P.; Schaller, T.; Seelbach, U. P.; Koziol, F.; Ochsenfeld, C.; Klärner, F. G.; Spiess, H. W. Structure and dynamics of the host-guest complex of a molecular tweezer: Coupling synthesis, solid-state NMR, and quantum-chemical calculations. *Angew. Chem., Int. Ed.* **2001**, *40*, 717−720.
(92) Trushin, E.; Thierbach, A.; Görling, A. Toward chemical accuracy at low computational cost: Density-functional theory with σ-functionals for the correlation energy. *J. Chem. Phys.* **2021**, *154*, No. 014104.
(93) Fauser, S.; Trushin, E.; Neiss, C.; Görling, A. Chemical accuracy with σ-functionals for the Kohn−Sham correlation energy optimized for different input orbitals and eigenvalues. *J. Chem. Phys.* **2021**, *155*, No. 134111.
(94) Erhard, J.; Fauser, S.; Trushin, E.; Görling, A. Scaled σ-functionals for the Kohn−Sham correlation energy with scaling functions from the homogeneous electron gas. *J. Chem. Phys.* **2022**, *157*, No. 114105.
(95) Lemke, Y.; Graf, D.; Kussmann, J.; Ochsenfeld, C. An assessment of orbital energy corrections for the direct random phase approximation and explicit σ-functionals. *Mol. Phys.* **2023**, *121*, No. e2098862.
(96) Lemke, Y.; Ochsenfeld, C. Highly accurate σ-and τ-functionals for beyond-RPA methods with approximate exchange kernels. *J. Chem. Phys.* **2023**, *159*, No. 194104.

https://doi.org/10.1021/acs.jpca.4c02773
J. Phys. Chem. A 2024, 128, 7950−7965

Supporting Information: Low-Scaling, Efficient and Memory Optimized Computation of Nuclear Magnetic Resonance Shieldings within the Random Phase Approximation using Cholesky-Decomposed Densities and an Attenuated Coulomb Metric

Viktoria Drontschenko[†] and Christian Ochsenfeld[*,†,‡]

†*Chair of Theoretical Chemistry, Department of Chemistry, University of Munich (LMU), D-81377 Munich, Germany*

‡*Max Planck Institute for Solid State Research, D-70569 Stuttgart, Germany*

E-mail: christian.ochsenfeld@cup.uni-muenchen.de

Contents

1 Memory Efficient Implementation

1.1 Batching Scheme: $\mathbf{\Sigma}(\mathrm{i}\tau)$

The computation of the self-energy is shown in Algorithm 1. First the intermediate $\mathbb{W}$ is computed (lines 1-12) and written on disk. For efficiency, lines 5-9 are implemented as a matrix multiplication. Then, within a separate batching scheme, $\mathbb{W}$ and the three-center integrals are read into memory for one auxiliary function batch (aux-batch) (lines 14 and 15, respectively). It should be noted that quantities are read into memory for one aux-batch at a time, rather than one auxiliary function, in order to optimize reading performance, since processing larger data in fewer instances is more efficient than repeatedly processing smaller amounts of data. Then, in lines 17-21, the self-energy in the negative imaginary time domain is computed for one auxiliary function at a time. In lines 23-27 the self-energy in the positive imaginary time domain is computed, again, for one auxiliary function at a time. To increase computational efficiency, we parallelize over the auxiliary function indices (lines 17-21 and 23-27). It should be noted that $\mathbf{\Sigma}(\mathrm{i}\tau)$ and $\mathbf{\Sigma}(-\mathrm{i}\tau)$ are computed within the same batching scheme, since the memory demanding third order tensors are computed for one auxiliary function at a time and, thus, do not show high memory requirements. The memory requirements for the batching method are rather determined by the memory demands of $\mathbb{W}$ and $\mathbb{B}$, which are loaded into memory for one aux-batch.

Algorithm 1 $\mathbf{\Sigma}(\pm \mathrm{i}\tau)$ per $\tau \geq 0$

1: ▷ Calculate $\mathbb{W}^P(\mathrm{i}\tau)(\forall P)$ and write on disk
2: **for** aux-batch1 **do**
3: **for** aux-batch2 **do**
4: read $\mathbf{B}^Q \quad \forall Q \in$ aux-batch2
5: **for** $P \in$ aux-batch1 **do**
6: **for** $Q \in$ aux-batch2 **do**
7: $\mathbb{W}^P_{\mu\nu}(\mathrm{i}\tau)$ += $W_{\mathrm{c},PQ}(\mathrm{i}\tau)\mathbb{B}^Q_{\mu\nu} \quad \forall \mu, \nu$
8: **end for**
9: **end for**
10: **end for**
11: write on disk $\mathbb{W}^P_{\mu\nu}(\mathrm{i}\tau) \quad \forall \mu, \nu, P \in$ aux-batch1
12: **end for**
13: **for** aux-batch1 **do**
14: read $\mathbb{W}^P(\mathrm{i}\tau) \quad \forall P \in$ aux-batch1
15: read $\mathbb{B}^P \quad \forall P \in$ aux-batch1
16: ▷ Calculate $\mathbf{\Sigma}(-\mathrm{i}\tau)$
17: **for** $P \in$ aux-batch1 **do** ▷ parallel
18: $\underline{\mathbb{W}}^P_{\mu\underline{i}}(\mathrm{i}\tau) = \mathbb{W}^P_{\mu\nu}(\mathrm{i}\tau)L_{\nu\underline{i}} \quad \forall \mu, \underline{i}$
19: $\underline{\mathbb{B}}^P_{\nu\underline{j}} = \mathbb{B}^P_{\nu\lambda}L_{\lambda\underline{j}} \quad \forall \nu, \underline{j}$
20: $\Sigma_{\mu\nu}(-\mathrm{i}\tau)$ += $\underline{\mathbb{W}}^P_{\mu\underline{i}}(\mathrm{i}\tau)\underline{G}_{=0,\underline{i}\underline{j}}(-\mathrm{i}\tau)\underline{\mathbb{B}}^P_{\nu\underline{j}} \quad \forall \mu, \nu$
21: **end for**
22: ▷ Calculate $\mathbf{\Sigma}(\mathrm{i}\tau)$
23: **for** $P \in$ aux-batch1 **do** ▷ parallel
24: $\overline{\mathbb{W}}^P_{\mu\underline{a}}(\mathrm{i}\tau) = \mathbb{W}^P_{\mu\nu}(\mathrm{i}\tau)L_{\mathrm{virt},\nu\underline{a}}(\mathrm{i}\tau) \quad \forall \mu, \underline{a}$
25: $\overline{\mathbb{B}}^P_{\nu\underline{a}}(\mathrm{i}\tau) = \mathbb{B}^P_{\nu\lambda}L_{\mathrm{virt},\lambda\underline{a}}(\mathrm{i}\tau) \quad \forall \nu, \underline{a}$
26: $\Sigma_{\mu\nu}(\mathrm{i}\tau)$ += $\overline{\mathbb{W}}^P_{\mu\underline{a}}(\mathrm{i}\tau)\overline{\mathbb{B}}^P_{\nu\underline{a}}(\mathrm{i}\tau) \quad \forall \mu, \nu$
27: **end for**
28: **end for**

1.2 Batching Scheme: $\mathbf{X}_0(\mathrm{i}\tau)$

For the computation of the response function in Algorithm 2, the three-center integrals are read into memory for one aux-batch (line 2) and subsequently transformed with the Cholesky matrix $\mathbf{L}$ (line 4) and used for the computation of the intermediate $\tilde{\underline{\mathbb{B}}}^P_{\underline{a}i}(\mathrm{i}\tau)$ (line 5). In a second aux-batch loop, the three-center integrals are read into memory for the respective aux-batch (line 8) and used to compute the intermediate $\overline{\underline{\mathbb{B}}}^Q_{\underline{a}i}(\mathrm{i}\tau)$. Finally, in line 14 the response function is computed by multiplying both intermediates. It should be noted that the symmetry of the response function is exploited for the second aux-batch loop (lines 7-17). Further, lines 12-16 are implemented as a matrix multiplication. The loops over the auxiliary function indices are parallelized (lines 3-6 and 9-11).

Algorithm 2 $\mathbf{X}_0(\mathrm{i}\tau)$ per $\tau \geq 0$

1: **for** aux-batch1 **do**
2: read $\mathbb{B}^P_{\mu\nu} \quad \forall \mu, \nu, P \in$ aux-batch1
3: **for** $P \in$ aux-batch1 **do** ▷ parallel
4: $\underline{\mathbb{B}}^P_{\mu \underline{j}} = \mathbb{B}^P_{\mu\nu} L_{\nu \underline{j}} \quad \forall \underline{j}, \mu$
5: $\tilde{B}^P_{\underline{a}\underline{i}}(\mathrm{i}\tau) = \underline{\underline{G}}_{0,\underline{i}\underline{j}}(-\mathrm{i}\tau) \underline{\mathbb{B}}^P_{\mu \underline{j}} L_{\mathrm{virt},\mu\underline{a}}(\mathrm{i}\tau) \quad \forall \underline{i}, \underline{a}$
6: **end for**
7: **for** aux-batch2 $\geq$ aux-batch1 **do**
8: read $\mathbb{B}^Q_{\mu\nu} \quad \forall \mu, \nu, Q \in$ aux-batch2
9: **for** $Q \in$ aux-batch2 **do** ▷ parallel
10: $\overline{\underline{\mathbb{B}}}^Q_{\underline{a}\underline{i}}(\mathrm{i}\tau) = L_{\mathrm{virt},\mu\underline{a}}(\mathrm{i}\tau) \mathbb{B}^Q_{\mu\nu} L_{\nu \underline{i}} \quad \forall \underline{i}, \underline{a}$
11: **end for**
12: **for** $P \in$ aux-batch1 **do**
13: **for** $Q \in$ aux-batch2 **do**
14: $X_{0,PQ}(\mathrm{i}\tau) = \tilde{B}^P_{\underline{a}\underline{i}}(\mathrm{i}\tau) \overline{\underline{\mathbb{B}}}^Q_{\underline{a}\underline{i}}(\mathrm{i}\tau)$
15: **end for**
16: **end for**
17: **end for**
18: **end for**

1.3 Batching Scheme: $\boldsymbol{\Sigma}^{\mathbf{B}}(\mathrm{i}\tau)$

A general outline for the computation of $\boldsymbol{\Sigma}^{\mathbf{B}}(\mathrm{i}\tau)$ is provided in Algorithm 3. First, the partial derivative with respect to $\tilde{\mathbf{W}}_{\mathrm{c}}(-\mathrm{i}\tau)$ is computed (line 2). Next, the intermediate $\mathbb{W}(\mathrm{i}\tau)$ is computed and written on disk as shown in Algorithm 1 lines 1-13. This intermediate is read into memory for the computation of the remaining partial derivatives, that is, the partial derivative with respect to the Green's function (line 4) and three-center integrals (line 5). All partial derivative terms (lines 2-4) are computed for the **B**-field derivative of the self-energy in the positive and negative imaginary time domain within the same batching scheme.

Algorithm 3 $\boldsymbol{\Sigma}^{\mathbf{B}}(\mathrm{i}\tau) \quad \forall \tau \in (-\infty, +\infty)$

1: **for all** τ **do**
2: calc. $\frac{\partial \boldsymbol{\Sigma}(\mathrm{i}\tau)}{\partial \tilde{\mathbf{W}}_{\mathrm{c}}(-\mathrm{i}\tau)} \frac{\partial \tilde{\mathbf{W}}_{\mathrm{c}}(-\mathrm{i}\tau)}{\partial \mathbf{B}}$
3: calc. batched $\mathbb{W}^P(\mathrm{i}\tau)(\forall P)$; write on disk
4: calc. $\frac{\partial \boldsymbol{\Sigma}(\mathrm{i}\tau)}{\partial \mathbf{G}_0(\mathrm{i}\tau)} \frac{\partial \mathbf{G}_0(\mathrm{i}\tau)}{\partial \mathbf{B}}$
5: calc. $\frac{\partial \boldsymbol{\Sigma}(\mathrm{i}\tau)}{\partial \mathbb{B}^P} \frac{\partial \mathbb{B}^P}{\partial \mathbf{B}}(\forall P)$
6: **end for**

Algorithm 4 $\mathbf{X}^{\mathbf{B}}_0(\mathrm{i}\tau) \quad \forall \tau \geq 0$

1: **for all** τ **do**
2: calc. $\frac{\partial \mathbf{X}_0(\mathrm{i}\tau)}{\partial \mathbf{G}_0(-\mathrm{i}\tau)} \frac{\partial \mathbf{G}_0(-\mathrm{i}\tau)}{\partial \mathbf{B}}$
3: calc. batched $\underline{\tilde{\mathbb{B}}}^P_{\mu \underline{i}}(-\mathrm{i}\tau)(\forall P, \mu, \underline{i})$; write on disk
4: calc. $\frac{\partial \mathbf{X}_0(\mathrm{i}\tau)}{\partial \mathbf{G}_0(\mathrm{i}\tau)} \frac{\partial \mathbf{G}_0(\mathrm{i}\tau)}{\partial \mathbf{B}}$
5: calc. $\frac{\partial \mathbf{X}_0(\mathrm{i}\tau)}{\partial \mathbb{B}^P} \frac{\partial \mathbb{B}^P}{\partial \mathbf{B}}(\forall P)$
6: **end for**

1.3.1 Partial Derivative Term: $\frac{\partial \mathbf{\Sigma}(\pm i\tau)}{\partial \mathbb{B}} \frac{\partial \mathbb{B}}{\partial \mathbf{B}}$

The computation of the partial derivative with respect to the three-center integrals is shown Algorithm 5. Here, first, $\mathbb{W}(i\tau)$ is read into memory for one aux-batch. Next, the $\mathbf{B}$-field derivatives of the three-center integrals are read into memory for one aux-batch and all magnetic field directions. Next, the contribution to $\mathbf{\Sigma}^{\mathbf{B}}(-i\tau)$ is computed for one aux-function at a time (lines 7-13). Here, the intermediate $\underline{\mathbb{W}}(i\tau)$ is computed first and subsequently used to compute the contribution to $\mathbf{\Sigma}^{\mathbf{B}}(-i\tau)$ for one magnetic field direction at a time. The contribution to $\mathbf{\Sigma}^{\mathbf{B}}(i\tau)$ is computed in lines 15-21. A similar loop structure is used, starting with a loop over auxiliary functions, where $\overline{\mathbb{W}}(i\tau)$ is computed and used to compute the contribution to $\mathbf{\Sigma}^{\mathbf{B}}(i\tau)$ (lines 18 and 19) for one $\mathbf{B}$-field direction at a time. The loops over the auxiliary function indices (lines 7-13 and 15-21) are parallelized. Since the contribution to the derivative of the self-energy in the positive and negative imaginary time domain is computed for one auxiliary function at a time, the memory demand of this algorithm is determined by $\mathbb{W}(i\tau)$ and the derivatives of the three-center integrals. Therefore, it is sensible to combine the computation of the partial derivatives of the self-energy in the positive and negative imaginary time domain in one batching scheme.

Algorithm 5 $\frac{\partial \boldsymbol{\Sigma}(\pm \mathrm{i}\tau)}{\partial \mathbb{B}} \frac{\partial \mathbb{B}}{\partial \mathbf{B}}$ per $\tau \geq 0$

1: **for** aux-batch1 **do**
2: read $\mathbb{W}^P(\mathrm{i}\tau) \quad \forall P \in$ aux-batch1
3: **for** $B \in \mathbf{B} = \{B_x, B_y, B_z\}$ **do**
4: read $\left(\mathbb{B}^P_{\lambda\nu}\right)^B \quad \forall \lambda, \nu, P \in$ aux-batch1
5: **end for**
6: ▷ Calculate contribution to $\boldsymbol{\Sigma}^{\mathbf{B}}(-\mathrm{i}\tau)$
7: **for** $P \in$ aux-batch1 **do** ▷ parallel
8: $\underline{\mathbb{W}}^P_{\mu \underline{j}}(\mathrm{i}\tau) = \mathbb{W}^P_{\mu\nu}(\mathrm{i}\tau) L_{\nu i} \underline{\underline{G}}_{0,\underline{i}\underline{j}}(-\mathrm{i}\tau) \quad \forall \mu, \underline{j}$
9: **for** $B \in \mathbf{B} = \{B_x, B_y, B_z\}$ **do**
10: $\Sigma^B_{\mu\nu}(-\mathrm{i}\tau)$ += $\underline{\mathbb{W}}^P_{\mu \underline{j}}(\mathrm{i}\tau) \left(\mathbb{B}^P_{\lambda\nu}\right)^B L_{\lambda \underline{j}} \quad \forall \mu, \nu$
11: $\Sigma^B_{\nu\mu}(-\mathrm{i}\tau)$ −= $\Sigma^B_{\mu\nu}(-\mathrm{i}\tau) \quad \forall \mu, \nu$
12: **end for**
13: **end for**
14: ▷ Calculate contribution to $\boldsymbol{\Sigma}^{\mathbf{B}}(\mathrm{i}\tau)$
15: **for** $P \in$ aux-batch1 **do** ▷ parallel
16: $\overline{\mathbb{W}}^P_{\mu \underline{a}}(\mathrm{i}\tau) = \mathbb{W}^P_{\mu\nu}(\mathrm{i}\tau) L_{\mathrm{virt},\nu \underline{a}}(\mathrm{i}\tau) \quad \forall \mu, \underline{a}$
17: **for** $B \in \mathbf{B} = \{B_x, B_y, B_z\}$ **do**
18: $\Sigma^B_{\mu\nu}(\mathrm{i}\tau)$ += $\overline{\mathbb{W}}^P_{\mu \underline{a}}(\mathrm{i}\tau) \left(\mathbb{B}^P_{\lambda\nu}\right)^B L_{\mathrm{virt},\lambda \underline{a}}(\mathrm{i}\tau) \quad \forall \mu, \nu$
19: $\Sigma^B_{\nu\mu}(\mathrm{i}\tau)$ −= $\Sigma^B_{\mu\nu}(\mathrm{i}\tau) \quad \forall \mu, \nu$
20: **end for**
21: **end for**
22: **end for**
23:

1.3.2 Partial Derivative Term: $\frac{\partial \boldsymbol{\Sigma}(\pm \mathrm{i}\tau)}{\partial \tilde{\mathbf{W}}_{\mathbf{c}}(\mp \mathrm{i}\tau)} \frac{\partial \tilde{\mathbf{W}}_{\mathbf{c}}(\mp \mathrm{i}\tau)}{\partial \mathbf{B}}$

Algorithm 6 displays the detailed procedure for the computation of the partial derivative $\frac{\partial \boldsymbol{\Sigma}(\pm \mathrm{i}\tau)}{\partial \mathbf{W}_{\mathrm{c}}(\mp \mathrm{i}\tau)} \frac{\partial \mathbf{W}_{\mathrm{c}}(\mp \mathrm{i}\tau)}{\partial \mathbf{B}}$. The contributions to $\boldsymbol{\Sigma}^{\mathbf{B}}(-\mathrm{i}\tau)$ and $\boldsymbol{\Sigma}^{\mathbf{B}}(\mathrm{i}\tau)$ are computed within the same batching scheme. Lines 5-9 are implemented as a matrix multiplication.

Algorithm 6 $\frac{\partial \boldsymbol{\Sigma}(\pm \mathrm{i}\tau)}{\partial \tilde{\mathbf{W}}_{\mathrm{c}}(\mp \mathrm{i}\tau)} \frac{\partial \tilde{\mathbf{W}}_{\mathrm{c}}(\mp \mathrm{i}\tau)}{\partial \mathbf{B}}$ per $\tau \geq 0$

for aux-batch1 **do**
  for aux-batch2 **do**
    read $\mathbb{B}^Q \quad \forall Q \in$ aux-batch2
    for $B \in \mathbf{B} = \{B_x, B_y, B_z\}$ **do**
      for $P \in$ aux-batch1 **do**
        for $Q \in$ aux-batch2 **do**
          $\left(\mathbb{W}^P_{\mu\nu}\right)^B(\mathrm{i}\tau) = W^B_{\mathrm{c},PQ}(\mathrm{i}\tau)\mathbb{B}^Q_{\mu\nu} \quad \forall \mu, \nu$
        end for
      end for
    end for
  end for
  read $\mathbb{B}^P \quad \forall P \in$ aux-batch1
  ▷ Calculate contribution to $\boldsymbol{\Sigma}^{\mathbf{B}}(-\mathrm{i}\tau)$
  for $P \in$ aux-batch1 **do** ▷ parallel
    $\underline{\mathbb{B}}^P_{\nu \underline{j}} = \mathbb{B}^P_{\nu\mu} L_{\mu \underline{j}} \quad \forall \nu, \underline{j}$
    $\tilde{\underline{\mathbb{B}}}^P_{\nu \underline{i}}(-\mathrm{i}\tau) = \underline{G}_{0,\underline{i}\underline{j}}(-\mathrm{i}\tau)\underline{\mathbb{B}}^P_{\nu \underline{j}} \quad \forall \nu, \underline{i}$
    for $B \in \mathbf{B} = \{B_x, B_y, B_z\}$ **do**
      $\left(\tilde{\mathbb{W}}^P_{\mu \underline{i}}\right)^B(\mathrm{i}\tau) = \left(\mathbb{W}^P_{\mu\nu}\right)^B(\mathrm{i}\tau) L_{\nu \underline{i}} \quad \forall \mu, \nu, \underline{i}$
      $\Sigma^B_{\mu\nu}(-\mathrm{i}\tau) \mathrel{+}= \left(\tilde{\mathbb{W}}^P_{\mu \underline{i}}\right)^B(\mathrm{i}\tau) \tilde{\underline{\mathbb{B}}}^P_{\nu \underline{i}}(-\mathrm{i}\tau) \quad \forall \mu, \nu$
    end for
  end for
  ▷ Calculate contribution to $\boldsymbol{\Sigma}^{\mathbf{B}}(\mathrm{i}\tau)$
  for $P \in$ aux-batch1 **do** ▷ parallel
    $\overline{\underline{\mathbb{B}}}^P_{\mu \underline{a}} = \mathbb{B}^P_{\mu\nu} L_{\mathrm{virt},\nu \underline{a}}(\mathrm{i}\tau) \quad \forall \mu, \underline{a}$
    for $B \in \mathbf{B} = \{B_x, B_y, B_z\}$ **do**
      $\left(\tilde{\mathbb{W}}^P_{\mu \underline{a}}\right)^B(\mathrm{i}\tau) = \left(\mathbb{W}^P_{\mu\nu}\right)^B(\mathrm{i}\tau) L_{\mathrm{virt},\nu \underline{a}}(\mathrm{i}\tau) \quad \forall \mu, \underline{a}$
      $\Sigma^B_{\mu\nu}(\mathrm{i}\tau) \mathrel{+}= \left(\tilde{\mathbb{W}}^P_{\mu \underline{a}}\right)^B(\mathrm{i}\tau) \overline{\underline{\mathbb{B}}}^P_{\nu \underline{a}}(\mathrm{i}\tau) \quad \forall \mu, \nu$
    end for
  end for
end for

1.3.3 Partial Derivative Term: $\frac{\partial \boldsymbol{\Sigma}(\pm \mathrm{i}\tau)}{\partial \mathbf{G}_0(\pm \mathrm{i}\tau)} \frac{\partial \mathbf{G}_0(\pm \mathrm{i}\tau)}{\partial \mathbf{B}}$

Algorithm 7 shows the computation of the partial derivative $\frac{\partial \boldsymbol{\Sigma}(\pm \mathrm{i}\tau)}{\partial \mathbf{G}_0(\pm \mathrm{i}\tau)} \frac{\partial \mathbf{G}_0(\pm \mathrm{i}\tau)}{\partial \mathbf{B}}$. The contributions to $\boldsymbol{\Sigma}^{\mathbf{B}}(-\mathrm{i}\tau)$ and $\boldsymbol{\Sigma}^{\mathbf{B}}(\mathrm{i}\tau)$ are computed within the same batching scheme.

Algorithm 7 $\frac{\partial \boldsymbol{\Sigma}(\pm \mathrm{i}\tau)}{\partial \mathbf{G}_0(\pm \mathrm{i}\tau)} \frac{\partial \mathbf{G}_0(\pm \mathrm{i}\tau)}{\partial \mathbf{B}}$ per $\tau \geq 0$

1: **for** aux-batch1 **do**
2: read $\mathbb{B}^P \quad \forall P \in$ aux-batch1
3: read $\mathbb{W}^P(\mathrm{i}\tau) \quad \forall P \in$ aux-batch1
4: ▷ Calculate contribution to $\boldsymbol{\Sigma}^{\mathbf{B}}(-\mathrm{i}\tau)$
5: **for** $P \in$ aux-batch1 **do** ▷ parallel
6: **for** $B \in \mathbf{B} = \{B_x, B_y, B_z\}$ **do**
7: $\Sigma^B_{\mu\nu}(-\mathrm{i}\tau) \mathrel{-}= \mathbb{W}^P_{\mu\lambda} \underline{\underline{G}}^B_{0,\lambda\sigma}(-\mathrm{i}\tau) \mathbb{B}^P_{\sigma\nu} \quad \forall \mu, \nu$
8: **end for**
9: **end for**
10: ▷ Calculate contribution to $\boldsymbol{\Sigma}^{\mathbf{B}}(\mathrm{i}\tau)$
11: **for** $P \in$ aux-batch1 **do** ▷ parallel
12: **for** $B \in \mathbf{B} = \{B_x, B_y, B_z\}$ **do**
13: $\Sigma^B_{\mu\nu}(\mathrm{i}\tau) \mathrel{-}= \mathbb{W}^P_{\mu\lambda} \overline{G}^B_{0,\lambda\sigma}(\mathrm{i}\tau) \mathbb{B}^P_{\sigma\nu} \quad \forall \mu, \nu$
14: **end for**
15: **end for**
16: **end for**

1.4 Batching Scheme: $\mathbf{X}_0^{\mathbf{B}}(\mathrm{i}\tau)$

A general outline for the computation of $\mathbf{X}_0^{\mathbf{B}}(\mathrm{i}\tau)$ is provided in Algorithm 4.

$$\underline{\tilde{\mathbb{B}}}^P_{\mu \underline{i}}(-\mathrm{i}\tau) := \underline{\underline{G}}_{0,\underline{i}\underline{j}}(-\mathrm{i}\tau) \underline{\mathbb{B}}^P_{\mu \underline{j}} \tag{1}$$

is precomputed and written on disk (line 3) by batching over the auxiliary function index. This intermediate is then read into memory for the computation of the partial derivative with respect to $\overline{\mathbf{G}}_0(\mathrm{i}\tau)$ (line 4) as well as $\mathbb{B}$ (line 5).

1.4.1 Partial Derivative Term: $\frac{\partial \mathbf{X}_0(\mathrm{i}\tau)}{\partial \mathbb{B}} \frac{\partial \mathbb{B}}{\partial \mathbf{B}}$

The detailed computation of the partial derivative with respect to the three-center integrals is shown in Algorithm 8. First, the intermediate $\underline{\tilde{\mathbb{B}}}(-\mathrm{i}\tau)$ is read into memory for one aux-batch (line 2) and transformed with $\mathbf{L}_{\mathrm{virt}}(\mathrm{i}\tau)$ (line 4). In a second aux-batch loop, the $\mathbf{B}$-field derivatives of the three-center integrals are read into memory for one $\mathbf{B}$-field direction and one aux-batch and subsequently transformed in line 10. Finally, in lines 12-17 the derivative of the response function is computed per $\mathbf{B}$-field direction. Lines 12-17 are implemented as a matrix multiplication. Further, the loops over the auxiliary function indices are parallelized

(lines 3-5 and 9-11).

Algorithm 8 $\frac{\partial \mathbf{X}_0(\mathrm{i}\tau)}{\partial \mathbb{B}} \frac{\partial \mathbb{B}}{\partial \mathbf{B}}$ per $\tau \geq 0$

1: **for** aux-batch1 **do**
2: read $\tilde{\underline{\mathbb{B}}}^P_{\mu\underline{i}}(-\mathrm{i}\tau) \quad \forall \underline{i}, \mu, P \in$ aux-batch1
3: **for** $P \in$ aux-batch1 **do** ▷ parallel
4: $\tilde{B}^P_{\underline{a}\underline{i}}(\mathrm{i}\tau) = \tilde{\underline{\mathbb{B}}}^P_{\mu\underline{i}}(-\mathrm{i}\tau) L_{\mathrm{virt},\mu\underline{a}}(\mathrm{i}\tau) \quad \forall \underline{i}, \underline{a}$
5: **end for**
6: **for** aux-batch2 **do**
7: **for** $B \in \mathbf{B} = \{B_x, B_y, B_z\}$ **do**
8: read $\left(\mathbb{B}^Q_{\mu\nu}\right)^B \quad \forall \mu, \nu, Q \in$ aux-batch2
9: **for** $Q \in$ aux-batch2 **do** ▷ parallel
10: $\left(\overline{\underline{\mathbb{B}}}^Q_{\underline{a}\underline{i}}\right)^B(\mathrm{i}\tau) = L_{\mathrm{virt},\mu\underline{a}}(\mathrm{i}\tau)\left(\mathbb{B}^Q_{\mu\nu}\right)^B L_{\nu\underline{i}} \quad \forall \underline{i}, \underline{a}$
11: **end for**
12: **for** $P \in$ aux-batch1 **do**
13: **for** $Q \in$ aux-batch2 **do**
14: $X^B_{0,PQ}(\mathrm{i}\tau) \mathrel{+}= \tilde{B}^P_{\underline{a}\underline{i}}(\mathrm{i}\tau)\left(\overline{\underline{\mathbb{B}}}^Q_{\underline{a}\underline{i}}\right)^B(\mathrm{i}\tau)$
15: $X^B_{0,QP}(\mathrm{i}\tau) \mathrel{-}= X^B_{0,PQ}(\mathrm{i}\tau)$
16: **end for**
17: **end for**
18: **end for**
19: **end for**
20: **end for**

1.4.2 Partial Derivative Term: $\frac{\partial \mathbf{X}_0(\mathrm{i}\tau)}{\partial \underline{\mathbf{G}}_0(-\mathrm{i}\tau)} \frac{\partial \underline{\mathbf{G}}_0(-\mathrm{i}\tau)}{\partial \mathbf{B}}$

The computation of the partial derivative $\frac{\partial \mathbf{X}_0(\mathrm{i}\tau)}{\partial \underline{\mathbf{G}}_0(-\mathrm{i}\tau)} \frac{\partial \underline{\mathbf{G}}_0(-\mathrm{i}\tau)}{\partial \mathbf{B}}$ is given in Algorithm 9. Lines 15-19 are implemented as a matrix multiplication.

Algorithm 9 $\frac{\partial \mathbf{X}_0(\mathrm{i}\tau)}{\partial \underline{\mathbf{G}}_0(-\mathrm{i}\tau)} \frac{\partial \underline{\mathbf{G}}_0(-\mathrm{i}\tau)}{\partial \mathbf{B}}$ per $\tau \geq 0$

1: **for** aux-batch1 **do**
2: read $\mathbb{B}^P \quad \forall P \in$ aux-batch1
3: **for** $P \in$ aux-batch1 **do** ▷ parallel
4: $\overline{\mathbb{B}}^P_{\mu\underline{a}} = \mathbb{B}^P_{\mu\nu} L_{\mathrm{virt},\nu\underline{a}}(\mathrm{i}\tau) \quad \forall \mu, \underline{a}$
5: **end for**
6: **for** aux-batch2 $\geq$ aux-batch1 **do**
7: read $\mathbb{B}^Q \quad \forall Q \in$ aux-batch2
8: **for** $Q \in$ aux-batch2 **do** ▷ parallel
9: $\overline{\mathbb{B}}^Q_{\mu\underline{a}}(\mathrm{i}\tau) = \mathbb{B}^Q_{\mu\nu} L_{\mathrm{virt},\nu\underline{a}}(\mathrm{i}\tau) \quad \forall \mu, \underline{a}$
10: **end for**
11: **for** $B \in \mathbf{B} = \{B_x, B_y, B_z\}$ **do**
12: **for** $Q \in$ aux-batch2 **do** ▷ parallel
13: $\big(\tilde{\mathbb{B}}^Q_{\mu\underline{a}}\big)^B(\mathrm{i}\tau) = \overline{\mathbb{B}}^Q_{\nu\underline{a}} \underline{G}^B_{0,\nu\mu}(-\mathrm{i}\tau) \quad \forall \mu, \underline{a}$
14: **end for**
15: **for** $P \in$ aux-batch1 **do**
16: **for** $Q \in$ aux-batch2 **do**
17: $X^B_{0,PQ}(\mathrm{i}\tau)$ += $\overline{\mathbb{B}}^P_{\mu\underline{a}} \big(\tilde{\mathbb{B}}^Q_{\mu\underline{a}}\big)^B$
18: **end for**
19: **end for**
20: **end for**
21: **end for**
22: **end for**

1.4.3 Partial Derivative Term: $\frac{\partial \mathbf{X}_0(\mathrm{i}\tau)}{\partial \overline{\mathbf{G}}_0(\mathrm{i}\tau)} \frac{\partial \overline{\mathbf{G}}_0(\mathrm{i}\tau)}{\partial \mathbf{B}}$

The computation of the partial derivative $\frac{\partial \mathbf{X}_0(\mathrm{i}\tau)}{\partial \overline{\mathbf{G}}_0(\mathrm{i}\tau)} \frac{\partial \overline{\mathbf{G}}_0(\mathrm{i}\tau)}{\partial \mathbf{B}}$ is shown in Algorithm 4. Lines 12-16 are implemented as a matrix multiplication.

Algorithm 10 $\frac{\partial \mathbf{X}_0(\mathrm{i}\tau)}{\partial \overline{\mathbf{G}}_0(\mathrm{i}\tau)} \frac{\partial \overline{\mathbf{G}}_0(\mathrm{i}\tau)}{\partial \mathbf{B}}$ per $\tau \geq 0$

for aux-batch1 **do**
  read $\mathbb{B}^P \quad \forall P \in$ aux-batch1
  for $P \in$ aux-batch1 **do** ▷ parallel
    $\underline{\mathbb{B}}^P_{\mu \underline{i}} = \mathbb{B}^P_{\mu\nu} L_{\nu \underline{i}} \quad \forall \mu, \underline{i}$
  end for
  for aux-batch2 $\geq$ aux-batch1 **do**
    read $\underline{\tilde{\mathbb{B}}}^Q_{\mu \underline{i}}(-\mathrm{i}\tau) \quad \forall \underline{i}, \mu, Q \in$ aux-batch2
    for $B \in \mathbf{B} = \{B_x, B_y, B_z\}$ **do**
      for $P \in$ aux-batch1 **do** ▷ parallel
        $\left(\tilde{\mathbb{B}}^P_{\mu \underline{i}}\right)^B(\mathrm{i}\tau) = \overline{\mathbb{B}}^P_{\nu \underline{i}} \overline{G}^B_{0,\nu\mu}(\mathrm{i}\tau) \quad \forall \mu, \underline{i}$
      end for
      for $P \in$ aux-batch1 **do**
        for $Q \in$ aux-batch2 **do**
          $X^B_{0,PQ}(\mathrm{i}\tau)$ += $\left(\tilde{\mathbb{B}}^P_{\mu \underline{i}}\right)^B(\mathrm{i}\tau) \underline{\tilde{\mathbb{B}}}^Q_{\mu \underline{i}}(-\mathrm{i}\tau)$
        end for
      end for
    end for
  end for
end for

2 Batching-Results: Linear Alkanes

Tab. S1 provides the number of batches corresponding to Fig. 7.

Table S1: Number of auxiliary function batches for various intermediates for linear alkanes of increasing size. Calculations were carried out on a compute node with 250 GB of RAM.

Quantity	Number of aux-batches				
	$N = 1690$	$N = 1970$	$N = 2250$	$N = 2530$	$N = 2810$
$\mathbf{X}_0(\mathrm{i}\tau)$	1	1	1	1	3
$\mathbf{X}_0^{\mathbf{B}}(\mathrm{i}\tau)$					
$\frac{\partial \mathbf{X}_0(\mathrm{i}\tau)}{\partial \underline{\mathbf{G}}_0(-\mathrm{i}\tau)} \frac{\partial \underline{\mathbf{G}}_0(-\mathrm{i}\tau)}{\partial \mathbf{B}}$	1	3	4	5	7
$\frac{\partial \mathbf{X}_0(\mathrm{i}\tau)}{\partial \overline{\mathbf{G}}_0(\mathrm{i}\tau)} \frac{\partial \overline{\mathbf{G}}_0(\mathrm{i}\tau)}{\partial \mathbf{B}}$	1	1	1	3	3
$\frac{\partial \mathbf{X}_0(\mathrm{i}\tau)}{\partial \mathbb{B}} \frac{\partial \mathbb{B}}{\partial \mathbf{B}}$	1	1	1	3	5
$\mathbf{\Sigma}(\mathrm{i}\tau)$	1	1	1	1	2
$\mathbf{\Sigma}^{\mathbf{B}}(\mathrm{i}\tau)$					
$\frac{\partial \mathbf{\Sigma}(\mathrm{i}\tau)}{\partial \tilde{\mathbf{W}}_{\mathrm{c}}(-\mathrm{i}\tau)} \frac{\partial \tilde{\mathbf{W}}_{\mathrm{c}}(-\mathrm{i}\tau)}{\partial \mathbf{B}}$	1	1	1	2	2
$\frac{\partial \mathbf{\Sigma}(\mathrm{i}\tau)}{\partial \mathbf{G}_0(\mathrm{i}\tau)} \frac{\partial \mathbf{G}_0(\mathrm{i}\tau)}{\partial \mathbf{B}}$	1	1	1	1	1
$\frac{\partial \mathbf{\Sigma}(\mathrm{i}\tau)}{\partial \mathbb{B}} \frac{\partial \mathbb{B}}{\partial \mathbf{B}}$	1	1	1	2	2

3 Timings: Dense vs. Sparse Implementation

NMR shieldings were computed at the RPA@HF level of theory using the cc-pwCVDZ basis set with the corresponding RI basis set for linear alkanes. The computations were carried out using the ω-CDD-RI-RPA-NMR method, that is, the atomic-orbital RPA NMR formulation with an attenuated Coulomb RI metric and Cholesky decomposed density type matrices. Tab. S2 compares the timings for the computations using dense matrix algebra, denoted as 'Dense', and using sparse matrix algebra, denoted as 'Sparse'. The computations were carried out on a compute node with AMD EPYC 7302 processors using 64 threads, 250 GB of RAM, and 1.7 TB of disk space. For dense matrix algebra routines the Intel Math Kernel Library (version 2022.0.0) was employed.

Table S2: Timings for the computation of the RPA correlation part within the computation of NMR shieldings at the RPA@HF/cc-pwCVDZ level of theory for the ω-CDD-RI-RPA-NMR method using dense and sparse matrix algebra for linear alkanes.

System	Wall Time [s]	
	Dense	Sparse
C_5H_{12}	61.34	72.38
$C_{10}H_{22}$	312.81	309.13
$C_{20}H_{42}$	1775.70	1418.08
$C_{30}H_{62}$	5689.82	3415.05

4 Isotropic NMR shielding constants for $(DNA)_4$/cc-pwCVDZ

Table S3: Isotropic NMR shielding constants for $(DNA)_4$ computed using RPA@HF (RPA based on a preceding HF calculation) and the cc-pwCVDZ basis set with the corresponding RI basis set.

Nucleus	Shieldings [ppm]
H	1.57833
H	1.390977

Table S3: (continued)

H	0.74982
O	39.625412
C	1.525101
C	18.766431
H	4.234651
C	8.601825
H	1.334232
N	5.214792
O	17.11874
H	0.619695
C	17.137739
C	13.991661
O	0.76482
H	0.011777
H	-0.037214
N	3.382744
H	0.71742
C	-0.030678
O	-4.852926
H	0.164014
C	-1.494732
H	0.8372
H	0.626706

Table S3: (continued)

C	-0.995834
C	0.181645
H	0.264816
H	1.446535
H	1.880048
H	1.201433
O	22.899628
H	0.90182
C	-0.18823
C	1.699186
C	17.939165
H	4.876313
O	5.865786
O	-0.517268
O	3.17016
C	8.729024
H	1.672155
N	9.706986
O	18.694527
P	-5.558484
C	17.851583
C	15.038718
O	-1.16659

Table S3: (continued)

H	0.551018
H	0.292424
N	3.527311
H	1.234812
C	-0.122849
O	-4.047136
H	0.476733
C	-1.016173
H	1.023262
H	0.81029
C	-1.005319
C	0.469242
H	0.401737
H	0.972414
H	1.431564
H	1.057215
O	28.595151
H	0.713146
C	0.058148
C	1.184723
C	17.507499
H	5.095655
O	5.81443

Table S3: (continued)

O	-1.839941
O	5.196133
C	8.006601
H	1.577159
N	11.366697
O	19.340224
P	-6.552366
C	18.108446
C	15.040221
O	-0.071245
H	0.736576
H	0.389637
N	3.613857
H	1.191251
C	0.015605
O	-3.912513
H	0.634324
C	-1.013577
H	0.765568
H	0.746337
C	-0.87146
C	0.277107
H	0.422746

Table S3: (continued)

H	0.708284
C	0.121936
O	6.030582
O	-1.702112
O	7.620857
P	-6.168668
H	0.550693
O	-0.527313
H	0.730181
H	0.358968
O	0.543564
H	0.208021
C	0.101372
H	0.601108
C	-0.243286
H	0.405819
H	0.393301
C	-0.907799
C	0.163644
O	-3.917446
H	0.707194
O	15.168253
C	-1.382187

Table S3: (continued)

C	13.889823
H	2.942117
N	3.281975
H	1.113149
N	12.03376
O	29.206439
C	17.825503
C	15.360425
C	6.329633
H	0.608848
H	0.514207
C	0.423383
H	0.392887
H	2.627137
H	-1.669095
N	23.600778
N	14.486347
H	1.437691
C	-12.18866
C	19.393901
C	10.615719
N	10.929766
N	35.457777

Table S3: (continued)

H	0.541916
C	16.505611
C	14.777031
H	0.531465
N	4.828071
H	0.67236
O	0.971618
H	-0.012738
H	-0.085093
H	5.723445
H	3.634883
C	-1.569247
H	0.549683
H	0.996448
C	-0.036606
O	-4.625606
H	0.132045
N	3.035753
N	8.401628
H	3.482241
C	0.35842
C	-1.211749
H	0.295052

Table S3: (continued)

C	17.904118
C	22.012332
H	0.649918
C	0.083592
C	7.155296
N	14.804725
N	38.438202
H	2.121572
O	5.909475
O	-1.372144
O	8.308139
C	18.475192
C	17.977088
P	-5.856548
N	6.676367
H	1.644376
O	-0.548599
H	0.368341
H	0.672384
H	6.422013
H	6.702008
C	-0.441486
H	1.286438

Table S3: (continued)

H	1.551719
C	0.094695
O	-3.279313
H	0.656462
N	20.344932
N	17.348439
H	4.026186
C	0.978224
C	-0.8653
H	0.619598
C	22.681794
C	22.697891
H	0.765969
C	0.563298
C	10.044622
N	13.580254
N	41.966413
H	2.404027
O	5.971144
O	-1.176067
O	8.216446
C	20.655167
C	18.88493

Table S3: (continued)

P	-5.806898
N	7.221697
H	1.41152
O	-0.545968
H	0.470987
H	0.947656
C	-0.63689
H	0.879467
H	0.463376
C	0.180698
O	-3.046955
H	0.772728
C	0.383694
C	-0.789458
H	0.269318
C	-0.012608
H	0.427743
O	-1.47565
O	5.690395
O	2.276213
P	-6.347167
H	0.058347
O	-0.367606

Table S3: (continued)

H	0.227289
H	0.611955
O	0.100699
H	-0.239016
C	-0.088877
H	0.312979
C	-0.739927
H	-0.609891
H	-0.434058
C	-1.201207
C	-0.582964
O	-3.537079
H	-0.133302
C	-2.177435
H	-0.451347
N	4.87628
C	14.281054
N	8.532255
H	2.11225
C	14.638668
N	34.43981
C	21.046854
C	4.679381

Table S3: (continued)

N	44.749026
C	7.53773
H	-10.798186
N	43.585368
H	9.508841

3.5 Publication V: Accurate NMR shieldings with σ-functionals

S. Fauser, V. Drontschenko, C. Ochsenfeld, A. Görling
J. Chem. Theory Comput., **20**, 6028 (2024).

Abstract

In recent years, density-functional methods relying on a new type of fifth-rung correlation functionals called σ-functionals have been introduced. σ- Functionals are technically closely related to the random phase approximation and require the same computational effort but yield distinctively higher accuracies for reaction and transition state energies of main group chemistry and even outperform double-hybrid functionals for these energies. In this work, we systematically investigate how accurate σ-functionals can describe nuclear magnetic resonance (NMR) shieldings. It turns out that σ-functionals yield very accurate NMR shieldings, even though in their optimization, exclusively, energies are employed as reference data and response properties such as NMR shieldings are not involved at all. This shows that σ-functionals combine universal applicability with accuracy. Indeed, the NMR shieldings from a σ-functional using input orbitals and eigenvalues from Kohn–Sham calculations with the exchange-correlation functional of Perdew, Burke and Ernzerhof (PBE) turned out to be the most accurate ones among the NMR shieldings calculated with various density-functional methods including methods using double-hybrid functionals. That σ-functionals can be used for calculating both reliable energies and response properties like NMR shieldings characterizes them as all-purpose functionals, which is appealing from an application point of view.

Reprinted with permission from:

S. Fauser, V. Drontschenko, C. Ochsenfeld, A. Görling
"Accurate NMR Shieldings with σ-Functionals"
J. Chem. Theory Comput., **20**, 6028 (2024).

JCTC Journal of Chemical Theory and Computation

pubs.acs.org/JCTC Article

Accurate NMR Shieldings with σ-Functionals

Steffen Fauser,[#] Viktoria Drontschenko,[#] Christian Ochsenfeld, and Andreas Görling*

Cite This: J. Chem. Theory Comput. 2024, 20, 6028−6036 Read Online

ACCESS | Metrics & More | Article Recommendations | Supporting Information

ABSTRACT: In recent years, density-functional methods relying on a new type of fifth-rung correlation functionals called σ-functionals have been introduced. σ-Functionals are technically closely related to the random phase approximation and require the same computational effort but yield distinctively higher accuracies for reaction and transition state energies of main group chemistry and even outperform double-hybrid functionals for these energies. In this work, we systematically investigate how accurate σ-functionals can describe nuclear magnetic resonance (NMR) shieldings. It turns out that σ-functionals yield very accurate NMR shieldings, even though in their optimization, exclusively, energies are employed as reference data and response properties such as NMR shieldings are not involved at all. This shows that σ-functionals combine universal applicability with accuracy. Indeed, the NMR shieldings from a σ-functional using input orbitals and eigenvalues from Kohn−Sham calculations with the exchange-correlation functional of Perdew, Burke and Ernzerhof (PBE) turned out to be the most accurate ones among the NMR shieldings calculated with various density-functional methods including methods using double-hybrid functionals. That σ-functionals can be used for calculating both reliable energies and response properties like NMR shieldings characterizes them as all-purpose functionals, which is appealing from an application point of view.

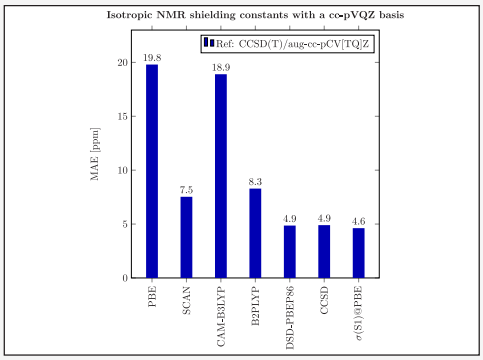

1. INTRODUCTION

In recent years, a new class of density-functional theory (DFT) methods, σ-functional methods, have been introduced.[1,2] Within these methods, all parts of the electronic energy, including the exchange energy, are calculated exactly, with the exception of the correlation energy. The latter is obtained by the σ-functional, which is a fifth-rung functional in the common classification of density functionals[3] and therefore depends on occupied as well as unoccupied Kohn−Sham (KS) orbitals and their eigenvalues. Technically, σ-functionals are closely related to the random phase approximation (RPA),[4−7] and like the RPA, they emerge from the adiabatic-connection fluctuation−dissipation (ACFD) theorem.[8,9] The formal foundation of σ-functionals is many-body perturbation theory along the adiabatic connection.[10,11]

Both within the RPA and with σ-functionals, the correlation energy is evaluated from the eigenvalues $-\sigma_n(\omega)$ of the dynamic, i.e., frequency-dependent, KS response function by integrating functions $H^{\sigma f}(\sigma_n(\omega))$ of $\sigma_n(\omega)$ along the complex-valued frequency $i\omega$. The difference between the RPA and σ-functionals lies in the function $H^{\sigma f}$. Within σ-functionals, the function $H^{\sigma f}$ equals the RPA function $H^{\mathrm{RPA}}(\sigma_n(\omega)) = -\ln(1 + \sigma_n(\omega)) + \sigma_n(\omega)$ supplemented by a correction function H to obtain a modified function $H^{\sigma f} = H^{\mathrm{RPA}} + H$.[1,2] This means the RPA can be considered as a σ-functional with the correction term H being zero. The correction function $H(\sigma_n(\omega))$ to the RPA function $H^{\mathrm{RPA}}(\sigma_n(\omega))$ is obtained by optimizing atomization, reaction, and transition state energies as well as noncovalent interaction energies from various established reference sets.[1,2,12,13] Like the RPA, σ-functionals are usually employed in a post-self-consistent-field (post-SCF) manner by evaluating the total electronic energy with orbitals and eigenvalues from a previous self-consistent KS calculation using exchange-correlation functionals of a lower rung. σ-Functionals were optimized[1,2] for orbitals and eigenvalues from KS calculations with the generalized gradient approximation (GGA) functional PBE,[14] the meta-GGA functional TPSS,[15] as well as the hybrid functionals PBE0[16,17] and B3LYP.[18]

In main group chemistry, σ-functionals yield reaction and transition state energies that are distinctively more accurate than those of the RPA.[2,13] Compared to lower rung functionals of the GGA, meta-GGA, or hybrid type, the gain in accuracy is even higher. Even double-hybrid functionals, which are also fifth-rung functionals, are outperformed in accuracy by σ-functionals in main group chemistry.[13] Indeed, σ-functionals reach chemical accuracy of 1 kcal/mol in main group chemistry.[2,13] Furthermore, σ-functionals, like the RPA, can

Received: April 17, 2024
Revised: June 13, 2024
Accepted: June 17, 2024
Published: July 5, 2024

https://doi.org/10.1021/acs.jctc.4c00512
J. Chem. Theory Comput. 2024, 20, 6028−6036

describe noncovalent interactions highly accurately in a seamless way. Molecular geometries and vibrational frequencies,[19] as well as singlet−triplet gaps,[20] can also be obtained very accurately with σ-functionals. Using orbitals and eigenvalues from the hybrid functionals PBE0 and B3LYP within σ-functionals leads to the most accurate results; however, orbitals and eigenvalues from the GGA functional PBE still yield results with accuracies that are much higher than that of GGA, meta-GGA, or hybrid functionals. Besides the original σ-functionals of refs 1 and 2, other versions of σ-functionals have been introduced recently.[12,21,22] In this work, however, we will focus on the original σ-functionals of refs 1 and 2.

σ-Functionals exhibit an excellent ratio of accuracy to computational effort. The evaluation of the total energy with σ-functionals or the RPA requires for medium-size molecules of about 100 to 200 atoms less computational effort than a preceding KS calculation with a hybrid functional for the input orbitals and eigenvalues (within the program package Molpro, using a canonical implementation).[13] Recently, efficient setups with basis sets of different quality were introduced both for Gaussian-type and Slater-type basis sets.[13] σ-Functionals have been implemented in a number of established quantum chemistry packages, e.g., Molpro,[1,2] Turbomole,[19] ADF,[13,20] PySCF, and FermiONs++.[21,22]

While σ-functional methods have been shown to be valuable approaches for calculating energetic data, like reaction or transition state energies, and molecular properties that are directly related to energies such as molecular geometries or vibrational frequencies, it is still largely unknown whether they are also able to accurately predict other molecular properties. NMR shieldings are such a property and, indeed, represent a quantity of great practical relevance. Recently, NMR shieldings were calculated for the first time within the RPA using numerical second derivatives and an extensive benchmark study was carried out.[23] Due to the good results of the RPA, analytical RPA NMR shieldings were also introduced recently[24] to extend the applicability of RPA NMR to larger systems. Among the RPA setups tested in ref 23, the one employing orbitals and eigenvalues from a preceding Hartree−Fock (HF) calculation turned out to provide the most accurate NMR shieldings. This setup, however, is not well suited for the calculation of energies within the RPA. For the latter, orbitals and eigenvalues from hybrid KS methods, e.g., using the PBE0 functional, lead to the best RPA results. This means, there seems to be no all-purpose RPA setup suitable for both energies and response properties like NMR shieldings. In ref 23, a first test of the performance of σ-functionals in the calculation of NMR shieldings was presented for one setup using PBE input orbitals and eigenvalues. The results were encouraging with NMR shieldings that were more accurate than those from the RPA with the same input data but less accurate than the results from the RPA based on HF orbitals and eigenvalues.

In this work, we present a systematic investigation of the performance of σ-functionals within the calculation of NMR shielding parameters. We consider the influence of the exchange-correlation functional used in the KS calculation to generate the input orbitals and eigenvalues. In particular, we study the effect of varying the amount of nonlocal exchange in hybrid functionals. Besides the PBE and PBE0 functionals, with 0% and 25% nonlocal exchange, respectively, we test the PBEh33, PBEh50, and PBEh100 functionals with 33%, 50%, and 100% nonlocal exchange, respectively. Additionally, input data from HF calculations are tested (HF is equal to PBEh100 except for the missing PBE correlation). Furthermore, we consider how strong NMR shieldings depend on the choice of the optimization of σ-functionals. Finally, the effect of the basis set size is investigated.

2. THEORY

2.1. RPA and σ-Functionals. The ACFD theorem provides an exact expression for the KS correlation energy. Its application, however, requires approximations for the not exactly known Hartree-exchange-correlation kernel, the frequency-dependent functional derivative of the sum of the Hartree and the exchange-correlation potential with respect to the electron density. The RPA can be obtained via the ACFD theorem by invoking a single but drastic approximation, that is to completely neglect the exchange-correlation kernel and to account only for the known Hartree kernel.

An RPA calculation requires to construct the KS response matrix $\mathbf{X}_0(\omega)$, represented in an RI (resolution of identity) auxiliary basis set $\{f_\mu\}$. Its matrix elements are given by

$$X_{0,\mu\nu}(\omega) = \sum_i^{\text{occ}} \sum_a^{\text{unocc}} (\phi_i\phi_a|f_\mu)\frac{1}{(\varepsilon_i - \varepsilon_a) + \mathrm{i}\omega}(\phi_a\phi_i|f_\nu) + (\phi_a\phi_i|f_\mu)\frac{1}{(\varepsilon_i - \varepsilon_a) - \mathrm{i}\omega}(\phi_i\phi_a|f_\nu) \tag{1}$$

with the three-index integrals

$$(\phi_i\phi_a|f_\mu) = \int\int d\mathbf{r}\, d\mathbf{r}' \frac{\phi_i^\dagger(\mathbf{r}')\phi_a(\mathbf{r}')f_\mu(\mathbf{r})}{|\mathbf{r} - \mathbf{r}'|} \tag{2}$$

and with ϕ_i and ϕ_a denoting occupied and unoccupied orbitals, respectively, and ε_i and ε_a the corresponding eigenvalues. For real-valued orbitals, eq 1 simplifies to

$$X_{0,\mu\nu}(\omega) = \sum_i^{\text{occ}} \sum_a^{\text{unocc}} (\phi_i\phi_a|f_\mu)\frac{2(\varepsilon_i - \varepsilon_a)}{(\varepsilon_i - \varepsilon_a)^2 + \omega^2}(\phi_i\phi_a|f_\nu) \tag{3}$$

For closed-shell systems, it is possible to sum over spatial instead of spin orbitals and to take into account spin by an additional factor of 2.

Diagonalization of $\mathbf{X}_0$ (or more precisely, of its negative) yields the eigenvalues $\sigma_n(\omega)$[25]

$$-\mathbf{X}_0(\omega) = \mathbf{V}(\omega)\boldsymbol{\sigma}(\omega)\mathbf{V}^{\mathrm{T}}(\omega) \tag{4}$$

with the matrix $\mathbf{V}$ containing the eigenvectors and the diagonal matrix $\boldsymbol{\sigma}(\omega)$ containing the eigenvalues $\sigma_n(\omega)$. Since $\mathbf{X}_0$ is negative definite, all $\sigma_n(\omega)$ are positive. The RPA correlation energy can then be written exclusively in terms of the $\sigma_n(\omega)$

$$E_c^{\text{RPA}} = -\frac{1}{2\pi}\int_0^\infty \mathrm{d}\omega\ \mathrm{Tr}\{-\ln[\mathbf{1} + \boldsymbol{\sigma}(\omega)] + \boldsymbol{\sigma}(\omega)\} \tag{5}$$

$$= -\frac{1}{2\pi}\int_0^\infty \mathrm{d}\omega\ \mathrm{Tr}\{H^{\text{RPA}}(\boldsymbol{\sigma}(\omega))\} \tag{6}$$

$$= -\frac{1}{2\pi}\int_0^\infty \mathrm{d}\omega \sum_n H^{\text{RPA}}(\sigma_n(\omega)) \tag{7}$$

with

$$H^{\text{RPA}}(\sigma) = -\ln[1 + \sigma] + \sigma \tag{8}$$

https://doi.org/10.1021/acs.jctc.4c00512
J. Chem. Theory Comput. 2024, 20, 6028−6036

Table 1. Overview of Parametrizations for σ-Functionals and their Differences in Number and Position of Spline Abscissae Values as well as the Reference Sets and Weights Used in the Optimization of the Respective Parametrization[a]

name	description	input	#param.	ref
P1, P2, P3	first parametrization based only on few reference sets and abscissae points	PBE	11 (P1,P2)	1
			17 (P3)	
W1	parametrization using more reference sets and abscissae points	PBE, TPSS,	19	2
		PBE0, B3LYP	18	
S1, S2	parametrizations with systematically reworked reference sets and abscissae points; S2 is identical to S1, except that it additionally contains total energies with a small weight	PBE	18	12
		PBE0	17	
S1re	reparametrization with same sets and weights as S1 for the use with small basis sets	PBE	18	13
		PBE0	17	
A1, A2	alternative parametrization with the same abscissae points as W1 but different reference sets, uses frozen core approximation for generating input data	PBE	19	22
		PBE0	18	

[a]The exact setup for each parametrization can be found in the cited references, respectively. The column "input" relates the parametrizations indicated in the first column with the functionals that can be used to generate input orbitals and eigenvalues. For each of the functionals in the column "Input," a parametrization indicated in the first column exists. The column "#param." indicates how many parameters are involved in the respective parametrization, which depends on the number of abscissae points selected for the spline function.

The frequency integration has to be performed numerically. The total energy for RPA (and equivalently for σ-functionals, see below) is given by

$$E^{\mathrm{RPA}} = \langle \Phi_0 | \hat{H} | \Phi_0 \rangle + E_{\mathrm{c}}^{\mathrm{RPA}} \tag{9}$$

i.e., the sum of the Hartree−Fock energy expression evaluated with KS orbitals and the RPA correlation energy.

σ-Functionals can be considered a generalization of the RPA, meaning that they replace the function H^{RPA} by a different one, $H^{\sigma f}$. This function $H^{\sigma f}$ is optimized with the help of (energetic) reference data in order to correct the error introduced in RPA by neglecting the exchange-correlation kernel.

The approach of refs 1 and 2 decomposes $H^{\sigma f}$ as the sum of H^{RPA} and a correction function H represented by cubic splines

$$H^{\sigma f}(\sigma) = H^{\mathrm{RPA}}(\sigma) + H(\sigma) \tag{10}$$

but there are also other possible ways to represent $H^{\sigma f}$, for example, by a power series approximation. $H(\sigma)$ is defined as[2]

$$H(\sigma) = \begin{cases} 0 & \text{for } \sigma \in I_1 \\ c_{0,2}(\sigma - x_2) + \frac{1}{2}c_{1,2}(\sigma - x_2)^2 + \frac{1}{3}c_{2,2}(\sigma - x_2)^3 + \frac{1}{4}c_{3,2}(\sigma - x_2)^4 & \text{for } \sigma \in I_2 \\ \sum_{i=2}^{m-1}\left[c_{0,i}\Delta x_i + \frac{1}{2}c_{1,i}\Delta x_i^2 + \frac{1}{3}c_{2,i}\Delta x_i^3 + \frac{1}{4}c_{3,i}\Delta x_i^4\right] + c_{0,m}(\sigma - x_m) & \text{for } \sigma \in I_m \text{ with } 3 \le m \le M-2 \\ \quad + \frac{1}{2}c_{1,m}(\sigma - x_m)^2 + \frac{1}{3}c_{2,m}(\sigma - x_m)^3 + \frac{1}{4}c_{3,m}(\sigma - x_m)^4 & \\ \sum_{i=2}^{M-2}\left[c_{0,i}\Delta x_i + \frac{1}{2}c_{1,i}\Delta x_i^2 + \frac{1}{3}c_{2,i}\Delta x_i^3 + \frac{1}{4}c_{3,i}\Delta x_i^4\right] & \text{for } \sigma \in I_{M-1}, I_M \end{cases} \tag{11}$$

with $\Delta x_i = x_{i+1} - x_i$ and with the intervals

$$I_m = \begin{cases} [x_m, x_{m+1}] & \text{for } 1 \le m \le M-1 \\ [x_m, \infty] & \text{for } m = M \end{cases} \tag{12}$$

The abscissae points x_m are selected before the optimization. Note that in the optimization process the coefficients $c_{p,m}$ of eq 11 are not optimized directly, but instead piecewise cubic Hermite interpolating polynomials (PCHIPs)[26] are used. PCHIPs are monotonous within each interval and are described by one parameter per interval. The PCHIP parameters for the first two and the last two intervals are set to zero, i.e., the number of parameters involved in the optimization equals $M - 4$. For more details on the optimization process, see refs 2 and 12. The parametrizations presented in Table 1 differ in the selection of abscissae values and in which reference sets are included in the optimization process and the weights assigned to them.

It is important to emphasize that the construction of σ-functionals is not just an optimization of empirical parameters, but that it is was developed on the basis of an expansion of the exact exchange-correlation kernel with respect to the coupling strength of the electrons[10,11] and follows the strategy underlying τ-functionals, which model the effect of the correlation kernel by a function of eigenvalues τ of a combination of the exact Hartree-exchange kernel with the KS response function.[10,11,22] Because of their physically motivated form, σ-functionals have shown a high degree of transferability to describe properties not included in their optimization. How far this transferability extends to the description of NMR shieldings is investigated in this work.

2.2. NMR with RPA-Based Methods. The nuclear magnetic resonance shielding tensor $\tilde{\boldsymbol{\sigma}}^A$ of a nucleus A is given by the mixed second derivative of the electronic energy E with respect to the nuclear magnetic moment $\mathbf{m}^A = (m_x^A, m_y^A, m_z^A)^{\mathrm{T}}$ and the magnetic field $\mathbf{B} = (B_x, B_y, B_z)^{\mathrm{T}}$, both evaluated at zero according to

https://doi.org/10.1021/acs.jctc.4c00512
J. Chem. Theory Comput. 2024, 20, 6028−6036

$$\tilde{\sigma}_{rs}^{A} = \left.\frac{\partial^2 E}{\partial B_r \partial m_s^A}\right|_{\mathbf{m}^A=\mathbf{0},\mathbf{B}=\mathbf{0}} \qquad \forall\, r, s \in \{x, y, z\} \tag{13}$$

In this work, we employ numerical second derivatives for the computation of the NMR shielding tensor within the RPA and σ-functionals as introduced in ref 23. This requires the computation of the energy $E(\mathbf{B}, \mathbf{m}^A)$ for different values of the magnetic field strength and size of the nuclear magnetic moment to compute a component of the NMR shielding tensor, e.g., $\tilde{\sigma}_{xy}^{A}$, as[23]

$$\tilde{\sigma}_{xy}^{A} \approx \frac{1}{2m_y^A B_x}[E((B_x, 0, 0)^{\mathrm{T}}, (0, m_y^A, 0)^{\mathrm{T}}) - E((B_x, 0, 0)^{\mathrm{T}}, (0, -m_y^A, 0)^{\mathrm{T}}] \tag{14}$$

As done in ref 23, both B_x and m_y^A are set to a constant value δ yielding

$$\tilde{\sigma}_{xy}^{A} \approx \frac{1}{2\delta^2}[E((\delta, 0, 0)^{\mathrm{T}}, (0, \delta, 0)^{\mathrm{T}}) - E((\delta, 0, 0)^{\mathrm{T}}, (0, -\delta, 0)^{\mathrm{T}}] \tag{15}$$

In the implementation, a value of $\delta = 0.1$ a.u. is used, which proved to provide accurate results in ref 23. The remaining components can be computed accordingly.

In this work, all errors are given for the isotropic NMR shielding constants

$$\tilde{\sigma}_{\mathrm{iso}}^{A} = \frac{1}{3}(\tilde{\sigma}_{xx}^{A} + \tilde{\sigma}_{yy}^{A} + \tilde{\sigma}_{zz}^{A}) = \frac{1}{3}\mathrm{Tr}(\tilde{\boldsymbol{\sigma}}^{A}) \tag{16}$$

in ppm.

Furthermore, gauge-including atomic orbitals (GIAOs)[27−30] denoted by $\{\chi_p(\mathbf{r}, \mathbf{B})\}$ are utilized to ensure gauge origin independence

$$\chi_p(\mathbf{r}, \mathbf{B}) = \chi_p(\mathbf{r}, \mathbf{B} = \mathbf{0}) \exp\left(-\frac{\mathrm{i}}{2}[\mathbf{B} \times (\mathbf{R}_p - \mathbf{R}_0)]\mathbf{r}\right) \tag{17}$$

where i is the imaginary unit, p denotes a GIAO index, $\chi_p(\mathbf{r}, \mathbf{B} = \mathbf{0})$ is a field-independent atomic orbital basis function centered at $\mathbf{R}_p$, and $\mathbf{R}_0$ is the gauge origin. Thus, by employing GIAOs, complex-valued quantities are introduced.

Using eq 15, the components of the NMR shielding tensor based on the RPA or σ-functionals can be computed by evaluating the total RPA or σ-functional energy resulting from eq 9 for different perturbations given by magnetic fields and nuclear magnetic moments in different directions. Specifically, the computation of the perturbed energy encompasses the following steps: first, a HF or KS-DFT calculation is carried out in the presence of a perturbation to obtain the orbitals and orbital energies. Due to the use of complex-valued orbitals, i.e., GIAOs, the SCF has to be carried out using complex matrix algebra. The detailed procedure is described in ref 23. The complex-valued orbitals and the orbital energies are then used to compute the perturbed total RPA or σ-functional energy (eq 9).

3. COMPUTATIONAL DETAILS

The optimizations of the new parametrizations for σ-functionals based on PBEh33, PBEh50, PBEh100, and HF input data were performed as described in ref 12 using the basis sets and the reference sets and weights of parametrization S1, i.e., parametrizations S1 for PBEh33, PBEh50, PBEh100, and HF input data were made (most reference data were taken from the GMTKN55 database,[31] see Supporting Information). The selection of abscissae points is identical to σ(S1)@PBE0 of ref 12. The required molecular calculations of those reference sets included in the parametrization S1 of ref 12, see Table 2 of ref 12 for details, were carried out with Molpro 2023.1.[32] For the SCF calculations, the keyword "old" was specified in order to use an older version of the SCF algorithm since the newer version turned out to cause convergence problems in some cases.

Nuclear magnetic resonance shielding tensors were computed for the RPA and σ-functionals using the finite-field method[23] implemented in a development version of the FermiONs++ program.[33−35] In this context, the perturbed RPA and σ-functional energies were computed using the RI approximation as introduced by Furche and coworkers[6] employing GIAOs.[27−30] The numerical frequency integration was carried out using the Clenshaw−Curtis scheme[6,36] with 120 grid points, which has been shown to yield accurate results.[23] The frozen core approximation was not employed. The SCF convergence criteria, DFT settings, and finite-field parameters were set as in ref 23. A range of different DFT functionals were used as a starting point for the RPA and σ-functional calculations, such as PBE,[14] B3LYP,[37] PBE0,[16,17] as well as hybrid PBE functionals with various amounts of nonlocal exchange, that is PBEh33, PBEh50, and PBEh100. Further, NMR shielding tensors based on the meta-GGA functionals SCAN[38] and revTPSS[39] were also computed using the finite-field method within the FermiONs++ program using the same SCF, DFT, and finite-field settings as ref 23.

NMR shielding tensors based on double-hybrid DFT,[40] specifically employing the functionals B2PLYP[41] and DSD-PBEP86,[42] have been computed using the ORCA program (version 5.0.1).[42,43] For the computation of the MP2 part, the RI approximation was employed and the frozen core approximation was not used.

The correlation consistent basis sets of the types cc-pVXZ (X ∈ D, T, Q),[44,45] cc-pwCVXZ (X ∈ T, Q),[45,46] and aug-cc-pwCVXZ (X ∈ T, Q)[47] have been used together with their corresponding RI basis sets.[48,49]

All calculations were carried out for the molecules in the test set assembled by Gauss and coworkers[49] (excluding O_3 and SO_2 like in refs 23 and 50). This comprises a total of 26 molecules with 68 nuclei, specifically 18 hydrogen nuclei, 17 carbon nuclei, 10 oxygen nuclei, 9 fluoride nuclei, 7 nitrogen nuclei, and 2 sulfur, phosphor, and lithium nuclei, as well as one aluminum nucleus. The complete list of molecules can be found in the Supporting Information. For calculations using basis sets with core-weighted functions, the molecules LiF and LiH were removed from the test set.

As reference serves data from the coupled cluster singles doubles with perturbative triples (CCSD(T)) method. The CCSD(T)/cc-pVXZ (X ∈ D, T, Q) data has been obtained from ref 23, while CCSD(T)/cc-pwCVXZ (X ∈ T, Q) reference values have been computed using the CFOUR program.[51] Further, basis set extrapolated CCSD(T) data, denoted as aug-cc-pCV[TQ]Z, have been obtained from ref 49.

As an error measurement in this work, we employ mean average errors of isotropic NMR shielding constants taken over all nuclei of the molecules in the benchmark set. While the

https://doi.org/10.1021/acs.jctc.4c00512
J. Chem. Theory Comput. 2024, 20, 6028−6036

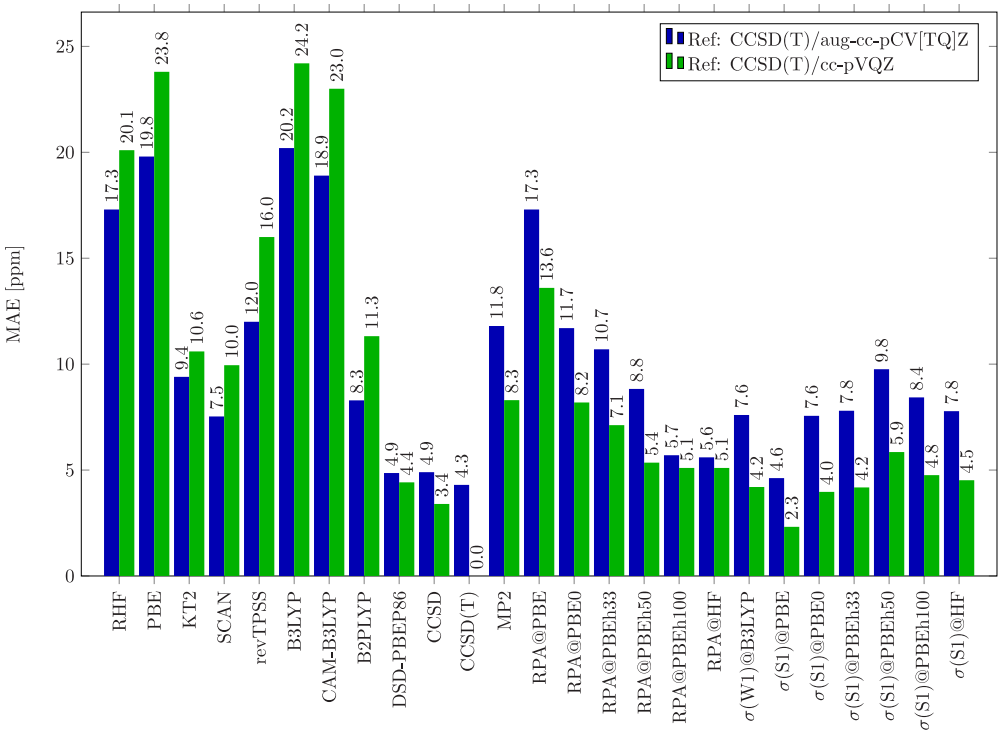

Figure 1. MAEs (ppm) of isotropic NMR shielding constants for different methods, including RPA and σ-functionals using the cc-pVQZ basis set (and corresponding RI basis set) compared to CCSD(T)/aug-cc-pCV[TQ]Z shieldings (blue) and CCSD(T)/cc-pVQZ shieldings (green). The data for RHF, PBE, KT2, CAM-B3LYP, and CCSD were obtained from ref 50, while data for CCSD(T), MP2, RPA@HF, and RPA@PBE were taken from ref 23. The shieldings based on the functionals SCAN[38] and revTPSS[39] were computed using the finite field method of ref 23. The individual shielding constants can be found in the Supporting Information.

absolute values of isotropic shielding constants vary significantly between nuclei and studying each type separately would certainly be beneficial, the key trends in methodological accuracy are also reflected in the combined error analysis of all nuclei. A detailed account of the absolute isotropic NMR shielding constants for each nucleus in the molecules from the Gauss benchmark set is provided in the Supporting Information.

4. RESULTS

4.1. RPA and σ-Functional Calculations with Different Input Orbitals and Eigenvalues and Comparison to Other Methods. Figure 1 shows mean average errors (MAEs) of NMR shieldings computed with several methods with respect to CCSD(T) using the cc-pVQZ basis set as well as CCSD(T) with the basis set extrapolation aug-cc-pCV[TQ]Z. The basis set extrapolated reference data is expected to be the most accurate. In Figure 1, the MAE of 4.3 ppm of the CCSD(T)/cc-pVQZ shieldings with respect to the corresponding basis set extrapolated CCSD(T) data shows the basis set incompleteness error of CCSD(T) at the QZ level (for RPA and σ-functionals, this error is much lower, see Section 4.3).

Figure 1 shows that the σ-functional setup σ(S1)@PBE, i.e., the σ-functional resulting from parametrization S1 of ref 12 for PBE input orbitals and eigenvalues, yields the lowest MAE of all considered methods. The NMR shieldings from CCSD and the double-hybrid DSD-PBEP86 exhibit MAEs that are only slightly higher and represent the next accurate results. The comparison with double-hybrid functionals is especially interesting because these functionals are fifth-rung functionals like σ-functionals. While the double-hybrid functional DSD-PBEP86 performs very well, the double hybrid functional B2PLYP is considerably less accurate. The DFT methods PBE, B3LYP, and CAM-B3LYP[52] of GGA, hybrid, and range-separated hybrid type, respectively, exhibit MAEs that are a factor of 5 to 10 larger than the MAE of the σ-functional approach σ(S1)@PBE. The DFT method KT2[53] shows MAEs about half as large as the DFT methods PBE, B3LYP, and CAM-B3LYP but still more than twice as large as those of σ(S1)@PBE. The meta-GGA functional SCAN has a similar accuracy as B2PLYP, while the revTPSS functional is less accurate.

The NMR shieldings from the RPA based on HF or PBEh100 input data, i.e., RPA@HF or RPA@PBEh100, are quite accurate and show only somewhat larger MAEs than those of σ(S1)@PBE. The admixture of exact nonlocal exchange in the functional used for generating the input data has a different effect for σ-functionals compared to the RPA. While σ(S1)@PBE has clearly the lowest MAE, the σ-functionals based on HF or hybrid DFT methods with the amount of exact exchange ranging from 25% to 100% yield all similar MAEs (with σ(S1)@PBEh50 being a slight outlier) of about 8 ppm. For RPA, on the other hand, the MAEs of NMR shieldings strongly and continuously become smaller from RPA@PBE over RPA@PBE0 (=RPA@PBEh25) and RPA@PBEh33 to RPA@PBEh50, and the lowest MAEs are obtained for RPA with HF or PBEh100 input data, RPA@HF or RPA@PBEh100, respectively. The RPA NMR shieldings depend much stronger on the amount of admixture of exact exchange in the KS calculations generating the input orbitals and eigenvalues than the NMR shieldings from σ-functionals. The

https://doi.org/10.1021/acs.jctc.4c00512
J. Chem. Theory Comput. 2024, 20, 6028−6036

MAEs of NMR shieldings of σ-functionals in contrast to those of RPA setups never become very large. A similar behavior is seen for the weighted deviation of relative energies that were used in the optimization process of σ-functionals, see Table S1. The energies for σ-functionals are much less dependent on the amount of exact exchange than for RPA. In particular, RPA@HF and RPA@PBEh100 yield very high errors for energies.

The MAEs of RPA as well as of σ-functional shieldings calculated with the cc-pVQZ basis set compared to CCSD(T) reference data for the same basis set are much smaller (typically by about 3−4 ppm) than the MAEs compared to the CCSD(T) reference data obtained with the basis set extrapolation aug-cc-pCV[TQ]Z. This difference is similar to the corresponding difference of 4.3 ppm of the CCSD(T) reference data when going from the cc-pVQZ basis sets to the extrapolation aug-cc-pCV[TQ]Z. The reason is that the CCSD(T)/cc-pVQZ shieldings are systematically too large compared to the extrapolated values, see Figure S1 for the results evaluated on mean signed error (MSE). While it is known that conventional DFT methods usually yield systematically too low shieldings,[50] it is found that RPA and σ-functionals (which are converged at the QZ level, see Section 4.3) have positive MSE, see Figure S1. Calculated NMR shieldings can be combined with vibrational corrections,[50] which are mostly negative, and thus typically worsen conventional DFT methods but improve CCSD(T) results. The findings of this work suggest that also RPA and σ-functionals should benefit from vibrational corrections.

4.2. Influence of the Parametrization. Figure 2 displays the effect of different parametrizations for the σ-functional with

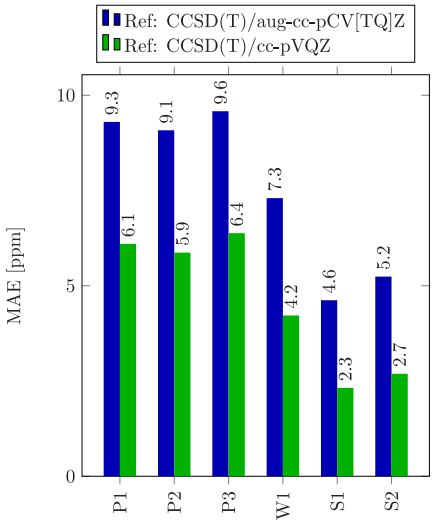

Figure 2. MAEs (ppm) of σ@PBE isotropic NMR shielding constants for different parametrizations using the cc-pVQZ basis set (and corresponding RI basis set) compared to CCSD(T)/aug-cc-pCV[TQ]Z shieldings (blue) and CCSD(T)/cc-pVQZ shieldings (green). The individual shielding constants can be found in the Supporting Information.

PBE input data, see Table 1 for an overview of available parametrizations. Figure 2 illustrates that the parametrization has a significant influence. The latest and arguably best balanced parametrizations, S1 and S2, clearly demonstrate superior performance. The dependence of the accuracy of NMR shieldings on the parametrization is distinctively larger than that on the accuracy of energies, see refs 1, 2, and 12. This indicates that response properties like NMR shieldings are more sensitive to the setup than energies. To keep things in perspective, we note that even the MAEs of the least good performing parametrization P3 of σ-functionals are still about a factor of 2 smaller than the MAEs of the DFT methods PBE, B3LYP, and CAM-B3LYP.

4.3. Influence of Basis Sets. Figure 3 shows the MAEs of NMR shieldings for calculations employing the cc-pVTZ

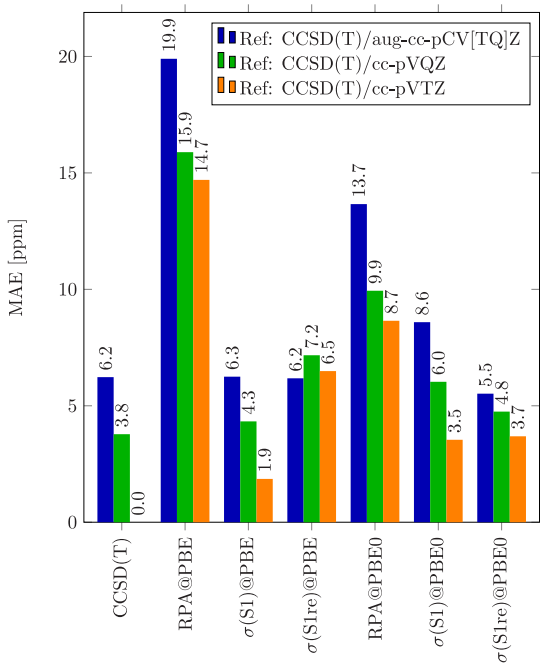

Figure 3. MAEs (ppm) of isotropic NMR shielding constants using the cc-pVTZ basis set (and corresponding RI basis set) compared to CCSD(T)/aug-cc-pCV[TQ]Z shieldings (blue), CCSD(T)/cc-pVQZ shieldings (green), and CCSD(T)/cc-pVTZ shieldings (orange). The individual shielding constants can be found in the Supporting Information.

atomic orbital (AO) basis set. Again σ(S1)@PBE yields clearly the best results, followed by σ(S1)@PBE0. In ref 13, the parametrization S1re was presented as a reoptimization of S1 (with identical weights as S1) specifically for small basis sets. It was shown to clearly reduce the error of reaction energies when using triple-ζ basis sets for reference data included in the optimization and for reference data that was not included. Applying optimization S1re to NMR shieldings, σ(S1re)@PBE0 has a lower error than σ(S1)@PBE0 compared to the extrapolated CCSD(T) results. σ(S1re)@PBE yields results of a similar quality as σ(S1)@PBE when compared with the extrapolated reference but clearly higher errors when compared to CCSD(T) data of the same basis set (cc-pVTZ). The explanation for this behavior is that the reparametrization S1re corrects the basis set error to some extent.

Figure 4 shows the basis set dependence of NMR shieldings obtained with the most accurate σ-functional approach σ(S1)@PBE. Compared to the basis set-extrapolated CCSD(T)/aug-cc-pCV[TQ]Z reference data, an inclusion of core polarization functions leads to a moderate improvement of the MAE from 4.6 to 3.8 ppm, see entries cc-pVQZ and cc-pwCVQZ in Figure 4. The quality of the shieldings with the smaller cc-pVTZ basis set benefits somewhat stronger from the

https://doi.org/10.1021/acs.jctc.4c00512
J. Chem. Theory Comput. 2024, 20, 6028−6036

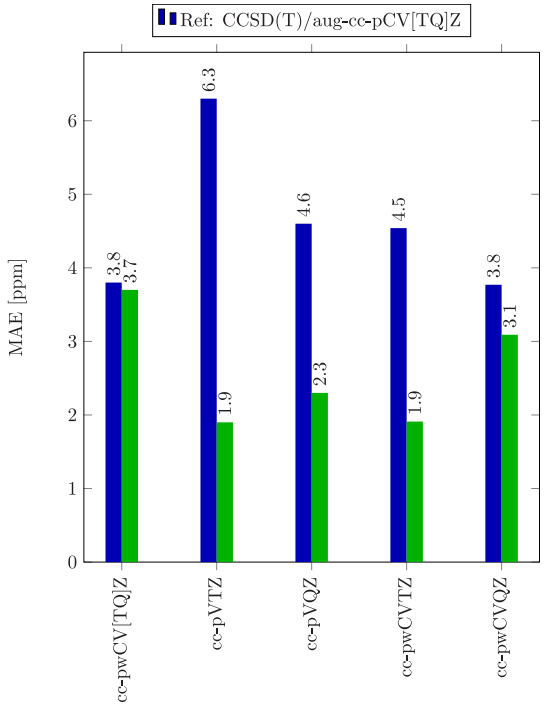

Figure 4. MAEs (ppm) of isotropic NMR shielding constants for σ(S1)@PBE computed with different basis sets compared to CCSD(T)/aug-cc-pCV[TQ]Z (blue) and CCSD(T) with the same basis set (green). Further, cc-pwCV[TQ]Z denotes basis set extrapolated σ(S1)@PBE results. The individual shielding constants can be found in the Supporting Information.

inclusion of core polarization functions, with a reduction of the MAE from 6.3 to 4.5 ppm. A basis set extrapolation from the cc-pwCVTZ to the cc-pwCVQZ basis set, see entry cc-pwCV[TQ]Z in Figure 4, does not lead to changes in the MAE compared to the shieldings obtained with the cc-pwCVQZ basis set; in both cases, an MAE of 3.8 ppm is found. This indicates that the σ(S1)@PBE shieldings are well converged with the cc-pwCVQZ basis set, and a basis set extrapolation is not necessary. We also considered the effect of augmentations of the cc-pwCVTZ and cc-pwCVQZ to aug-cc-pwCVTZ and aug-cc-pwCVTZ basis sets. The comparison of the basis set-extrapolated cc-pwCV[TQ]Z and aug-cc-pwCV[TQ]Z shieldings suggests that augmentation functions are not required (see Figure S2 and discussion in the Supporting Information).

In summary, the setup σ(S1)@PBE with the cc-pwCVQZ basis set yields the most accurate NMR shieldings, while the setup σ(S1)@PBE with the cc-pVQZ basis set is only slightly less accurate.

In ref 13, it was furthermore reported that the RI auxiliary basis can be chosen one cardinal number smaller than the AO basis without significantly affecting the accuracy for reaction energies. Table 2 shows that this finding can also be applied to NMR shieldings. This is an important result because a smaller auxiliary basis greatly reduces the required computational effort, see ref 13.

5. CONCLUSION

The comparison of NMR shieldings calculated from σ-functionals with CCSD(T) reference values and with other DFT methods shows that σ-functionals using PBE input orbitals and eigenvalues, i.e., σ(S1)@PBE, yield the most accurate NMR shieldings. Compared to the GGA and hybrid DFT functionals PBE, B3LYP, or CAM-B3LYP, the difference in accuracy is large, with MAEs of σ(S1)@PBE compared to the CCSD(T) reference data being up to an order of magnitude smaller. Compared to NMR shieldings from the RPA, the gain in accuracy is not as distinct but still clearly noticeable, and even compared to the best performing double-hybrid functional DSD-PBEP86, the σ-functional setup σ(S1)@PBE shows a slightly better performance. NMR shieldings from a σ-functional based on PBE0 input orbitals and eigenvalues, i.e., σ(S1)@PBE0, exhibit MAEs that are a bit larger than those of the setup σ(S1)@PBE but still highly accurate. Thus, both σ-functional setups, σ(S1)@PBE and σ(S1)@PBE0, are well-suited for the calculation of NMR shieldings.

Table 2. Comparison of MAEs in ppm (Relative to CCSD(T) with the Respective AO Basis Set) for σ(S1)@PBE and σ(S1)@PBE0 Using Different Combinations of AO Basis Sets and RI Basis Sets

		MAE [ppm]	
AO basis	RI basis	σ(S1)@PBE	σ(S1)@PBE0
cc-pVQZ	cc-pVQZ/mp2fit	2.32	3.97
	cc-pVTZ/mp2fit	2.40	4.02
cc-pVTZ	cc-pVTZ/mp2fit	1.86	3.54
	cc-pVDZ/mp2fit	1.97	3.07

Both setups, σ(S1)@PBE and σ(S1)@PBE0, have been shown previously[12,13] to yield very good reaction, transition state, and noncovalent interaction energies. Thus, both setups are generally applicable setups for investigating both energies and NMR shieldings. The setup σ(S1)@PBE is computationally somewhat more efficient than the setup σ(S1)@PBE0 because instead of a hybrid KS calculation, PBE0, a GGA KS calculation, PBE, is carried out for generating the input data. Moreover, the setup σ(S1)@PBE yields slightly more accurate NMR shieldings but somewhat less accurate energetic data than σ(S1)@PBE0. Therefore, the choice of which of the two setups to use depends on the computational effort that shall be invested and the main quantity of interest.

Due to the high accuracy obtained by σ-functionals for NMR shielding constants, an analytical implementation for second-order properties based on σ-functionals would be desirable, which we intend to explore in future work. In this context, the implementation can be built on an existing RPA NMR implementation with moderate programming effort. The computation of analytical NMR shielding constants would extend the applicability of σ-functionals to even larger systems and provide a very accurate method for potential computational applications.

The finding that σ-functionals yield highly accurate NMR shieldings is remarkable not only from an application point of view but also because the optimization of σ-functionals is carried out exclusively using energetic reference data. Response properties like NMR shieldings are not involved at all in the optimization of σ-functionals. That σ-functionals nevertheless yield accurate NMR shieldings shows a high transferability of the constructed σ-functionals out of the realm they were optimized in. This is important from the perspective of the goal of constructing all-purpose correlation functionals of universal validity.

https://doi.org/10.1021/acs.jctc.4c00512
J. Chem. Theory Comput. 2024, 20, 6028−6036

■ ASSOCIATED CONTENT

Data Availability Statement

Additional data are provided at the data repository Zenodo at https://doi.org/10.5281/zenodo.10974893. These contain the coefficients for the new parametrizations σ(S1)@PBEh33, σ(S1)@PBEh50, σ(S1)@PBEh100, and σ(S1) @HF.

Supporting Information

The Supporting Information is available free of charge at https://pubs.acs.org/doi/10.1021/acs.jctc.4c00512.

The mean absolute errors (MAEs) of all reference sets that were involved in the optimization of σ-functionals with parametrization S1, an evaluation of NMR shieldings based on mean signed errors instead of mean absolute errors, and information on the effect of augmented basis sets in the calculation of NMR shieldings with the setup σ(S1)@PBE. Furthermore, the individual shielding constants underlying the presented results are provided (PDF)

■ AUTHOR INFORMATION

Corresponding Author

Andreas Görling − *Lehrstuhl für Theoretische Chemie, Universität Erlangen-Nürnberg, D-91058 Erlangen, Germany; Erlangen National High Performance Computing Center (NHR@FAU), D-91058 Erlangen, Germany;* orcid.org/0000-0002-1831-3318; Email: andreas.goerling@fau.de

Authors

Steffen Fauser − *Lehrstuhl für Theoretische Chemie, Universität Erlangen-Nürnberg, D-91058 Erlangen, Germany;* orcid.org/0000-0002-8201-8989

Viktoria Drontschenko − *Chair of Theoretical Chemistry, Department of Chemistry, University of Munich (LMU), D-81377 Munich, Germany*

Christian Ochsenfeld − *Chair of Theoretical Chemistry, Department of Chemistry, University of Munich (LMU), D-81377 Munich, Germany; Max Planck Institute for Solid State Research, D-70569 Stuttgart, Germany*

Complete contact information is available at: https://pubs.acs.org/10.1021/acs.jctc.4c00512

Author Contributions

#S.F. and V.D. contributed equally.

Notes

The authors declare no competing financial interest.

■ ACKNOWLEDGMENTS

C.O. acknowledges financial support by the "Deutsche Forschungsgemeinschaft" (DFG, German Research Foundation) under grant TRR325 "Assembly Controlled Chemical Photocatalysis" (grant no. 444632635) and the cluster of excellence (EXC2111-390814868) "Munich Center for Quantum Science and Technology" (MCQST) and additional support as Max-Planck-Fellow at the MPI-FKF Stuttgart. A.G acknowledges support by the DFG by grant no. 431791331-SFB 1452 "Catalysis at Liquid Interfaces." The authors thank Dr. J. Kussmann (LMU Munich) for providing a development version of the FermiONs++ program package.

■ REFERENCES

(1) Trushin, E.; Thierbach, A.; Görling, A. Toward chemical accuracy at low computational cost: Density-functional theory with σ-functionals for the correlation energy. *J. Chem. Phys.* **2021**, *154*, 014104.

(2) Fauser, S.; Trushin, E.; Neiss, C.; Görling, A. Chemical accuracy with σ-functionals for the Kohn−Sham correlation energy optimized for different input orbitals and eigenvalues. *J. Chem. Phys.* **2021**, *155*, 134111.

(3) Perdew, J. P.; Schmidt, K. Jacob's ladder of density functional approximations for the exchange-correlation energy. *AIP Conf Proc.* **2001**, *577*, 1−20.

(4) Heßelmann, A.; Görling, A. Random-phase approximation correlation methods for molecules and solids. *Mol. Phys.* **2011**, *109*, 2473−2500.

(5) Furche, F. Developing the random phase approximation into a practical post−Kohn−Sham correlation model. *J. Chem. Phys.* **2008**, *129*, 114105.

(6) Eshuis, H.; Yarkony, J.; Furche, F. Fast computation of molecular random phase approximation correlation energies using resolution of the identity and imaginary frequency integration. *J. Chem. Phys.* **2010**, *132*, 234114.

(7) Ren, X.; Rinke, P.; Joas, C.; Scheffler, M. Random-phase approximation and its applications in computational chemistry and materials science. *J. Mater. Sci.* **2012**, *47*, 7447−7471.

(8) Langreth, D. C.; Perdew, J. P. The exchange−correlation energy of a metallic surface. *Solid State Commun.* **1975**, *17*, 1425.

(9) Langreth, D. C.; Perdew, J. P. Exchange−correlation energy of a metallic surface: Wave−vector analysis. *Phys. Rev. B* **1977**, *15*, 2884.

(10) Erhard, J.; Bleiziffer, P.; Görling, A. Power Series Approximation for the Correlation Kernel Leading to Kohn-Sham Methods Combining Accuracy, Computational Efficiency, and General Applicability. *Phys. Rev. Lett.* **2016**, *117*, 143002.

(11) Görling, A. Hierarchies of methods towards the exact Kohn-Sham correlation energy based on the adiabatic-connection fluctuation-dissipation theorem. *Phys. Rev. B* **2019**, *99*, 235120.

(12) Erhard, J.; Fauser, S.; Trushin, E.; Görling, A. Scaled σ-functionals for the Kohn−Sham correlation energy with scaling functions from the homogeneous electron gas. *J. Chem. Phys.* **2022**, *157*, 114105.

(13) Fauser, S.; Förster, A.; Redeker, L.; Neiss, C.; Erhard, J.; Trushin, E.; Görling, A. Basis Set Requirements of σ-Functionals for Gaussian- and Slater-Type Basis Functions and Comparison with Range-Separated Hybrid and Double Hybrid Functionals. *J. Chem. Theory Comput.* **2024**, *20*, 2404−2422.

(14) Perdew, J. P.; Burke, K.; Ernzerhof, M. Generalized gradient approximation made simple. *Phys. Rev. Lett.* **1996**, *77*, 3865.

(15) Tao, J. M.; Perdew, J. P.; Staroverov, V. N.; Scuseria, E. Climbing the density functional ladder: Nonempirical meta-generalized gradient approximation designed for molecules and solids. *Phys. Rev. Lett.* **2003**, *91*, 146401.

(16) Perdew, J. P.; Ernzerhof, M.; Burke, K. Rationale for mixing exact exchange with density functional approximations. *J. Chem. Phys.* **1996**, *105*, 9982−9985.

(17) Ernzerhof, M.; Scuseria, G. E. Assessment of the Perdew−Burke−Ernzerhof exchange-correlation functional. *J. Chem. Phys.* **1999**, *110*, 5029−5036.

(18) Becke, A. D. Density-functional thermochemistry. III. The role of exact exchange. *J. Chem. Phys.* **1993**, *98*, 5648−5652.

(19) Neiss, C.; Fauser, S.; Görling, A. Geometries and vibrational frequencies with Kohn−Sham methods using σ-functionals for the correlation energy. *J. Chem. Phys.* **2023**, *158*, 044107.

(20) Dhingra, D.; Shori, A.; Förster, A. Chemically accurate singlet-triplet gaps of organic chromophores and linear acenes by the random phase approximation and σ-functionals. *J. Chem. Phys.* **2023**, *159*, 194105.

(21) Lemke, Y.; Graf, D.; Kussmann, J.; Ochsenfeld, C. An assessment of orbital energy corrections for the direct random

phase approximation and explicit σ-functionals. *Mol. Phys.* **2023**, *121*, No. e2098862.
(22) Lemke, Y.; Ochsenfeld, C. Highly accurate σ- and τ-functionals for beyond-RPA methods with approximate exchange kernels. *J. Chem. Phys.* **2023**, *159*, 194104.
(23) Glasbrenner, M.; Graf, D.; Ochsenfeld, C. Benchmarking the Accuracy of the Direct Random Phase Approximation and σ-Functionals for NMR Shieldings. *J. Chem. Theory Comput.* **2022**, *18*, 192−205.
(24) Drontschenko, V.; Bangerter, F. H.; Ochsenfeld, C. Analytical Second-Order Properties for the Random Phase Approximation: Nuclear Magnetic Resonance Shieldings. *J. Chem. Theory Comput.* **2023**, *19*, 7542−7554.
(25) Note that the formally correct definiton of σ is

$$(-\mathbf{X}_0)^{1/2}\mathbf{F}_H(-\mathbf{X}_0)^{1/2} = \mathbf{V}\boldsymbol{\sigma}\mathbf{V}^{\mathrm{T}}$$

with $\mathbf{F}_H$ the matrix representation of the Hartree kernel. However, when the RI auxiliary basis is orthonormalized with respect to the Coulomb norm, as in our Molpro implementation, $\mathbf{F}_H$ becomes the unit matrix and thus $(-\mathbf{X}_0)^{1/2}\mathbf{F}_H(-\mathbf{X}_0)^{1/2} = -\mathbf{X}_0$
(26) Fritsch, F. N.; Carlson, R. E. Monotone Piecewise Cubic Interpolation. *SIAM J. Numer. Anal.* **1980**, *17*, 238−246.
(27) London, F. Théorie quantique des courants interatomiques dans les combinaisons aromatiques. *J. Phys. Radium.* **1937**, *8*, 397−409.
(28) Wolinski, K.; Hinton, J. F.; Pulay, P. Efficient implementation of the gauge-independent atomic orbital method for NMR chemical shift calculations. *J. Am. Chem. Soc.* **1990**, *112*, 8251−8260.
(29) Helgaker, T.; Jørgensen, P. An electronic Hamiltonian for origin independent calculations of magnetic properties. *J. Chem. Phys.* **1991**, *95*, 2595−2601.
(30) Ditchfield, R. Self-consistent perturbation theory of diamagnetism: I. A gauge-invariant LCAO method for NMR chemical shifts. *Mol. Phys.* **1974**, *27*, 789−807.
(31) Goerigk, L.; Hansen, A.; Bauer, C.; Ehrlich, S.; Najibi, A.; Grimme, S. A look at the density functional theory zoo with the advanced GMTKN55 database for general main group thermochemistry, kinetics and noncovalent interactions. *Phys. Chem. Chem. Phys.* **2017**, *19*, 32184−32215.
(32) Werne, H.-J; Knowles, P. J.; Knizia, G.; Manby, F. R.; Schütz, M.; Celani, P.; Györffy, W.; Korona, T.; Lindh, R.; Mitrushenkov, A.; Rauhut, G.; Shama-sundar, K. R.; Adler, T. B.; Amos, R. D.; Bennie, S. J.; Bernhardsson, A.; Berning, A.; Cooper, D. L.; Deegan, M. J. O.; Dobbyn, A. J.; Eckert, F.; Goll, E.; Hampel, C.; Heäÿelmann, A.; Hetzer, G.; Hrenar, T.; Jansen, G.; Köppl, C.; Lee, S. J. R.; Liu, Y.; Lloyd, A. W.; Ma, Q.; Mata, R. A.; May, A. J.; McNicholas, S. J.; Meyer, W.; Miller, T. F., III; Mura, M. E.; Nicklass, A.; O'Neill, D. P.; Palmieri, P.; Peng, D.; Pflüger, K.; Pitzer, R.; Shiozaki, T.; Stoll, H.; Tarroni, R.; Stoll, H.; Thorsteins-son, T.; Wang, M.; Welborn, M. *MOLPRO, version 2023.1, a package of ab initio programs*, 2023, see https://www.molpro.net (accessed April 4 2024).
(33) Kussmann, J.; Ochsenfeld, C. Pre-selective screening for matrix elements in linear-scaling exact exchange calculations. *J. Chem. Phys.* **2013**, *138*, 134114.
(34) Kussmann, J.; Ochsenfeld, C. Preselective screening for linear-scaling exact exchange-gradient calculations for graphics processing units and general strong-scaling massively parallel calculations. *J. Chem. Theory Comput.* **2015**, *11*, 918−922.
(35) Kussmann, J.; Ochsenfeld, C. Hybrid CPU/GPU Integral Engine for Strong-Scaling Ab Initio Methods. *J. Chem. Theory Comput.* **2017**, *13*, 3153−3159.
(36) Boyd, J. P. Exponentially convergent Fourier-Chebshev quadrature schemes on bounded and infinite intervals. *J. Sci. Comput.* **1987**, *2*, 99−109.
(37) Stephens, P. J.; Devlin, F. J.; Chabalowski, C. F.; Frisch, M. J. Ab initio calculation of vibrational absorption and circular dichroism spectra using density functional force fields. *J. Phys. Chem.* **1994**, *98*, 11623−11627.
(38) Sun, J.; Ruzsinszky, A.; Perdew, J. P. Strongly constrained and appropriately normed semilocal density functional. *Phys. Rev. Lett.* **2015**, *115*, 036402.
(39) Perdew, J. P.; Ruzsinszky, A.; Csonka, G. I.; Constantin, L. A.; Sun, J. Workhorse semilocal density functional for condensed matter physics and quantum chemistry. *Phys. Rev. Lett.* **2009**, *103*, 026403.
(40) Stoychev, G. L.; Auer, A. A.; Neese, F. Efficient and accurate prediction of nuclear magnetic resonance shielding tensors with double-hybrid density functional theory. *J. Chem. Theory Comp.* **2018**, *14*, 4756−4771.
(41) Grimme, S. Semiempirical hybrid density functional with perturbative second-order correlation. *J. Chem. Phys.* **2006**, *124* (3), 034108.
(42) Kozuch, S.; Martin, J. M. Spin-component-scaled double hybrids: an extensive search for the best fifth-rung functionals blending DFT and perturbation theory. *J. Comput. Chem.* **2013**, *34*, 2327−2344.
(43) Neese, F. The ORCA program system. *Wiley Interdiscip. Rev.: Comput. Mol. Sci.* **2012**, *2*, 73−78.
(44) Neese, F. Software update: The ORCA program system—Version 5.0. *Wiley Interdiscip. Rev.: Comput. Mol. Sci.* **2022**, *12*, No. e1606.
(45) Dunning, T. H. Gaussian basis sets for use in correlated molecular calculations. I. The atoms boron through neon and hydrogen. *J. Chem. Phys.* **1989**, *90*, 1007.
(46) Woon, D.; Dunning, T. H., Jr Gaussian basis sets for use in correlated molecular calculations. III. The atoms aluminum through argon. *J. Chem. Phys.* **1993**, *98*, 1358.
(47) Peterson, K. A.; Dunning, T., Jr H. Accurate correlation consistent basis sets for molecular core−valence correlation effects: The second row atoms Al−Ar, and the first row atoms B−Ne revisited. *J. Chem. Phys.* **2002**, *117*, 10548−10560.
(48) Weigend, F.; Köhn, A.; Hättig, C. Efficient use of the correlation consistent basis sets in resolution of the identity MP2 calculations. *J. Chem. Phys.* **2002**, *116*, 3175−3183.
(49) Hättig, C. Optimization of auxiliary basis sets for RI-MP2 and RI-CC2 calculations: Core-valence and quintuple-[small zeta] basis sets for H to Ar and QZVPP basis sets for Li to Kr. *Phys. Chem. Chem. Phys.* **2005**, *7*, 59−66.
(50) Teale, A. M.; Lutnæs, O. B.; Helgaker, T.; Tozer, D. J.; Gauss, J. Benchmarking density-functional theory calculations of NMR shielding constants and spin−rotation constants using accurate coupled-cluster calculations. *J. Chem. Phys.* **2013**, *138*, 024111.
(51) Matthews, D. A.; Cheng, L.; Harding, M. E.; Lipparini, F.; Stopkowicz, S.; Jagau, T.-C.; Szalay, P. G.; Gauss, J.; Stanton, J. F. Coupled-cluster techniques for computational chemistry: The CFOUR program package. *J. Chem. Phys.* **2020**, *152* (21), 214108.
(52) Yanai, T.; Tew, D. P.; Handy, N. C. A new hybrid exchange−correlation functional using the Coulomb-attenuating method (CAM-B3LYP). *Chem. Phys. Lett.* **2004**, *393*, 51−57.
(53) Keal, T. W.; Tozer, D. J. The exchange-correlation potential in Kohn−Sham nuclear magnetic resonance shielding calculations. *J. Chem. Phys.* **2003**, *119*, 3015−3024.

https://doi.org/10.1021/acs.jctc.4c00512
J. Chem. Theory Comput. 2024, 20, 6028−6036

Supporting Information: Accurate NMR shieldings with σ-functionals

Steffen Fauser[1,a], Viktoria Drontschenko[2,a], Christian Ochsenfeld[2,3], and Andreas Görling[*,1,4]

[1] *Lehrstuhl für Theoretische Chemie, Universität Erlangen-Nürnberg, Egerlandstr. 3, D-91058 Erlangen, Germany*

[2] *Chair of Theoretical Chemistry, Department of Chemistry, University of Munich (LMU), D-81377 Munich, Germany*

[3] *Max Planck Institute for Solid State Research, D-70569 Stuttgart, Germany*

[4] *Erlangen National High Performance Computing Center (NHR@FAU), Martensstr. 1, D-91058 Erlangen, Germany*

[a] These authors contributed equally

[*] Email: andreas.goerling@fau.de

1 Content

This supporting information contains, (i) the mean absolute errors (MAEs) of all reference sets that were involved in the optimization of σ-functionals with parametrization S1 (Sec. 2), (ii) the mean signed errors (as opposed to the mean absolut errors discussed in the main text) of the considered isotropic NMR shielding constants (Sec. 3), (iii) a discussion of the effect of augmented basis sets in the calculation of NMR shieldings with the σ-functional setup σ(S1)@PBE (Sec. 4), and (iv) tables with all calculated absolute isotropic NMR shieldings (Sec. 5).

Additionally, in separate files, we provide the coefficients for the new parametrizations σ(S1)@PBEh33, σ(S1)@PBEh50, σ(S1)@PBEh100, and σ(S1)@HF. These data are available on Zenodo (https://doi.org/10.5281/zenodo.10974893).

2 MAEs of reference sets for new parametrizations σ(S1)@PBEh33, σ(S1)@PBEh50, σ(S1)@PBEh100, and σ(S1)@HF

Table S1: MAEs in kcal/mol of RPA and σ(S1) calculations of those reference sets that enter the optimization for the parametrization S1 for σ-functionals using input data from PBE, PBE0, PBEh33, PBEh50, PBEh100, and HF. (The entries for σ-functionals based on PBE and PBE0 input data have already been published in Ref. [1] but are included here for completeness). Additionally the weighted deviation is shown using the weights of parametrization S1 according to Table 2 in Ref. [1]. Basis sets were used according to 'Setup 0' of Ref. [2] (see Table 2 there). For the nature of the reference sets see Table 1 of Ref. [2]. Reference sets were taken from the GMTKN55 database [3] unless noted otherwise.

Testset	**RPA**	**σ(S1)**	**RPA**	**σ(S1)**	**RPA**	**σ(S1)**	**RPA**	**σ(S1)**	**RPA**	**σ(S1)**	**RPA**	**σ(S1)**
	@PBE		@PBE0		@PBEh33		@PBEh50		@PBEh100		@HF	
W4-17[a,b]	26.35	6.48	21.91	5.85	23.03	6.49	26.07	6.78	37.89	6.59	37.49	7.15
YBDE18	3.34	1.54	3.25	1.15	3.38	1.16	3.75	1.14	5.77	1.57	5.68	1.94
MOR41-3d9[c,d]	1.96	1.8	1.59	1.85	1.55	1.67	1.38	1.59	2.83	3.65	3.66	4.2
MOBH35-3d9BH[c,e]	1.72	1.68	1.22	1.37	1.21	1.24	1.28	0.99	3.1	1.36	3.28	1.71
MOBH35-3d9RE[c,e]	1.96	2.25	2.1	2.11	2.15	2.04	2.15	1.81	4.46	2.51	4.74	3.18
W4-17RE[a,b,f]	2.96	1.38	1.9	0.99	2.09	1.01	2.72	1.17	4.92	2.7	5.22	3.7
PA26	3.67	1.52	4.04	1.05	4.15	0.97	4.34	0.95	4.6	0.94	4.36	0.91
ISO34	0.78	0.5	0.64	0.32	0.63	0.31	0.61	0.42	0.8	0.74	0.87	0.78
BH76	1.66	1.21	1.02	1.22	1.1	1.23	1.76	1.23	4.87	2.73	5.62	3.73
PX13	0.56	0.43	0.98	0.54	1.23	0.57	1.96	0.46	4.57	0.19	4.7	0.2
WCPT18	1.06	0.54	0.86	0.55	1.32	0.56	2.23	0.57	5.15	0.43	5.15	0.57
BHPERI	0.71	0.92	1.81	1.1	2.22	1.14	3.01	0.82	5.17	0.6	4.64	1.1
PCONF21	0.41	0.54	0.21	0.43	0.14	0.42	0.08	0.26	0.39	0.22	0.53	0.21
MCONF	0.26	0.17	0.15	0.11	0.11	0.12	0.05	0.06	0.26	0.11	0.36	0.13
S22[g,h]	0.96	0.46	0.88	0.31	0.88	0.3	0.92	0.26	1.14	0.14	1.28	0.43
G2RC	3.84	1.1	1.49	0.93	1.31	0.88	1.36	0.83	3.23	1.29	3.54	1.28
PNICO23[g]	1.56	0.91	1.1	0.46	1.03	0.4	0.97	0.39	1.08	0.25	1.13	0.32
WeightedDev(S2h)	2.27	1.23	1.78	1.04	1.88	1.01	2.22	0.99	3.97	1.69	4.18	2.14

[a] Atomization and reaction energies containing C_2 and ClOO are excluded because KS calculations for the input orbitals and eigenvalues did not converge. [b] Reference [4] [c] Using only a subset of those reactions with 3d transition metals (reactions 1-6,12,15,40 in MOR41 and reactions 1-9 in MOBH35). [d] Reference [5] [e] Reference [6] [f] Reference [7] [g] Using counterpoise correction. [h] Reaction 21 is excluded because KS calculation did not converge.

3 Mean signed errors of isotropic NMR shielding constants based on various density functionals, as well as RPA, and σ-functionals

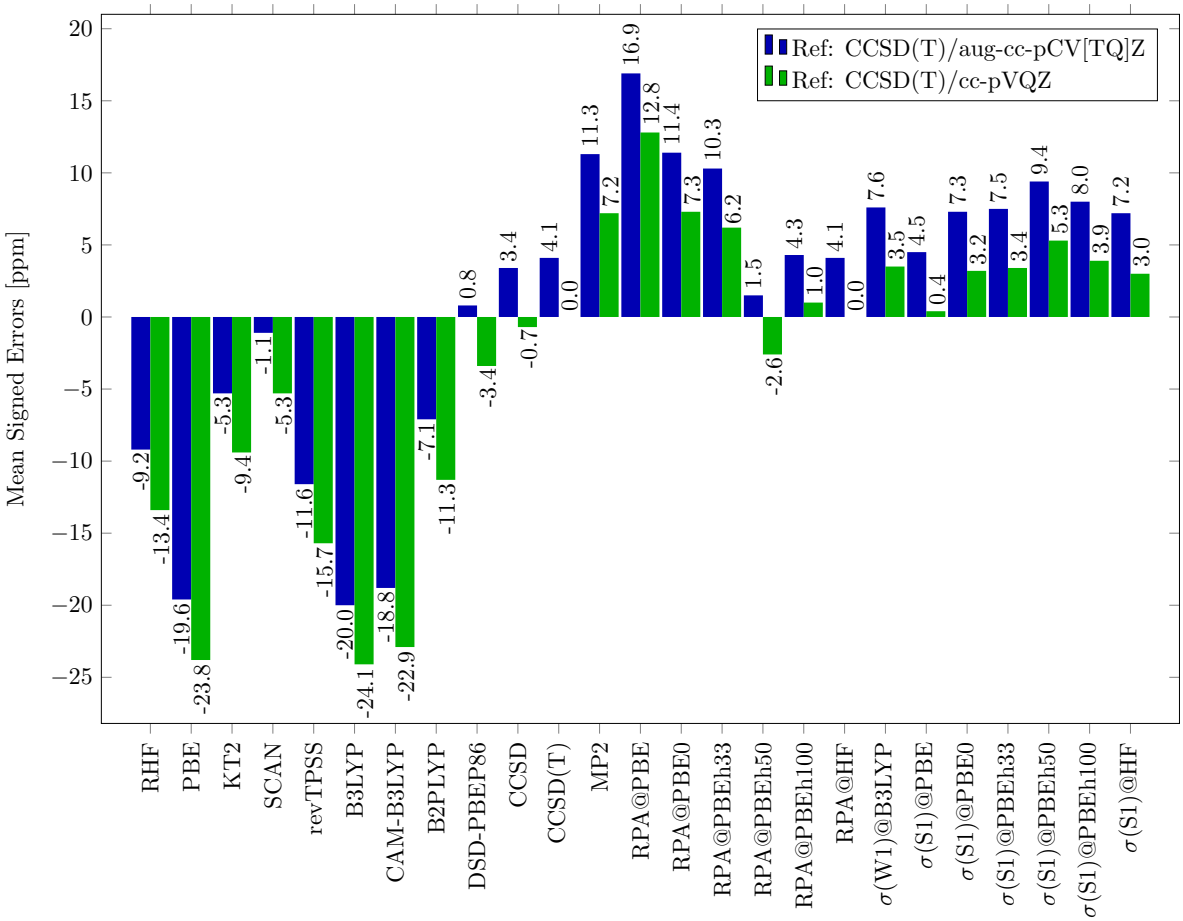

Figure S1: Mean signed errors (ppm) of isotropic NMR shielding constants based on various methods in a cc-pVQZ basis set compared to basis set extrapolated CCSD(T) data, denoted as CCSD(T)/aug-cc-pCV[TQ]Z (blue), and CCSD(T)/cc-pVQZ data (green). For all calculations the Gauss benchmark set [8] was used.

4 Effect of augmentation of the basis set

Figure S2 shows the basis set dependence of σ(S1)@PBE NMR shieldings similar to Figure 4 of the main paper, but now additionally results from extrapolated aug-cc-pwCV[TQ]Z basis sets are included. For technical reasons the molecules H_4C_2O and C_3H_4 could not be calculated with aug-cc-pwCVQZ basis sets and were therefore excluded from the benchmark set of Gauss and coworkers [8] in all cases. Due to the two missing molecules the MAEs for those basis sets included in Table 4 of the main text as well as Table S2 in this supporting information are not identical. The removal of the two molecules leads to a slightly higher MAE of 4.2 ppm for the cc-pwCV[TQ]Z shieldings compared to 3.8 ppm for the full reference set, see Table 4 main text. The MAE of the aug-cc-pwCV[TQ]Z shieldings and of the cc-pwCV[TQ]Z shieldings for the benchmark set of Ref. [8] without H_4C_2O and C_3H_4 is identical (4.2 ppm) which suggests that augmentation functions are not required.

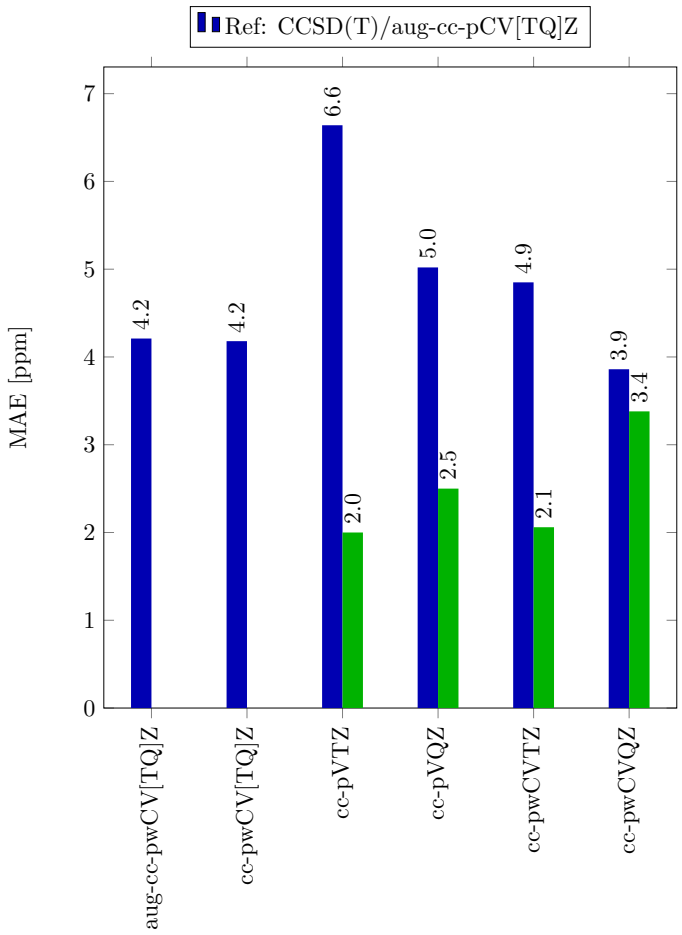

Figure S2: MAEs (ppm) of NMR shieldings for σ(S1)@PBE computed with different basis sets compared to CCSD(T)/aug-cc-pCV[TQ]Z (blue) and CCSD(T) with the same basis set (green). Further, aug-cc-pwCV[TQ]Z and cc-pwCV[TQ]Z denote basis set extrapolated σ(S1)@PBE results. For all calculations the Gauss benchmark set [8] was used with the molecules H_4C_2O and C_3H_4 excluded.

5 Absolute isotropic NMR shieldings

5.1 Absolute isotropic NMR shieldings at the RPA level of theory with a cc-pVQZ basis set

Table S2: Absolute isotropic NMR shieldings (ppm) for each nucleus (nuc.) of the molecules (mol.) in the Gauss benchmark set [8] with a cc-pVQZ basis set (with the corresponding RI basis set). As reference serve CCSD(T)/cc-pVQZ shieldings (taken from Ref. [9]) as well as basis set extrapolated CCSD(T)/aug-cc-pCV[TQ]Z shieldings (extrap.) taken from Ref. [8].

mol.	nuc.	CCSD(T)	extrap.	RPA@PBE0	RPA@PBEh33	RPA@PBEh50	RPA@PBEh100
AlF							
	AL	587.7	572.9	588.5	588.4	588.5	589.9
	F	212.2	211.8	227.5	227.0	226.3	227.6
C_2H_4							
	C	72.9	69.7	75.1	74.2	72.7	69.7
	H	26.1	26.0	26.5	26.5	26.4	26.4
C_3H_4							
	C	193.2	192.1	191.7	191.5	191.3	191.3
	C	86.5	83.7	88.7	87.9	86.4	83.5
	H	24.5	24.4	24.8	24.8	24.8	24.7
	H	30.7	30.6	30.9	30.9	30.9	30.9
CH_2O							
	O	-377.2	-378.6	-300.3	-306.2	-317.4	-351.8
	C	6.5	1.5	16.5	14.8	12.0	7.2
	H	22.1	22.0	22.8	22.7	22.7	22.7
CH_3F							
	C	124.5	122.1	125.6	125.2	124.7	124.7
	F	482.7	482.9	476.9	477.3	478.0	480.0
	H	27.5	27.3	27.7	27.7	27.7	27.8
CH_4							
	C	199.9	198.9	197.3	197.1	196.9	196.7
	H	31.4	31.3	31.5	31.5	31.5	31.5
CO							
	C	5.8	2.2	13.5	11.5	8.0	0.6
	O	-51.9	-55.0	-34.5	-36.6	-40.3	-49.8
FCCH							
	C	181.4	179.9	180.8	180.5	180.0	179.2
	C	102.6	100.1	104.3	103.9	103.2	102.7
	H	30.6	30.5	30.8	30.8	30.7	30.7
	F	424.0	423.5	425.1	425.5	426.1	426.1
FCN							

Table S2: (continued)

	F	375.1	374.1	377.9	378.1	378.4	379.5
	C	84.8	82.2	86.7	86.1	85.0	82.6
	N	120.1	117.9	125.0	123.9	121.5	114.2
H_2C_2O							
	C	194.4	193.3	192.8	192.6	192.3	192.0
	C	-2.0	-6.3	3.0	2.2	0.7	-3.1
	O	-4.3	-5.9	13.7	12.9	11.1	2.4
	H	29.3	29.2	29.6	29.6	29.5	29.5
H_2O							
	O	341.0	338.0	338.5	338.4	338.2	337.0
	H	30.9	30.6	31.1	31.1	31.0	30.9
H_2S							
	S	759.6	739.0	749.2	748.3	746.5	742.1
	H	30.7	30.5	30.9	30.9	30.9	30.9
H_4C_2O							
	O	364.7	363.2	363.4	364.1	365.1	366.3
	C	155.1	153.2	155.1	154.8	154.5	154.5
	H	29.2	29.1	29.4	29.4	29.5	29.5
HCN							
	H	29.1	29.0	29.3	29.3	29.3	29.3
	C	87.3	84.6	90.4	89.5	87.8	83.8
	N	-11.3	-14.1	-0.4	-2.5	-6.3	-15.6
HCP							
	H	29.7	29.6	29.9	29.9	29.9	30.0
	C	41.1	37.6	44.9	43.7	41.4	34.1
	P	426.9	388.0	440.4	439.5	436.2	410.9
HF							
	H	29.1	28.8	29.4	29.3	29.2	29.0
	F	419.9	420.3	418.7	418.7	418.7	418.3
HFCO							
	O	-91.0	-94.3	-65.0	-66.7	-70.3	-85.7
	C	43.1	39.6	46.4	45.7	44.5	41.7
	F	166.9	165.3	182.3	181.9	181.6	184.0
	H	24.0	23.9	24.3	24.3	24.3	24.4
HOF							
	O	-58.7	-68.9	-27.9	-34.6	-45.2	-59.3
	H	20.0	19.6	21.1	21.0	20.7	20.6
	F	191.6	192.2	211.2	211.6	212.9	216.8
LiF							
	LI	89.4	89.3	89.5	89.5	89.5	89.7

Table S2: (continued)

	F	377.0	382.5	382.2	381.8	381.6	384.9
LiH							
	H	26.6	26.6	26.7	26.8	26.8	26.9
	LI	89.3	89.3	89.6	89.5	89.4	89.2
N_2							
	N	-57.6	-60.4	-46.2	-48.8	-53.4	-62.9
N_2O							
	N	109.4	106.4	114.1	112.5	109.6	102.4
	N	16.0	12.6	21.1	19.4	16.1	7.6
	O	199.9	199.0	205.9	205.2	204.0	199.8
NH_3							
	N	273.1	270.7	270.3	270.1	269.8	268.7
	H	31.6	31.4	31.8	31.8	31.8	31.8
OCS							
	O	98.7	96.8	108.1	107.2	105.5	100.4
	C	33.8	30.2	37.9	36.7	34.4	28.1
	S	815.1	796.7	818.6	818.3	817.6	813.3
OF_2							
	O	-430.3	-447.1	-353.9	-368.4	-388.4	-407.1
	F	-12.7	-24.0	21.0	19.0	16.4	13.5
PN							
	N	-340.7	-344.0	-307.4	-314.0	-325.7	-355.6
	P	118.2	50.6	150.1	141.7	127.1	92.3
AlF							
	AL	587.7	572.9	588.5	588.4	588.5	589.9
	F	212.2	211.8	227.5	227.0	226.3	227.6
C_2H_4							
	C	72.9	69.7	75.1	74.2	72.7	69.7
	H	26.1	26.0	26.5	26.5	26.4	26.4
C_3H_4							
	C	193.2	192.1	191.7	191.5	191.3	191.3
	C	86.5	83.7	88.7	87.9	86.4	83.5
	H	24.5	24.4	24.8	24.8	24.8	24.7
	H	30.7	30.6	30.9	30.9	30.9	30.9
CH_2O							
	O	-377.2	-378.6	-300.3	-306.2	-317.4	-351.8
	C	6.5	1.5	16.5	14.8	12.0	7.2
	H	22.1	22.0	22.8	22.7	22.7	22.7
CH_3F							
	C	124.5	122.1	125.6	125.2	124.7	124.7

Table S2: (continued)

	F	482.7	482.9	476.9	477.3	478.0	480.0
	H	27.5	27.3	27.7	27.7	27.7	27.8
CH_4							
	C	199.9	198.9	197.3	197.1	196.9	196.7
	H	31.4	31.3	31.5	31.5	31.5	31.5
CO							
	C	5.8	2.2	13.5	11.5	8.0	0.6
	O	-51.9	-55.0	-34.5	-36.6	-40.3	-49.8
FCCH							
	C	181.4	179.9	180.8	180.5	180.0	179.2
	C	102.6	100.1	104.3	103.9	103.2	102.7
	H	30.6	30.5	30.8	30.8	30.7	30.7
	F	424.0	423.5	425.1	425.5	426.1	426.1
FCN							
	F	375.1	374.1	377.9	378.1	378.4	379.5
	C	84.8	82.2	86.7	86.1	85.0	82.6
	N	120.1	117.9	125.0	123.9	121.5	114.2
H_2C_2O							
	C	194.4	193.3	192.8	192.6	192.3	192.0
	C	-2.0	-6.3	3.0	2.2	0.7	-3.1
	O	-4.3	-5.9	13.7	12.9	11.1	2.4
	H	29.3	29.2	29.6	29.6	29.5	29.5
H_2O							
	O	341.0	338.0	338.5	338.4	338.2	337.0
	H	30.9	30.6	31.1	31.1	31.0	30.9
H_2S							
	S	759.6	739.0	749.2	748.3	746.5	742.1
	H	30.7	30.5	30.9	30.9	30.9	30.9
H_4C_2O							
	O	364.7	363.2	363.4	364.1	365.1	366.3
	C	155.1	153.2	155.1	154.8	154.5	154.5
	H	29.2	29.1	29.4	29.4	29.5	29.5
HCN							
	H	29.1	29.0	29.3	29.3	29.3	29.3
	C	87.3	84.6	90.4	89.5	87.8	83.8
	N	-11.3	-14.1	-0.4	-2.5	-6.3	-15.6
HCP							
	H	29.7	29.6	29.9	29.9	29.9	30.0
	C	41.1	37.6	44.9	43.7	41.4	34.1
	P	426.9	388.0	440.4	439.5	436.2	410.9

Table S2: (continued)

HF							
	H	29.1	28.8	29.4	29.3	29.2	29.0
	F	419.9	420.3	418.7	418.7	418.7	418.3
HFCO							
	O	-91.0	-94.3	-65.0	-66.7	-70.3	-85.7
	C	43.1	39.6	46.4	45.7	44.5	41.7
	F	166.9	165.3	182.3	181.9	181.6	184.0
	H	24.0	23.9	24.3	24.3	24.3	24.4
HOF							
	O	-58.7	-68.9	-27.9	-34.6	-45.2	-59.3
	H	20.0	19.6	21.1	21.0	20.7	20.6
	F	191.6	192.2	211.2	211.6	212.9	216.8
LiF							
	LI	89.4	89.3	89.5	89.5	89.5	89.7
	F	377.0	382.5	382.2	381.8	381.6	384.9
LiH							
	H	26.6	26.6	26.7	26.8	26.8	26.9
	LI	89.3	89.3	89.6	89.5	89.4	89.2
N_2							
	N	-57.6	-60.4	-46.2	-48.8	-53.4	-62.9
N_2O							
	N	109.4	106.4	114.1	112.5	109.6	102.4
	N	16.0	12.6	21.1	19.4	16.1	7.6
	O	199.9	199.0	205.9	205.2	204.0	199.8
NH_3							
	N	273.1	270.7	270.3	270.1	269.8	268.7
	H	31.6	31.4	31.8	31.8	31.8	31.8
OCS							
	O	98.7	96.8	108.1	107.2	105.5	100.4
	C	33.8	30.2	37.9	36.7	34.4	28.1
	S	815.1	796.7	818.6	818.3	817.6	813.3
OF_2							
	O	-430.3	-447.1	-353.9	-368.4	-388.4	-407.1
	F	-12.7	-24.0	21.0	19.0	16.4	13.5
PN							
	N	-340.7	-344.0	-307.4	-314.0	-325.7	-355.6
	P	118.2	50.6	150.1	141.7	127.1	92.3

5.2 Absolute isotropic NMR shieldings at the RPA@PBE0 level of theory with a cc-pVTZ basis set

Table S3: Absolute isotropic NMR shieldings (ppm) for each nucleus (nuc.) of the molecules (mol.) in the Gauss benchmark set [8] with a cc-pVTZ basis set (with the corresponding RI basis set). As reference serve CCSD(T)/cc-pVTZ shieldings (taken from Ref. [9]) as well as basis set extrapolated CCSD(T)/aug-cc-pCV[TQ]Z shieldings (extrap.) taken from Ref. [8].

mol.	nuc.	CCSD(T)	extrap.	RPA@PBE0
AlF				
	AL	576.5	572.9	582.0
	F	200.2	211.8	215.8
C_2H_4				
	C	77.3	69.7	79.4
	H	26.3	26.0	26.7
C_3H_4				
	C	194.9	192.1	193.3
	C	90.3	83.7	92.4
	H	24.6	24.4	25.0
	H	30.9	30.6	31.1
CH_2O				
	O	-376.5	-378.6	-297.7
	C	13.2	1.5	23.3
	H	22.3	22.0	23.0
CH_3F				
	C	127.4	122.1	128.3
	F	479.2	482.9	473.3
	H	27.7	27.3	27.9
CH_4				
	C	201.3	198.9	198.7
	H	31.5	31.3	31.6
CO				
	C	11.3	2.2	19.6
	O	-49.8	-55.0	-31.6
FCCH				
	C	183.1	179.9	183.1
	C	105.3	100.1	107.0
	H	30.7	30.5	31.0
	F	421.2	423.5	422.6
FCN				
	F	373.2	374.1	376.9
	C	88.2	82.2	90.2

Table S3: (continued)

	N	122.4	117.9	127.7
H_2C_2O				
	C	196.3	193.3	194.9
	C	3.4	-6.3	8.5
	O	-3.9	-5.9	15.1
	H	29.5	29.2	29.8
H_2O				
	O	344.3	338.0	341.2
	H	31.3	30.6	31.6
H_2S				
	S	758.5	739.0	748.5
	H	30.9	30.5	31.2
H_4C_2O				
	O	362.1	363.2	361.4
	C	158.1	153.2	158.0
	H	29.4	29.1	29.6
HCN				
	H	29.2	29.0	29.5
	C	91.5	84.6	94.7
	N	-7.4	-14.1	3.7
HCP				
	H	29.7	29.6	29.9
	C	45.4	37.6	48.7
	P	412.9	388.0	427.0
HF				
	H	29.5	28.8	29.9
	F	419.8	420.3	418.2
HFCO				
	O	-88.0	-94.3	-61.3
	C	47.0	39.6	50.5
	F	167.2	165.3	182.5
	H	24.3	23.9	24.6
HOF				
	O	-44.4	-68.9	-12.0
	H	20.7	19.6	21.9
	F	188.3	192.2	209.4
LiF				
	LI	90.8	89.3	90.7
	F	370.3	382.5	368.9
LiH				

Table S3: (continued)

	H	26.5	26.6	26.7
	LI	90.0	89.3	90.3
N_2				
	N	-52.5	-60.4	-40.3
N_2O				
	N	114.3	106.4	119.5
	N	22.1	12.6	27.4
	O	197.0	199.0	204.2
NH_3				
	N	276.2	270.7	272.8
	H	32.0	31.4	32.2
OCS				
	O	98.7	96.8	108.9
	C	37.9	30.2	42.2
	S	810.9	796.7	817.9
OF_2				
	O	-402.8	-447.1	-323.5
	F	0.0	-24.0	34.8
PN				
	N	-336.0	-344.0	-301.1
	P	89.4	50.6	128.1

5.3 Absolute isotropic NMR shieldings at the σ-functional level of theory with a cc-pVQZ basis set

Table S4: Absolute isotropic NMR shieldings (ppm) for each nucleus (nuc.) of the molecules (mol.) in the Gauss benchmark set [8] with a cc-pVQZ basis set (with the corresponding RI basis set) for σ-functionals based on various parametrizations and references. As reference serve CCSD(T)/cc-pVQZ shieldings (taken from Ref. [9]) as well as basis set extrapolated CCSD(T)/aug-cc-pCV[TQ]Z shieldings (extrap.) taken from Ref. [8].

mol.	nuc.	CCSD(T)	extrap.	W1@B3LYP	W1@PBE	S1@PBE	S2@PBE	S1@PBE0	S1@PBEh33	S1@PBEh50	S1@PBEh100	S1@HF
AlF												
	AL	587.7	572.9	584.2	584.7	583.3	584.5	585.6	585.8	587.6	585.5	585.8
	F	212.2	211.8	223.9	227.4	222.6	222.3	219.8	218.1	220.0	216.6	215.8
C_2H_4												
	C	72.9	69.7	74.8	73.9	72.8	73.4	73.6	72.8	72.8	72.5	71.6
	H	26.1	26.0	26.2	26.2	26.2	26.3	26.3	26.3	26.3	26.3	26.3
C_3H_4												
	C	193.2	192.1	192.3	192.8	192.7	192.5	191.6	191.3	191.2	191.0	191.0
	C	86.5	83.7	87.5	87.7	86.7	87.2	87.3	87.2	87.0	87.0	86.2
	H	24.5	24.4	24.6	24.6	24.6	24.6	24.6	24.6	24.6	24.7	24.7
	H	30.7	30.6	30.7	30.8	30.8	30.8	30.8	30.8	30.8	30.8	30.8
CH_2O												
	O	-377.2	-378.6	-335.0	-341.2	-365.2	-359.5	-338.0	-335.0	-313.8	-329.0	-330.6
	C	6.5	1.5	9.7	10.0	7.0	7.7	9.0	8.7	9.5	9.4	7.1
	H	22.1	22.0	22.4	22.5	22.3	22.4	22.3	22.3	22.4	22.6	22.5
CH_3F												
	C	124.5	122.1	125.5	126.0	125.5	125.4	124.3	123.9	123.7	124.3	124.1
	F	482.7	482.9	481.3	483.1	482.9	481.7	480.1	479.7	479.1	477.2	476.6
	H	27.5	27.3	27.5	27.6	27.6	27.6	27.5	27.5	27.5	27.6	27.6
CH_4												
	C	199.9	198.9	199.6	199.3	199.4	199.1	198.5	198.5	198.7	198.6	198.5

Table S4: (continued)

	H	31.4	31.3	31.4	31.3	31.3	31.4	31.4	31.4	31.4	31.4	31.4
CO												
	C	5.8	2.2	5.7	8.4	5.5	6.5	8.3	8.2	10.1	8.6	6.8
	O	-51.9	-55.0	-41.0	-42.5	-48.4	-47.2	-41.4	-41.3	-36.0	-42.4	-44.6
FCCH												
	C	181.4	179.9	181.6	179.6	179.7	180.1	180.6	180.7	180.9	180.7	180.2
	C	102.6	100.1	103.9	103.2	102.6	102.8	102.6	102.4	101.5	101.6	101.1
	H	30.6	30.5	30.6	30.5	30.5	30.6	30.6	30.6	30.6	30.6	30.7
	F	424.0	423.5	424.0	424.0	423.2	422.9	424.2	423.9	424.8	423.0	421.4
FCN												
	F	375.1	374.1	374.9	375.0	373.6	373.0	374.6	374.9	375.8	376.5	375.5
	C	84.8	82.2	86.2	84.9	83.9	84.3	85.2	85.3	84.8	83.5	82.6
	N	120.1	117.9	125.1	119.8	119.2	120.5	125.1	125.7	127.3	123.5	122.3
H_2C_2O												
	C	194.4	193.3	193.5	193.3	193.4	193.3	193.4	193.5	193.8	194.6	194.4
	C	-2.0	-6.3	-0.8	-1.6	-3.5	-4.7	-0.4	-0.3	0.6	0.3	-1.2
	O	-4.3	-5.9	12.1	6.0	1.9	2.1	11.7	12.8	21.1	13.6	12.7
	H	29.3	29.2	29.3	29.3	29.3	29.3	29.3	29.4	29.4	29.4	29.5
H_2O												
	O	341.0	338.0	340.2	339.5	339.7	339.2	339.9	340.2	341.4	341.0	342.1
	H	30.9	30.6	30.8	30.8	30.8	30.9	30.9	30.9	30.9	31.0	31.1
H_2S												
	S	759.6	739.0	752.9	752.1	751.1	749.1	751.3	751.5	754.8	758.7	760.7
	H	30.7	30.5	30.7	30.7	30.7	30.7	30.7	30.8	30.7	30.7	30.7
H_4C_2O												
	O	364.7	363.2	363.4	361.3	360.9	360.7	363.1	363.3	363.7	361.9	361.7
	C	155.1	153.2	155.1	155.3	155.1	155.2	154.2	153.9	153.8	154.5	154.4
	H	29.2	29.1	29.2	29.3	29.3	29.3	29.3	29.3	29.3	29.4	29.4

Table S4: (continued)

HCN												
	H	29.1	29.0	29.1	29.2	29.2	29.2	29.1	29.1	29.1	29.2	29.2
	C	87.3	84.6	88.6	87.4	86.2	86.8	88.4	88.5	88.8	86.7	86.1
	N	-11.3	-14.1	-0.5	-6.9	-8.3	-6.7	-2.7	-2.1	-1.3	-4.6	-5.3
HCP												
	H	29.7	29.6	29.7	29.8	29.8	29.8	29.7	29.7	29.7	29.7	29.7
	C	41.1	37.6	43.9	41.4	39.2	40.6	44.8	44.8	44.0	38.5	38.9
	P	426.9	388.0	424.5	417.6	412.8	414.9	440.1	441.8	443.0	421.7	417.5
HF												
	H	29.1	28.8	29.0	28.9	29.0	29.1	29.2	29.2	29.1	29.3	29.4
	F	419.9	420.3	420.7	421.0	420.9	420.4	419.7	420.0	421.8	420.2	420.5
HFCO												
	O	-91.0	-94.3	-73.6	-81.4	-89.9	-87.7	-74.8	-72.2	-63.1	-73.4	-75.4
	C	43.1	39.6	44.1	42.8	41.4	41.9	43.2	43.1	43.5	42.5	41.2
	F	166.9	165.3	174.3	175.7	170.1	170.0	170.8	170.6	173.5	173.9	171.8
	H	24.0	23.9	24.1	24.1	24.1	24.1	24.5	24.1	24.1	24.2	24.2
HOF												
	O	-58.7	-68.9	-49.7	-40.1	-52.9	-48.6	-50.1	-48.8	-37.0	-26.3	-27.4
	H	20.0	19.6	20.2	20.6	20.3	20.4	20.2	20.2	20.5	21.2	21.2
	F	191.6	192.2	200.1	203.4	195.3	195.9	197.3	196.6	200.3	193.0	191.2
LiF												
	LI	89.4	89.3	89.2	89.4	89.2	89.2	89.0	88.9	88.8	89.3	89.3
	F	377.0	382.5	384.6	387.4	384.3	383.4	380.0	378.1	377.1	377.3	374.4
LiH												
	H	26.6	26.6	26.7	26.7	26.7	26.7	26.6	26.6	26.6	26.7	26.7
	LI	89.3	89.3	89.3	89.3	89.2	89.2	89.2	89.1	89.0	89.0	89.3
N_2												
	N	-57.6	-60.4	-50.0	-54.6	-58.7	-57.3	-53.0	-51.8	-48.0	-48.2	-51.0

Table S4: (continued)

N_2O												
	N	109.4	106.4	114.1	109.9	108.2	109.1	113.3	114.4	112.9	116.5	115.1
	N	16.0	12.6	21.3	18.9	17.0	17.4	20.4	21.0	21.5	18.6	17.1
	O	199.9	199.0	203.1	200.5	197.9	198.2	203.1	204.1	207.9	207.8	206.0
NH_3												
	N	273.1	270.7	271.9	271.3	271.4	271.0	271.7	271.9	272.3	272.4	273.5
	H	31.6	31.4	31.6	31.6	31.6	31.6	31.6	31.7	31.7	31.7	31.8
OCS												
	O	98.7	96.8	107.2	104.6	102.0	102.5	107.1	107.4	108.8	105.3	103.8
	C	33.8	30.2	37.6	36.1	34.5	34.9	37.3	37.0	36.6	34.0	32.8
	S	815.1	796.7	809.3	808.9	808.8	808.9	813.5	812.1	818.6	819.6	819.3
OF_2												
	O	-430.3	-447.1	-410.7	-372.8	-409.9	-402.8	-419.7	-420.5	-399.9	-390.0	-391.4
	F	-12.7	-24.0	-2.1	2.2	-10.9	-8.6	-4.4	-4.0	7.5	8.3	8.6
PN												
	N	-340.7	-344.0	-316.3	-329.8	-337.6	-333.7	-313.4	-310.8	-306.4	-316.1	-316.6
	P	118.2	50.6	126.5	119.2	111.2	113.7	135.3	137.0	137.7	125.1	111.4

5.4 Absolute isotropic NMR shieldings at the σ-functional level of theory with a cc-pVTZ basis set

Table S5: Absolute isotropic NMR shieldings (ppm) for each nucleus (nuc.) of the molecules (mol.) in the Gauss benchmark set [8] with a cc-pVTZ basis set (with the corresponding RI basis set) for σ-functionals based on various parametrizations and references. As reference serve CCSD(T)/cc-pVTZ shieldings (taken from Ref. [9]) as well as basis set extrapolated CCSD(T)/aug-cc-pCV[TQ]Z shieldings (extrap.) taken from Ref. [8].

mol.	nuc.	CCSD(T)	extrap.	S1@PBE	S1re@PBE	S1@PBE0	S1re@PBE0
AlF							
	AL	576.5	572.9	577.5	571.4	575.8	569.8
	F	200.2	211.8	206.6	194.1	205.3	198.3
C_2H_4							
	C	77.3	69.7	77.3	77.4	77.6	77.4
	H	26.3	26.0	26.5	26.4	26.5	26.4
C_3H_4							
	C	194.9	192.1	194.8	195.9	193.1	194.1
	C	90.3	83.7	90.5	90.4	90.6	90.2
	H	24.6	24.4	24.8	24.7	24.9	24.7
	H	30.9	30.6	31.0	31.0	31.0	31.0
CH_2O							
	O	-376.5	-378.6	-376.0	-431.2	-344.1	-398.0
	C	13.2	1.5	14.8	10.1	16.8	10.2
	H	22.3	22.0	22.6	22.3	22.6	22.3
CH_3F							
	C	127.4	122.1	128.4	128.3	127.2	126.5
	F	479.2	482.9	477.8	477.8	474.6	476.9
	H	27.7	27.3	27.9	27.8	27.8	27.7
CH_4							
	C	201.3	198.9	200.2	201.0	199.3	200.2
	H	31.5	31.3	31.5	31.5	31.5	31.5
CO							
	C	11.3	2.2	10.2	3.5	13.4	6.2
	O	-49.8	-55.0	-49.2	-65.3	-42.4	-58.4
FCCH							
	C	183.1	179.9	181.4	182.4	182.8	183.6
	C	105.3	100.1	105.0	105.2	105.6	105.0
	H	30.7	30.5	30.8	30.7	30.9	30.8
	F	421.2	423.5	419.7	420.0	420.3	421.5
FCN							
	F	373.2	374.1	369.7	366.5	371.5	369.9

Table S5: (continued)

	C	88.2	82.2	87.9	87.2	88.9	87.7
	N	122.4	117.9	119.9	119.0	126.0	125.6
H_2C_2O							
	C	196.3	193.3	194.7	195.7	195.0	196.2
	C	3.4	-6.3	2.1	-0.1	5.0	2.1
	O	-3.9	-5.9	-2.7	-13.7	8.6	-1.5
	H	29.5	29.2	29.6	29.5	29.7	29.5
H_2O							
	O	344.3	338.0	341.2	343.3	340.8	343.6
	H	31.3	30.6	31.4	31.4	31.5	31.4
H_2S							
	S	758.5	739.0	746.9	746.5	745.7	751.8
	H	30.9	30.5	31.1	31.0	31.1	31.0
H_4C_2O							
	O	362.1	363.2	359.1	357.9	359.8	361.2
	C	158.1	153.2	158.4	158.8	157.2	157.5
	H	29.4	29.1	29.6	29.5	29.6	29.4
HCN							
	H	29.2	29.0	29.4	29.3	29.4	29.2
	C	91.5	84.6	90.8	89.2	92.7	90.0
	N	-7.4	-14.1	-6.4	-10.3	-0.6	-4.7
HCP							
	H	29.7	29.6	29.9	29.8	29.9	29.8
	C	45.4	37.6	44.4	43.4	48.5	48.2
	P	412.9	388.0	416.5	411.2	422.0	419.2
HF							
	H	29.5	28.8	29.7	29.8	29.9	29.8
	F	419.8	420.3	419.0	419.0	417.8	418.7
HFCO							
	O	-88.0	-94.3	-91.7	-109.1	-75.1	-92.7
	C	47.0	39.6	45.7	44.4	47.5	44.8
	F	167.2	165.3	166.8	153.3	168.7	157.6
	H	24.3	23.9	24.5	24.3	24.4	24.3
HOF							
	O	-44.4	-68.9	-38.1	-72.9	-34.1	-67.9
	H	20.7	19.6	21.2	20.2	21.2	20.2
	F	188.3	192.2	191.8	174.4	193.3	187.0
LiF							
	LI	90.8	89.3	90.7	90.6	90.5	90.4
	F	370.3	382.5	367.9	362.2	365.3	362.4

Table S5: (continued)

LiH							
	H	26.5	26.6	26.5	26.5	26.6	26.6
	LI	90.0	89.3	90.6	90.9	90.3	90.5
N_2							
	N	-52.5	-60.4	-55.4	-65.9	-48.9	-60.3
N_2O							
	N	114.3	106.4	111.8	109.8	117.5	114.8
	N	22.1	12.6	22.9	21.5	26.0	23.5
	O	197.0	199.0	194.0	189.8	199.4	194.7
NH_3							
	N	276.2	270.7	273.3	275.4	273.2	275.2
	H	32.0	31.4	32.1	32.0	32.1	32.0
OCS							
	O	98.7	96.8	99.4	93.5	104.8	100.6
	C	37.9	30.2	38.6	37.8	41.2	39.4
	S	810.9	796.7	805.5	802.5	808.5	806.0
OF_2							
	O	-402.8	-447.1	-381.6	-484.6	-392.5	-466.4
	F	0.0	-24.0	3.3	-24.4	8.9	-14.5
PN							
	N	-336.0	-344.0	-338.1	-358.6	-318.2	-333.1
	P	89.4	50.6	84.6	58.8	100.8	79.2

5.5 Absolute isotropic NMR shieldings at the σ(S1)@PBE level of theory with a cc-pwCVXZ basis set (X$\in$ T, Q)

Table S6: Absolute isotropic NMR shieldings (ppm) for each nucleus (nuc.) of the molecules (mol.) in the Gauss benchmark set [8] with a cc-pwCVTZ and cc-pwCVQZ basis (with their corresponding RI basis sets). 'extrap.' denotes basis set extrapolated CCSD(T)/aug-cc-pCV[TQ]Z shieldings (taken from Ref. [8]) and 'S1@PBE' denotes σ(S1)@PBE shieldings. The CCSD(T)/cc-pwCVTZ and CCSD(T)/cc-pwCVQZ calculations were carried out using the CFOUR program [10].

mol.	nuc.	extrap.	cc-pwCVTZ		cc-pwCVQZ	
			CCSD(T)	S1@PBE	CCSD(T)	S1@PBE
AlF						
	AL	572.9	571.7	567.6	572.1	568.3
	F	211.8	198.2	203.2	206.6	218.2
C_2H_4						
	C	69.7	74.7	74.7	71.1	72.7
	H	26.0	26.3	26.4	26.1	26.2
C_3H_4						
	C	192.1	193.7	193.1	192.6	192.3
	C	83.7	88.0	87.9	84.9	86.6
	H	24.4	24.6	24.7	24.4	24.6
	H	30.6	30.9	31.0	30.7	30.8
CH_2O						
	O	-378.6	-380.8	-380.1	-382.2	-359.6
	C	1.5	10.5	12.2	4.5	8.0
	H	22.0	22.3	22.6	22.1	22.4
CH_3F						
	C	122.1	126.0	127.2	123.3	125.3
	F	482.9	480.4	478.3	482.3	482.6
	H	27.3	27.6	27.9	27.4	27.6
CH_4						
	C	198.9	200.4	198.8	199.3	198.6
	H	31.3	31.4	31.5	31.4	31.3
CO						
	C	2.2	8.7	7.3	4.1	6.0
	O	-55.0	-50.0	-49.6	-54.4	-46.9
FCCH						
	C	179.9	182.2	180.6	180.6	179.7
	C	100.1	104.1	104.3	101.2	102.4
	H	30.5	30.6	30.7	30.5	30.5
	F	423.5	422.1	420.1	422.6	423.7

Table S6: (continued)

FCN						
	F	374.1	373.7	369.5	373.7	374.1
	C	82.2	87.0	86.5	83.6	84.1
	N	117.9	120.9	118.4	118.5	119.5
H_2C_2O						
	C	193.3	195.0	193.1	193.8	192.9
	C	-6.3	0.9	-0.6	-4.2	-2.6
	O	-5.9	-5.3	-5.0	-6.7	2.5
	H	29.2	29.5	29.5	29.3	29.3
H_2O						
	O	338.0	344.8	341.1	340.7	339.1
	H	30.6	31.2	31.4	30.9	30.8
H_2S						
	S	739.0	734.3	727.0	736.9	733.4
	H	30.5	30.7	30.8	30.6	30.5
H_4C_2O						
	O	363.2	362.4	358.8	363.2	361.4
	C	153.2	156.3	156.6	154.1	155.0
	H	29.1	29.4	29.5	29.2	29.3
HCN						
	H	29.0	29.2	29.3	29.1	29.2
	C	84.6	89.9	89.0	86.1	86.4
	N	-14.1	-9.8	-8.2	-13.4	-7.4
HCP						
	H	29.6	29.6	29.8	29.6	29.7
	C	37.6	43.0	42.1	39.0	39.4
	P	388.0	389.4	390.8	388.8	390.3
HF						
	H	28.8	29.4	29.7	29.1	29.0
	F	420.3	420.7	419.4	419.8	420.6
HFCO						
	O	-94.3	-90.7	-95.0	-94.3	-87.6
	C	39.6	45.5	44.2	41.3	42.0
	F	165.3	167.6	166.6	165.3	172.3
	H	23.9	24.2	24.4	24.0	24.1
HOF						
	O	-68.9	-47.2	-40.4	-61.2	-51.0
	H	19.6	20.6	21.2	20.0	20.3
	F	192.2	186.0	188.5	189.4	196.8
N_2						

Table S6: (continued)

	N	-60.4	-54.8	-58.0	-59.9	-57.8
N_2O						
	N	106.4	111.6	109.2	108.0	108.8
	N	12.6	20.1	20.6	14.3	17.4
	O	199.0	197.7	194.1	197.7	198.4
NH_3						
	N	270.7	275.7	272.2	272.8	270.8
	H	31.4	31.9	32.0	31.6	31.6
OCS						
	O	96.8	97.9	98.8	96.6	102.5
	C	30.2	35.9	36.5	31.7	34.3
	S	796.7	797.2	791.6	797.6	796.6
OF_2						
	O	-447.1	-409.5	-387.3	-434.0	-402.3
	F	-24.0	-4.7	-2.4	-15.1	-8.0
PN						
	N	-344.0	-339.8	-338.4	-344.8	-332.7
	P	50.6	53.9	51.3	52.9	56.9

5.6 Absolute isotropic NMR shieldings at the σ(S1)@PBE level of theory for different combinations of AO and RI basis sets

Table S7: Absolute isotropic NMR shieldings (ppm) for each nucleus (nuc.) of the molecules (mol.) in the Gauss benchmark set [8]. 'extrap.' denotes basis set extrapolated CCSD(T)/aug-cc-pCV[TQ]Z shieldings (taken from Ref. [8]). The CCSD(T) and σ(S1)@PBE (abbreviated as 'σ') shieldings are given for the atomic orbital basis sets cc-pVQZ (for σ(S1)@PBE the RI basis sets cc-pVQZ/mp2fit and cc-pVTZ/mp2fit were used) as well as cc-pVTZ (with the RI basis sets cc-pVTZ/mp2fit and cc-pVDZ/mp2fit for σ(S1)@PBE). The CCSD(T) data was obtained from Ref. [9].

mol	element	extrap.	AO basis-set: cc-pVQZ			AO basis-set: cc-pVTZ		
			CCSD(T)	σ/cc-pVQZ-ri	σ/cc-pVTZ-ri	CCSD(T)	σ/cc-pVTZ-ri	σ/cc-pVDZ-ri
AlF								
	AL	572.9	587.7	585.8	583.5	576.5	577.5	577.4
	F	211.8	212.2	218.1	223.3	200.2	206.6	204.6
C_2H_4								
	C	69.7	72.9	72.8	72.8	77.3	77.3	76.9
	H	26.0	26.1	26.3	26.2	26.3	26.5	26.4
C_3H_4								
	C	192.1	193.2	191.3	192.8	194.9	194.8	194.9
	C	83.7	86.5	87.2	86.8	90.3	90.5	90.0
	H	24.4	24.5	24.6	24.6	24.6	24.8	24.8
	H	30.6	30.7	30.8	30.8	30.9	31.0	31.0
CH_2O								
	O	-378.6	-377.2	-335.0	-364.2	-376.5	-376.0	-382.4
	C	1.5	6.5	8.7	7.4	13.2	14.8	13.8
	H	22.0	22.1	22.3	22.4	22.3	22.6	22.6
CH_3F								
	C	122.1	124.5	123.9	125.5	127.4	128.4	128.5
	F	482.9	482.7	479.7	483.2	479.2	477.8	478.2
	H	27.3	27.5	27.5	27.6	27.7	27.9	27.9

Table S7: (continued)

CH_4								
	C	198.9	199.9	198.5	199.3	201.3	200.2	200.5
	H	31.3	31.4	31.4	31.3	31.5	31.5	31.5
CO								
	C	2.2	5.8	8.2	5.5	11.3	10.2	9.8
	O	-55.0	-51.9	-41.3	-48.2	-49.8	-49.2	-50.4
FCCH								
	C	179.9	181.4	180.7	179.9	183.1	181.4	181.2
	C	100.1	102.6	102.4	102.7	105.3	105.0	105.2
	H	30.5	30.6	30.6	30.5	30.7	30.8	30.8
	F	423.5	424.0	423.9	423.4	421.2	419.7	418.9
FCN								
	F	374.1	375.1	374.9	373.8	373.2	369.7	368.7
	C	82.2	84.8	85.3	84.0	88.2	87.9	87.7
	N	117.9	120.1	125.7	119.1	122.4	119.9	119.5
H_2C_2O								
	C	193.3	194.4	193.5	193.5	196.3	194.7	194.8
	C	-6.3	-2.0	-0.3	-2.8	3.4	2.1	1.9
	O	-5.9	-4.3	12.8	2.2	-3.9	-2.7	-4.1
	H	29.2	29.3	29.4	29.3	29.5	29.6	29.6
H_2O								
	O	338.0	341.0	340.2	339.9	344.3	341.2	341.4
	H	30.6	30.9	30.9	30.8	31.3	31.4	31.4
H_2S								
	S	739.0	759.6	751.5	751.5	758.5	746.9	748.9
	H	30.5	30.7	30.8	30.7	30.9	31.1	31.1
H_4C_2O								
	O	363.2	364.7	363.3	361.1	362.1	359.1	358.9

Table S7: (continued)

	C	153.2	155.1	153.9	155.1	158.1	158.4	158.4
	H	29.1	29.2	29.3	29.3	29.4	29.6	29.6
HCN								
	H	29.0	29.1	29.1	29.2	29.2	29.4	29.4
	C	84.6	87.3	88.5	86.1	91.5	90.8	90.3
	N	-14.1	-11.3	-2.1	-8.3	-7.4	-6.4	-7.4
HCP								
	H	29.6	29.7	29.7	29.8	29.7	29.9	29.9
	C	37.6	41.1	44.8	38.9	45.4	44.4	43.5
	P	388.0	426.9	441.8	412.5	412.9	416.5	414.3
HF								
	H	28.8	29.1	29.2	29.0	29.5	29.7	29.8
	F	420.3	419.9	420.0	421.1	419.8	419.0	419.1
HFCO								
	O	-94.3	-91.0	-72.2	-89.6	-88.0	-91.7	-93.8
	C	39.6	43.1	43.1	41.4	47.0	45.7	45.5
	F	165.3	166.9	170.6	170.6	167.2	166.8	164.8
	H	23.9	24.0	24.1	24.1	24.3	24.5	24.5
HOF								
	O	-68.9	-58.7	-48.8	-52.4	-44.4	-38.1	-40.1
	H	19.6	20.0	20.2	20.2	20.7	21.2	21.2
	F	192.2	191.6	196.6	196.0	188.3	191.8	190.2
LiF								
	LI	89.3	89.4	88.9	89.2	90.8	90.7	90.7
	F	382.5	377.0	378.1	384.8	370.3	367.9	367.2
LiH								
	H	26.6	26.6	26.6	26.7	26.5	26.5	26.5
	LI	89.3	89.3	89.1	89.2	90.0	90.6	90.6

Table S7: (continued)

N_2								
	N	-60.4	-57.6	-51.8	-58.7	-52.5	-55.4	-56.7
N_2O								
	N	106.4	109.4	114.4	108.2	114.3	111.8	111.5
	N	12.6	16.0	21.0	17.1	22.1	22.9	22.8
	O	199.0	199.9	204.1	198.0	197.0	194.0	193.4
NH_3								
	N	270.7	273.1	271.9	271.4	276.2	273.3	273.6
	H	31.4	31.6	31.7	31.6	32.0	32.1	32.1
OCS								
	O	96.8	98.7	107.4	102.2	98.7	99.4	98.1
	C	30.2	33.8	37.0	34.5	37.9	38.6	38.5
	S	796.7	815.1	812.1	808.7	810.9	805.5	804.1
OF_2								
	O	-447.1	-430.3	-420.5	-409.2	-402.8	-381.6	-388.4
	F	-24.0	-12.7	-4.0	-10.2	0.0	3.3	1.5
PN								
	N	-344.0	-340.7	-310.8	-338.5	-336.0	-338.1	-344.0
	P	50.6	118.2	137.0	110.1	89.4	84.6	78.6

5.7 Absolute isotropic NMR shieldings at the σ(S1)@PBE0 level of theory for different combinations of AO and RI basis sets

Table S8: Absolute isotropic NMR shieldings (ppm) for each nucleus (nuc.) of the molecules (mol.) in the Gauss benchmark set [8]. 'extrap.' denotes basis set extrapolated CCSD(T)/aug-cc-pCV[TQ]Z shieldings (taken from Ref. [8]). The CCSD(T) and σ(S1)@PBE0 (abbreviated as 'σ') shieldings are given for the atomic orbital basis sets cc-pVQZ (for σ(S1)@PBE0 the RI basis sets cc-pVQZ/mp2fit and cc-pVTZ/mp2fit were used) as well as cc-pVTZ (with the RI basis sets cc-pVTZ/mp2fit and cc-pVDZ/mp2fit for σ(S1)@PBE0). The CCSD(T) data was obtained from Ref. [9].

mol	element	extrap.	AO basis-set: cc-pVQZ			AO basis-set: cc-pVTZ		
			CCSD(T)	σ/cc-pVQZ-ri	σ/cc-pVTZ-ri	CCSD(T)	σ/cc-pVTZ-ri	σ/cc-pVDZ-ri
AlF								
	AL	572.9	587.7	585.6	586.0	576.5	575.8	586.0
	F	211.8	212.2	219.8	220.7	200.2	205.3	220.7
C_2H_4								
	C	69.7	72.9	73.6	73.4	77.3	77.6	73.4
	H	26.0	26.1	26.3	26.2	26.3	26.5	26.2
C_3H_4								
	C	192.1	193.2	191.6	191.7	194.9	193.1	191.7
	C	83.7	86.5	87.3	87.4	90.3	90.6	87.4
	H	24.4	24.5	24.6	24.6	24.6	24.9	24.6
	H	30.6	30.7	30.8	30.8	30.9	31.0	30.8
CH_2O								
	O	-378.6	-377.2	-338.0	-337.5	-376.5	-344.1	-337.5
	C	1.5	6.5	9.0	8.9	13.2	16.8	8.9
	H	22.0	22.1	22.3	22.3	22.3	22.6	22.3
CH_3F								
	C	122.1	124.5	124.3	124.4	127.4	127.2	124.4
	F	482.9	482.7	480.1	480.5	479.2	474.6	480.5
	H	27.3	27.5	27.5	27.5	27.7	27.8	27.5

Table S8: (continued)

CH_4								
	C	198.9	199.9	198.5	198.7	201.3	199.3	198.7
	H	31.3	31.4	31.4	31.4	31.5	31.5	31.4
CO								
	C	2.2	5.8	8.3	8.3	11.3	13.4	8.3
	O	-55.0	-51.9	-41.4	-41.6	-49.8	-42.4	-41.6
FCCH								
	C	179.9	181.4	180.6	180.5	183.1	182.8	180.5
	C	100.1	102.6	102.6	102.7	105.3	105.6	102.7
	H	30.5	30.6	30.6	30.6	30.7	30.9	30.6
	F	423.5	424.0	424.2	424.3	421.2	420.3	424.3
FCN								
	F	374.1	375.1	374.6	374.8	373.2	371.5	374.8
	C	82.2	84.8	85.2	85.3	88.2	88.9	85.3
	N	117.9	120.1	125.1	124.9	122.4	126.0	124.9
H_2C_2O								
	C	193.3	194.4	193.4	193.5	196.3	195.0	193.5
	C	-6.3	-2.0	-0.4	-0.3	3.4	5.0	-0.3
	O	-5.9	-4.3	11.7	12.1	-3.9	8.6	12.1
	H	29.2	29.3	29.3	29.3	29.5	29.7	29.3
H_2O								
	O	338.0	341.0	339.9	340.3	344.3	340.8	340.3
	H	30.6	30.9	30.9	30.9	31.3	31.5	30.9
H_2S								
	S	739.0	759.6	751.3	752.0	758.5	745.7	752.0
	H	30.5	30.7	30.7	30.7	30.9	31.1	30.7
H_4C_2O								
	O	363.2	364.7	363.1	363.4	362.1	359.8	363.4

Table S8: (continued)

	C	153.2	155.1	154.2	154.3	158.1	157.2	154.3
	H	29.1	29.2	29.3	29.2	29.4	29.6	29.2
HCN								
	H	29.0	29.1	29.1	29.1	29.2	29.4	29.1
	C	84.6	87.3	88.4	88.4	91.5	92.7	88.4
	N	-14.1	-11.3	-2.7	-2.7	-7.4	-0.6	-2.7
HCP								
	H	29.6	29.7	29.7	29.7	29.7	29.9	29.7
	C	37.6	41.1	44.8	44.7	45.4	48.5	44.7
	P	388.0	426.9	440.1	439.4	412.9	422.0	439.4
HF								
	H	28.8	29.1	29.2	29.2	29.5	29.9	29.2
	F	420.3	419.9	419.7	420.1	419.8	417.8	420.1
HFCO								
	O	-94.3	-91.0	-74.8	-73.9	-88.0	-75.1	-73.9
	C	39.6	43.1	43.2	43.2	47.0	47.5	43.2
	F	165.3	166.9	170.8	171.8	167.2	168.7	171.8
	H	23.9	24.0	24.5	24.1	24.3	24.4	24.1
HOF								
	O	-68.9	-58.7	-50.1	-49.5	-44.4	-34.1	-49.5
	H	19.6	20.0	20.2	20.2	20.7	21.2	20.2
	F	192.2	191.6	197.3	197.9	188.3	193.3	197.9
LiF								
	LI	89.3	89.4	89.0	89.0	90.8	90.5	89.0
	F	382.5	377.0	380.0	380.4	370.3	365.3	380.4
LiH								
	H	26.6	26.6	26.6	26.6	26.5	26.6	26.6
	LI	89.3	89.3	89.2	89.2	90.0	90.3	89.2

Table S8: (continued)

N_2								
	N	-60.4	-57.6	-53.0	-50.4	-52.5	-48.9	-50.4
N_2O								
	N	106.4	109.4	113.3	113.4	114.3	117.5	113.4
	N	12.6	16.0	20.4	20.6	22.1	26.0	20.6
	O	199.0	199.9	203.1	203.2	197.0	199.4	203.2
NH_3								
	N	270.7	273.1	271.7	272.0	276.2	273.2	272.0
	H	31.4	31.6	31.6	31.6	32.0	32.1	31.6
OCS								
	O	96.8	98.7	107.1	107.4	98.7	104.8	107.4
	C	30.2	33.8	37.3	37.4	37.9	41.2	37.4
	S	796.7	815.1	813.5	813.2	810.9	808.5	813.2
OF_2								
	O	-447.1	-430.3	-419.7	-419.5	-402.8	-392.5	-419.5
	F	-24.0	-12.7	-4.4	-3.9	0.0	8.9	-3.9
PN								
	N	-344.0	-340.7	-313.4	-314.0	-336.0	-318.2	-314.0
	P	50.6	118.2	135.3	133.7	89.4	100.8	133.7

5.8 Absolute isotropic NMR shieldings for double hybrid density functionals

Table S9: Absolute isotropic NMR shieldings (ppm) for each nucleus (nuc.) of the molecules (mol.) in the Gauss benchmark set [8] for the double hybrid functionals B2PLYP [11] and DSD-PBEP86 [12]. 'extrap.' denotes basis set extrapolated CCSD(T)/aug-cc-pCV[TQ]Z shieldings (taken from Ref. [8]). The CCSD(T) data was obtained from Ref. [9].

mol.	nuc.	CCSD(T)	extrap.	B2PLYP	DSD-PBEP86
AlF					
	AL	587.7	572.9	571.1	579.0
	F	212.2	211.8	184.7	197.2
C_2H_4					
	C	72.9	69.7	58.8	65.4
	H	26.1	26.0	26.0	26.0
C_3H_4					
	C	193.2	192.1	185.4	190.3
	C	86.5	83.7	66.2	70.1
	H	24.5	24.4	24.2	24.1
	H	30.7	30.6	30.8	30.8
CH_2O					
	O	-377.2	-378.6	-406.3	-378.7
	C	6.5	1.5	-10.1	-1.8
	H	22.1	22.0	21.7	21.9
CH_3F					
	C	124.5	122.1	114.7	120.5
	F	482.7	482.9	476.0	482.1
	H	27.5	27.3	27.4	27.4
CH_4					
	C	199.9	198.9	194.5	198.3
	H	31.4	31.3	31.5	31.4
CO					
	C	5.8	2.2	-7.3	-0.2
	O	-51.9	-55.0	-68.4	-59.8
FCCH					
	C	181.4	179.9	175.9	179.2
	C	102.6	100.1	91.8	97.4
	H	30.6	30.5	30.7	30.6
	F	424.0	423.5	413.8	420.0
FCN					
	F	375.1	374.1	364.2	370.9
	C	84.8	82.2	74.9	80.2

Table S9: (continued)

	N	120.1	117.9	110.1	118.7
H_2C_2O					
	C	194.4	193.3	190.3	194.2
	C	-2.0	-6.3	-11.9	-4.4
	O	-4.3	-5.9	-6.2	6.4
	H	29.3	29.2	29.4	29.3
H_2O					
	O	341.0	338.0	337.8	341.4
	H	30.9	30.6	31.0	30.8
H_2S					
	S	759.6	739.0	741.1	757.5
	H	30.7	30.5	30.8	30.6
H_4C_2O					
	O	364.7	363.2	357.4	368.1
	C	155.1	153.2	147.0	152.6
	H	29.2	29.1	29.5	29.5
HCN					
	H	29.1	29.0	29.2	29.1
	C	87.3	84.6	78.0	82.7
	N	-11.3	-14.1	-28.8	-17.1
HCP					
	H	29.7	29.6	29.8	29.6
	C	41.1	37.6	27.3	35.4
	P	426.9	388.0	395.4	412.1
HF					
	H	29.1	28.8	29.2	29.0
	F	419.9	420.3	417.0	419.8
HFCO					
	O	-91.0	-94.3	-104.0	-87.9
	C	43.1	39.6	31.3	37.9
	F	166.9	165.3	137.4	152.8
	H	24.0	23.9	23.8	23.9
HOF					
	O	-58.7	-68.9	-99.3	-76.1
	H	20.0	19.6	19.6	19.8
	F	191.6	192.2	188.5	198.8
LiF					
	LI	89.4	89.3	88.4	89.1
	F	377.0	382.5	356.8	370.2
LiH					

Table S9: (continued)

	H	26.6	26.6	26.6	26.5
	LI	89.3	89.3	88.7	89.0
N_2					
	N	-57.6	-60.4	-74.0	-62.9
N_2O					
	N	109.4	106.4	101.4	111.4
	N	16.0	12.6	7.3	16.8
	O	199.9	199.0	189.1	199.3
NH_3					
	N	273.1	270.7	269.1	272.8
	H	31.6	31.4	31.8	31.7
OCS					
	O	98.7	96.8	87.3	96.6
	C	33.8	30.2	26.5	32.6
	S	815.1	796.7	799.2	813.1
OF_2					
	O	-430.3	-447.1	-527.3	-480.5
	F	-12.7	-24.0	-38.9	-16.5
PN					
	N	-340.7	-344.0	-369.6	-333.0
	P	118.2	50.6	74.4	105.1

5.9 Absolute isotropic NMR shieldings for meta-GGA density functionals

Table S10: Absolute isotropic NMR shieldings (ppm) for each nucleus (nuc.) of the molecules (mol.) in the Gauss benchmark set [8] for the meta-GGA functionals SCAN [13] and revTPSS [14]. 'extrap.' denotes basis set extrapolated CCSD(T)/aug-cc-pCV[TQ]Z shieldings (taken from Ref. [8]). The CCSD(T) data was obtained from Ref. [9].

mol.	nuc.	CCSD(T)	extrap.	SCAN	revTPSS
AlF					
	AL	587.7	572.9	559.5	557.5
	F	212.2	211.8	191.2	161.6
C_2H_4					
	C	72.9	69.7	66.0	60.2
	H	26.1	26.0	25.8	26.3
C_3H_4					
	C	193.2	192.1	182.6	177.7
	C	86.5	83.7	78.5	73.5
	H	24.5	24.4	24.2	24.7
	H	30.7	30.6	30.6	30.9
CH_2O					
	O	-377.2	-378.6	-331.7	-372.7
	C	6.5	1.5	-1.8	-6.4
	H	22.1	22.0	21.5	21.9
CH_3F					
	C	124.5	122.1	116.3	111.1
	F	482.7	482.9	471.7	459.4
	H	27.5	27.3	27.2	27.6
CH_4					
	C	199.9	198.9	197.5	189.4
	H	31.4	31.3	31.4	31.8
CO					
	C	5.8	2.2	7.0	0.9
	O	-51.9	-55.0	-36.7	-59.4
FCCH					
	C	181.4	179.9	178.4	175.1
	C	102.6	100.1	93.9	92.7
	H	30.6	30.5	30.5	31.1
	F	424.0	423.5	404.6	389.2
FCN					
	F	375.1	374.1	359.6	340.3
	C	84.8	82.2	80.0	77.9

Table S10: (continued)

	N	120.1	117.9	123.0	111.2
H_2C_2O					
	C	194.4	193.3	194.7	186.7
	C	-2.0	-6.3	1.1	-7.7
	O	-4.3	-5.9	29.5	-9.9
	H	29.3	29.2	29.3	29.8
H_2O					
	O	341.0	338.0	346.5	334.1
	H	30.9	30.6	31.0	31.7
H_2S					
	S	759.6	739.0	755.0	719.3
	H	30.7	30.5	30.7	31.3
H_4C_2O					
	O	364.7	363.2	345.8	335.9
	C	155.1	153.2	145.2	141.9
	H	29.2	29.1	29.0	29.5
HCN					
	H	29.1	29.0	29.0	29.4
	C	87.3	84.6	83.6	80.9
	N	-11.3	-14.1	-13.0	-20.8
HCP					
	H	29.7	29.6	29.6	29.9
	C	41.1	37.6	29.0	22.2
	P	426.9	388.0	359.8	347.2
HF					
	H	29.1	28.8	29.3	30.2
	F	419.9	420.3	432.4	415.7
HFCO					
	O	-91.0	-94.3	-72.0	-99.4
	C	43.1	39.6	35.5	31.0
	F	166.9	165.3	141.7	115.5
	H	24.0	23.9	23.4	23.7
HOF					
	O	-58.7	-68.9	-68.6	-84.9
	H	20.0	19.6	20.1	20.7
	F	191.6	192.2	185.4	162.9
LiF					
	LI	89.4	89.3	88.8	87.8
	F	377.0	382.5	385.5	352.8
LiH					

Table S10: (continued)

	H	26.6	26.6	26.7	26.6
	LI	89.3	89.3	89.2	89.4
N_2					
	N	-57.6	-60.4	-57.9	-67.7
N_2O					
	N	109.4	106.4	108.1	100.2
	N	16.0	12.6	14.7	9.3
	O	199.9	199.0	190.3	174.9
NH_3					
	N	273.1	270.7	273.5	264.5
	H	31.6	31.4	31.8	32.3
OCS					
	O	98.7	96.8	105.9	77.8
	C	33.8	30.2	36.7	30.9
	S	815.1	796.7	804.1	765.2
OF_2					
	O	-430.3	-447.1	-490.1	-525.5
	F	-12.7	-24.0	-26.2	-51.1
PN					
	N	-340.7	-344.0	-358.4	-383.2
	P	118.2	50.6	41.4	23.9

References

[1] Jannis Erhard et al. "Scaled σ-functionals for the Kohn–Sham correlation energy with scaling functions from the homogeneous electron gas". In: *J. Chem. Phys.* 157.11 (Sept. 2022), p. 114105. ISSN: 0021-9606. DOI: 10.1063/5.0101641. URL: https://doi.org/10.1063/5.0101641.

[2] Steffen Fauser et al. "Basis Set Requirements of σ-Functionals for Gaussian- and Slater-Type Basis Functions and Comparison with Range-Separated Hybrid and Double Hybrid Functionals". In: *Journal of Chemical Theory and Computation* 20.6 (2024), pp. 2404–2422. DOI: 10.1021/acs.jctc.3c01132. URL: https://doi.org/10.1021/acs.jctc.3c01132.

[3] Lars Goerigk et al. "A look at the density functional theory zoo with the advanced GMTKN55 database for general main group thermochemistry, kinetics and noncovalent interactions". In: *Phys. Chem. Chem. Phys.* 19 (48 2017), pp. 32184–32215. DOI: 10.1039/C7CP04913G. URL: http://dx.doi.org/10.1039/C7CP04913G.

[4] Amir Karton, Nitai Sylvetsky, and Jan M. L. Martin. "W4-17: A diverse and high-confidence dataset of atomization energies for benchmarking high-level electronic structure methods". In: *J. Comp. Chem.* 38.24 (2017). Note that parts of the SI of this reference, containing the reference geometries, are no longer available at the publisher's website, instead they can be found at A. Karton's website https://www.chemtheorist.com/w4-17-database.html (accessed 03.06.2021), pp. 2063–2075. DOI: https://doi.org/10.1002/jcc.24854. URL: https://onlinelibrary.wiley.com/doi/pdf/10.1002/jcc.24854.

[5] Sebastian Dohm et al. "Comprehensive Thermochemical Benchmark Set of Realistic Closed-Shell Metal Organic Reactions". In: *J. Chem. Theory Comput.* 14.5 (2018), pp. 2596–2608. DOI: 10.1021/acs.jctc.7b01183. URL: https://doi.org/10.1021/acs.jctc.7b01183.

[6] Mark A. Iron and Trevor Janes. "Evaluating Transition Metal Barrier Heights with the Latest Density Functional Theory Exchange–Correlation Functionals: The MOBH35 Benchmark Database". In: *J. Phys. Chem. A* 123.17 (2019), pp. 3761–3781. DOI: 10.1021/acs.jpca.9b01546. URL: https://doi.org/10.1021/acs.jpca.9b01546.

[7] Johannes T. Margraf, Duminda S. Ranasinghe, and Rodney J. Bartlett. "Automatic generation of reaction energy databases from highly accurate atomization energy benchmark sets". In: *Phys. Chem. Chem. Phys.* 19 (15 2017), pp. 9798–9805. DOI: 10.1039/C7CP00757D. URL: http://dx.doi.org/10.1039/C7CP00757D.

[8] Andrew M Teale et al. "Benchmarking density-functional theory calculations of NMR shielding constants and spin–rotation constants using accurate coupled-cluster calculations". In: *J. Chem. Phys.* 138.2 (2013), p. 024111.

[9] Michael Glasbrenner, Daniel Graf, and Christian Ochsenfeld. "Benchmarking the Accuracy of the Direct Random Phase Approximation and σ-Functionals for NMR Shieldings". In: *J. Chem. Theory Comput.* 18.1 (2022), pp. 192–205.

[10] Devin A Matthews et al. "Coupled-cluster techniques for computational chemistry: The CFOUR program package". In: *J. Chem. Phys.* 152.21 (2020).

[11] Stefan Grimme. "Semiempirical hybrid density functional with perturbative second-order correlation". In: *J. Chem. Phys.* 124.3 (2006).

[12] Sebastian Kozuch and Jan ML Martin. "Spin-component-scaled double hybrids: an extensive search for the best fifth-rung functionals blending DFT and perturbation theory". In: *J. Comput. Chem.* 34.27 (2013), pp. 2327–2344.

[13] Jianwei Sun, Adrienn Ruzsinszky, and John P Perdew. "Strongly constrained and appropriately normed semilocal density functional". In: *Phys. Rev. Lett.* 115.3 (2015), p. 036402.

[14] John P Perdew et al. "Workhorse semilocal density functional for condensed matter physics and quantum chemistry". In: *Phys. Rev. Lett.* 103.2 (2009), p. 026403.

Chapter 4

Conclusion

In this thesis several novel methods were introduced for the efficient calculation of RPA energies and properties based on first and second-order derivatives of the energy.

For the memory-efficient computation of RPA energies, an optimized batching scheme was introduced, completely alleviating the memory bottleneck of the method. This advancement allowed the computation of systems with up to 1,052 atoms and 11,230 basis functions on a single compute node, something that was not possible before. The introduced method can also be adapted for related electron correlation methods that come with high memory demands, which makes this method widely applicable and transferable.

For nuclear gradients within RPA an efficient method was presented to introduce the frozen-core approximation. Since nuclear gradients are typically unaffected by the correlation between core electrons and between core and valence electrons, the error introduced by the frozen-core approximation was shown to be minimal, while performance gains of 20-30% were observed. Further, most atomic and auxiliary basis sets are designed to correlate only the valence electrons, thus, they do not include any additional tight Gaussians for the core region. These basis sets can now be used for the computation of RPA gradients leading to accurate results and further performance gains due to the smaller size of the basis set.

Furthermore, this thesis described, for the first time, the derivation and implementation of analytical second-order derivatives for the computation of NMR shieldings within RPA. The implementation, based on a formulation in the atomic-orbital space, has been validated by comparison with numerical RPA NMR shieldings. By using a local RI metric, Cholesky decomposed density type matrices, sparse matrix algebra techniques, and a memory efficient batching scheme, an efficient and low-scaling formulation was obtained. This made the computation of NMR shieldings of a DNA strand with 260 atoms and 3408 AO basis functions on a single compute node possible. Since RPA has been previously shown to yield accuracies comparable to CCSD, the introduced efficient and low-scaling analytical NMR method opens the door for applications to large systems with high accuracy.

σ-Functionals are closely related to RPA, with a σ-functional implementation building directly upon an RPA implementation. Thus, all improvements that were introduced for RPA can also be employed for the σ-functionals with moderate additional programming effort. σ-Functionals have been shown to yield high accuracy for energetic data as well as nuclear gradients and vibrational frequencies. In this

work, a comprehensive benchmark study was conducted to study the accuracy of σ-functionals for NMR shieldings using numerical second-order derivatives. It has been found that σ-functionals perform exceptionally well, achieving accuracies comparable to CCSD(T) and outperforming RPA, all investigated density functionals, and MP2. Therefore, analytical σ-functional NMR shieldings would be beneficial in the future, where the efficient RPA NMR method presented in this work can be utilized for the implementation. This would provide another highly accurate and efficient method for the computation of NMR shieldings.

Therefore, the methods introduced in this thesis play a crucial role in advancing RPA, moving it closer to being established as the preferred functional of choice for various computational applications.

Bibliography

[1] Schrödinger, E. *Phys. Rev.* **1926**, *28*, 1049.

[2] Born, M.; Oppenheimer, R. *Ann. Phys.* **1927**, *389*, 457.

[3] Shankar, R. *Principles of Quantum Mechanics*; Springer New York, 2012.

[4] Levine, I. N. *Quantum Chemistry*; Pearson, 2014.

[5] Hartree, D. R. *Math. Proc. Camb. Philos. Soc.* **1928**, *24*, 89.

[6] Slater, J. C. *Phys. Rev.* **1930**, *35*, 210.

[7] Fock, V. *Z. Phys.* **1930**, *61*, 126.

[8] Møller, C.; Plesset, M. S. *Phys. Rev.* **1934**, *46*, 618.

[9] Kohn, W.; Sham, L. J. *Phys. Rev.* **1965**, *140*, A1133.

[10] Sholl, D. S.; Steckel, J. A. *Density Functional Theory: A Practical Introduction*; Wiley, 2023.

[11] Norman, P.; Ruud, K.; Saue, T. *Principles and Practices of Molecular Properties: Theory, Modeling, and Simulations*; Wiley, 2018.

[12] Langreth, D. C.; Perdew, J. P. *Solid State Commun.* **1975**, *17*, 1425.

[13] Langreth, D. C.; Perdew, J. P. *Phys. Rev. B* **1977**, *15*, 2884.

[14] Callen, H. B.; Welton, T. A. *Phys. Rev.* **1951**, *83*, 34.

[15] Perdew, J. P.; Schmidt, K. Jacob's ladder of density functional approximations for the exchange-correlation energy. AIP Conf. Proc. 2001; p 1.

[16] Chen, G. P.; Voora, V. K.; Agee, M. M.; Balasubramani, S. G.; Furche, F. *Annu. Rev. Phys. Chem.* **2017**, *68*, 421.

[17] Scuseria, G. E.; Henderson, T. M.; Sorensen, D. C. *J. Chem. Phys.* **2008**, *129*, 231101.

[18] Onida, G.; Reining, L.; Rubio, A. *Rev. Mod. Phys.* **2002**, *74*, 601.

[19] Bohm, D.; Pines, D. *Phys. Rev.* **1951**, *82*, 625.

[20] Pines, D.; Bohm, D. *Phys. Rev.* **1952**, *85*, 338.

[21] Bohm, D.; Pines, D. *Phys. Rev.* **1953**, *92*, 609.

[22] de la Roza, A. O.; DiLabio, G. A. *Non-Covalent Interactions in Quantum Chemistry and Physics: Theory and Applications*; Elsevier, 2012.

[23] Furche, F. *Phys. Rev. B* **2001**, *64*, 195120.

[24] Eshuis, H.; Yarkony, J.; Furche, F. *J. Chem. Phys.* **2010**, *132*, 234114.

[25] Schurkus, H. F.; Ochsenfeld, C. *J. Chem. Phys.* **2016**, *144*, 031101.

[26] Luenser, A.; Schurkus, H. F.; Ochsenfeld, C. *J. Chem. Theory Comput.* **2017**, *13*, 1647.

[27] Graf, D.; Beuerle, M.; Schurkus, H. F.; Luenser, A.; Savasci, G.; Ochsenfeld, C. *J. Chem. Theory Comput.* **2018**, *14*, 2505.

[28] Kaltak, M.; Klimeš, J.; Kresse, G. *J. Chem. Theory Comput.* **2014**, *10*, 2498.

[29] Sacchetta, F.; Graf, D.; Laqua, H.; Ambroise, M. A.; Kussmann, J.; Dreuw, A.; Ochsenfeld, C. *J. Chem. Phys.* **2022**, *157*, 104104.

[30] Eshuis, H.; Furche, F. *J. Chem. Phys.* **2012**, *136*, 084105.

[31] Distasio Jr, R. A.; Steele, R. P.; Rhee, Y. M.; Shao, Y.; Head-Gordon, M. *J. Comput. Chem.* **2007**, *28*, 839.

[32] Baeck, K. K.; Watts, J. D.; Bartlett, R. J. *J. Chem. Phys.* **1997**, *107*, 3853.

[33] Rekkedal, J.; Coriani, S.; Iozzi, M. F.; Teale, A. M.; Helgaker, T.; Pedersen, T. B. *J. Chem. Phys.* **2013**, *139*, 081101.

[34] Burow, A. M.; Bates, J. E.; Furche, F.; Eshuis, H. *J. Chem. Theory Comput.* **2014**, *10*, 180.

[35] Ramberger, B.; Schäfer, T.; Kresse, G. *Phys. Rev.Lett.* **2017**, *118*, 106403.

[36] Beuerle, M.; Ochsenfeld, C. *J. Chem. Phys.* **2018**, *149*, 244111.

[37] Thierbach, A.; Görling, A. *J. Chem. Phys.* **2020**, *153*, 134113.

[38] Thierbach, A.; Görling, A. *J. Chem. Phys.* **2020**, *152*, 114113.

[39] Thierbach, A.; Görling, A. *The Journal of Chemical Physics* **2020**, *153*, 134113.

[40] Stein, F.; Hutter, J. *J. Chem. Phys.* **2024**, *160*, 024120.

[41] Stevens, R. M.; Pitzer, R. M.; Lipscomb, W. N. *J. Chem. Phys.* **1963**, *38*, 550.

[42] Ditchfield, R. *Mol. Phys.* **1974**, *27*, 789.

[43] Wolinski, K.; Hinton, J. F.; Pulay, P. *J. Am. Chem. Soc.* **1990**, *112*, 8251.

[44] Häser, M.; Ahlrichs, R.; Baron, H. P.; Weis, P.; Horn, H. *Theor. Chim. Acta* **1992**, *83*, 455.

[45] Larsen, H.; Helgaker, T.; Olsen, J.; Jørgensen, P. *J. Chem. Phys.* **2001**, *115*, 10344.

[46] Schreckenbach, G.; Ziegler, T. *J. Phys. Chem.* **1995**, *99*, 606.

[47] Cheeseman, J. R.; Trucks, G. W.; Keith, T. A.; Frisch, M. J. *J. Chem. Phys.* **1996**, *104*, 5497.

[48] Rauhut, G.; Puyear, S.; Wolinski, K.; Pulay, P. *J. Phys. Chem.* **1996**, *100*, 6310.

[49] Gauss, J. *Chem. Phys. Lett.* **1992**, *191*, 614.

[50] Gauss, J.; Stanton, J. F. *Adv. Chem. Phys.* **2002**, *123*, 355.

[51] Gauss, J.; Stanton, J. F. *J. Chem. Phys.* **1995**, *102*, 251.

[52] Gauss, J.; Stanton, J. F. *J. Chem. Phys.* **1996**, *104*, 2574.

[53] Kállay, M.; Gauss, J. *J. Chem. Phys.* **2004**, *120*, 6841.

[54] Ruud, K.; Helgaker, T.; Kobayashi, R.; Jørgensen, P.; Bak, K. L.; Jensen, H. J. A. *J. Chem. Phys.* **1994**, *100*, 8178.

[55] Glasbrenner, M.; Graf, D.; Ochsenfeld, C. *J. Chem. Theory Comput.* **2021**, *18*, 192.

[56] Eshuis, H.; Bates, J. E.; Furche, F. *Theor. Chem. Acc.* **2012**, *131*, 1084.

[57] Eshuis, H.; Furche, F. *J. Phys. Chem. Lett.* **2011**, *2*, 983.

[58] Fuchs, M.; Niquet, Y. M.; Gonze, X.; Burke, K. *J. Chem. Phys.* **2005**, *122*, 094116.

[59] Henderson, T. M.; Scuseria, G. E. *Mol. Phys.* **2010**, *108*, 2511.

[60] Fuchs, M.; Gonze, X. *Phys. Rev. B* **2002**, *65*, 235109.

[61] Furche, F.; Voorhis, T. V. *J. Chem. Phys.* **2005**, *122*, 164106.

[62] Grüneis, A.; Marsman, M.; Harl, J.; Schimka, L.; Kresse, G. *J. Chem. Phys.* **2009**, *131*, 154115.

[63] Jansen, G.; Liu, R.-F.; Ángyán, J. G. *J. Chem. Phys.* **2010**, *133*, 154106.

[64] Heßelmann, A.; Görling, A. *Mol. Phys.* **2010**, *108*, 359.

[65] Ángyán, J. G.; Liu, R. F.; Toulouse, J.; Jansen, G. *J. Chem. Theory Comput.* **2011**, *7*, 3116.

[66] Verma, P.; Bartlett, R. J. *J. Chem. Phys.* **2012**, *136*, 044105.

[67] Bleiziffer, P.; Heßelmann, A.; Görling, A. *J. Chem. Phys.* **2012**, *136*, 134102.

[68] Heßelmann, A. *Phys. Rev. A* **2012**, *85*, 012517.

[69] Heßelmann, A. *Phys. Rev. A* **2012**, *85*, 012517.

[70] Bates, J. E.; Furche, F. *J. Chem. Phys.* **2013**, *139*, 171103.

[71] Nguyen, N. L.; Colonna, N.; De Gironcoli, S. *Phys. Rev. B* **2014**, *90*, 045138.

[72] Hellgren, M.; Caruso, F.; Rohr, D. R.; Ren, X.; Rubio, A.; Scheffler, M.; Rinke, P. *Phys. Rev. B* **2015**, *91*, 165110.

[73] Erhard, J.; Bleiziffer, P.; Görling, A. *Phys. Rev. Lett.* **2016**, *117*, 143002.

[74] Dixit, A.; Ángyán, J. G.; Rocca, D. *J. Chem. Phys.* **2016**, *145*, 104105.

[75] Mussard, B.; Rocca, D.; Jansen, G.; Ángyán, J. G. *J. Chem. Theory Comput.* **2016**, *12*, 2191.

[76] Beuerle, M.; Ochsenfeld, C. *J. Chem. Phys.* **2017**, *147*, 204107.

[77] Görling, A. *Phys. Rev. B* **2019**, *99*, 235120.

[78] Graf, D.; Beuerle, M.; Ochsenfeld, C. *J. Chem. Theory Comput.* **2019**, *15*, 4468.

[79] Graf, D.; Ochsenfeld, C. *J. Chem. Phys.* **2020**, *153*, 244118.

[80] Lemke, Y.; Graf, D.; Kussmann, J.; Ochsenfeld, C. *Mol. Phys.* **2023**, *121*, e2098862.

[81] Trushin, E.; Thierbach, A.; Görling, A. *J. Chem. Phys.* **2021**, *154*, 014104.

[82] Fauser, S.; Trushin, E.; Neiss, C.; Görling, A. *J. Chem. Phys.* **2021**, *155*, 134111.

[83] Erhard, J.; Fauser, S.; Trushin, E.; Görling, A. *J. Chem. Phys.* **2022**, *157*, 114105.

[84] Fauser, S.; Forster, A.; Redeker, L.; Neiss, C.; Erhard, J.; Trushin, E.; Gorling, A. *J. Chem. Theory Comput.* **2024**, *20*, 2404.

[85] Neiss, C.; Fauser, S.; Görling, A. *J. Chem. Phys.* **2023**, *158*, 044107.

[86] Heisenberg, W. *Z. Phys.* **1926**, *38*, 411.

[87] Dirac, P. A. M. *Proc. R. Soc.r* **1926**, *112*, 661.

[88] Pauli, W. *Z. Phys.* **1925**, *31*, 373.

[89] Pauli, W. *Z. Phys.* **1925**, *31*, 765.

[90] Szabo, A.; Ostlund, N. S. *Modern Quantum Chemistry: Introduction to Advanced Electronic Structure Theory*; Dover, Mineola, New York, 1996.

[91] Roothaan, C. C. J. *Rev. Mod. Phys.* **1951**, *23*, 69.

[92] Hall, G. G. *Proc. R. Soc. A* **1951**, *205*, 541.

[93] Hohenberg, P.; Kohn, W. *Phys. Rev.* **1964**, *136*, B864.

[94] Parr, R.; Weitao, Y. *Density-Functional Theory of Atoms and Molecules*; Oxford University Press, 1989.

[95] Ullrich, C. *Time-Dependent Density-Functional Theory: Concepts and Applications*; Oxford University Press, 2012.

[96] Feynman, R. P. *Phys. Rev.* **1939**, *56*, 340.

[97] Marques, M. A. L.; Maitra, N. T.; Nogueira, F. M. S.; Gross, E. K. U.; Rubio, A. *Fundamentals of Time-Dependent Density Functional Theory*; Springer Berlin Heidelberg, 2012.

[98] Lehmann, H. *Nuovo Cim.* **1954**, *11*, 342.

[99] Bak, J.; Newman, D. *Complex Analysis*; Springer New York, 2010.

[100] Petersilka, M.; Gossmann, U. J.; Gross, E. K. U. *Phys. Rev. Lett.* **1996**, *76*, 1212.

[101] Whitten, J. L. *J. Chem. Phys.* **1973**, *58*, 4496.

[102] Baerends, E. J.; Ellis, D. E.; Ros, P. *Chem. Phys.* **1973**, *2*, 41.

[103] Dunlap, B. I.; Connolly, J. W. D.; Sabin, J. R. *J. Chem. Phys.* **1979**, *71*, 4993.

[104] Alsenoy, C. V. *J. Comput. Chem.* **1988**, *9*, 620.

[105] Feyereisen, M.; Fitzgerald, G.; Komomicki, A. *Chem. Phys. Lett.* **1993**, *208*, 359.

[106] Vahtras, O.; Almlöf, J.; Feyereisen, M. *Chem. Phys. Lett.* **1993**, *213*, 514.

[107] Schurkus, H. F.; Luenser, A.; Ochsenfeld, C. *J. Chem. Phys.* **2017**, *146*, 211106.

[108] Jung, Y.; Sodt, A.; Gill, P. M. W.; Head-Gordon, M. *Proc. Natl. Acad. Sci.* **2005**, *102*, 6692.

[109] Jung, Y.; Shao, Y.; Head-Gordon, M. *J. Comput. Chem.* **2007**, *28*, 1953.

[110] Zwillinger, D.; Jeffrey, A. *Table of Integrals, Series, and Products*; Elsevier Science, 2007.

[111] Bracewell, R. N. *The Fourier Transform and Its Applications: Solutions Manual*; McGraw-Hill, 1978.

[112] Jensen, F. *Introduction to Computational Chemistry*; Wiley, 2006.

[113] Riley, K. F.; Hobson, M. P.; Bence, S. J. *Mathematical Methods for Physics and Engineering: A Comprehensive Guide*; Cambridge University Press, 2006.

[114] Gauss, J. *Modern methods and algorithms of quantum chemistry* **2000**, *3*, 541.

[115] Pulay, P. *Wiley Interdiscip. Rev. Comput. Mol. Sci.* **2014**, *4*, 169.

[116] Wigner, E. P. In *Part I: Physical Chemistry. Part II: Solid State Physics*; Wightman, A. S., Ed.; Springer Berlin Heidelberg: Berlin, Heidelberg, 1997; p 131.

[117] Handy, N. C.; Schaefer III, H. F. *J. Chem. Phys.* **1984**, *81*, 5031.

[118] Helgaker, T.; Jørgensen, P. *Theor. Chim. Acta* **1989**, *75*, 111.

[119] Schweizer, S.; Doser, B.; Ochsenfeld, C. *J. Chem. Phys.* **2008**, *128*, 128.

[120] Ayala, P. Y.; Scuseria, G. E. *J. Chem. Phys.* **1999**, *110*, 3660.

[121] Surján, P. R. *Chem. Phys. Lett.* **2005**, *406*, 318–320.

[122] Beer, M.; Ochsenfeld, C. *J. Chem. Phys.* **2008**, *128*, 221102.

[123] Kaupp, M.; Bühl, M.; Malkin, V. G. *Calculation of NMR and EPR Parameters: Theory and Applications*; Wiley, 2006.

[124] London, F. *J. Phys. Radium* **1937**, *8*, 397.

[125] Helgaker, T.; Jørgensen, P. *J. Chem. Phys.* **1991**, *95*, 2595.

[126] Fukui, H.; Baba, T.; Matsuda, H.; Miura, K. *J. Chem. Phys.* **1994**, *100*, 6608.

[127] Maurer, M.; Ochsenfeld, C. *J. Chem. Phys.* **2013**, *138*, 174104.

[128] Glasbrenner, M.; Vogler, S.; Ochsenfeld, C. *J. Chem. Phys.* **2021**, *155*, 224107.